

THE UNIVERSITY OF SHEFFIELD

# Layout Optimization of Structures: Novel Methods and Applications

by

**Helen E. Fairclough**

A thesis submitted in partial fulfilment for  
the degree of Doctor of Philosophy.

in the

Department of Civil and Structural Engineering

September 2019





# Declaration of Authorship

I, Helen E. Fairclough, declare that the work in this thesis, entitled, ‘Layout Optimization of Structures: Novel methods and Applications’, is my own unless referenced to the contrary in the text.

Signed:

Date:

## Acknowledgements

I would like to thank my supervisors, Matthew Gilbert and Andy Tyas, for their continued guidance and support, without which this study would not have been possible.

I am also grateful to my colleagues, at both the University of Sheffield and Expedition Engineering, for their camaraderie and for our engaging discussions, which provided invaluable perspective.

I would like to thank my parents for believing in me from the very beginning. I also wish to express my appreciation to my friends, who were always there and without whom these years would have been far less enjoyable. Particular thanks must go to Robert Middleton, for all his love and support.

I would also like to acknowledge the financial support of the University of Sheffield and Expedition Engineering Ltd.

# Abstract

Computational optimization methods have become widely used in various fields of engineering in recent years. However, the field of structural design still largely relies on past experience and a limited number of well known structural forms for the majority of problems. This thesis aims to identify and address factors that limit the uptake of computational optimization methods for the design of structural frameworks in practice. Novel methods to address three major issues are presented here: the accurate modelling of self-weight of structural elements and auxiliary components, user-friendly methods for reducing the complexity of the resulting structures, and numerical methods that produce a more easily interpretable output.

The contribution of the self-weight of a structure to the loads it must carry is often significant for structures of large dimensions. Here a novel formulation of the ground structure based layout optimization method is presented; this uses curved elements that must take the form of an equally stressed catenary. This is the minimum weight form for an axially loaded member that must also support its own weight, and allows accurate numerical results to be obtained for long span problems, eliminating the non-conservative errors that are caused by current methods. Using this formulation novel layouts are proposed, which can allow much longer spans to be obtained with the same amount of material. A further extension is also presented that allows modelling of lumped masses at points where they are of use. This allows generation of solutions incorporating counterweights, anchorages and abutments.

A further issue that is addressed in this work is the complexity of the structures typically produced by numerical optimization methods. Two approaches to reducing complexity are considered, addressing physical and conceptual complexity respectively. Resolving the former involves using mixed integer programming to impose specific constraints designed to improve the buildability of the identified truss structures. Several different constraint types are compared, including limiting the number of joints and the angle between adjacent members. So-called ‘lazy constraints’, generated at run-time, are used to efficiently allow consideration of these constraints at the large number of potential crossover joints. Simple example problems are used to allow more detailed analytical examination of the characteristics of structures subjected to these constraints. It is observed that the set of optimal structures may be discontinuous, and that symmetrical problems under these constraints may not have symmetrical optimal solutions.

The second approach to reducing complexity is based on allowing better understanding of the identified form, by increasing the level of abstraction of the results. A method is proposed by which region based elements are incorporated into the ground structure method. This is found to be capable of producing numerical results that very closely approach the volumes of known theoretical solutions, whilst simultaneously allowing for easier interpretation and communication. This can then be used to suggest discretised layouts of the required degree of complexity.

A number of case studies based on real-world projects are used alongside more academic numerical examples to demonstrate the applicability and relevance of the proposed methods.

# Contents

Declaration of Authorship . . . . .	i
Acknowledgements . . . . .	ii
Abstract . . . . .	iii
Contents . . . . .	iv
List of Figures . . . . .	vii
List of Tables . . . . .	xi
List of Symbols . . . . .	xiii
List of Abbreviations . . . . .	xvii

## I Preliminaries 1

### 1 Introduction 3

1.1 Objectives and scope of work . . . . .	4
--	---

1.2 Organisation of the thesis . . . . .	4
--	---

### 2 Literature review 7

2.1 Layouts of minimum weight structures . . . . .	8
--	---

2.2 An overview of mathematical optimization . . . . .	14
--	----

2.3 Numerical structural optimization methods . . . . .	19
---	----

2.4 The use of optimization in structural engineering practice . . . . .	25
--	----

2.5 Observations . . . . .	29
----------------------------	----

### 3 Evaluating the applicability of current methods 31

3.1 Introduction . . . . .	32
----------------------------	----

3.2 Three dimensional ‘chassis’ problem . . . . .	32
---	----

3.3 Two dimensional ‘mother’ truss problem . . . . .	33
--	----

3.4 Observations . . . . .	41
----------------------------	----

Requirements identified in Part I . . . . .	42
---	----

## II Modelling self-weight 43

### 4 Modelling of distributed self-weight 45

4.1 Introduction . . . . .	46
----------------------------	----

4.2 Elements of equal strength . . . . .	47
--	----

4.3 Layout optimization . . . . .	49
-----------------------------------	----

4.4 Application to very long span bridges . . . . .	52
---	----

4.5 Conclusions . . . . .	61
---------------------------	----

### 5 Lumped masses and frictional foundations 63

5.1 Introduction . . . . .	64
----------------------------	----

5.2 Layout optimization with distributed self-weight . . . . .	65
--	----

5.3 Proposed formulations . . . . .	68
-------------------------------------	----

5.4 Bridge example . . . . .	70
------------------------------	----

5.5 Concluding remarks . . . . .	75
----------------------------------	----

<b>III</b>	<b>Simplification strategies</b>	<b>77</b>
<b>6</b>	<b>Identification of structures with limited complexity</b>	<b>79</b>
6.1	Introduction . . . . .	80
6.2	A simple illustrative example . . . . .	84
6.3	Case study to compare complexity measures . . . . .	89
6.4	Adaptive solution methods . . . . .	93
6.5	Concluding remarks . . . . .	106
<b>7</b>	<b>Region based Adaptive Ground Structure (RAGS) method</b>	<b>107</b>
7.1	Introduction . . . . .	108
7.2	Methodology . . . . .	109
7.3	Three node (fan) elements . . . . .	110
7.4	Application of fan regions . . . . .	117
7.5	Discrete approximation of four node regions . . . . .	123
7.6	Discussion . . . . .	129
<b>IV</b>	<b>Discussion and closure</b>	<b>131</b>
<b>8</b>	<b>Discussion</b>	<b>133</b>
8.1	Combined application of the proposed methods . . . . .	134
8.2	Scaling and numerical issues . . . . .	136
8.3	The solution spaces of layout optimization problems . . . . .	140
8.4	Simplification and interpretation in practice . . . . .	149
<b>9</b>	<b>Conclusions</b>	<b>157</b>
<b>10</b>	<b>Suggestions for future work</b>	<b>159</b>
	<b>References</b>	<b>161</b>
	<b>Appendices</b>	<b>175</b>
<b>A</b>	<b>Numerical analysis of regions in known optimal solutions</b>	<b>177</b>
A.1	Definitions of functions and constants . . . . .	178
A.2	Tabulated results . . . . .	179
<b>B</b>	<b>Further applications of counterweights</b>	<b>183</b>
B.1	Crane structure example . . . . .	184
B.2	Counterbalance bridge example . . . . .	190
B.3	Foundations on inclined frictional planes . . . . .	191
<b>C</b>	<b>Derivation of further region types for RAGS method</b>	<b>193</b>
C.1	Type $T_3$ regions . . . . .	194
C.2	Type $T_2$ regions . . . . .	195
C.3	Type $T_1$ regions . . . . .	197
C.4	Type $R$ regions . . . . .	210
C.5	Type $S$ regions . . . . .	210
<b>D</b>	<b>The solution spaces of layout optimization problems</b>	<b>211</b>
D.1	Sensitivity analysis of layout optimization problems . . . . .	212
D.2	Vertex enumeration by pivoting methods . . . . .	217
D.3	Vertex enumeration by incremental algorithms . . . . .	219
<b>E</b>	<b>Additional contributions to the literature</b>	<b>221</b>
E.1	Application of layout optimisation for building structures . . . . .	222
E.2	Optimisation-driven conceptual design: Case study of a large transfer truss . . . . .	226
E.3	Optimization-driven conceptual design of long span bridges . . . . .	234
E.4	Automatic identification of structurally efficient layouts with limited complexity . . . . .	243
E.5	Balancing complexity and structural efficiency in the design of optimal trusses . . . . .	247
E.6	Layout optimization of simplified trusses using MILP with runtime generation of constraints . . . . .	256



# List of Figures

1.1	Two traditionally conceived structural forms for long span bridges . . . . .	3
1.2	Three railway stations in London, each with different structural forms . . . . .	4
2.1	Example problem with support conditions that imply either fixed or variable support forces . . .	8
2.2	Regions of types $R^+$ , $R^-$ , $S^+$ , $S^-$ , $T$ and $O$ . . . . .	9
2.3	Regions of types $T_1$ , $T_2$ and $T_3$ . . . . .	10
2.4	A selection of known Michell structures, colour added according to the different region types. . .	11
2.5	Minimum volume plastic designs for multiple load case problems . . . . .	13
2.6	Convex and non-convex functions and sets. . . . .	15
2.7	Examples of solution spaces of linear programming problems with two or three variables. . . . .	16
2.8	Stress-strain curves based on ductile materials . . . . .	19
2.9	The solutions from analytical and numerical methods . . . . .	20
2.10	The stages of the layout optimization method . . . . .	21
2.11	Results with self-weight, using the formulation in equation (2.13) . . . . .	23
2.12	The geometry optimization procedure. . . . .	24
2.13	Stages in the design and construction process . . . . .	25
2.14	Examples of physical models . . . . .	26
2.15	Example of form generation using the popular parametric modelling software Grasshopper . . . .	28
3.1	Hotel basement study - 3D chassis: Problem specification . . . . .	32
3.2	Hotel basement study - 3D chassis: Result. . . . .	33
3.3	Hotel basement study - 2D mother truss: Problem specification. . . . .	34
3.4	Hotel basement study - 2D mother truss: Results of single load case problems . . . . .	34
3.5	Linear approximation of buckling in commercially available RHS sections. . . . .	35
3.6	Hotel basement study - 2D mother truss: Results of initial study into deflection limits. . . . .	36
3.7	Hotel basement study - 2D mother truss: Comparison of options for structural layout . . . . .	38
3.8	Hotel basement study - 2D mother truss: Rationalized truss using optimized topology . . . . .	39
3.9	Hotel basement study - 2D mother truss: Contributions of different design decisions to volume .	40
4.1	Approximate shape of an equally stressed element AB in compression . . . . .	48
4.2	Forces acting on an infinitesimal slice of a vertical, equally stressed element. . . . .	49
4.3	Procedure employed to identify optimal (minimum volume) bridge structures. . . . .	50
4.4	Bridge forms for various spans and associated volumes. . . . .	53
4.5	Split pylon concept bridge to cross Strait of Gibraltar, with two 5km main spans. . . . .	55
4.6	Volume vs. span for various bridge forms, using equal stress catenary elements . . . . .	56
4.7	Span-to-dip ratio of 4.4 - Volume vs. span for different bridge designs . . . . .	57
4.8	Span-to-dip ratio of 9 - Volume vs. span for different bridge designs . . . . .	57
4.9	Effect of reducing the limiting compressive stress. . . . .	59
4.10	Effect of changing the relative cost of compressive and tensile members . . . . .	60
4.11	Appraising the relative efficiency of bridge forms by considering how deck loads are transmitted back to a support. . . . .	61
5.1	The distributed self-weight method, geometry and end forces of a single catenary member . . . .	65
5.2	Simple example: Results for increasing material weight . . . . .	66
5.3	Simple example: Volumes of structures after layout optimization and geometry optimization . . .	66
5.4	Cantilever example: Forms of optimal structures with restricted and extended design domains . .	67
5.5	Cantilever example: Volumes of structures using the restricted and extended design domains . .	68
5.6	Cantilever example: Improved solutions with unstressed counterweights of various relative costs .	69

5.7	Reaction and counterweight forces acting on a frictional foundation node. . . . .	70
5.8	Bridge example: Results for scenarios with pinned or roller pinned supports . . . . .	71
5.9	Bridge example: Results for roller pin supports with and without arching permitted . . . . .	72
5.10	Bridge example: Structures with frictional foundations at both tower base and anchorage. . . . .	73
5.11	Bridge example: Structures with frictional support at anchorage and roller pin at tower base . . .	74
5.12	Bridge example: Simplified proposed designs for three span bridge . . . . .	76
6.1	Stages in the truss layout optimization method . . . . .	82
6.2	Simple cantilever: Problem specification and component load cases . . . . .	85
6.3	Simple cantilever: Volume of two member truss for $0 \leq y_A \leq 2d$ and $0 \leq y_B \leq 2d$ . . . . .	86
6.4	Simple cantilever: Theoretical results . . . . .	88
6.5	Roof transfer truss: Problem Specification. . . . .	89
6.6	Roof transfer truss: High resolution layout optimization result. . . . .	89
6.7	Roof transfer truss: 9 node structure . . . . .	90
6.8	Roof transfer truss: Exhaustive enumeration of designs with 11 nodes. . . . .	90
6.9	Roof transfer truss: Lower resolution layout optimization result. . . . .	91
6.10	Roof transfer truss: Results with limited numbers of nodes . . . . .	92
6.11	Roof transfer truss: Results with minimum cross-section area . . . . .	93
6.12	Roof transfer truss: Correlation between complexity measures. . . . .	94
6.13	Procedure for runtime constraint generation . . . . .	96
6.14	Approximation of members crossing a line of symmetry . . . . .	98
6.15	Handling of crossover joints in geometry optimization stage. . . . .	98
6.16	Handling of branched member forms in geometry optimization stage. . . . .	99
6.17	Simple cantilever: Numerical results with limits on the minimum angle between members . . . .	100
6.18	Michell cantilever: Problem specification. . . . .	100
6.19	Michell cantilever: Results after MILP stage and after GO stage. . . . .	100
6.20	Michell cantilever: Results with limits imposed on the total number of joints. . . . .	102
6.21	Michell cantilever: Results with limited joint angle. . . . .	103
6.22	Spanning example: Problem specification . . . . .	104
6.23	Spanning example: Results after MILP and GO showing asymmetric optimal solutions. . . . .	104
6.24	Spanning example: Results with limited numbers of joints. . . . .	105
6.25	Spanning example: Correlation between number of joints and members in solutions . . . . .	106
7.1	Results for the problem of Ghista & Resnikoff (1968) . . . . .	108
7.2	Fan region: Geometry and behaviour . . . . .	111
7.3	Offset fan region: Node positions and angle definitions . . . . .	113
7.4	Discrete approximation of fan element: Geometry and virtual deflections . . . . .	115
7.5	Graphical interpretation of the member adding method for bar elements . . . . .	118
7.6	Graphical interpretation of the member adding method for fan elements . . . . .	119
7.7	Point load example: Problem specification. . . . .	120
7.8	Point load example: Results of layout and geometry optimization. . . . .	121
7.9	Bridge example: solutions . . . . .	122
7.10	Discrete approximation of four node region: Labels and angles . . . . .	123
7.11	The range of possible layouts of the approximated four node region . . . . .	124
7.12	Further relationships and quantities for a given value of $\hat{p}$ and inclination of line $R_{AP}P$ . . . . .	125
7.13	Primal (static) derivation of a discrete approximated quad element. . . . .	127
7.14	Michell cantilever: Result of iteration 1 . . . . .	128
7.15	Michell cantilever: Result of iteration 2 . . . . .	128
7.16	Michell cantilever: Result of iteration 3 (final iteration) . . . . .	128
7.17	Michell cantilever: Result with bars and increased number of ground structure nodes . . . . .	129
8.1	Issues caused by the interaction of self-weight modelling and symmetry conditions . . . . .	134
8.2	Solutions for a simple cantilever problem under substantial self-weight loading . . . . .	135
8.3	Comparison of heuristics for member adding sequence . . . . .	136
8.4	A comparison of the effectiveness of the member adding method with light and heavy materials .	137
8.5	A simple example to demonstrate the limits of $M$ and $\hat{M}$ . . . . .	139
8.6	Variation in time required to solve problem using various values of $\hat{M}$ . . . . .	139
8.7	Square cantilever - 6 nodes: Basic and non-basic solutions . . . . .	141
8.8	Square cantilever - 6 nodes: Values of complexity measures on a plane of the solution space. . . .	142
8.9	Square cantilever - 4 nodes: All vertices of the solution space . . . . .	144



8.10	Square cantilever - 6 nodes: All vertices of the solution space . . . . .	145
8.11	Square cantilever - 25 nodes: Complexity of 200 basic solutions . . . . .	147
8.12	Square cantilever - 25 nodes: Structural forms for points on the Pareto fronts in Figure 8.11 . . . . .	148
8.13	Square cantilever - 9 nodes: Results of modified double description method . . . . .	148
8.14	Two span footbridge: Design domains . . . . .	149
8.15	Two span footbridge: Minimum volume structures for single load case problem . . . . .	150
8.16	Two span footbridge: Minimum volume structure for multiple load cases . . . . .	150
8.17	Two span footbridge: Intermediate structures between truss and arch designs. . . . .	151
8.18	Two span footbridge: Structures with one non-essential node. . . . .	152
8.19	Two span footbridge: Intermediate structures between cable stayed and arch designs. . . . .	153
8.20	3D transfer truss example: Design domain . . . . .	154
8.21	3D transfer truss example: Solutions with limited numbers of nodes. . . . .	154
A.1	Normalised values of the coefficients $D_n$ for selected regions of type $T_2$ . . . . .	179
A.2	Normalised values of the coefficients $C_n$ for regions of type $T_1$ in the exterior of a square . . . . .	181
A.3	Normalised values of the coefficients $C_n$ for regions of type $T_1$ in a long cantilever . . . . .	181
B.1	A variety of designs of tower crane in use. . . . .	184
B.2	Crane example: Problem specification . . . . .	184
B.3	Crane example: Results of layout optimization with 0.5m nodal grid . . . . .	185
B.4	Crane example: Results of layout optimization using 4m nodal grid followed by GO . . . . .	185
B.5	Crane example: Results of layout optimization using 2m nodal grid . . . . .	185
B.6	Crane example: Results of layout optimization with minimal nodes followed by GO . . . . .	185
B.7	Crane example: Effect of variations in material strengths and costs on the use of counterweights . . . . .	187
B.8	Crane example: Results when the cost of the material in the tower is included . . . . .	188
B.9	Crane example: Results for problem with two load cases . . . . .	189
B.10	Cantilever bridge example: Resulting structures . . . . .	190
B.11	Reaction and counterweight forces acting on a frictional foundation node. . . . .	191
C.1	Type $T_3$ region: Virtual deflections and possible static forms from duality principles . . . . .	194
C.2	Type $T_2$ region: Definitions of points and angles . . . . .	195
C.3	A discrete approximation of a region using a $1 \times 2$ cell mesh . . . . .	196
C.4	Type $T_1$ region: Definitions of points and angles . . . . .	197
C.5	The range of possible geometries for a region of type $T_1$ where $\alpha = 0$ and $\beta = 0$ are circular arcs . . . . .	200
C.6	Relationship between regions constructed from two arcs, $\theta_A = \theta_B$ , for varying $\frac{r_A}{r_B}$ . . . . .	200
C.7	Relationship between different regions constructed from arcs with varying $\theta_A$ , $\theta_B$ and $\frac{r_A}{r_B}$ . . . . .	201
C.8	Two fields of curvilinear coordinate lines based on circular arcs . . . . .	203
C.9	Test of uniqueness of areas cut from circular based fields: Resulting layouts . . . . .	205
C.10	Normalised coefficients defining regions cut from the field based on circular arcs with equal radius . . . . .	207
C.11	Micell cantilever: Results with bars and four node elements . . . . .	207
C.12	A four cell approximated element, with the associated circles of relative displacements . . . . .	208
C.13	Four cell approximated element: local displacements of points . . . . .	209
C.14	Apparent regions of type $S$ occurring due to limited resolution . . . . .	210
D.1	Square cantilever - 4 node: sensitivity analysis for external forces . . . . .	213
D.2	Square cantilever - 25 nodes, 2 load case: Sensitivity analysis of cost coefficients . . . . .	215
D.3	Square cantilever - 25 nodes, 2 load case: Sensitivity analysis of cost coefficients . . . . .	216
D.4	Square cantilever - 25 nodes: Volumes of 200 basic solutions found by pivoting type method . . . . .	218
D.5	Square cantilever - 25 nodes: Structural forms for points labelled in Figure D.4 . . . . .	218
D.6	Number of points and rays at each step of complexity constrained double description method . . . . .	219



# List of Tables

4.1	Numerical volumes for various bridge spans and nodal resolutions. . . . .	54
4.2	Comparison of volumes of traditional bridge forms with those of new reference solutions. . . . .	58
6.1	Simple cantilever: Behaviour of volume function in the vicinity of $\vartheta_2$ . . . . .	87
6.2	Simple cantilever: Comparison of theoretical and numerical methods . . . . .	89
6.3	Speed comparison between formulations for defining the node flag variables, $\mathbf{v}$ . Problem is the Michell cantilever with limited number of joints, as shown in Table 6.4 and Figure 6.20. . . . .	97
6.4	Michell cantilever: Results with limits imposed on the total number of joints. . . . .	102
6.5	Michell cantilever example: Results with limited joint angle. . . . .	103
6.6	Spanning example: Results with limited numbers of joints. . . . .	105
8.1	3D transfer truss example: Load case definitions. . . . .	154
A.1	Details of selected known regions of type $T_2$ . . . . .	179
A.2	Details of selected known regions of type $T_1$ . . . . .	180
C.1	Test of uniqueness of areas cut from circular based fields: Optimized parameter values . . . . .	205



# List of Symbols

This section lists the symbols used in this thesis. The page number where the symbol is defined or first used is given for each. Symbols which are used as parameters of example problems, and therefore defined in various locations, are denoted by var. The symbols are divided by alphabet (Latin/Greek); Latin letters are further divided by case, then by style.

## Latin

### Capitals

#### Italic

	Description	Page
$A$	Lamé coefficient . . . . .	10
$\hat{A}$	Interior angle of quadrilateral OAPB at A . . . . .	197
$B$	Lamé coefficient . . . . .	10
$\hat{B}$	Interior angle of quadrilateral OAPB at B . . . . .	197
$C$	Coefficients in series expansions of $A$ and $B$ . . . . .	198
$D$	Coefficients in series expansion of $F(\beta)$ . . . . .	178
$E$	Youngs Modulus . . . . .	19
$F$	Function of $\beta$ for a region of type $T_2$ , $B(\alpha, \beta) = \alpha + F(\beta)$ . . . . .	195
$G$	Function used for simplifying notation of $A$ and $B$ . . . . .	178
$H$	Function defining a circular based region of type $T_1$ . . . . .	202
$I$	Modified Bessel function of the first kind . . . . .	199
$J_j$	The set containing the indices of all ground structure members which connect to node $j$ . . . . .	83
$K$	Joint complexity score . . . . .	146
$L$	Length scale in example problems . . . . .	var.
$M$	Large Number, integer programming . . . . .	83
$\bar{M}$	Another large number, integer programming . . . . .	83
$N$	Number of negative rays . . . . .	219
$O$	Region type with no fully strained directions . . . . .	9
$\hat{O}$	Interior angle of quadrilateral OAPB at O . . . . .	197
$P$	Number of positive rays . . . . .	219
$\hat{P}$	Interior angle of quadrilateral OAPB at P . . . . .	197
$Q$	Force value in an example problem . . . . .	var.
$R$	Region type with fully strained members in one direction only . . . . .	9
$S$	Region type with uniform dilation . . . . .	9
$T$	Region type with fully strained members in orthogonal directions . . . . .	9
$T_1$	Region with fully strained members lying along two sets of mutually orthogonal curves . . . . .	10
$T_2$	Region with set of straight fully strained members and one orthogonal set of curved members . . . . .	10
$T_3$	Region with fully strained straight orthogonal Cartesian members . . . . .	10
$U$	Upper bound for number of points in next iteration . . . . .	219
$V$	Total structural volume . . . . .	21
$W$	Total external work. . . . .	21
$W_D$	Deck level weight (i.e. traffic plus road surface) . . . . .	71
$W_S$	Structural weight . . . . .	71
$X$	Local horizontal direction . . . . .	109
$Y$	Local vertical direction . . . . .	110
$Z$	Number of zero rays . . . . .	219

**Roman**

	Description	Page
A	Extreme point of region with local curvilinear coordinates $(\theta_A, 0)$ . . . . .	110
B	Extreme point of region with local curvilinear coordinates $(0, \theta_B)$ . . . . .	110
C	Midpoint of line OP . . . . .	125
E	Centres of circles of relative displacement . . . . .	115
J	Intersections of bisectors of $\hat{o}$ and $\hat{p}$ and circle with diameter OP . . . . .	125
M	Center of rotation for points A and B, for approximated type $T_1$ region . . . . .	125
	for exact circular based region . . . . .	201
O	Extreme point of region with local curvilinear coordinates $(0, 0)$ . . . . .	110
P	Extreme point of region with local curvilinear coordinates $(\theta_A, \theta_B)$ . . . . .	110
R	Intermediate points in discrete approximations of: type $T_1$ regions . . . . .	123
	fan regions . . . . .	115
Z	Point of line OP defining an edge of quads $\mathbb{A}$ and $\mathbb{B}$ . . . . .	124

**Calligraphy**

	Description	Page
$\mathcal{A}$	A formulation where node flags are set based on member areas . . . . .	95
$\mathcal{C}$	Cost function . . . . .	9
$\mathcal{G}$	Sub-gradient operator . . . . .	9
$\mathcal{L}$	A polytope in $d$ -dimensional space . . . . .	143
$\mathcal{P}$	Problem specific constant relating to the relative quantities of tension and compressive material . . . . .	8
$\mathcal{V}$	Set of pairs of members which form an angle smaller than $\Psi$ . . . . .	98
$\mathcal{W}$	A formulation where node flags are set based on member flag variables . . . . .	97
$\mathcal{X}$	Set of pairs of members which intersect (excluding those which meet at a node) . . . . .	94

**Double struck**

	Description	Page
$\mathbb{A}$	Possible (normalised) locations of point A . . . . .	123
$\mathbb{B}$	Possible (normalised) locations of point B . . . . .	123
$\mathbb{J}$	Mesh cell in approximated fan . . . . .	115
	in approximated type $T_1$ region . . . . .	208
$\mathbb{K}$	Mesh cell in approximated fan . . . . .	115
	in approximated type $T_1$ region . . . . .	208
$\mathbb{L}$	Mesh cell in approximated type $T_1$ region . . . . .	208
$\mathbb{M}$	Mesh cell in approximated type $T_1$ region . . . . .	208

**Bold**

	Description	Page
<b>A</b>	Constraint matrix . . . . .	15
<b>B</b>	Equilibrium matrix . . . . .	21
<b>C</b>	Equilibrium matrix for frictional support forces . . . . .	70
<b>D</b>	Equilibrium matrix for normal support forces . . . . .	70
<b>K</b>	Joint complexity matrix . . . . .	146
<b>P</b>	Imposed load case . . . . .	84
<b>P*</b>	Component load case, for superposition method of solving 2 load case problems . . . . .	84
<b>V</b>	Matrix containing all vertices of a polytope . . . . .	143
<b>W</b>	Lumped self-weight coefficients . . . . .	23
<b>Z</b>	Matrix of unit vectors in the direction of gravity (for converting c/w masses to forces) . . . . .	68

**Lower case****Italic**

	Description	Page
$a$	Cross sectional area of a bar . . . . .	22
$\hat{a}$	Internal angle of a mesh cell in a a discrete approximation of a: Fan region (type $T_2$ ) . . . . .	115
	$T_1$ region . . . . .	123
$b$	Number of pool variables . . . . .	95
$\hat{b}$	Internal angle of a mesh cell in a discrete approximation of a $T_1$ region . . . . .	123
$c$	Total structure cost: With different material prices in tension and compression . . . . .	60
	Including both stressed and unstressed material . . . . .	68
	Including a fixed cost per joint . . . . .	101
$d$	Length scale . . . . .	var.
$e$	$= \sin^2 \hat{p}$ . . . . .	125
$f$	External force, at point indicated by subscript, and in direction indicated by superscript . . . . .	21
$g$	Local gravitational constant ( $\approx 9.8\text{N/kg}$ ) . . . . .	47
$h$	Hypotenuse of a right angled triangle in the circle of relative displacements . . . . .	116
$i$	Index of a member . . . . .	21
$j$	Index of a node . . . . .	23
$k$	Loadcase iterator . . . . .	22
$l$	Member length . . . . .	21
$m$	Number of potential members (in ground structure) . . . . .	21
$n$	Number of potential nodes (in ground structure) . . . . .	21
$o$	Coefficients of quartic in $e$ . . . . .	125
$\hat{o}$	Internal angle of a mesh cell in a discrete approximation of a $T_1$ region . . . . .	123
$p$	Price: per unit volume of $p_S$ structural and $p_U$ non structural (lumped mass) materials . . . . .	68
	per unit volume of material in $p_C$ compression and $p_T$ tension . . . . .	60
	per joint, $p_J$ . . . . .	101
$\hat{p}$	Internal angle of a mesh cell in a a discrete approximation of a: Fan region (type $T_2$ ) . . . . .	115
	$T_1$ region . . . . .	123
$q$	Member internal force . . . . .	21
$\tilde{q}$	Critical axial force in member for Euler buckling . . . . .	35
$r$	Radius: Italic subscripts, radius is the distance from point O to subscripted point . . . . .	110
	Roman subscripts, radius of the arc connecting point O and subscripted point . . . . .	199
$s$	Frictional support, reaction force parallel to plane . . . . .	70
$t$	Frictional support, reaction force normal to plane . . . . .	70
$u$	Virtual deflection, at point indicated by subscript, and in direction indicated by superscript . . . . .	21
$\dot{u}$	Virtual deflections, within a local frame of reference for overall translation . . . . .	116
$\bar{u}$	Virtual deflections, within a local frame of reference for overall translation and rotation . . . . .	111
$v_j$	Node integer flag representing the existence of node $j$ . . . . .	83
$w$	Intensity of distributed load . . . . .	var.
$w_i$	Integer ‘flag’ variable representing the existence of member $i$ . . . . .	83
$x$	Global Cartesian direction . . . . .	21
$y$	Global Cartesian direction . . . . .	21
$z$	Perpendicular distance from line AB to C in discrete approximation of $T_1$ region . . . . .	125
$\bar{z}$	Distance, perpendicular to line AB, between M and C in discrete approximation of $T_1$ region . . . . .	125

**Bold**

	Description	Page
<b>a</b>	Vector of member areas . . . . .	22
<b>b</b>	Right hand sides of constraints . . . . .	15
<b>c</b>	Vector of objective coefficients . . . . .	15
<b>e</b>	Vector where every entry has value 1 . . . . .	68
<b>f</b>	External force vector . . . . .	21
<b>g</b>	Topology vector . . . . .	146
<b>l</b>	Member length vector . . . . .	22
<b>q</b>	Vector of internal member forces. (possible subscript for load case) . . . . .	21
<b>r</b>	Vector of counterweight variables . . . . .	68
<b>s</b>	Vector of frictional shear forces . . . . .	70
<b>t</b>	Vector of support forces perpendicular to frictional surfaces . . . . .	70
<b>u</b>	Virtual nodal displacement vector . . . . .	21
<b>v</b>	Vector of node flags (integer variables) . . . . .	83
<b>w</b>	Vector of member flags (integer variables) . . . . .	83
<b>x</b>	Primal problem variables . . . . .	14
<b>y</b>	Dual problem variables . . . . .	16
<b>z</b>	A vector representing a point in a polytope as a convex combination of its vertices . . . . .	143

**Greek**

	Description	Page
$\alpha$	Local curvilinear coordinate . . . . .	10
$\beta$	Local curvilinear coordinate . . . . .	10
$\Gamma$	Gamma function, $\Gamma(n) = (n-1)!$ for positive integers . . . . .	206
$\gamma$	Ratio of radii of base arcs . . . . .	202
$\Delta$	Discriminant of a polynomial . . . . .	87
$\epsilon$	Strain of a bar . . . . .	8
$\varepsilon$	Allowable strain . . . . .	110
$\zeta$	Maximum permitted number of joints . . . . .	83
$\eta$	Maximum permitted number of nodes . . . . .	83
$\Theta$	Angle between a line and the global $X$ -axis . . . . .	var.
$\theta$	Angle turned through by a set of coordinate lines in a region . . . . .	111
$\vartheta$	Angular parameter of example problem, e.g. force inclination . . . . .	var.
$\iota$	Offset angle of the curved coordinate lines in an offset fan region . . . . .	112
$\kappa$	Signed strength to weight ratio of a material . . . . .	47
$\Lambda$	Vector containing minimum cross-section areas for each member in the ground structure . . . . .	83
$\lambda$	$\beta$ coordinate of point O for a region cut from a circular field . . . . .	204
$\mu$	Coefficient of friction . . . . .	69
$\nu$	Angle between tangents to coordinate lines and sides of parallelogram at a corner point of a region . . . . .	197
$\Xi$	Reciprocal gamma function, $\Xi(n) = \frac{1}{\Gamma(n)}$ . . . . .	206
$\xi$	Angle between opposing sides of a quadrilateral . . . . .	197
$\rho$	Density . . . . .	47
$\sigma$	Permitted stress, subscripts $T$ and $C$ represent value in tension and compression respectively . . . . .	8
$\tau$	Minimum distance between perpendicular bisector of AB and point C . . . . .	125
$\Phi$	Inclination of an equally stressed catenary member at a point . . . . .	48
$\phi$	Angle between $\alpha$ -lines and local $x$ axis . . . . .	10
$\varphi$	Offset angle for an approximated $T_1$ element, (=angle between OP and bisector of angle at P) . . . . .	126
$\chi$	$\alpha$ coordinate of point O for a region cut from a circular field . . . . .	204
$\Psi$	Minimum permitted angle between connected members . . . . .	99
$\psi$	Angle of frictional plane to horizontal . . . . .	191
$\Omega$	Constants of integration for function describing a catenary element . . . . .	47
$\omega$	Rotation . . . . .	110



# List of Abbreviations

	Description	Page
CHS	Circular Hollow Section . . . . .	35
GO	Geometry Optimization . . . . .	24
IP	Integer Programming . . . . .	17
LO	Layout Optimization . . . . .	21
LP	Linear Programming . . . . .	14
MILP	Mixed Integer Linear Programming . . . . .	17
MIP	Mixed Integer Programming . . . . .	17
MIQCP	Mixed Integer Quadratically Constrained Programming . . . . .	17
MIQP	Mixed Integer Quadratic Programming . . . . .	17
MISOCP	Mixed Integer Second Order Cone Programming . . . . .	17
NLP	Non-Linear Programming . . . . .	17
RAGS	Region based Adaptive Ground Structure (method) . . . . .	107
RHS	Rectangular Hollow Section . . . . .	35
SLS	Serviceability Limit State . . . . .	37
ULS	Ultimate Limit State . . . . .	32



Part I

Preliminaries



# Chapter 1

## Introduction

The field of structural design is still dominated by designs conceived by ‘engineering intuition’ and previous experience. Often several different solutions are common for the same scenario; see figures 1.1 and 1.2 for some examples of common forms found in bridges and buildings respectively. Decisions on the overall layout must be taken very early in a project’s conception, yet can have huge impacts on the feasibility and effectiveness of the whole project. Despite this, there are currently very few tools available to designers that can allow them to make an informed choice on which of the many options will be the most effective, or indeed if there are alternative options which may perform even better.

The increasing awareness of the importance of efficiently using natural resources leads to greater urgency in these matters. In other fields of engineering, such as aerospace and mechanical engineering, this has already led to widespread use of optimization methods, allowing the creation of increasingly lightweight and materially efficient components, whilst maintaining the required performance. However, similar tools for structural engineers are not yet so well developed.

The constraints and challenges specific to structural design stem from a variety of factors. The physical scale of the problem requires that structures be assembled from discrete elements, and often causes the weight of the structure itself to be a significant source of loading. The number and variety of stakeholders, and the public nature of projects, necessitate forms that may be easily communicated, and a design work-flow capable of adapting to rapidly changing demands and collaborative decision making. There may also be additional architectural and aesthetic considerations applied on a problem specific basis, and each site may present its own logistical constraints.

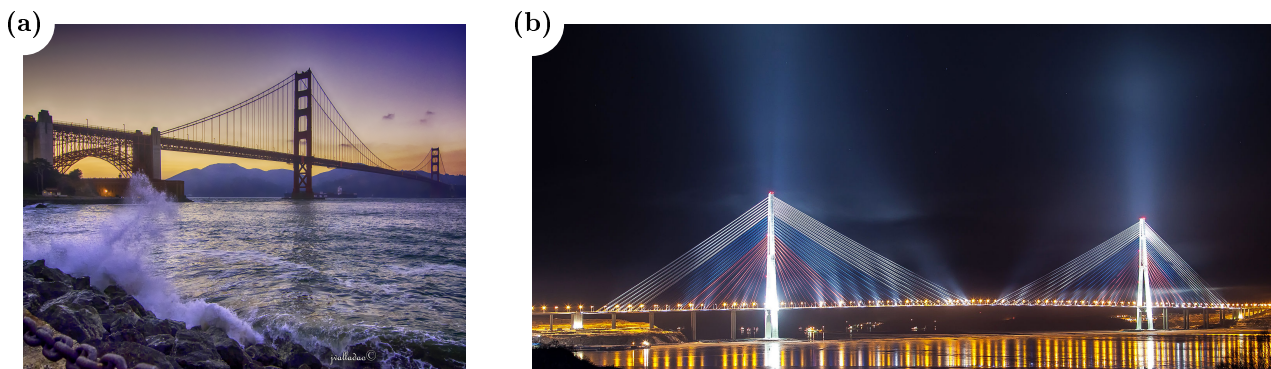


**Figure 1.1:** Two traditionally conceived structural forms for long span bridges. (a) A suspension bridge, the Golden Gate bridge, USA (photo by Walladao, 2018, used under CC BY-SA 4.0). (b) A cable stayed bridge, the Russky bridge, Russia (photo by Александрович, 2013, used under CC BY 3.0).



**Figure 1.2:** Three railway stations in London, each with different structural forms. **(a)** Waterloo station, showing a series of Warren trusses of varying depth (photo by Brown, 2011, used under CC BY 2.0). **(b)** St Pancras International station, with arched roof vault (photo by Sakrajda, 2010, used under CC BY-SA 3.0). **(c)** Cannon Street station with Cannon Place office block above, the exoskeleton of the office block comprises transfer trusses, using Pratt trusses and cross braced cantilever layouts (photo by Prasannan, 2012, CC BY-SA 3.0).

## 1.1 Objectives and scope of work

The aim of the present study is to identify and address issues that limit the application of optimization methods in structural engineering practice. The intention is to target a wide range of applications encompassing elements of buildings, bridges and other structures which are constructed using broadly truss-like, axially loaded components. The methods used in this work centre around the ground structure layout optimization approach (Dorn et al., 1964), due to the ease with which this can be integrated into the frame based analysis programs currently in use in structural engineering practices. Compared to the continuum based topology optimization methods used in mechanical engineering applications, the ground structure method also has far fewer difficulties in dealing with problems that require a very low quantity of structural material compared to the size of the design domain; this is often the case in structural design problems.

This thesis primarily focuses on methods that are applicable in the early stages of the design process. This is where the greatest potential for material savings are available, yet also where the tools required are least developed. In this stage of design development, it is common to consider only the most important influences on the design; with more detailed concerns being added as the design develops. For example, often in the current design process only a sub-set of the loading scenarios are initially considered, with further checks for the omitted cases occurring at a later stage.

Recently, there has been growing interest in innovative construction methods based on additive manufacturing (3D printing). Whilst these approaches have the potential to allow more complex designs to be realised, they are still in the early stages of development, and have not yet achieved widespread application, regulatory acceptance and affordability. Instead, this work will focus on obtaining designs that could be constructed using broadly familiar techniques, with perhaps some modification such as allowing bespoke cast nodes at the most critical joints.

## 1.2 Organisation of the thesis

This thesis begins by investigating current methods available in the field of structural optimization and evaluating their applicability for practical structural design, this forms Part I. Several methods are then proposed to address factors that could limit the uptake of optimization methods. The factors addressed are the non-conservative errors caused by the modelling of self-weight, addressed in Part II, and the often complex and seemingly incomprehensible nature of solutions obtained using numerical optimization methods, which is addressed in Part III. The proposed methods are combined, compared and tested on real-world projects, and suggestions for further work are made in Part IV.

This work is split into chapters as follows:

1. This introduction forms Chapter 1.
2. Chapter 2 presents a review of previous studies and methods that are related to work in this thesis. This includes theories underlying the study of minimum weight structures, as well as numerical methods of

obtaining the same. These are contrasted with methods for ‘form finding’ and initial structural design used in practice. Features that make methods attractive for practical application are noted.

3. Several of the numerical optimization methods considered in the previous chapter appear to be highly suitable for use in design practice. However, their uptake is still limited. To establish why this may be, in Chapter 3 these methods are applied to a real-world case study, thereby identifying several challenges that still need to be addressed.
4. Long span bridges are one category of structure where the engineer traditionally has the most design freedom. Typically these employ suspension or cable-stayed forms (see Figure 1.1). At long spans, the self-weight of the structure itself becomes dominating; however existing numerical optimization methods model this with non-conservative approximations. As such, the optimality of traditional forms over very long spans appears never to have been rigorously assessed, and the theoretically optimal form for a given span carrying gravity loading has remained unknown. To address this, Chapter 4 describes a new numerical layout optimization procedure capable of intrinsically modelling the self-weight of the constituent structural elements. The bridge forms identified are complex and differ markedly to traditional suspension and cable-stayed bridge forms. Simplified variants incorporating split pylons are also presented.
5. The modelling approach developed in the previous chapter can produce unclear results in cases where the self-weight of the structure has a favourable role in supporting the applied loads. Therefore, Chapter 5 presents an improved formulation that explicitly includes the possibility of favourable unstressed masses, such as counterweights, in the optimal solution. Extension to frictional boundary conditions, which are more realistic than traditional pinned supports, are also considered, and the cost of abutments and anchorages is also included within the optimization. The method is demonstrated by application to the initial conceptual design of a simplified bridge structure. This allows for comparison of ground anchored and self anchored structural forms, thereby showing that use of standard support types may produce sub-optimal results.
6. Attempts to apply topology or layout optimization methods at the conceptual design stage can be hampered by the complex and impractical nature of the forms that are often generated; in the previous two chapters manual intervention has been required to convert these into potentially buildable proposals. In Chapter 6, the standard truss layout optimization formulation is extended to allow introduction of constraints designed to increase buildability and reduce fabrication costs. A number of different constraints are compared, including means of controlling the numbers of joints, eliminating overly thin members and limiting the minimum angle between connected members. Joints arising from crossover of pairs of members are accounted for using so-called ‘lazy constraints’, allowing speedups of more than 20 times whilst ensuring that there is no loss of solution quality. It is also shown that symmetric problems may not have symmetric optimal solutions, and that multiple distinct and equally optimal solutions may be found.
7. In Chapter 7, a novel extension to the truss layout optimization method is proposed that greatly improves the clarity and accuracy of numerically identified solutions. The method adds ground structure elements based on *regions*, of the type used in the analytical construction of minimum weight layouts. This not only allows for a level of abstraction that can greatly improve the users understanding of the result, but simultaneously allows numerical identification of minimum volume structures to within a fraction of a percent of known analytical solutions.
8. Implications of the findings of the previous chapters are discussed in Chapter 8. Points that must be considered in the application of the proposed techniques are also explored, and some initial investigations into suggested alternatives are considered. This chapter also describes application of the suggested methods to real-world scenarios.
9. The contributions and conclusions of the work are summarised in Chapter 9.
10. Finally, suggestions for future work are presented in Chapter 10.





# Chapter 2

## Literature review

This thesis is concerned with the application of optimization to the field of structural engineering. As such, knowledge of both existing optimization methods and current engineering practice is required.

This chapter contains a review of current work in the identification of optimal structural forms, including both analytical (Section 2.1) and numerical (Section 2.3) approaches. Additional background on mathematical optimization techniques, which are required for application of the numerical methods, are also presented in Section 2.2.

Methods used by practitioners to assist in the initial design of structural form are reviewed in Section 2.4. Finally, the differences between these practical methods and the more rigorous techniques from Sections 2.1 and 2.3 are evaluated in Section 2.5, and key requirements for improvement are identified.

---

2.1	Layouts of minimum weight structures . . . . .	8
2.1.1	Classical Michell structures . . . . .	8
	Known analytical solutions for classical Michell trusses . . . . .	11
2.1.2	Extensions of Michell's theory . . . . .	12
2.1.3	Minimum weight continuum structures . . . . .	14
2.2	An overview of mathematical optimization . . . . .	14
2.2.1	General optimization concepts . . . . .	14
2.2.2	Linear Programming . . . . .	14
	Duality . . . . .	16
	Algorithms . . . . .	16
2.2.3	Non-linear programming . . . . .	17
2.2.4	Discrete Optimization . . . . .	17
	Algorithms . . . . .	17
2.2.5	Meta-heuristic methods . . . . .	18
2.3	Numerical structural optimization methods . . . . .	19
2.3.1	Categories of structural optimization . . . . .	19
	Scope of problem . . . . .	19
	Structural modelling approach . . . . .	19
2.3.2	The layout optimization method and its extensions . . . . .	21
2.3.3	Geometry Optimization . . . . .	24
2.4	The use of optimization in structural engineering practice . . . . .	25
2.4.1	Form Finding . . . . .	25
2.4.2	Construction factors influencing optimality . . . . .	27
2.5	Observations . . . . .	29

---

## 2.1 Layouts of minimum weight structures

The identification of an efficient, economic and safe arrangement of structural members is one of the main goals of structural design. Lightweight forms reduce material usage in both the design itself and the supporting structures. However, direct implementation of true minimum weight structures is challenging, due to the very high level of complexity that they are characterised by. Nonetheless, these minimum volume forms can suggest an appropriate layout for a simpler solution, and it is possible to maintain much of the material savings with significantly simpler designs.

True minimum weight structures are also useful in benchmarking the efficiency of proposed designs. Cox (1965) has likened the study of minimum volume structures to that of the theoretical Carnot engine (Carnot, 1897), used to quantify the efficiency of heat engines. Similarly, Palmer & Sheppard (1970) defined the term Michell efficiency as the ratio of the weight of a suggested design to that of the optimal Michell structure for the same problem and material.

### 2.1.1 Classical Michell structures

**The Michell-Hemp criteria** The absolute minimum volume structure required to transmit a given set of loads to a set of supports is obtained through use of a structural layout obeying simple criteria, which were first noted by Michell (1904). The first of these criteria is that all members must have an axial stress that is equal in magnitude to the maximum permissible value, and the second is that the strain in all members should be equal, and there should be no other point in the domain with a strain higher than this value.

This was later generalised to cases with unequal permitted stresses in compression ( $\sigma_C$ ) and tension ( $\sigma_T$ ) by Hemp (1973). In this case, the strain  $\epsilon$  at any point in the domain must be in the range

$$-\frac{1}{\sigma_C} \leq \epsilon \leq \frac{1}{\sigma_T} \quad (2.1)$$

with the appropriate constraint satisfied with equality in cases where members are present.

This differs slightly from Michell's second criteria (Rozvany, 1996), and thus equation (2.1) and Michell's first criteria are often known as the Michell-Hemp criteria. Michell's original criteria produce correct results only when  $\sigma_T = \sigma_C$ , or when the support conditions of the structure are statically determinate. In Michell's original criteria, the 'comparison' displacements are independent of the values of  $\sigma_T$  and  $\sigma_C$ . Thus, in cases where this criteria is valid, e.g. Figure 2.1a, only the thicknesses of members change when  $\sigma_C$  is varied. In more general cases, e.g. Figure 2.1b, the layout of members, and the values of the reaction forces, change with  $\sigma_C$ .

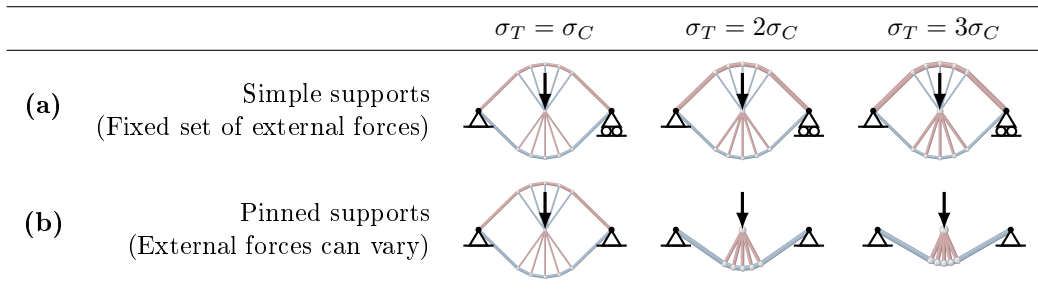


**Figure 2.1:** Example problem with two different sets of support conditions. (a) Fixed support forces, therefore Michell's original criteria, and Maxwell's theorem in equation (2.2), are valid, and the form does not change with relative strength. (b) Multiple possible sets of support forces and only the criteria of Hemp (1973), from equation (2.1), produce the optimal result.

**Maxwell's (1870) Theorem** This seemingly unintuitive result may be better understood by referring to the earlier theorem of Maxwell (1870), on which this part of Michell's theory was based. This is also restricted in applicability to statically determinate cases (Rozvany, 1996). Maxwell's theorem states that

$$\sum_{\forall i | q_i > 0} l_i q_i + \sum_{\forall i | q_i < 0} l_i q_i = P \quad (2.2)$$

where  $l_i$  and  $q_i$  are the length and internal force of bar  $i$ , and  $P$  is a constant for a given problem. This states that, for a statically determinate problem, an increase in the force carried by members in tension, must be transmitted back to the supports by incurring a corresponding increase in the force in the compression members. However,

when multiple options for the support forces are available, these extra forces can be resolved in other ways, e.g. by the additional horizontal thrust in the examples in Figure 2.1. This finding may be of interest to structural engineers, as thermal stresses in large structures are often avoided by the use of movement joints, which lead to almost statically determinate problems. In these cases, it is therefore feasible to obtain general benchmark layouts, from which minimum volumes for any ratio of  $\sigma_T$  to  $\sigma_C$  may be easily obtained.

**Hencky's Theorem** Most structures that obey the Michell-Hemp criteria (often termed Michell structures) are not trusses in the usual sense, but instead truss-like continua, where the lines of principal strain generally form two sets of orthogonal curves. These take a form consistent with those of the slip-lines in perfectly plastic flow (Hemp, 1958; Johnson, 1961), allowing the application of existing work from this field.

The theory of perfectly plastic plane flow was initially developed by Hencky and then further by Prandtl, leading to the term Hencky-Prandtl net to describe a such a layout (Prager & Hodge, 1951). Such layouts contain two families of orthogonal curves, often referred to as  $\alpha$ -lines and  $\beta$ -lines, based on their coordinates in a curvilinear system  $(\alpha, \beta)$  (Hill, 1950).

Hencky's first theorem (as cited by Hill, 1950, p. 136) states 'the angle between two slip-lines of one family, where they are cut by a slip-line of another family, is constant along their length'. Hencky's second theorem states that for two adjacent  $\alpha$ -lines at their point of intersection with a given  $\beta$ -line, the difference in the radii of curvature is equal to the distance along the  $\beta$ -line (Hill, 1950).

**Prager-Shield Optimality criteria** Prager & Shield (1967) generalised the design of optimal plastic structures to include both trusses and beams in bending, defining a relationship between the optimal statically admissible stress field and kinematically admissible strain field. This is stated by Rozvany (1989) as

$$\mathbf{u}^K = \mathcal{G}(\mathcal{C}(\mathbf{q}^S)) \quad (2.3)$$

where  $\mathbf{u}^K$  is a kinematically admissible strain field,  $\mathbf{q}^S$  is a statically admissible stress field,  $\mathcal{C}$  is the cost function and  $\mathcal{G}$  is the subgradient function. For a truss, where the cost of the beam is proportional to its force divided by the permissible stress in tension or compression respectively, this relationship becomes identical to the Michell Hemp criteria.

**Classification of regions of the domain** Despite the apparent simplicity of these criteria, a wide variety of structural regions are possible. These are divided into types according to the directions and magnitudes of the strains in the two principal directions  $(\epsilon_1, \epsilon_2)$ . This then prescribes in which of these directions members may be present (i.e. carry non-zero forces,  $q_1$  and  $q_2$  respectively).

Type $R^+$ :	$\epsilon_1 = \frac{1}{\sigma_T}$	$-\frac{1}{\sigma_C} < \epsilon_2 < \frac{1}{\sigma_T}$	$q_1 \geq 0$	$q_2 = 0$
Type $R^-$ :	$-\frac{1}{\sigma_C} < \epsilon_1 < \frac{1}{\sigma_T}$	$\epsilon_2 = -\frac{1}{\sigma_C}$ ,	$q_1 = 0$	$q_2 \leq 0$
Type $S^+$ :	$\epsilon_1 = \epsilon_2 = \frac{1}{\sigma_T}$		$q_1 \geq 0$	$q_2 \geq 0$
Type $S^-$ :	$\epsilon_1 = \epsilon_2 = -\frac{1}{\sigma_C}$		$q_1 \leq 0$	$q_2 \leq 0$
Type $T$ :	$\epsilon_1 = \frac{1}{\sigma_T}$	$\epsilon_2 = -\frac{1}{\sigma_C}$	$q_1 \geq 0$	$q_2 \leq 0$
Type $O$ :	$-\frac{1}{\sigma_C} < \epsilon_1 < \frac{1}{\sigma_T}$	$-\frac{1}{\sigma_C} < \epsilon_2 < \frac{1}{\sigma_T}$	$q_1 = 0$	$q_2 = 0$

Examples of possible layouts in these regions are shown in Figure 2.2. Types  $R, S$  and  $T$  were identified for optimal grillage design (Prager & Rozvany, 1977), type  $O$  regions only were explicitly specified later (Melchers, 2005; Lewiński et al., 2019).

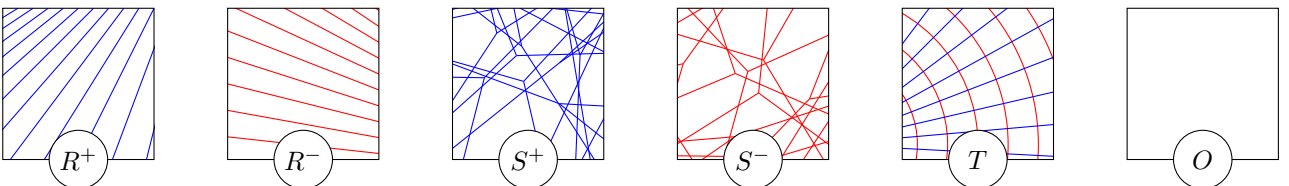


**Figure 2.2:** Regions of types  $R^+$ ,  $R^-$ ,  $S^+$ ,  $S^-$ ,  $T$  and  $O$ .

Therefore within  $R$  regions, members run in one direction only and must all be of either tension or compression respectively. In  $S$  regions, a uniform strain is observed, and members will be of the same sense and may run in any direction, leading to the possibility of multiple equivalent layouts with the same overall volume. The presence of these regions was noted by Maxwell (1870) and therefore optimal structures consisting only of type  $S$  regions are sometimes referred to as Maxwell trusses (Prager, 1978b).

Regions of type  $T$  contain two mutually orthogonal sets of members, one set in compression and one set in tension. As these regions made up the majority of the early solutions that were identified, it was often stated (Parkes, 1965; Hemp, 1973) that orthogonality of adjoining compression and tension members is a general characteristic of a minimum weight structure. This was shown to be somewhat inaccurate by Rozvany (1996), who demonstrated that the corrected statement is "If a pair of tension and compression members *cross* each other, they must be orthogonal... No other members can be coplanar with them".

Chan (1960) restricted his attention to  $T$  regions and went on to introduce three special cases of coordinate parametrisation, as shown in Figure 2.3. These special cases are

- Type 1, TWO SETS OF CURVES WITH NO INFLEXIONS parametrised by setting  $\alpha$  and  $\beta$  as equal to the angle turned through by two axis lines from some origin. These will be herein referred to as type  $T_1$ .
- Type 2, ONE SET OF CURVED LINES, ONE SET OF STRAIGHT LINES parametrised by the angle turned through by the curved lines, and the distance along the straight lines from some origin. Herein referred to as  $T_2$ .
- Type 3, TWO SETS OF STRAIGHT LINES parametrised by the distance along the line in each direction from some origin. Herein referred to as  $T_3$ .

These cases cover most  $T$  regions in solutions known to date; some examples are shown in Figure 2.4.

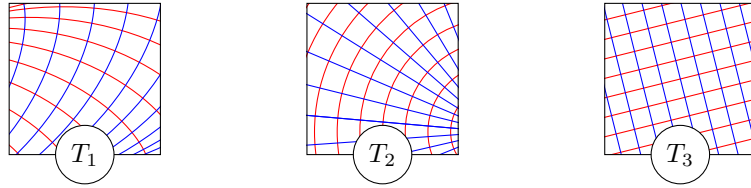


Figure 2.3: Regions of types  $T_1$ ,  $T_2$  and  $T_3$ .

**Construction of potential layouts** Identification of a solution for a given problem is very challenging. Therefore most solutions in the literature begin by assuming a given layout of regions and then define the applied forces for which these regions are valid. This process is very much the opposite of that used in practical structural design. Ghista & Resnikoff (1968) divided problems into smaller sections that may have known solutions; a similar approach was used to propose initial solutions by Rozvany et al. (1993a). Within a known strain field, Cox (1965) noted that a system of any number of loads may be added, requiring only that they observe the requirement for tension and compression in appropriate members and overall static equilibrium.

Prager & Hodge (1951) outlined the construction of Hencky-Prandtl nets in the context of plastic flow, including a graphical method by which an approximation to a net may be found from two intersecting shear lines, producing an approximation consisting of arc segments. Parkes (1965) provided a simpler construction method, using straight segments; this method would require a smaller step size ( $15^\circ$  is suggested) than Prager's to ensure accuracy, however construction is considerably simpler. This results in the angles at each joint throughout the structure being kept constant.

Mathematically, the geometric definition of a region usually begins by defining a function  $\phi(\alpha, \beta)$  representing the inclination of the co-ordinate lines.  $\alpha$  and  $\beta$  are the coordinates of a point, in a local curvilinear coordinate system, as for a Henky-Prandtl net. Two other positive functions of  $\alpha$  and  $\beta$  are also defined, often referred to as  $A$  and  $B$ , which define the radii of curvature of each line at a point (Chan, 1960). These are sometimes known as the Lamé coefficients (Lamé, 1859; Lewiński et al., 1994a). These functions can be used to give differential equations defining the deflections of points, relative to the imposed strains and rotations (Love, 1920; Chan, 1960). The compatibility of adjoining regions and the imposed boundary conditions can then be checked, and the deflections and required member thicknesses can be calculated. A more detailed description of this process may be found in Lewiński et al. (2019).

Ewing (1967) developed a computational method of calculating Hencky-Prandtl net layouts to arbitrary precision by expanding the functions  $A$ ,  $B$  as a double power series. The geometric implications of this were studied by Hill (1967) and Collins (1968). Dewhurst & Collins (1973) later extended this to a matrix based technique, allowing matrix inversion to be used to find power series coefficients for indirect problems.

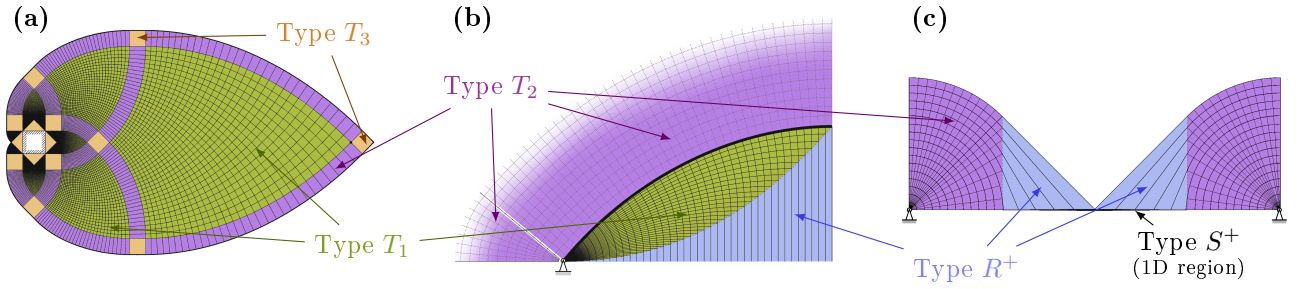


**Figure 2.4:** A selection of known Michell structures, colour added according to the different region types.

(a) Structure supported on a square shaped line support, based on a figure of Lewiński & Rozvany (2008b, reused with permission). (b) Hemp's arch with vertical hangers for a distributed load between pinned supports, including regions outside the structure itself, based on a figure of Pichugin et al. (2012, reused with permission). (c) Structure supporting a uniform load over multiple spans, based on a figure of Pichugin et al. (2015, used under CC BY 4.0)

### Known analytical solutions for classical Michell trusses

This section briefly outlines known analytical results for minimum volume structures; several of these are compared numerically in Appendix A. It is shown that the  $T$  type regions in these results can be considered to fall into the categories  $T_1$ ,  $T_2$  and  $T_3$  as described above. Although over a century has elapsed since Michell's seminal paper, only a handful of solutions have been obtained.

Michell (1904) proposed solutions for several classic examples, including a region of equiangular spirals extending from a circular support (type  $T_1$ ). Additionally, solutions to the problem of three equally spaced parallel forces (i.e. a simply supported point load) were considered, and solutions obtained for both the full plane and the half plane. These solutions contain regions of Cartesian members (type  $T_3$ ), and regions with straight radial members and curved members forming circular arcs (a degenerate case of type  $T_2$ ). A variation of this problem requires the addition of regions of type  $S^-$  (Michell, 1904, Figure 4).

Chan (1960) considered the design of a cantilever. In addition to the type  $T_3$  and degenerate  $T_2$  fan regions of Michell (1904), this includes a region of type  $T_1$  that is bounded by two circular arcs. This solution, in the context of plastic slip lines was also given by Hill (1950). Chan (1963) further developed this by the addition of a region of type  $T_2$ , extending from the outer limit of the solution of Chan (1960), and followed by another region of type  $T_1$ . This field was extended in a similar manner to the whole plane in Hemp (1973, figure 4.19). Solutions to additional three force cantilever problems were found by Sokół & Lewiński (2010), these are also used to construct solutions to spanning problems supporting multiple point loads (Lewiński et al., 2019).

Solutions for problems with a limited design domain were considered by Chan (1967) and Hemp (1976), who produced solutions for three force problems lying within a half plane. A more restricted domain was considered by Prager & Hodge (1951) who gave a slip line solution for the shearing of two parallel plates, consisting of two families of cycloids (a region of type  $T_1$ ). Hemp (1973) uses this field for the design of a long cantilever with an unusual loading regime. Long cantilevers with more standard loading were considered by Lewiński et al. (1994a,b), consisting of multiple regions of type  $T_1$ . These solutions have been numerically shown to tend towards the cycloid solution when far from the supports by Dewhurst (2001), who also proposed an alternative support case that would require the purely cycloidal solution. Graczykowski & Lewiński (2006a,b, 2007) consider the case where the design domain has non-parallel sides, resulting in a solution of similar form.

A wider variety of polygonal supports and design domains have been considered by Lewiński & Rozvany (2007, 2008b,a). In Lewiński & Rozvany (2008a) further regions with restrictive design domains have been developed, with subsequent refinement by Lewiński et al. (2013). In both cases, forms similar to those in Lewiński et al. (1994b) are identified. Lewiński & Rozvany (2007, 2008b) focus on the identification of layouts covering an unrestricted domain, supported by polygonal forms. These are similar to the whole plane field for two point supports illustrated by Hemp (1973, figure 4.19) in that each region of type  $T_2$  is bordered on opposite edges by a pair of regions of type  $T_3$  and a pair of regions of type  $T_1$ , as shown in Figure 2.4a.

Problems requiring the support of distributed loads were first considered by Hemp (1974). His proposed solution was later shown to be optimal for a non-uniform load distribution (Chan, 1975) and unequal tension and compression strengths (Pichugin et al., 2012). This single span solution is shown in Figure 2.4b. For a multiple span structure lying above the line of application of loads the optimal solution has been identified by Pichugin et al. (2015), and is shown in Figure 2.4c. Unusually in the literature this includes a region of type  $R$ , and a degenerate 1D region of type  $S$ . A related solution for the case where the whole plane is considered as the design domain has been proposed by Beghini & Baker (2015).

### 2.1.2 Extensions of Michell's theory

**Further applications of the theory** It was previously noted that the forms of minimum weight structural layouts correspond to those of slip lines in plastic flow; one of the most important applications of this in building design scenarios is the solution of geotechnical problems (Smith & Gilbert, 2007). The kinematic criteria for yield line analysis of slabs also implies an analogous result (Schumann, 1958).

Within the field of structural design, Hegemier & Prager (1969) show that the minimum volume layout is also optimal for a range of other problems in structural design, including the maximisation of stiffness in either the elastic range or in stationary creep (for a constant volume), and the minimisation of the volume for a given fundamental frequency (assuming that the mass of structure is negligible compared to the masses that must be supported).

The optimal design of pure bending structures, known as grillages, is another related problem, whereby the optimal solution consists of a grillage-like continua consisting of regions of type  $R$ ,  $S$  and  $T$  (Prager & Rozvany, 1977). The forms observed in typical solutions are significantly different to the common Hencky-Prandtl nets in truss design, and often consist of polygonal regions that lend themselves more easily to automatic construction, e.g. by computer (Hill & Rozvany, 1985).

**Three dimensions** Although one example of an optimal structure in 3D (the so-called Michell sphere) was given by Michell (1904), few other examples have been identified since, and the theory behind them is far less developed than for the plane case.

Cox (1965) divides the possible values of the 3D principal strains, into two classes. The first has values  $\frac{1}{\sigma_T}, -\frac{1}{\sigma_C}$  and 0, and takes the form of orthogonal curves lying on some surface (e.g. the Michell sphere) or a series of plane frameworks arrayed linearly or cylindrically. The second type proposed by Cox (1965) has principal strains  $\frac{1}{\sigma_T}, \frac{1}{\sigma_T}$  and  $-\frac{1}{\sigma_C}$  (or  $-\frac{1}{\sigma_C}, -\frac{1}{\sigma_C}$  and  $\frac{1}{\sigma_T}$ ), implying a system of surfaces in uniform tension (resp. compression), orthogonal to a series of curved linear members in compression (resp. tension).

Results available in the literature generally take the form of orthogonal curves lying on a surface; for example Lewiński (2004) produces results analogous to the Michell sphere but restricted to lie on cones or cylinders. Jacot & Mueller (2017) provide a more general formulation and thereby identify novel solutions to a 3D cantilever problem; again these take the form of orthogonally fibrous surfaces, as the intermediate strain is assumed to be zero.

Solutions for axisymmetric problems can often be found by rotating a planar structure around an axis. In many cases this results in a circumferential strain that is less than the limiting value, and therefore no circumferential bars are required (Lewiński et al., 2019, sect. 5.1). Similarly, it is possible to produce one-way spanning structures by replicating a series of planar trusses. Both of these cases still fall into the first of the categories considered by Cox (1965).

**Multiple load cases** For a single load case, there should always be at least one statically determinate optimal structure (Fleron, 1964 as reported by Topping, 1983). Any statically determinate solution for plastic limit design is also a feasible solution for elastic design (Hemp, 1966). In such cases the virtual deflections that are referred to in the Michell-Hemp criteria will be proportional to a permissible real strain field (Hemp, 1973). In other words, for a single load case problem, the optimal layout is the same for elastic or plastic design.

However, when multiple load cases are imposed, the structures resulting from plastic design are normally statically indeterminate (Chan, 1964); therefore plastic designs will differ from elastic designs. Most attention in the literature has been devoted to plastic design due to the relative simplicity of the calculations involved.

When only two load cases are considered, the optimal plastic solution may be found by use of a superposition principle developed by Spillers & Lev (1971) and Nagtegaal & Prager (1973). In this, two related load cases (found by taking half of the sum and difference of the original load cases) are solved; the optimal solutions can then be combined to give the minimum weight structure for the original multiple load case problem. Examples of these superimposed designs are shown in Figure 2.5a and 2.5b. This principle has been extended to more than two loading cases by Rozvany & Hill (1978), although this applies only to a limited range of circumstances. However, later numerical results do seem to suggest that a similar ‘multi-layered lamina’ form is prevalent in a wider range of multiple load case problems; examples may be seen in 2.5c and in Sokół & Rozvany (2013b).

The elastic design problem generally considers some combination of stress and/or displacement constraints. Chern & Prager (1972) considered simple three bar trusses subjected to stress constraints, and found that optimal truss were usually statically determinate, i.e. that one of the bars had zero area. These so called ‘singular’ solutions can cause substantial difficulties in identifying optimal solutions (Rozvany & Birker, 1994) and have been the subject of much investigation (Sved & Ginos, 1968; Nagtegaal, 1973a; Kirsch, 1990).

Displacement constraints were considered by Prager & Shield (1968), and applied to truss design by Rozvany (1992). As with the stress constraints, statically determinate structures were found to be optimal for the problem under consideration. However, solutions identified under displacement constraints and under stress constraints

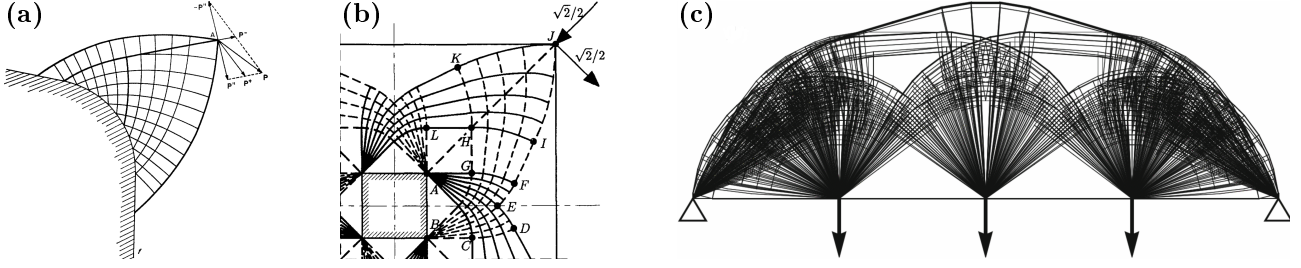


**Figure 2.5:** Minimum volume plastic designs for multiple load case problems. (a) and (b) analytical solutions for two load cases using the superposition principle. From Nagtegaal & Prager (1973, used with permission) and Rozvany (1998, used with permission) respectively. (c) Numerical result for three load cases from Lewiński et al. (2019, used with permission), showing a multi-layered structure.

are not identical. Rozvany et al. (1993b) and Rozvany & Birker (1994) consider the same problem under displacement and stress constraints respectively, with different optimal layouts being identified.

Multiple load case problems have also been considered with explicit inclusion of bending. Prager & Shield (1968) treated the design of a beam that must resist (separately) bending and axial load. Nagtegaal (1973b) generalised the plastic superposition principle to include sandwich beams and frames.

**Design dependent loading and self-weight** In many practical problems, a portion of the loading that the structure must support depends on the material distribution of the chosen design. The most common example of this is that structures must carry their own weight; other design dependent loads include external loads such as snow, which will be imposed on the upper surface of a roof, whatever height that may be.

A specific class of arch grid type structures with external loads that may vary in their point of application have been studied by Rozvany & Prager (1979); these were later referred to as Prager structures (Rozvany et al., 1982) and have the additional restriction that all stresses should be of one sense (Rozvany & Wang, 1983). For a system of parallel arches, this method identifies a parabolic arch; this is the correct optimum structure only when the structural material can support only compressive stresses. It was later shown (Darwich et al., 2010; Tyas et al., 2011) that when both tensile and compressive forces are possible, the true optimum is more complex.

The inclusion of self-weight is one of the most critical applications of design dependent loading. Rozvany (1977) extends the Prager-Shield optimality criteria to include self-weight to give

$$\mathbf{u}^K = (1 + u_k^K) \mathcal{G}(\mathcal{C}(\mathbf{q}^S)) \quad (2.4)$$

where  $\mathbf{u}^K$  a kinematically admissible strain field,  $\mathbf{q}^S$  a statically admissible stress field,  $\mathcal{C}$  the cost function and  $\mathcal{G}$  the subgradient function and  $u_k^K$  the vertical deflection. Compare this to equation (2.3). Wang & Rozvany (1983) apply this self-weight formulation to the design of Prager structures, producing funicular forms for various combinations of external and self-weight loading.

**Discretised optimal trusses** Pure Michell trusses are impractical for construction as they typically consist of a continuum of members. To address this, several workers have suggested the use of additional costs relating to the material volume or expense of forming a joint. Parkes (1975) suggests that such a cost should be proportional to the thickness of the bars connected to the joint; by assuming a topology similar to that of the known Michell structure, he demonstrated that a close approximation of the absolute minimum volume can be found using structures with as few as 7 joints. However, this approach disproportionately penalises shorter members, and as such it may not always be effective.

Prager (1977) suggests that the cost per joint should be constant, regardless of the number or dimensions of the members connected there. As in the method of Parkes (1975), minimum weight structures with given numbers of joints are first identified, and the ranges of joint costs for which they are optimal are later found. Prager (1977) identifies discretised optimal structures by making use of Maxwell’s reciprocal diagrams, and the self-adjoint nature of optimal trusses.

Prager (1978b) provides an alternative theory underpinning the optimization of trusses with discrete members. A small increase in volume over the absolute minimum is permitted, and a strain state is sought that has a maximum strain correspondingly slightly over the original value. This strain field is mesh-wise constant, i.e. produces equal strains in all non-vanishing bars of the mesh. Through use of the circle of relative displacements (analogous to Mohr’s circle in plastic plane strain), geometric rules governing the angles at every joint are found.

### 2.1.3 Minimum weight continuum structures

It has been recognised from as early as Cox (1965) that the basis for the Michell-Hemp criteria is not consistent with solid construction from an isotropic material. Cox (1965) mentions that an isotropic material could carry tension and compression within the same region of material, and that the permitted value of shear stress may also be limiting. Similarly, Prager (1978b) states that the classical solution for the Michell sphere is equivalent to a shell where the maximum shear stress is double the maximum axial stress of the fibrous material.

Sigmund et al. (2016) significantly expand on this principle, noting that the stiffness of an optimal perforated or variable thickness plate structure approaches that of the Michell structure only as the volume fraction approaches zero. For higher volume fractions, variable thickness plates or shells are preferred.

However, it is the aim of the present thesis to address the requirements of structural engineers, who generally tackle problems where a very small volume fraction is required (in the region of 1%, Baandrup et al., 2019). Furthermore, such structures are often constructed using pinned joints, as it is desirable for logistical purposes that they may be transported in smaller pieces. Thus the focus here will remain on frames, trusses and truss-like continua. However, the analytical methods described in this section are unlikely to be well suited to engineering practice. Therefore, Section 2.3 will focus on numerical methods for identifying optimal skeletal structures. The necessary mathematical background to this is outlined in the next Section, 2.2.

## 2.2 An overview of mathematical optimization

### 2.2.1 General optimization concepts

A very general statement of a mathematical optimization problem can be formulated (Boyd & Vandenberghe, 2004) as

$$\text{minimise } f_0(\mathbf{x}) \tag{2.5a}$$

$$\text{subject to } f_i(\mathbf{x}) \geq b_i, \quad i = 1, \dots, m \tag{2.5b}$$

where  $\mathbf{x} = [x_1, x_2, \dots, x_n]$  is a vector containing the optimization variables, the function  $f_0 : \mathbb{R}^n \rightarrow \mathbb{R}$  is the objective function,  $f_i : \mathbb{R}^n \rightarrow \mathbb{R}$  are the constraint functions and  $b_i$  is the bound for the constraint  $i$ .

A point, represented by  $\mathbf{x}$  is *feasible* if  $f_i(\mathbf{x}) \leq b_i$  for all constraints  $i$ . If there are no feasible values of  $\mathbf{x}$  then the problem is often said to be infeasible.

**Convexity** An optimization problem is called convex if all the functions  $f_0, f_1, \dots, f_n$  in equation (2.5) are convex functions. A function  $f$  is defined as convex (Boyd & Vandenberghe, 2004) if

$$f(\alpha\mathbf{x} + \beta\mathbf{\hat{x}}) \leq \alpha f(\mathbf{x}) + \beta f(\mathbf{\hat{x}}) \quad \forall \quad \mathbf{x}, \mathbf{\hat{x}} \in \mathbb{R}^n, \quad \alpha + \beta = 1, \quad \alpha, \beta \geq 0 \tag{2.6}$$

This is illustrated graphically in Figure 2.6a-b.

Convexity is also a property of some sets; in a convex set, a line segment between any two points is contained within the set, as in Figure 2.6c. Note that the set of points above the plot of a convex function is a convex set, and the set of points above a non-convex function is a non-convex set.

**Global and local optima** A local optimum of an optimization problem is a point that has a lower value of the objective function than all feasible neighbouring points; optima for minimising the functions in Figures 2.6a-b are marked with red crosses. If a local optimum is also the minimum value for the function over the whole of the domain then that point is also the global optimum, as shown in Figure 2.6a.

In convex optimization, any local optimum will also be the global optimum. This makes convex problems significantly easier to solve and eliminates any uncertainty as to the quality of the solution. Note that there may still be multiple solutions that have an equally optimal value; these will form another convex set, although many algorithms will return only a single one of these results.

### 2.2.2 Linear Programming

Linear programming (LP) is the most prominent technique in the field of operations research (Taha, 2007), this is due to the availability of rapid and robust solution algorithms that can find the globally optimal solution. A problem is said to be linear if all functions  $f$  in equation (2.5) are linear in the optimization variables. All linear programming problems are convex, and they are often most conveniently written using matrix notation.



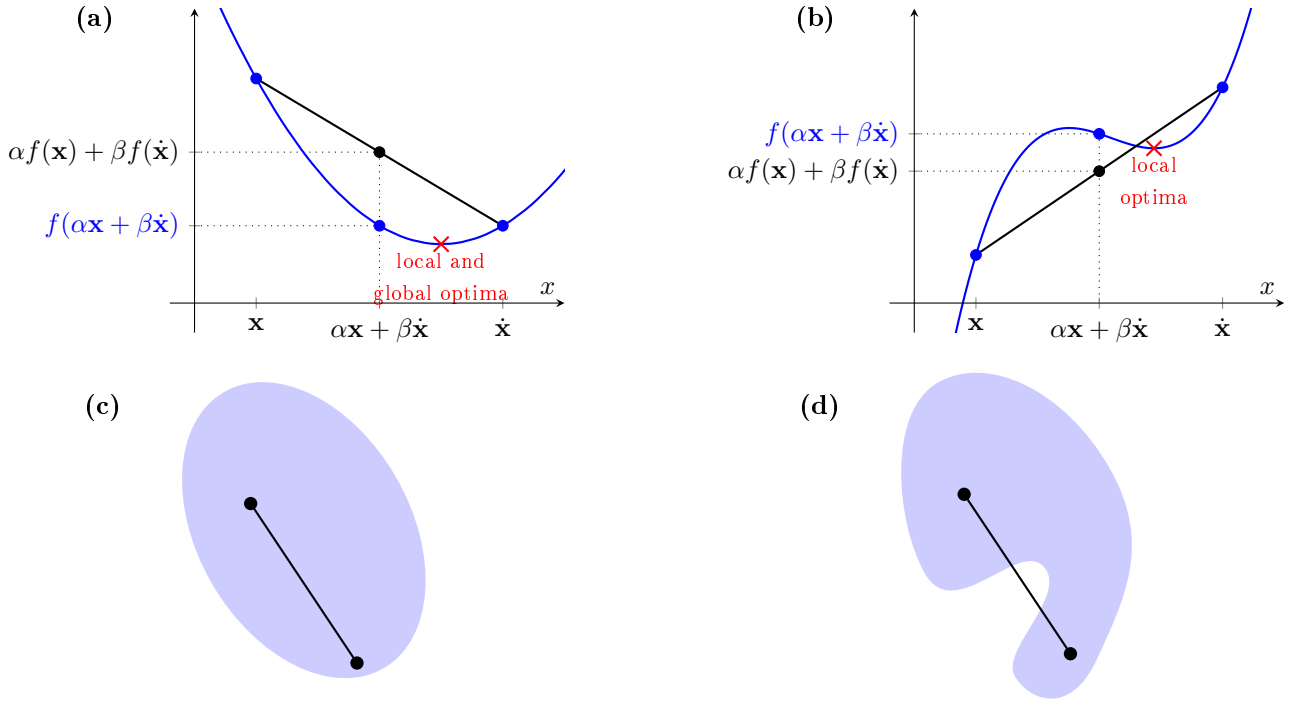


**Figure 2.6:** Convex and non-convex functions and sets. (a) A convex (quadratic) function, global optimum of  $\min_x f(x)$  shown. (b) A non-convex (cubic) function, a local optimum of  $\min_x f(x)$  is shown, the global optimum is unbounded as  $x \rightarrow -\infty$ . (c) A convex set. (d) A non-convex set.

Several variants what constitutes the ‘standard’ or ‘canonical’ form of a linear program have been proposed by different authors. For example, Vanderbei (2001) uses

$$\text{maximise } \mathbf{c}^T \mathbf{x} \quad (2.7a)$$

$$\text{subject to } \mathbf{A} \mathbf{x} \leq \mathbf{b} \quad (2.7b)$$

$$\mathbf{x} \geq \mathbf{0} \quad (2.7c)$$

where  $\mathbf{x}$  is a vector containing the optimization variables,  $\mathbf{c}$  contains the objective coefficients,  $\mathbf{A}$  the coefficients for the constraints, and  $\mathbf{b} = [b_1, b_2, \dots, b_m]^T$  are the constant parts of the constraints.

**Solution spaces** A set of linear constraints over 2 optimization variables  $x_1, x_2$  defines a polygonal region as shown in Figure 2.7a this known as the feasible region or solution space (in this thesis, the term solution space is preferred to avoid ambiguity with the physical space allowed for a structure). Each constraint of the problem defines an edge of the polygon, and vertices are formed at the intersection of two (or more) edges. For three optimization variables, the solution space becomes a polyhedron, with each constraint forming a face, Figure 2.7b. For larger numbers of variables, the solution space is referred to as a polytope, where each constraint forms a hyperplane where the corresponding slack variable (or variable, for non-negativity constraints) is equal to 0.

Any point within the solution space defines a feasible solution to the problem, of which there are an infinite number. Vertices of the solution space represent what are known as basic feasible solutions; these are finite in number and any non-basic feasible solution can be expressed as a convex combination of two or more basic feasible solutions. Normally, the optimal solution to a problem will be a basic feasible solution, although it is also possible for multiple basic solutions to have the same, optimal objective value, in which case any convex combination of these solutions will also be equally optimal. Intersections of constraint planes outside the solution space form basic non-feasible solutions.

Usually, a vertex of a 2D solution space is formed by the intersection of 2 lines; in 3D solution space by the intersection of 3 planes and in  $nd$  solution space by the intersection of  $n$  hyperplanes. It is sometimes convenient to identify a basic solution using the the variables/slack variables associated with these hyperplanes, these are known as *non-basic variables* and must be equal to zero.

The remaining variables are then known as *basic variables*, which are generally non-zero. However, it may be the case that one or more basic variables are found to be equal to zero; this is referred to as a degenerate

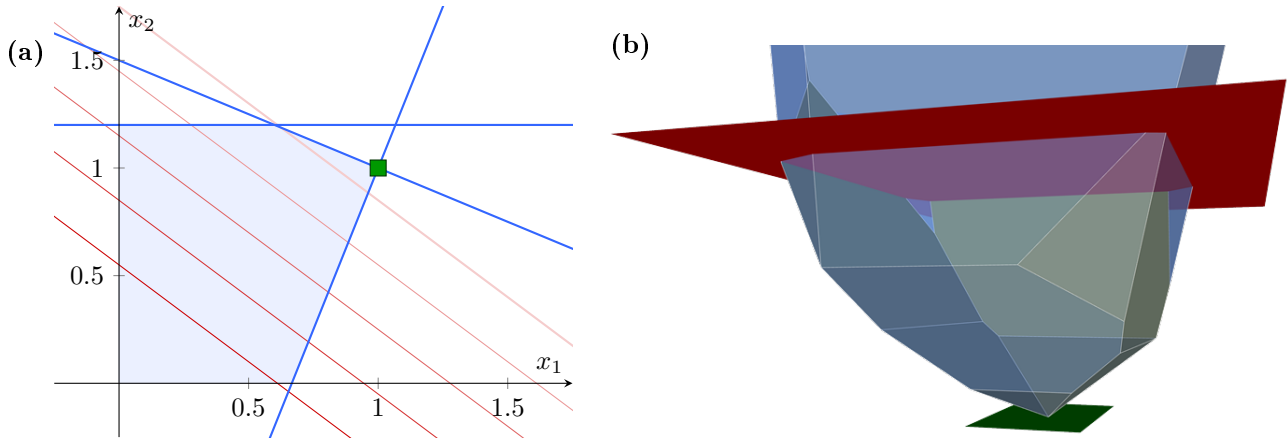


**Figure 2.7:** Examples of solution spaces of linear programming problems with (a) two or (b) three variables. Solution spaces, and bounding constraints shown in blue. Optimal value shown in green, and lines/planes of constant objective value shown in red (lighter showing more optimal values).

solution. Graphically, this corresponds to 3 or more lines intersecting in 2D or 4 or more planes intersecting in 3D. This can cause significant challenges for some algorithms.

### Duality

For every linear problem (known as the primal problem), an associated problem called the dual can be defined. This is stated as

$$\text{minimise } \mathbf{b}^T \mathbf{y} \quad (2.8a)$$

$$\text{subject to } \mathbf{A}^T \mathbf{y} \geq \mathbf{c} \quad (2.8b)$$

$$\mathbf{y} \geq \mathbf{0} \quad (2.8c)$$

where  $\mathbf{b}$ ,  $\mathbf{A}$  and  $\mathbf{c}$  are as given for the primal problem in equation (2.7), and  $\mathbf{y}$  is the vector containing the dual optimization variables. Note that each variable in the primal problem implies a constraint in the dual problem, and vice versa.

The strong duality theorem states that the optimal solution of the primal problem is equal to the optimal solution of the dual problem. For linear problems, this holds in all cases where an optimal solution exists (Vanderbei, 2001).

### Algorithms

**The simplex algorithm** The simplex algorithm was proposed by Dantzig (1949), and solves a linear programming problem by moving between basic solutions (pivoting), with each pivot improving the value of the objective function. Once no more pivots that improve the objective value are possible, the current basic solution must be optimal. Note that the solution identified by this method will always be basic, and if multiple basic solutions are equally optimal any may be returned depending on the heuristics used to choose the route through the solution space.

Later developments to the method have improved the behaviour of the algorithm when faced with degenerate problems (Bland, 1977; Perold, 1980), improved the choice of pivots (Goldfarb & Reid, 1977), leading to quicker convergence or to allowed the algorithm to operate over both the primal and dual problems (Dantzig et al., 1956; Forrest & Goldfarb, 1992). However, the Simplex algorithm is still exponential in problem size (Taha, 2007), therefore the interior point algorithm is preferred for very large problems.

**Interior point algorithm** The interior point algorithm differs from the simplex algorithm in that it moves through the interior of the solution space; it is preferred for very large problems as its computational difficulty is polynomial in problem size. The method was proposed by Karmarkar (1984), and simplified somewhat by Gill et al. (1986).

The algorithm moves through the interior of the solution space, with the distance from the boundary generally reducing at each iteration as the barrier function is reduced. When the barrier function is sufficiently small, the solution approaches an optimum for the original problem.

The output of this algorithm differs from that of the simplex algorithm when multiple optima are present. The interior point algorithm will generally produce a convex combination of the different optimal basic solutions, in roughly equal proportions. Methods have been developed to identify a basic solution based on the solution from the interior point method (e.g. Bixby & Saltzman, 1994), and this feature is now available in the major commercial codes (Gurobi Optimization, LLC, 2018; IBM Corp., 2015; Fair Isacc Corp., 2018).

### 2.2.3 Non-linear programming

Non-linear programming (NLP) refers to the more general case of equation (2.5), where the constraints and objective function are formed of non-linear functions. The interior point algorithm, as described above, is often used to attempt to solve these problems. This is a local optimization algorithm, and it is probable that a local optimum may be identified if the problem is non-convex and the starting point has not been appropriately chosen.

Global optimization methods that can deterministically find global optima for non-convex problems are available only for certain classes of problems, and are generally very computationally expensive (Horst & Tuy, 1995). In many practical scenarios, these rigorous methods have fallen out of use and been largely replaced with meta-heuristic methods (see Section 2.2.5). Optimization with discrete variables is one case where deterministic methods are still fairly common, see Section 2.2.4.

Convex optimization problems avoid the issue of local optima, allowing the interior point method to be used to identify the globally optimal value. A wide range of formulations can be shown to be convex, including several variations of conic optimization (Mosek ApS, 2019). These problems are substantially easier to solve than the general case; Boyd & Vandenberghe (2004) claim that by formulating a problem as a convex problem, one has essentially solved the problem.

### 2.2.4 Discrete Optimization

Discrete optimization refers to any optimization problem where one or more variables are restricted to a discrete set of possible values. Most commonly the variables will be restricted to integer values  $\mathbb{N}$ , giving rise to the term integer programming (IP), or mixed integer programming (MIP) for problems where some variables may take continuous values (Taha, 1975).

MIP may be used in conjunction with many classes of optimization problems, some of the most common non-linear types are mixed integer second order cone (MISOCP), mixed integer quadratic (MIQP) and mixed integer quadratically constrained (MIQCP). However, mixed integer linear programming (MILP) is the most common form. The algorithms for these problems generally require the solution of multiple relaxations of the problem (i.e. problems with the integer constraints removed); the underlying convexity or otherwise of the problem is crucial in determining whether globally optimal solutions can be obtained.

MIP may be used to model a wide range of phenomena, Taha (2007) classifies these as *direct* applications, for quantities that are inherently integer, or *transformed* where an auxiliary integer variable is used to represent constraints that could not otherwise be represented, such as *either-or* and *if-then* constraints. This flexibility, combined with algorithms that are capable of finding global optima, has led to the development of many commercially available solvers including Gurobi (Gurobi Optimization, LLC, 2018), CPLEX (IBM Corp., 2015) and Xpress (Fair Isacc Corp., 2018).

## Algorithms

The two main solution algorithm types for solving problems with integer constraints are branch and bound algorithms and cutting plane algorithms. Many commercial solvers use a mixture of the two strategies, with an overall branch and bound structure but incorporating some cutting planes within sub-problems (Gurobi Optimization, LLC, 2018; IBM Corp., 2015).

**Branch and bound algorithm** Branch and bound type algorithms are applicable to a large array of discrete problems; it will here be discussed in the context of mixed integer programming. The method was first proposed by Land & Doig (1960), who applied it to MILP problems. However, note that any mixed integer programming problem may be solved to global optimality by this method providing that its continuous relaxation is convex.

The algorithm begins by solving the continuous relaxation of the problem; this provides an upper (here a maximisation problem is assumed) bound on the optimal value. One variable that has a fractional value in the relaxation solution, but must be an integer in the original problem, is chosen for branching. Two new sub-problems are generated, one limits the chosen variable to be less than or equal to the integer below its relaxed value, and the other limits the variable to be greater than or equal to the integer above its relaxed value.

The procedure is then repeated on a sub-problem, choosing a different branching variable each time. Once a solution satisfying all integer requirements is found, that branch is referred to as being fathomed, and the solution becomes a lower bound (again, assuming a maximisation problem) on the optimal value if it is better than the incumbent lower bound solution.

**Cutting plane algorithm** A cutting plane is an additional constraint that is added to the linear relaxation of a problem, removing some non-integer solutions but keeping all integer solutions feasible. To solve a problem in this way, cuts must be added until the solution of the relaxed problem satisfies the integrality constraints. One of the earliest practical cut generation methods for mixed problems was due to Gomory (1960), but many other methods have been proposed since (Taha, 1975). The cutting plane algorithm is generally inferior, in terms of performance, to the branch and bound algorithm (Taha, 2007). However, cutting planes are still often used to improve the solutions of sub-problems in the branch and bound method.

Modern solvers are capable of generating many types of cuts (Gurobi Optimization, LLC, 2018; IBM Corp., 2015). Additionally, commercial solvers have the capability to take cutting planes generated by the user from problem specific heuristics or knowledge, often during the solution process.

**Lazy constraints** A feature related to that of the user-provided cut, is the idea of so-called lazy constraints. These differ from cutting planes as they may exclude some otherwise feasible integer solutions. They may be entirely generated before the solver commences, and simply stored and checked each time a new (currently) feasible integer solution is found. However, it is often much simpler to check if a given solution violates any constraint than to generate all potential constraints. Therefore it is also possible to generate lazy constraints during the solution process

The classic problem to demonstrate this principle is the travelling salesman problem. To fully formulate this problem as an MIP, an exponential number of constraints to eliminate sub-tours would be required (one for every sub-set, of any size, of the cities to be visited). However, checking if a solution contains sub-tours is significantly easier and very good performance is therefore seen if subtour constraints are added only when that sub-tour appears in a candidate solution (Dantzig et al., 1954).

### 2.2.5 Meta-heuristic methods

The field of meta-heuristic algorithms for optimization comprises a vast number of methodologies; these are typically based on real world processes, rather than strict mathematical reasoning (Yang, 2010). In many cases, there is no guarantee that the solution found will be even a local optimum. This may not be crucial for practical application however, as it is likely to be preferable to find a lower volume solution (e.g. a non-optimal point that is near the global minimum) than a local optimum point, which may have a higher volume.

Meta-heuristics are also popular in practice due to their versatility, as they can usually handle arbitrary functions. It may not be possible to explicitly write these functions; they may consist of outputs from simulations or finite element analysis. However, the ‘no free lunch’ theorems, proven by Wolpert & Macready (1997), show that there cannot be a universally efficient algorithm, but that incorporating problem specific knowledge in the algorithm provides an important advantage.

Some of the most common meta-heuristic methods are

- **GENETIC ALGORITHMS** (Holland, 1992), are based on the theory of evolution, with possible solutions described using a genome. At each generation, a population of possible solutions is generated by combining the fittest of the previous generation. Mutation is used to mitigate the risk of local optima.
- **SIMULATED ANNEALING** (Kirkpatrick et al., 1983), moves through a solution space by moving from the current point to a nearby point, modelling the cooling of a material. Initially the ‘temperature’ is high, and it is likely that a move will be accepted whether it improves or worsens the objective function. Gradually, the temperature reduces and it becomes less likely that detrimental moves will be accepted.
- **PARTICLE SWARM OPTIMIZATION** (Kennedy & Eberhart, 1995) is based on a number of agents, each with a position within the solution space and a velocity. They move towards their individual, and the overall best known positions, moderated by the inertia of their current velocity. Other swarm intelligence methods have been inspired by bees, ants, fireflies and many other creatures.

Many of these methods have a large number of parameters that should be tuned for best results (e.g. population sizes, cooling rates, inertia levels) often this must be done by trial and error. Additionally, many methods are stochastic in nature, relying on random values for starting points, mutation or moves through the solution space. Therefore the algorithms produce different results each time, and multiple runs may be required.

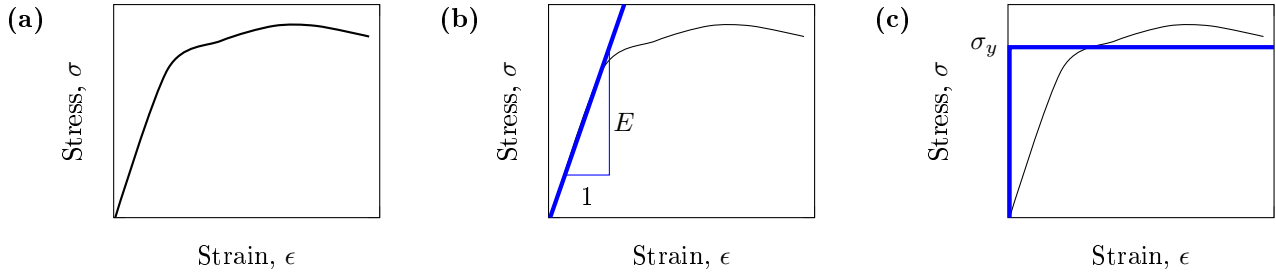


**Figure 2.8:** Stress-strain curves. (a) A stress-strain curve for a ductile material. (b) An elastic stress-strain relationship. (c) A rigid-plastic stress-strain relationship.

## 2.3 Numerical structural optimization methods

### 2.3.1 Categories of structural optimization

The field of structural optimization may be divided into categories based on several different parameters.

#### Scope of problem

Structural optimization problems may be categorised as size, shape or topology optimization problems (Bendsoe & Sigmund, 2004). Size optimization consists of the identification of dimensions (e.g. member cross-section diameters or plate thickness) for a problem where the layout is already fixed. Shape optimization allows for the geometry of the problem (e.g. the locations of joints or holes) to be altered. Finally topology optimization allows for significant changes from the starting structure (if a starting structure is even required), including the addition of new holes or changes in the connectivity of the structure.

Topology optimization provides the potential for the most significant material savings as the most design freedom is permitted, however it also presents the most challenges in both accurate modelling of real world behaviour and the solving of the resulting optimization problems.

#### Structural modelling approach

**Elastic v.s. Plastic design** Various models of the stress-strain relationship for a given material may be assumed during the design process. The simplest is linear elasticity, in which  $\frac{\sigma}{\epsilon} = E$ , with  $\sigma$  and  $\epsilon$  the stress and strain at a point, and  $E$  the Young's modulus of the material (Benham et al., 1996). Most engineering materials approximately demonstrate this behaviour at a stress below  $\sigma_y$ , the yield stress (Figure 2.8a).

Once the yield stress is reached the behaviour changes, this is most simply modelled as a non-hardening plastic relationship, in which the stress remains constant as the strain increases. The strains that may be reached in this stage are generally much larger than those in the elastic region, therefore the rigid-plastic model may be assumed, in which the strains in the elastic region are neglected and a stress of  $\sigma_y$  is assumed for all non-zero strains. The use of plasticity can allow significantly higher loading to be carried by a structure, for example a beam with rectangular cross section may carry a moment 1.5 times larger when designed to utilise plasticity instead of just elasticity (Benham et al., 1996).

Both the pure elastic (Figure 2.8b) and the rigid-plastic (Figure 2.8c) approach have been frequently used in optimization methods, with more complex models such as elastoplasticity (Maute et al., 1998) being considered only occasionally. When elastic methods are employed, the problem is classically (Bendsoe & Sigmund, 2004) the minimisation of compliance subject to a limit on the volume of the structure (often reported as a percentage of the design domain and termed the volume fraction). In these formulations the restriction that the stress should be kept below  $\sigma_y$  is often neglected, although some methods are available to incorporate it (e.g. Duysinx & Bendsoe, 1998; Ohsaki, 2011). For plastic design, the problem is usually to minimise the volume of the structure subject to the limits on stress in the members.

When designing for minimum compliance it is possible to formulate the problem such that it is convex (Bendsoe et al., 1994), but this is only possible in cases where a non-zero lower bound is provided to ensure that the stiffness matrix is positive definite. Providing a non-zero lower bound is inconsistent with use for topology optimization, and restricts the applicability to sizing problems.

In the elastic formulation with stress constraints, the problem is non-convex, and the removal of the stress constraint for bars that are removed can cause significant difficulty (Nagtegaal, 1973a; Hansen & Vanderplaats, 1990). Iterative numerical methods are often required to obtain solutions, methods have been proposed by workers including Hansen & Vanderplaats (1990), Zhou & Rozvany (1991), Rozvany & Zhou (1991).

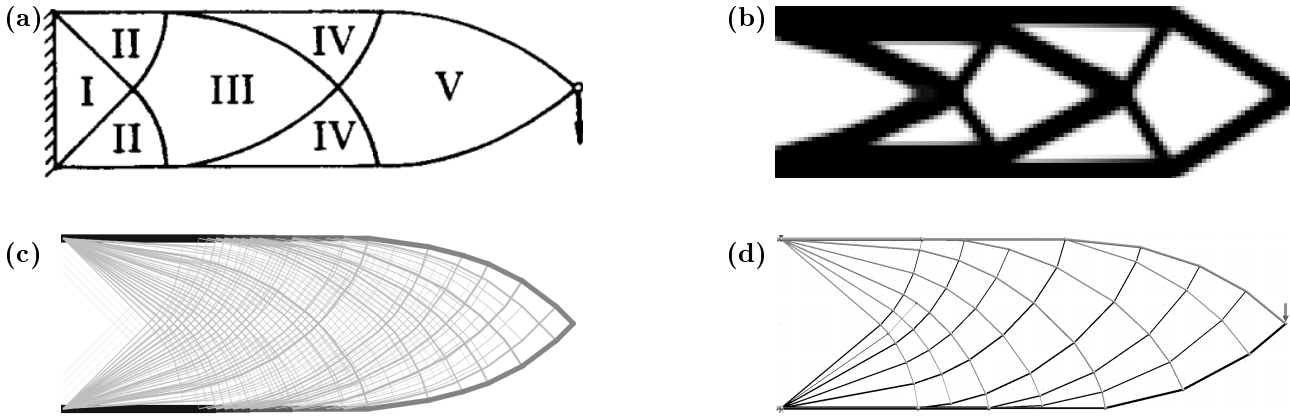


**Figure 2.9:** The solutions from analytical and numerical methods. (a) Analytical result presented as a small number of regions, from Lewiński et al. (1994a, used with permission). (b) Numerical result from density based continuum method, using the Matlab script of Sigmund (2001). (c) Numerical result from ground structure method, by Sokół (2011a, used under CC BC-NC 2.0). (d) Numerical result from growth type truss optimization method, using software by Martinez et al. (2007).

In this thesis, the rigid-plastic formulation is preferred due to the higher strengths that are available and the greater similarity between the optimization problem as typically posed and the current process of structural design.

**Discrete vs continuum representations** Two methods of modelling a material and design domain are relevant for the purposes of structural optimization. Both result in solutions comprising many individual components, without the overall structural insight of analytical results, see Figure 2.9.

The most popular approach is to consider the design domain as a continuum, in which each location may or may not have material assigned to it (Bendsøe, 1989). The leading method using a continuum representation is the Solid Isotropic Material with Penalisation (SIMP) method, shown in Figure 2.9b, in which ‘gray’ areas, of intermediate density, are penalised by use of a disproportionate decrease in stiffness (Bendsøe & Sigmund, 1999). The evolutionary structural optimization (ESO) method, developed by Xie & Steven (1993), is also popular due to its intuitive concept. At each stage, stresses are found using standard finite element analysis, then the elements with lowest utilization are removed.

The second method of modelling, which is perhaps more familiar to structural engineers in practice, is to consider the final structure to be assembled from a series of individual members. The topology optimization problem then becomes to identify the optimal sizes and connectivity of members and the locations of joints that connect them, early work in this area was reviewed by Topping (1983). The assumptions of these methods, such as the uniformity of axial stress distributions across the relatively slender members, match those common in structural engineering practice (Benham et al., 1996).

Most applications to these discrete trusses make use of ground structure type methods (Dorn et al., 1964; Chan, 1964), in which a large number of potential nodes and members are considered, and the optimal subset are assigned a non-zero area, an example result using this method is shown in Figure 2.9. Achtziger et al. (1992) give a number of formulations for elastic design within this framework, and demonstrates that alternative formulations may lead to more computationally efficient algorithms.

Alternative truss based methods have also been explored, such as methods that grow the structure from a very simple starting point (McKeown, 1998; Martinez et al., 2007), although these can be susceptible to local optima, e.g. see the asymmetry in the solution of Figure 2.9. To more directly seek Michell structures rather than directly minimising volume, Kwok et al. (2016) and Arora et al. (2019) propose methods, in 2D and 3D respectively, based on identifying principal stresses from a finite element solution. These are then used to align the truss members.

Continuum based methods have enjoyed much popularity, particularly in the fields of aerospace and automotive engineering, and even more so since the advent of additive manufacturing methods. However, for the purposes of structural engineering, the monolithic structures that are output would prove very challenging to build. Additionally, the typical structural design values for both the volume fractions and the sizes of members relative to the domain are far smaller than those for which continuum methods are ideal. Bendsøe & Haber (1993) showed that at such very low volume fractions, the continuum perforated plate problem tends towards the problem of Michell’s least weight trusses. For these reasons, the focus of this thesis will be on the use of truss based methods.

### 2.3.2 The layout optimization method and its extensions

When applied to truss or frame type structures, topology optimization is often referred to as layout optimization (LO). The classic formulation of the plastic layout optimization method was given by Dorn et al. (1964) and also in parallel by Chan (1964). This involves producing a densely connected ground structure, and then finding the optimal sub-set of members. These are found by solving a linear programming problem; by the use of duality principles, a pair of problems are defined. Today it is usual to consider the static formulation as the primal, this is stated for a single load case problem with  $n$  ground structure nodes and  $m$  potential members as

$$\text{minimise } V = \mathbf{c}^T \mathbf{q} \quad (2.9a)$$

$$\text{subject to } \mathbf{B}\mathbf{q} = \mathbf{f} \quad (2.9b)$$

$$\mathbf{q} \geq 0 \quad (2.9c)$$

where  $V$  is the total structural volume, the objective coefficients  $\mathbf{c} = [\frac{l_1}{\sigma_T}, \frac{l_1}{\sigma_C}, \frac{l_2}{\sigma_T}, \dots, \frac{l_m}{\sigma_C}]$  with  $l_i$  the length of member  $i$  and  $\sigma_T, \sigma_C$  the limiting stresses in tension and compression.  $\mathbf{q}$  is the vector of optimization variables, containing the tensile and compressive forces in each bar  $[q_1^T, q_1^C, q_2^T, \dots, q_m^C]^T$ . The  $2n \times 2m$  matrix  $\mathbf{B}$  contains suitable equilibrium coefficients and  $\mathbf{f} = [f_1^x, f_1^y, f_2^x, \dots, f_n^y]^T$  is the vector of externally applied forces.

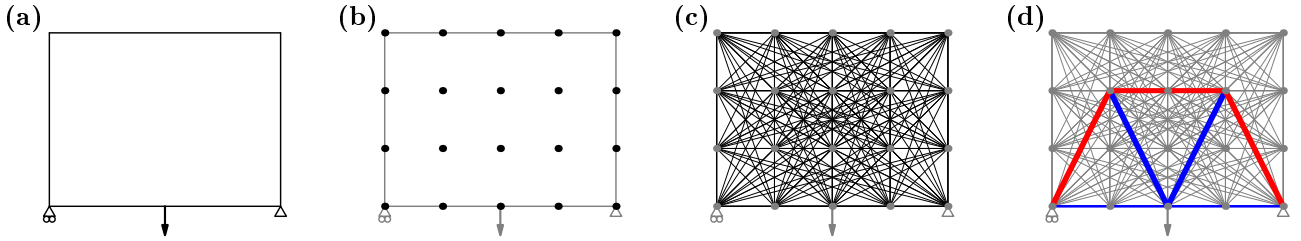


**Figure 2.10:** The stages of the layout optimization method. (a) Problem specification. (b) Design domain discretised with nodes. (c) Each pair of nodes connected with a potential truss member. (d) The optimal members are identified using the problem of equation (2.9).

The kinematic problem forms the dual of problem (2.9). This is stated as

$$\text{maximise } W = \mathbf{f}^T \mathbf{u} \quad (2.10a)$$

$$\text{subject to } \mathbf{B}^T \mathbf{u} \leq \mathbf{c} \quad (2.10b)$$

$$\mathbf{u} \in \mathbb{R} \quad (2.10c)$$

where  $\mathbf{c}, \mathbf{B}$  and  $\mathbf{f}$  are carried through from the primal problem. The dual optimization variables  $\mathbf{u} = [u_1^x, u_1^y, u_2^x, \dots, u_n^y]^T$  are the virtual displacements at each node in the  $x$  and  $y$  (i.e. global horizontal and vertical) directions. The value of the objective function  $W$  represents the virtual work done by the external forces.

Observe that each bar in the ground structure implies two force variables in the primal problem, and two strain constraints in the dual. Each node in the ground structure implies two (or three, in 3D cases) equilibrium constraints in the primal problem, and two (resp. three) virtual displacement variables in the dual problem.

The problem structure is broadly unchanged between two and three dimensional problems, with the main issues stemming from the increased number of nodes required to populate a 3D domain to the same density. Other practical issues with the application of the layout optimization method concern the specification of design domains, particularly ensuring that concavities and holes are respected, and that appropriate nodal grids can be generated for a variety of domain shapes. Several practical and educational scripts provide implementations of the layout optimization method including Sokół (2011a); Zegard & Paulino (2014, 2015); He et al. (2019).

**Adaptive solution methods** For true topology optimization to be achieved, it should be possible to connect any point in the design domain to any other. This requires a so called ‘fully connected’ ground structure, where every node is connected to every other. In such a ground structure, the number of potential members is proportional to the square of the number of nodes. This leads to a rapid increase in problem size, limiting the resolution of problems that may be solved.

Gilbert & Tyas (2003) proposed a member adding technique that increased the size of numerically tractable problems by more than 2 orders of magnitude. This approach can find optimal layouts from ground structures with several billion potential members. This makes use of the mathematical principle of column generation, specifically interpreting it in the context of the layout optimization problem to provide suitable explanations and heuristics.

The method begins by solving a problem using a minimally connected ground structure. The values of the dual variables are then examined for every pair of nodes to see if the dual constraint that corresponds to the potential member between them is violated. This check is essentially equivalent to that of Hemp's strain limit (equation (2.1)). Note that this check may be performed even for potential members that were not in the original ground structure, and indeed the constraint will always be satisfied for any member that is present in the current ground structure.

Some or all of the potential members that violate the dual constraint should be added to the ground structure for the next iteration, Gilbert & Tyas (2003) add up to a fixed number of new members (chosen as 5% of the number of members in the initial ground structure) in each iteration, choosing those that have the largest violation of the constraint. The method continues until no potential members violate their dual constraints. At this point the solution is feasible for the dual problem with fully connected ground structure. The solution could be made feasible for the fully connected primal problem by simply adding variables with a value of 0. From this it is evident that the member adding technique will provide the same, globally optimal solution as direct solving of the full problem.

Sokół (2011a,b) outlines a related method, which leverages the regularity of the Cartesian nodal grids that are often used for layout optimization. Rather than checking all potential members at every step, only those shorter than a certain length are checked, this critical length is increased at each iteration until all potential members have been checked. Sokół & Rozvany (2015) further extended the method to allow the temporary 'deactivation' of a node in intermediate iterations, providing particular advantage in the solution of 3D problems, which often contain large regions with no structure.

Regardless of the heuristic used to order the checks on potential members, the final solution of these methods will be the same, and equivalent to the solution found by directly solving the fully connected ground structure. These methods allow very large ground structures to be considered. Darwich et al. (2010) make use of these high resolution results to provide an extrapolation scheme that can provide an approximation to the volume with infinitely many ground structure nodes (i.e. the continuum solution).

**Multiple load cases** This problem in equations (2.9) and (2.10) can be extended to consider the design of structures that must resist multiple different load cases. The primal (static) problem then requires variables representing both member areas and internal forces. It is stated as

$$\text{minimise } V = \mathbf{l}^T \mathbf{a} \quad (2.11a)$$

$$\text{subject to } (\mathbf{B}\mathbf{q}_k = \mathbf{f}_k)_{\forall k} \quad (2.11b)$$

$$\left( a_i - \frac{q_{i,k}^T}{\sigma_T} - \frac{q_{i,k}^C}{\sigma_C} \geq 0 \right)_{\forall i,k} \quad (2.11c)$$

$$\mathbf{a}, \mathbf{q} > 0 \quad (2.11d)$$

where  $\mathbf{l} = [l_1, l_2, \dots, l_m]^T$  is the vector of member lengths,  $\mathbf{a} = [a_1, a_2, \dots, a_m]^T$  with  $a_i$  representing the area of bar  $i$ .  $\mathbf{q}_k = [q_{1,k}^T, q_{1,k}^C, q_{2,k}^T, \dots, q_{m,k}^C]$  is the vector of tensile and compressive member forces for load case  $k$  and  $\mathbf{f}_k$  is the vector of externally applied forces for load case  $k$ .

The dual of this problem is

$$\text{maximise } W = \sum_{\forall k} \mathbf{f}_k^T \mathbf{u}_k \quad (2.12a)$$

$$\text{subject to } \left( -\frac{y_{i,k}}{\sigma_T} \leq \mathbf{B}_i^T \mathbf{u}_{i,k} \leq \frac{y_{i,k}}{\sigma_C} \right)_{\forall i,k} \quad (2.12b)$$

$$\left( \sum_{\forall k} y_{i,k} \leq l_i \right)_{\forall i} \quad (2.12c)$$

where  $\mathbf{u}$  is the vector of nodal virtual displacements in load case  $k$ .  $y_{i,k}$  may be interpreted as the consumed length of bar  $i$  in load case  $k$ . The total of these consumed lengths for all load cases must be less than the real length  $l$  of the bar.  $\mathbf{u}_{i,k}$  refers to the components of  $\mathbf{u}_k$  that relate to the nodes connected to bar  $i$ .  $\mathbf{B}_i$  refers to the  $1 \times 4$  ( $1 \times 6$  for 3D) section of  $\mathbf{B}$  related to the variable  $q_i^T$  and the equilibrium constraints of the nodes connected to bar  $i$ .

In this formulation each potential bar requires two force variables per load case, which are coupled to an overall area variable. In the dual, these correspond to bounds on a consumed length variable for each load case, coupled by the limit on the total for each bar. Nodes each require two (resp. three for 3D) primal equilibrium constraints in each load case. These correspond to two (resp. three) displacement variables in the dual.

The adaptive solution methodology has been extended to cover multiple load cases by Pritchard et al. (2005).



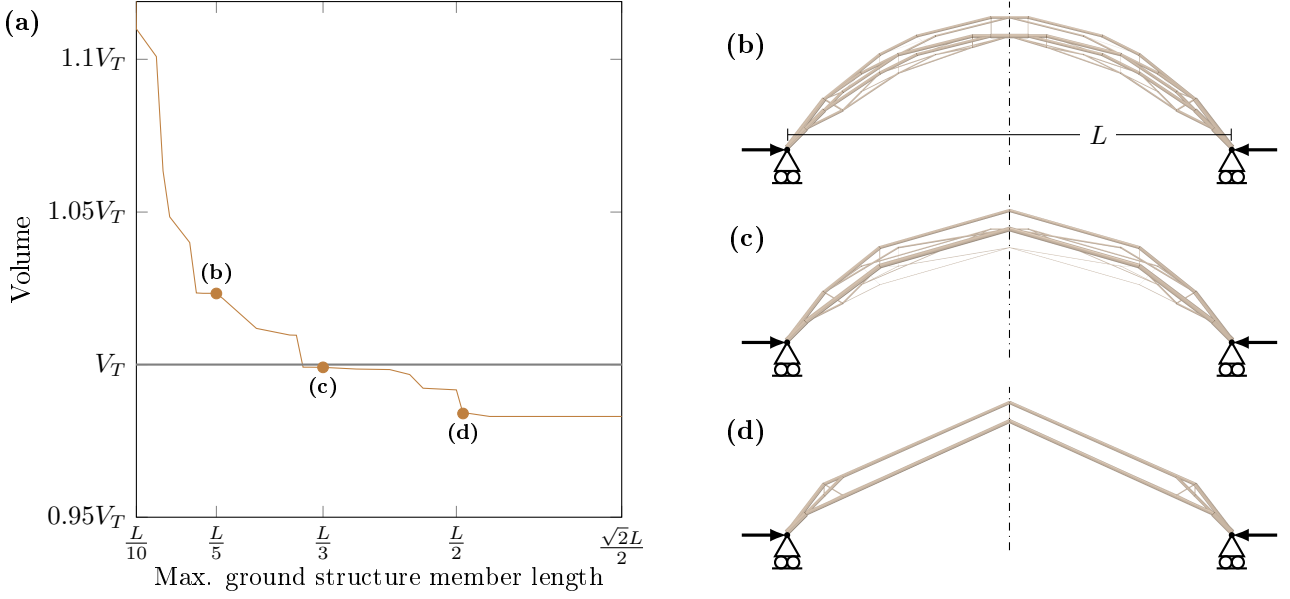


**Figure 2.11:** Results with self-weight, using the formulation in equation (2.13). (a) Plot of the volumes found from layout optimization, using ground structures where bars over a certain length are not permitted, with volumes shown relative to the analytical volume for this problem,  $V_T$ . (b), (c) & (d) Forms identified by layout optimization for the points indicated.

**Self-weight** When the self-weight of a bar is considered, it is standard to assume that the bar weight is carried equally at both end nodes, and that no increase in the bar dimensions are needed to permit this (Bendsøe et al., 1994; Pritchard et al., 2005). For the plastic layout optimization formulation this becomes

$$\text{minimise } V = \mathbf{l}^T \mathbf{a} \quad (2.13a)$$

$$\text{subject to } (\mathbf{B}\mathbf{q}_k + \mathbf{W}\mathbf{a} = \mathbf{f}_k)_{\forall k} \quad (2.13b)$$

$$(a_i - \frac{q_{i,k}^T}{\sigma_T} - \frac{q_{i,k}^C}{\sigma_C} \geq 0)_{\forall k,i} \quad (2.13c)$$

$$\mathbf{a}, \mathbf{q}_k \geq \mathbf{0} \quad (2.13d)$$

where  $\mathbf{W}$  is a  $m \times n$  matrix containing all zeros except where bar  $i$  is connected to node  $j$ , in which case  $w_{i,j} = -0.5l_i\rho g$ , with  $\rho g$  being the unit weight of the material.

If the dual of this formulation is considered for a single load case, then it can be shown that the constraints become very similar to the extended Prager-Shield criterion in equation (2.4) but with the exception that the brackets  $(1 + u_y^K)$  are instead  $(1 - 0.5u_y^A - 0.5u_y^B)$ . Clearly, as the length of the bar tends to zero this will approach the true optimality criteria, but at any finite length (as will always be considered in ground structure type methods) errors will be introduced.

The physical interpretation of these errors is based on the exclusion of the bending stresses that will be caused by the member's own self-weight. An example demonstrating this is shown in Figure 2.11. This is clearly non-conservative; the solution in Figure 2.11d is significantly lower volume than the theoretical minimum volume solution, as it contains several very long members, exploiting the maximum amount of 'free' bending capacity. Limiting the maximum length of members that are added to the ground structure can minimise the errors induced in this way. This comes at the cost of reducing the available design freedom and potentially leading to results substantially above the optimum, such as Figure 2.11b. Even for results that have a volume close to the optimum, such as Figure 2.11c, the solution may not be accurate; Figure 2.11c still contains reasonably long bars that will need to carry significant bending.

**Discrete cross sections** Often in structural design, the structures are to be constructed from a set of catalogue sections, with predefined structures. This is then a discrete optimization problem, which has received significant attention. Stolpe (2016) provides an overview of both rigorous (e.g. integer programming) and meta-heuristic approaches, and also observes that in many cases these problems are restricted to tackling problems of *sizing* optimization rather than true *topology* optimization.

**Other practical constraints** A number of other practical constraints can be incorporated within an MILP framework. Kanno & Fujita (2018) consider an upper bound on the number of joints permitted. Mela (2014) uses integer variables to prevent overlapping members from appearing in the solution, and to prevent unstable chains of compression members. In each of these cases, binary variables are used to represent the existence of a given member or node. Again, this leads to a significantly increased computational requirements.

Optimizing for ‘cost’ has also been attempted; early semi-analytical methods such as those of (Parkes, 1975) and (Prager, 1977) have been discussed earlier in Section 2.1.2. Many of the more rigorous numerical methods adopt a similar approach, whereby the cost function is defined as the sum of a material cost and a cost per member or joint. Asadpoure et al. (2015) use a continuous approximation of the Heaviside function to penalise the approximate number of members, whilst Torii et al. (2016) use a similar method to penalise the number of joints.

Designs in the real world are often required to conform to design codes, these frequently contain complex non-convex and even non-continuous constraints, which pose challenges for their integration in optimization methods. Integer programming (Van Mellaert et al., 2016), sequential programming (Pedersen & Nielsen, 2003) and meta-heuristic methods (Koumoussis & Georgiou, 1994; Villar et al., 2016) have all been used with some success, but problem sizes are severely limited. Additionally, codes vary in different countries, for example Saka (1990) compares American and German codes, resulting in substantially different optimal values and designs. This restricts the applicability of any results and leads to the questionable conclusion that the optimal structure for a given problem could vary by jurisdiction.

### 2.3.3 Geometry Optimization

Shape optimization, when applied to truss models, may be referred to as geometry optimization (GO). It concerns optimization of the positions of a structure’s joints, usually in addition to their cross-sectional area. When the topology is also to be optimized, it may be referred to as configuration optimization (Ohsaki, 2011).

These problems are non-linear and generally non-convex. One major issue occurs when two potential nodes move to be in the same location, this is referred to as melting nodes (Achtziger, 2007) or coalescent nodes (Ohsaki, 1998). Achtziger (2007) uses an approach where the reformulation prevents numerical issues with zero length bars by reducing them to a trivial inequality.

Due to the difficulties in solving the fully coupled problem, several approaches have been proposed to separate it into multiple sequential problems. Gil & Andreu (2001) use fully stressed design, alongside an unconstrained NLP problem with a penalty function. Bendsøe et al. (1994) discuss an implicit programming approach, with an inner problem of layout optimization, and an outer problem varying the nodal positions. The outer problem may become non-differentiable, leading to difficulties in solving the problem. He & Gilbert (2015) take an initial starting point from standard layout optimization, then solve a sequence of NLPs varying both position and area variables with extra limits on the distances the nodes can move; topology altering operations (merging nodes/creating crossover nodes) occur between solves. This method produces good results, provided that the original solution is sufficiently close to the true optimum.

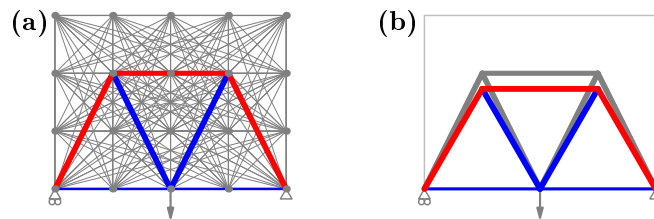


**Figure 2.12:** The geometry optimization procedure. (a) Starting point, obtained from layout optimization. (b) Solution after geometry optimization, showing optimized positions of joints.

Due to the complexity of the problem, meta-heuristic methods have been used with some success, these also often incorporate additional practical constraints. Ahrari et al. (2015) use a genetic algorithm, whilst Mortazavi & Toğan (2016) employ the particle swarm method. Reddy & Cagan (1995) make use of a method similar to simulated annealing, using so called shape grammars to define possible changes in size, geometry or topology at each stage, in this way, significant modifications to the topology are can also be achieved.

Numerous modifications have been proposed for the purposes of increasing the attractiveness of methods to practitioners. For example, Mueller & Ochsendorf (2015) modified genetic algorithms to allow designer’s input during the solution process. Multi-objective genetic algorithms aim to provide designers with a choice of outcomes, which is likely to make this more attractive to industry (Balling, 2006). They make use of the population based structure of the genetic algorithm by seeking a final generation that contains individuals who

are spread over the a Pareto front of two or more objectives. Objectives may include structural weight, deflection or embodied/operational energy (Brown & Mueller, 2016) amongst others.

## 2.4 The use of optimization in structural engineering practice

It is widely expected that structural engineering practice will, in the near future, be revolutionised by the application of digital design and optimization methods (Tranau, 2018; Wainwright, 2018) and that this will free engineers to focus on the more imaginative and innovative elements of the process (Firth, 2017). This section discusses current practices in structural design, with emphasis on methods that are in some respects related to optimization, and also on factors that should be taken into consideration to produce an effective design. It will be observed that there are some areas that may cause challenges in the application of previously discussed optimization techniques, but that there are also many opportunities.

The usual design process for a building consists of a number of stages, these are usually<sup>1</sup> described using the RIBA plan of work (Sinclair, 2013). This is illustrated in Figure 2.13a. The majority of activity for the structural aspects of the design occur in stages 2 to 4. Paulson (1976) discussed how the potential for influence over the final outcomes of the design changes throughout the process, as visualised in Figure 2.13b. Initially, the design team have full control over the possible outcomes and full flexibility to make changes. As the design is finalised, alterations become increasingly difficult, expensive and limited in scope. Around 70% to 80% of project resources will be committed during the concept design phase (Rafiq & Beck, 2008), therefore it is likely to be most advantageous to provide tools that target this stage.

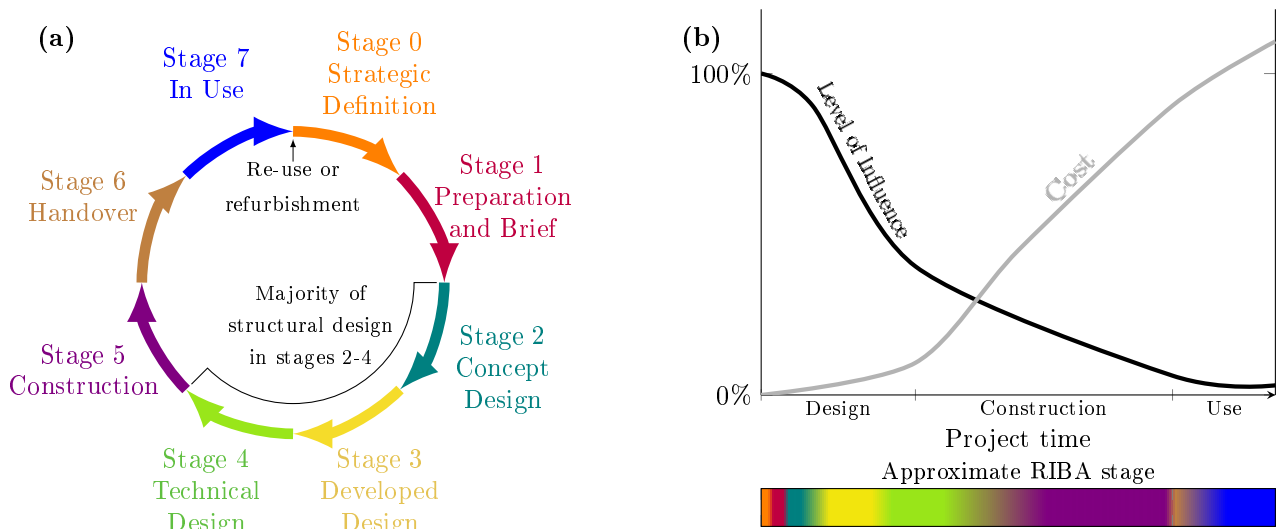


**Figure 2.13:** Stages in the design and construction process (a) Stages of the RIBA plan of work (after Sinclair, 2013). (b) Changes in potential level of influence and project costs over time (after Paulson, 1976).

Typical design practice begins with selection of an overall layout in the concept design stage. This is usually decided based on experience and ‘engineering judgement’. True *topology* optimization is not commonly used, and manual trial-and-error improvements of member sizing and possibly positions may be the only revisions that are made in the later ‘developed design’ stage. However, some optimization-like techniques are occasionally employed, especially for unusual or monumental structures; these are generally referred to as ‘form finding’.

### 2.4.1 Form Finding

The practice of form finding is linked to that of optimization, as both involve altering a design in order to achieve a better result. However form finding generally seeks only a *feasible* solution, albeit often with some additional constraints such as elimination of bending stresses. Usually these methods do not directly seek e.g. a maximal stiffness solution, although there have been some attempts to explicitly include optimization, e.g. Bletzinger & Ramm (2001); Beghini et al. (2014).

Long before the formal theories of minimum weight design, the importance of geometry in designing a safe and efficient structure was well understood. The earliest studies often concerned masonry arches, where pure

<sup>1</sup>The previous edition of the RIBA plan of work (RIBA, 2007) is still occasionally referred to, particularly with relation to long term projects. The terminology of concept, developed/development and technical design stages are similar, although the numbering system is altered.

compression was necessary for stability. Later, as suspension bridges became popular, form finding for tensile cables and surfaces also flourished, and more recently a desire for thin shell and tensile membrane structures have led to an increase in methods for analysing surfaces.

**Physical modelling** The equivalence between hanging chains and arches was identified by Hooke (1676) and published as a Latin anagram, unscrambled and translated it becomes ‘as hangs the flexible line, so but inverted will stand the rigid arch’ (Heyman, 1998). This principle allowed for design without requiring complex mathematics, leading to structures from as early as Wren’s 1675 design for St Paul’s cathedral (Heyman, 1998) to Gaudí’s early 20th century design for the Colònia Güell church (Huerta, 2006), see Figure 2.14.

A further form finding problem that has received attention by way of physical modelling is that of finding a surface of minimum area bounded by a given curve. A physical model of such a surface can be found by a soap film suspended from a thin rigid framework (Plateau, 1869); an example is shown in Figure 2.14b. Such surfaces are popular as designs for membrane structures, with well known proponents including Frei Otto (Goldsmith, 2016) and Heinz Isler (Chilton, 2009).

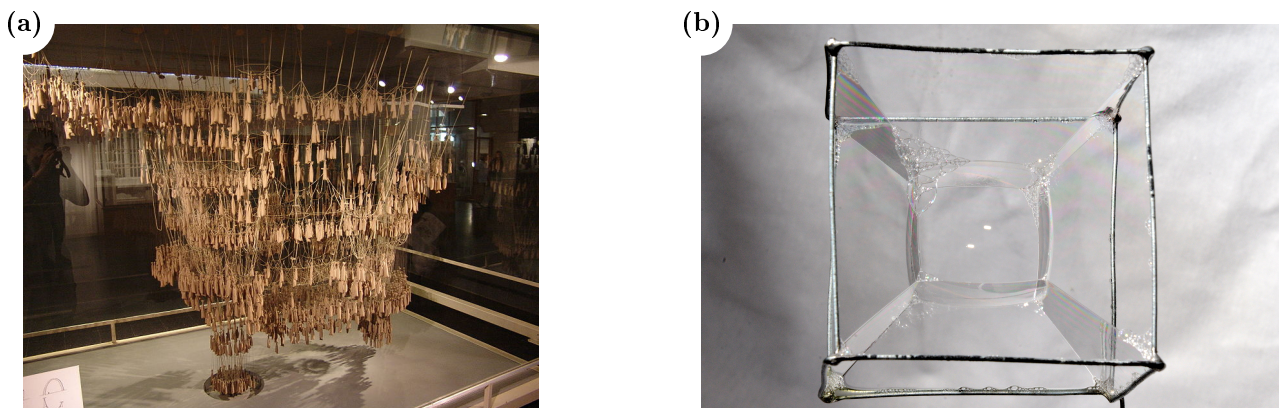


**Figure 2.14:** Examples of physical models, (a) Hanging model by Antonio Gaudí for the Church of Colònia Güell, photo by Marmulla (2008, used under CC BY-SA 3.0). (b) Minimal surface formed by a soap film on a wire frame, photo by de Gol (2014, used under CC BY 4.0).

Later, a number of computational methods became available to emulate these processes of physical modelling. Popular examples for minimal surfaces include the force density method (Schek, 1974) and dynamic relaxation (Barnes, 1999); for simulation of hanging models large displacement finite element analysis can be used (Bletzinger & Ramm, 2001). However, the importance of physical models is still recognised by practitioners (Azagra & Hay, 2012; Addis, 2013). They are particularly common for evaluating a design’s aerodynamic performance, Cammelli (2018) describes a day long physical workshop in which the outer shape of a skyscraper was ‘optimized’ by trial and error over a number of iterations.

**Mathematical forms** Alongside physical hanging models, mathematical descriptions of useful funicular structures were developed. The parabolic arch (e.g.  $y = x^2$ ) was the first equation proposed for the form of a pure compression arch by Galileo (1954), it was shown by Huygens in 1646 (Heyman, 1998) that this is the correct solution only when the load is evenly distributed horizontally, rather than along the arch.

The correct solution for the arch/cable (of constant cross section) under its own self-weight is the catenary (e.g.  $y = \cosh(x)$ ), discovered by Huygens, Bernoulli and Leibnitz in 1690 (Heyman, 1998). Intermediate moment-free forms are also possible under a combination of these two loading types (Lewis, 2016). However, these forms do not describe the minimum material use for their relevant cases, as they each assume a constant cross section throughout the arch, leading some regions to be less stressed than others.

Gilbert (1826) developed equations for a cable subject to the loading from its own self-weight, the cable width varied such that the stress at each point was equal (taking a form described by the function  $y = \ln(\cos(x))$ ), these were presented alongside tables showing the impact of the choice of geometric parameters on the levels of force in the cables. Routh (1896) further develops this to the general case of a cable under load from its own weight, a horizontally distributed deck load and loading from hangers, i.e. a suspension bridge.

**Bridges** As bridge forms can usually be well approximated by simple scenarios, general purpose structures can be proposed. Several standard forms are well known for the design of bridges. Early bridges often favoured

arch forms, as discussed above. For modern long spans, cable stayed or suspension bridges are the most common forms.

As these forms are of such widespread use, a number of parametric studies have compared them, using a variety of assumptions and parameters. One early approach was made by Croll (1997a), with subsequent discussions by Dalton (1997) and French (1997). This study neglected the influence of self-weight, and considered somewhat unusual cable stayed forms with a deck partially in tension and partially in compression to ensure the same support forces in each case. Suspension bridges were found to be more economical for span to dip ratios above 4, whilst cable stayed forms were preferred for lower ratios.

Gimsing & Georgakis (2011) included the self-weight of the towers. Lewis (2012) also included an approximation of the self-weight of the cables, thereby giving a limit for the maximum span possible for a given material and span to dip ratio, suggested to be in the region of 5 km for a suspension bridge constructed of current materials.

The accurate inclusion of self-weight is critical as spans increase, it is one of the two limiting factors for a very long span bridge, alongside control of dynamic effects (Ostenfeld, 1996; Brancaloni et al., 2011). Even in the longest span in existence today, the Akashi Kaikyo bridge, over 90% of the main cable capacity is devoted to carrying the bridge's self-weight (Ito, 1996)

**Graphic Statics** Prior to the ready availability of computers, equilibrium of a joint subjected to only axial loads could be verified graphically by ensuring that the force vectors formed a closed polygon. This led to the principle of reciprocal diagrams (Maxwell, 1864), and the field of graphic statics (Culmann, 1875), which became the most common method of identifying structures in equilibrium for the end of the nineteenth and beginning of the twentieth centuries (Block et al., 2006).

Graphic statics then fell into disuse for much of the 20th century, however interest in the area was renewed at the beginning of the 21st century. This particularly focussed on extensions to 3D forms (Block, 2009; Akbarzadeh et al., 2015; Beghini et al., 2013), interactive computational tools (Kilian & Ochsendorf, 2005; Rippmann et al., 2012; Harding & Shepherd, 2011) and more explicit links to optimality (Baker et al., 2013; Beghini et al., 2014).

**Computational parametric modelling** The term parametric design was first coined by an architect, Luigi Moretti, in 1939 (Tedeschi, 2014). These early studies resulted in mathematical expressions of surfaces and curves. Generally the time investment of manual treatment would be justified only for fairly general problems; in Moretti's case the viewing angles of sports stadia.

More recently, software is used to allow designers to model forms using parameters of their choice. Lin et al. (1981) describe an early version of this method. There are several popular commercial software packages implementing these methods. Grasshopper is a plugin for the Rhino modelling software, which provides a graphical interface for parametric relationships (Davidson, 2019); a similar functionality is provided by the Dynamo interface for Revit (Autodesk, Inc, 2016). The visual programming environment of Grasshopper is shown in Figure 2.15a, this includes a set of input parameters (in the pink box) and the operations that relate these to an output geometry.

One of the main advantages of parametric modelling is that parameters may be changed at any point in the design process. Figures 2.15b and c, show two forms that may be produced by varying the parameters in Figure 2.15a; many other variations may also be obtained. Parameters may be tuned manually to find the preferred values, especially when aesthetic design criteria are involved or substantial collaboration with architects or clients is to be undertaken (Leach et al., 2016). For more quantifiable criteria, optimization methods may be used. Some workers have studied mathematical optimization of parametrically modelled forms (Ohsaki, 1998) but the mathematical formulations and limited user interface have hindered their uptake in practice.

One of the most popular commercially available packages for optimizing parametric models, is the Galapagos genetic algorithm solver that is embedded within the Rhino/Grasshopper software package. As a genetic algorithm, it can be used with almost any parameters, and has been used to solve not only standard structural problems (Gerbo & Saliklis, 2014) but also ones regarding more unusual parameters such as irregularity (Mele et al., 2018) and even optimization of solar gains (González & Fiorito, 2015). The power of this approach is best utilised in optimizing very complex functions that do not have a simple mathematical description, such as daylight calculations. For simpler problems, better results could likely be obtained using mathematical methods.

## 2.4.2 Construction factors influencing optimality

Optimality of real-world designs is difficult to define. Isolating a single element, such as the superstructure, may lead to very different results compared to solutions that also include the substructure (Nolan, 2016). Furthermore, the quantity to be optimized may vary for different projects; least-weight, least-cost or environmental impact may be considered as objectives for designers (Debney, 2016).

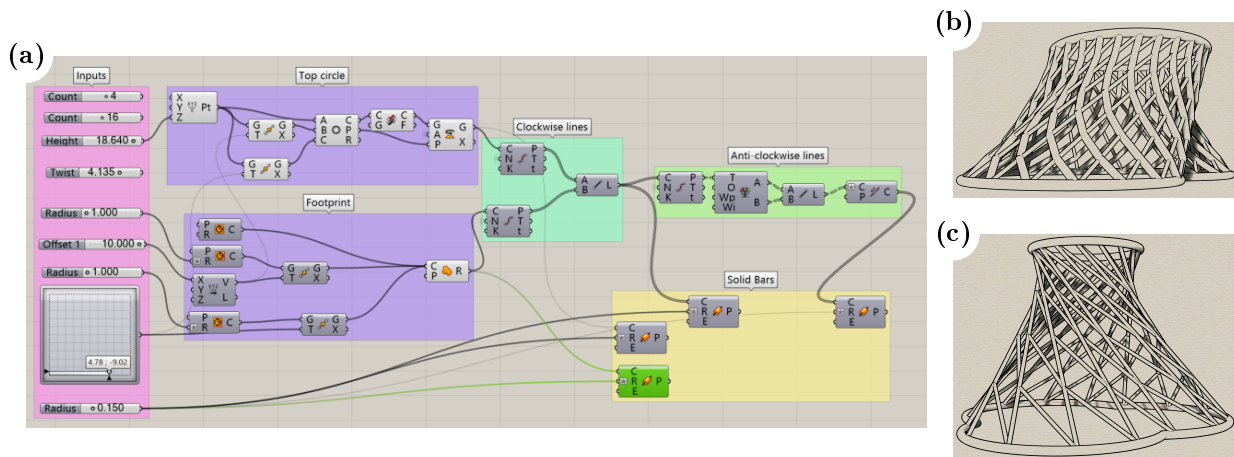


**Figure 2.15:** Example of form generation using the popular parametric modelling software Grasshopper. (a) Visual programming environment. (b) & (c) Two example forms using different values for the input parameters.

**Cost** Cost is usually a driving factor in the procurement of real world structures. However, estimating the total cost of any given design is a very complex task. The standard estimating procedure involves quantifying all materials, plant and labour required (Potts, 2008), and is therefore suited to the later stages of design, tender and construction. It is also common for companies to produce estimates based on similar projects, either from their own experience or documented data.

At the early stages, estimates must be made using incomplete data. Creese & Li (1995) and Arafa & Alqedra (2011) use neural networks to predict final costs, it is possible to use very early stage information such as number of storeys or floor area. Case based reasoning (Perera & Watson, 1998) identifies projects from a database that are similar to the current project and uses these to generate an estimate. Kim et al. (2004) compares both neural networks and case-based reasoning to statistical regression methods, finding that whilst the neural network was the most accurate, the time to train the model was slow and the clarity of explanation was lacking, leading them to suggest that case-based reasoning was likely to be the preferable solution. Both neural networks and case based reasoning rely on banks of existing data to produce their results, therefore they may perform poorly when faced with unusual solutions.

**Buildability and complexity** Buildability is a very general term that refers to the ease with which a design may be constructed. Lam et al. (2006) conducted a survey of 111 members of project teams; of the 10 attributes of buildability ranked as most important, only three relate to the design output (as opposed to the design process and documents). The identified attributes were: allowing safe sequences of trades, efficient site layout for storage/access, and allowing a high degree of standardisation.

Fischer & Tatum (1997) collect a range of knowledge items relating to the buildability of reinforced concrete structures, and propose a classification system that could be used to formalise this information. A numeric 'constructability score' was proposed by Tauriainen et al. (2014) for an overall project, with contributing scores calculated for components including trusses. For trusses, the score included contributions based on number of section types, lengths of elements and weights of elements.

Horn (2015) proposes a number of different metrics to measure complexity, including number of lorry loads required to transport all members, number of connections, number of different cross sections, numbers of members at each node, and the angles between connecting members. Pareto fronts of complexity vs weight are then identified to show the trade-off that designers must tackle. However, the designs tested are near-randomly generated, and there is no attempt to specifically seek high performing designs.

Havelia (2016) develops an optimization method to incorporate costs associated with joint complexity, this is similar to ESO, where inefficiently used members are sequentially removed. For this the efficiency of a member was estimated by the ratio of its internal force to its total cost, including connections. The method has been further extended to allow continuous members through joints by Ranalli et al. (2018).

Connections can form a substantial proportion of the cost of a structure. As such optimization techniques to reduce their complexity may be very useful. However, alternative methods are also possible; the Leadenhall building uses prefabricated joint pieces, meaning only splice connections need to be assembled on-site (Eley & Annereau, 2018). Additive manufacturing may also provide additional flexibility, either through direct printing of metal (Block, 2018) or using printed moulds to cast joints (Niehe, 2017).

**Environmental impact** When two possible designs for the same scenario and using the same materials and technologies are compared, the embodied energy of a building is usually well correlated to its material usage (Lagaros, 2018). However, selection of alternative materials and technologies may make a substantial difference, for example a timber office building may produce only 30% of the net CO<sub>2</sub> emissions of a comparable steel framed building (Buchanan & Honey, 1994).

Reuse of structural elements is growing in popularity as a possible means to reduce carbon emissions associated with buildings, although its uptake is mainly limited to clients who are sufficiently ideologically committed to permit the additional perceived risk (Gorgolewski, 2008). Additionally, extra constraints based on the availability of cross sections and lengths are generated, Bukauskas et al. (2018) assigns a catalogue of available components to a structure to minimise the amount of offcuts produced.

## 2.5 Observations

The fields of practical structural design, numerical optimization and the analytical study of minimum weight structures are often very divided. Methods used in structural design generally employ techniques that aid interpretation by the user, such as the graphical representations of graphic statics, or the physical intuitiveness of model making. In contrast, the results from numerical optimization methods are complex assemblies of bars, from which it can be difficult to extract a structural logic.

The results of analytical methods are significantly easier to interpret than numerical methods, albeit still not as intuitive as e.g. physical modelling. However, the mathematical difficulties in identifying minimum weight structures analytically mean that these methods have time commitments that are well beyond the time-scales required for practical design. Furthermore, the difficulties in identifying a solution for a given problem (as opposed to vice versa), mean that numerical methods are the most appropriate for application in practice. However, these methods are still subject to a number of limitations.

**Practicality of numerical solutions** The solutions obtained from both numerical and analytical methods are often too complex to be practical for real-world construction. However, whilst the region-based representation of analytical results can suggest simplified variants, this is generally much more challenging to obtain from numerical results. Formulations that exist to simplify numerical results generally lead to significant limitations on the size of problem that may be solved.

**Missing functionality** The layout optimization method has many qualities that appear to suggest its suitability for application in the field of structural design, for example the use of distinct structural elements and the ease of handling problems with very low volume fractions. A major drawback in its application to very long span structures is the errors introduced by the current approaches to modelling self-weight. These errors become increasingly significant as span increases. As they are non-conservative, they substantially undermine the reliability of the method.

**Computational efficiency** There has been no major improvement in algorithms for numerical layout opt since Gilbert & Tyas (2003) almost 2 decades ago. However, further developments that aim to simply increase the size of feasible ground structures may provide diminishing returns. The extrapolation scheme of Darwich et al. (2010) has been shown to be capable of obtaining solutions that have a volume within 0.01% of analytical optima (Pichugin et al., 2015), by using ground structures that may be solved using current adaptive layout optimization methods. Furthermore, results using dense nodal grids become visually congested at levels somewhat below the maximum resolution that may be solved. Therefore, methods should be developed that can increase the comprehensibility of the solutions.

Further evaluation of the applicability of layout optimization methods will be undertaken in the next chapter; this will be achieved through application to a real-world case study. Part I then concludes by cataloguing the main issues that have been identified, and outlining how they will be addressed in the remainder of the thesis; this can be found on page 42.





## Chapter 3

# Evaluating the applicability of current methods

This chapter contains the results of a case study drawn from a real world project. The aim of this study was to investigate the effectiveness of currently available methods of structural optimization when applied to realistic scenarios.

Some material in this chapter has previously been presented as a conference poster<sup>†</sup> (see Appendix E.1) and has also formed part of an article<sup>‡</sup> (see Appendix E.2) that has been accepted for publication in *The Structural Engineer*; this aims to inform practitioners of the current capabilities of optimization software.

---

3.1	Introduction . . . . .	32
3.2	Three dimensional ‘chassis’ problem . . . . .	32
3.3	Two dimensional ‘mother’ truss problem . . . . .	33
3.3.1	Consideration of buckling . . . . .	34
3.3.2	Deflection . . . . .	36
3.3.3	Rationalisation . . . . .	37
	Automatic layout rationalization . . . . .	37
	Human-in-the-loop layout rationalization . . . . .	37
	Cross section rationalization . . . . .	37
3.3.4	Results . . . . .	39
3.4	Observations . . . . .	41

---

<sup>†</sup> Fairclough, H., (2017) Application of layout optimisation for building structures. In *Proceedings of the 19th Young Researchers Conference*. The Institute of Structural Engineers, (pp. 44-45).

<sup>‡</sup> Fairclough, H., Gilbert, M., Thirion, C., Tyas, A., & Winslow, P. (in press) Optimization-driven conceptual design: Case study of a large transfer truss. *The Structural Engineer*.

### 3.1 Introduction

Many of the methods described in Section 2.3 appear to have the potential to be of great use in the practice of structural design. However, their application to real-world projects is still very limited. The aim of this chapter is to identify the major issues that arise when applying these techniques. This will allow prioritising of the issues that should be addressed in later chapters.

In choosing the project, its suitability for application of optimization was considered in several ways. Firstly, scenarios where the structure would be mostly hidden or in ‘back of house’ spaces were preferred, such scenarios generally allow the structural designer more freedom, potentially allowing for greater savings. Additionally, scenarios with well defined loadings are preferable. Furthermore, loading combinations that are further from everyday cases with well known ‘textbook’ solutions are more likely to produce innovative design solutions.

The project described below fulfils each of these criteria well and should therefore be an ideal candidate for the use of optimization methods.

This chapter will primarily focus on the use of truss based methods, including adaptive layout optimization (Dorn et al., 1964; Gilbert & Tyas, 2003) and geometry optimization (He & Gilbert, 2015), although some comparisons with continuum modelling approaches will also be made.

### 3.2 Three dimensional ‘chassis’ problem

The chosen project consists of a system of interconnected transfer trusses creating an approximately 50m by 50m clear space in the basement of a hotel development project. The system is to consist of two north-south trusses, with two storey depth. These are supported by an east-west, 3 storey ‘mother’ truss part way along their span, and at one end by another transfer truss, as shown in Figure 3.1a. The remaining ends of each truss are supported on the basement walls. This assemblage of trusses was referred to as the ‘chassis’ by the design team, due to its critical role in the project and similarity to the layout of a vehicle chassis.

Loads from the basement levels are transferred through columns and applied at the base of the design domain, whilst additional loads from a garden and a 5 storey building above are applied at the top of the domain along the mother truss, as shown in Figure 3.1a. The magnitudes of the loads at each location vary according to the usage of the surrounding areas, the factored ultimate limit state (ULS) loads are given in Figure 3.1b.

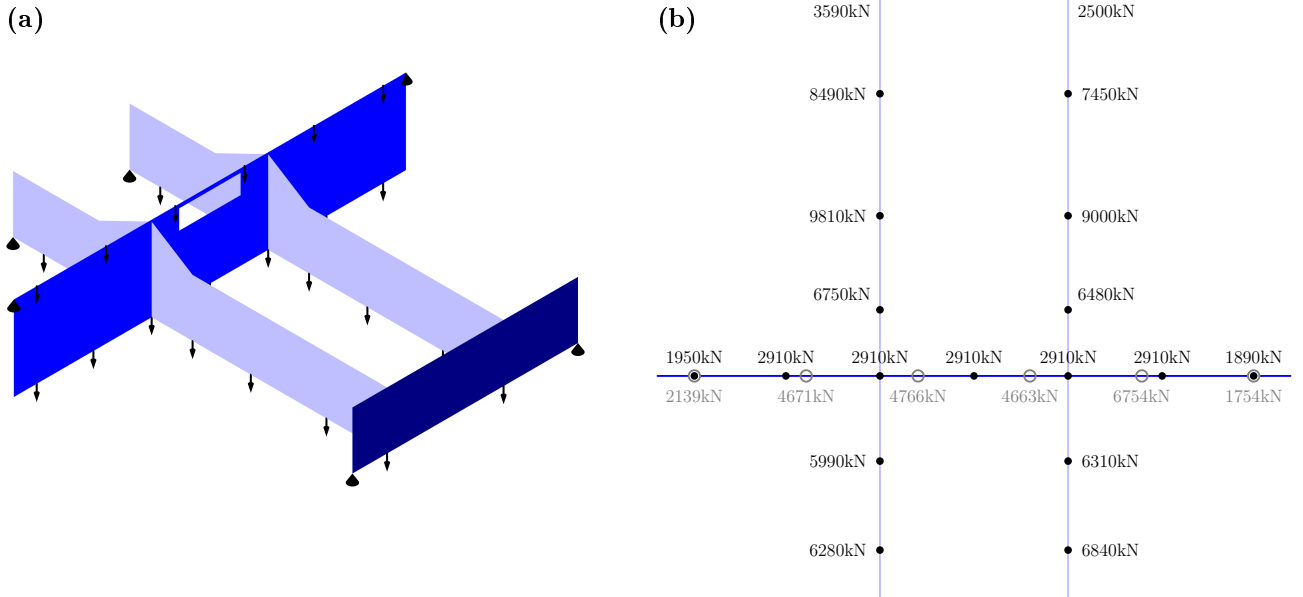


**Figure 3.1:** Hotel basement study - 3D chassis: Problem specification. (a) Geometry of truss planes, supports and loading. (b) Magnitudes of loads applied to the structure, black dots are applied at the base of the design domain, whilst grey circles are applied to the top.

The large loads carried by the structure meant that the sections required were often beyond the ranges available in catalogue sections. Therefore the structure was to be constructed from hollow square or rectangular sections fabricated from S355 steel. Initially, the maximum stress was set to 355MPa in both tension and compression, consideration for buckling was added only later in the study (see Section 3.3.1).

Due to the large area supported by the chassis, a large number of pattern load cases are possible. The results of layout and geometry optimization can be seen in Figure 3.2. These results are very complex and difficult to interpret, there are several reasons for this.

The size of the problem is fairly large, in terms of both the number of load cases and the number of ground structure nodes that are required for even the low resolution shown in Figure 3.2. This can lead to numerical difficulties, particularly in convergence of the non-linear optimization problem in geometry optimization. In the results in Figure 3.2 it can be observed that the resulting nodal positions along the bottom chord of the mother truss have particularly been affected by this. The low resolution, which is necessitated by the problem size, also leads to difficulties as some regions do not have sufficient design freedom to see what is happening, for example the end transfer truss at the lower right of Figure 3.2.

However much of the reason for the difficulty in interpreting this solution is also caused by difficulties inherent in *presenting* optimized 3D structures. For example overlapping members are much more difficult to decipher when there is not a simple pattern or some other hierarchy by which the solution can be abstracted into fewer components. In this problem, the effects of this are somewhat mitigated as the design domain was already defined as a number of component planar trusses. This problem will therefore be exacerbated in fully volumetric problems, as there are the far fewer familiar structural forms for fully 3D problems than for planar cases.

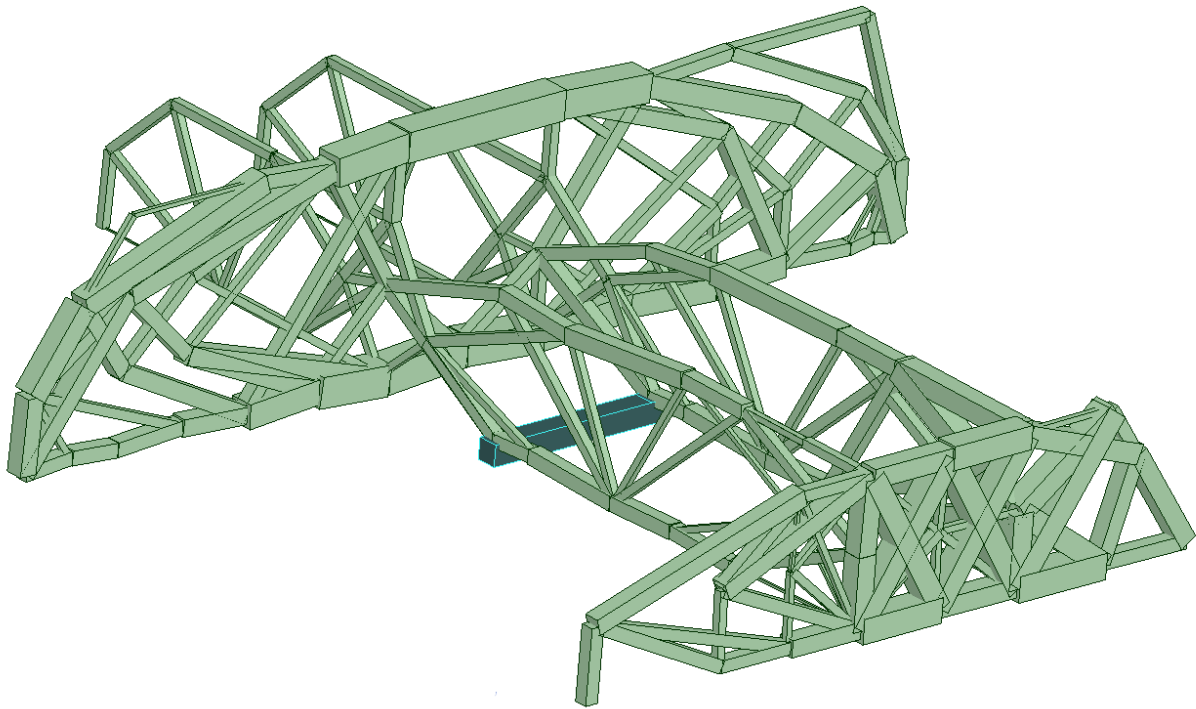


**Figure 3.2:** Hotel basement study - 3D chassis: Result.

### 3.3 Two dimensional ‘mother’ truss problem

In light of these results, it was decided to focus on just the 3 storey ‘mother Truss’. This would allow a more detailed investigation and more easily interpreted results.

The problem that will be considered for the remainder of this chapter is outlined in Figure 3.3, which shows the characteristic values of loading. The structure was again to be constructed from steel sections, fabricated from S355 grade steel. Two results for this problem, with a single load case containing all loads factored unfavourably, are shown in Figure 3.4. The first was calculated using an adaptive truss layout optimization method, minimising the total volume of material whilst limiting the stress in each bar.

Figure 3.4b is calculated using the continuum method of Sigmund (2001), this minimises the compliance, subject to a constraint on the fraction of the design domain that is filled with structure, in this case the so-called

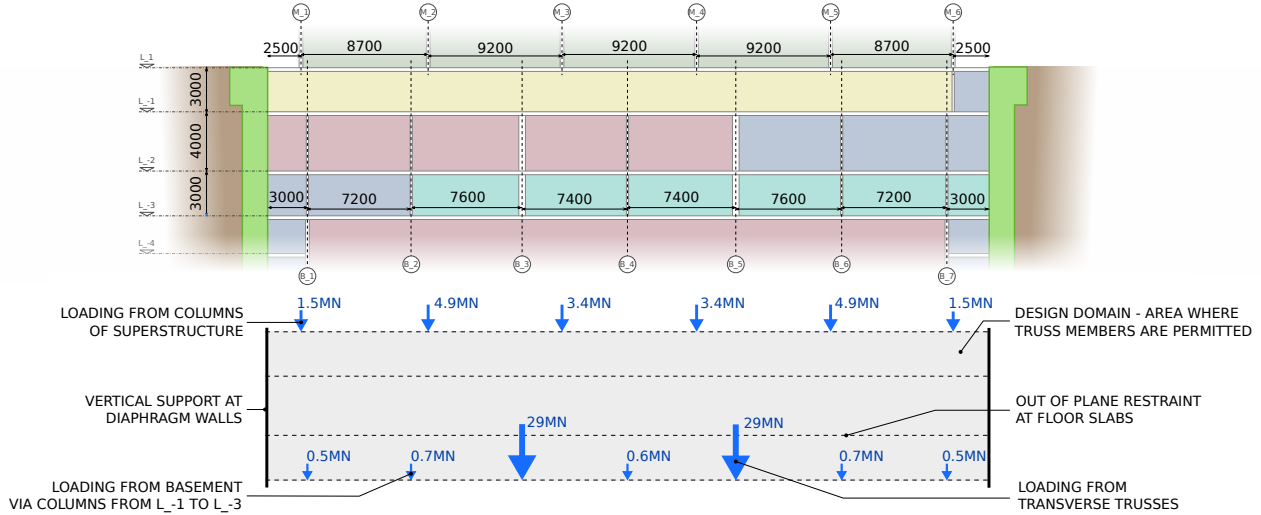


**Figure 3.3:** Hotel basement study - 2D mother truss: Problem specification.

volume fraction was set to 0.3. Selecting a value for the volume fraction is difficult in the context of structural engineering problems, as it is not a constraint that arises naturally from the problem specification. Particular issues have been encountered in this case due to the differences in magnitude between the loading from the transverse trusses and the other loads applied. Some loads on the structure are supported by ‘grey’ elements, physical realisation of these is sometimes achieved through the use of microstructures, however this is unlikely to be practical for building scale structures. Increasing the volume fraction may provide more available material for these regions. However, observe that the smaller central loads are carried by bending of the thick top and bottom chords at this point, these are likely to be making use of a much larger structural depth than would be realistically provided; increasing the volume fraction would exacerbate this problem. In contrast, the layout optimization result in Figure 3.4a can easily consider both the large and smaller loads.

However, the loads applied to a structure are rarely constant, in building design codes this is often considered by factoring loads according to whether their effects are favourable or unfavourable. The single load case structures in figure 3.4 are both susceptible to issues from unbalanced loading, however it is not necessarily clear a-priori which load combinations should be considered. For the purposes of this study, 3 load cases have been considered, one where all loads are factored unfavourably, and two where the loading from one transverse truss was taken to be favourable. Compliance based formulations generally approach multiple load case problems by considering a weighted average of the compliance in each load case, this is not ideal for the purposes of structural design, where each load case must be satisfied to ensure a safe structure is obtained. The layout optimization method can easily consider stress constraints in multiple load cases by using a plastic formulation, this approach will therefore be adopted for the remainder of the chapter.

### 3.3.1 Consideration of buckling

Within the linear programming formulation to be used in this study, buckling cannot be accurately modelled. Two distinct issues arise from this, global buckling of the entire pin jointed truss, and local buckling of individual members.

The layout optimization method models the structure as a pure truss, i.e. with zero bending resistance at all joints. However, this case study example, as is common with real-world problems, consists of a planar truss in free space. Therefore there is no mechanism by which nodes (other than those at supports) may be restrained

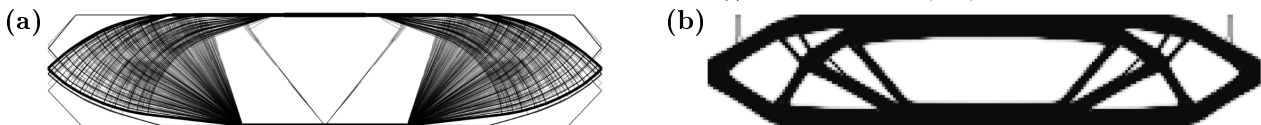


**Figure 3.4:** Hotel basement study - 2D mother truss: Results of single load case versions of current scenario. (a) Minimising volume subject to a stress constraint, using an adaptive layout optimization method based on Gilbert & Tias (2003). (b) Minimising compliance subject to a volume fraction constraint, using the MATLAB code of Sigmund (2001).

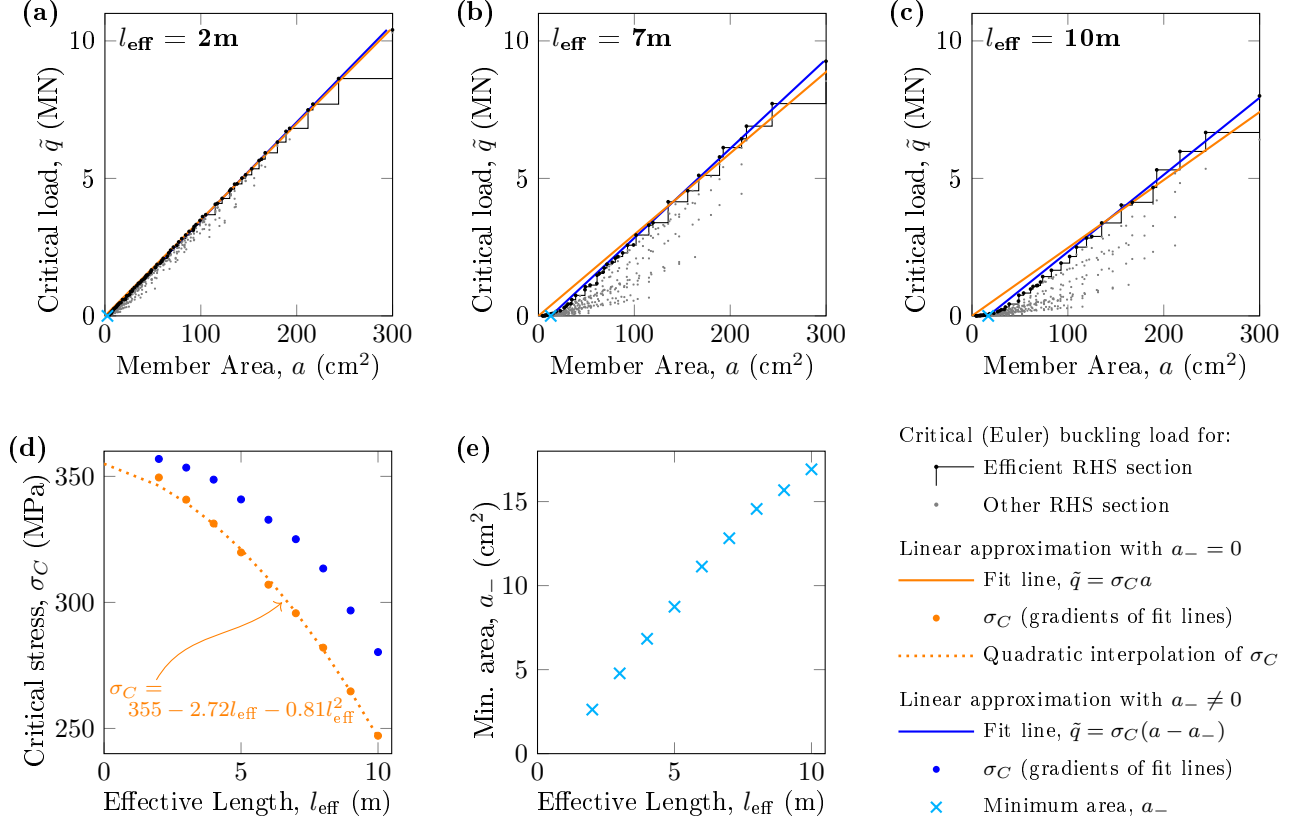


**Figure 3.5:** Linear approximation of buckling in commercially available RHS sections. Orange interpolation results are based on assuming a continuous linear relationship (suitable for implementation with a linear programming approach). Blue interpolation results are based on allowing a discontinuity at  $a = 0$  (suitable for implementation with a MILP approach).

(a)-(c) Critical compression force for RHS sections at lengths of 2m, 7m and 10m. The most efficient cross section for a given load is given in black, sections that are never most efficient are given in gray.

(d) Effective compression strengths (i.e. slopes of fit lines) for lengths of 2 to 10m.

(e) Minimum permissible cross-section areas, from intercept points of fit lines.

from buckling out of the plane of the truss. Second-order effects from tension members connected to such joints may provide a possible restraint mechanism, although the use of either continuous members or moment-resisting joints are a more practical solution. To avoid such issues in this study, the floor plates and the diaphragm wall will be used to provide out-of-plane restraint. Nodes will only be permitted at these locations, therefore no nodes that are unrestrained will exist. The single load case layout optimization solution for this restricted ground structure is shown in Figure 3.7b, and incurs a volume penalty of only 1.5% over the benchmark value shown in Figures 3.4a and 3.7a.

This method also simplifies the consideration of local buckling. The effective buckling length of a member can be taken to be equal to its overall length. The problem of compressive chains (Mela, 2014) is avoided as intermediate nodes are supported. However, member buckling is still a non-linear and highly non-convex problem when simple, solid sections are considered. When more realistic sections (e.g. I-beams, hollow sections) are used the non-linearities become less significant, as shown by Tyas (2002) for commercial circular hollow sections (CHS).

Similar calculations have here been carried out for commercially available rectangular hollow sections (RHS) buckling about their minor axis. This involved calculating the buckling force for each available cross section at lengths of 2m to 10m, and selecting the most efficient (lightest) cross section to carry any given axial load. A linear best fit of member area vs. allowable compression force was then found for the efficient cross sections. These best fit lines furnish an expression of the form

$$\tilde{q} = \sigma_C (a - a_-) \quad (3.1)$$

where  $\tilde{q}$  is the allowable compressive force,  $a$  is the member cross-section area,  $\sigma_C$  is the allowable compressive stress, and  $a_-$  is the minimum permitted cross section area. Best fit lines have been found for  $a_- = 0$  and un-

restricted  $a_-$  for each length, some examples are shown in Figure 3.5a-c. These values of  $\sigma_C$  and  $a_-$  can then be plotted against the relevant length, as in Figure 3.5d-e and relationships can be found to interpolate/extrapolate values for any length.

Here, the values of  $\sigma_C$  for  $a_- = 0$  have been used as this provides a continuous, linear formulation. This is less accurate than the non-smooth formulation; however the formulation with  $a_- \neq 0$  would require integer variables to implement. It can be seen from Figure 3.5b-c that the continuous formulation is non-conservative for member areas below approximately  $130\text{cm}^2$ .

The resulting equation for the compressive strength,  $\sigma_C$ , of a bar of effective length  $l_{\text{eff}}$  was therefore found to be

$$\sigma_C = 355 - 272l_{\text{eff}} - 0.81l_{\text{eff}}^2 \quad (3.2)$$

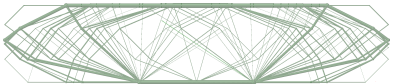


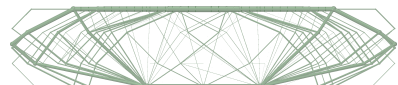
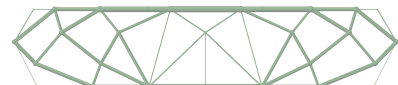







as shown in Figure 3.5d. This was interpolated under the requirement that a bar of zero effective length should have equal tensile and compressive strengths (i.e.  $\sigma_C = 355\text{MPa}$ ). However, from Figure 3.5 it appears that a more accurate (quadratic) interpolation would have a higher  $\sigma_C$  at  $L = 0$ , this would therefore require that the function was capped, with short members failing by crushing rather than buckling. This function would then be non-smooth, potentially leading to difficulties in implementing geometry optimization. Therefore the more conservative equation (3.2) is used. The effective length of a bar was set equal to its length, except in the case where the bar was entirely contained within a single slab, in which case the effective length was zero. The result of layout optimization with the nodes on the slab lines, and also with the member compressive strengths reduced according to equation (3.2) is shown in Figure 3.7c.

### 3.3.2 Deflection

For single load case problems, the lightest fully stressed layout also corresponds to the stiffest layout. As such, the lightest structure with a limit on the deflection can be found by simply scaling the result of the layout optimization problem. However, this is no longer the case when multiple load cases exist and the structure is no longer fully stressed.

A commercial implementation of the layout optimization method, LimitState:FORM (Limitstate Ltd., 2019), uses a simplified method to impose deflection constraints. The problem is first solved with no deflection constraints imposed, with elastic analysis methods then used to calculate the resulting deflections. For deflection constraints that are violated by this solution, the allowable stresses in the relevant load case are reduced, and the problem is solved again. Thus, for single load cases this approach corresponds to the appropriate scaling of the original solution.

When applied to multiple load cases, the theoretical backing for this approach is less clear. As elastic and plastic methods are combined, the deflections calculated in this stage may involve some members being stressed beyond the linear elastic region. However, the method does appear to produce practically useful results; Table

	LO Result	Rationalized Form	Traditional Form
No deflection limit	 Weight = 288t = $V_\infty$ Deflection = 148mm = $u_\infty$	 Weight = 233t = $1.02V_\infty$ Deflection = 164mm = $1.11u_\infty$	 Weight = 319t = $1.40V_\infty$ Deflection = 196mm = $1.32u_\infty$
Span/500 (100mm)	 Weight = 342t = $V_{100}$	 Weight = 359t = $1.049V_{100}$	 Weight = 562t = $1.643V_{100}$
Span/1000 (50mm)	 Weight = 679t = $V_{50}$	 Weight = 711t = $1.047V_{50}$	 Weight = 1116t = $1.644V_{50}$
Span/2000 (25mm)	 Weight = 1358t = $V_{25}$	 Weight = 1418t = $1.044V_{25}$	 Weight = 2227t = $1.640V_{25}$

**Figure 3.6:** Hotel basement study - 2D mother truss: Results of initial study into influence of deflection limits.

3.6 shows the resulting forms for the three load case problem with a range of deflection limits imposed at mid-span. The deflection limits are imposed at the serviceability limit state (SLS), by adding an additional load case with all loads factored unfavourably (using SLS factors).

From the top row of Table 3.6, which shows stress based designs, it can be seen that the form based on the optimized result is both lighter and stiffer than the traditional layout. When deflection limits become governing, this translates into an increased difference in volume. Also note that the overall layouts of all the layout optimization results are broadly similar.

A number of different deflection limits were tested, as the design team had not yet decided the appropriate criteria for the project. This demonstrates the subjective nature of serviceability constraints such as deflection limits. There is some movement within the community to consider reducing the strictness of these constraints (Orr, 2008), or to use alternative methods to address them (Senatore, 2016). Because of this, the remainder of this chapter will consider stress based designs. Therefore larger material savings than those shown in the figures below (e.g. Figure 3.7) may be possible in a case where displacements are limiting.

### 3.3.3 Rationalisation

#### Automatic layout rationalization

The structures resulting from layout optimization (such as Figures 3.7a-c) are frequently very complex, this is further exacerbated when multiple load cases are concerned - as shown in Figure 3.7d. One method of rationalizing these structures is the joint cost method of Parkes (1975), this can be easily implemented as part of the linear programming problem for layout optimization (He & Gilbert, 2015). This approach has been applied to the current problem in Figure 3.7e. This approach has the advantage of being automatic, allowing result to be obtained quickly and reproducibly. However, the resulting structure still has a number of features that would be challenging to construct, including members that meet at narrow angles and very fine members.

#### Human-in-the-loop layout rationalization

An alternative method involves a ‘human-in-the-loop’ approach (He et al., 2017). In such a process, the rationalization is manually controlled by the operator who has the ability to edit the solution of the layout optimization problem. The LimitState:FORM (Limitstate Ltd., 2019) software also implements a similar approach by allowing the user to delete unwanted members or add new members. The geometry optimization method (He & Gilbert, 2015) can then be used to find the optimal positions of the remaining nodes.

Here an additional step was also included, in which all nodes remaining in the structure after geometry optimization are taken as the basis for a fully connected ground structure, on which layout optimization is performed. This was found to be helpful in avoiding the local optima that may result from manual intervention. For example, Figure 3.7f shows an intermediate solution identified during the manual rationalization process; whilst this structure is simple, it has a volume some 13% above the equivalent un-rationalized solution (Figure 3.7d). The fully connected layout optimization based on this is shown in Figure 3.7g, and allows much of this volume penalty to be eliminated with only a small increase in complexity. Much of this complexity is then removed again in the next iteration of manual intervention, producing the structure shown in Figure 3.7h. Overall, this manual rationalization increases the volume of the structure by only 5%.

The truss based nature of the layout optimization method means that interaction with solutions should be fairly intuitive to anyone familiar with more conventional frame analysis programs. Developing a feel for the best members to add or remove comes with practice. This intuition may be obtained through experience, improved by knowledge of the fundamental features of minimum weight structures, such as preferring the use of purely axially loaded members, and the fact that tension and compression members should ideally intersect at close to 90 degrees in problems dominated by a single load case.

#### Cross section rationalization

Another feature of optimized structures which can cause challenges for production is the fact that each member will generally require a different cross-section area. As the problem currently under consideration is to be constructed from fabricated sections, the requirements for rationalizing the number of sections are somewhat different from the catalogue section constraints commonly implemented using MILP (Stolpe, 2016). As the sizes of the cross sections are not known in advance, they cannot be used as coefficients of a linear problem.

Instead, the rationalization of the cross sections has here been undertaken as a post processing step. This adopted a simple brute-force approach, with every combination of cross sections present in the solution being considered as a potential solution. For each potential set of cross sections, every element was assigned the smallest available cross section that was at least as large as its original cross section. The set of cross sections that produced the smallest total volume was then returned. The result of applying this process to the structure

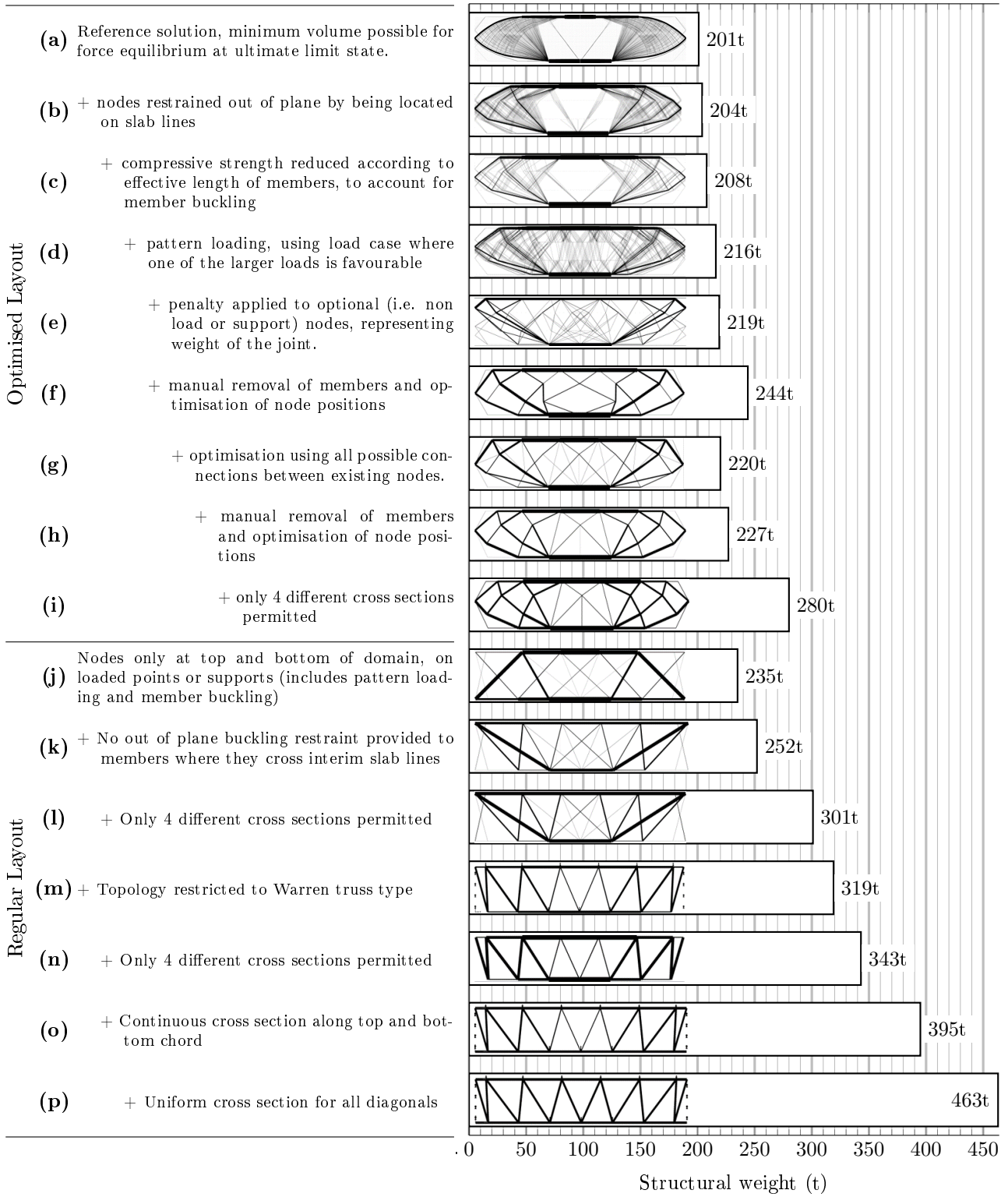


**Figure 3.7:** Hotel basement study - 2D mother truss: Comparison of options for structural layout.



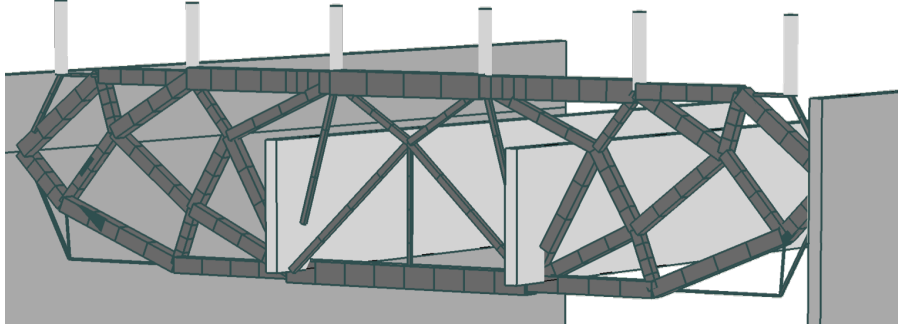


**Figure 3.8:** Hotel basement study - 2D mother truss: Rationalized truss using optimized topology (dark grey), showing supporting walls (mid grey) and main loading sources (light grey).

in Figure 3.7h is shown in Figure 3.7i, and with the context of the surrounding structure in Figure 3.8. This process is shown to increase the volume by 23%. It may be possible to reduce this value by, for example, geometry optimizing the structure whilst maintaining the current sets of linked member cross sections.

### 3.3.4 Results

The manual rationalization approach can also be used to force structures to take on well known forms for comparison purposes. To assist with the comparison of the optimized layout and the more regular structures that will now be described, Figure 3.9 shows the volumes of the two structures alongside one another. The structures of Figure 3.9a-e correspond to Figure 3.7i, h, d, c, and a respectively. The bars show the volume added by each decision made during the modelling and rationalization process, and how it contributes to the overall material usage.

Figures 3.7j and 3.9i show the results of a very low resolution layout optimization for the current problem with member buckling and pattern loading. the ground structure used here allows nodes only at the locations of the loads, plus the top and bottom of the supports. The contributions of the different decisions made in moving from Figure 3.9j (i.e. Figure 3.7a) to 3.9i are split into the increase from the use of the ground structure of only 17 nodes, and the increases from adding the pattern load cases and reducing  $\sigma_C$  to model member buckling. In this case, the permissible stress of each member was set assuming that the effective length was equal to the maximum distance it travelled between two floor slabs.

Figures 3.7k and 3.9h show the case where the effective buckling length of the members was set based on their whole length rather than the free length between floors. Figure 3.7l then uses the procedure described above to limit the problem to only 4 different cross-section types.

The set of nodes used in these three structures is the same as that which would be used for a conventional Warren truss solution, however the optimized layouts are substantially different. The number of joints used in Figures 3.7j-k is difficult to evaluate as many pairs of members in these solutions intersect partway along their lengths. Realising this physically may require an additional joint at these points, making these solutions significantly more complex than a Warren truss despite having the same number of ground structure nodes.

The manual rationalization process can be used to eliminate these crossover joints, although it is not always clear which of the two intersecting members should be removed. The structure has been manually rationalized, removing crossovers and giving a Warren truss form, in Figures 3.7m and 3.9g. This has a volume increase of 27% over the layout optimized solution with a the same number of ground structure nodes. This is a significant increase, as can be seen from Figure 3.9, yet to manually establish if there was may be more efficient layout using these nodes (without crossovers) would be a challenging and time consuming task.

The Warren truss topology was limited to only four different cross sections, this structure is shown in Figure 3.7n. The locations of these automatically assigned cross sections are not related to the convenient conceptual groupings of the structure (i.e. top chord, bottom chord and diagonals). Therefore Figures 3.7o-p show the cases where the top and bottom chord are required to be of constant cross sections, and also where all diagonal members should have the same cross section.

The design in Figure 3.9f (and also Figure 3.7p), is reasonably similar to what may be proposed from the conventional practice of structural design. However, this has a volume of 2.3 times larger than the theoretical benchmark value in Figure 3.9j, and it is also 65% heavier than the rationalized structure based on the optimal layout shown in Figure 3.9a. Thus it seems that substantial material savings can be made possible using the methods demonstrated here.

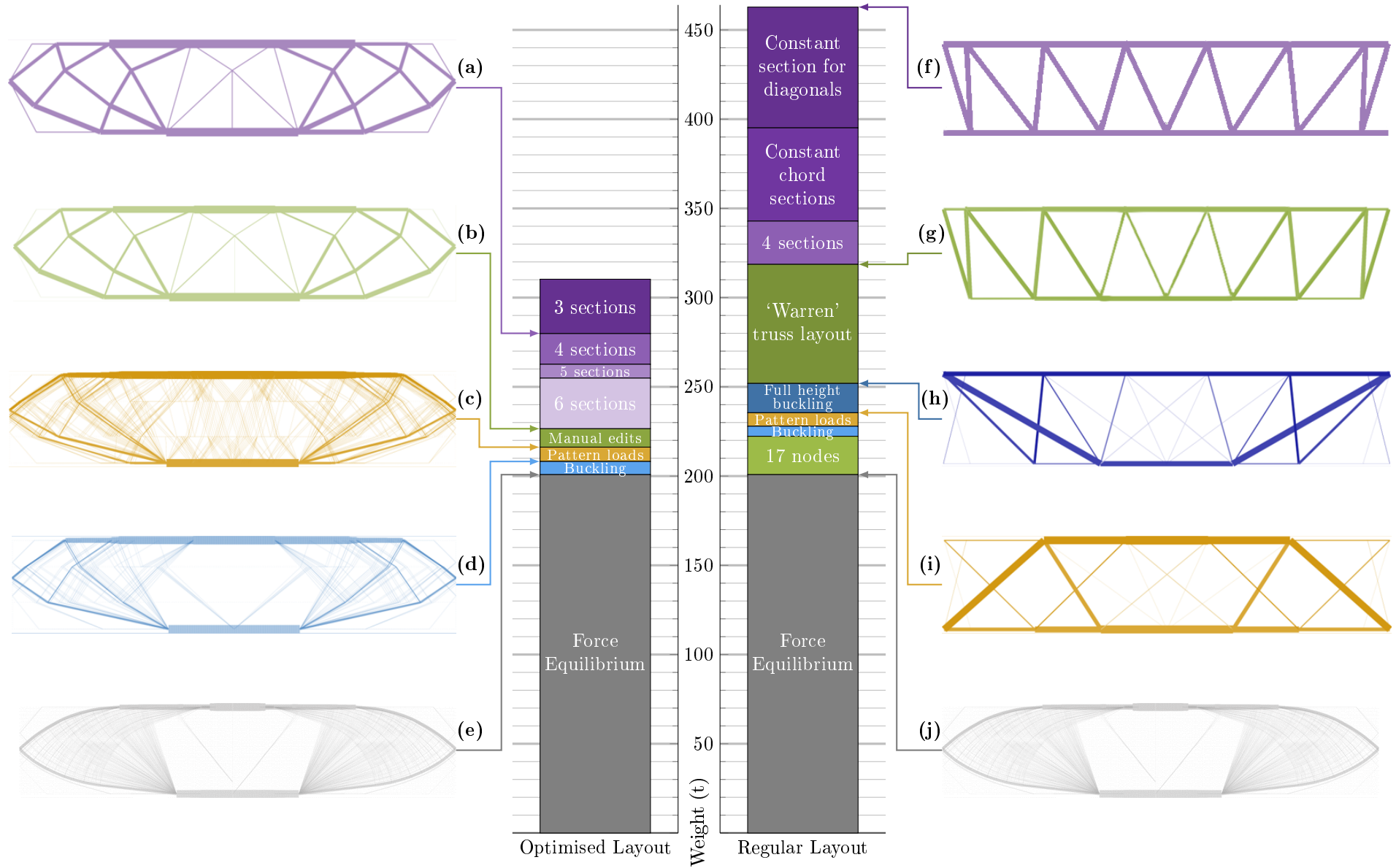


**Figure 3.9:** Hotel basement study - 2D mother truss: Contributions of different design decisions to the volume of the final designs of optimized and regular layouts. Blue steps relate to the modelling of buckling, yellow refers to pattern loading, green to rationalization of layout and purple to rationalization of sections.

### 3.4 Observations

This chapter has demonstrated that there is the potential for substantial material savings through the use of numerical optimization. In the undertaking of the case study presented here a number of issues have been encountered in applying current optimization methods to a real world design project.

Interpretation of results, particularly for complex 3D problems such as Figure 3.2, can be challenging and this may limit the users confidence in the structural form. This also causes issues in applying the manual rationalization process as it is unclear which members should be removed. These complex and incomprehensible designs would cause significant difficulties in communicating the intention to other parties, such as the client or architect. This is likely to limit the uptake of optimization methods.

For simpler problems a manual rationalization method proved fairly effective, however this process is time consuming. Different users will likely obtain different designs and, whilst some level of empowerment is useful to allow for ill-defined or subjective constraints, a level of repeatability would increase confidence. From Figure 3.7e it can be seen that the joint cost method (Parkes, 1975) is not very effective at reducing the complexity of the structure. A more automated method for rationalizing the structures could also provide a more refined benchmark value to compare structures with similar levels of complexity.

The Pareto front style representation of Figure 3.7 is effective at allowing rapid comparison of different structures. However, the vertical axis represents a very vague concept of complexity. There are a wide variety of measures that could be used to quantify this; it is not yet known which measure would be most effective, or if they would all be equivalent to one another.

# Requirements identified in Part I

This thesis concerns the development of methods to facilitate the practical application of layout optimization techniques in structural engineering practice. To this end, a number of features of the real-world design process are noted. Parts II and III will develop methods to address these concerns within numerical optimization methods, in order to ensure maximum applicability to structural design.

- For long span structures, self-weight can be a significant contributor. Current methods of modelling self-weight within layout optimization can cause non-conservative errors. A novel method by which the self-weight may be accurately modelled will be developed in Part II. Firstly, the self-weight of structural members will be modelled in a distributed manner in Chapter 4, then consideration of the weight of non-structural material will be incorporated in Chapter 5.
- Cost is generally the driving objective in practical design. Cost estimation methods in use by practitioners rely on the existence of similar previous projects and therefore may not be reliable when a novel layout is used. Therefore optimization methods should consider additional factors that will contribute to the cost.
  - There are several elements of a structure that are frequently neglected or considered separately to the main structural design, however they may make a substantial contribution to the overall cost. Foundations are one of the most significant of these elements, and a formulation to incorporate these into the optimization will be proposed in Chapter 5.
  - Cost is also significantly impacted by additional complexity of construction. Where optimization algorithms have incorporated this, they have often used methods of quantifying complexity that greatly reduce the size of problem that can be solved. Part III considers approaches that may address this. The most direct approach is considered in Chapter 6; this discusses formulations including constraints that aim to reduce the complexity of the resulting structures, whilst still allowing problems of reasonable size to be addressed.
- Optimization methods are often too opaque and produce designs that are difficult to interpret. Conversely, design methodologies in use in practice today favour structures that can be explained using a reasonably small number of elements (e.g. pylon, main cable, hangers for a suspension bridge), and are therefore controlled by small numbers of parameters. In contrast, numerical optimization methods output complex arrangements of bars, with no hierarchical structure. Analytical methods of identifying minimum weight structures do produce structures that can be interpreted reasonably easily, however they are very challenging to identify for a given problem. Therefore, Chapter 7 will describe a framework within which numerical methods may be used to obtain optimal layouts that are expressed using regions, in the same way as analytical results. This not only increases the ease with which the results may be interpreted, but also clarifies how a structure should be modified to produce simpler designs.

## Part II

# Modelling self-weight



## Chapter 4

# Modelling of distributed self-weight

This chapter concerns the development of a novel method to identify optimal layouts for structures where the self-weight of the structure itself makes a substantial contribution to the overall loading. The impact of self-weight increases with span, and this chapter therefore applies the method to the initial design of long span bridge structures.

This work builds on the basic method outlined in the masters dissertation of the present author (Fairclough, 2015) which initially proposed the idea of replacing the straight bars of the ground structure, with optimally curved catenary forms. However a number of significant improvements are demonstrated herein. Most notably, the method has been extended to incorporate the member adding technique developed by Gilbert & Tyas (2003), resulting in significant increases in computational speed during the layout optimization phase and allowing high resolution numerical results (see Table 4.1) for benchmarking other designs. The results are also compared over a range of spans, to allow the increasing influence of self-weight loading to be seen. Additionally, a number of new considerations of practical relevance are incorporated, such as considering the possibility that members may have different costs and/or strengths in tension vs compression.

The contents of this chapter was originally prepared for a journal paper<sup>†</sup> (note that some notation has been changed for consistency) in collaboration with a number of co-authors. These include bridge designer Ian Firth, who offered practical guidance on which additional considerations would be most useful to include. Aleksey Pichugin was of particular assistance in the application of the extrapolation scheme used in Table 4.1. The implementation of the methods described and numerical optimization runs were performed by the author of the present thesis.

---

4.1	Introduction . . . . .	46
4.2	Elements of equal strength . . . . .	47
4.2.1	Catenary elements . . . . .	47
4.2.2	Vertical elements . . . . .	48
4.3	Layout optimization . . . . .	49
4.3.1	Standard formulation . . . . .	49
4.3.2	Formulation with elements of equal strength . . . . .	51
4.3.3	Rationalization via geometry optimization . . . . .	51
4.4	Application to very long span bridges . . . . .	52
4.4.1	Problem definition . . . . .	52
4.4.2	New reference volumes . . . . .	52
4.4.3	New structural forms . . . . .	52
4.4.4	Influence of span-to-dip ratio . . . . .	55
4.4.5	Influence of reducing the limiting compressive stress . . . . .	58
4.4.6	Commentary . . . . .	60
4.5	Conclusions . . . . .	61

---

<sup>†</sup> Fairclough, H. E., Gilbert, M., Pichugin, A. V., Tyas, A., & Firth, I. (2018). Theoretically optimal forms for very long-span bridges under gravity loading. *Proceedings of the Royal Society A: Mathematical, Physical and Engineering Sciences*, 474(2217)

## 4.1 Introduction

Since construction of the 137m span Union bridge on the England-Scotland border in 1820, the world's longest bridge span has doubled approximately every 50 years, and nine out of the ten longest bridge spans in history have been constructed in the last 20 years. In recent years plans have been developed for bridges in Italy, Norway and Indonesia with spans of in excess of 3km, whilst a more speculative, though still potentially feasible, proposal has been mooted for a bridge with 5km spans over the Strait of Gibraltar. Whilst these specific structures face challenges of a technical as well as economic and political nature, it is likely that bridge spans will continue to increase in the 21st century.

Forms for long span bridges have evolved over several centuries. The modern suspension bridge form, pioneered by James Finlay in the U.S., started to find favour at the turn of the nineteenth century (Drewry, 1832), and is still employed in the world's longest span bridge structures, such as the 1,991m span Akashi Kaikyo Bridge in Japan (Gregorski, 1998). In the past few decades the ease and speed of construction of cable-stayed bridge forms has led to an increase in their popularity, particularly for spans up to approx. 1200m. This development has led to debate about the relative merits of suspension vs. cable-stayed bridges (Hansford, 2012). However, debate has often centred on the importance of various practical considerations, for example relating to ease of construction or susceptibility to dynamic effects, rather than on a comparison of the theoretical efficiency of these forms. Furthermore, and most significantly, it has seldom been questioned whether these forms are appropriate when very long spans are involved, or whether more optimal structural forms exist. This is important as a non-optimal form will consume more material than is necessary, in some cases considerably more.

Also, it is important to bear in mind that for any given material the form will limit the overall span that can be attained. In the case of the Akashi Kaikyo Bridge, consultant M. Ito stated that high-strength steel wire was developed to reduce the dead weight *"because more than 90 percent of the cross section of the main cables is used to carry the bridge's own weight"* (Ito, 1996). Similarly, K. H. Ostenfeld, Project Director for the Great Belt (East) Bridge with the longest span in the world prior to Akashi Kaikyo at 1,624m, has stated that one of two limiting factors for long span bridges is *"the limits for known materials in carrying their own weight"* (Ostenfeld, 1996), governed by the well known square-cube law (Galileo, 1954). Also Lewis (2012) indicates a practical limiting span of less than 5km for a suspension bridge when using steel, suggesting that materials with a higher specific strength (the strength/weight ratio) might be necessary to achieve longer spans. However, although lightweight composite materials (Meier, 1987; Xiong et al., 2011), and even carbon nanotubes (Damolini, 2009), have been proposed for long span bridges, metals such as steel have advantages, such as far greater fracture toughness (Lu, 2010). This coupled with plentiful supply and low cost means that steel is likely to remain the dominant material for suspension cables for the foreseeable future. Thus, whilst materials are unlikely to revolutionise longer span bridges in the near term, and recognising that constructability factors still dominate consideration of economical solutions, there is the possibility for new, more materially-efficient, structural forms to do so. This is the focus of the present study.

Although there have been attempts to identify improved designs for very long span bridges by using engineering intuition (Lin & Chow, 1991; Starossek, 1996), an alternative is to use layout optimization, the theoretical basis of which was developed by A.G.M. Michell (1904) in the early 20th century, building on earlier work by J. Clerk Maxwell (1870). This theory later stimulated the development of computer-based numerical layout optimization methods (Dorn et al., 1964; Gilbert & Tyas, 2003). Modern numerical layout optimization methods have been found to be capable of identifying new forms and of obtaining very close estimates of the volumes of the corresponding exact solutions. For example, layout optimization was used to show that the minimum volume structure to carry a uniformly distributed load between pinned supports was not the parabolic arch (or cable) form which had presumed to be optimal since the time of Christiaan Huygens (Darwich et al., 2010), but instead a more complex form comprising networks of orthogonal tensile and compressive elements near the supports and a central parabolic section; in this case the numerical volume obtained via extrapolation techniques was later shown to be within 0.001% of the exact analytical solution subsequently derived (Tyas et al., 2011). Layout optimization has also been used to investigate bridge-like forms, for example being used to show that changing the ratio of the limiting compressive to tensile material strength gives rise to a family of optimal structures which range from arch to cable-stayed forms (Pichugin et al., 2015), prompting follow on analytical studies by practitioners (Beghini & Baker, 2015).

However, long-span bridge structures are dominated by self-weight and standard layout optimization techniques are not suitable in this case, since phenomena such as cable sag are not modelled intrinsically as part of the formulation. Simplified models which assume self-weight to be 'lumped' at end-nodes, and which implicitly assume that bending can be carried by the element between nodes (Bendsoe & Sigmund, 2004) are problematic in cases where self-weight effects are significant. This is because in such a formulation the flexural effect of self-weight on the element itself is ignored, and physically meaningful solutions may not be generated (e.g. a



solution might comprise long-spanning straight bars of constant cross section, which transmit a large proportion of their self-weight directly to supports).

In fact when self-weight is taken into account it has been known for almost two centuries that each (non-vertical) element in an optimal structure must take the form of a *catenary of equal strength* (Gilbert, 1826; Calladine, 2015). This is an element which is free of bending and has a cross section which varies along its length, thus ensuring no excess material is present, a requirement in a rigorously optimal solution (notwithstanding that uniform cross sections are normally preferred in practice, for practical reasons). A key feature of such an element is that if the spatial positions of its end points are known in advance then that element can take up one of only two possible shapes, depending only on whether the force to be carried is compressive or tensile. This is significant as it means that the standard layout optimization procedure (Dorn et al., 1964; Gilbert & Tyas, 2003) can be modified such that every potential (non-vertical) member is an equal stress catenary element with an *a priori* defined shape. Thus straight elements are replaced with suitably curved compression and/or tension elements. This also means that applications where self-weight effects are significant can be tackled, such as very long span bridges, enabling new reference solutions for bridge structures subjected to gravity loadings to be obtained.

In this paper the formulation for elements of equal strength will first be outlined and then used to provide a new layout optimization formulation. This will then be used to determine the theoretically optimal form for a very long span bridge of given span carrying gravity loading, with the volume of material required compared with that required to construct traditional bridge forms of the same span. Note that the influence of wind and other dynamic effects, while significant in the design and construction of such spans, are beyond the scope of the present study, although they can, in principle, be incorporated into structural optimization schemes.

## 4.2 Elements of equal strength

### 4.2.1 Catenary elements

Gilbert (1826) developed relations to describe the shape of the *catenary of equal strength*, a structural form transferring its self-weight to two level end points. Its cross-sectional area  $a$  is proportional to the axial force  $q$ , hence its weight per unit length is  $\kappa q$ , where  $\kappa$  is a proportionality constant. In an optimal skeletal structure the stresses at all points in an element must be purely axial, and equal to the value of the limiting material stress. For a material with unit weight  $\rho g$  then the weight per unit length is  $a\rho g$ . If the limiting stress in tension and compression is  $\sigma_T$  and  $\sigma_C$  respectively, then  $q = a\sigma_T$  and  $\kappa = \rho g/\sigma_T$  for tensile elements, and  $q = -a\sigma_C$  and  $\kappa = -\rho g/\sigma_C$  for compressive elements. Unless otherwise stated, in this paper the limiting material stress will be taken to be the same in tension and compression, such that  $\sigma_T = \sigma_C = \sigma$ .

Routh (1896, Art. 453) provides a concise derivation of the equation for this catenary in Cartesian coordinates, which for our purposes can be reformulated as

$$\kappa y = \log(\cos(\Omega_1 - \kappa x)) + \Omega_2 \quad (4.1)$$

If the origin is placed at the highest point of the curve  $\Omega_1 = \Omega_2 = 0$ . A plot of the curve is shown in Figure 4.1. The curve has vertical asymptotes at  $\pm\pi/2|\kappa|$ . Therefore, elements with a span of  $\pi/|\kappa|$  are not possible, as they would have infinite length and volume. (For the steel material used in this study, unless stated otherwise, the limiting material stress  $\sigma$  has been taken as 500MPa and the unit weight  $\rho g$  as 80kN/m<sup>3</sup>, so that the maximum span of an element is approximately 20km.)

We will need relations for elements connecting two arbitrary points on a plane, allowing these to be incorporated in the layout optimization formulation that will be described in Section 4.3. It can be shown, see Figure 4.1, that an equally stressed element connecting any two arbitrary points will consist of a segment of the curve defined by equation (4.1) with non-zero  $\Omega_1$  and  $\Omega_2$ . If the coordinates of two nodes are denoted by  $(x_A, y_A)$  and  $(x_B, y_B)$ , the expressions for the associated constants  $\Omega_1$  and  $\Omega_2$  can be established to be in the form

$$\Omega_1 = \kappa x_A - \arctan\left(\frac{\cos(\kappa(x_B - x_A)) - e^{\kappa(y_B - y_A)}}{\sin(\kappa(x_B - x_A))}\right) \quad (4.2)$$

$$\Omega_2 = \kappa y_A - \log\left(\cos\left(\arctan\left(\frac{\cos(\kappa(x_B - x_A)) - e^{\kappa(y_B - y_A)}}{\sin(\kappa(x_B - x_A))}\right)\right)\right) \quad (4.3)$$

The parameters that will be required in the layout optimization formulation are the reaction forces exerted on the element end points, and the volume of the element. Note also that the horizontal distance between the two connected points must be below  $\pi/|\kappa|$  in order for it to be possible to connect them; thus elements with a span greater or equal to this limit will not be added to the ground structure in the layout optimization formulation.

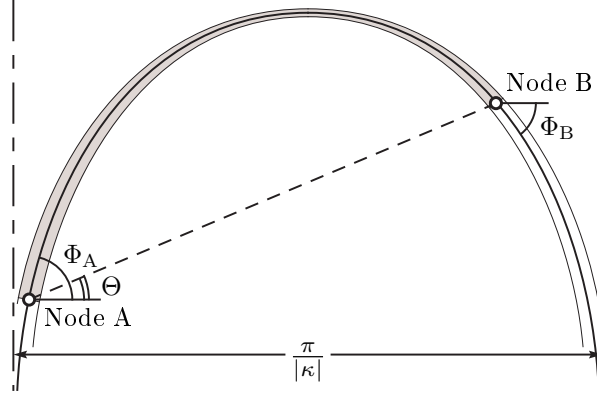


**Figure 4.1:** Approximate shape of an equally stressed element AB in compression

**Reaction Forces:** The angle of inclination of the centreline of the element at any point is given by

$$\Phi = \Omega_1 - \kappa x \quad (4.4)$$

In order to produce purely axial stresses the force must also be inclined at the angle  $\Phi$ . Therefore

$$q_y = q_x \tan(\Phi) \quad (4.5)$$

where  $q_y$  and  $q_x$  are the vertical and horizontal components of the force  $q$  at the given point. Component  $q_x$  will be constant over the length of the element as only vertical self-weight forces are applied between the end points. Given that an external force  $q$  is to be transmitted directly between the end points,  $q_x = q \cos(\Theta)$ , where  $\Theta$  is as shown in Figure 4.1. Combining this with equation (4.5), gives

$$q_y = q \cos(\Theta) \tan(\Phi) \quad (4.6)$$

which, when used with values of  $\Phi_A$  and  $\Phi_B$  from equation (4.4), allows the vertical reaction forces  $q_y$  to be determined at the supports. Note that when self-weight effects become negligible,  $\Phi$  will tend to  $\Theta$  and hence  $q_y$  in equation (4.6) will tend to  $q \sin(\Theta)$ .

**Volume:** The volume  $V$  of an element AB with unit width is given by

$$V_{AB} = \int_A^B a ds \quad (4.7)$$

where  $a$  is the cross-sectional area of the element at a given position along the element. By noting that the cross-sectional area at a point is proportional to the force at that point, it can be shown that

$$V_{AB} = -\frac{q_x}{\rho g} (\tan(\Phi_B) - \tan(\Phi_A)) = -\frac{q \cos(\Theta)}{\rho g} (\tan(\Phi_B) - \tan(\Phi_A)) \quad (4.8)$$

Note that there will be two sets of values for  $\Phi_A$  and  $\Phi_B$ , one set for tensile elements and one set for compressive elements (see equation (4.4), noting that the sign of  $\kappa$  changes depending on whether tensile or compressive elements are involved).

#### 4.2.2 Vertical elements

The equations presented in the preceding section cannot be applied to perfectly vertical elements as the curve never becomes completely vertical. Complementary equations for the thickness of an optimal vertical element of varying cross section are therefore now derived.

If an infinitesimal slice of a vertical element is considered, as shown in Figure 4.2, vertical equilibrium and the requirement that the stress is always equal to the limiting stress gives

$$-\frac{1}{q} dq = \kappa ds \quad (4.9)$$

Integrating both sides between the endpoints A and B gives

$$q_B = q_A \exp(\kappa(y_A - y_B)) \quad (4.10)$$

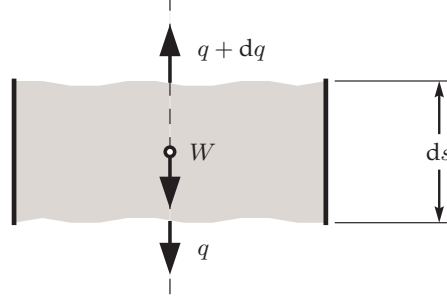


**Figure 4.2:** Forces acting on an infinitesimal slice of a vertical, equally stressed element.

**Reaction Forces:** Equation (4.10) relates the forces at each end of the element; however, unlike the catenary form, there is no value  $q$  which relates this to the force to be transmitted. Therefore the reaction forces at the ends of vertical elements are defined in terms of  $q_A$ . Trivially, the vertical reaction force at point A is defined as  $1 \times q_A$  and Eq. (4.10) provides the definition of the vertical reaction at point B. Also, since the element is vertical,  $q_{Ax} = q_{Bx} = 0$ .

**Volume:** The volume of the vertical element is found by integrating the cross-sectional area of the element over its length, which, due to (4.10), yields

$$V_{AB} = \int_A^B A \, ds = \frac{q_A}{\rho g} (\exp(\kappa(y_A - y_B)) - 1) \quad (4.11)$$

## 4.3 Layout optimization

### 4.3.1 Standard formulation

The standard (weightless) numerical layout optimization procedure involves discretising a design domain with  $n$  nodes, usually positioned on a uniform grid. These nodes are interconnected with  $m$  potential truss elements, forming a ‘ground structure’, and optimization is then used to find the minimum volume truss structure satisfying force equilibrium conditions, explained diagrammatically in Figure 4.3a–c.

The classical ‘equilibrium’ plastic truss layout optimization formulation for a single load case is defined as

$$\min V = \mathbf{c}^T \mathbf{q}$$

subject to:

$$\mathbf{B}\mathbf{q} = \mathbf{f} \quad (4.12)$$

$$\mathbf{q} \geq \mathbf{0}$$

where  $V$  is the total volume of the structure. In the standard formulation not involving self-weight  $\mathbf{q} = [q_1^T, q_1^C, q_2^T, q_2^C, \dots, q_m^C]^T$ , and  $q_i^T, q_i^C$  are the tensile and compressive internal forces in bar  $i$  ( $i = 1, \dots, m$ );  $\mathbf{c} = [l_1/\sigma_T, l_1/\sigma_C, l_2/\sigma_T, l_2/\sigma_C, \dots, l_m/\sigma_C]^T$ , where  $l_i$  is the length of bar  $i$  and  $\sigma_T$  and  $\sigma_C$  are respectively the limiting material stress in tension and compression. Note that in the classical layout optimization formulation buckling instability is not modelled directly, though the specified limiting material stress in compression can if necessary be reduced to account for this.  $\mathbf{B}$  is a suitable  $(2n \times 2m)$  equilibrium matrix containing direction cosines and  $\mathbf{f} = [f_1^x, f_1^y, f_2^x, f_2^y, \dots, f_n^y]^T$ , where  $f_j^x$  and  $f_j^y$  are the  $x$  and  $y$  components of the external load applied to node  $j$  ( $j = 1, \dots, n$ ). The presence of supports at nodes can be accounted for by omitting the relevant terms from  $\mathbf{f}$ , together with the corresponding rows from  $\mathbf{B}$ .

Consider now the contribution of a single element  $i$  to the volume of the structure and to the global equilibrium matrix, which can be written as  $V_i = \mathbf{c}_i^T \mathbf{q}_i$  and  $\mathbf{B}_i \mathbf{q}_i$ , where  $\mathbf{c}_i$ ,  $\mathbf{B}_i$  and  $\mathbf{q}_i$  are, respectively, a vector containing terms that allow the volume to be derived from the element force, the local equilibrium matrix, and the vector containing element force terms. The relevant expressions can be written in expanded form as

$$V_i = \begin{bmatrix} \frac{l_i}{\sigma_T} & \frac{l_i}{\sigma_C} \end{bmatrix} \begin{bmatrix} q_i^T \\ q_i^C \end{bmatrix}, \quad (4.13)$$

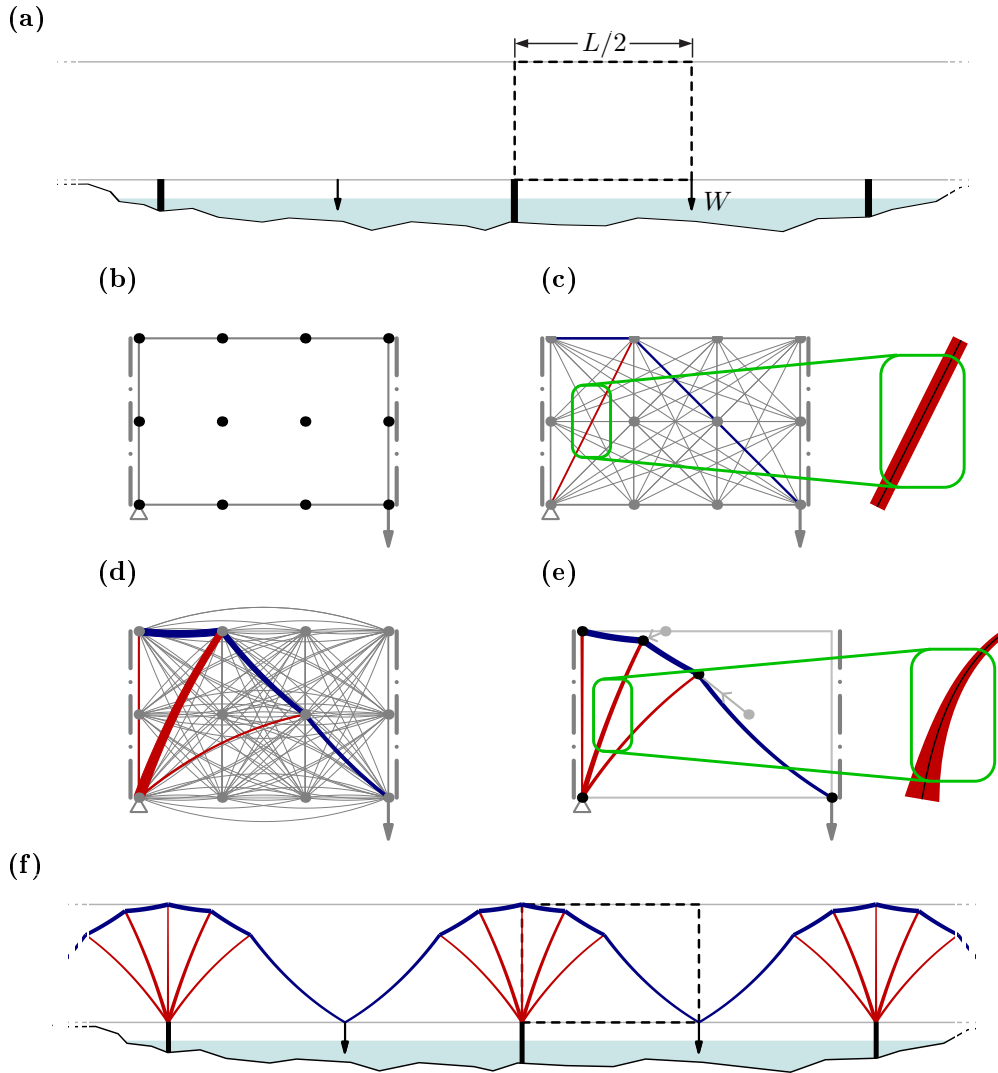


**Figure 4.3:** Procedure employed to identify optimal (minimum volume) bridge structures. Steps (a)-(c) describe the standard layout optimization formulation while steps (a)-(b) and (d) describe the new layout optimization formulation, used when self-weight effects are significant. Steps (e)-(f) show the result of subsequently applying geometry optimization.

(a) Problem definition (simplified multi-span bridge problem with multiple spans, with point load applied at the centre of each span; the highlighted half span can be modelled due to symmetry).

(b) Design domain discretized with nodes and assumed boundary and load conditions.

(c) Layout of straight (weightless) elements identified via layout optimization. (Compressive and tensile elements shown in red and blue respectively.)

(d) Layout of curved elements identified via layout optimization. (Curved elements may lie slightly outside the domain.)

(e) Improved design, obtained by adjusting the positions of active nodes using geometry optimization. (Detail shows an element with exaggerated self-weight, demonstrating the curvature and non-uniform cross sections of these elements.)

(f) Resulting optimized design for the problem.

$$\mathbf{B}_i \mathbf{q}_i = \begin{bmatrix} \cos \Theta_i & -\cos \Theta_i \\ \sin \Theta_i & -\sin \Theta_i \\ -\cos \Theta_i & \cos \Theta_i \\ -\sin \Theta_i & \sin \Theta_i \end{bmatrix} \begin{bmatrix} q_i^T \\ q_i^C \end{bmatrix}, \quad (4.14)$$

where  $\Theta_i$  is the angle of inclination of the element.

This problem is in a form which can be solved using linear programming (LP), with the member forces in  $\mathbf{q}$  being the LP variables. Although posed as a plastic design problem, when only a single load case is involved, as is the case here, the formulation furnishes solutions which are identical to those obtained when using an elastic (minimum compliance) formulation Bendsoe & Sigmund (2004).

#### 4.3.2 Formulation with elements of equal strength

To take account of the effects of self-weight, the standard formulation can be modified to include elements with equal strength along their length. Thus straight elements are replaced with suitably curved compression and/or tension members, as indicated on Figure 4.3d. By using the relations given in Section 4.2, new terms for  $V_i$  and  $\mathbf{B}_i \mathbf{q}_i$  can be established which take account of self-weight effects as follows.

**Inclined element with self-weight:** the element volume and equilibrium expressions can be obtained using (4.8) and (4.6) respectively, and written in expanded form as

$$V_i = \left[ \frac{\cos(\Theta_i) [\tan \Phi_A^T - \tan \Phi_B^T]}{\rho g} \quad \frac{\cos(\Theta_i) [\tan \Phi_B^C - \tan \Phi_A^C]}{\rho g} \right] \begin{bmatrix} \hat{q}_i^T \\ \hat{q}_i^C \end{bmatrix} \quad (4.15)$$

$$\mathbf{B}_i \mathbf{q}_i = \begin{bmatrix} \cos \Theta_i & -\cos \Theta_i \\ \cos \Theta_i \tan \Phi_A^T & -\cos \Theta_i \tan \Phi_A^C \\ -\cos \Theta_i & \cos \Theta_i \\ -\cos \Theta_i \tan \Phi_B^T & \cos \Theta_i \tan \Phi_B^C \end{bmatrix} \begin{bmatrix} \hat{q}_i^T \\ \hat{q}_i^C \end{bmatrix}, \quad (4.16)$$

where  $\Phi_A^T$ ,  $\Phi_A^C$  and  $\Phi_B^T$ ,  $\Phi_B^C$  are the angles of inclination of the tensile and compressive equal stress catenary elements at points A and B respectively which are calculated from Eq. (4.4), and  $\hat{q}_i^T$  and  $\hat{q}_i^C$  are the tensile and compressive forces in the element (equivalent to  $q_i^T$  and  $q_i^C$  given in the previous section).

**Vertical element with self-weight:** in this case the element volume and equilibrium expressions can be obtained using (4.11) and (4.10) respectively, and written in expanded form as

$$V_i = \left[ \frac{1 - \exp[\kappa(y_A - y_B)]}{\rho g} \quad \frac{\exp[\kappa(y_A - y_B)] - 1}{\rho g} \right] \begin{bmatrix} \hat{q}_i^T \\ \hat{q}_i^C \end{bmatrix} \quad (4.17)$$

$$\mathbf{B}_i \mathbf{q}_i = \begin{bmatrix} 0 & 0 \\ 1 & -1 \\ 0 & 0 \\ -\exp(\kappa(y_A - y_B)) & \exp(\kappa(y_A - y_B)) \end{bmatrix} \begin{bmatrix} \hat{q}_i^T \\ \hat{q}_i^C \end{bmatrix}, \quad (4.18)$$

where in this case  $\hat{q}_i^T$ ,  $\hat{q}_i^C$  are tensile and compressive force components, equal to  $q_A$ , the force exerted on node A.

It is entirely possible for the ground structure, and therefore the resulting solution, to contain any desired combination of weightless, inclined and vertical elements.

#### 4.3.3 Rationalization via geometry optimization

When using layout optimization the solution accuracy is controlled by the number of nodes used to discretise the design domain. If large numbers of nodes are employed then highly accurate numerical solutions can be obtained. However, the associated forms will often be complex, and also difficult to realise in practice. To address this a relatively coarse nodal discretisation can instead be used to obtain a layout that can then be improved by adjusting the locations of nodes using the geometry optimization procedure described by He & Gilbert (2015), though with standard weightless bars replaced with elements of equal strength, using the relations described in the preceding section; sample results are shown in Figure 4.3e, f.

## 4.4 Application to very long span bridges

### 4.4.1 Problem definition

The modified layout optimization procedure can now be used to identify theoretically optimal forms for very long span bridges. For sake of simplicity it is here assumed that the central span of a notional multi-span bridge structure is being modelled, with the problem being as described in Figure 4.3, but with the point loads  $W$  replaced with a uniformly distributed load  $w$ , applied at the same elevation. This configuration can also be used to approximately represent a bridge with a central main span and shorter side-spans. (In fact this representation will be exact if the side-spans are equal to half the main span, and if reactions at the ends of the bridge are purely horizontal, as is approximately the case e.g. for the Akashi Kaikyo Bridge.) However, other specific scenarios can readily be modelled using the general numerical procedure described. The magnitude of  $w$  is assumed to include both traffic loading and the self-weight of deck elements required to provide a continuous level traffic surface, though it does not include the self-weight of material required in the deck to carry axial forces, if present, which is automatically included in the model as part of the optimization process. Note also that in very long span bridges traffic loading becomes less significant than the self-weight of the deck and cables, which means that the problem can justifiably be posed as a single load case layout optimization problem, furnishing a structural form which consumes the minimum possible volume of material to carry the distributed load  $w$  and the self-weight of the structural elements employed.

The inherent bending resistance of the pylons and deck is not considered in the optimization directly, but will be required to ensure that alternative load cases can be carried. Also, although wind and other dynamic effects are very important in cable supported bridges, particularly when spans are long, various mitigation strategies can often be applied once the basic form has been established. For example, to counter wind-induced vibration it has recently been suggested that the use of slotted box girder decks will permit 5km suspension bridge spans to be achieved (Ge, 2016), or alternatively active control systems can potentially be employed (Xu, 2013). These are therefore not considered further here.

In the interests of computational efficiency a half span was modelled (taking advantage of symmetry) and the adaptive solution strategy developed by Gilbert & Tyas (2003) was employed to enable problems with increasingly fine nodal resolutions to be solved. The load discretisation strategy used by Darwich et al. (2010) was also employed in order to reduce the discretisation error associated with the load. The largest model run contained 68,026 nodes and 2,313,734,325 potential connections, including overlaps (i.e. over 2 *billion* potential connections).

### 4.4.2 New reference volumes

Using the aforementioned assumptions, the layout optimization procedure has been used to obtain new reference solutions for a range of bridge span lengths  $L$ , obtained by using increasingly fine nodal resolutions; numerical results are shown in Table 4.1. The spans quoted in the table assume high strength steel is employed for all elements, with a limiting material strength in tension and compression of 500MPa and a unit weight of 80kN/m<sup>3</sup> - though other scenarios can readily be modelled using the general numerical procedure described. Also shown are extrapolated volumes computed using the power law extrapolation scheme described in Darwich et al. (2010). Models comprising  $n_x = 200, 240, \dots, 600$  divisions were used to provide source data, where  $n_x$  is the number of nodal divisions across the full span (the number of nodal divisions in the height of the domain,  $n_y$  was taken as  $n_x \times 3/8$ ). A weighted nonlinear least-squares approach was used to find best-fit coefficient values for use in the extrapolation, with the weighting factor taken as  $n_x$ , to increase the influence of fine resolution solutions.

For the 0km span (weightless) case the extrapolated value was found to compare closely with a recently published analytical value Pichugin et al. (2015), showing that high precision results can be obtained. For the other spans considered the extrapolated values furnish new reference volumes, providing benchmark values against which alternative bridge designs can be judged. (As suggested by Cox (1965), just as there is a limit on the thermal efficiency of a heat engine, set by the Carnot cycle, so there is a lower limit on the volume of material necessary to form a structure. Even though this will not normally be achievable in practice, it provides a useful basis on which to judge alternative designs.)

### 4.4.3 New structural forms

Structural forms corresponding to the new reference solutions for 1km, 2.5km and 5km span lengths are shown in Figure 4.4a. To provide visually clear solutions a layout optimization discretisation involving 30 nodal spacings across the full span was used prior to rationalizing the solutions using geometry optimization.

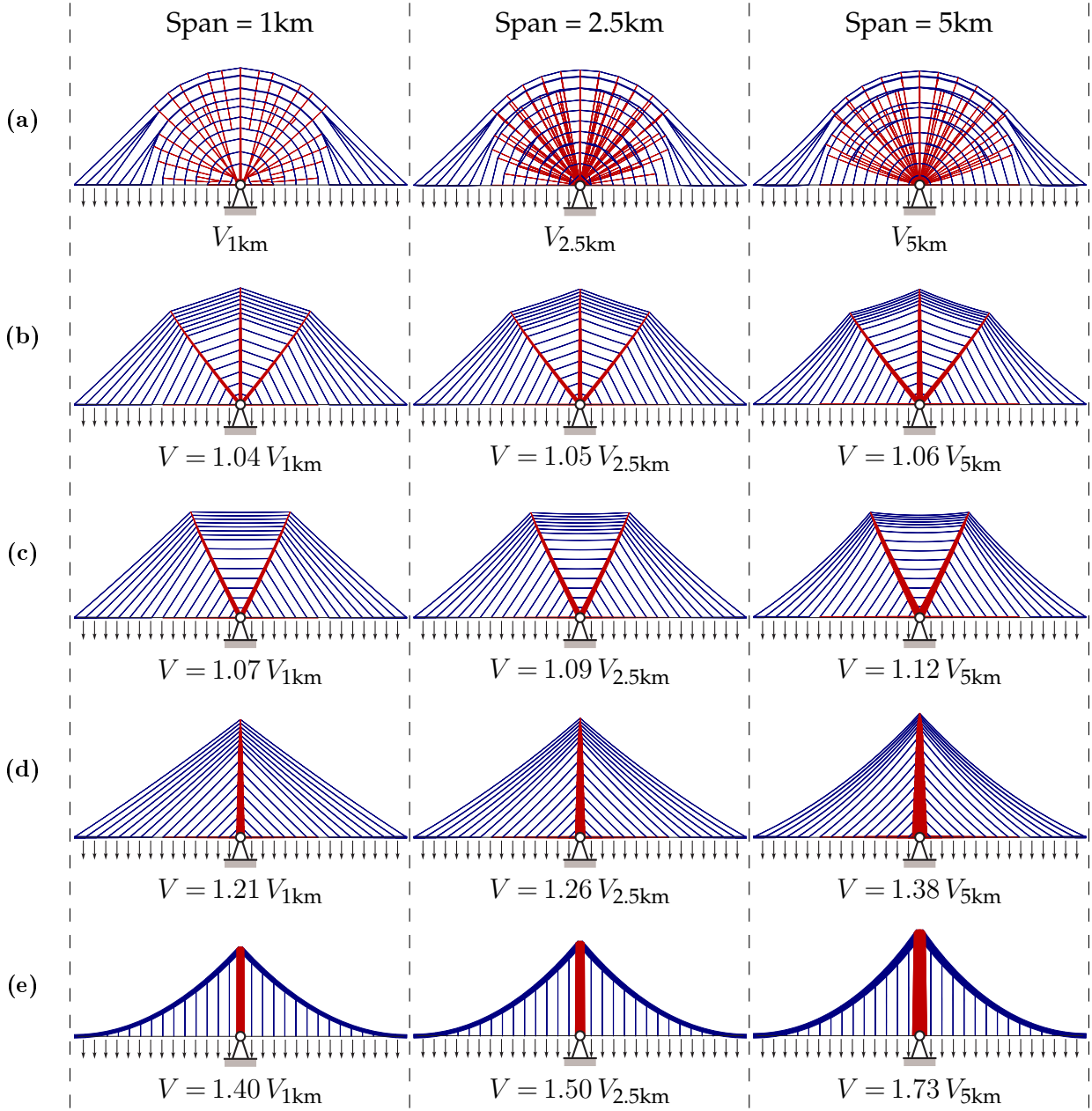


**Figure 4.4:** Bridge forms for various spans and associated volumes, expressed in terms of the reference volume, where  $V_{1\text{km}} = 0.7805wL^2/\sigma$ ,  $V_{2.5\text{km}} = 0.8737wL^2/\sigma$  and  $V_{5\text{km}} = 1.0662wL^2/\sigma$  (where  $w$  is the load applied at deck level,  $L$  is the span and  $\sigma$  is the limiting strength of the material). The three span lengths considered,  $0.16 \frac{\sigma}{\rho g}$ ,  $0.4 \frac{\sigma}{\rho g}$  and  $0.8 \frac{\sigma}{\rho g}$ , correspond to 1km, 2.5km and 5km respectively when  $\sigma$  is taken as 500MPa and the unit weight  $\rho g$  as 80kN/m<sup>3</sup>. All solutions shown were optimized via geometry optimization. (a) Reference design (simplified layout shown for clarity). (b) Optimized triple split pylon design. (c) Optimized double split pylon design. (d) Optimized cable stayed design. (e) Optimized suspension bridge design. (All with variable cross-section cables.)

	$n_x$	Span			
		0 km (weightless)	1 km ( $0.16 \frac{\sigma}{\rho g}$ )	2.5 km ( $0.4 \frac{\sigma}{\rho g}$ )	5 km ( $0.8 \frac{\sigma}{\rho g}$ )
Numerical	200	0.726937	0.781744	0.875206	1.068504
	240	0.726759	0.781493	0.874886	1.067978
	280	0.726624	0.781327	0.874680	1.067679
	320	0.726535	0.781206	0.874535	1.067468
	360	0.726475	0.781120	0.874425	1.067293
	400	0.726425	0.781050	0.874337	1.067149
	440	0.726378	0.780995	0.874262	1.067038
	480	0.726342	0.780945	0.874201	1.066947
	520	0.726313	0.780903	0.874150	1.066866
	560	0.726286	0.780871	0.874109	1.066804
	600	0.726267	0.780844	0.874075	1.066753
	$\infty^\dagger$	0.726031	<b>0.780531</b>	<b>0.873674</b>	<b>1.066152</b>
Analytical	-	0.7260325 $^\ddagger$	-	-	-
Diff. (%)	-	0.0002%	-	-	-

$^\dagger$  Obtained by extrapolation, using a power-law extrapolation scheme as used in Darwich et al. (2010).

$^\ddagger$  Analytical solution obtained by Pichugin et al. (2015)

**Table 4.1:** Numerical volumes ( $\times \frac{wL^2}{\sigma}$ ) for various bridge spans and nodal resolutions. The new reference solutions are shown in bold typeface. (Quoted span lengths assume a limiting material stress  $\sigma = 500\text{MPa}$  and unit weight  $\rho g = 80\text{kN/m}^3$ .)

The new reference forms shown on Figure 4.4a quite closely resemble the weightless Michell structure that was fully described analytically by Pichugin et al. (2015), with tension and compressive elements aligned (near)orthogonally. They also include a series of inclined compressive elements radiating out from the supports, just as in Pichugin et al. (2015). The forms are also markedly different to traditional cable stayed or suspension bridge forms, though would clearly be extremely difficult to construct in practice. However, to allow comparison with the former, the inclined compressive elements can readily be removed by omitting candidate inclined compressive elements when setting up the layout optimization problem. The resulting optimized cable stayed bridge forms are shown in Figure 4.4d, and differ slightly from the standard ‘harp’ cable arrangement in that they have non-uniform spacing of stays along the height of the pylon. However, most significantly, the consumed material is up to 38 percent greater than that required for the corresponding (near) optimal reference designs shown in Figure 4.4a. Although the latter would be much more difficult to fabricate than the more conventional cable stayed forms shown in Figure 4.4d, they can be used to inspire a range of simplified forms. Thus Figure 4.4b & 4.4c show simplified split pylon bridge structures comprising respectively three and two pylons, consuming respectively approx. 6 percent and 12 percent more material than the corresponding reference designs in the 5km span case; a computer generated render of a bridge comprising two 5km spans designed to be potentially suitable for the hypothetical Strait of Gibraltar crossing is also shown in Figure 4.5.

The optimized locations of all elements in the single, double and triple split-pylon cable stayed structures shown in Figure 4.4b-d were found using geometry optimization techniques, indicating that a harp rather than fan style cable arrangement is most materially-efficient.

Also, for comparative purposes, optimized suspension bridge configurations were obtained by applying geometry optimization to the standard suspension bridge layout, as shown in Figure 4.4e. These bridges consume up to 73 percent more material than the corresponding reference designs shown in Figure 4.4a. (The bridge structures described here are actually somewhat lighter than those found in constructed suspension bridges as the cable areas were here allowed to vary along the lengths of the cables.)

Figure 4.6 presents results for all the cases described in normalised form, covering spans of up to 10km when using the same steel material as assumed before. Volumes for the fan style cable stayed bridge form are also included for comparative purposes, along with those for cable stayed and suspension bridge forms constrained to use the larger span-to-dip ( $L/h$ ) ratios currently employed in the world’s current longest cable stayed and suspension bridge spans, respectively found in the 1,104m span Russky Bridge, Russia ( $L/h = 4.4$ ) and the 1,991m span Akashi-Kaikyo Bridge, Japan ( $L/h = 9$ ). (Traditional suspension bridges have generally been built with span-to-dip ratios of 8.5 - 13.5 and cable stayed bridges with span-to-dip ratios of 3.4-4.9 (Lewis, 2012).) It is evident that traditional bridge forms with larger span-to-dip ratios become very inefficient as spans increase, but that the simplified double and triple split pylon forms remain comparatively efficient even when the span is long.



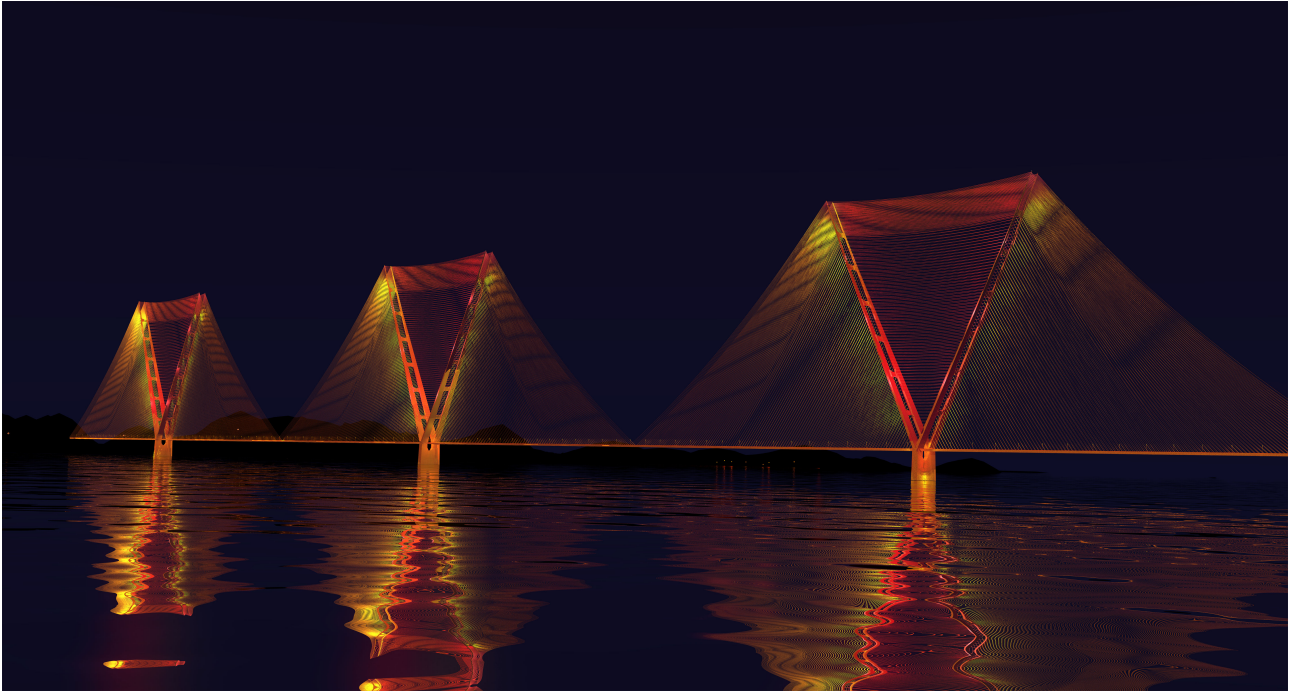


**Figure 4.5:** Split pylon concept bridge to cross Strait of Gibraltar, with two 5km main spans (not showing additional measures likely to be needed to counteract unbalanced live load effects - e.g. see Gimsing & Georgakis (2011)).

#### 4.4.4 Influence of span-to-dip ratio

The fact that a high span-to-dip ratio in a cable supported bridge can lead to a high volume of material being required has been known for many years (indeed this prompted the seminal work of Davies Gilbert, who wanted to demonstrate to Thomas Telford that the initial shallow suspension bridge design for the Menai Straits was structurally inefficient (Calladine, 2015)). However, a low span-to-dip ratio also requires the use of tall pylons, which can be problematic to construct. Also, when non-uniform loadings are present it has been observed that midspan deflections increase in suspension bridges when lower span-to-dip ratios are employed (Gimsing & Georgakis, 2011). It is therefore of interest to explore the influence of the limiting span-to-dip ratio on the volume of material required, and to evaluate the performance of the new simplified forms when such limits are imposed. Figures 4.7 and 4.8 present volumes and corresponding forms when the span-to-dip ratios are limited to 4.4 and 9 respectively; key results from Figures 4.6, 4.7 and 4.8 are also tabulated on Table 4.2, showing that the span-to-dip ratios identified as being optimal in the present study are considerably lower than those typically used in practice.

From Figures 4.7 and 4.8 it is clear that even when a limit is placed on the span-to-dip ratio, the corresponding reference form consumes considerably less material than traditional forms. The simplified double split pylon form is also much more materially-efficient than traditional forms, suggesting that this latter form could prove popular in practice. When the span-to-dip ratio is increased to 9 the resulting double split pylon form quite closely resembles the split pylon design tentatively proposed by Starossek (1996) some years ago, though the latter uses a fan style cable arrangement rather than the hybrid cable arrangement observed to be optimal here. (A small number of split pylon cable stayed bridges have been constructed in practice, though these have generally spanned relatively short distances, and aesthetic or specific practical reasons for their form have usually been cited by their designers. For example, the double split pylon cable stayed bridge constructed near Düsseldorf Airport in Germany in 2002 was so designed to keep the height of the structure low in order to avoid impeding air traffic (Prehn & Mertens, 2002). Also, this bridge uses a fan style cable arrangement, rather than the hybrid cable arrangement found to be most materially-efficient here.)

When the height available is unrestricted the optimal cable stayed form resembles the harp style form but has a non-uniform spacing of cables up the pylon (see Figure 4.6); this also leads to a lower pylon height being required. As the height available is reduced the traditional harp style form (with uniform spacing of cables up the pylon) becomes less efficient than both the fan style form and also the suspension bridge form. Also, the optimal cable stayed form begins to resemble the fan style form, and has a similar volume.

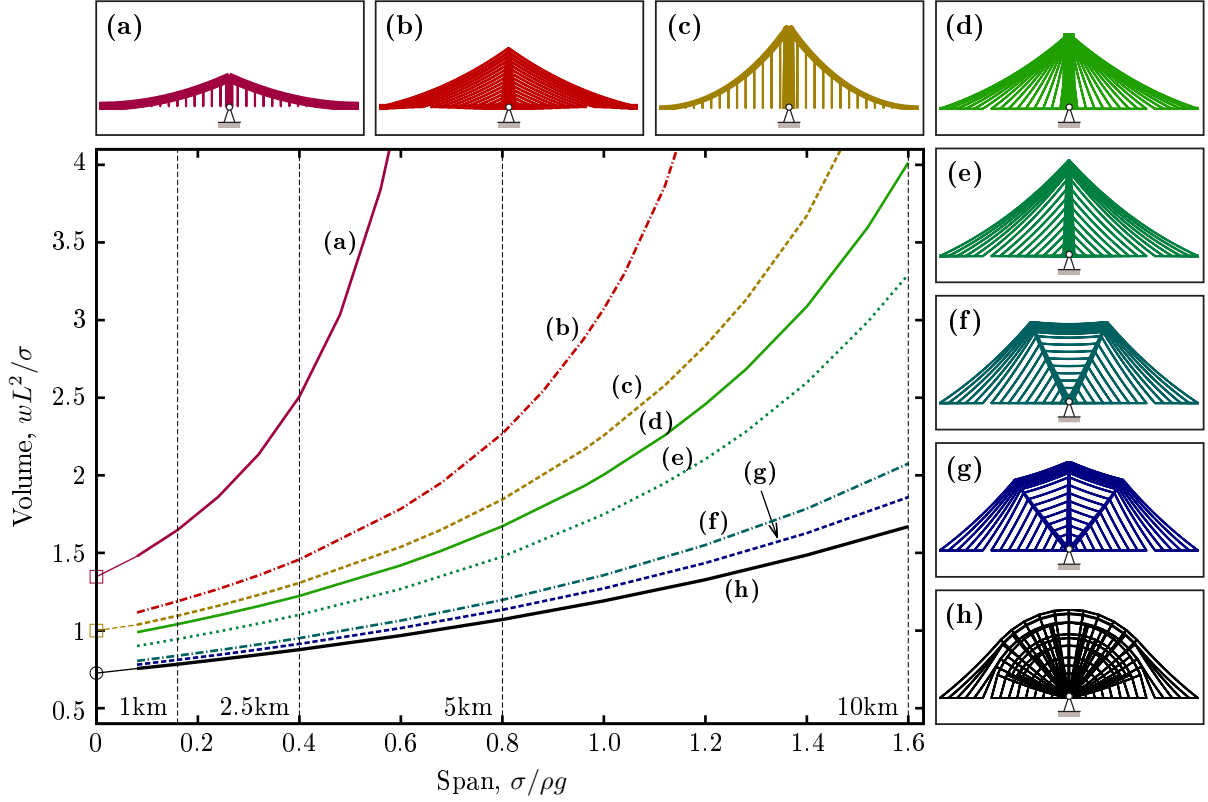


**Figure 4.6:** Volume vs. span for various bridge forms, using equal stress catenary elements and with nodal positions identified via geometry optimization (Span  $L = 0$  data points are taken from the literature; see Table 2 for details). Indicated span distances of 1km, 2.5km, 5km and 10km assume  $\sigma$  is taken as 500MPa and the unit weight  $\rho g$  as 80kN/m<sup>3</sup>. **(a)** Suspension bridge, with span-to-dip ratio of 9, as in the Akashi Kaikyo Bridge, Japan. **(b)** Cable stayed bridge with span-to-dip ratio of 4.4, as in the Russky Bridge, Russia (harp cable arrangement assumed here). **(c)** Suspension bridge with optimal pylon height. **(d)** Cable stayed bridge with fan cable arrangement and optimal pylon height. **(e)** Cable stayed bridge with optimal pylon height. **(f)** Optimized double split pylon design. **(g)** Optimized triple split pylon design. **(h)** Reference bridge design.

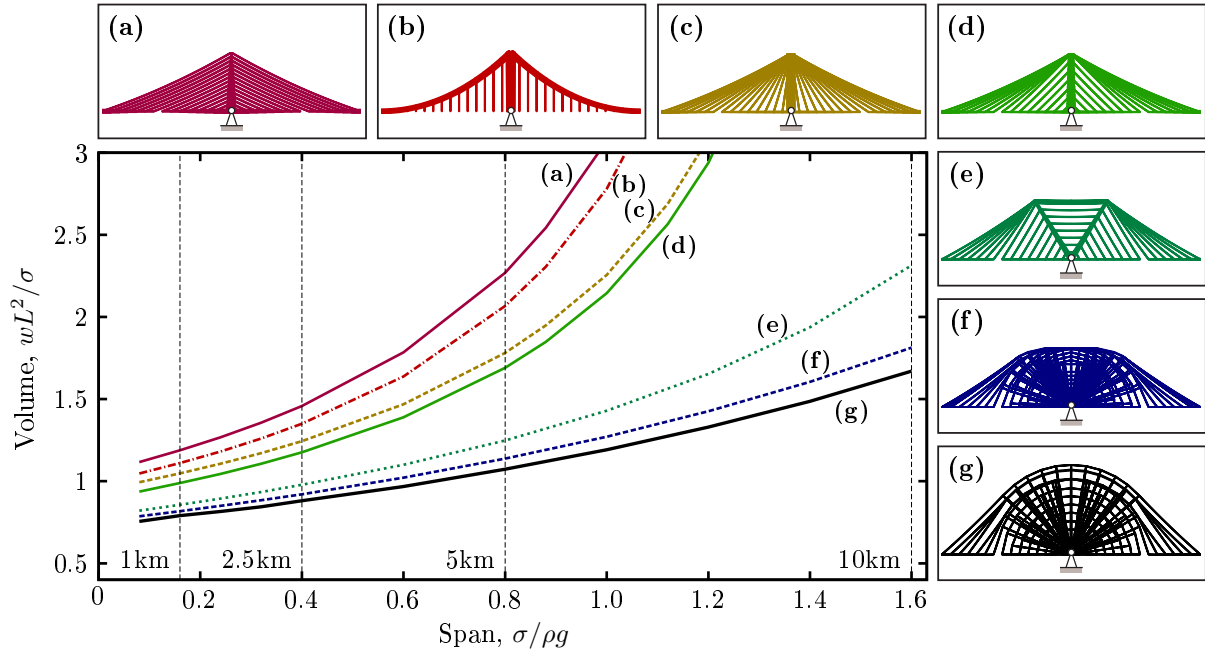


**Figure 4.7:** Span-to-dip ratio of 4.4 - Volume vs. span for different bridge designs. (a) Harp style cable stayed. (b) Suspension. (c) Fan style cable stayed. (d) Optimized cable stayed. (e) Optimized double split pylon. (f) Reference optimum form for the given span-to-dip ratio. (g) Reference with unrestricted span-to-dip ratio for comparative purposes.

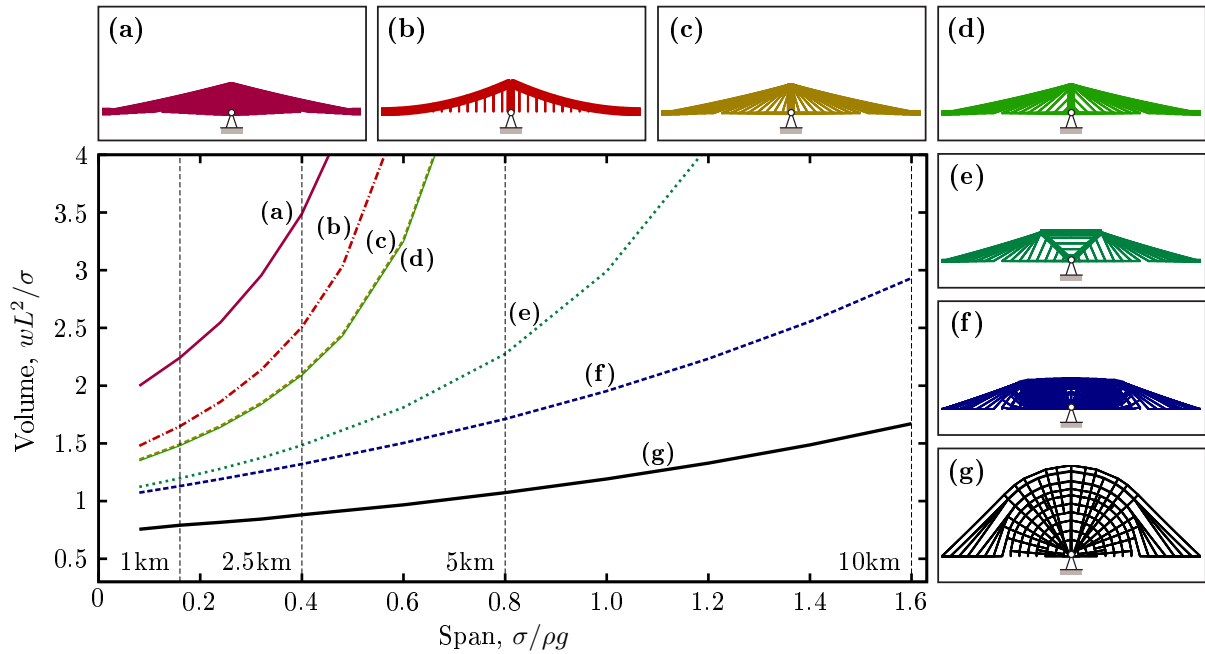


**Figure 4.8:** Span-to-dip ratio of 9 - Volume vs. span for different bridge designs. (a) Harp style cable stayed. (b) Suspension. (c) Fan style cable stayed. (d) Optimized cable stayed. (e) Optimized double split pylon. (f) Reference optimum form for the given span-to-dip ratio. (g) Reference with unrestricted span-to-dip ratio for comparative purposes.

Form	$L/h$ (*)	figure	Span			
			0 km (weightless)	1 km ( $0.16 \frac{\sigma}{\rho g}$ )	2.5 km ( $0.4 \frac{\sigma}{\rho g}$ )	5 km ( $0.8 \frac{\sigma}{\rho g}$ )
Suspension	9	6a,8b	1.347222 <sup>a,b</sup>	1.648	2.508	18.985
	optimal (4)	6c	1.000000 <sup>a,b</sup>	1.096	1.307	1.845
Cable stayed (fan)	4.4	7c		1.048	1.244	1.781
	optimal	6d		1.041	1.224	1.672
Cable stayed (harp)	4.4	6b	1.052273 <sup>a</sup>	1.189	1.458	2.269
	optimal ( $4/\sqrt{3}$ )	-	0.866025 <sup>a</sup>	0.954	1.112	1.492
Cable stayed (optimal)	4.4	7d		0.989	1.176	1.691
	optimal	6e		0.946	1.102	1.476
Split pylon (double)	9	8e		1.197	1.483	2.275
	4.4	7e		0.856	0.978	1.248
	optimal	6f		0.838	0.951	1.197
Split pylon (triple)	optimal	6g		0.811	0.914	1.134
Reference	9	8f		1.130	1.320	1.711
	4.4	7f		0.817	0.921	1.137
	optimal ( $2\sqrt{2}$ )	6h, 7g, 8g	0.726031 <sup>c</sup>	0.780531	0.873674	1.066152

\* Optimal span-to-dip ( $L/h$ ) ratios for weightless designs indicated in parenthesis, where available in the cited sources. (The optimal span-to-dip ratios for the longer span designs, which include self-weight, are similar, though not identical.)

<sup>a</sup> Croll (1997a)

<sup>b</sup> Croll (1997b); Dalton (1997); French (1997)

<sup>c</sup> Pichugin et al. (2015)

**Table 4.2:** Comparison of volumes ( $\times \frac{wL^2}{\sigma}$ ) of traditional bridge forms with those of new reference solutions. (A discretisation of 30 nodal spacings across the full span and geometry optimization was used except for the optimal reference forms. Quoted span lengths assume a limiting material stress  $\sigma = 500\text{MPa}$  and unit weight  $\rho g = 80\text{kN/m}^3$ .) The quoted volumes for the weightless designs are computed using explicit analytical expressions given by Croll (1997a,b); Dalton (1997); French (1997) (for suspension bridges), Croll (1997a) (for cable-stayed bridges) and Pichugin et al. (2015) (for optimal Michell structures).

#### 4.4.5 Influence of reducing the limiting compressive stress

In the present study the limiting material stress has thus far been assumed to be the same in tension and compression. However, it can be argued that a higher limiting stress should be adopted for tension elements, to account for the likelihood that higher strength steel will be used for the cables, and to account for a reduction in the stress sustainable by compression elements due to buckling effects. On the other hand, in recent years very high strength hot rolled steel has become available which can potentially be used in the construction of pylon and deck elements carrying compressive stresses, and appropriate detailing can be used to try to mitigate the detrimental effects of buckling on the allowable stress. Nevertheless, it is of interest to explore cases when the limiting tensile stress  $\sigma_T$  exceeds the limiting compressive stress  $\sigma_C$ . For example, Figure 4.9 shows optimized bridge forms when the limiting stress in compression is reduced to one third and then one ninth of the limiting stress in tension (the latter case could e.g. represent a case where the limiting tensile stress is 1800MPa and the limiting compressive stress is 200MPa). Firstly, it is clear from the figure that the overall form of the optimal reference structure is largely unaffected, though the horizontal extent of the fan region over a support reduces (as was also shown by Pichugin et al. (2015) for the case when self-weight effects are neglected). Also the optimal span-to-dip ratio increases for the reference structure, and also for all the other bridge forms considered. The relative volumes of the cable stayed and suspension bridges fall respectively to 1.30 and 1.54 for the  $\sigma_T/\sigma_C = 3$  case, and to 1.25 and 1.36 respectively for the  $\sigma_T/\sigma_C = 9$  case. This indicates that the advantage of the new forms over traditional forms remains, though does reduce somewhat when the limiting compressive stress is lower than the limiting tensile stress.

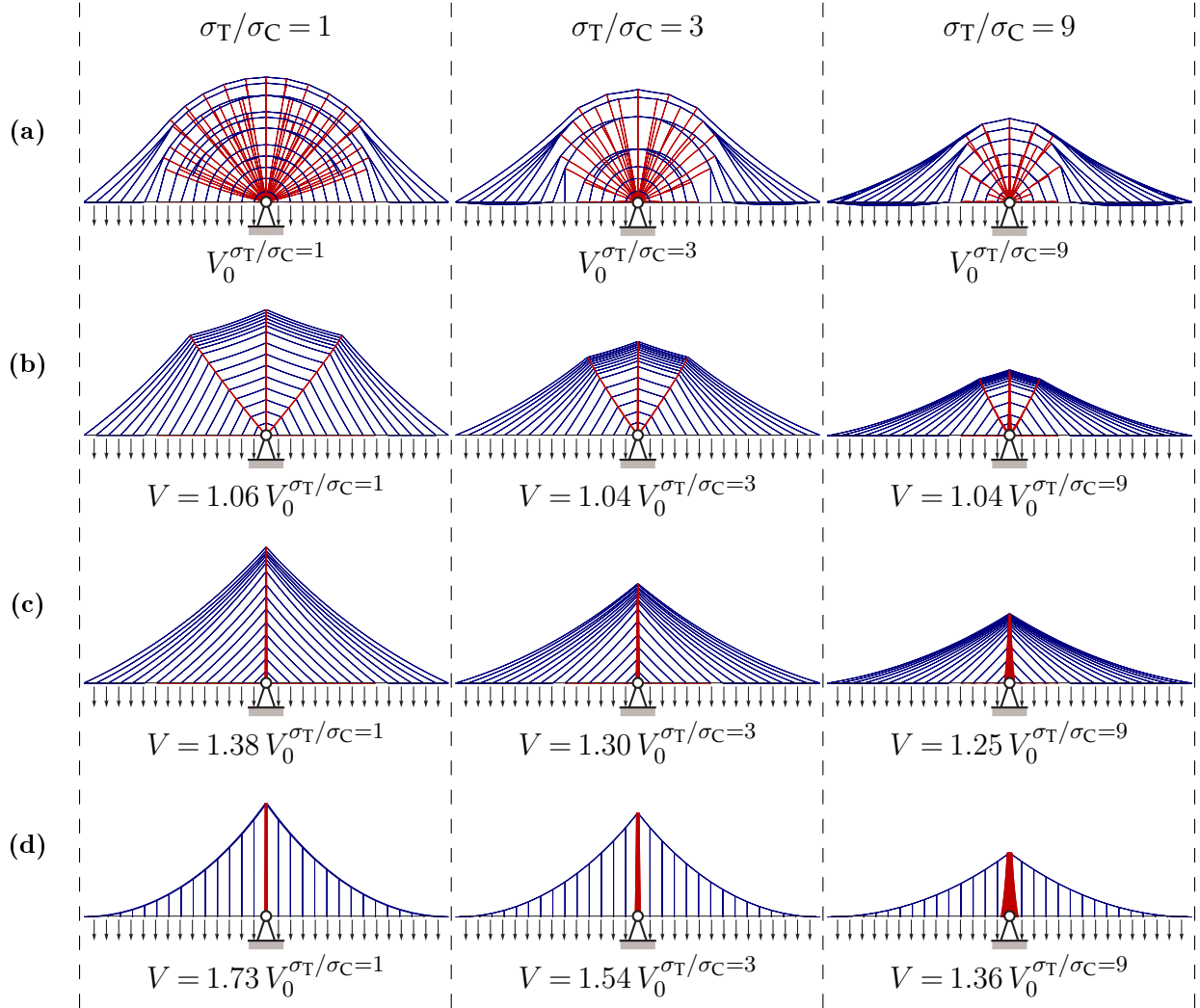


**Figure 4.9:** Effect of reducing the limiting compressive stress on selected forms shown in Figure 4.4, for the span =  $0.8 \frac{\sigma}{\rho g}$  case (where the limiting tensile stress  $\sigma_T = \sigma_0$  and the limiting compressive stress is reduced as indicated). Volumes shown are expressed in terms of the relevant reference volume. **(a)** Reference design (simplified layout shown for clarity). **(b)** Optimized triple split pylon design. **(c)** Optimized cable stayed design. **(d)** Optimized suspension bridge design. (All with variable cross-section cables.)

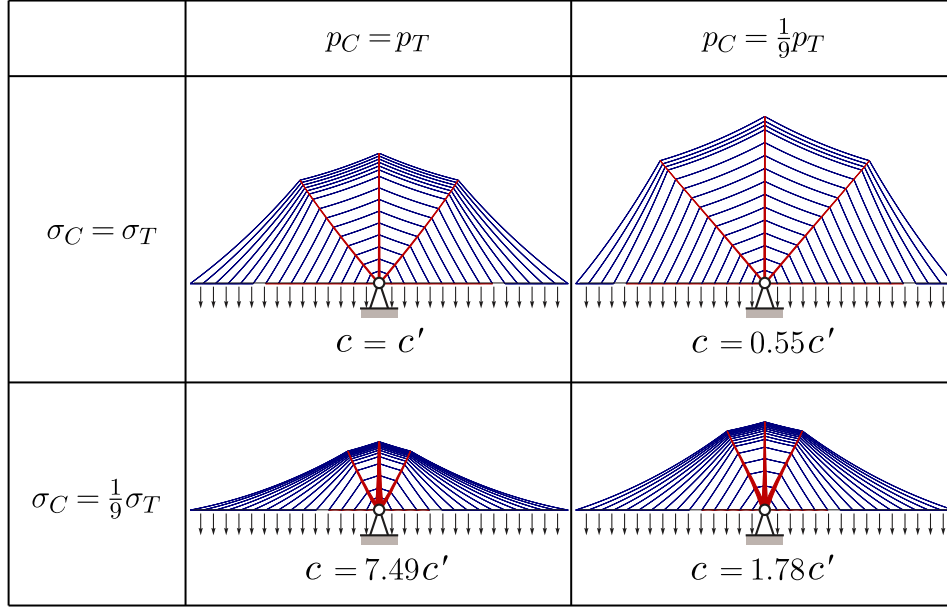


**Figure 4.10:** Effect of changing the relative cost of compressive and tensile members on the minimum cost  $c$  and corresponding geometry of the triple split pylon bridge form considered in Figure 4.9, where  $c = \sum p_T V_T + \sum p_C V_C$ , and where  $p_T$ ,  $V_T$  and  $p_C$ ,  $V_C$  are the cost coefficients and volumes for tensile and compressive members respectively. (Two limiting tensile to compressive stress and cost ratios considered.)

#### 4.4.6 Commentary

This study has focussed on identifying theoretically optimal forms for carrying the predominant load case for a hypothetical very long bridge span structure, i.e. self-weight loading, comprising the weight of the cables, pylons and deck, together with uniformly distributed traffic loading. It is sometimes argued that certain structural configurations become efficient when asymmetric loadings due to traffic are involved (e.g. considering the fan style cable stayed bridge configuration, the pylons are not subject to bending when asymmetric loadings due to traffic are involved, which is advantageous if traffic loads are high). However, in the case of very long span bridges the magnitude of traffic loading in relation to self-weight becomes comparatively small, reducing this effect. For example, in studies recently undertaken by a bridge design consultancy for proposed suspension bridges incorporating spans ranging from 1.3km to 3.3km, traffic loads contributed only between 15 and 23 percent of the unfactored loads carried by the main cables (Jensen & Bloomstine, 2009). Thus although non-uniform traffic loading would need to be considered as part of the detailed design phase it is unlikely to change the overall findings of the present study when very long spans are involved. (In contrast when shorter spans are involved, of the sort likely to be constructed in the immediate future, non-uniform traffic loading can be expected to have an influence on form, with, in the case of multi-span bridges, alternate span traffic loading scenarios being particularly important. This for example led to a ‘crossing stay’ cable arrangement being chosen for the three-span Queensferry Crossing bridge across the Firth of Forth in Scotland, completed in 2017 (Carter et al., 2010). Also, cable size may need to be increased to reduce deflections if these prove to be excessive.)

In this paper elements with non-uniform cross sections have been employed for all bridge forms considered, both new and traditional. This means that material in all cross sections is fully stressed, ensuring that the structures are as materially-efficient as possible, thereby allowing reference solutions to be obtained. However, it should be noted that whilst methods of realising non-uniform elements have been proposed (e.g. Gokyu, 1970), usually uniform cross sections are preferred in practice, which will slightly increase the overall weight of all bridge forms considered.

Although the present study has focused on efficiency, the method proposed can potentially be modified so as to minimise the likely cost of the overall bridge construction. For example, as the cost of cables is likely to be higher than the cost of compression elements, this can be accounted for by including suitable cost coefficients in the optimization objective function. For example, in Figure 4.10 the minimum cost triple split pylon design is sought, with the ratio of limiting tensile and compressive stress varied together with the relative cost of tensile and compressive members. Also, when modelling a bridge containing end spans, a cost could potentially be ascribed to the resultant horizontal reaction forces, which would in practice need to be carried by costly anchorages. These forces will generally be greatest in the case of suspension bridge forms, adding to their

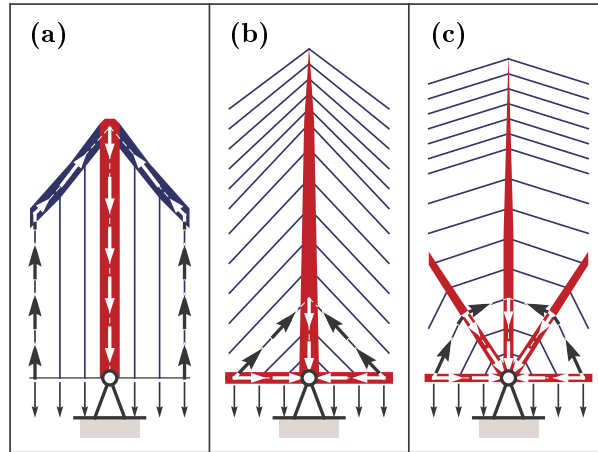


**Figure 4.11:** Appraising the relative efficiency of bridge forms by considering how deck loads are transmitted back to a support. **(a)** Suspension bridge: the load path is comparatively long, so a large volume of material is required to transmit the forces involved. (The same situation occurs in a fan cable stayed bridge.) **(b)** Harp cable-stayed bridge: the load path is kept short, but acute angles between the elements lead to high cable forces, and also to significant induced forces in the deck. **(c)** Split pylon cable-stayed bridge: the load path remains relatively short but the angles between the elements are less acute, ensuring cable and induced deck forces are lower.

relative cost, though the other cable supported forms considered herein would also require the use of external earth anchorages, due to the presence of tension at the supports. Although ‘self-anchored’ cable-stayed bridge designs have become popular due to ease of construction, a benefit of using earth anchorages for very long spans is that compression in the deck can be controlled; this is discussed further by Gimsing (1994). Alternatively boundary conditions in the optimization problem can easily be changed to, for example, prevent a solution being generated which requires transmission of horizontal forces to supports.

Finally, an explanation for the comparative efficiency of the split pylon form is given in Figure 4.11; this involves considering how directly deck loads are transmitted back to the supports. Although constructing very long span bridges based on these latter designs would no doubt be challenging, the reward – significantly reduced material consumption – is clear.

## 4.5 Conclusions

A means of obtaining the theoretically optimal bridge form to span a given distance under the action of gravity loading has been described. This required the development of a new numerical layout optimization procedure capable of intrinsically modelling the self-weight of the constituent structural elements. To achieve this, equal strength catenary elements were employed, allowing phenomena such as cable sag to be modelled in the optimization process in an entirely natural manner. The procedure has been applied to the design of hypothetical very long span bridges, enabling the optimal reference form and associated required volume of material to be established for a given span. The reference volume provides a benchmark against which traditional or proposed new bridge designs can be objectively judged.

It has been found that the reference bridge forms differ markedly to traditional suspension bridge and cable stayed bridge forms involving vertical pylons, and also require much less material to construct, especially when very long spans are involved. For example, a conventional suspension bridge form spanning 5km requires up to 73 percent more material than the corresponding reference design when using steel. The reference designs have also been used as inspiration for simple yet highly efficient bridge designs involving split pylons, which require comparatively little more material than the reference designs.





## Chapter 5

# Lumped masses and frictional foundations

This chapter further develops the distributed self-weight method of the previous chapter by incorporating potential lumped masses which may be added at any point. This allows for accurate modelling of cases where structural mass is used favourably, such as in counterweights and anchorages. To allow accurate interpretation of structures involving anchorages and abutments, a frictional support type is introduced.

In this chapter, the new methods are principally demonstrated using a bridge type problem. Unlike the previous chapter this example has only three spans, which allows the effect of the boundary conditions to be studied. Further examples using the counterweight formulation are available in Appendix B, where the method is applied to the design of a crane structure and a cantilever spar cable-stayed bridge.

The contents of this chapter has been prepared with the intention of submitting it for publication as a journal article<sup>†</sup>.

---

5.1	Introduction . . . . .	64
5.2	Layout optimization with distributed self-weight . . . . .	65
5.2.1	Formulation . . . . .	65
5.2.2	Change of form with span . . . . .	66
5.2.3	Cantilever with favourable use of self-weight . . . . .	67
5.3	Proposed formulations . . . . .	68
5.3.1	Formulation incorporating self-weight of unstressed lumped masses . . . . .	68
	Improved solution of cantilever making favourable use of self-weight . . . . .	69
5.3.2	Frictional foundations . . . . .	69
	Interpretation of boundary conditions . . . . .	70
5.4	Bridge example . . . . .	70
5.4.1	Standard support types . . . . .	71
5.4.2	Frictional supports . . . . .	72
5.4.3	Mixed support types . . . . .	74
5.4.4	Simplified designs . . . . .	75
5.5	Concluding remarks . . . . .	75

---

<sup>†</sup> Fairclough, H. E., Gilbert, M., and Tyas, A., (2019), *Truss topology optimization of structures with distributed self-weight, lumped masses and frictional supports*. Manuscript in preparation.

## 5.1 Introduction

The theory of minimum volume structures was developed by Michell (1904) and Hemp (1973). However, these classical solutions neglect many real-world considerations and are time consuming and difficult to identify. Rozvany & Wang (1984), provide an extension to the theory which incorporates self-weight, however this adds further challenges and solutions have only been found for a certain class of trusses which are restricted to be entirely in compression or entirely in tension (Wang & Rozvany, 1983).

Numerical methods, such as the layout optimization method developed by Dorn et al. (1964) provide the potential for significantly more flexibility in extending the applicability of optimal solutions. Modern computing hardware, and improvements in computational efficiency (e.g. Gilbert & Tyas, 2003) have allowed such numerical methods to be used to quickly identify structures which are within a fraction of a percent of theoretical values.

These numerical results may also suggest layouts leading to analytical solutions, or to support a partial solution. For a pin supported single span, an arch bridge type solution was proposed by Hemp (1974), later shown to be optimal in restricted cases by Chan (1975) and Pichugin et al. (2012). For a multiple span structure, a solution was provided by Pichugin et al. (2015), with further studies undertaken by Beghini & Baker (2015).

Numerical methods have been extended to include a range of additional practical considerations. Existing methods of modelling self-weight within ground structure type methods, such as those of Bendsoe & Sigmund (2004) and Pritchard et al. (2005), generally assume that the weight of a truss member may act directly on the member's end nodes. However, this formulation neglects the bending stresses which are imposed by the self-weight of a non-vertical bar, potentially leading to significantly non-conservative designs, particularly when long members are present.

Fairclough et al. (2018) have proposed an alternative method of modelling self-weight, this distributed self-weight method is based on the use of catenaries in place of straight bar elements. This allows the self-weight to be applied continuously across the structure without the generation of bending stresses, allowing for accurate results at all spans. The method was principally applied to long span bridges consisting of an infinite number of spans. This allowed for comparison between cable-stayed and suspension bridges, alongside the newly identified forms, thereby demonstrating the potential for material savings of up to 70% over suspension forms and 40% over cable stayed forms.

The material savings identified by Fairclough et al. (2018) were most significant at the longest spans due to the increase in the relative importance of self-weight loading. This has also been observed in practice; in the record 1991m span of the Akashi Kaikyo bridge, the bridge's self-weight accounts for over 90% of the capacity of the suspension cable (Ito, 1996). The limit of materials to carry their own self-weight has been recognised as one of the two major limiting factors by the designers of both the 1624m span Great Belt bridge (Ostenfeld, 1996) and of the proposed 3300m span Messina bridge (Brancaloni et al., 2011). Optimization methods therefore have the potential to be of great benefit in this area.

In practice, suspension bridges have long been the preferred solution for long spans. They must transmit the force at the end of the main cable into the ground, this generally requires a structure of significant mass to provide sufficient anchorage (Gimsing & Georgakis, 2011). Self-anchored suspension bridges are possible, but are generally considered impractical for spans of more than a few hundred metres (Ochsendorf & Billington, 1999). Conversely, an 'outstanding advantage' (Troitsky, 1988) of cable stayed bridges is that they are usually self-anchored with no horizontal force transmitted at the ends of the structure, this permits efficient construction using the cantilever method, but also leads to significant compressive forces in the deck. Ground anchored cable stayed bridges have been proposed (Shao et al., 2013) but are still rare in practice.

These different boundary conditions can cause issues for theoretical comparative studies. To allow fair comparison between suspension and cable stayed forms, Croll (1997a) and Croll (1997b) considered a ground anchored cable stayed bridge which requires the same reactions as the suspension form. Lewis (2012) extends this to include some consideration of the self-weight of the structure but, as with Croll (1997a), the study is limited to the classical forms, with parabolic suspension cables and parallel (harp style) cable stays.

Some novel designs for very long spans have been proposed, such as the designs of Lin & Chow (1991) and Starossek (1996), which both utilise a split pylon concept, based on a ground anchored suspension form and a self anchored fan type cable stayed form respectively. Other proposals also address more complex issues such as out of plane stability (Menn & Billington, 1995). However very few bridges of significant span have been constructed using non-traditional forms, one recent exception being the Yavuz Sultan Selim Bridge which uses a hybrid cable stayed and suspension form for increased stiffness (Virlogeux, 2018), it also includes some regions with ground anchored cable stays (de Ville de Goyet et al., 2018).

Consideration of scenarios with support types beyond classical pin or roller pin supports is rare within the optimization literature. Rozvany & Sokół (2012) consider support types where reaction forces incur a cost proportional to their magnitude. In further discussions of this paper (Espí, 2013; Sokół & Rozvany, 2013a) some solutions with frictional foundations were identified, although these required *a priori* knowledge of the

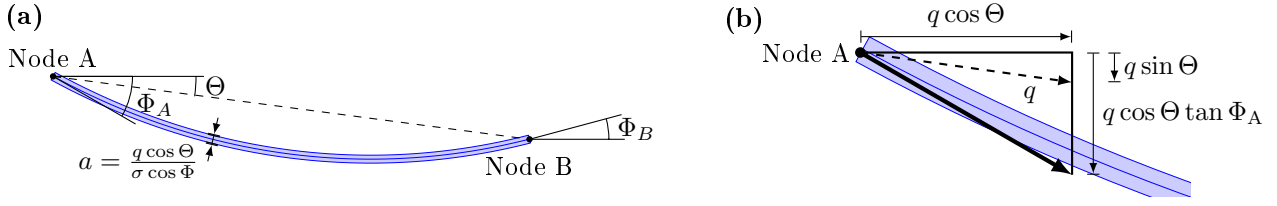


**Figure 5.1:** The distributed self-weight method. (a) Geometry and (b) end forces of a single equally stressed catenary member. Dashed lines show the equivalent member without self-weight.

optimal solution's use of the foundation. Furthermore these solutions did not consider self-weight, which may be usefully employed to increase the possible horizontal force, such as in an anchorage block.

To allow for consideration of these differing boundary conditions, the distributed self-weight method will here be extended to allow the inclusion of the costs of unstressed material, such as in anchorage or abutment structures. This will allow investigation of the potential for material savings through the use of layout optimization in both ground-anchored and self-anchored cases, as well as potentially more realistic cases with an intermediate level of friction. The inclusion of unstressed material will also permit investigation of cases where counterweights can be used as part of a structural solution.

This chapter is organised as follows; Section 5.2 provides a brief overview of the distributed self-weight formulation for modelling self-weight, and then provides some illustrative examples which demonstrate mechanisms by which the optimal forms identified may change with span. Section 5.3 then proposes new formulations which extend the range of boundary conditions which may be considered using this method. These are applied to the initial design of a bridge type structure in Section 5.4.

## 5.2 Layout optimization with distributed self-weight

### 5.2.1 Formulation

The overall structure of the distributed self-weight formulation is very similar to the classical formulation found in literature, with the differences occurring only within the coefficient matrices. Therefore the layout optimization problem is written as

$$\text{minimise} \quad V = \mathbf{c}^T \mathbf{q} \quad (5.1a)$$

$$\text{subject to} \quad \mathbf{B}\mathbf{q} = \mathbf{f} \quad (5.1b)$$

$$\mathbf{q} \geq \mathbf{0} \quad (5.1c)$$

where  $V$  is the total volume of all members in the structure.  $\mathbf{q} = [q_1^T, q_1^C, q_2^T, \dots, q_m^C]^T$ , and  $q_i^T, q_i^C$  are the tensile and compressive member forces.  $\mathbf{f} = [f_1^x, f_1^y, f_2^x, \dots, f_n^y]^T$  is the vector of externally applied forces at each node.  $\mathbf{c} = [\frac{l_1}{\sigma_T}, \frac{l_1}{\sigma_C}, \frac{l_2}{\sigma_T}, \dots, \frac{l_m}{\sigma_C}]^T$  where  $l_i$  is the length of member  $i$  and  $\sigma_T$  and  $\sigma_C$  are the allowable stresses in tension and compression, and  $\mathbf{B}$  is a suitable  $2m \times 2n$  (for 2D problems) equilibrium matrix.

The coefficients in  $\mathbf{B}$  and  $\mathbf{c}$  are found from the geometry of the catenary member as shown in Figure 5.1. The centreline of any member of a given material consists of a section of an equally stressed catenary (Routh, 1896). This centreline is independent of the magnitude of the load and is given by the relations

$$\Phi = \Omega_1 - \kappa x \quad (5.2)$$

$$\kappa y = \log(\cos(\Phi)) + \Omega_2 \quad (5.3)$$

where  $x$  and  $y$  are the coordinates of the centreline,  $\Phi$  is the inclination of the centreline at  $(x, y)$ ,  $\kappa$  is the signed strength to weight ratio of the material, which may also differ in magnitude in tension and compression, and  $\Omega_1$  and  $\Omega_2$  are constants of integration.

The coefficients in  $\mathbf{c}$  are given by integrating the expression for the area  $a = \frac{q \cos \Theta}{\sigma \cos \Phi}$  (where  $\sigma = \sigma_T$  or  $\sigma_C$  as appropriate), between the two end nodes. For a single catenary element,  $i$ , this implies that

$$\mathbf{c}_i = \left[ \frac{\cos \Theta_i (\tan \Phi_A^T - \tan \Phi_B^T)}{\rho g} \quad \frac{\cos \Theta_i (\tan \Phi_B^C - \tan \Phi_A^C)}{\rho g} \right]^T \quad (5.4)$$

where  $\Phi^T$  and  $\Phi^C$  are the values of  $\Phi$  assuming tension and compression stress respectively, and  $\Phi_A$  and  $\Phi_B$  are the values at points A and B.  $\rho g$  is the unit weight of the material, and  $\Theta_i$  is the angle directly between the end nodes, as in Figure 5.1.

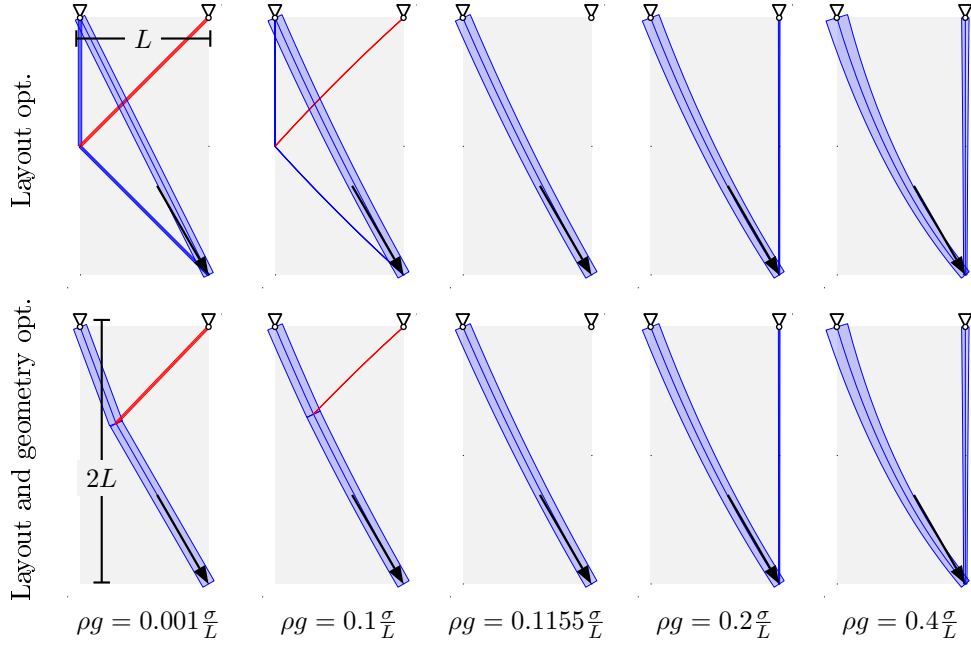


**Figure 5.2:** Simple example: Results for increasing material weight, showing how changes in the optimal topology of the function correspond to changes in the geometry of the elements.

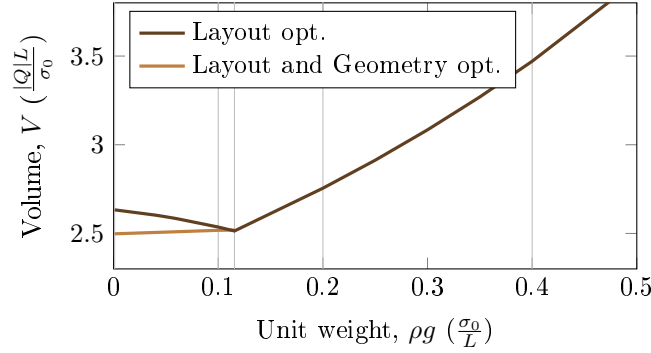


**Figure 5.3:** Simple example: Volumes of structures after layout optimization and geometry optimization.

The coefficients of matrix  $\mathbf{B}$  are such that end forces are aligned to the centreline, with the horizontal components being unchanged by the addition of self-weight, as shown in Figure 5.1. Therefore for a single bar  $i$  the relevant coefficients are

$$\mathbf{B}_i = \begin{bmatrix} \cos \Theta_i & -\cos \Theta_i \\ \cos \Theta_i \tan \Phi_A^T & -\cos \Theta_i \tan \Phi_A^C \\ -\cos \Theta_i & \cos \Theta_i \\ -\cos \Theta_i \tan \Phi_B^T & \cos \Theta_i \tan \Phi_B^C \end{bmatrix} \quad (5.5)$$

For more details of this formulation see Fairclough et al. (2018).

When the self-weight is insignificant, i.e. at short spans or with very strong materials, the members are almost straight, with almost constant cross sections. As spans increase, the members gradually increase their sag. This gradual change in individual member geometry can combine to cause significant and abrupt changes in to overall optimal topology.

Once the result of the layout optimization is known, a geometry optimization method based on that developed by He & Gilbert (2015) can be used to further refine the joint positions within the solution. Again, further details can be found in Fairclough et al. (2018).

### 5.2.2 Change of form with span

To illustrate how this change in the geometry of individual elements can lead to substantial changes in overall topology, a simple example is considered. This consists of a design domain of width  $L$  and height  $2L$ , with pin supports at the top corners and a force of magnitude  $Q$  applied at an angle  $30^\circ$  from vertical. The structure

is constructed from a material with limiting strength in tension and compression of  $\sigma$ , and a given unit weight denoted by  $\rho g$ . The resulting structures are shown in Figure 5.2, and their volumes are plotted in Figure 5.3.

When the unit weight of the material is small, the elements in the ground structure approximate straight lines. The longest diagonal member in the solution lies above the line of action of the applied force, and a 3 bar supporting structure is required to ensure equilibrium. During geometry optimization, the bar connecting to the force is aligned to the line of action, this then requires a kink, supported by an additional compression member, to reach the support point. The thickness of the supporting structure reduces as the material weight, and therefore also the cable sag, increases.

When  $\rho g = 0.1155 \frac{\sigma}{L}$ , the main diagonal member is parallel to the applied force at the point of application. The redirecting force is now provided by the self-weight of the structure itself. As the unit weight increases further, the sag of this element takes it below the line of action of the force. Therefore, additional support from above is required, leading to the addition of a new tension member and a change in optimal topology.

### 5.2.3 Cantilever with favourable use of self-weight

The classic Michell cantilever problem will be used to illustrate some interesting possibilities which become available in the presence of self-weight. Generally, this is analytically considered to be a whole plane problem (e.g. Hemp, 1973). However, in the most common cases, the solution requires structure only in one half plane, leading many numerical studies to consider a design domain within the half plane containing the force (e.g. Gilbert & Tyas, 2003).

The distributed self-weight method has been used to find solutions for this problem with a given material unit weight,  $\rho g$  and limiting stress  $\sigma$ . The results are shown in Figures 5.4 and 5.5. Two design domains were considered; a ‘restricted domain’, entirely within one half plane, and an ‘extended domain’ which continues behind the supports. The dimensions of the problems are shown in Figure 5.4.

In the presence of small to moderate levels of self-weight, the layout and volume identified in the ‘restricted domain’ is very similar to the known analytical solution. When self-weight is a significant factor, the geometry of the form changes somewhat. The overall depth of the structure increases and a larger proportion of the material is used close to the supports.

If the larger design domain is used, no change is observed at small values of self-weight. However, as the self-weight increases, sudden and significant change in the overall topology is seen. The new structure makes

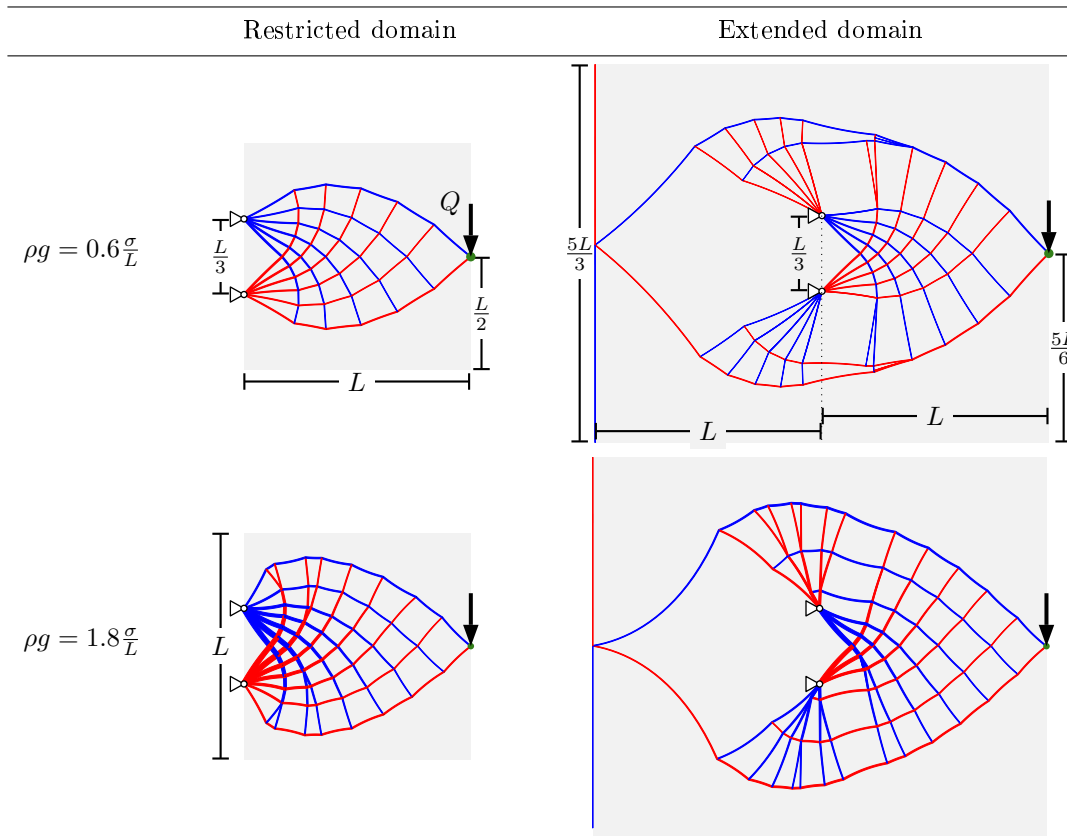


**Figure 5.4:** Cantilever example: Forms of optimal structures with restricted and extended design domains.

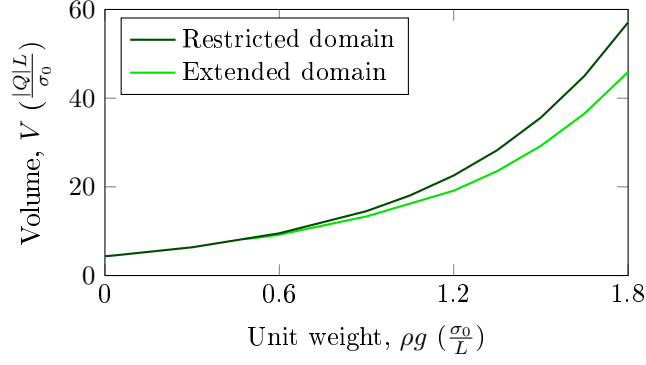


**Figure 5.5:** Cantilever example: Volumes of structures using the restricted and extended design domains.

use of the back-span to provide a counterweight to the applied load, thereby reducing the moment which must be provided by the supports and allowing for an even greater structural depth. However, as the method is based on the assumption that all material should be fully stressed, these counterweights take the form of tall thin members aligned to the leftmost edge of the permitted domain.

Figure 5.5 shows that the use of this counterweight form gives a lower volume than is possible with the restricted domain by up to 20%, the counterweight solution is preferred for cases where the unit weight is greater than approximately  $0.48 \frac{\sigma}{L}$ . However, the modelling of the form of the solution is unsatisfactory, therefore the next section proposes an improved formulation which allows for unstressed material to be present in the optimal solution. This problem will be revisited in Section 5.3.1 using the improved formulation.

## 5.3 Proposed formulations

### 5.3.1 Formulation incorporating self-weight of unstressed lumped masses

The layout optimization method is easily extended to include unstressed lumped masses by the introduction of an additional variable,  $r_j$ , at each node representing the volume of unstressed material at that point.

This volume is added to the total volume in the objective function, it is also used to calculate the force from the self-weight of the unstressed material ( $\rho g r_j$ ), which is then added to the equilibrium calculation for that node in the vertical direction (by use of a matrix of unit vectors,  $\mathbf{Z}$ ).

Therefore, the optimization problem becomes

$$\text{minimise} \quad V = \mathbf{c}^T \mathbf{q} + \mathbf{e}^T \mathbf{r} \quad (5.6a)$$

$$\text{subject to} \quad \mathbf{Bq} + \rho g \mathbf{Zr} = \mathbf{f} \quad (5.6b)$$

$$\mathbf{q}, \mathbf{r} \geq \mathbf{0} \quad (5.6c)$$

where  $\mathbf{r}$  is a vector of length  $n$ , containing the volumes of the counterweight at each node and  $\mathbf{e}$  is a vector of length  $n$  with all elements equal to one.  $\mathbf{Z}$  is a  $2n \times n$  matrix where  $z_{i,j} = \begin{cases} 1 & \text{if } i=2j \\ 0 & \text{if } i \neq 2j \end{cases}$ .

It would be unusual for material in bulk form to be equal in cost to the same volume of structural members. To model this, the formulation is modified to have the objective of minimising the total material cost,  $c$ . The formulation thus becomes

$$\text{minimise} \quad c = p_S \mathbf{c}^T \mathbf{q} + p_U \mathbf{e}^T \mathbf{r} \quad (5.7a)$$

$$\text{subject to} \quad \mathbf{Bq} + \rho g \mathbf{Zr} = \mathbf{f} \quad (5.7b)$$

$$\mathbf{q}, \mathbf{r} \geq \mathbf{0} \quad (5.7c)$$

where  $p_S$  and  $p_U$  are the prices per unit volume of stressed and unstressed material respectively.

Note that the value of  $\rho g$  used for the unstressed material need not be the same as that used in the calculations of the stressed material. However, the important quantity for a counterweight material is the cost to weight ratio,  $\frac{p_U}{\rho g}$ . In problem (5.7), materials with the same cost to weight ratio are interchangeable in terms of their effect on the rest of the problem, and the values for volumes at each point can be obtained by simple scaling.

Herein, for the sake of simplicity, counterweights will be assumed to have a density equal to that of the structural material. No generality is lost through this assumption.

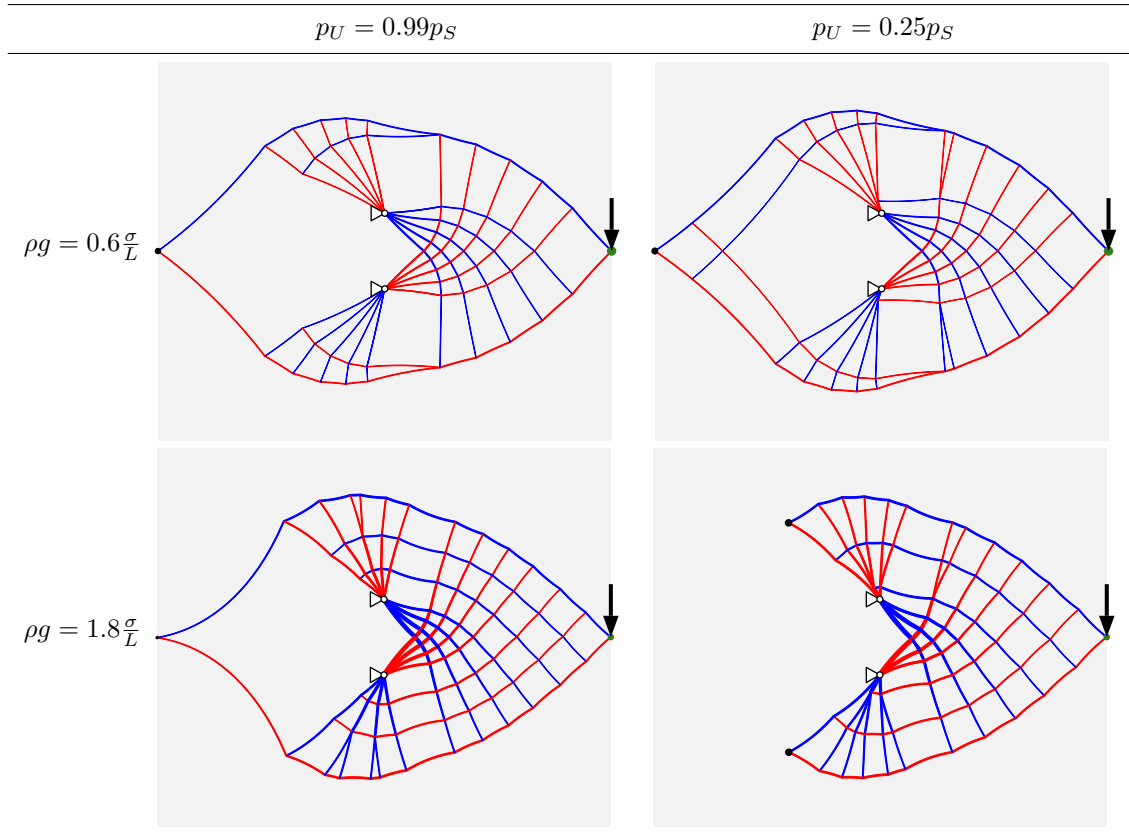


**Figure 5.6:** Cantilever example: Improved solutions with unstressed counterweights of various relative costs. Problem specification is as shown for the ‘extended domain’ in Figure 5.4.

### Improved solution of cantilever making favourable use of self-weight

The problem of Section 5.2.3 will now be revisited with a view to providing a clearer optimal structure and considering the effect of altering the relative cost of unstressed material.

Figure 5.6 shows the resulting optimal forms within the extended domain at the same two values of unit weight as were illustrated in Figure 5.4. When  $p_U$  is almost equal to  $p_S$ , the overall form is almost unchanged between Figures 5.6 and 5.4, except that the tower of members in the counterweight has been replaced by an equivalent unstressed mass.

When the cost of the unstressed material is significantly less than that of the structural members, it can become advantageous to use a larger counterweight, closer to the supports, in order to reduce the quantity of structural material required. The structures where  $p_U = 0.25p_S$  have a higher overall volume than those where  $p_U = 0.99p_S$ , however a greater proportion of this volume is unstressed, leading to lower overall costs.

### 5.3.2 Frictional foundations

One of the most common uses of large quantities of unstressed material in structural design is in abutments and anchorages. These can cause significant costs in a design as well as using large volumes of material, therefore it is important to include them to give a good understanding of the total costs/volume of the structure.

Here we will model the boundary conditions of the structure by assuming that a gravity type anchorage is used; these are commonly found in suspension bridges (Gimsing & Georgakis, 2011). For the purposes of preliminary design, the anchorage is required to have sufficient weight, or applied downwards forces, that frictional forces on the base are able to withstand the necessary horizontal force component. Further detailed considerations such as the design of the anchorage to resist overturning, or the details of the connection of the cable to the anchor block are not considered here.

The foundation nodes will be modelled as resting on a solid frictional plane. Within the main body of this chapter, these planes will be assumed to be horizontal, although Appendix B.3 discusses the case where the plane is inclined. The coefficient of friction between the plane and the construction material will be denoted by  $\mu$ . This gives rise to support forces normal and perpendicular to the supporting plane, denoted for a node  $j$  by  $t_j$  and  $s_j$  respectively, as shown in Figure 5.7.

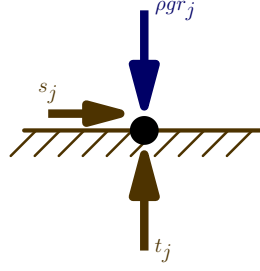


**Figure 5.7:** Reaction and counterweight forces acting on a frictional foundation node.

Standard Coulomb friction is assumed, leading to a constraint on  $s_j$  and  $t_j$  of

$$|s_j| \leq \mu t_j \quad (5.8)$$

For a scenario with  $n$  nodes of which  $k$  are supported, the formulation becomes

$$\text{minimise} \quad c = p_S \mathbf{c}^T \mathbf{q} + p_U \mathbf{e}^T \mathbf{r} \quad (5.9a)$$

$$\text{subject to} \quad \mathbf{B}\mathbf{q} + \rho g \mathbf{Z}\mathbf{r} + \mathbf{C}\mathbf{s} + \mathbf{D}\mathbf{t} = \mathbf{f} \quad (5.9b)$$

$$\mathbf{s} \leq \mu \mathbf{t} \quad (5.9c)$$

$$\mathbf{s} \geq -\mu \mathbf{t} \quad (5.9d)$$

$$\mathbf{q}, \mathbf{r}, \mathbf{t} \geq \mathbf{0} \quad (5.9e)$$

where  $\mathbf{s} = [s_1, s_2, \dots, s_k]^T$  is a vector containing the reaction forces parallel to the frictional faces at supported nodes,  $\mathbf{t} = [t_1, t_2, \dots, t_k]^T$  is a vector containing the reaction forces normal to the frictional faces at supported nodes.  $\mu$  is the coefficient of friction between the foundation node and the supporting planes.  $\mathbf{C}$  and  $\mathbf{D}$  are  $2n \times k$  equilibrium matrices such that for a single supported node,  $j$ , equation (5.9b) becomes

$$\mathbf{B}_j \mathbf{q} + \rho g \begin{bmatrix} 0 \\ 1 \end{bmatrix} r_j + \begin{bmatrix} 1 \\ 0 \end{bmatrix} s_j + \begin{bmatrix} 0 \\ 1 \end{bmatrix} t_j = \begin{bmatrix} f_j^x \\ f_j^y \end{bmatrix} \quad (5.10)$$

where  $\mathbf{B}_j$  represents the rows of  $\mathbf{B}$  relating to node  $j$ . Note that the value of  $\rho g$  will usually be negative, such that the self-weight of a lumped mass acts as in the opposite direction to the normal reaction force.

### Interpretation of boundary conditions

In cases where  $p_U = 0$ , an arbitrary amount of load parallel to the plane can be supported at no additional cost by increasing the volume of unstressed material at that point. This is equivalent to a pinned support. Similarly, an infinite value of  $\mu$  will give behaviour which is almost identical to a pin, although only in cases where the normal reaction force,  $t_j$ , is positive.

At the other extreme, if  $\mu = 0$  it is not possible to carry any horizontal force; this is broadly equivalent to a roller pin support, but again with the additional constraint that no upwards reaction forces are possible. If  $\mu = 0$  and  $p_U = 0$  then the presence of an upwards reaction is possible with no added cost by adding a sufficient quantity of unstressed material.

Other values for  $\mu$  and  $p_U$  will produce intermediate behaviour, allowing us to find a full range of structural options. Gimsing & Georgakis (2011) recommend a value of  $\mu = 0.3$  for preliminary calculations, although values of  $\mu = 0.55$  may be possible in certain ground conditions (Mathur & Molina, 2005). Here, larger values are also considered to demonstrate how the behaviour tends towards the fixed pin case. A possible physical interpretation of these high  $\mu$  values can be found in Appendix B.3.

## 5.4 Bridge example

The proposed method will now be applied to the initial conceptual design of a three span bridge structure. The idealised scenario to be considered consists of a main span of length  $L$ , and two side spans each with length  $\frac{L}{2}$ . The maximum height of the structure is permitted to be up to  $\frac{L}{2}$  as shown in Figure 5.8a. The allowable stress of the material is 1500MPa in tension and 150MPa in compression, with a unit weight of 0.08MN/m<sup>3</sup>.

The bridge is modelled with a uniform loading across all spans comprising the weight of traffic and the components of the deck concerned with providing a flat surface spanning between superstructure support points.



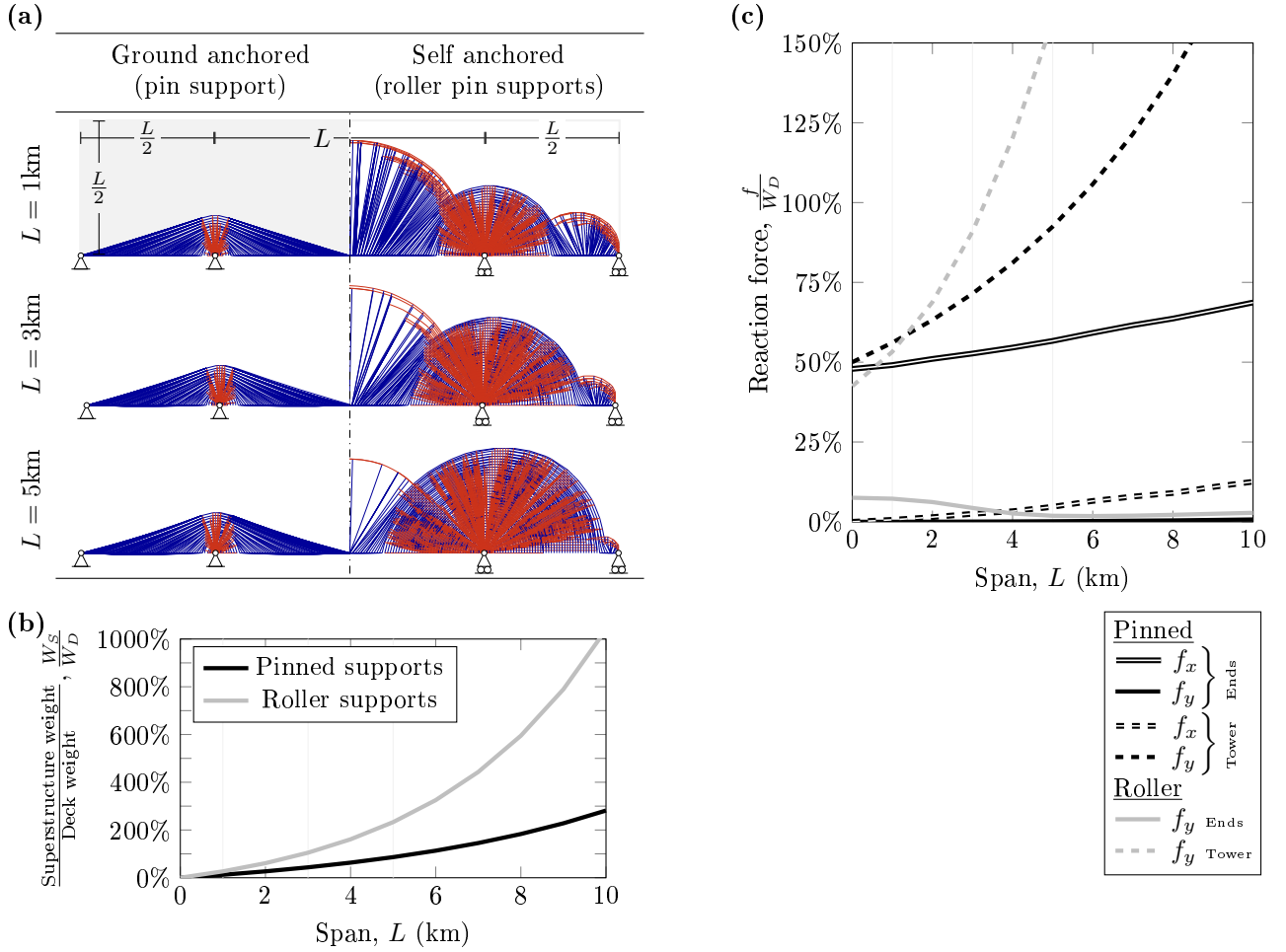


**Figure 5.8:** Bridge example: Results for scenarios with pinned or roller pinned supports. **(a)** Forms of optimized structures for spans of 1km, 3km and 5km. Design domain dimensions also shown, dash-dotted line represents line of symmetry. **(b)** Structural weight, note that this is proportional to total cost in this case. **(c)** Magnitudes of reaction forces required for optimized structures.

The total force imposed by these deck level loads across the whole structure is denoted by  $W_D$ . It is assumed that the dead load is dominating, and therefore only a single load case is modelled.

The symmetry of the problem has been exploited to allow half of the domain to be modelled. A total of 100 nodal divisions was used across this halved domain (nodal spacing =  $0.01L$ ).

#### 5.4.1 Standard support types

Initially, pinned (ground anchored) and roller pinned (self-anchored) support conditions are tested for a range of span lengths. The results are shown in Figure 5.8.

The pinned support case produces a ground anchored cable stay type structure, with tower height increasing at longer spans to counteract the effects of cable sag. This is similar to the results of Fairclough et al. (2018), as the symmetry boundary conditions considered there also provide an unlimited horizontal reaction force. However, these horizontal reaction forces are substantial, with a magnitude of over half the imposed deck level load (see Figure 5.8c). Resisting these would be challenging. Additionally, a significant horizontal force begins to develop at the tower base as the region containing compression members becomes asymmetric, note that this force is in the opposite direction to the outer anchorage and provides an abutment to the central compression ribs.

The roller pin model, at short spans, produces a form which resembles a series of tied arches with additional webbing providing continuity over the intermediate supports. This structure changes significantly as span increases, with the arched sections reducing in size and being replaced with a fan type form from the central supports. This form is somewhat asymmetrical, favouring material usage over the side span to counterweight the forces of the main span. The super structure weight ( $W_S$ ) of these structures is between 1.6 and 3.7 times heavier than the equivalent pinned structure (see Figure 5.8b).

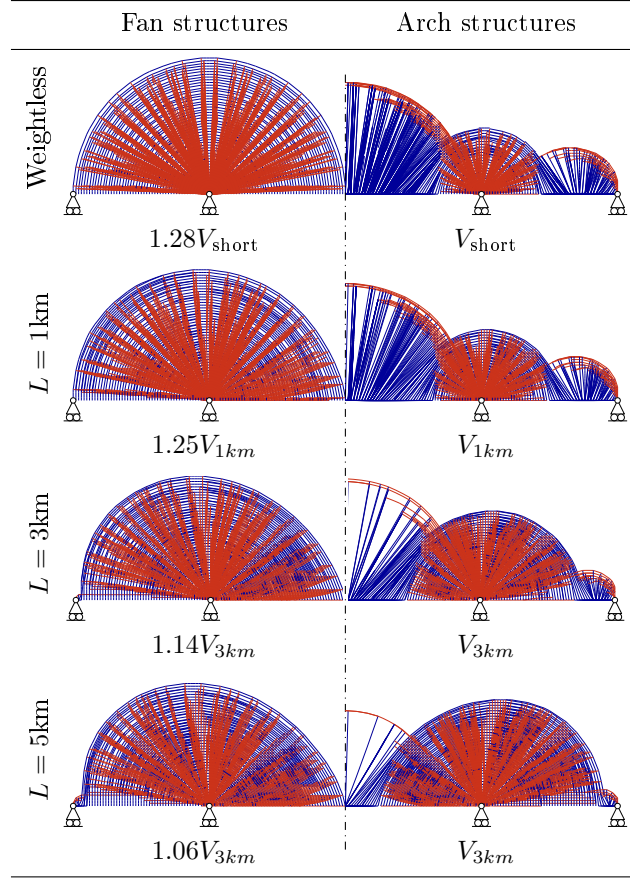


**Figure 5.9:** Bridge example: Results for roller pin supports with and without arching permitted. Arching is prevented by disallowing compression members across the line of symmetry.

If a roller pin support is used and arch type forms are not permitted (for example by preventing compressive forces being transmitted over the symmetry plane) then a bicycle wheel structure is always identified, at short spans this is a further 28% heavier than the self anchored arch although this reduces with span as shown in Figure 5.9. Simplification of the bicycle wheel would involve a reduced number of spokes being permitted from the tower support; at its most extreme this would result in a single vertical spoke and two horizontal ones, i.e. a self anchored cable stayed bridge. In the weightless case, no vertical reaction force is required at the anchorage point, as would be the case during construction with the balanced cantilever method. However, at longer spans, the fan becomes asymmetric and more self-weight is located over the side span, resulting in a vertical force on the outer support.

### 5.4.2 Frictional supports

To find a compromise between the high volumes of the roller pin solutions, and the large reaction forces required by the pinned structures, all supports will now be replaced by frictional foundations. A range of values for the counterweight cost,  $p_U$ , have been tested at spans of  $L = 3\text{km}$  and  $L = 5\text{km}$ . The effect of varying the coefficient of friction,  $\mu$ , has been tested up to a value of 2. This is a value much larger than that possible in real-world construction, and is considered here to give an indication of how the results change as  $\mu$  tends to infinity, i.e. the support type tends towards a pin (an alternative interpretation can be found in Appendix B.3). The results can be seen in Figure 5.10.

Approximately similar behaviour is observed at 3km and 5km spans. When  $\mu = 0$ , the structures are identical to the relevant roller pin solutions for any value of  $p_U$ . No unstressed anchorage material is present in these solutions, resulting in the lack of dependence on the value of  $p_U$ .

For each value of  $p_U$  a critical value of  $\mu$  is reached where a ground-anchored solution becomes preferable, at this point the solutions diverge, with total cost and structural weight decreasing, whilst total weight increases (potentially very significantly). As the coefficient of friction approaches infinity, the weight and cost of the structure will tend towards the appropriate pinned solution, although this often occurs at values of  $\mu$  well beyond those practical in the real world.

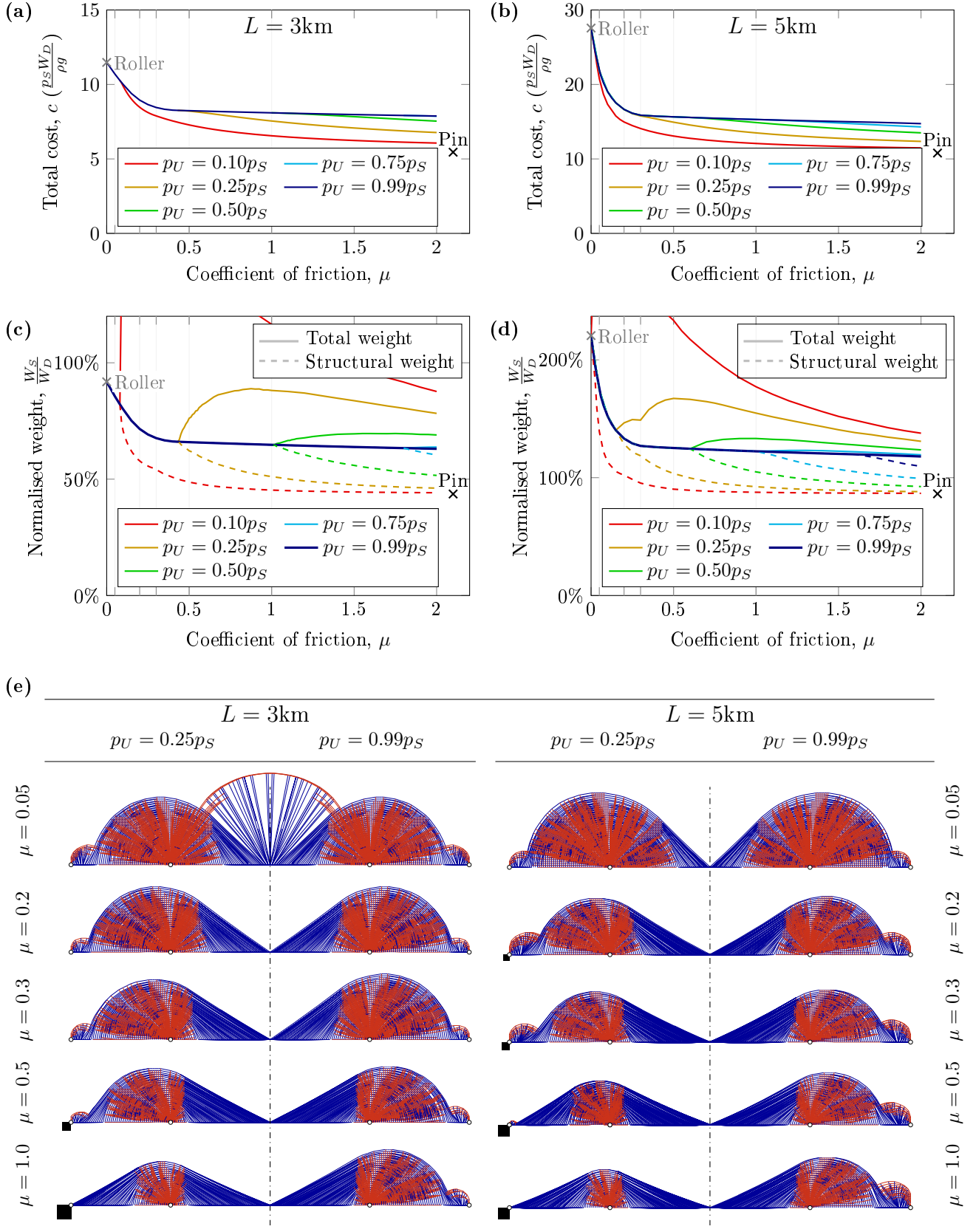


**Figure 5.10:** Bridge example, structures with frictional foundations at both tower base and anchorage. (a) & (b) Total cost,  $c$ , when  $L = 3\text{km}$  and  $5\text{km}$  respectively. (c) & (d) Structural and total weights for  $L = 3\text{km}$  and  $5\text{km}$  respectively. These all include pinned and roller results for comparison. (e) Optimal forms for selected values of  $p_U$  and  $\mu$ , the dash dotted line represents the line of symmetry.

When the relative cost of the counterweight material is small, the point of divergence occurs at low  $\mu$  and the cost and structural weight then rapidly approach the pin value. The form of these structures also soon resembles that of the pinned problem. However, when the relative cost of the foundation is high, there is a rapid initial decrease in weight/cost but then a plateau is reached, where further reductions are much slower. This plateau is roughly halfway between the cost of the roller and pin solution for the 3km span, but much closer to the cost of the pinned solution for the 5km span.

This plateau corresponds to a solution which makes use of the horizontal force from the frictional support at the intermediate towers. As there is a substantial vertical load supported here, horizontal forces are carried without requiring additional unstressed masses. This results in a structure where the central span is cable-stayed, but the side spans are a hybrid of a fan structure from the tower support and an arch form which redirects the thrust at the anchorage points. This structure cannot be identified using the standard support types, and for many values of  $p_U$  it is optimal over much of the realistic range of  $\mu$ . This structure is observed in most solutions for  $p_U = 0.99p_S$  in Figure 5.10e.

The most significant variation with increasing span is, for a given ratio of  $\frac{p_U}{p_S}$ , the critical point at which ground anchored solutions become preferable occur at lower values of  $\mu$ . This is approximately in line with current practice, whereby self anchored structures are preferred at shorter spans, and ground anchored forms become more common as span increases.

### 5.4.3 Mixed support types

Many of the forms in Figure 5.10 make use of horizontal reaction forces at the intermediate tower bases. This is advantageous as a significant downwards force is already present at these points, reducing the need for additional anchorage mass. However, it is often the case that these intermediate points must be supported on towers, which may be fairly tall and/or involve complex marine construction, in such cases the choice of a frictional support would be questionable.

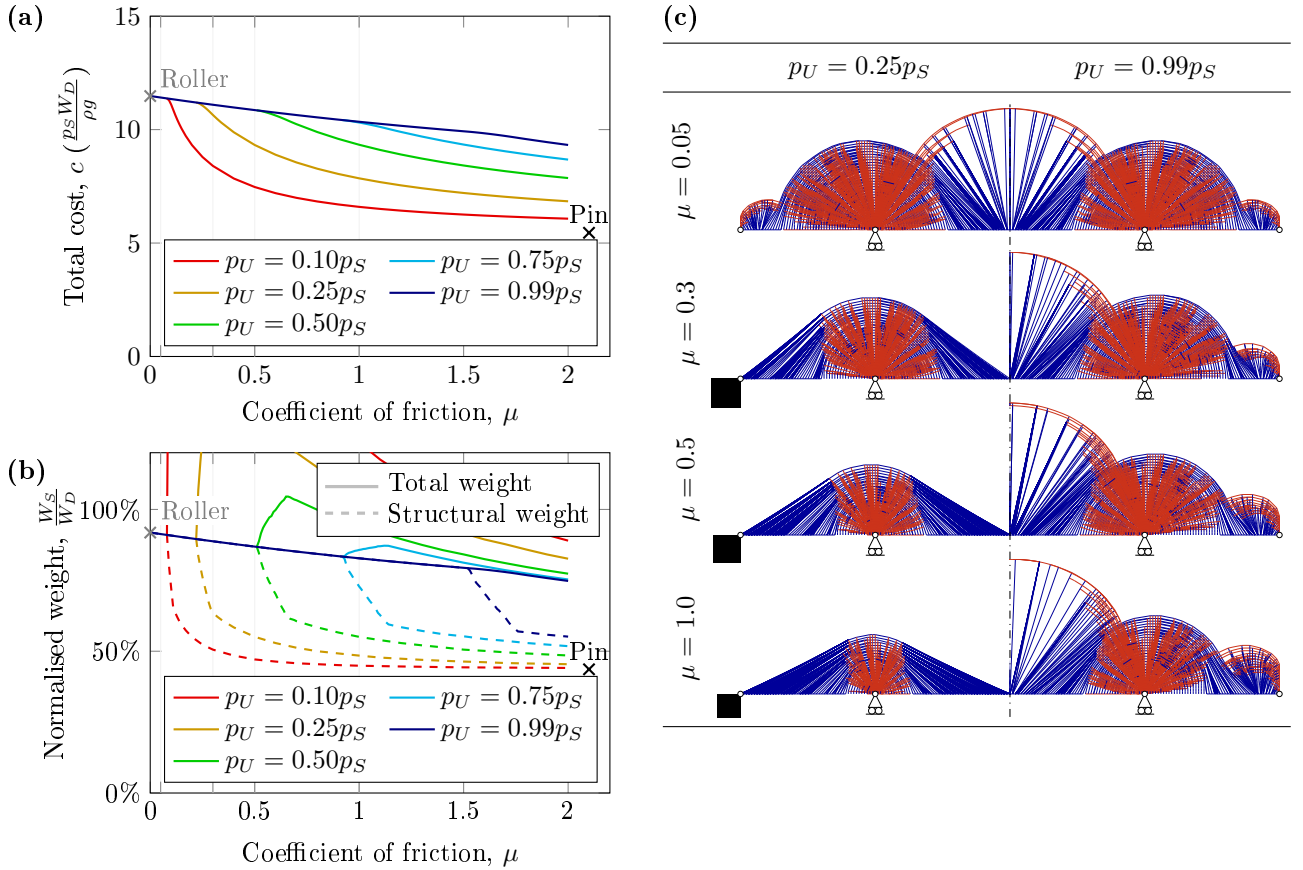


**Figure 5.11:** Bridge example: Structures with frictional support at anchorage and roller pin at tower base, with span  $L = 3\text{km}$ . (a) Total cost,  $c$ . (b) Total and structural weight. Both of these include the pinned and roller pinned solutions for comparison. (c) Optimal forms for various values of  $p_U$  and  $\mu$ , with the dash dotted line indicating the line of symmetry.

Therefore, a similar study has been undertaken for  $L = 3\text{km}$ , assuming that the intermediate support points can provide only vertical reaction forces (i.e. roller supports). The costs and volumes of the results are shown in Figures 5.11.

It can be seen that the initial rapid reduction in cost, and subsequent plateau are no longer present. Instead, the reduction in cost is fairly constant at high values of counterweight cost (e.g.  $p_U = 0.99p_S$ ), with only minimal change in optimal form. At lower counterweight costs (e.g.  $p_U = 0.25p_S$ ), a sudden divergence at a critical value of  $\mu$  is again observed, at this point the arched sections of the form are replaced by horizontal reaction forces at the anchorage points; little difference is seen in the layout in the vicinity of the intermediate roller supports. The span to dip ratio of these cable stayed structures is low initially, but increases at higher values of  $\mu$ .

#### 5.4.4 Simplified designs

The structures identified in this section thus far have been the output of high resolution layout optimization. Whilst these are useful for benchmarking the minimum cost for a given problem, and suggesting potential forms, they are too complex to be considered for real-world construction.

Therefore, simplified forms for  $L = 3\text{km}$  have been manually identified based on the layouts above (see the Online Resources). Geometry optimization is then used to refine the nodal positions. Simplified forms have been identified for both the entirely frictional support case (based on the layout from Figure 5.10), and the mixed frictional/roller support case (based on the layout from Figure 5.11). The value of  $\mu$  was taken to be 0.3, and the value of  $p_U$  as  $0.25p_S$ .

The resulting structures can be seen in Figure 5.12c-d. These have costs of only a few percent more than the equivalent layout optimization result, yet are much simpler.

For comparison purposes, two cable stayed forms were also created, and refined using geometry optimization. When only vertical support is permitted at the outer supports, a self anchored cable stay bridge will be identified. This would have an optimal span-dip ratio of 2:1, as it is essentially a rationalized form of the half bicycle wheel shown in Figure 5.9. However, to allow comparison with the other illustrated designs and to better reflect real world designs, Figure 5.12a shows the form when the height is limited to give a span:dip ratio of 3.3.

When the outer supports can support a frictional force, a partially ground anchored cable stayed bridge is identified, the optimal span:dip for this structure was found to be 3.28. This structure is essentially identical to the infinite span bridges identified by Fairclough et al. (2018).

By comparing Figures 5.12b and 5.12c (which have identical boundary conditions) several beneficial features of the proposed optimal design can be seen. Firstly, the steeper angle of the stay cables reduces the horizontal load at the anchorages, therefore requiring a smaller unstressed mass. The presence of multiple split pylons allows for some asymmetry about the tower support points. The inclined pylons in the side spans are longer, prioritising reduction of the horizontal thrust at the anchorages, whilst the main span reduces the volume of the pylon by reducing its length.

### 5.5 Concluding remarks

The distributed self-weight method of modelling self-weight has been extended to incorporate the costs of unstressed material used in structural forms such as counterweights and anchorage blocks. Additionally, a friction based support type has been proposed. This increases the range of applicability of the method and allows for fair comparison between ground anchored and self anchored structural forms.

As the formulation still remains linear, high resolution problems can be solved, whilst accurately accounting for the effects of both favourable and unfavourable self-weight. This allows accurate benchmark results to be identified. The geometry optimization method has been shown to be a practical option for refining simplified versions of these structures.

The method has been applied to initial concept design of a bridge type structure consisting of one main span and two shorter side spans. Unlike the infinite bridges which have been the subject of previous studies using the distributed self-weight method, this allows comparison between ground anchored and self anchored bridge types. When other variables were kept constant, self anchored structures were more likely to be preferred for short to moderate spans, whilst at very long spans ground anchored structures are more often optimal. However, it was also found that the optimal result may lie between these two classes, resulting in a novel hybrid structure which could only be identified through the use of the improved boundary conditions proposed here.

The developments described herein are still subject to several of the restrictions of the distributed self-weight method. Notably, that only problems with a single load case can be addressed, and also that buckling cannot be explicitly considered.

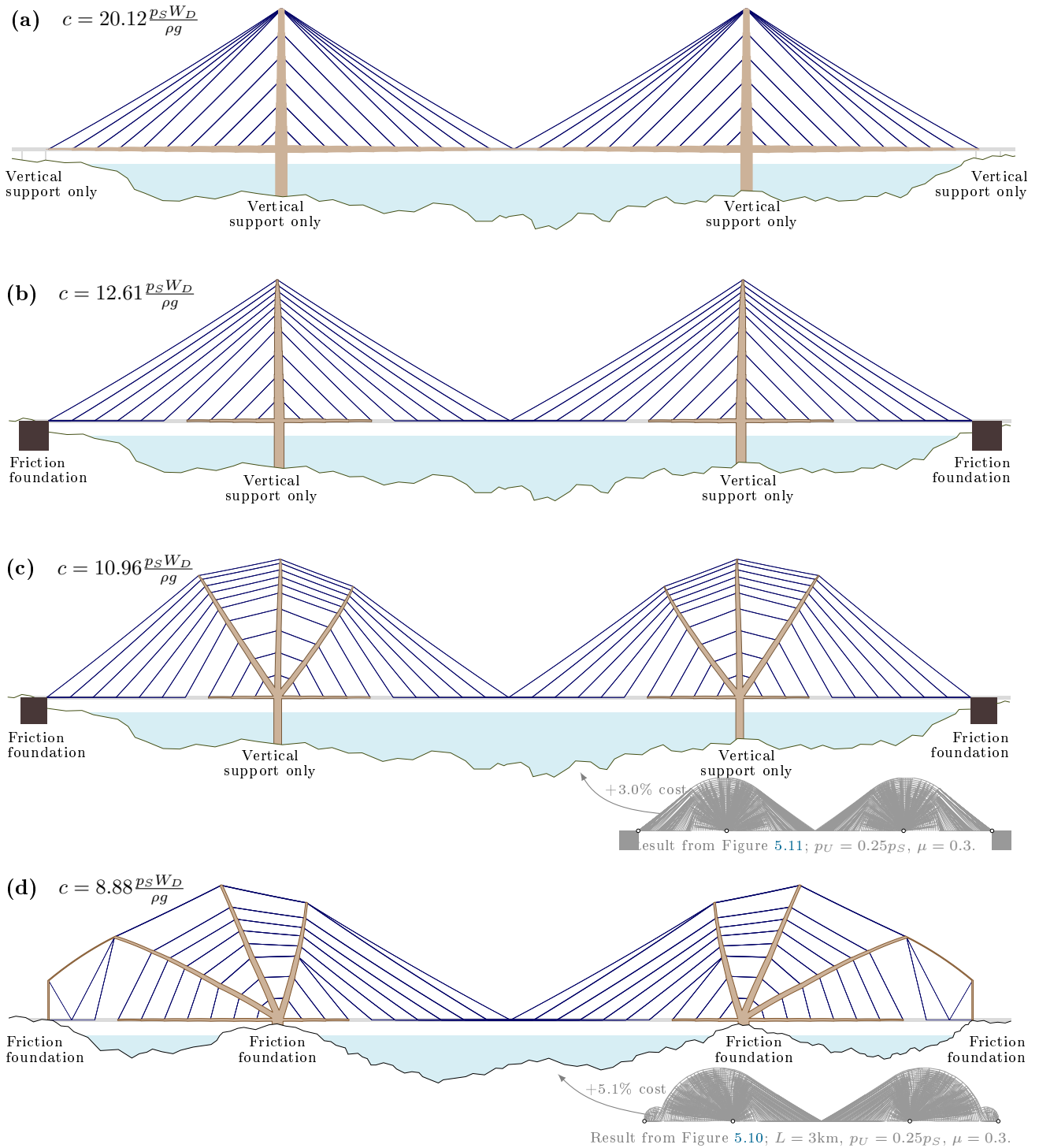


**Figure 5.12:** Bridge example: Simplified designs for three span bridges with  $L = 3\text{km}$ ,  $\mu = 0.3$ , and counter-weight material unit cost  $p_U = 0.25p_S$ .

(a) Cable stayed design with purely vertical support (self-anchored) with span:dip ratio limited to 3.3.

(b) Cable stayed design with frictional supports at anchorages (self anchored), span:dip unrestricted, optimal span:dip = 3.28.

(c) Proposed design supported vertically at intermediate towers, with frictional supports at anchorages, span:dip unrestricted, optimal span:dip = 3.34.

(d) Proposed design for frictional supports at both anchorages and intermediate supports, span:dip unrestricted, optimal span:dip = 3.43.

## Part III

# Simplification strategies





## Chapter 6

# Identification of structures with limited complexity

This chapter contains formulations and results based on the use of discrete optimization methods to impose constraints designed to reduce the complexity of the designs which are identified. A range of possible quantities which may be taken as defining complexity are compared in order to establish whether it is necessary to explicitly impose many different constraint types. Characteristics of structures subjected to limits on complexity are observed from a simple example and from numerical results. A novel method of using dynamically generated constraints is then presented, which is capable of greatly reducing the computational requirements for implementation of some practical constraints which involve consideration of crossover joints.

Some material in this chapter, principally Section 6.3, has been previously presented as part of a conference paper<sup>†</sup>. Material in the remainder of the chapter was originally prepared for a journal paper which has been accepted for publication<sup>‡</sup>.

---

6.1	Introduction . . . . .	80
6.1.1	Previous Work . . . . .	80
6.1.2	Formulations . . . . .	82
6.2	A simple illustrative example . . . . .	84
6.2.1	Minimum volume solution . . . . .	84
6.2.2	Limited complexity solution - maximum 3 joints permitted . . . . .	85
6.2.3	Results from theoretical and numerical methods . . . . .	88
6.3	Case study to compare complexity measures . . . . .	89
6.3.1	Structures with limited numbers of nodes . . . . .	89
6.3.2	Structures with limited cross-section area . . . . .	93
6.3.3	Comparison of complexity measures . . . . .	93
6.4	Adaptive solution methods . . . . .	93
6.4.1	Formulations . . . . .	94
6.4.2	Simple cantilever example revisited . . . . .	99
6.4.3	Michell cantilever example . . . . .	100
6.4.4	Spanning example . . . . .	104
6.5	Concluding remarks . . . . .	106

---

<sup>†</sup> Fairclough, H., Gilbert, M., Thirion, C., & Tyas, A. (2018). Balancing complexity and structural efficiency in the design of optimal trusses. In *Proceedings of IASS Annual Symposia 2018: Creativity in Structural Design*. International Association for Shell and Spatial Structures (IASS)

<sup>‡</sup> Fairclough, H. & Gilbert, M. (in press) Layout optimization of simplified trusses using mixed integer linear programming with runtime generation of constraints. *Structural and Multidisciplinary Optimization*

## 6.1 Introduction

In a world increasingly driven by resource scarcity, minimising material usage in construction projects is a challenge of increasing importance. The theory of minimum volume structures is well established (Michell, 1904) and can provide benchmark values to help evaluate the structural efficiency of proposed designs. However, for practical usage, the truss-like continua generated by classical methods are often challenging or impossible to construct in practice. Whilst novel construction methods may allow more complex designs to be realised in the future, more immediate benefits may arise through the use of optimization methods that produce less complex solutions.

In the previous chapters (Chapters 3, 4 & 5) simplified structures were produced manually, by following the approximate forms of the complex numerical results or by iteratively removing undesirable members. Whilst reasonable results have been obtained, the process is time consuming, subjective and is not guaranteed to find the best solution.

Further difficulties in manually rationalizing results are encountered due to the nature of the solutions found by multiple load case plastic design methods. Optimality criteria for multiple load case plastic design problems were first given by Prager & Shield (1967). For scenarios with two load cases, it is possible to use the superposition principle derived by Nagtegaal & Prager (1973) to split the problem into two single load case problems that can then be superimposed. The superposition principle was later extended to problems with more than two load cases by Rozvany & Hill (1978), although this has a restricted range of applicability. Numerical results for various problems demonstrate this ‘overlapping’ nature in many of the optimal layouts identified. In such cases, manually identifying the ideal layout for a discretised structure becomes very challenging, and there are very few benchmark examples available.

Therefore, this chapter will focus on automated methods by which optimized structures with lower complexity may be obtained. Generally, these require the quantification of complexity by some measure. Conceptually, the simplest measures of complexity are the numbers of joints or members in a given structure. Additionally, significant attention has been devoted to limiting the numbers of different cross sections present in a given solution.

### 6.1.1 Previous Work

One potential method for limiting the complexity of a structure was suggested by Parkes (1975). This involves adding a volume penalty to represent the material required in the connections joining each member in a structure, known as a joint cost. The penalty is linearly related to the member volume, and this method can therefore readily be integrated with numerical ground structure based layout optimization methods, to provide an automated method of reducing complexity whilst retaining computational efficiency. However, as this method penalises short members, rather than the number of members, its efficacy is problem dependent.

Another, similar concept was presented by Prager (1977); however, here the cost of a joint was assumed to be constant. With Prager’s approach minimum volume trusses with fixed numbers of joints are first found, and the ranges of costs for which they are optimal are later established. The minimum volume trusses are based on use of a mesh-wise constant strain field, although with a manually identified topology. This furnishes a set of geometrical rules for the joints. Mazurek et al. (2011) identify the same rules by direct optimization of joint positions for simple structures, building on the principles of graphical statics. These rules imply that the angles between members at every non-supported joint should be identical. Prager (1978b) extends these rules to the case where  $\sigma_T \neq \sigma_C$ , where  $\sigma_T$  and  $\sigma_C$  are respectively the limiting stress in tension and compression. This approach is not suited to multiple load case problems as the topology must be set in advance.

Kanno & Fujita (2018) limit the number of joints in solutions whilst minimising the compliance of the structure, considering both a heuristic method and a mathematical programming formulation including integer variables. However, although the resulting mixed integer second order cone programming (MISOCP) problem could solve problems with up to 1500 potential members reasonably quickly (in a time of 112s), larger problems had rapidly increasing demands, and the accuracy of the heuristic method appears to reduce with problem size.

A similar approach, but based on plastic design principles with volume minimisation, was used by Park (2013), resulting in a mixed integer linear programming (MILP) problem. Here, complexity was reduced by imposing limits on the numbers of members in the solution; he also used a similar approach to identify tensegrity forms.

Tensegrity forms were also identified by Kanno (2013), using another MILP formulation considering both compliance and stress constraints, as well as a number of practical considerations. This formulation prevents the inclusion of intersecting members, by including constraints for every intersecting pair of potential members in the ground structure. As the problems considered are limited in size (with ground structures containing up to 18 nodes and 99 potential members), the number of potential intersection points is small ( $\leq 32$ ). Nonetheless,

times of 67000s were required to solve the problem, and the number of intersection points and time required would rapidly increase at higher resolutions.

The great majority of work on truss based optimization methods with discrete constraints have focused on restricting the cross sections of each member to be chosen from a given list of catalogue sections. A comprehensive review of methods for approaching this problem can be found in Stolpe (2016), covering both deterministic (e.g. integer programming) and meta-heuristic methods. In this it is observed that complex formulations generally restrict the size of problems, such that these fall within the realm of ‘size optimization’ rather than true layout or topology optimization. Identification of global optima (deterministic methods) generally has a high computational cost; for example when Achtziger & Stolpe (2007) identify the global optimum for a problem with 131 potential members and 6 possible cross sections, the associated computational time is 488592s.

Heuristic methods are simple to implement and are therefore popular with many researchers (e.g. Ahrari et al., 2015; Mortazavi & Toğan, 2016; Gonçalves et al., 2015). However, the number of independent design variables is limited ( $\ll$  100 independent members). Therefore these methods generally employ very low resolution and/or restricted ground structures, often tailored to individual problems.

The Moving Morphable Components (MMC) method, developed by Guo et al. (2014), combines a continuum level-set model and explicit description of geometry. This allows complexity to be controlled in intuitive ways; for example Hoang & Jang (2017) limit the thickness of members, and Zhang et al. (2017) limit the number of ‘effective components’ ( $\approx$  number of members). However, the problem is highly non-linear and prone to identification of local optima; there are also issues treating problems with low volume fractions.

Identification of local optima is also an issue for ground structure based methods involving continuous non-linear approximations of a complexity function, such as number of members (Asadpoure et al., 2015) or number of nodes (Torii et al., 2016), these approximations are usually non-convex. Leng & Duan (2012) use a continuum approximation based on the Heaviside function to prevent intersecting bars; however, only problems with up to 68 potential members are considered, and no times are reported.

Ohsaki & Katoh (2005) also include a constraint on member intersection, as well as nodal stability and stress constraints. They use non-linear programming (NLP) and MILP in combination to provide both upper and lower bounds on solutions; problems solved have a maximum of 72 bars, and the ground structure is such that very few members can intersect. Times of up to 3000s are reported.

Ohsaki (2011) provides an introduction to the truss topology optimization problem with discrete cross sections, and additionally considers the problem of combined topology and geometry optimization of trusses, i.e. where the nodal locations are also included as design variables. In this, it is noted that these problems may be both non-convex and non-smooth, and therefore solving them is very difficult. A number of other means of addressing this are also possible, such as the implicit programming approach of Achtziger (2007), and the post-processing method used by He & Gilbert (2015).

MILP formulations have also been used to incorporate a range of other constraints, including buckling (Groenwold & Stander, 1997; Mela, 2014), stress constraints (Kanno & Guo, 2010), and the requirements of real world design codes (Van Mellaert et al., 2018). Complex real world and design code constraints have also been studied using meta-heuristic methods (e.g. Koumoutsis & Georgiou, 1994; Villar et al., 2016; Huang & Xie, 2007). However, for both MILP and metaheuristic methods the additional complexity that these cause limit their applicability to size optimization or very low resolution layout optimization (up to around 200 potential member) problems.

Most numerical approaches in the literature which consider buildability constraints can therefore be seen to fall into one of the following categories: (i) those that present topology optimization problem formulations of such complexity that only trivial scenarios can be solved; (ii) those that present solution algorithms that produce structures with no guarantee or measure of optimality. The methodology presented in this paper seeks to extend the achievable scale of truss layout optimization problems with basic buildability constraints, so as to provide a potentially useful conceptual design tool for practitioners.

To this end, MILP formulations are used to find a globally optimal solution for a ground structure of finite resolution. This is embedded within a two stage design process. The MILP problem forms the first stage, followed by a second stage of non-linear refinement i.e. geometry optimization. An important finding is that the outputs from the first stage are sufficiently accurate to be used as starting points for the second stage. Additional findings of this chapter stem from observations on the nature of the structures identified as optimal under the imposed buildability constraints, these are drawn from both the numerical results and analytical results which are obtained for a simple benchmark problem. The speed with which the MILP problems may be solved, and hence the practicable problem size, are substantially increased through the runtime generation of some constraints (so-called ‘lazy constraints’).

The chapter is organized as follows: Section 6.1.2 describes the combination of methods and formulations which will be applied and extended herein. Section 6.2 first derives a theoretical results for a simple multiple load case plastic design with a limit on the number of joints, then uses this to validate the numerical approach.

Section 6.3 applies the numerical methods to a real-world example to compare the influence of the chosen complexity measure; a number of issues with the method are also highlighted. Section 6.4 proposes novel methods to overcome these issues, and applies the improved method to a number of examples. Conclusions from the study are drawn in Section 6.5.

### 6.1.2 Formulations

#### Linear programming formulation

The well known plastic layout optimization formulation for volume minimisation of trusses subject to stress constraints (Dorn et al., 1964) is used herein; the process is described in Figure 6.1.

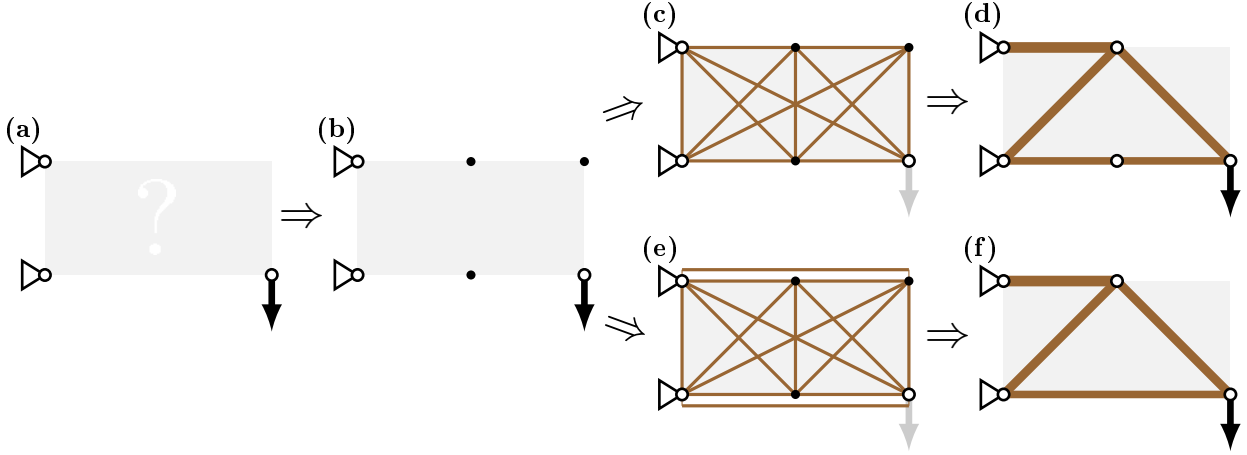


**Figure 6.1:** Stages in the truss layout optimization method. (a) Problem specification (load(s), support(s) and design domain). (b) Discretisation with nodes. (c) A ground structure without overlapping members. (d) Unique optimal solution when overlapping members are removed (uses 5 nodes of the ground structure). (e) Ground structure including overlapping members (as used herein) (f) Optimal solution which may be obtained only when overlapping members are included (uses only 4 nodes of the ground structure).

To obtain the optimal structure (e.g. Figures 6.1d and f) from a ground structure (e.g. Figures 6.1c or e) requires the solution of the following linear programming problem,

$$\text{minimise } V = \mathbf{l}^T \mathbf{a} \quad (6.1a)$$

$$\text{subject to } (\mathbf{B}\mathbf{q}_k = \mathbf{f}_k)_{\forall k} \quad (6.1b)$$

$$(\sigma_T \mathbf{a} - \mathbf{q}_k \geq 0)_{\forall k} \quad (6.1c)$$

$$(\sigma_C \mathbf{a} + \mathbf{q}_k \geq 0)_{\forall k} \quad (6.1d)$$

$$\mathbf{a} \geq 0 \quad (6.1e)$$

where  $V$  is the total volume of all members,  $\mathbf{l}$  is a vector of all potential members' lengths,  $\mathbf{a}$  is a vector of all potential members' areas.  $\mathbf{B}$  is a suitable  $2n \times 2m$  equilibrium matrix (for planar problems, for 3D problems  $\mathbf{B}$  is  $3n \times 2m$ ), where  $n$  is the number of nodes and  $m$  the number of potential truss members in the ground structure.  $\mathbf{q}_k$  is the vector of member internal forces and  $\mathbf{f}_k$  is the externally applied loading, in load case  $k$ .  $\sigma_T$  and  $\sigma_C$  are the limiting stresses in tension and compression.

Note that fully connected ground structures including overlapping members, see Figure 6.1e, are employed in this chapter. This will allow accurate modelling under limits on the number of joints. For example, consider the problem of Figure 6.1 subjected to a limit of up to 4 joints. The ground structure of Figure 6.1e would still identify the structure of Figure 6.1f, however the solution in Figure 6.1d would not be feasible, so the ground structure in Figure 6.1c would produce a sub-optimal result.

#### MILP formulations

The previous formulation can be extended using mixed integer linear programming (MILP) to provide a flexible method capable of imposing a wide range of constraints, including constraints designed to increase the practicality and buildability of a truss structure. In this formulation a new set of binary variables are added using the big- $M$  modelling method, as used by Park (2013) and Kanno & Fujita (2018). These new variables represent

the existence of a given potential member or node. The member flag variables are set based on the cross-section areas, using the constraint

$$M\mathbf{w} - \mathbf{a} \geq 0 \quad (6.2a)$$

$$w_i \in \{0, 1\} \quad i = 1, 2, \dots, m \quad (6.2b)$$

where  $\mathbf{w} = [w_1, w_2, \dots, w_m]^T$  is the vector of flag variables for each potential member in the ground structure.  $M$  is a large number, which becomes effectively an upper bound on the cross-section areas and must therefore be larger than any required cross section in the final solution. However if  $M$  is too large, numeric issues can result, here  $M$  was chosen to be 20 times the maximum point load magnitude divided by the minimum of the permitted stresses.

To provide flag variables to represent the existence of a joint, the sum of all members linked to the relevant node is used, in the form

$$\hat{M}v_j - \sum_{i \in J_j} a_i \geq 0 \quad j = 1, 2, \dots, n \quad (6.3a)$$

$$v_j \in \{0, 1\} \quad j = 1, 2, \dots, n \quad (6.3b)$$

where  $J_j$  is the set of member indices for all members connected to node  $j$ .  $\mathbf{v} = [v_1, v_2, \dots, v_n]^T$  is the vector of flag variables, such that  $v_j$  is relevant to the presence of node  $j$ .  $\hat{M}$  is another sufficiently large number. In this case  $\hat{M}$  should be bigger than the total area of members connected to any node; here  $\hat{M}$  was pragmatically taken to be 4 times  $M$ .

These flag variables can then be used to form a wide variety of constraints to increase the practicality of the forms produced.

One such constraint is to limit the number of members to be fewer than some quantity  $\zeta$ , a continuous approximation to this was considered by Asadpoure et al. (2015). In this discrete setting, this constraint can be simply expressed by

$$\sum_{i=1}^m w_i \leq \zeta \quad (6.4)$$

To numerically identify the optimal structure with a limited number of members, the constraints of (6.2) and (6.4) should be added to the problem of equation (6.1).

The number of potential members in the ground structure increases at a much higher rate than the number of nodes ( $\propto n^2$  instead of  $\propto n$ ). Therefore, it will generally be far more computationally efficient to impose a limit on the number of joints in the structure. Such a limit has been considered by Kanno & Fujita (2018) and via a continuous approximation by Torii et al. (2016). The simplest method to limit the number of joints to some given value  $\eta$  is to add the constraints from equations (6.3) and (6.5) to the problem of equation (6.1).

$$\sum_{j=1}^n v_j \leq \eta \quad (6.5)$$

Initial studies have suggested that other constraints based on the member flag variables may be more efficient than the constraint of equation (6.4). This is likely to be due to the highly coupled nature of that constraint; one of the least coupled constraints is to restrict the presence of very thin members. This is achieved by the constraint

$$M(1 - \mathbf{w}) + \mathbf{a} \geq \Lambda \quad (6.6)$$

where  $\Lambda$  is a vector containing the minimum permitted cross-section area for each member (usually all members of  $\Lambda$  will be identical, this value will then be denoted as  $a_{\min}$ ). A similar constraint has been considered by Kanno & Fujita (2018), although as the minimum area there was set based on element length, significant issues with chains of members were observed. A similar constraint is also implicitly imposed when the use of catalogue sections is enforced (Stolpe, 2016), although the substantially different formulation restricts the possible comparisons.

In light of the different possible measures of complexity, and their associated computational difficulties, it is of interest whether the choice of constraint has a substantial impact on the optimal form. For practical usage, it would be desirable to impose only the least computationally demanding constraint (likely to be the limit on the numbers of nodes), if it is possible for this to act as a surrogate for other limitations.

### Non-linear post processing formulations

Once the integer programming stage has been completed, the resulting structure can be further refined by the use of the geometry optimization (GO) method developed by He & Gilbert (2015). This adds the nodal positions of the structure as design variables, resulting in a non-linear and non-convex problem. As it is therefore not generally possible to solve this to a globally optimal solution, this method relies on the starting point provided by the topology optimization being sufficiently close to the optimal point. Additionally, in cases where a minimum cross-section area has been imposed, the lower bound on the member area variables must be changed appropriately.

The numerical results given in this chapter were run on an Intel Core i7-6700HQ CPU @ 2.60GHz, with 16GB of RAM. Gurobi 7.0.1 was used to solve the MILP problems, and up to 8 cores were permitted for use. All problems mentioned were solved to a 0.01% optimality gap (Gurobi's default). For practical usage, it may not be required to solve the problem with this level of accuracy, and a higher value may be preferred to reduce computation time. All other Gurobi parameters were set to their default value. The computational times reported are wall clock time, including the time taken to set up the problem.

## 6.2 A simple illustrative example

Due to the lack of benchmark solutions for multiple load case problems with limited complexity, a very simple example will here be considered in order to allow validation of the numerical approach. Solutions will be identified analytically for both unlimited complexity (Section 6.2.1) and with a limit of a maximum of three joints permitted (Section 6.2.2). Despite the apparently trivial nature of the problem, the results show complex and unexpected behaviour. Numerical solutions are also calculated using the methodology described in Section 6.1.2, and the numerical and analytical results are compared in Section 6.2.3.

The problem consists of 2 load cases denoted as  $\mathbf{P}_1$  and  $\mathbf{P}_2$ . These each contain a single point load, which are both applied at the point with coordinates  $(d, 0)$ , and with the same magnitude,  $Q$ . The two loads are applied orthogonally, and the load in  $\mathbf{P}_1$  is at an angle of  $\vartheta$  to the horizontal (Figure 6.2a-b), cases where  $0 \leq \vartheta \leq \frac{\pi}{2}$  will be considered. The loads are to be transmitted to supports on the line  $x = 0$ . Two special cases of this, with  $\vartheta = 0$  and  $\vartheta = \frac{\pi}{4}$ , were studied by Rozvany et al. (2014).

### 6.2.1 Minimum volume solution

First the component load cases are calculated, the sum component load case<sup>1</sup>  $\mathbf{P}_1^* = (\mathbf{P}_2 + \mathbf{P}_1)/\sqrt{2}$  contains a point load of magnitude  $Q$  and inclined at an angle of  $\vartheta - \frac{\pi}{4}$  (Figure 6.2c). The difference component  $\mathbf{P}_2^* = (\mathbf{P}_2 - \mathbf{P}_1)/\sqrt{2}$  is also of magnitude  $Q$  and inclined at an angle of  $\vartheta - \frac{3\pi}{4}$  (Figure 6.2d).

The solution for  $\mathbf{P}_1^*$  consists of a single member inclined at the same angle as the force (Figure 6.2e), i.e. connecting to the support at  $y = -d \tan(\vartheta - \frac{\pi}{4})$ . The member has an internal force of  $-Q$ . The length of the member is  $\frac{d}{\cos(\vartheta - \frac{\pi}{4})}$ . Therefore the component volume is

$$V_1^* = \frac{Qd}{\sigma \cos(\vartheta - \frac{\pi}{4})} \quad (6.7)$$

For  $\mathbf{P}_2^*$  the external load is again of magnitude  $Q$  and its direction varies by  $\frac{\pi}{4}$  either side of vertical, the solution to this was given by Rozvany et al. (1995). This consists of 2 symmetrical, orthogonal members, which connect to the support at heights  $y = \pm d$  (Figure 6.2f). The length of each member is  $d\sqrt{2}$ . The internal force in the top member is  $Q \sin \vartheta$  and in the bottom member is  $Q \cos \vartheta$ . Therefore the volume in this component is

$$V_2^* = \frac{Qd}{\sigma} \sqrt{2} \cos \vartheta + \sqrt{2} \sin \vartheta \quad (6.8)$$

By the superposition principle, these two component solutions are combined to give the optimal design (Figure 6.2g-h). The total volume is given by

$$V = \frac{V_1^* + V_2^*}{\sqrt{2}} = \frac{Qd}{\sigma} \left( \frac{1}{\sqrt{2} \cos(\vartheta - \frac{\pi}{4})} + \cos \vartheta + \sin \vartheta \right) \quad (6.9)$$

As there are no co-incident members, the final member areas are given by dividing the component areas by  $\sqrt{2}$ .

<sup>1</sup>Note that here we use the component load form of Rozvany & Hill (1978) which allows for generalisations to more than two load cases.

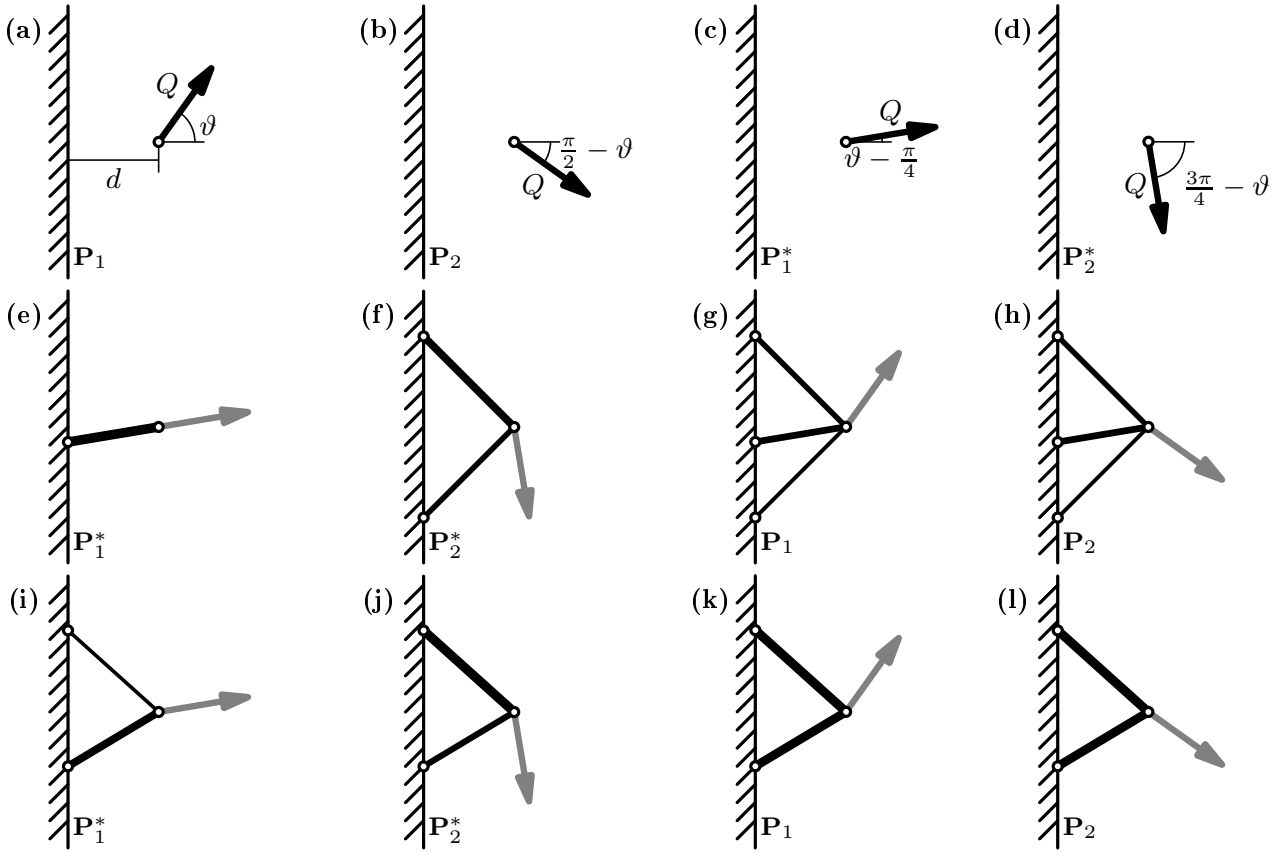


**Figure 6.2:** Simple cantilever: Problem specification and component load cases. (a)-(b) Imposed load cases. (c)-(d) Component load cases. (e)-(f) Component solutions with unlimited complexity. (g)-(h) Final optimal solution with unlimited complexity. (i)-(j) Component solutions with only 3 nodes. (k)-(l) Final solution with only 3 nodes.

### 6.2.2 Limited complexity solution - maximum 3 joints permitted

It is now required to find the minimum volume solution to the same problem, but with the additional constraint that only 3 joints are permitted. This permits only a single topology; two members reaching from the point of application of the forces to the support line. Therefore all potential solutions to this problem can be enumerated using 2 degrees of freedom, the vertical locations of the two support points, which will be denoted  $y_A$  and  $y_B$  (Figure 6.2i-j).

Calculating the solutions in this case is somewhat more complex than previously, three main steps will be undertaken. Firstly, expressions for the structural volume, in terms of  $y_A$ ,  $y_B$  and  $\vartheta$  will be found by using the component load cases. Then, the optimal values for these expressions will be identified; three cases depending on the value of  $\vartheta$  will be found where the solutions must be calculated differently. Finally, the critical values of  $\vartheta$  which form the boundaries between cases are found.

#### Expressions for structural volume

The two component load cases are identical to the previous section. The lengths of the members are given by  $l_A = \sqrt{y_A^2 + d}$  and  $l_B = \sqrt{y_B^2 + d}$  respectively. The member forces are found from equilibrium equations at the loaded point. In  $\mathbf{P}_1^*$  the member forces in members A and B are

$$q_1^A = Q \frac{(\sin(\frac{\pi}{4} + \vartheta)y_B - \cos(\frac{\pi}{4} + \vartheta)d)\sqrt{y_A^2 + 1}}{d(y_A - y_B)}, \quad q_1^B = Q \frac{(-\sin(\frac{\pi}{4} + \vartheta)y_A + \cos(\frac{\pi}{4} + \vartheta)d)\sqrt{y_B^2 + 1}}{d(y_A - y_B)} \quad (6.10)$$

In  $\mathbf{P}_2^*$  the member forces are

$$q_2^A = -Q \frac{(-\cos(\frac{\pi}{4} + \vartheta)y_B - \sin(\frac{\pi}{4} + \vartheta)d)\sqrt{y_A^2 + 1}}{d(y_A - y_B)}, \quad q_2^B = -Q \frac{(\cos(\frac{\pi}{4} + \vartheta)y_A + \sin(\frac{\pi}{4} + \vartheta)d)\sqrt{y_B^2 + 1}}{d(y_A - y_B)} \quad (6.11)$$

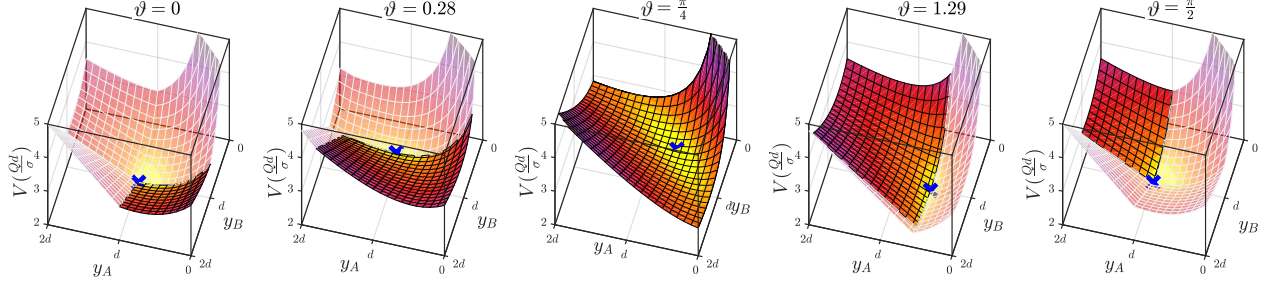


**Figure 6.3:** Simple cantilever: Volume of two member truss for  $0 \leq y_A \leq 2d$  and  $0 \leq y_B \leq 2d$  for various force inclinations,  $\vartheta$ . (The solid region shows where  $q_1^A < 0, q_1^B < 0, q_2^A < 0$  and  $q_2^B > 0$ , the blue cross shows the globally minimum volume/design to resist each set of forces.)

The superposition principle is again used to find the overall design (Figure 6.2k-l), and define the total volume as

$$V = \frac{V_1^* + V_2^*}{\sqrt{2}} = \frac{(|q_1^A l_A| + |q_1^B l_B|) + (|q_2^A l_A| + |q_2^B l_B|)}{\sigma \sqrt{2}} \quad (6.12)$$

By inspection of the graph of this function for all values of  $0 \leq \vartheta \leq \frac{\pi}{2}$  (see examples in Figure 6.3), it can be seen that the minimum volume solution falls within or on the border of the region where the member forces in  $\mathbf{P}_1^*$  are in the same direction, and the member forces in  $\mathbf{P}_2^*$  are in opposing directions. Based on this, the expression for  $V$  is re-written without using the absolute value operator, using the sign convention that tensile stresses are negative.

$$V = \frac{-q_1^A l_A - q_1^B l_B - q_2^A l_A + q_2^B l_B}{\sigma \sqrt{2}} \quad (6.13)$$

Additionally the cusps of the plots in Figure 6.3 must be considered, these define the limits of the region within which equation (6.13) is valid. They are given by:

$$q_1^A \leq 0 \quad q_2^A \leq 0 \quad (6.14a)$$

$$q_1^B \leq 0 \quad q_2^B \geq 0 \quad (6.14b)$$

For a given value of  $\vartheta$ , these equations each define a vertical plane. Equations (6.14a) are planes with constant  $y_B$ , and equations (6.14b) are planes with constant  $y_A$ .

### Optimal values in each case

The equations which describe the optimal solution vary depending upon the value of  $\vartheta$ . Three case are possible, and each of these are considered separately.

When  $\vartheta > \vartheta_2$  (where  $\vartheta_2$  is a critical value, approximately equal to 0.9), the minimal value is found on the cusp of the volume function defined by  $q_1^A = 0$ . The optimal point lies on the minima of the cusp line, i.e. where the partial derivative  $V_{y_A} = 0$ . In this region, the optimal values of  $y_A$  and  $y_B$ , and the optimal volume  $V$  are given by

$$y_A = \frac{1}{\tan(\frac{\pi}{4} + \vartheta)} + \frac{\sqrt{2}}{\sin(\frac{\pi}{4} + \vartheta)}, \quad y_B = \frac{-1}{\tan(\frac{\pi}{4} + \vartheta)}, \quad V = \frac{\sqrt{2}(\sin(\vartheta + \frac{\pi}{4}) + 2\sqrt{2} + 3\cos(\vartheta + \frac{\pi}{4}))}{2\sin^2(\vartheta + \frac{\pi}{4})} \quad (6.15)$$

Similarly, for values of  $\vartheta \leq \vartheta_1$  (where  $\vartheta_1 \approx 0.65$ ), the minimal value is found on the intersection of  $V_{y_B} = 0$  and  $q_1^B = 0$ . This gives

$$y_A = \frac{1}{\tan(\frac{\pi}{4} + \vartheta)}, \quad y_B = \frac{-1}{\tan(\frac{\pi}{4} + \vartheta)} + \frac{\sqrt{2}}{\sin(\frac{\pi}{4} + \vartheta)}, \quad V = \frac{\sqrt{2}(\sin(\vartheta + \frac{\pi}{4}) + 2\sqrt{2} - 3\cos(\vartheta + \frac{\pi}{4}))}{2\sin^2(\vartheta + \frac{\pi}{4})} \quad (6.16)$$



$\theta$	Point	$y_A$	$y_B$	$V$		
0.90011	C	1.30835	0.11521	2.49230		$\vartheta_1 < \vartheta < \vartheta_2$ optimum from eqn (6.17)
	S					
	M	1.19519	0.19318	<b>2.49217</b>		
0.90068	C	1.30786	0.11580	<b>2.49136</b>		$\vartheta = \vartheta_2$
	S	1.27886	0.13492	2.49138		
	M	1.22241	0.17384	<b>2.49136</b>		
0.90087	C	1.037709	0.11599	<b>2.49106</b>		$\vartheta > \vartheta_2$ optimum from eqn (6.15)
	S	1.25026	0.15444	2.49108		
	M					

**Table 6.1:** Simple cantilever: Behaviour of volume function in vicinity of optimal values for force inclinations in the vicinity of  $\vartheta_2$ . (Point M is a local minimum of equation (6.17), point S is a saddle point of equation (6.17), and point C is the minimum value along the cusp  $q_1^A = 0$ , with values given by equation (6.15). Values in boldface are the optimal points for that problem, note that when  $\vartheta = 0.90068$  two equally optimal solutions exist.)

In the inner region, where  $\vartheta_1 \leq \vartheta \leq \vartheta_2$ , the minimum volume structure is found at the local minima of equation (6.13), i.e. where the partial derivatives  $V_{y_A} = 0$  and  $V_{y_B} = 0$ . In this region, values for pairs of  $y_A$  and  $y_B$  are given by

$$\begin{aligned}
 0 = & \quad y_B^4 \\
 & -2y_A^2y_B^3 + 2y_Ay_B^3 \\
 & -2y_A^3y_B^2 + 4y_Ay_B^2 \\
 & +2y_A^3y_B + 4y_A^2y_B + 4y_Ay_B - 2y_B \\
 & +y_A^4 - 2y_A - 2
 \end{aligned} \tag{6.17}$$

To complete the system of equations and calculate the corresponding value of  $\vartheta$  for such a pair, the values of  $y_A$  and  $y_B$  are simply substituted into either  $V_{y_A} = 0$  or  $V_{y_B} = 0$ . For this region, it is quite difficult to begin with a value of  $\vartheta$  and calculate the optimal values of  $y_A$  and  $y_B$ .

### Boundaries between cases

The final task is to establish the boundary values,  $\vartheta_1$  and  $\vartheta_2$  between the outer and inner regions. To do this some points of interest must first be defined. The point C is defined as the minimum volume point lying on the cusp  $q_1^A = 0$ , this is the point given by the equations (6.15), and is the optimal value when  $\vartheta \geq \vartheta_2$ .

Next, the stationary points of equation (6.13) are considered, these lie on the line defined by equation (6.17). There are at most 2 stationary points in the region in which this function is valid. To characterise these, the discriminant of this function,  $\Delta = V_{y_A y_A} V_{y_B y_B} - (V_{y_A y_B})^2$ , is calculated. The stationary point at which  $\Delta > 0$  is defined as point M, this is a local minima, and additionally represents the optimal value in the central region ( $\vartheta_1 \leq \vartheta \leq \vartheta_2$ ). The stationary point where  $\Delta < 0$  is defined as S, this is a saddle point of the function. The critical value  $\vartheta_2$  is the point at which the optimal value switches from point C to point M.

Table 6.1 gives values of  $y_A, y_B$  and  $V$  for these three points at notable values of  $\vartheta$ . Additionally it provides illustrations of the topography of the volume function in the vicinity of C, M and P; these illustrations show the approximate profile the volume function at the bottom of a ‘valley’ which runs roughly parallel to the plane  $y_A + y_B = 1$ . This valley may also be observed in the plots in Figure 6.3, particularly when  $\vartheta = \frac{\pi}{4}$ .

Point S enters the valid region when the relations from equation (6.15) are substituted into equation (6.17), giving  $\vartheta = 0.900110$ . Here, points S and C are co-incident and have a volume which is 0.005% greater than the optimal value at M.

At the point where  $V_{y_A} = 0$ ,  $V_{y_B} = 0$  and  $\Delta = 0$  a single degenerate stationary point is formed as points S and M become co-incident. This occurs when  $\vartheta = 0.900874$ , and the volume at points S and M is 0.0008% higher than the volume at C. Therefore the value  $\vartheta_2$ , at which points M and C are equally optimal must lie in the region  $0.900110 \leq \vartheta_2 \leq 0.900874$ .

The value of  $\vartheta_2$  is found at the point where  $V_{y_A} = 0$ ,  $V_{y_B} = 0$  and the right hand side of equation (6.15c) is equal to the right hand side of equation (6.13) (where the values of  $y_A$  and  $y_B$  refer to the point M). From this it is found that  $\vartheta_2 = 0.9006836427$ . By a similar logic,  $\vartheta_1 = 0.6701126839$ .

It has been shown that within the the region  $0.900110 \leq \vartheta \leq 0.900874$ , the range of volumes is small ( $< 0.005\%$ ) over a wide range of possible values for  $y_A$  and  $y_B$  (of up to  $0.1d$ ). This may cause problems for numerical methods if accuracy levels are not set high enough. Additionally, when  $\vartheta = \vartheta_1$  or  $\vartheta_2$ , two distinct solutions are equally optimal.

### 6.2.3 Results from theoretical and numerical methods

The optimal volumes, member sizes and support locations calculated above for both the problem with unlimited complexity and the problem with only three joints permitted are shown in Figure 6.4a and b. Example structures for  $\vartheta = \frac{\pi}{4}, \vartheta_2, \frac{3\pi}{8}$  and  $\frac{\pi}{2}$  are also shown in Figure 6.4c-j.

It can be seen that even for this very simple problem, the behaviour is quite complex and unintuitive. The rationalized structures are not closely linked to the equivalent un-rationalized form, which may make such structures difficult to obtain by intuitive or mathematical post processing. The volume penalty caused by imposing the three joint limit is at most 20.3%.

Table 6.2 shows the difference between the theoretical and numerical results for this example under the three joint limit. The numerical results were found using the MILP method outlined in Section 6.1.2. The ground structure contained nodes only along the support, at  $0.02d$  spacing over  $-1.5d \leq y \leq 1.5d$  (i.e. 152 nodes, including the loaded node). Geometry optimization (GO) was also performed to further refine the results.

The numerical and analytical volumes can be observed to be in close agreement. At  $\vartheta = \vartheta_2$  two distinct results are equally optimal. Here, the MILP solver identifies one of these solutions. Then, use of the interior point method for the GO stage perturbs this solution, resulting in identification of the alternative solution. The non-linear interior point method used in the geometry optimization stage is only capable of returning a single solution, therefore it may not be apparent to the user that multiple optima exist. However, the branch and bound type algorithms generally used in MILP can maintain a pool of the best solutions found during the solve, potentially showing alternative possibilities. There is an additional computational cost involved in finding

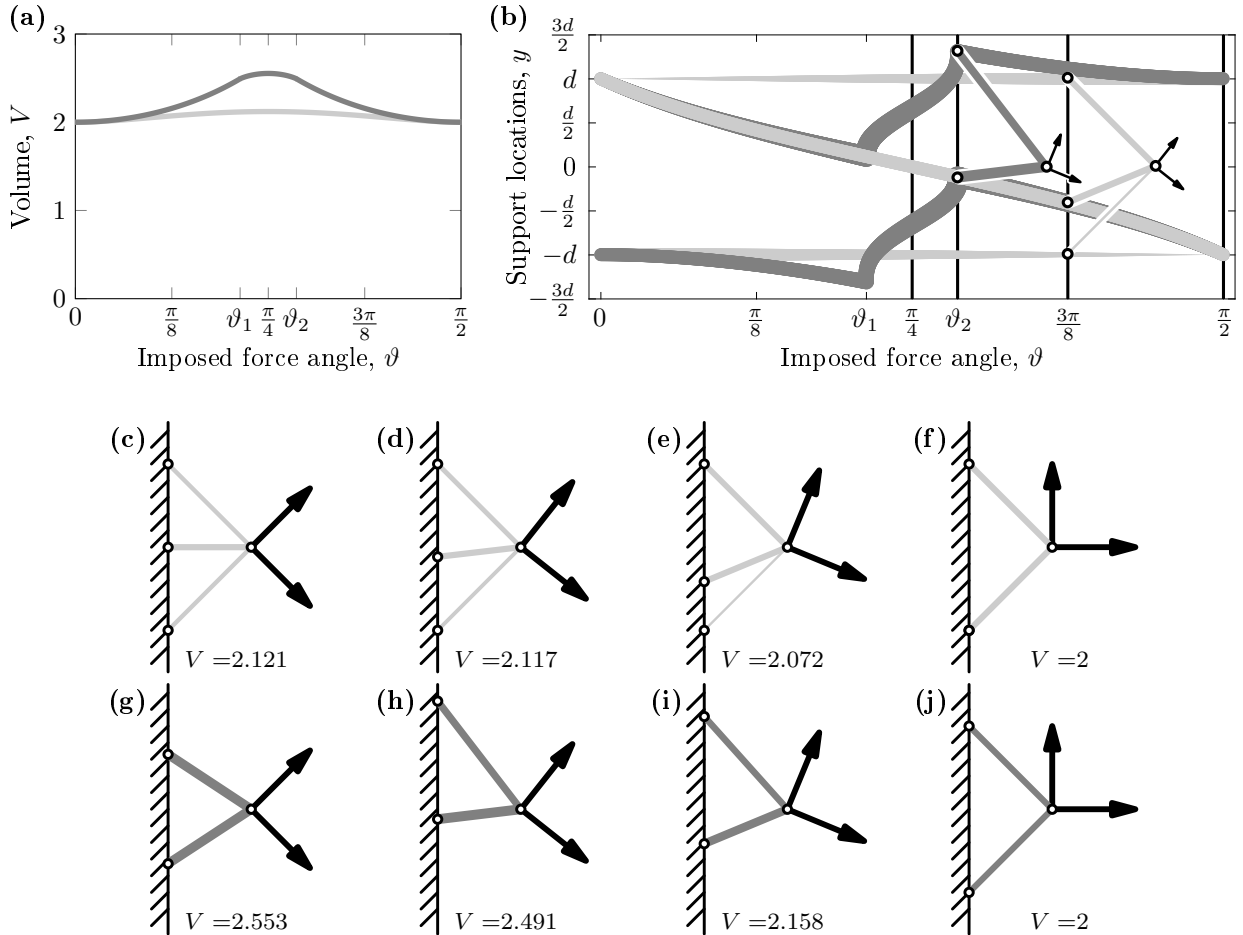


**Figure 6.4:** Simple cantilever: Theoretical results.

(a) Volumes of optimal structures with unlimited complexity (light grey) and maximum 3 joints (dark grey) for values of  $\vartheta$  between 0 and  $\frac{\pi}{2}$ .

(b) Locations of support points for optimal structures with unrestricted complexity (light grey) and maximum 3 joints (dark grey), with line width proportional to the area of the member which connects there (forms (e) and (h) shown for context).

(c)-(f) Forms of optimal structures with unlimited complexity for  $\vartheta = \frac{\pi}{4}, \vartheta_2, \frac{3\pi}{8}, \frac{\pi}{2}$ .

(g)-(j) Forms of optimal structures with only 3 joints for  $\vartheta = \frac{\pi}{4}, \vartheta_2, \frac{3\pi}{8}, \frac{\pi}{2}$ .

$\vartheta$	Theoretical			MILP results				MILP + GO results		
	$y_A(d)$	$y_B(d)$	$V\left(\frac{dQ}{\sigma}\right)$	$y_A(d)$	$y_B(d)$	$V\left(\frac{dQ}{\sigma}\right)$	Time (s)	$y_A(d)$	$y_B(d)$	$V\left(\frac{dQ}{\sigma}\right)$
$\frac{\pi}{4}$	0.657	0.657	2.553	0.660	0.660	2.553	10	0.659	0.659	2.553
$\vartheta_2$	1.308	0.116	2.491	1.300	0.120	2.491	7	1.222	0.174	2.491
	1.222	0.174								
$\frac{3\pi}{8}$	1.117	0.414	2.158	1.120	0.420	2.162	3	1.117	0.414	2.158
$\frac{\pi}{2}$	1.000	1.000	2.000	1.000	1.000	2.000	2	1.000	1.000	2.000

**Table 6.2:** Simple cantilever: Comparison of theoretical and numerical methods for problem with 3 joints.

the *best* alternative solutions, but good solutions may be obtained with almost no additional computations. Although these results are uncertain and non-deterministic, they may provide some extra context for the user.

### 6.3 Case study to compare complexity measures

The methods will now be tested using a case study drawn from a real world project. The case study concerns the identification of a structural layout for a transfer truss of 21m span, as shown in Figure 6.5. The truss is to carry 6 equally spaced column loads of equal magnitude in the Ultimate Limit State (ULS) load case, and a pattern load case is also included. The structure is to be constructed from S355 steel, giving a maximum stress of 355MPa in tension, reduced to 266MPa in compression to approximate the effects of buckling. The problem is symmetrical, and a symmetrical solution is desired, therefore only half the design domain is modelled, and symmetry boundary conditions will be used.

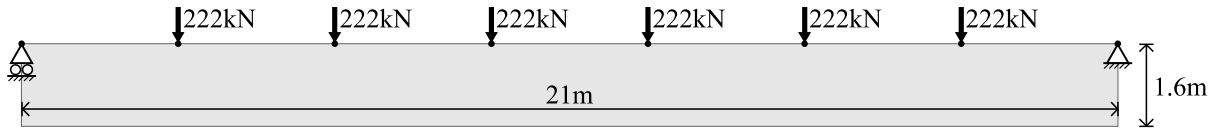


**Figure 6.5:** Roof transfer truss: Problem Specification.

For example, the layout optimization benchmark structure shown in Figure 6.6 was calculated from a fully connected ground structure with a Cartesian grid of nodes at spacings of 0.25m horizontal and 0.2m vertical. The problem was solved using the member adding method (Gilbert & Tyas, 2003) in under 4 minutes. This structure requires 2.73t of steel; this will be used as the benchmark value against which the weights of simplified structures can be compared.

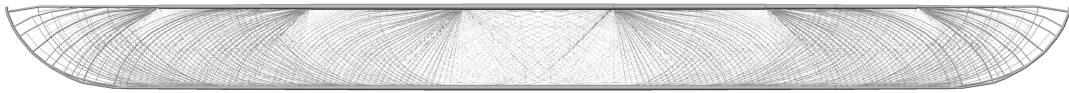


**Figure 6.6:** Roof transfer truss: High resolution layout optimization result. Steel weight 2.73t

#### 6.3.1 Structures with limited numbers of nodes

For trusses where very low complexity is desired, there are only limited options for possible forms. For a structure to be a true truss (i.e. with no bending stresses) it is necessary to ensure that a node is present at each applied load and support. Simply connecting these essential nodes will often provide a ground structure which is suitable for use to identify the minimum volume truss with fewest possible nodes.

##### Trusses comprising 9 nodes

For this case study, all the loads and supports are co-linear. Therefore, at least one additional node is required to form a feasible truss structure. To ensure symmetry, this node should be located on the central symmetry

plane of the problem. Also, to create the lightest structure, this node should be placed to maximise the depth of the truss, as shown in Figure 6.7.

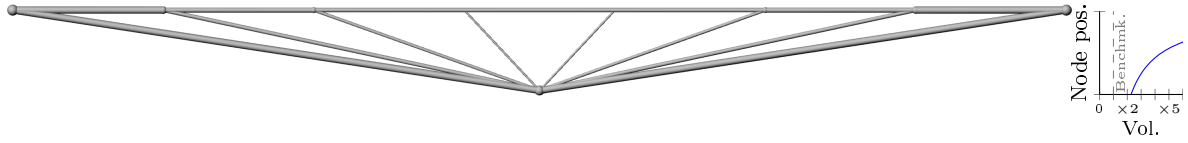


**Figure 6.7:** Roof transfer truss: 9 node structure. Steel weight 127% higher than benchmark. Also, plot of volumes for 9 node structures with varying depth.

### Trusses comprising 11 nodes

The above solution with 9 nodes has a volume over double that of the benchmark value. Therefore, to provide a lower weight, a pair of additional nodes will be added to the design, it is assumed that for maximum efficiency, the central joint in the 9 node structure will remain at the base of the design domain. This problem therefore adds only two degrees of freedom (the horizontal and vertical location of the new nodes), it is possible to enumerate the minimum structural volume for each possible position, see Figure 6.8. A 25mm spacing between adjacent locations was used, resulting in 27,365 structures analysed in a total time of 7 minutes.

Four principal topologies were identified, these are illustrated in Figure 6.8c-f, and the corresponding joint locations, and the regions over which the optimal topology is constant are indicated in Figure 6.8b. When the newly added joint was located inside the hull of the 9 node structure in Figure 6.7, similar topologies were identified, but with an additional member directly linking the central joint to the supports and/or the loaded points. The central (darkest) region represents where the additional nodes were ignored and the structure in Figure 6.7 was identified as optimal.

The optimal location is shown in the lightest blue, and illustrated in Figure 6.8d, its volume is 13% greater than the benchmark value. It can be seen that although the feasible solution space (i.e. the space above the surface in 6.8) is non-convex overall, in the region of the optimal solution it is convex and smooth. This suggests the viability that the proposed numerical approach using MILP then geometry optimization, provided that the results of MILP are sufficiently close to the optimal solution.

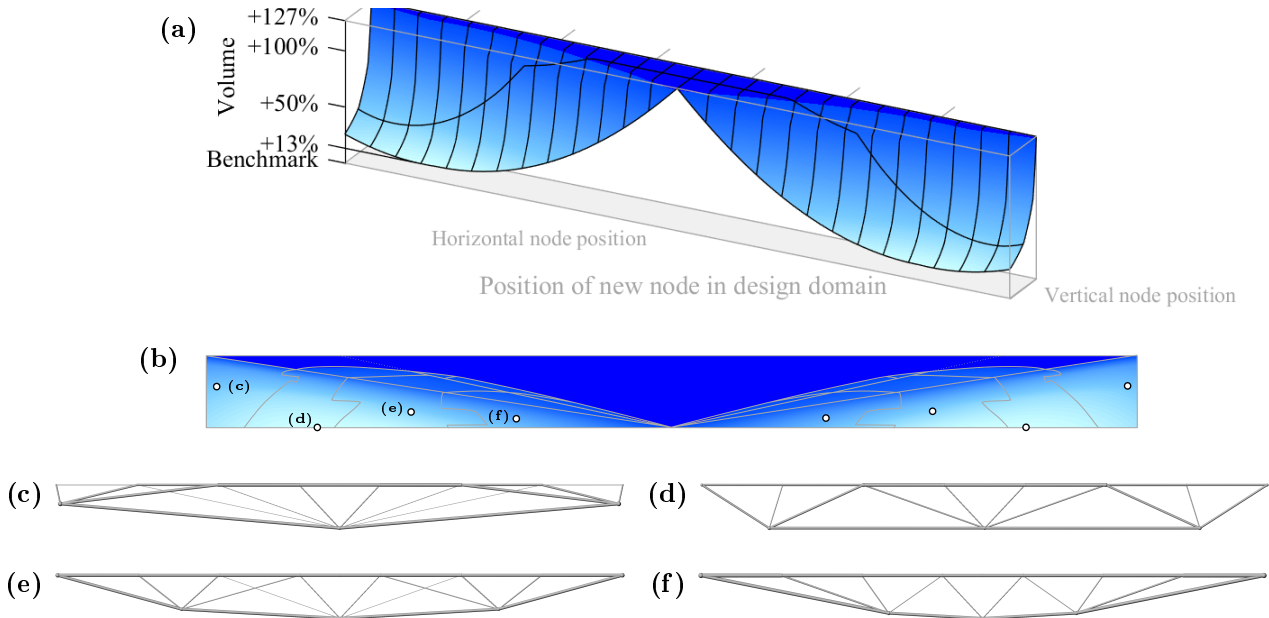


**Figure 6.8:** Roof transfer truss: Exhaustive enumeration of designs with 11 nodes.

(a) Total structural volume for each position of the newly added pair of nodes within the design domain.

(b) Positions of the newly added nodes within the design domain, showing regions where the minimum volume topology is uniform, and locations of added nodes for the sample layouts shown.

(c) – (f) Sample layouts for the main 4 topologies identified, total volumes 42%, 13%, 34% and 62% greater than the benchmark value respectively.

### Trusses comprising more than 11 nodes

As more nodes are added to the structure, the dimensionality of the problem quickly makes testing every location impractical. For example, adding one more pair of nodes to the previous problem will square the number of points which must be checked, leading to an expected computational time of 19 weeks. The non-convexity of the solution spaces of these problems (which can be seen in Figure 6.8a), means that more refined methods based on further sequential development of the problem (such as Martinez et al., 2007) become problematic, leaving them susceptible to identifying local optima (see He & Gilbert, 2015).

Instead the mixed integer-linear programming (MILP) formulation described in Section 6.1.2 is used. MILP solvers find a range of values (which may be very narrow, here a range of 0.01% was obtained) within which the global optimum of the problem lies. As the global solution is identified; the solution of a high resolution problem will give the globally minimum volume truss with the required number of nodes. However, MILP problems have greatly increased computational demands compared to standard linear problems. This necessitates the use of lower resolutions, which restricts the possible solutions. Here, a ground structure comprising 36 nodes and 666 potential members (in the half of the design domain under consideration) is used.

Figure 6.9a shows the result of standard layout optimization at this resolution; this structure is 4% heavier than the benchmark, and the form is quite restricted by the underlying Cartesian grid of nodes. To counter this, the resulting solutions of the layout optimization and MILP problems are subject to geometry optimization. This method has been applied to the result in Figure 6.9a, both with and without the merging of nearby nodes, leading to the structures in Figures 6.9c and 6.9b respectively. The geometry optimized structures are simpler and lower weight than the layout optimization result (although they are still around 2.5% higher in volume than the benchmark). However, there is little control over the level of simplification required, and some regions of the forms may still be challenging to construct.

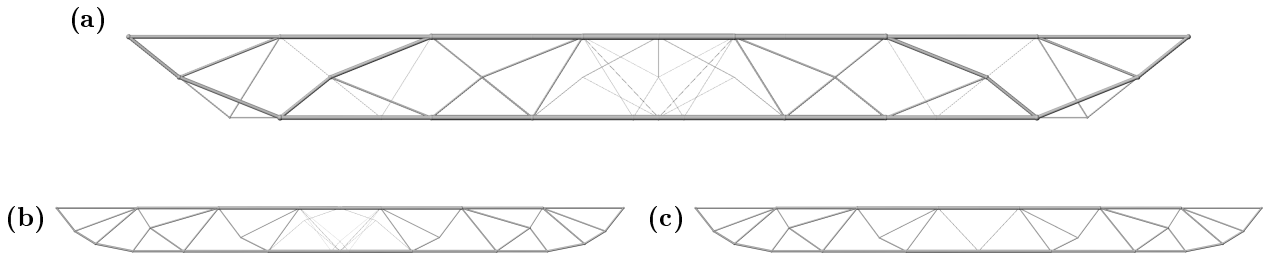
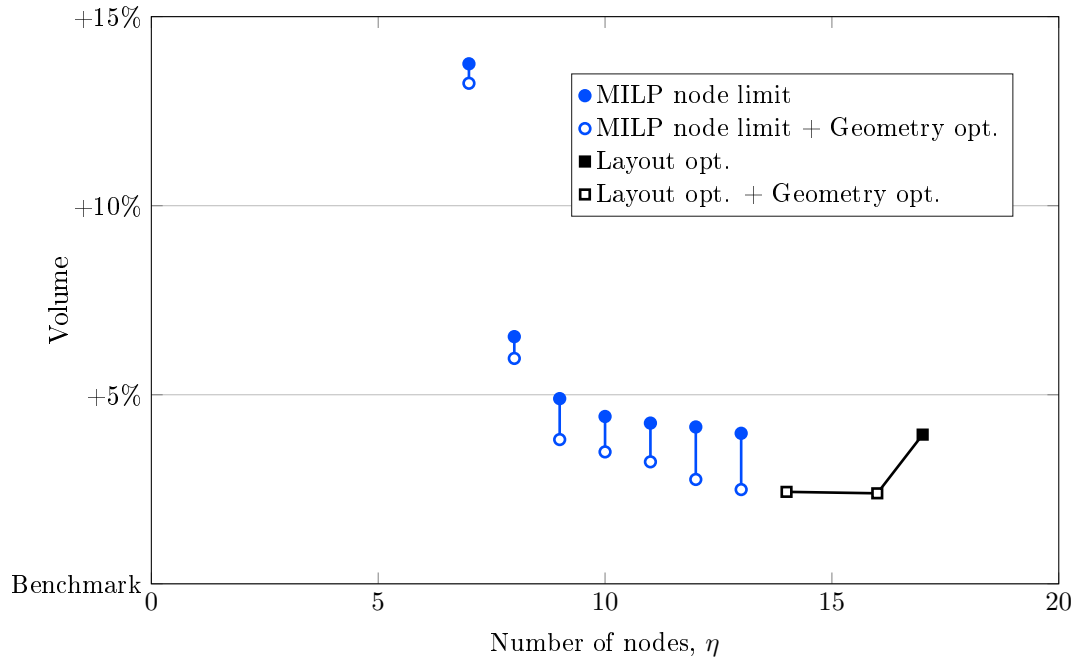


**Figure 6.9:** Roof transfer truss: Results for comparison with MILP formulations. **(a)** Lower resolution layout optimization result (3.9% above benchmark), **(b)** Geometry optimization result without node merging (2.4% above benchmark), **(c)** Geometry optimization result with node merging (2.5% above benchmark).

The results of the MILP problem, and of subsequent geometry optimization for various values of  $\eta$  is shown in Figure 6.10. Here,  $\eta$  refers to the number of nodes used in the half of the design domain under consideration. This causes some issues; firstly, nodes on the centerline are counted as equal to those away from the center, although the latter will imply two joints in the final structure. Secondly, nodes on the centerline are counted as joints even if they are only a location where a horizontal bar passes through the mirror plane, such as in the results for  $\eta = 8$ . These issues will be addressed in Section 6.4.

Nonetheless, it can be seen that the solution identified for 7 nodes after geometry optimization is identical to that illustrated in Figure 6.8d. It has also been successfully verified that imposing a limit of 9 nodes produces the form shown in Figure 6.7, although this was omitted from Figure 6.10 for clarity.

A further issue can be observed in Figure 6.10, particularly in the geometry optimized result with  $\eta = 12$ , and the MILP results with  $\eta = 8, 9, 11, 12$  and 13. In these cases, the number of joints in the structure from an engineering perspective is not equal to the number of active nodes. This is due to the presence of members which intersect at points partway between their supports. Preventing these crossover nodes implies constraints between pairs of members in the ground structure, which would give a very large number of constraints (roughly  $\propto n^4$ ). A more efficient method of tackling this will be described in Section 6.4.



$\eta$	MILP node limit	MILP node limit + Geometry opt.	MILP time
7			00:03:15
8			00:00:58
9			00:00:27
10			00:01:49
11			00:01:39
12			00:00:39
13			00:00:42

**Figure 6.10:** Roof transfer truss: Results with limited numbers of nodes.  $\eta$  gives the number of nodes permitted in the half design domain which was modelled. The layout optimization points represent the forms shown in Figure 6.9.

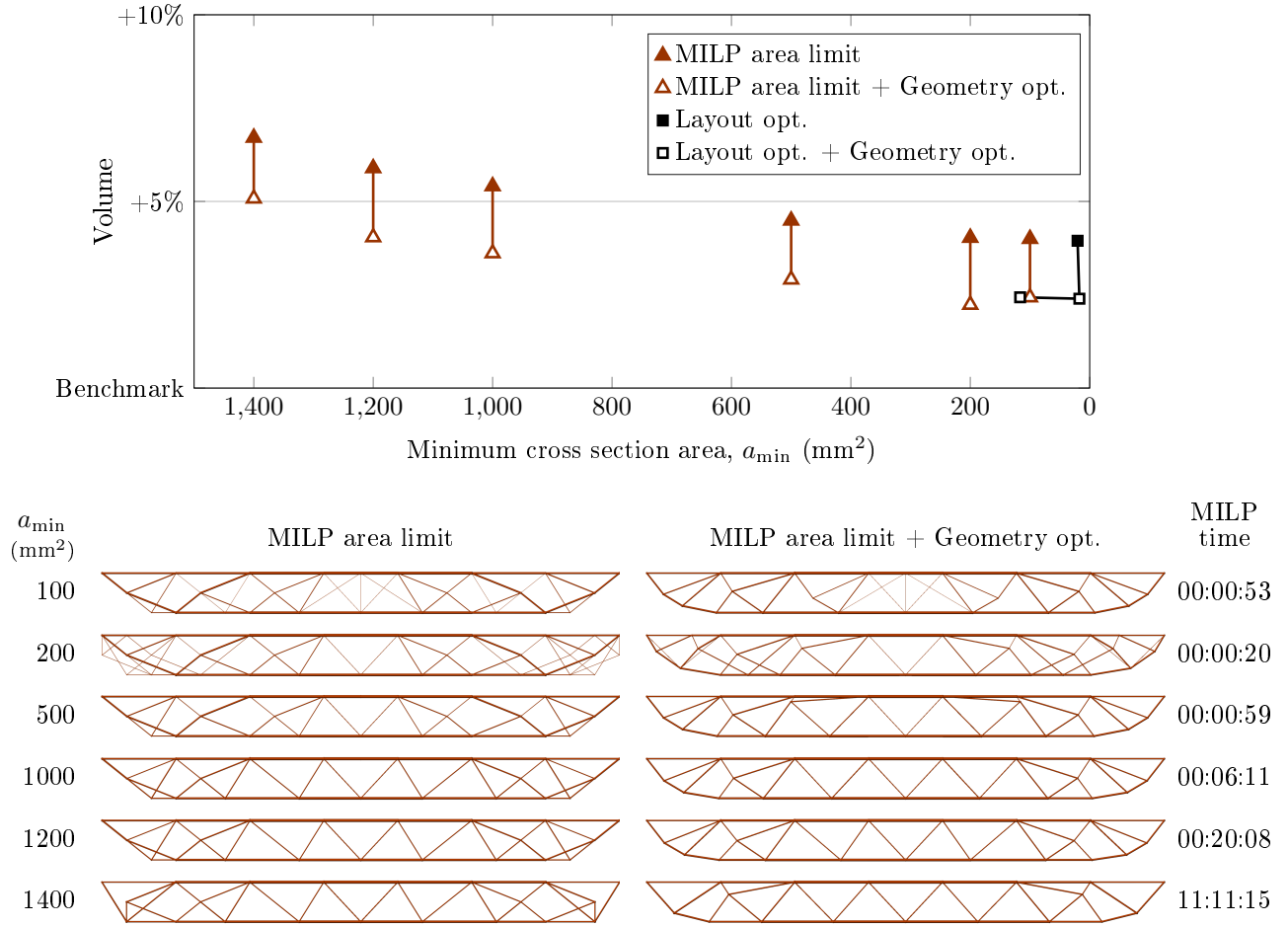


**Figure 6.11:** Roof transfer truss: Results with minimum cross-section area ( $a_{\min}$ ). The layout optimization points represent the forms shown in Figure 6.9.

### 6.3.2 Structures with limited cross-section area

Equation (6.6) has been used to impose a minimum cross-section area on the resulting structures. The minimum permitted area ranged from 100mm<sup>2</sup> to 1400mm<sup>2</sup>, and the results are shown in Figure 6.11, as are results post processed using geometry optimization. These results generally required a longer computational time to compute than the results in Figure 6.10, likely due to the increased number of integer variables.

The Pareto fronts shown in Figures 6.10 and 6.11 provide a powerful tool for designers, allowing them to choose the appropriate level of compromise between complexity and lightness required for a given project. They also place the options in context, both against each other and against the theoretical benchmark solution.

### 6.3.3 Comparison of complexity measures

Figure 6.12 shows the complexities, in terms of number of active nodes and minimum cross-section area, for all the structures in Figures 6.9, 6.7, 6.8d, 6.10 and 6.11. There is some correlation between the different measures, however it is not strong, implying that it may be necessary to impose multiple constraints to achieve a structure which is truly practical with current construction methods.

## 6.4 Adaptive solution methods

In light of the issues encountered in the previous section, a number of modifications to the numerical method will now be proposed and tested on a number of example problems. These aim to address the 'crossover joints' formed by members which intersect part-way along their lengths, and the inaccuracies encountered when using symmetry to reduce the size of the problem. The proposed technique also allows constraints on the angles between members to be considered with a reasonable degree of computational cost.

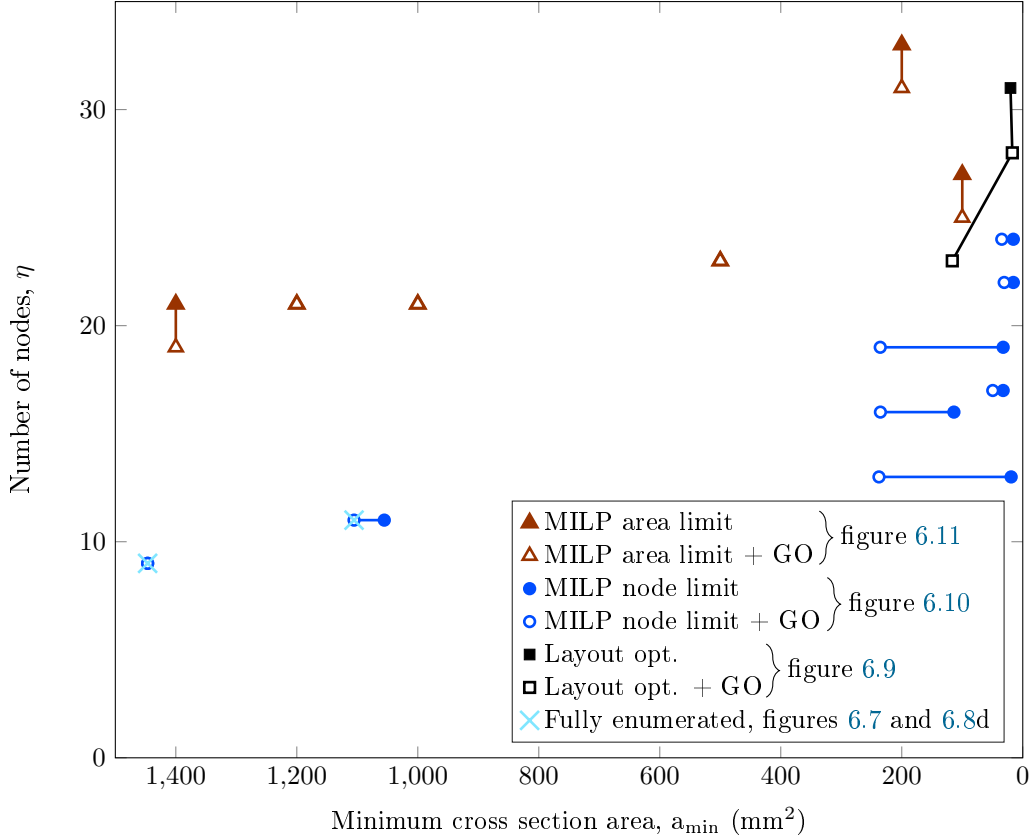


**Figure 6.12:** Roof transfer truss: Correlation between complexity measures.

### 6.4.1 Formulations

These formulations build on those of Section 6.1.2. Notably the flag variables  $\mathbf{w}$  and  $\mathbf{v}$  for members and nodes as defined in equations (6.2) and (6.3) are used.

#### Layout optimization

**Limits on the number of joints including ‘crossover joints’** The ‘crossover joints’ which appear in Figure 6.10, and may also be observed in the results of Kanno & Fujita (2018), will appear to be additional joints from the point of view of the designer, but will by default not be counted as such in the formulation.

To prevent this, constraints can be added for each pair of intersecting members, preventing both of them from being present in the solution at the same time,

$$\sum_{j=1}^n v_j \leq \eta \quad (6.18a)$$

$$(w_h + w_i \leq 1)_{\forall \{h,i\} \in \mathcal{X}} \quad (6.18b)$$

where  $\mathcal{X}$  is a set containing unordered pairs of indices,  $\{h, i\}$ , for each pair of intersecting elements.

However, the size of  $\mathcal{X}$  increases at a very high rate ( $\propto n^4$ ), meaning that the full form of this problem will be extremely computationally expensive to formulate and solve. Fortunately, since only a small subset of these constraints are likely to be used, these can instead be generated on-the-fly, during the running of the solver. Most commercial solvers, including CPLEX (IBM Corp., 2015) and Gurobi (Gurobi Optimization, LLC, 2018), are capable of implementing these so-called ‘lazy constraints’ by allowing user defined code (often referred to as a callback function) to be called at intervals *during* a single run of the solver. As any intermediate solution which violates one or more potential constraints will be eliminated, this methodology does not alter the final solution, which remains identical to the solution of the full MILP problem containing all constraints from the beginning.

Lazy constraints have previously been used when solving the travelling salesman and related problems (Dantzig et al., 1954), where they have been shown to provide significant advantages in terms of computational efficiency. More recently Haunert & Wolff (2010) have applied them to the simplification of building outlines for



maps. Here it is shown that, when applied to truss structures, the use of lazy constraints enables true topology optimization problems to be solved, i.e., layout optimization problems utilising fully connected, non-problem specific, ground structures to identify optimal topologies under various different constraints.

The problem is initially provided to the solver without the constraints of (6.18b). All member flags in  $\mathbf{w}$  can be initially set to be equal to 1 without violating any of the initial constraints. without violating any of the initial constraints. This can be used as a partial warm start, although the speed advantage in explicitly doing so is small as this fact is easily detected by a solver's built in heuristics. Nonetheless, the fact that these variables are somewhat irrelevant (before any lazy constraints are added) does provide a reasonable computational advantage.

When a feasible solution is found, the set of members with non-zero areas are identified and each pair from this set (of which there are several orders of magnitude fewer than all pairs of potential members) is checked to see if a crossover joint is produced. If a crossover is found, then an appropriate constraint of the form of equation (6.18b) is added to the problem, and remains present in the active problem until the final solution is found.

For multiple load case problems, optimal solutions are often made up of multiple, almost independent, forms overlain on top of each other. Therefore it is preferable to allow crossovers in the solutions, and to take account of them when computing the total number of joints. This is achieved when equation (6.18) becomes

$$\sum_{j=1}^n v_j + \sum_{g=1}^b \bar{v}_g \leq \eta \quad (6.19a)$$

$$(w_h + w_i - \bar{v}_g \leq 1)_{\forall h,i \in \mathcal{X}} \quad (6.19b)$$

where  $\bar{\mathbf{v}} = [\bar{v}_1, \bar{v}_2, \dots, \bar{v}_b]^T$  is a vector of flag variables representing the existence of each possible crossover between members of the ground structure. The length of  $\bar{\mathbf{v}}$ , denoted by  $b$ , will be equal to the size of  $\mathcal{X}$ , i.e. approximately proportional to  $n^4$ .

When the constraints of equation (6.19) are implemented using lazy constraints, the size of  $\bar{\mathbf{v}}$  can be greatly reduced.  $\bar{\mathbf{v}}$  becomes a pool of variables, which are assigned to crossovers as required. The pool size should be chosen to be larger than the number of lazy constraints expected to be added, but small enough to not require excessive memory. For the problems shown here, a pool size of 100 was found to be sufficient. In this case, the variables in  $\bar{\mathbf{v}}$  can be set to zero without affecting the optimality of the problem as initially provided, this is also used in a partial warm start.

Initial tests suggested that it was more advantageous to check and impose these lazy constraints each time a feasible integer solution was identified, rather than each time a continuous relaxation was solved. This also reduced the number of times the check was performed, and meant a smaller pool of constraints could be used. This approach has therefore been adopted here. As the solution is not changed by the proposed method, these heuristics impact only the speed with which the solution is obtained, and not the solution itself.

The procedure used to dynamically generate these constraints is shown in Figure 6.13. The process to instead forbid crossovers is similar, except that all references to  $\bar{\mathbf{v}}$  are removed, and the newly added lazy constraint is instead  $w_p + w_q \leq 1$ .

In the procedure, once a constraint has been added to the current reduced problem, it will not be removed. This ensures that the solution obtained by successively adding dynamically generated constraints will converge to the globally optimal solution for the original full problem (i.e., the problem that includes all constraints from the outset). This will occur when the solution for the current reduced problem, comprising only a subset of all possible constraints, is also found to be feasible for the original full problem. For continuous linear optimization problems a similar principle underpins the cutting plane method (Kelley, 1960) and analogous column generation method (Dantzig & Wolfe, 1960), which has been successfully used by Gilbert & Tyas (2003) to develop a computationally efficient ‘member adding’ procedure for large-scale truss layout optimization problems.

Finally, note that the optional geometry optimization post-processing step (see below) is not shown in Figure 6.13, and is performed following a successful termination of the solver.

**A comparison of problem formulations** Several equivalent formulations are possible to ensure that the variables  $\mathbf{v}$  accurately represent the existence of each node. The method that is used within this chapter links the value of  $v_j$  to the sum of the areas of the members connected to node  $j$  using equation (6.3a), i.e.

$$\hat{M}v_j - \sum_{i \in J_j} a_i \geq 0 \quad j = 1, 2, \dots, n$$

This formulation will be referred to as formulation  $\mathcal{A}$ . This formulation is the natural choice when considering limits on the number of joints without considering crossovers, as in Section 6.3, as flag variables are not required for each member.

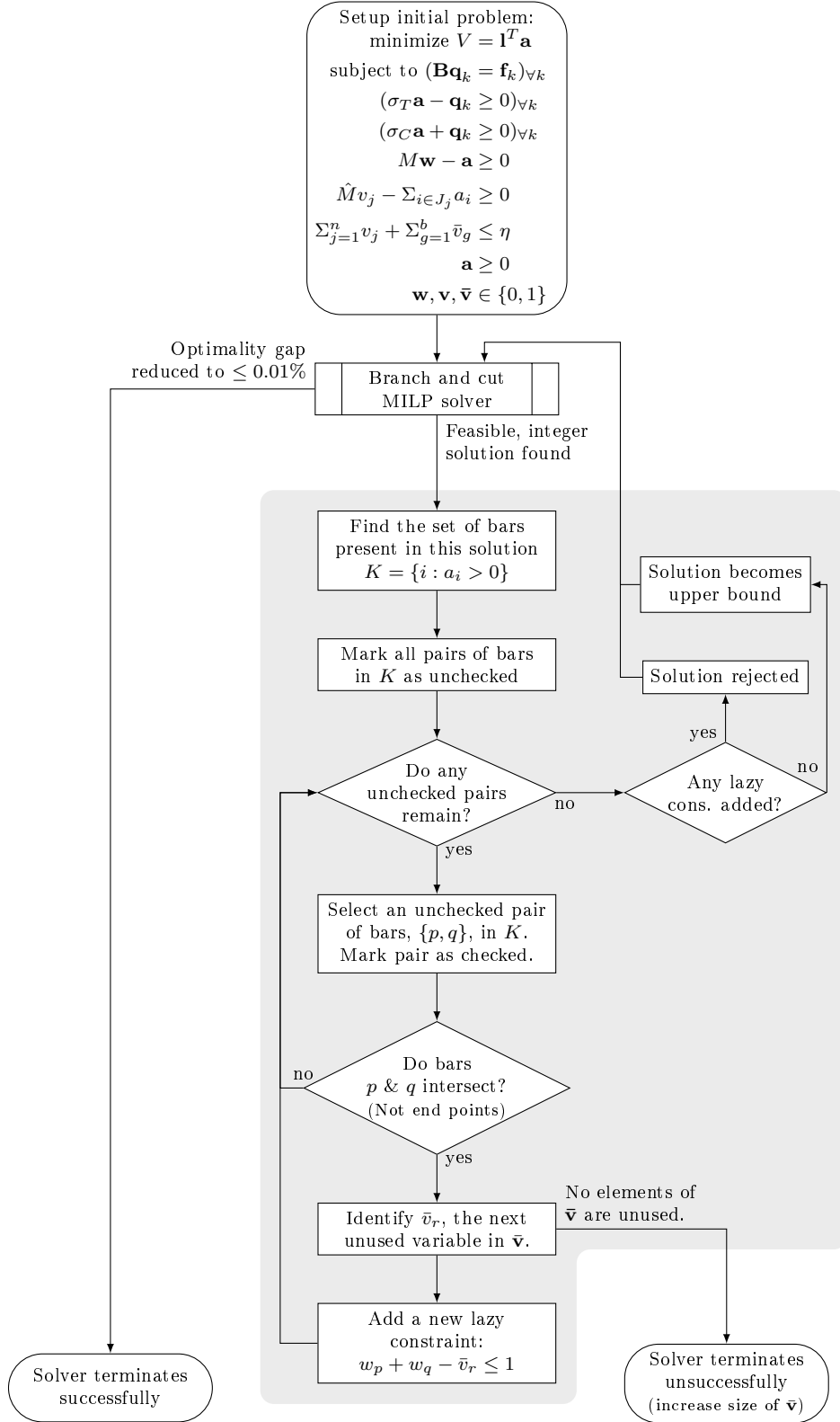


**Figure 6.13:** Procedure for runtime constraint generation. Problem shown involves imposing a limit on the number of joints, including ‘crossover joints’. The steps in the shaded region are performed within the callback function which is called by the MILP solver (e.g. Gurobi).

Permitted number of joints	Formulation $\mathcal{A}$		Formulation $\mathcal{W}$	
	No. of lazy cons. added	Time (s)	No. of lazy cons. added	Time (s)
3	0	10	0	14
4	0	16	0	58
5	3	74	8	137
6	4	72	0	95
7	4	117	7	222
8	0	257	0	686
9	3	291	1	571
10	9	196	10	376
11	17	133	17	224

**Table 6.3:** Speed comparison between formulations for defining the node flag variables,  $\mathbf{v}$ . Problem is the Michell cantilever with limited number of joints, as shown in Table 6.4 and Figure 6.20.

However, when crossovers are considered, member flag variables are required due to the constraints of equations (6.18) or (6.19). In this case an alternative formulation may be considered to be more standard in the general integer programming community. This avoids the need for the arbitrary large number  $\hat{M}$ , by linking the value of  $v_j$  to the *flag* variables of the members connected to node  $j$ , using

$$Nv_j - \sum_{i \in J_j} w_i \geq 0 \quad j = 1, 2, \dots, n \quad (6.20)$$

In this formulation,  $\hat{M}$ , is replaced by  $N$ , the maximum number of members which will be permitted to connect to any node. This formulation will be referred to as formulation  $\mathcal{W}$ .

For both  $\mathcal{A}$  and  $\mathcal{W}$ , the remainder of the formulation is as described above. The two formulations produce identical solutions; however the computational requirements may differ.

To investigate this, both formulations are tested on the same problem. The problem used is the Michell cantilever problem, as shown below in Section 6.4.3, with a limit set on the number of joints and crossover joints prevented. Table 6.3 shows the computational time required to solve the problem for different numbers of joints, using each formulation.

It can be seen that formulation  $\mathcal{A}$  takes roughly half the time to solve the problems compared to formulation  $\mathcal{W}$ . This is as expected if the characteristics of the two formulations prior to the addition of any lazy constraints is considered. Formulation  $\mathcal{A}$  initially begins with all the member flags,  $\mathbf{w}$ , unconstrained; i.e. they may all be set equal to 1 without making any potential solution infeasible. It only becomes necessary to begin to branch on any variable  $w_i$  once the member  $i$  is part of an added crossover constraint.

In contrast, formulation  $\mathcal{W}$  couples all integer variables from the outset, leading to a much more challenging initial problem. This outweighs the potential benefits of eliminating  $\hat{M}$ . Formulation  $\mathcal{A}$  is therefore used for the remainder of the chapter.

**Imposing symmetry with a limited number of joints** For a given problem with symmetrical design domain, loads and supports, it is known (Stolpe, 2010) that truss optimization with discrete cross sections may have an optimal solution that is not symmetrical; it will be shown that this is also the case when the MILP problem formulation proposed here is used to impose limits on the number of joints in the structure.

However, it is useful to consider how a requirement for a symmetrical solution can be imposed as an additional constraint, since symmetry will often be preferred for reasons of standardisation or aesthetics. It also allows problem size to be significantly reduced, as only half of the design domain is explicitly modelled. Thus to impose a symmetry condition, each symmetrical pair of members is assigned only a single area variable. Additionally, only one integer flag is added to each symmetrical pair of members or nodes. Members that cross the mirror line are not included, as they can be approximated by using the nodes which lie on the mirror line, as shown in Figure 6.14. Thus the number of potential members (and therefore variables) will be reduced to approximately a quarter of the initial number.

To avoid the issues encountered in Section 6.3, some modifications to the constraints are needed. A node which lies on the mirror plane, and which is connected only to members which are perpendicular to the mirror plane will not appear to be a joint in the final design (see for example the central point on the top chord of most results in Figure 6.10). Therefore for nodes lying on the mirror plane, equation (6.3a) is replaced by

$$\hat{M}v_j - \sum_{i \in J'_j} a_i \geq 0 \quad j = 1, 2, \dots, n \quad (6.21)$$

where  $J'_j$  is the set of member indices for members connected to node  $j$ , but not including those members which are perpendicular to the mirror plane.

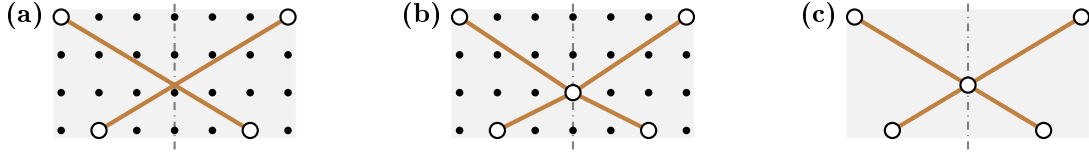


**Figure 6.14:** Approximation of members crossing a line of symmetry (the line of symmetry is shown as a dash-dotted line). **(a)** Section of a layout optimization result with members crossing the mirror line permitted, note that the crossover joint will be counted due to equation (6.19). **(b)** Section of a layout optimization result when members crossing the mirror line are not permitted, using a node on the mirror line to approximate the result. **(c)** Further improvement of the approximation is possible when geometry optimization is used, and the node on the mirror line may be moved to the location in part a.

The constraint on the total number of joints must also be modified such that joints that are formed by crossovers or nodes lying remote from the mirror plane are counted twice in the computations.

**Limits on the angle between members** Another feature that can make Michell structures difficult to manufacture is the presence of small angles between adjacent members, especially in fan-type regions. To prevent this, integer constraints can be added in the layout optimization stage using the equation

$$(w_h + w_i \leq 1)_{\forall \{h,i\} \in \mathcal{V}} \quad (6.22)$$

where  $\mathcal{V} = \{\{h_1, i_1\}, \{h_2, i_2\}, \dots\}$  is the set containing unordered pairs of indices for all pairs of members that form an angle that is smaller than  $\Psi$ , the minimum permitted joint angle. Note that this angle may be formed either at a node which is common to both members or at a point where the members intersect, partway along one or both of their lengths.

Again, the full formulation is very time consuming to compute as the number of these constraints is approximately proportional to  $n^4$ . These constraints are therefore also implemented as lazy constraints. The procedure is similar to that outlined in Figure 6.13; however references to  $\bar{\mathbf{v}}$  are removed, and the check on each pair of members,  $p$  &  $q$ , is checked to identify if they form an angle (either at a crossover point or at an end node) which is outside the permitted range.

### Geometry Optimisation

The solution found by solving the MILP problem will again be used as the starting point for geometry optimization. It will be important to ensure that the solutions continue to be feasible with respect to the practical constraints imposed in the previous sections. However, these need not be imposed as integer constraints at this stage, as the overall topology is generally not significantly changed. Instead the buildability constraints are reformulated as constraints on the nodal positions.

**Limiting the number of joints in geometry optimization** When only a limited number of joints are permitted, generally no additional constraints will be required in the geometry optimization stage. This is because the joints in the problem generally remain in a constant topology, with the number of joints only reducing due to merging or all connecting members vanishing.

The only possible method by which more apparent joints could appear is if the topology is changed by a bar passing over another joint, as shown in Figure 6.15. However, this situation can easily be avoided by converting the topology between the MILP and GO stages such that all crossover joints become standard joints.



**Figure 6.15:** Detail of a layout, showing the importance of converting crossover joints to full joints between the MILP and GO stages when imposing a limit on the total number of joints. **(a)** Before geometry optimization, containing 3 joints in this region. **(b)** After geometry optimization, containing 4 joints in this region.

**Limiting the angle between members in geometry optimization** When a limit on the angle between members has been imposed, this must be converted to a continuous constraint on the nodal coordinates. This will be in the form

$$\frac{\overrightarrow{DA} \cdot \overrightarrow{DB}}{|\overrightarrow{DA}| \cdot |\overrightarrow{DB}|} \leq \cos(\Psi) \quad (6.23)$$

where D is the node common to two members, A and B are the other nodes of each member, and  $\Psi$  is the imposed minimum angle. Note that this also means that crossover joints must be converted to standard joints before the geometry optimization phase.

In some cases where a minimum angle is imposed, a branch type form (as shown in Figure 6.16a) is identified as the optimal solution of the integer programming problem. As the joints move during geometry optimization, the branch joint tends to move towards the ‘root’ joint, as in Figure 6.16b. The joint merging phase of geometry optimization will then combine the two joints, however there then may be pairs of members which violate the angle constraint, Figure 6.16c. If the permitted movement radius of the joints is sufficiently large, the feasibility restoration phase of the non-linear solver is likely to be able to find a new feasible solution using the new topology, Figure 6.16d.

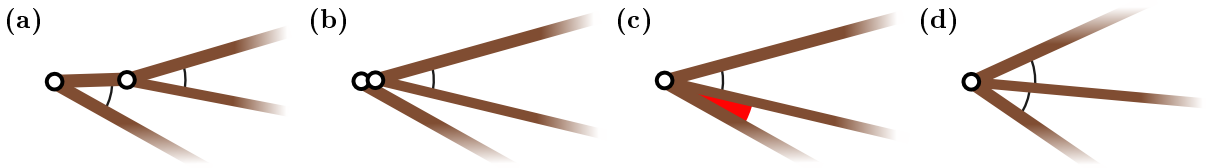


**Figure 6.16:** Detail of area containing branched members during geometry optimization stage.

- (a) Initial branched member topology.
- (b) The joints move close together, however as the bottom and middle member do not quite meet, the angle between them is not checked.
- (c) The joints are merged, the bottom and middle members now have an angle constraint, which is violated.
- (d) Feasibility restoration phase successfully finds a point at which all constraints are satisfied, although this is now quite different to the starting point from integer programming.

This new form may now be notably different from the initial starting point, and therefore potentially inefficient. However, simply eliminating the joint merging step would result in a final design where two joints were infinitesimally close together. A minimum member length constraint can be added to prevent this, i.e.

$$|\overrightarrow{AB}| \geq l_{min} \quad (6.24)$$

where A and B are the end points of the member, and  $l_{min}$  is the minimum permitted length. This constraint is only explicitly required during the geometry optimization stage, during layout optimization members with a length less than  $l_{min}$  can simply be omitted from the ground structure. Here, length limits have generally been added only in the geometry optimization phase, with  $l_{min}$  being set at or below the nodal spacing of the original ground structure.







### 6.4.2 Simple cantilever example revisited

The problem from Section 6.2 will now be revisited using the methods of Section 6.4. The simple topologies which are demanded in the case with limited numbers of joints mean that no crossover joints exist in these cases, and the results of Figure 6.4 remain valid for the case where only 3 joints are permitted.

However, when a limit on the angle between members is imposed, solutions may be more complex in form, involving members that do not simply directly connect the loaded point and a point on the support. Therefore, the methods outlined in the previous section can be of use. Numerical solutions for joint angle limits have been calculated using a  $5 \times 13$  grid of nodes, and a fully connected ground structure ( $m = 2080$ ).

Figure 6.17 shows results for the problem with loads inclined at the angle  $\vartheta = \frac{3\pi}{8}$ , i.e. as shown in Figures 6.4e and 6.4i which are duplicated in Figure 6.17 for comparison. The scenario is subjected to limits on the minimum angles between members of  $35^\circ$  and  $45^\circ$ . The unusual topologies identified demonstrate the difficulty in trying to identify optimal solutions for this problem analytically or manually.

The problem was solved firstly by imposing all angle constraints from the outset (‘basic formulation’), and then by implementing the angle limit (i.e. equation (6.22)) using lazy constraints. Both implementations produced identical final results; however it can be seen that the use of lazy constraints reduced the time required by approximately a factor of 20.

	35°	Minimum angle	45°	N/A	N/A ( $\eta = 3$ )
Results after MILP		2.160 167s 7s 23.8×	2.198 180s 11s 16.3×		
Results after MILP and GO		2.082	2.099		
		Volume	Volume	2.072	2.158

**Figure 6.17:** Simple cantilever: numerical results for problem with specified minimum angles between members (load inclination  $\vartheta = \frac{3\pi}{8}$ ). Additionally, results from Figure 6.4 with unrestricted complexity and with the limit on the number of joints  $\eta = 3$  are shown for comparison.

Figure 6.17 also shows the result of applying geometry optimization post-processing. Despite the different topologies identified in the MILP stage, similar topologies are found after geometry optimization. Additionally, it can be observed that the volumes after geometry optimization are both lower than the solution limited to three joints, demonstrating that the more complex topology is beneficial, albeit only by 3.6% and 2.8% respectively. This suggests that, although the geometry optimization process is non-convex and therefore cannot be proven to identify a global optimum, the starting points provided by the MILP formulation appear to be sufficient to provide good results.

### 6.4.3 Michell cantilever example

#### Problem specification

The proposed methods are now applied to a classical Michell cantilever problem, as shown in Figure 6.18. The theoretical minimum volume can be found using equations derived by Chan (1960) to be  $V_T = 39.43Qd$ . Discretised versions of this problem have been studied by Prager (1977) and Achtziger & Stolpe (2007). In both cases, the topology of the optimal structures was manually inferred from the continuum form; however their observations are useful for comparative purposes.

A fully connected ground structure of 99 nodes is used here; this contains 4851 potential members. The solution to the standard layout optimization problem at this resolution has a volume of  $40.45Qd$ , an increase of 2.6% over  $V_T$ , although this reduces to +0.8% after GO is applied, and the resulting solution has 20 joints.

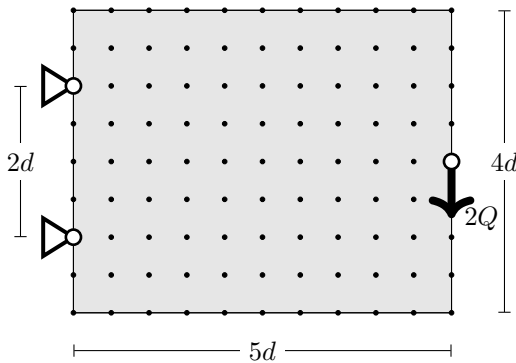


**Figure 6.18:** Michell cantilever: Problem specification. (Fully connected ground structure used.)

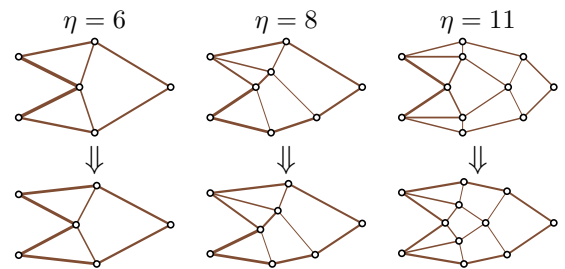


**Figure 6.19:** Michell cantilever: Results after MILP (top) and GO (bottom) stages. The volume difference between MILP and GO solutions is 1%, 1.4% and 1.6% respectively.

### Limiting the number of joints

To set up the problem with all crossover constraints from the beginning requires checking 11,763,675 pairs of members, of which 2,795,779 produce a constraint. (Simply performing these checks was found to take nearly 20 minutes with the C++ code used here.)

Alternatively, using lazy constraints, the problem can be set up almost instantly, producing an initial problem with 14,553 variables and 14,844 constraints. The problem was first solved using lazy constraints to prevent crossovers but without limiting the number of joints. This produced a structure with 12 joints, and required 240 lazy constraints, around 0.01% of the full number. This is shown as the 12 joint result in Table 6.4 and Figure 6.20.

The problem was then solved with limits imposed on the maximum numbers of joints,  $\eta$ , from 3 to 11. The results can be seen in Table 6.4 and Figures 6.20 and 6.19. Note that the longest time taken to solve any of these problems was under 5 minutes, around a quarter of the time needed just to formulate the full problem.

It may be observed that the forms for 3, 6, or 11 joints agree with those found by Prager (1977)<sup>2</sup>. Additionally the solution with 8 joints corresponds to similar ones mentioned by Mazurek et al. (2011, fig 22). This structure, along with the majority of the others in Figure 6.20, are asymmetric despite the anti-symmetry observed in the problem. A similar approach to that described in Section 6.4 could be adopted to enforce symmetry in anti-symmetrical problems, however this is likely to be less desirable than for symmetric problems, and will also be affected by differences in relative tension and compression strengths.

### Other related problems

Prager extended his results to postulate a solution to the related problem of minimising total cost, comprising a material cost and a fixed cost per joint. It is possible to reformulate the integer programming problem to consider this directly, by changing the objective function to be of the form

$$\text{minimise } c = \mathbf{l}^T \mathbf{a} + p_J \mathbf{v} \quad (6.25)$$

where  $p_J$  is the normalised cost of a joint, and  $c$  is the total normalised cost.

However, equation (6.25) may alternatively be expressed in the form of an equation, plotted as a straight line on Figure 6.20. The example objective function shown on Figure 6.20, is a line of constant cost when the joint cost,  $p_J$ , is equal to the cost of a volume increase of 0.69% of the minimum volume,  $V_T$ . In this case, the solutions with 6 and 8 joints are equally optimal. However, the 7 joint solution has a higher cost; it is therefore not optimal for any objective function in the form of equation (6.25).

Prager's solution to this problem over a range of values for  $p_J$  consisted of only the 3, 6 and 11 joint solutions. From Figure 6.20 this can now be extended to add solutions with 4, 5, and 8 joints. The ranges of joint cost  $p_J$  for which each solution is optimal is shown in the final column of Table 6.4.

Limiting the number of members in a solution is another concern for ensuring practicality. As this is a single load case problem, and due to the Simplex solver used to solve the LP sub-problems of the MILP problem, the optimal structures identified are all likely to be statically determinate, meaning that the number of joints is directly linked to the number of members (number of members =  $2\eta - 4$ ). Therefore this method can also be used as a proxy for limiting the number of members.

### Limiting the angles between members

Solutions for the same Michell truss problem, but with imposed minimum angle limits from 15° to 45°, are shown in Table 6.5 and Figure 6.21. It can be seen that the topologies shown in Figure 6.21 are symmetrical, and several are distinct from those shown in Figure 6.20.

In the layout optimization stage only a limited number of member angles are available; therefore the structures identified do not have a minimum angle that exactly corresponds to the limit. Generally, once the geometry optimization post-processing step has been applied, the angle limits become active, although this is not always the case (e.g. in the case of the 20° limit). In some cases, such as the 40° and 45° solutions, the same initial result is identified for multiple angle limits, and the solutions only diverge in the geometry optimization stage.

<sup>2</sup>Note that Prager (1977) gives a volume of 36.41Qd for the 11 joint solution; this can clearly be seen to be incorrect, as it is lower than the minimum value from the equations of Chan (1960). However, the form given by Prager is correct.

Permitted no. of joints, $\eta$	Number of Lazy constraints added	MILP time (s)	Volume after		Optimal for joint costs	
			MILP	MILP+GO		
3	0	10	+31.9%	+31.9%	$15.11\% \leq p_J \leq$	$\infty$
4	0	16	+17.4%	+16.8%	$6.25\% \leq p_J \leq$	15.11%
5	3	74	+10.7%	+10.5%	$6.24\% \leq p_J \leq$	6.25%
6	4	72	+ 5.3%	+ 4.3%	$0.69\% \leq p_J \leq$	6.24%
7	4	117	+ 4.9%	+ 3.9%	N/A	
8	0	257	+ 4.3%	+ 2.9%	$0.45\% \leq p_J \leq$	0.69%
9	3	291	+ 3.9%	+ 2.8%	N/A	
10	9	196	+ 3.6%	+ 2.6%	N/A	
11	17	133	+ 3.1%	+ 1.6%	$0.09\%^a \leq p_J \leq$	0.45%
12 <sup>b</sup>	240	44	+ 3.0%	+ 1.5%		
20 <sup>c</sup>	—	4	+ 2.6%	+ 0.8%		

<sup>a</sup>Assumes next optimal design is the continuous layout optimization solution; designs with 13-19 joints may increase this value.

<sup>b</sup>Result of preventing crossovers without limiting the total number of joints.

<sup>c</sup>Continuous layout optimization result, after crossover generation.

**Table 6.4:** Michell cantilever: Results with limits imposed on the total number of joints. Volumes given as percentage above the theoretical minimum volume,  $V_T$ . Optimal joint cost ranges are given as a percentage of the material cost of  $V_T$ .

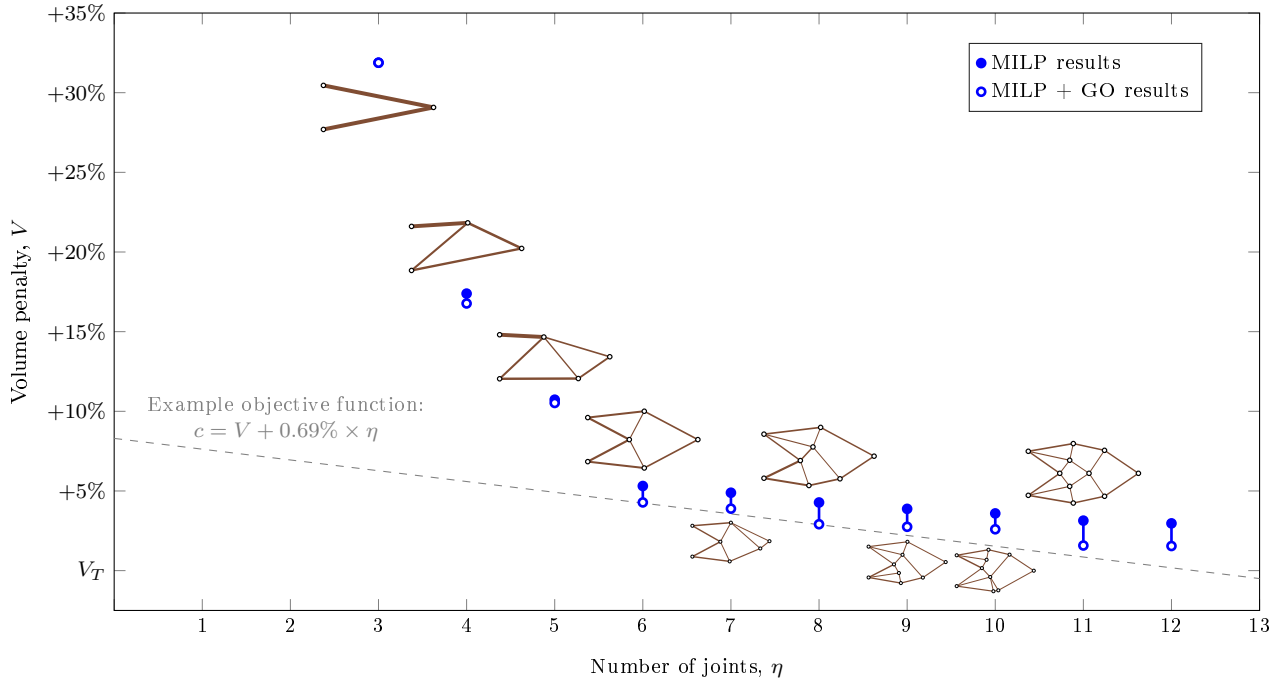


**Figure 6.20:** Michell cantilever: Results with limits imposed on the total number of joints. (Volume shown as percentage above theoretical minimum volume,  $V_T = 39.43Qd$ . Forms shown after MILP and GO. An example cost function is also shown where each joint has a constant cost, equal to an increase in volume 0.69% of  $V_T$ .)



Permitted angle between members, $\Psi$	Number of lazy constraints added	MILP time (s)	After MILP Min. angle	After MILP Volume	After MILP+GO Min. angle	After MILP+GO Volume
45°	3462	2341	47.7°	+6.3%	45°	+5.4%
40°	1415	2009	47.7°	+6.3%	40°	+4.6%
35°	805	234	37.9°	+5.1%	35°	+4.2%
30°	1377	537	33.7°	+5.0%	30°	+2.5% <sup>a</sup>
25°	665	344	26.6°	+4.4%	25°	+1.8%
20°	349	91	22.8°	+4.3%	21.9°	+1.6%
15°	73	21	18.4°	+3.8%	15°	+1.3%

<sup>a</sup> GO with a length limit of  $0.5d$  (i.e. equal to shortest length in ground structure) gives volume of +2.51%, GO without a length limit and after joint merging and subsequent feasibility restoration gives a volume of +2.55%.

**Table 6.5:** Michell cantilever: Results with limited joint angle. (Volume shown as percentage above  $V_T$ .)

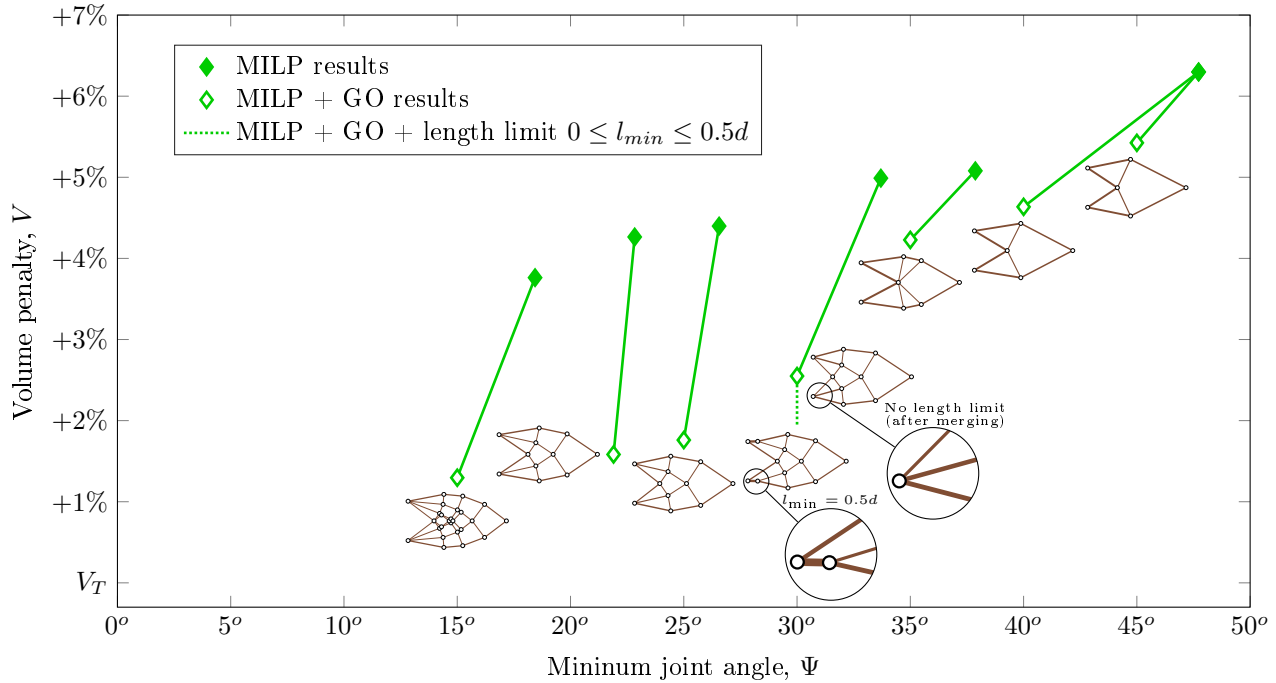


**Figure 6.21:** Michell cantilever: Results with limited joint angle. (Volume given as percentage above theoretical minimum volume. Forms shown after MILP and GO. For branched forms, results both with and without a length limit are shown.)

Most results in Figure 6.21 are shown after geometry optimization with no length limit imposed. However, for the limit of 30°, a branching form similar to that shown in Figure 6.16 was identified. During the geometry optimization stage for this result, the merging of the ‘root’ and ‘branch’ joint occurred, leading to a significant change in topology. The solution reduces in volume as the distance between the branching joints approaches zero, but then increases again in order to restore feasibility of the new angle constraint.

A length limit was therefore imposed to produce more meaningful results. For practical purposes, this is likely to be defined by the same manufacturing process that dictates the minimum angle between members; here  $l_{min}$  will be set at or below the length of the shortest member in the ground structure ( $0.5d$ ). When  $l_{min} = 0.5d$ , the new volume was only slightly smaller (+2.51% vs. +2.55%). However, for small values of  $l_{min}$  the volume reduced to +1.9%; this is shown as a dotted line in Figure 6.21. Both the result with no length limit, and with  $l_{min} = 0.5d$ , are illustrated in Figure 6.21.

By comparing the results in Table 6.4 and 6.5, it can be seen that the angle limits require a greater number of lazy constraints to be added, leading to correspondingly longer computational times. This is likely to be due to the fact that, when a limit on the number of joint is imposed, the initial constraints significantly reduce the number of feasible integer topologies before any lazy constraints are required. However, the maximum number of lazy constraints added in Table 6.5 was at most 0.3% of the total number possible (for the 45° limit), showing that the advantage of using lazy constraints is still very significant.

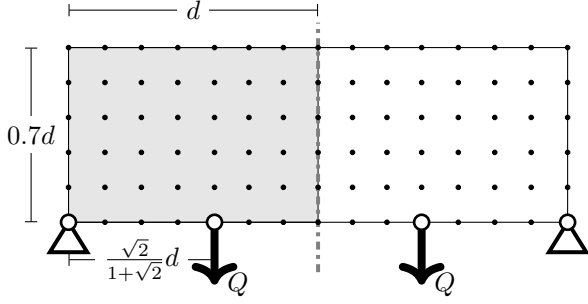


**Figure 6.22:** Spanning example: Problem specification, after Sokół & Rozvany (2013b). (The two point loads are applied separately. Grey shading shows the area modelled when the symmetry condition is imposed.)

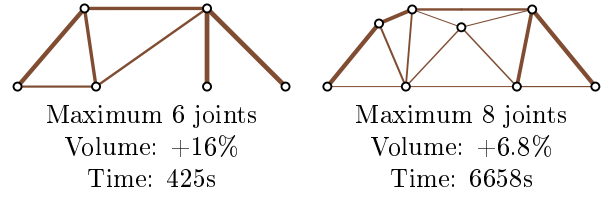


**Figure 6.23:** Spanning example: Results after MILP and GO showing asymmetric optimal solutions.

#### 6.4.4 Spanning example

A more complex, two load case problem is now considered. This consists of two point loads which are applied separately, and transmitted to a pair of pinned supports; the problem specification is shown in Figure 6.22.

This is a symmetrical problem, and therefore the minimum volume structure is also symmetrical when no discrete buildability constraints are imposed. The minimum volume solution,  $V_T$ , is given by Sokół & Rozvany (2013b) as  $3.44363 \frac{Qd}{\sigma}$ . The design domain is discretised using a grid of 90 nodes. The layout and geometry optimization solution for this resolution had a volume 1.2% greater than the theoretical optimal value.

The problem was first solved without imposing a requirement for a symmetrical solution. Solutions with maximum numbers of joints,  $\eta$ , ranging from 5 to 9 were found. Solutions with odd numbers of joints were found to be symmetrical, and were equal to the corresponding results shown in Figure 6.24 and Table 6.6. However, the solutions with 6 and 8 joints were asymmetric, as shown in Figure 6.23. Note that the 8 joint example approximately consists of one half from each of the topologies with 7 and 9 joints.

Due to these findings, and the general preference in practice for symmetrical designs, the model was modified to explicitly impose a symmetry condition about the centre line, using equation (6.21) and the method outlined in Section 6.4. Solutions were again sought for 6 and 8 joints; however, the optimal solutions were found to be identical to the solutions for 5 and 7 joints respectively. This demonstrates that the lack of a symmetrical optimal solution, a characteristic previously noted in the solutions of truss optimization problems with discrete cross sections, is also a characteristic of the problem with continuous cross sections when limits are imposed on the numbers of joints.

Results for various numbers of joints are given in Table 6.6 and Figure 6.24. The use of the constraints from equation (6.18) (to prevent ‘crossover joints’) and equation (6.19) (to include ‘crossover joints’ in the total number of joints to be limited), have both been tested. When ‘crossover joints’ are not permitted, only structures with up to 17 joints can be identified; results in the range  $17 < \eta < 45$  can only be identified by allowing ‘crossover joints’ and explicitly including them in the total limit.

The problem of including the ‘crossover joints’ is a more relaxed version of the problem where ‘crossover joints’ are prevented. Therefore solutions from the MILP problems that take account of crossovers must be at least as good as solutions found when these are prevented. However, the geometry optimization stage is non-linear, and therefore local optima may result, depending on the initial point provided. It can be seen that for the 15 and 17 joint solutions, local optima have been identified; both methods appear to be susceptible to this. However, the volume difference is less than 0.2%, demonstrating that at this point multiple options are available of similar volume and complexity, any one of which would likely be suitable for practical application. The ability of many commercial solvers (e.g. IBM Corp. 2015; Gurobi Optimization, LLC 2018) to record a pool of nearly optimal solutions may be of use in addressing this issue.

As a multiple load case problem, the solutions identified are generally not statically determinate and therefore there is not a direct relationship between number of members and number of joints. However, Figure 6.25 shows that there is still a very strong correlation between the number of members and the number of joints. Therefore, for practical purposes, this method is still likely to produce useful results when structures with few members are desired.

Permitted number of joints, $\eta$	Counting ‘crossover joints’				Preventing ‘crossover joints’			
	No. of lazy cons. added	MILP time (s)	Volume after		No. of lazy cons. added	MILP time (s)	Volume after	
			MILP	MILP+GO			MILP	MILP+GO
5	0	7	+59.5%	+58.1%	0	6	+59.5%	+58.1%
7	0	56	+8.8%	+8.4%	0	31	+8.8%	+8.4%
9	7	52	+5.9%	+5.1%	14	77	+5.9%	+5.1%
11	26	345	+5.2%	+4.1%	33	154	+5.2%	+4.1%
13	24	528	+ <b>4.5%</b>	+3.3%	154	446	+ <b>4.5%</b>	+3.3%
15	28	436	+ <b>3.5%</b>	+ <b>2.7%</b>	48	184	+ <b>3.7%</b>	+ <b>2.5%</b>
17	40	504	+ <b>3.4%</b>	+ <b>2.3%</b>	444 <sup>a</sup>	455 <sup>a</sup>	+ <b>3.5%</b>	+ <b>2.4%</b>
19	76	8150	+3.1%	+2.4%				
21	68	6833	+3.0%	+2.0%				
31	90	138265	+2.7%	+1.8%				
45 <sup>b</sup>	—	6	+2.3%	+1.2%				

<sup>a</sup> Refers to forbidding crossovers with no limit on number of joints, which produces a structure with 17 joints.

<sup>b</sup> Layout optimization result, which produces structure with 45 joints.

**Table 6.6:** Spanning example: Results with symmetry condition imposed and limits on numbers of joints. (Bold values highlight when the two methods produce different results.)

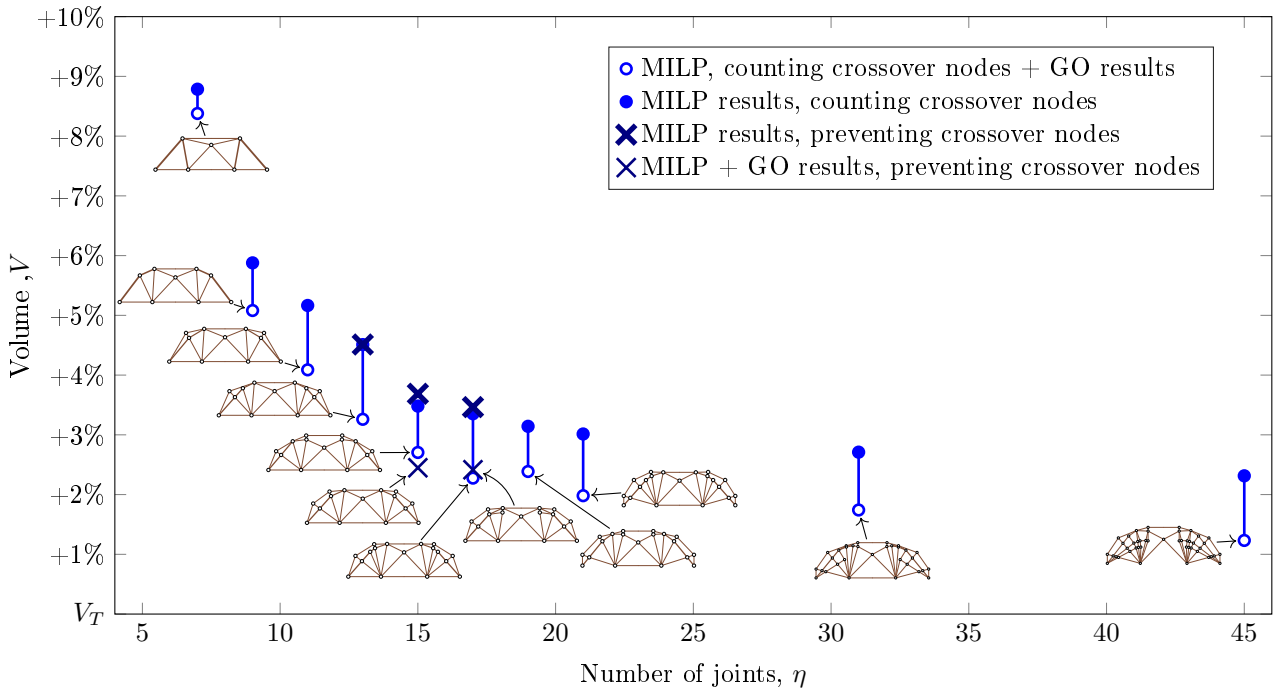


**Figure 6.24:** Spanning example: Results with symmetry condition imposed and limits on numbers of joints. (Volume shown as percentage above theoretical minimum volume. Forms shown are after MILP and GO, with symmetrical solutions required. Results preventing crossover joints are shown only where they differ from the result of counting the crossover joints.)

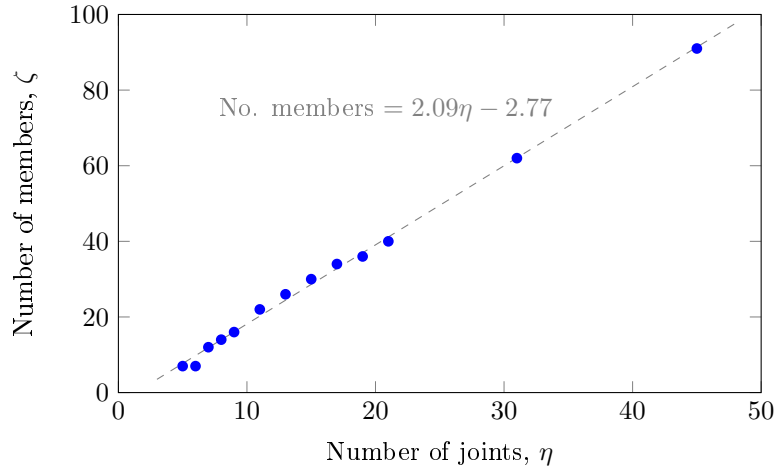


**Figure 6.25:** Spanning example: Correlation between number of joints and number of members in solutions where the number of joints has been limited, also showing best fit line. ( $R^2 = 0.997$ ).

## 6.5 Concluding remarks

The addition of MILP constraints to the standard layout optimization problem formulation has been shown to provide an effective means of including buildability constraints for low to medium resolution truss topology optimization problems. Issues relating to the presence of ‘crossover joints’ have been tackled through the use of dynamically generated lazy constraints, significantly reducing the computational time required. Improvements in computational time of over a factor of 20 were observed for relatively small problems; this difference is likely to increase further as problem size increases. This allows the proposed method to be used for problem sizes that would be intractable using the standard formulation.

Rationalized structures have been identified for a range of problems, including those with multiple load cases, using a two stage process incorporating a layout optimization stage and a geometry optimization stage. Using this process, results were found to agree with analytically derived results, suggesting that the proposed separation of topology and geometry/shape optimization is effective, and that MILP solutions are suitable starting points for a non-linear optimization stage.

The rationalized structures were often found to have a volume within a few percent of the corresponding minimum volume Michell structure, whilst being far more feasible to construct. A number of interesting features of these solutions have been observed:

- Symmetrical or anti-symmetrical problems do not always have symmetrical optimal solutions when limits on the numbers of joints are imposed. Therefore, the decision to use symmetry to reduce the computational expense of a problem should be made with care.
- Multiple optimal or near optimal solutions are possible. Many numerical methods, such as geometry optimization, will identify only one of these, although there may be many which would be acceptable for practical use.
- When the angle between adjacent members is limited, ‘branching’ type structures may occur. This may then require the addition of a minimum length constraint to produce practical results.

Different measures of complexity have been considered, leading to different levels of computational difficulty. When the number of joints is limited, it was found that the number of members in the solution was strongly linked to the number of joints. This may provide a computationally efficient proxy problem, as restricting the number of joints requires far fewer integer variables, thus is much quicker. Other complexity measures are not so closely correlated, for example the number of joints and minimum cross-section area. Therefore multiple complexity limits may need to be imposed simultaneously, increasing the size of the problem. It is possible that lazy constraints could be of use in this situation too, allowing an initial problem containing only the most computationally efficient restriction (e.g. number of joints), and reducing the number of constraints required for other complexity limits.

## Chapter 7

# Region based Adaptive Ground Structure (RAGS) method

This chapter contains formulations and results based on the use of a novel hybrid analytical-theoretical method for the identification of minimum volume structures. The approach is based on the ground structure method, but allows for structural elements representing larger regions to be adaptively added.

In this chapter, an element representing a fan type  $T$  region and a discretised approximation of a more general region of type  $T$  are presented. Discussion of further possible regions, including those of type  $R$ ,  $S$  and exact general regions of type  $T$ , can be found in Appendix C.

This method can identify the optimal volume to within  $1 \times 10^{-5}\%$ , whilst simultaneously providing an easily interpretable output. By presenting the solution using a small number of regions, it is clearer how the solution could be rationalized into a discrete structure.

---

7.1	Introduction . . . . .	108
7.2	Methodology . . . . .	109
7.2.1	General derivation of region of type $T$ . . . . .	109
7.3	Three node (fan) elements . . . . .	110
7.3.1	Derivation of exact form . . . . .	110
7.3.2	Offset fan region . . . . .	112
7.3.3	Discrete approximation . . . . .	115
7.4	Application of fan regions . . . . .	117
7.4.1	Application in layout optimization . . . . .	117
7.4.2	Graphical interpretation of member adding . . . . .	117
7.4.3	Application in geometry optimization . . . . .	119
7.4.4	Example: Simply supported central point load . . . . .	120
7.4.5	Example: Continuous multi-span bridge . . . . .	122
7.5	Discrete approximation of four node regions . . . . .	123
7.5.1	Geometry of a $2 \times 2$ cell mesh . . . . .	123
7.5.2	Static derivation of constraints . . . . .	127
7.5.3	Example: Michell cantilever . . . . .	127
7.6	Discussion . . . . .	129

---

## 7.1 Introduction

In the identification of a minimum volume truss-like structure for a given problem, both analytical and numerical methods have received significant attention. However, these fields have, for the most part, remained separate. In this chapter a methodology will be described which aims to combine the advantages of both approaches.

When these fields have interacted, it has primarily been for comparative or validation purposes. Results of numerical studies have been used to inspire later exact analytical solutions, e.g. the numerical study of Darwich et al. (2010), which led to the analytical result by Tyas et al. (2011). Conversely, numerical results can also provide confidence in analytical solutions, for example Sokół & Rozvany (2013b) use numerical methods both to check the analytical solutions, and also to contrast with results of related single load case problems.

Analytical methods generally proceed by the sequential identification of a number of regions satisfying the criteria laid down by Michell (1904). Each region is defined by a set of functions, which give the curves along which any members should lie (Chan, 1960). This process is described in more detail in Section 7.2.1.

It is often the case that the same regions occur in multiple problems. For example the fan type region, first identified in the solution for a simply supported point load by Michell (1904), also appears in the equivalent half plane solution, the cantilever of Chan (1960) and the multi-span bridge of Pichugin et al. (2015), as well as a great many more solutions. A comparison of regions in a wide range of known solutions may be found in Appendix A.

The recurrence of assemblages of regions has also been used to identify solutions to more complex problems, by manually combining the constituent parts. Rozvany (1998) combines equiangular spiral regions and Michell cantilevers to find solutions to the problem of a deep beam loaded by a moment. Sokół & Lewiński (2010) combine cantilever forms, and additional straight bar elements, to find solutions to a class of problems with two point loads and pinned supports. Beghini & Baker (2015) propose a structure for a multiple span viaduct by combining solutions for simply supported regions and double cantilevers.

Rigorously demonstrating the optimality of these combined structures is laborious, but necessary. Figure 7.1 shows how inaccuracies may be introduced by the choice of how to divide the problem and the boundary conditions imposed on the resulting sub-problems. Figure 7.1a shows the problem and result identified by Ghista & Resnikoff (1968); the result was obtained by dividing the problem into three sub problems. However, the result chosen for these sub-problems was the half plane solution from Michell (1904) which leads to a sub-optimal design. Figure 7.1b shows a numerical layout optimization result for the same problem; the divisions are the same but the overall solution is substantially changed.

Numerical methods of truss optimization are often based on the ground structure method (Dorn et al., 1964; Chan, 1964). This approach uses a large number of nodes, connected by potential members. The adaptive member adding approach of Gilbert & Tyas (2003) can be used to reduce the number of potential members which must be considered simultaneously. The members in the ground structure are generally straight truss bars; although moment-carrying members are sometimes used (e.g. Van Mellaert et al., 2016), they are substantially more computationally difficult to handle. Replacement of the straight bars with appropriately curved arches/sagging cables was shown to be an effective technique for modelling self-weight in Chapter 4. In the field of discontinuity layout optimization (a mathematically analogous application concerning the identification of geotechnical failure mechanisms) Smith & Gilbert (2013) employ connections in the form of circular arcs to more accurately identify mechanisms involving rotational movements.

This chapter proposes a method by which layout optimization can be extended to produce solutions which are in the style of analytical results. This involves the inclusion of region type elements within the ground structure. These elements are regions in the sense used in analytical results, i.e. they consist of members lying along curves described by a given function. From the forms of these region, and the deflection fields they define, constraints on the relevant ground structure nodes will be obtained. This method has the potential to not only increase the accuracy of solutions, but also provide a more interpretable result.

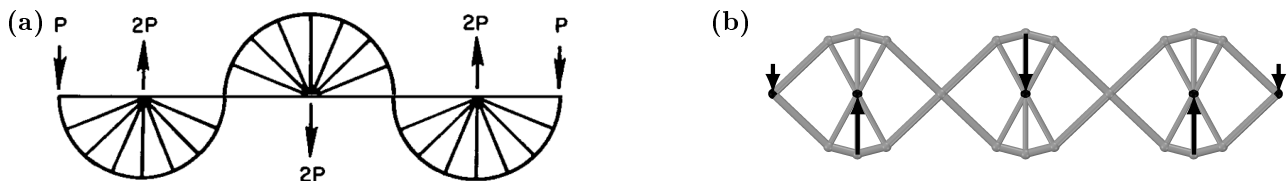


**Figure 7.1:** Results for the problem of Ghista & Resnikoff (1968) showing the difficulties in manually decomposing problems. (a) Result of Ghista & Resnikoff (1968) for the given problem (used under 17 U.S.C. §105). (b) layout optimization result for the same problem.

This chapter is organised as follows; the proposed methodology is discussed in Section 7.2. The derivation of first region element (the fan) is undertaken in Section 7.3, and fan elements are then applied in Section 7.4. A second region element which connects four nodes and is based on an approximation with a finite number of bars is discussed in Section 7.5. Finally, Section 7.6 provides some discussion on the potential of this method and its application.

## 7.2 Methodology

The proposed region based method aims to use novel potential structural elements in the layout optimization formulation. Instead of connecting two nodes with a straight line, these region elements will connect 3 or 4 nodes with a predetermined geometry based on forms which are commonly observed in known analytical solutions.

For a problem with  $n$  nodes, the number of possible region types will be approximately proportional to  $n^3$  or  $n^4$ , therefore the problem sizes using this method would increase rapidly. To ameliorate this we will make use of the principles of the member adding method developed by Gilbert & Tyas (2003). The problem will first be solved with a ground structure, containing only straight bar elements. Dual (kinematic) constraints for potential regions will then be checked based on the virtual displacements of the previous iteration, and regions which have a violated virtual strain constraint will be added. The key requirement to implement a region type within this framework is therefore the ability to calculate whether a potential region is over-strained based on the virtual displacements of the nodes in the previous iteration.

It may be the case that multiple region geometries are possible for a given set of points. A similar situation was encountered by Smith & Gilbert (2013) in the identification of circular arcs connecting two ground structure nodes, as infinitely many arcs are possible to connect two points. When the adaptive approach is used, the ‘most violated’ of the different possible geometries can be identified, and this element is then included in the next iteration. In subsequent iterations, it is possible for a different geometry between the same two nodes to become violated, requiring another different connection between the same two points to be added. Eventually no potential connections are violated; at this point the solution is identical to one considering all (infinitely many) circular arc connections. It may become necessary to adopt a similar approach for some regions in this framework, although it has not been required for the region types discussed within this chapter.

Once the optimal solution is obtained for the used set of ground structure nodes, further refinement can be performed using the geometry optimization method (He & Gilbert, 2015). This involves adding the positions of the nodes as variables within the optimization. Non-linear gradient based solvers are required to solve this problem; therefore derivatives with respect to nodal coordinates will be required for the problem coefficients.

Attention will be focused on deriving relationships for regions of type  $T$ , i.e. where principal virtual strains in two orthogonal directions reach the compressive and tensile limiting values respectively. These form the vast majority of regions found in structures in the literature. Most regions in known solutions can be parametrised by one of the three ‘special cases’ described by Chan (1960). These are here denoted by using Chan’s case number as a subscript, i.e.  $T_1$  regions are those parametrised by the angle turned by the pair of base curves;  $T_2$  regions are parametrised by the distance along one family of straight lines, and the angle turned through by the other, curved, family;  $T_3$  regions consist only of straight lines, and are parametrised by the distance along each. These region types are illustrated in Figure 2.3.

### 7.2.1 General derivation of region of type $T$

In this section, the principles for the construction of optimal regions will be recalled and presented in a form suited to the purposes of this method; much of this section is based on the derivations of Chan (1960).

For the purposes of the proposed method, a region is an area of the design domain in which the lines of principal strain lie on a curvilinear coordinate system  $(\alpha, \beta)$  which is defined by the relationship

$$ds^2 = (A d\alpha)^2 + (B d\beta)^2 \quad (7.1)$$

such that  $ds$  is a line element, and  $A$  and  $B$  are positive functions of  $\alpha, \beta$ , referred to as Lamé coefficients.

The angle  $\phi$  is defined as the angle between the positive  $\alpha$  direction and the positive  $X$  direction of a local Cartesian coordinate system.  $\phi$  is generally considered as a function of  $\alpha$  and  $\beta$ . The system of differential equations which links  $\phi(\alpha, \beta)$  to  $A(\alpha, \beta)$  and  $B(\alpha, \beta)$  is

$$\frac{d\phi}{d\alpha} = -\frac{1}{B} \frac{dA}{d\beta} \quad (7.2a)$$

$$\frac{d\phi}{d\beta} = \frac{1}{A} \frac{dB}{d\alpha} \quad (7.2b)$$

From equation (7.1) it can be seen that the equation for a line element along an  $\alpha$  line ( $\beta$  constant) is

$$(ds)^2 = (Ad\alpha)^2 + (B \times 0)^2 = (Ad\alpha)^2 \rightarrow ds = Ad\alpha \quad (7.3)$$

Combining this with the system of (7.2), gives us differential equations for the  $\alpha$  lines,

$$dx = A \cos(\phi) d\alpha, \quad dy = A \sin(\phi) d\alpha \quad (7.4a)$$

By similar reasoning we find the equations for the  $\beta$  lines to be

$$dx = -B \sin(\phi) d\beta \quad dy = B \cos(\phi) d\beta \quad (7.4b)$$

Integrating these will allow us to find the coordinates of a point in local Cartesian coordinates. Also note that converting between the global  $(x, y)$  axis and the local  $(X, Y)$  axis will be necessary, this may be achieved by a simple rigid body rotation.

Here, only regions which are bordered by lines of constant  $\alpha$  or  $\beta$  are considered, i.e. the valid area of the region is the area where  $\alpha_- \leq \alpha \leq \alpha_+$  and  $\beta_- \leq \beta \leq \beta_+$ . Generally, this will imply a four sided region, with four corner points. The symbols representing the four corner points, and their corresponding curvilinear coordinates  $(\alpha, \beta)$  are

$$O = (\alpha_-, \beta_-) \quad A = (\alpha_+, \beta_-) \quad B = (\alpha_-, \beta_+) \quad P = (\alpha_+, \beta_+) \quad (7.5)$$

For the purpose of this method, the process described here will be reversed. First, locations of these corner points will be chosen from nodes in the ground structure. These will then be used as the boundary conditions for the solution of the system (7.4) to find the functions  $A(\alpha, \beta)$  and  $B(\alpha, \beta)$ .

### Local Deflections

The strains along  $\alpha$  lines ( $\beta$  constant) are equal to  $\varepsilon$  and along  $\beta$  lines ( $\alpha$  constant) the strains are  $-\varepsilon$ . The rotation of a point in the region is defined by  $\omega$ , a function of  $\alpha$  and  $\beta$  which is given by the differential equations (Chan, 1960)

$$\frac{d}{d\alpha}(\omega - 2\varepsilon\phi) = 0 \quad (7.6a)$$

$$\frac{d}{d\beta}(\omega + 2\varepsilon\phi) = 0 \quad (7.6b)$$

From the functions  $A$ ,  $B$  and  $\omega$ , we now need to solve a system of equations to give us the displacements of a point in the region. The displacement in the  $\alpha$  direction is given as  $u^\alpha$  and in the  $\beta$  direction as  $u^\beta$ .

$$\frac{du^\alpha}{d\alpha} = A\varepsilon + u^\beta \frac{d\phi}{d\alpha}, \quad \frac{du^\alpha}{d\beta} = -B\omega + u^\beta \frac{d\phi}{d\beta} \quad (7.7a)$$

$$\frac{du^\beta}{d\alpha} = A\omega - u^\alpha \frac{d\phi}{d\alpha}, \quad \frac{du^\beta}{d\beta} = -B\varepsilon - u^\alpha \frac{d\phi}{d\beta} \quad (7.7b)$$

This system will require additional boundary conditions to solve. The choice of boundary conditions will give a frame of reference (which could be thought of physically as a template/overlay fixed to certain points on the element) local to the current element. We will refer to displacements measured in this local frame of reference as  $\bar{u}$ . It will then be necessary to convert this local frame of reference back to the global deflection field,  $u$ .

## 7.3 Three node (fan) elements

One of the most common patterns seen in solutions in the literature is that of a fan of straight members radiating from a point, alongside an orthogonal series of circular arcs, this is a region of type  $T_2$ . Such a fan element will have three vertices/nodes, this is because nodes O and B (as described in equation (7.5)) are co-incident. This point will be referred to as point O. Points A and P will continue to be defined as in equation (7.5).

### 7.3.1 Derivation of exact form

In order for this region to exist, the radial distances to the two outer nodes must be equal, i.e.  $|OA| = |OP|$ , this value is equal to the radius of the outermost curved coordinate arc, and will be denoted by  $r$ . Cases where  $|OA| \neq |OP|$  will be discussed in Section 7.3.2.



### Geometry

The  $(\alpha, \beta)$  co-ordinates of a point S are defined as follows;  $\alpha_S$  is the distance to the origin  $|\mathbf{OS}|$ , and  $\beta_S$  is the angle  $\angle AOS$  as shown in Figure 7.2a. The relevant ranges for the coordinates are

$$0 \leq \alpha \leq r = |\mathbf{OA}| = |\mathbf{OP}| \quad (7.8a)$$

$$0 \leq \beta \leq \theta = \angle AOP \quad (7.8b)$$

The  $\alpha$  co-ordinate curves are straight lines radiating out from the point O. The  $\beta$  lines form circular arcs centred on the point O which each turn through an angle  $\theta$ .

The local Cartesian coordinate system for a fan element is chosen such that the local  $X$  axis is along the line  $\overrightarrow{OA}$ , i.e.  $Y_A = 0$ . The equation for  $\phi$  for this element is

$$\phi = \beta \quad (7.9)$$

Therefore the geometry functions will be

$$A(\alpha, \beta) = 1 \quad (7.10a)$$

$$B(\alpha, \beta) = \alpha \quad (7.10b)$$

It is simple to show that integration of these functions in the system (7.4) produces the correct nodal positions in local  $(X, Y)$  coordinates:  $A = (r, 0)$  and  $P = (r \cos \theta, r \sin \theta)$ .

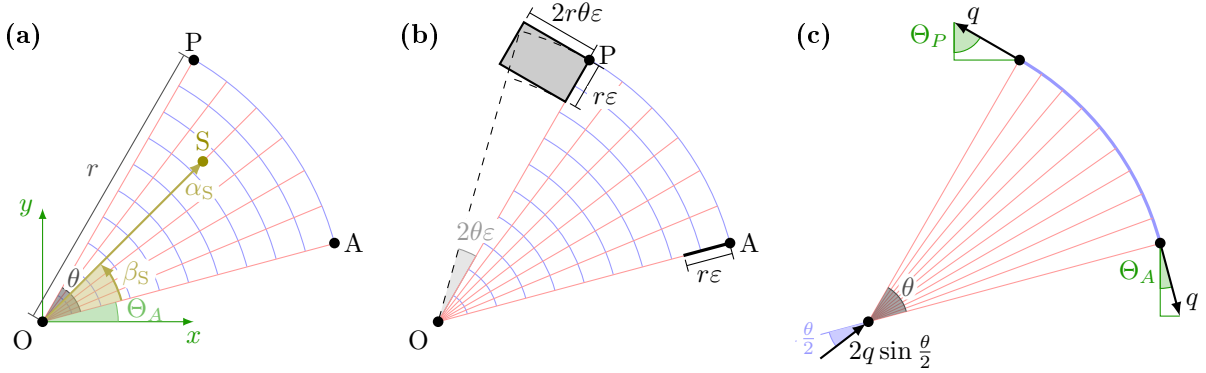


**Figure 7.2:** Fan element: Geometry and behaviour (a) Definition of coordinate systems, points and quantities. (b) Kinematic interpretation of behaviour within local  $\bar{u}$  reference frame; point A must deflect to a point within the thick black line, and point P must deflect to a point within the shaded region. The dotted lines show a more intuitive interpretation which tends towards the true result at small deflections. (c) Static interpretation of behaviour, with external forces shown.

### Kinematic form

Within a fan region, the local deflection reference frame,  $\bar{u}$  is defined such that  $\bar{u}_O^x = \bar{u}_O^y = 0$  and  $\omega_{OA} = 0$ . The system (7.7) is solved to give expressions for local deflections,

$$\bar{u}^\alpha = \alpha\varepsilon \quad \bar{u}^\beta = -2\alpha\beta\varepsilon \quad (7.11)$$

Noting that  $\bar{u}_O^\alpha$ ,  $\bar{u}_O^\beta$  and  $\bar{u}_A^\beta$  will be equal to zero by definition, the limiting deflections at the remaining degrees of freedom are

$$\begin{bmatrix} \bar{u}_A^\alpha \\ \bar{u}_P^\alpha \\ \bar{u}_P^\beta \end{bmatrix} \leq \begin{bmatrix} r\varepsilon \\ r\varepsilon \\ -2r\theta\varepsilon \end{bmatrix} \quad (7.12)$$

The geometrical interpretation of this equation is shown in Figure 7.2b. It consists of a 1D slot within which the deflected location of A must fall, the deflection of A perpendicular to this will define the local reference frame. The deflected location of P must then fall within the 2D shaded region. Note that deflections are assumed to be small, and have been enlarged for clarity.

Transforming the left side of the equation into global deflection coordinates gives the constraints

$$\begin{bmatrix} -\cos(\Theta_A) & -\cos(\Theta_P) & \sin(\Theta_P) - \sin(\Theta_A) \\ -\sin(\Theta_A) & -\sin(\Theta_P) & \cos(\Theta_A) - \cos(\Theta_P) \\ \cos(\Theta_A) & 0 & \sin(\Theta_A) \\ \sin(\Theta_A) & 0 & -\cos(\Theta_A) \\ 0 & \cos(\Theta_P) & -\sin(\Theta_P) \\ 0 & \sin(\Theta_P) & \cos(\Theta_P) \end{bmatrix}^T \begin{bmatrix} u_O^x \\ u_O^y \\ u_A^x \\ u_A^y \\ u_P^x \\ u_P^y \end{bmatrix} \leq \begin{bmatrix} r\varepsilon \\ r\varepsilon \\ -2r\theta\varepsilon \end{bmatrix} \quad (7.13)$$

where  $\Theta_A$  is the inclination of the bar OA and  $\Theta_P$  is the inclination of the bar OP. Values of  $u$  are the virtual deflection for the indicated point and direction.

The first two columns are identical to the constraints of the straight bars OA and OP and will therefore not need to be checked separately. Therefore the final column gives the constraint which will be critical to check for the addition of this element.

### Static form

It is equally reasonable to derive the necessary equations for a region within the static formulation (i.e. the primal problem).

Consider a fan region where  $\alpha$  lines have infinitesimal thickness, and all  $\beta$  lines have zero thickness, with the exception of the  $\beta$  line containing A and P which has a finite thickness (i.e. it is a concentrated member).

The (finite) external forces imposed on points A and P may only be aligned to the concentrated member. Furthermore, to ensure equilibrium of moments about point O, they must be equal in magnitude and opposite in direction as shown in Figure 7.2c. The magnitude of these forces will be referred to as  $q$ . Once these forces have been resolved relative to the global axes, the forces at point O can be found by considering equilibrium in the horizontal and vertical directions. Therefore the external forces on this member are given by

$$\begin{bmatrix} \sin(\Theta_P) - \sin(\Theta_A) \\ \cos(\Theta_A) - \cos(\Theta_P) \\ \sin(\Theta_A) \\ -\cos(\Theta_A) \\ -\sin(\Theta_P) \\ \cos(\Theta_P) \end{bmatrix} q = \begin{bmatrix} f_O^x \\ f_O^y \\ f_A^x \\ f_A^y \\ f_P^x \\ f_P^y \end{bmatrix} \quad (7.14)$$

The cross-sectional area of the concentrated member must be equal to  $\frac{q}{\sigma}$ , and its length is equal to  $r\theta$ . Therefore its volume will be  $r\theta\frac{q}{\sigma}$ . The volume of all other  $\beta$  lines will be zero.

The infinitesimal members aligned to the  $\beta$  lines have a constant total cross section over any given range of  $\alpha$ . Considering equilibrium of the concentrated member AP over a small section subtended by the angle  $d\beta$ , it is found that the infinitesimal members normal to this carry a total force of  $qd\beta$ , requiring a total cross section area of  $\frac{qd\beta}{\sigma}$ . These members all have a length of  $r$ . The total volume of members is therefore given by

$$V = r\theta\frac{q}{\sigma} + r \int_0^\theta \frac{q}{\sigma} d\beta = q\frac{2r\theta}{\sigma} \quad (7.15)$$

By duality principles, equations (7.14) and (7.15) can be combined to give a constraint, which will be identical to that shown in equation (7.13), once the relationship  $\varepsilon = \frac{1}{\sigma}$  is used.

### 7.3.2 Offset fan region

As fans with equal radii are not always possible when fixed nodal positions are imposed, an approximate region for arbitrary |OA| and |OP| is required. To facilitate the calculation of the derivatives required for geometry optimization, this region should be as simple as possible, ideally still consisting of straight  $\alpha$  lines.

#### Geometry

Numerical tests have suggested that under these conditions, the minimum volume structure has a constant (but non-right angle) angle between the  $\alpha$  and  $\beta$  lines. The difference between this angle and  $\frac{\pi}{2}$  will be denoted by  $\iota$ . This region consists of straight  $\alpha$  lines radiating from the point O, and curved  $\beta$  lines, which are no longer circular arcs, as shown in Figure 7.3a.

To calculate the value of  $\iota$ , an arbitrary point S on the co-ordinate curve connecting A and P is considered. Two points which are close to S are also defined as shown in Figure 7.3b;  $\hat{S}$  is a point along an arc subtended

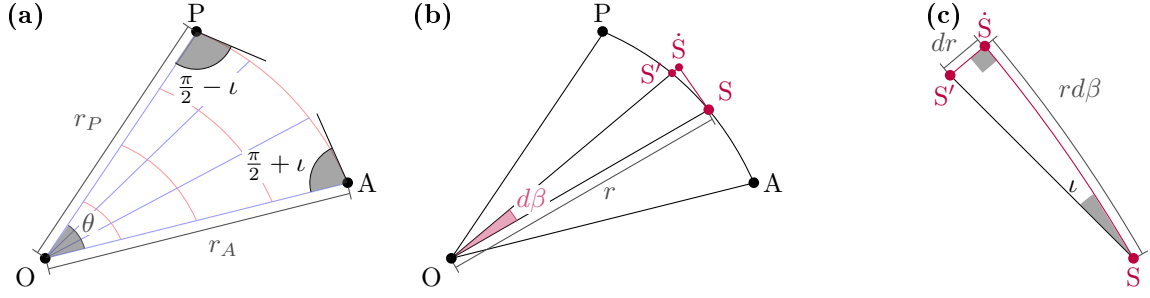


**Figure 7.3:** Offset circle region: Node positions and angle definitions. (a) Overall layout and dimensions. (b) Points on a small slice of the region. (c) Locations of nearby points relative to point S.

by a small angle  $d\beta$  from S centred on O. The point S' is the point on the same co-ordinate curve as S and on the line  $\dot{S}O$ . The distance from O to S is denoted as  $r_S$ .

The distance from  $\dot{S}$  to S' is the change in the radius between S and S', i.e.  $dr$ , note that this may be positive or negative, and the sign of this change also gives the sign of  $\iota$ . As  $d\beta$  becomes small, the arc  $\dot{S}S$  tends towards a line of length  $r_S d\beta$ . The right angled triangle  $\dot{S}SS'$ , shown in Figure 7.3c, is then considered;  $\iota$  is given by the angle  $\angle \dot{S}SS'$ .

$$\tan \iota = \frac{dr}{r d\beta} \quad (7.16)$$

$$\rightarrow \int \tan \iota d\beta = \int \frac{1}{r} dr \quad \rightarrow \quad \beta \tan \iota = \ln r + c \quad (7.17)$$

The integration constant,  $c$ , is found by use of the boundary condition at point A; when  $\beta = 0$ ,  $r = r_A$ . Thus,

$$c = -\ln r_A \quad \rightarrow \quad \beta \tan \iota = \ln \left( \frac{r}{r_A} \right) \quad (7.18)$$

From the boundary condition at point P, that when  $\beta = \theta$ ,  $r = r_P$ , the expression for  $\iota$  is found, and subsequently the expression for the radius at an arbitrary point.

$$\theta \tan \iota = \ln \left( \frac{r_P}{r_A} \right) \quad \rightarrow \quad \iota = \arctan \left( \frac{\ln \left( \frac{r_P}{r_A} \right)}{\theta} \right) \quad (7.19)$$

$$\rightarrow \quad r = r_A^{(1-\frac{\beta}{\theta})} r_P^{\frac{\beta}{\theta}} \quad (7.20)$$

### Static Form

As this region is necessarily sub-optimal, the static (primal) principles are the most appropriate setting for the derivation of the optimization coefficients.  $q_A$  and  $q_P$  represent the magnitudes of the force applied by the element on node A and P respectively. Similarly to the exact formulation, we assume a single concentrated  $\beta$  line, AP, and infinitesimal  $\alpha$  lines.

Forces applied at points A or P must be in line with the outer coordinate line at that point. The components of these which are perpendicular to the lines OA and OP are  $q_A \cos \iota$  and  $q_P \cos \iota$  respectively. Then equilibrium of moments about point O implies

$$r_P q_P \cos \iota = r_A q_A \cos \iota \quad (7.21)$$

$$\rightarrow \quad q_P = \frac{r_A}{r_P} q_A \quad (7.22)$$

The remaining external force at O can be found by simply using horizontal and vertical equilibrium equations.

It has magnitude  $q \sqrt{1 + \frac{r_A^2}{r_B^2} - 2 \frac{r_A}{r_B} \cos \theta}$ . Therefore, the complete set of external forces is given as

$$\begin{bmatrix} \frac{r_A}{r_P} \sin(\Theta_P - \iota) - \sin(\Theta_A - \iota) \\ -\frac{r_A}{r_P} \cos(\Theta_P - \iota) + \cos(\Theta_A - \iota) \\ \sin(\Theta_A - \iota) \\ -\cos(\Theta_A - \iota) \\ -\frac{r_A}{r_P} \sin(\Theta_P - \iota) \\ \frac{r_A}{r_P} \cos(\Theta_P - \iota) \end{bmatrix} q_A = \begin{bmatrix} f_O^x \\ f_O^y \\ f_A^x \\ f_A^y \\ f_P^x \\ f_P^y \end{bmatrix} \quad (7.23)$$

To derive an expression for the volume, consider again the triangle  $\dot{SS}'$ ; the hypotenuse  $S$  to  $S'$  defines a short distance along the coordinate curve,  $dL$ . The expression for this is

$$dL = \sqrt{(dr)^2 + (rd\beta)^2} \quad (7.24)$$

This can then be combined with equations (7.16) and (7.19) to give

$$dL = \sqrt{\left(\frac{\ln \frac{r_P}{r_A}}{\theta} rd\beta\right)^2 + (rd\beta)^2} \rightarrow dL = rd\beta \sqrt{\left(\frac{\ln \frac{r_P}{r_A}}{\theta}\right)^2 + 1} \quad (7.25)$$

The cross-sectional area of the concentrated member from  $A$  to  $P$  at the arbitrary point,  $S$  will be proportional to the force,  $q_S$ , at that point. This is found by extending the reasoning of equation (7.22) to the arbitrary point.

$$A_S = \frac{q_S}{\sigma} \quad (7.26)$$

$$\rightarrow A_S = \frac{1}{\sigma} \left( \frac{r_A}{r_S} q_A \right) \quad (7.27)$$

The volume of the concentrated member is found by integrating between point  $A$  and  $P$ .

$$V_+ = \int_A^P (A) dL = \int_A^P \left( \frac{r_A}{\sigma r} q_A \right) rd\beta \sqrt{\left(\frac{\ln \frac{r_P}{r_A}}{\theta}\right)^2 + 1} \quad (7.28)$$

$$= \frac{r_A q_A}{\sigma} \sqrt{\left(\frac{\ln \frac{r_P}{r_A}}{\theta}\right)^2 + 1} \int_0^\theta d\beta \quad (7.29)$$

$$= \frac{r_A q_A \theta}{\sigma} \sqrt{\left(\frac{\ln \frac{r_P}{r_A}}{\theta}\right)^2 + 1} \quad (7.30)$$

$$= \frac{r_A q_A \theta}{\sigma} \sqrt{\tan^2 \iota + 1} \quad (7.31)$$

To find the volume of the infinitesimal members, consider a small segment subtended by  $d\beta$ . The forces along the outer concentrated member are related using the relationship of equation (7.16) to be in the ratio  $1 : (1 + d\beta \tan \iota)$ . Equilibrium of this segment can then be considered to find that the force to be carried by the infinitesimal radial elements in this segment (as  $d\beta \rightarrow 0$ ) is  $q\sqrt{1 + \tan^2 \iota} d\beta$ . This can be combined with the expression for the radius (i.e. the length of the infinitesimal members) and the allowable stress to give the volume in this segment. That expression is then integrated throughout the region  $A$  to  $P$  to find the total contribution of all infinitesimal members.

$$V_- = \int_A^P r_S \frac{1}{\sigma} (A_S) \sqrt{1 + \tan^2 \iota} d\beta \quad (7.32)$$

$$= \frac{1}{\sigma} \sqrt{1 + \tan^2 \iota} \int_A^P r_S \left( \frac{r_A}{r_S} q_A \right) d\beta \quad (7.33)$$

$$= \frac{r_A q_A}{\sigma} \sqrt{1 + \tan^2 \iota} \int_0^\theta d\beta \quad (7.34)$$

$$= \frac{r_A q_A \theta}{\sigma} \sqrt{1 + \tan^2 \iota} \quad (7.35)$$

Note that the values for  $V_+$  and  $V_-$  are identical, this follows from Maxwell's theorem (see equation (2.2)) as the constant  $\mathcal{P}$  is zero in this case. Combining the two relationships gives

$$V = V_+ + V_- = q_A \left( 2 \frac{r_A \theta}{\sigma} \sqrt{\left(\frac{\ln \frac{r_P}{r_A}}{\theta}\right)^2 + 1} \right) = q_A \left( 2 \frac{r_A \theta}{\sigma} \sqrt{\tan^2 \iota + 1} \right) \quad (7.36)$$

Thus all required coefficients for this member have been found. Note that at  $r_A = r_P$ ,  $\iota = 0$  and these expressions become equal to those for the perfect fan region.

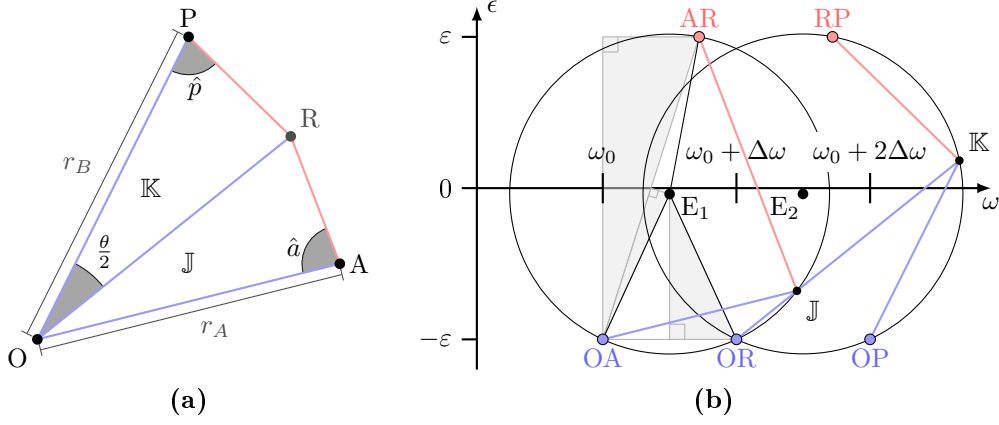


**Figure 7.4:** Discrete approximation of a fan element. **(a)** Geometric definition of points and quantities. **(b)** Circles of relative displacements, the red and blue lines are parallel to their respective lines in the physical plane in (a). Also shown are the three right-angled triangles used to calculate  $\Delta\omega$ .

### 7.3.3 Discrete approximation

We can alternatively approximate the truss-like continuum structural regions discussed above by considering discrete trusses of similar geometry. Figure 7.4a shows such a layout. Prager (1978b) considered trusses similar to this, where  $\hat{a} = \frac{\pi}{2}$ ; Zhou & Li (2004) also considered similar regions where  $\hat{p} = \hat{a}$ . In both cases, the triangles OPR and ORA (as shown in Figure 7.4) were similar; this relationship will be maintained here, and these mesh cells will be referred to as  $\mathbb{J}$  and  $\mathbb{K}$  respectively.

#### Geometry

For a general set of points O, A and P, the values of  $\hat{a}$  and  $\hat{p}$  can be found using the similar triangles OPR and ORA.

$$\frac{r_P}{\sin(\hat{a})} = \frac{r_R}{\sin(\hat{p})}, \quad \frac{r_R}{\sin(\hat{a})} = \frac{r_A}{\sin(\hat{p})} \quad (7.37)$$

$$\frac{r_P \sin(\hat{p})}{\sin(\hat{a})} = r_R, \quad r_R = \frac{r_A \sin(\hat{a})}{\sin(\hat{p})} \quad (7.38)$$

These relationships are combined to give,

$$\frac{r_P \sin(\hat{p})}{\sin(\hat{a})} = \frac{r_A \sin(\hat{a})}{\sin(\hat{p})} \quad (7.39)$$

$$\frac{r_P}{r_A} = \left( \frac{\sin(\hat{a})}{\sin(\hat{p})} \right)^2 \quad (7.40)$$

By also noting that  $\hat{a} + \hat{p} + \frac{\theta}{2} = \pi$ , we find that

$$\tan(\hat{p}) = \frac{\sin(\frac{\theta}{2})}{\sqrt{\frac{r_P}{r_A}} - \cos(\frac{\theta}{2})} \quad (7.41)$$

Additionally, the unknown bar lengths are given by

$$|\text{OR}| = r_R = \sqrt{r_A r_P} \quad |\text{PR}| = r_P \frac{\sin \frac{\theta}{2}}{\sin \hat{a}} \quad |\text{RA}| = r_A \frac{\sin \frac{\theta}{2}}{\sin \hat{p}} \quad (7.42)$$

#### Static form

To calculate the optimization coefficients based on static principles, the external force at point A is assumed to be aligned to the bar AR and of value  $q_A$ . Equilibrium at point R requires that the force in bar PR is equal to  $q_A \frac{\sin \hat{p}}{\sin \hat{a}} = q_A \sqrt{\frac{r_A}{r_P}}$ . Similarly, the force in bar OR will be  $q_A \frac{\sin \frac{\theta}{2}}{\sin \hat{a}}$ . Bars OA and OP will have zero force from this element, although separate straight bar elements may be present.

Therefore the external forces acting on this element will be

$$\begin{bmatrix} -\cos(\hat{a} - \Theta_A) - \sqrt{\frac{r_A}{r_P}} \cos(\Theta_P + \hat{p}) \\ \sin(\hat{a} - \Theta_A) - \sqrt{\frac{r_A}{r_P}} \sin(\Theta_P + \hat{p}) \\ \cos(\hat{a} - \Theta_A) \\ -\sin(\hat{a} - \Theta_A) \\ \sqrt{\frac{r_A}{r_P}} \cos(\Theta_P + \hat{p}) \\ \sqrt{\frac{r_A}{r_P}} \sin(\Theta_P + \hat{p}) \end{bmatrix} q_A = \begin{bmatrix} f_O^x \\ f_O^y \\ f_A^x \\ f_A^y \\ f_P^x \\ f_P^y \end{bmatrix} \quad (7.43)$$

Note that if  $\hat{a} = \hat{p} = \frac{\pi}{2}$  then these equations would become identical to the constraints of equation (7.14) for exact fans. However, clearly a triangle with two right angles does not practically exist, and as such this is better thought of as a limit, indicating that these approximate elements become increasingly accurate when  $\theta$  is small.

By combining the forces above with the lengths from equation (7.42) the volume of this element is shown to be

$$V = \frac{q_A}{\sigma} \left( \frac{2\sqrt{r_A r_P} \sin(\frac{\theta}{2})}{\sin \hat{a}} + \frac{r_P \sin \hat{p} \sin \frac{\theta}{2}}{\sin^2 \hat{a}} \right) \quad (7.44a)$$

$$= \frac{q_A}{\sigma} (3r_A \cos \hat{a} + 3\sqrt{r_A r_P} \cos \hat{p}) \quad (7.44b)$$

### Kinematic form

To calculate the virtual deflection field, the circle of relative displacements (Prager, 1978b) is used, as shown in Figure 7.4b. This shows the rotation and longitudinal strains of each bar as points on a circle(s) which represents the strain of the relevant cell(s) of the mesh. Lines from each point to a pole on the circle are parallel to the respective line in the physical plane. The poles for the mesh cells  $\mathbb{J}$  and  $\mathbb{K}$  are indicated.

The local displacement field  $\dot{u}$  is defined such that  $\dot{u}_O^x = 0, \dot{u}_O^y = 0$ . Each bar has a longitudinal strain equal to  $\pm\varepsilon$ ; therefore to find the deflections of all the points, it remains only to find the values of  $\Delta\omega$  and  $\omega_0$ .

Consider the right-angled triangle aligned to the  $\varepsilon$  and  $\omega$  axes with hypotenuse  $OA \rightarrow AR$ , the length of the hypotenuse will be referred to as  $h$ .

$$h = \frac{2\varepsilon}{\sin((\frac{\pi}{2} - \hat{a}) + (\frac{\pi}{2} - \frac{\theta}{2}))} = \frac{2\varepsilon}{\sin(\hat{p})} \quad (7.45)$$

Now consider one half of the isosceles triangle between  $\overrightarrow{OA}, \overrightarrow{AR}$  and  $E_1$ , the centre of the circle. This forms a right angled triangle with a hypotenuse equal to the radius of the circle,  $R_1$ .

$$R_1 = \frac{0.5h}{\sin(\hat{a})} = \frac{\varepsilon}{\sin(\hat{a}) \sin(\hat{p})} \quad (7.46)$$

From this, the value of  $\Delta\omega$  can be found.

$$\Delta\omega = 2R_1 \sin(\frac{\theta}{2}) = 2\varepsilon(\cot(\hat{a}) + \cot(\hat{p})) \quad (7.47)$$

Consider the local,  $\dot{u}$ , reference frame at point A, in the direction parallel to the bar AR.

$$\dot{u}_A^{\parallel AR} = r_A \varepsilon \cos \hat{a} + r_A \omega_0 \sin \hat{a} \quad (7.48)$$

$$\rightarrow \quad \omega_0 = \frac{\dot{u}_A^{\parallel AR}}{r_A \sin \hat{a}} - \frac{\varepsilon}{\tan \hat{a}} \quad (7.49)$$

The deflection at the point P in the direction parallel to bar PR is

$$\dot{u}_P^{\parallel PR} = \sin(\hat{p}) (r_P \omega_0 + 4r_P \varepsilon (\cot \hat{a} + \cot \hat{p})) - r_P \varepsilon \cos \hat{p} \quad (7.50)$$

Combining these gives

$$\dot{u}_P^{\parallel PR} = r_P \sin(\hat{p}) \left( \frac{\dot{u}_A^{\parallel AR}}{r_A \sin \hat{a}} - \frac{\varepsilon}{\tan \hat{a}} + 4\varepsilon(\cot \hat{a} + \cot \hat{p}) \right) - r_P \varepsilon \cos \hat{p} \quad (7.51)$$

$$\dot{u}_P^{\parallel PR} - \sqrt{\frac{r_P}{r_A}} \dot{u}_A^{\parallel AR} = 3r_P \varepsilon \left( \sqrt{\frac{r_A}{r_P}} \cos \hat{a} + \cos \hat{p} \right) \quad (7.52)$$

or equivalently

$$\sqrt{\frac{r_A}{r_P}} \dot{u}_P^{\text{PR}} - \dot{u}_A^{\text{AR}} = 3\varepsilon(r_A \cos \hat{a} + \sqrt{r_A r_P} \cos \hat{p}) \quad (7.53)$$

which, after appropriate transformation of the deflections, becomes identical to the values found from the primal form.

## 7.4 Application of fan regions

### 7.4.1 Application in layout optimization

To implement the above fan elements in layout optimization, the problem is first solved using the standard layout optimization method, i.e. with straight bar elements. Each set of three nodes is then checked. For each triplet, three possible fans should be identified, corresponding to the cases where O is located at each of the three nodes. Points A and P are then assigned by ensuring that the angle  $\angle AOP$  is less than  $180^\circ$  when measured anti-clockwise.

If the three points are co-linear then the only element possible is when point O is the centre of the three nodes, in which case  $\theta = \pi$ . However, there is uncertainty as to the direction in which the region should lie. Furthermore such regions will be fairly large compared to the nodal resolution of the problem; thus it is likely that other nodes will allow it to be equivalently formed of multiple fan regions (noting that these need not be in an exact position, which can instead be recovered during the layout optimization stage).

Similarly, it is simple at this stage to impose a limit on how far from a perfect circle the regions are allowed to be, as either a value of the offset angle,  $\iota$ , or based on the difference between  $r_A$  and  $r_P$ . Any potential region outside of this limit is simply omitted from the procedure. Limits on the design domain can also be imposed once the geometry of a potential region has been calculated.

For each potential element, the constraints are then checked; using the offset fan constraints from equations (7.23) and (7.36) is simplest as it allows the same equations to be used in all cases. However, the equation for a perfect fan, equation (7.13), may also be used for cases where  $r_A = r_P$  to obtain the same results. If the discrete approximation of this region is required (for example for compatibility with the region to be derived in Section 7.5), then equations (7.43) and (7.44) are used.

### 7.4.2 Graphical interpretation of member adding

The member adding method of Gilbert & Tyas (2003) can be interpreted graphically. This section will first outline this for the simple bar elements of standard layout optimization; a similar interpretation will then be given for the fan elements.

#### The member adding method for bar elements

Figure 7.5a shows the resulting structure from the first iteration of the simple single load case problem shown. The allowable stresses for compression and tension are equal, and will be denoted by  $\sigma$ . By the Michell-Hemp criteria, the strain at any point in the domain must be less than  $\frac{1}{\sigma}$ , i.e.  $\varepsilon$ .

The initial ground structure was constructed using adjacent connectivity. Figure 7.5a also shows the corresponding virtual displacement field for this solution. Two nodes are highlighted with circles; currently the ground structure does not contain a member connecting these two circles. However, the dual constraint for such a member can still be calculated using

$$\begin{bmatrix} \sin \Theta \\ \cos \Theta \\ -\sin \Theta \\ -\cos \Theta \end{bmatrix}^T \begin{bmatrix} u_A^x \\ u_A^y \\ u_B^x \\ u_B^y \end{bmatrix} \leq \varepsilon l \quad (7.54)$$

where  $\Theta$  is the inclination of the relevant potential member,  $l$  is the length of the relevant member and  $u$  are the virtual displacements of the end nodes A and B in the  $x$  and  $y$  directions. This constraint relates to the compressive strain, a second constraint with the signs of the coefficients reversed relates to the tensile strain. As values for  $u$  may be obtained at all points in the ground structure, this constraint can be evaluated for any pair of nodes, regardless of whether they are connected by a member in the ground structure.

If the virtual displacements at A and B are taken from the resulting displacement field in Figure 7.5a, only  $u_B^x$  and  $u_B^y$  remain as unknowns. Therefore equation (7.54) (as an equality) can be expressed as a straight line. These lines, for both the compressive and tensile limits, have been plotted over the displacement field in Figure 7.5a, as has the line of zero virtual strain. It can be seen that the virtual displacement of the point B moves it outside these lines; this indicates that the corresponding constraint is violated.

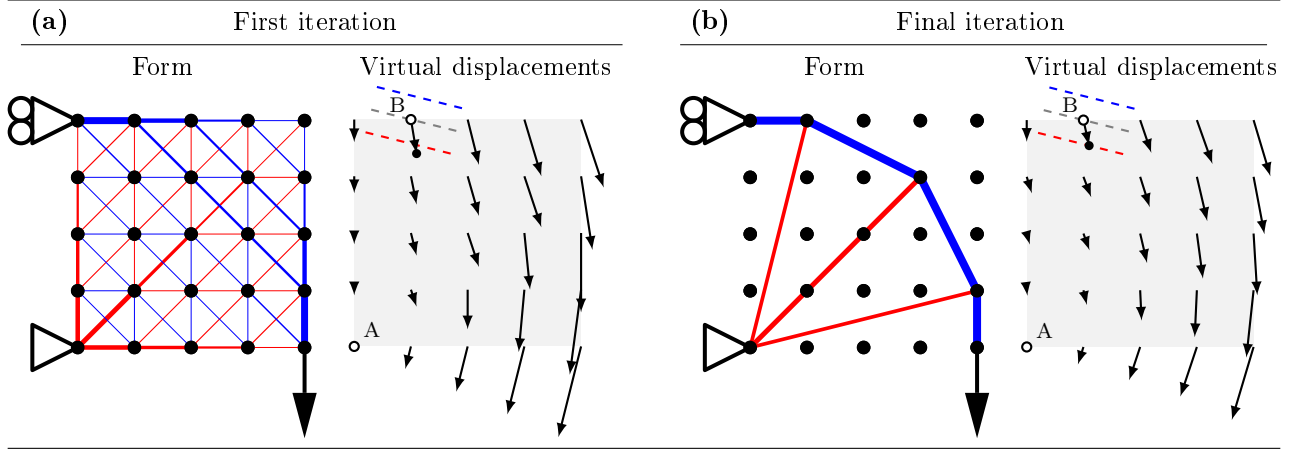


**Figure 7.5:** Graphical interpretation of the member adding method for bar elements. (a) Form and virtual deflection field after first iteration (adjacent connectivity ground structure). (b) Form and virtual deflection field of final solution.

The final solution, after all member adding iterations have occurred, is shown in Figure 7.5b; the member from A to B is now present in the structure. The virtual strain field is also shown, again with the limiting lines for the member under consideration. It is now seen that the displacement of node B lies directly on the line of the compressive limit, as must be the case for the member to have a non-zero area.

### The member adding method for fan elements

The graphical interpretation will now be extended to cover the newly derived fan elements. The structure from Figure 7.5b is reproduced as Figure 7.6a, except that now the labels superimposed on the virtual deflection field relate to a potential fan element connecting the indicated points O, A and P.

The constraints for a perfect fan element from equation (7.13) are used to provide the most intuitive interpretation. Duality principles could be used on equations (7.23) and (7.36) to the same effect, but with increased complexity of calculation.

The limits imposed by straight bars OA and OP are marked; these members have already been checked as part of the standard layout optimization procedure and therefore will not be violated at this point. These correspond to the first two constraints of equation (7.13).

The third constraint of equation (7.13) will now be considered. By considering it at equality and rearranging it is possible to obtain

$$u_A^y = \frac{\sin \Theta_A}{\cos \Theta_A} u_A^x + \left( \begin{bmatrix} \sin \Theta_P - \sin \Theta_A \\ \cos \Theta_A - \cos \Theta_P \\ -\sin \Theta_P \\ \cos \Theta_P \end{bmatrix}^T \begin{bmatrix} u_O^x \\ u_O^y \\ u_P^x \\ u_P^y \end{bmatrix} - 2r\theta\varepsilon \right) \quad (7.55)$$

If the deflections of points O and P are taken as fixed, then this defines a limiting line for the virtual deflection of A. This limiting line has a gradient of  $\tan \Theta_A$ , i.e. it is parallel to the line OA. Different values for the displacements of points O and A will cause the line to be translated; moving of the point O will appear to approximately move the line in the same manner, whilst movement of the point P will result in a movement similar to a rotation about the point O.

The line of equation (7.55), and the corresponding line of the opposite sense, are marked on the virtual displacement field of Figure 7.6a as solid lines, with the colours corresponding to the sense of the force in the infinitesimal radial members. The virtual deflection of point A takes it over this line (although as the violation is only 2.5% this is not immediately obvious).

Therefore, when the member adding procedure evaluates the potential fan OAP it identifies it as a potentially advantageous element, and it is added in the next iteration. This iteration then produces the result in Figure 7.6b. From the virtual deflection field it can be seen that the deflection of point A now causes it to lie on the limiting line. Furthermore, no other potential elements are found to violate the relevant constraint; thus the algorithm terminates and the structure in Figure 7.6b is returned as the overall solution.

As the theoretical solution for this problem consists of only a single fan region, the numerical result obtained by this method is limited in its accuracy only by the tolerances of the solver and the precision with which



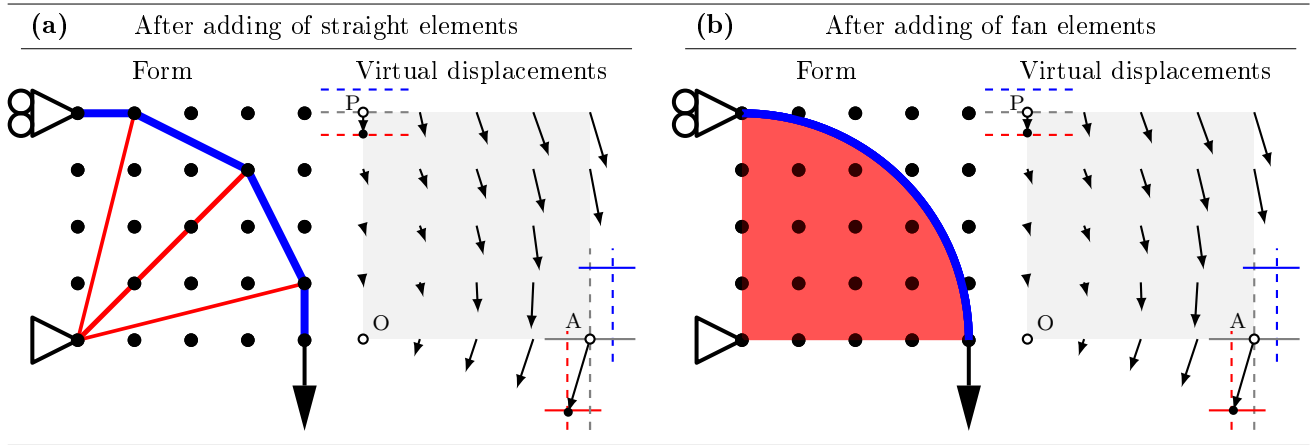


**Figure 7.6:** Graphical interpretation of the member adding method for fan elements.

(a) Form and virtual deflection field after final iteration using only bars, i.e. Figure 7.5b.

(b) Form and virtual deflection field of final solution including fan elements.

The virtual deflections of some points in the vicinity of A have been omitted for clarity.

the calculations have been performed. Here the solution matches the theoretical volume ( $= \pi$ ) to 8 significant figures.

### 7.4.3 Application in geometry optimization

To further refine the solutions, the geometry optimization method of He & Gilbert (2015) is extended to incorporate the fan regions described here. The layout optimization solution is first filtered to remove members with essentially zero cross-section areas, and also nodes which connect only to the removed members. The problem is then reformulated, incorporating the positions of the nodes as variables. This problem becomes non-linear, but the use of a starting point derived from layout optimization ensures that it is possible to find good results.

The problem is solved using an open source implementation of the primal-dual interior point method (Wächter & Biegler, 2006). This method makes use of gradient information; specifically, it requires partial derivatives of objective and constraint values for each variable. If the constraints derived from the exact form in equations (7.14) and (7.15) are used then an issue is encountered. This is because the value of  $r$  does not have a well defined derivative with respect to the position variables, even when the positions of the nodes are such that the member is a perfect fan.

Instead equations (7.23) and (7.36) for the offset fan are used to find the constraint values and derivatives. Equations (7.23) and (7.36) can be written explicitly in the geometry optimization variables using simple geometrical expressions ( $\sqrt{(x_A - x_O)^2 + (y_A - y_O)^2} = r_A$  etc.), and the required derivatives then obtained.

It is found that, when the true solution consists of fan regions, the optimization naturally causes these regions to tend towards perfectly circular fans; no artificial penalisation of highly offset regions is required. When the true solution consists of more complex curves, these may be approximated more accurately by offset fan regions than by straight bars. In this case, the fan elements may not tend to perfect circles after geometry optimization. However, once more advanced regions (see Appendix C) are incorporated, these should provide an even better approximation in these areas, eliminating the offset fans.

Several further details of the method require care. Removal of in-line (straight bar) members is necessary in the geometry optimization procedure as they may otherwise freely migrate along an axis (He & Gilbert, 2015). A similar phenomenon can be observed if two fans share a central point O, and an end node A / P which has no other members connecting to it. The mitigation is again similar to the 1D case, the two fans and the shared A / P node should be removed and replaced by a single, larger fan. Furthermore, care must be taken during operations such as node merging to preserve the orders of the nodes O, A and P.

#### 7.4.4 Example: Simply supported central point load

The proposed method will first be applied to the problem shown in Figure 7.7, consisting of a point load of magnitude  $Q$ , located equidistant between simple supports which are positioned  $2L$  apart. The point load is applied at a height of  $d$  above the level of the supports.

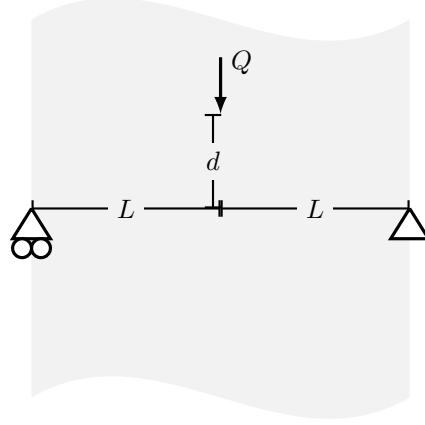


**Figure 7.7:** Point load example: Problem specification.

This example, with  $d = 0$ , was one of Michell's original 1904 problems. The support conditions are statically determinate, and thus the optimal layout will not change based on the material's relative strength in tension and compression. The problem, for a range of values of  $d$ , was also considered by Hemp (1973, eqn 4.70) who gives the total volume,  $V$ , as

$$V = \frac{\frac{1}{2}QL}{\sigma_C \sigma_T} \left( (\sigma_T + \sigma_C) \left( 1 + \frac{\pi}{2} \right) + (\sigma_T - \sigma_C) \frac{h}{L} \right) \quad (7.56)$$

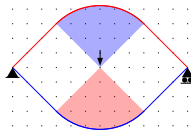
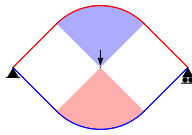
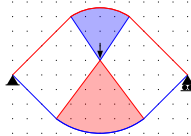
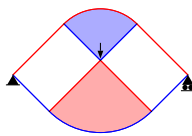
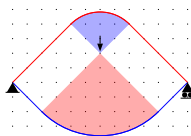
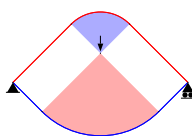
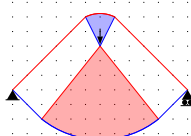
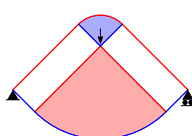
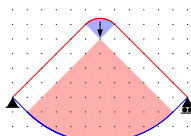
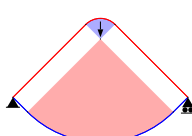
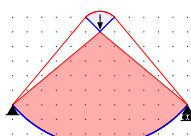
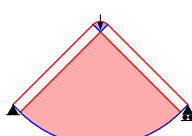
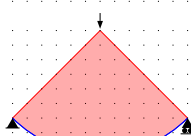
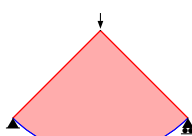
where  $\sigma_T$  and  $\sigma_C$  are the permissible stresses in tension and compression respectively. Here, only the case  $\sigma_T = \sigma_C = \sigma$  will be considered. In this case, the volume may be given by

$$V = \frac{QL}{\sigma} \left( 1 + \frac{\pi}{2} \right) \approx 2.570796 \frac{QL}{\sigma} \quad (7.57)$$

The problem was solved using the proposed numerical method, using a nodal grid with spacing of  $\frac{L}{6}$  (total 169 nodes, 14,196 potential bars and 2,370,732 potential fans); results are shown in Figure 7.8. No limits were imposed on regions extending outside the area, as this is generally considered to be a full plane problem. However, the initial ground structure nodes were spread only over a  $2L \times 2L$  square.

The resulting structures were then subjected to geometry optimization for further refinement, and these results are also shown in Figure 7.8. These results show excellent agreement with the analytical result, in terms of both the overall volume and the form of the solutions. In addition, the make-up of the solution from two fans and four straight bars is very clear. These results generally required less than two minutes to solve both the layout and geometry optimization stages.

After the layout optimization stage, it can be seen in some cases that ground structure nodes were already appropriately located to provide a solution which is very close to the optimal. In these cases, the error slightly increased after geometry optimization, due to the higher tolerances which are preferred to solve the NLP problem. However, in all cases, very good agreement with the analytical solution is seen after both layout and geometry optimization.

$d$	Layout optimization				Layout and geometry optimization			
	$t$ (s)	Vol. $\left(\frac{QL}{\sigma}\right)$	Error		$t^\dagger$ (s)	Vol. $\left(\frac{QL}{\sigma}\right)$	Error	
0	54	2.5708	$9 \times 10^{-11}\%$		0.8	2.5708	$3 \times 10^{-6}\%$	
$\frac{L}{6}$	65	2.5741	0.13%		22	2.5708	$4 \times 10^{-6}\%$	
$\frac{2L}{6}$	65	2.5708	$1 \times 10^{-11}\%$		0.9	2.5708	$3 \times 10^{-6}\%$	
$\frac{3L}{6}$	44	2.5772	0.25%		14	2.5708	$4 \times 10^{-6}\%$	
$\frac{4L}{6}$	87	2.5708	$1 \times 10^{-7}\%$		1	2.5708	$3 \times 10^{-6}\%$	
$\frac{5L}{6}$	77	2.5854	0.57%		98	2.5708	$4 \times 10^{-6}\%$	
$\frac{6L}{6}$	56	2.5708	$2 \times 10^{-11}\%$		0.8	2.5708	$3 \times 10^{-6}\%$	

† Time for geometry optimization step only.

**Figure 7.8:** Point load example: Results of layout and geometry optimization for various values of  $d$ . Errors are compared to the analytical value given by equation (7.57).

### 7.4.5 Example: Continuous multi-span bridge

The next problem that will be considered is a simplified bridge structure similar to that studied by Pichugin et al. (2015). The structure must support a uniform load along the bottom of the design domain, and has infinitely many spans of length  $2L$ . Pichugin et al. (2015) propose a minimum volume (for a distributed load of  $w$  per unit length) of

$$V = \left( \frac{3\Delta_\sigma + 5}{6\sqrt{\Delta_\sigma}} + \frac{(1 + \Delta_\sigma)^2}{2\Delta_\sigma} \arctan \sqrt{\Delta_\sigma} \right) \frac{wL^2}{\sigma} \quad (7.58)$$

where  $\Delta_\sigma = \frac{\sigma_C}{\sigma_T}$  and  $\sigma = \frac{\sigma_T + \sigma_C}{2}$ .

Here, the cases where  $\sigma_T = \sigma_C$  or  $\sigma_T = 2\sigma_C$  will be considered. For equal tension and compression strength ( $\sigma_T = \sigma_C = \sigma$ ) the volume is  $\left(\frac{4}{3} + \frac{\pi}{2}\right) \frac{wL^2}{\sigma} \approx 2.90413 \frac{wL^2}{\sigma}$ . For  $\sigma_T = 2\sigma_C$  equation (7.58) gives a volume of approximately  $2.916894 \frac{wL^2}{\sigma} = 3.88919 \frac{wL^2}{\sigma_T}$ .

Extending the derivation of Section 7.3.2 to unequal stresses is fairly simple; equations (7.31) and (7.35) are altered to use  $\sigma_T$  or  $\sigma_C$  as appropriate, before being combined to form equation (7.36).

The problem has been solved using the RAGS method, one half span was modelled using symmetry boundary conditions. A maximum height of  $0.8L$  was allowed and a  $20 \times 10$  grid of nodes was used, the forces were discretised in accordance with the method of Darwich et al. (2010). Results for  $\sigma_T = \sigma_C$  and for  $\sigma_T = 2\sigma_C$  are shown in Figure 7.9. The errors here are somewhat higher than those found in the previous example, however a significant proportion of this error is likely to be caused by the discretisation of the load.

In the layout optimization result of Figure 7.9a, a faint arching fan region (i.e. with tensile spokes) can be observed. This was suggested to be the form of the strain field outside of the structure by Pichugin et al. (2015, figure 4). This shows the potential that this method has for finding not only regions within the structure but through the remainder of the plane as well. This could be further developed by outputting region elements which are fully strained even if they are not carrying any force; this may provide considerable assistance in analytically verifying the optimal solutions.

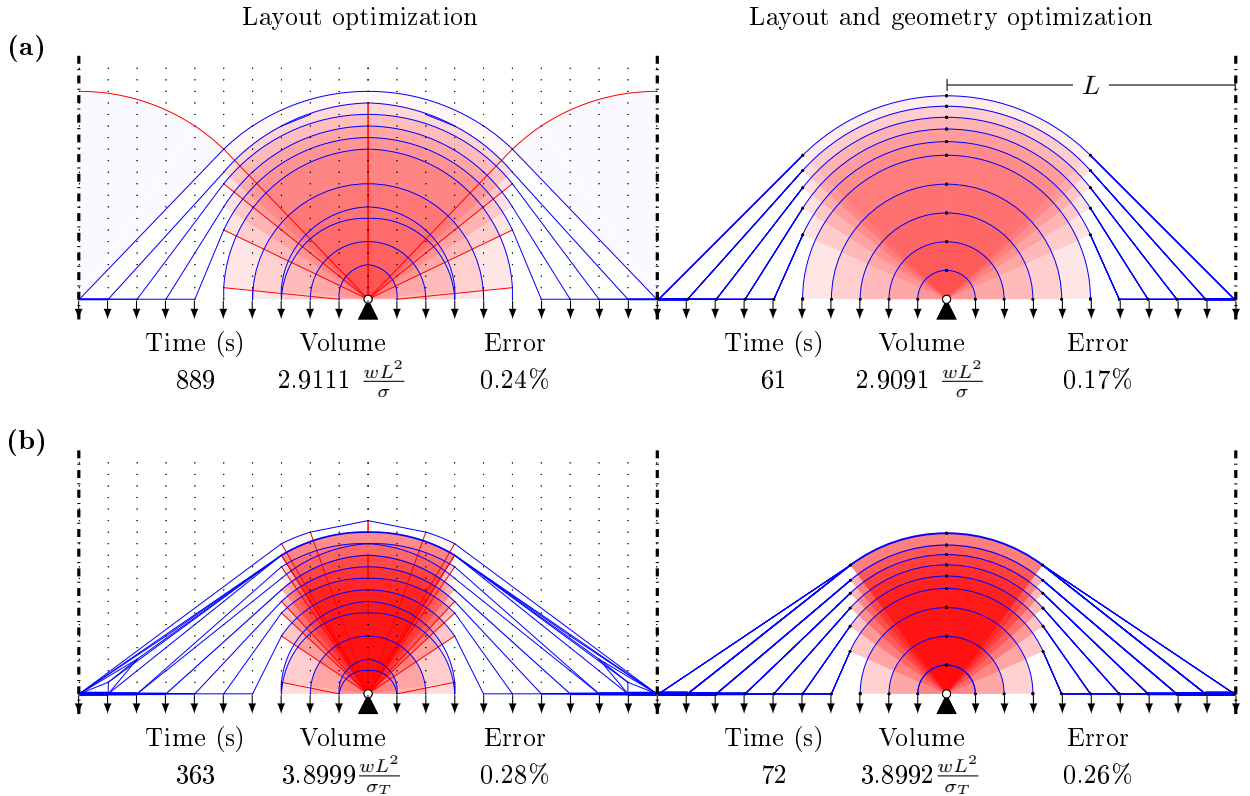


**Figure 7.9:** Bridge example: solutions with (a)  $\sigma_T = \sigma_C$  and (b)  $\sigma_T = 2\sigma_C$ . Errors are relative to the analytical solution for a problem with continuously distributed loading.

## 7.5 Discrete approximation of four node regions

The next element to be considered will be of type  $T_1$ , i.e. consisting of two sets of curvilinear members. However, the equations of such elements are rather complex; therefore this section will consider a discrete approximation of this region. Work towards obtaining a solution for the continuum region may be found in Appendix C.3.

The discrete approximation method applied previously in Section 7.3.3 can be extended to cover more complex regions. Such elements have been studied by (Prager, 1978a,b) and Mazurek et al. (2011) amongst others. Such structures are constructed from a mesh of members forming quadrilateral or triangle mesh cells, where each cell forms the same angles at corresponding corners; these will be referred to as  $\hat{a}$ ,  $\hat{b}$ ,  $\hat{o}$  and  $\hat{p}$  according to which corner point they are adjacent to. Each cell must be a cyclic quadrilateral, and two opposite angles  $\hat{a}$  and  $\hat{b}$  are determined by the ratio of the material's tensile and compressive strengths, being right angles when they are equal, as shown in Figure 7.10b.

Thus the first problem to be tackled, in Section 7.5.1, is to establish the geometry of such a region (if such a geometry is possible) for a given set of 4 arbitrary points. This can then be used to find the appropriate constraint on the nodal displacements.

The number of cells in the mesh region under consideration must be decided. To allow symmetry, it has been chosen that the number cells should be equal in each direction. For a  $1 \times 1$  grid of mesh cells, the geometrical rules can be obeyed only if the 4 points lie on a single circle; this is generally not true. Grids of  $3 \times 3$  can be shown to produce multiple possible solutions for the same set of input nodes; whilst this problem could be tackled using an approach similar to Smith & Gilbert (2013), the additional complexity is undesirable. Therefore a  $2 \times 2$  grid, as shown in Figure 7.10, will be used here.

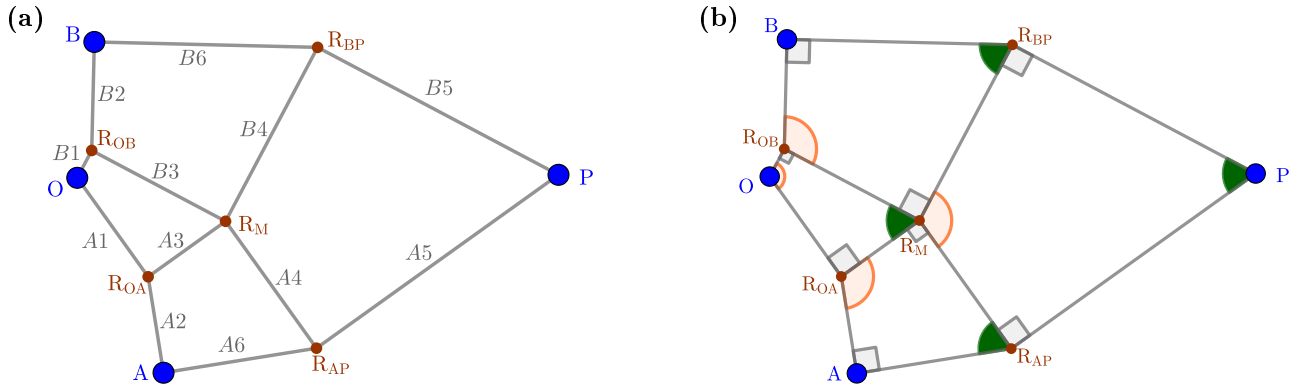


**Figure 7.10:** Discrete approximation of four node region: Labels and angles. (a) Labels of points and bars, large blue points are nodes of the ground structure and smaller brown points are internal points of the region. (b) Internal angles of each mesh cell, case where  $\sigma_T = \sigma_C$ , and therefore two opposing right angles are present. All solid green angles are equal, and will be denoted by  $\hat{p}$ . All outlined orange angles are equal and will be denoted by  $\hat{o}$ .

### 7.5.1 Geometry of a $2 \times 2$ cell mesh

This section concerns identification of the geometry of the region obeying the above rules and connecting an arbitrary set of four nodes, O, A, B and P. The additional points within this element will be denoted by R and subscripts indicating the joints to which they connect; the subscript M will denote the middle point. These labels are shown in Figure 7.10. The relevant geometrical relationships and associated equations are first found; a summary of the required procedure is given at the end of the section.

All possible regions with a fixed O and P are considered; by simple scaling and rotation, this may be applied to any set of positions and so generality is not affected. For a given value of  $\hat{p}$  and a given inclination of the bar  $R_{AP} - P$ , there are four possible degenerate extreme cases which occur when one or more edges of the layout have a zero length. These are illustrated in Figure 7.11a-d. The locations of points A and B given by these layouts form two cyclic quadrilaterals,  $\mathbb{A}$  and  $\mathbb{B}$ , with angles equal to those found in the mesh.  $\mathbb{A}$  and  $\mathbb{B}$  are shaded in blue in Figures 7.11 and 7.12

These two quadrilaterals are rotational images of each other; specifically a rotation of  $2\hat{p}$  about a point which will be referred to as M. Furthermore, any point A within the quadrilateral  $\mathbb{A}$  permits the construction of a permissible layout with the given values of  $\hat{p}$  and inclination of  $R_{AP} - P$ , resulting in point B lying in the corresponding rotated location in  $\mathbb{B}$ . This is shown in Figure 7.12a.

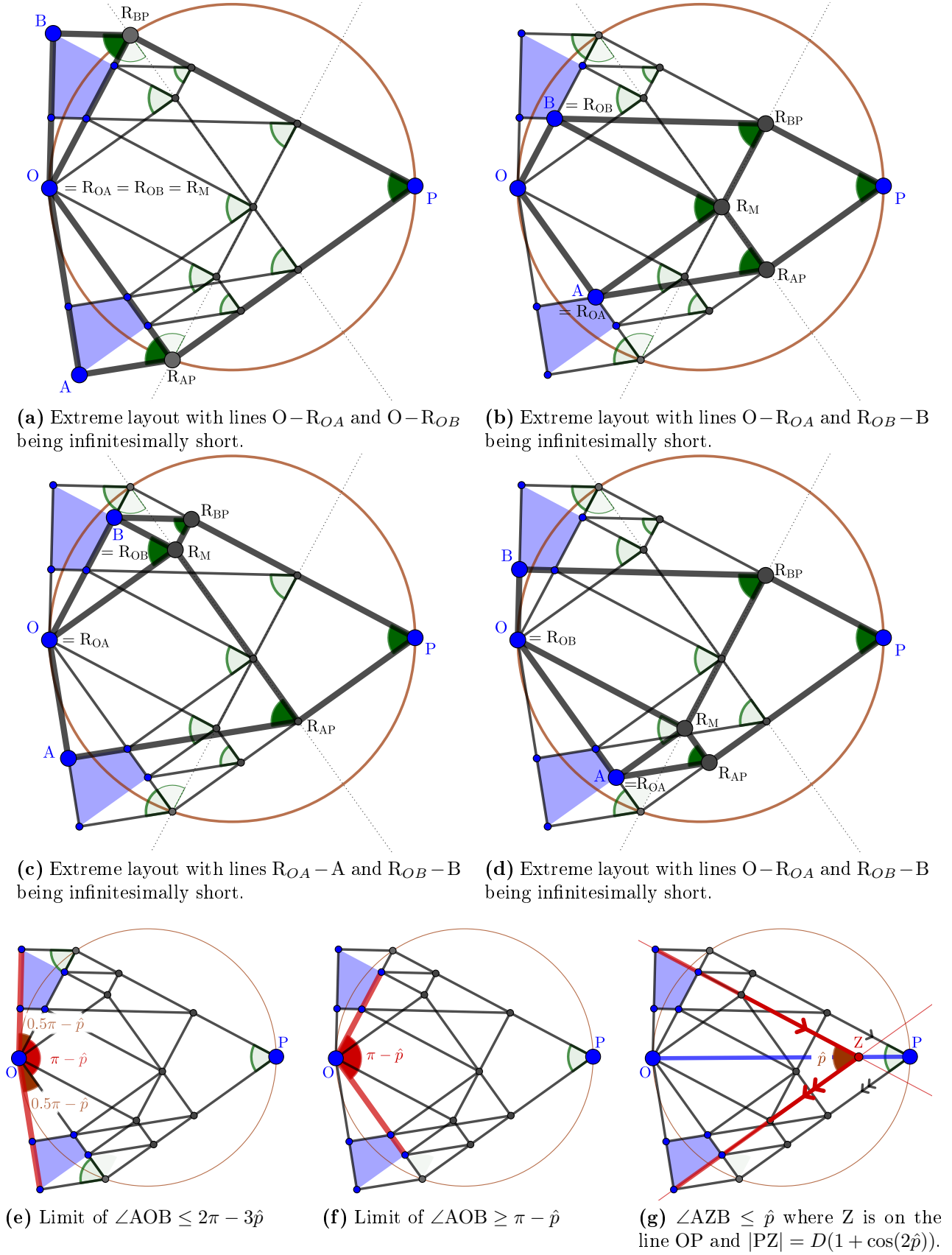
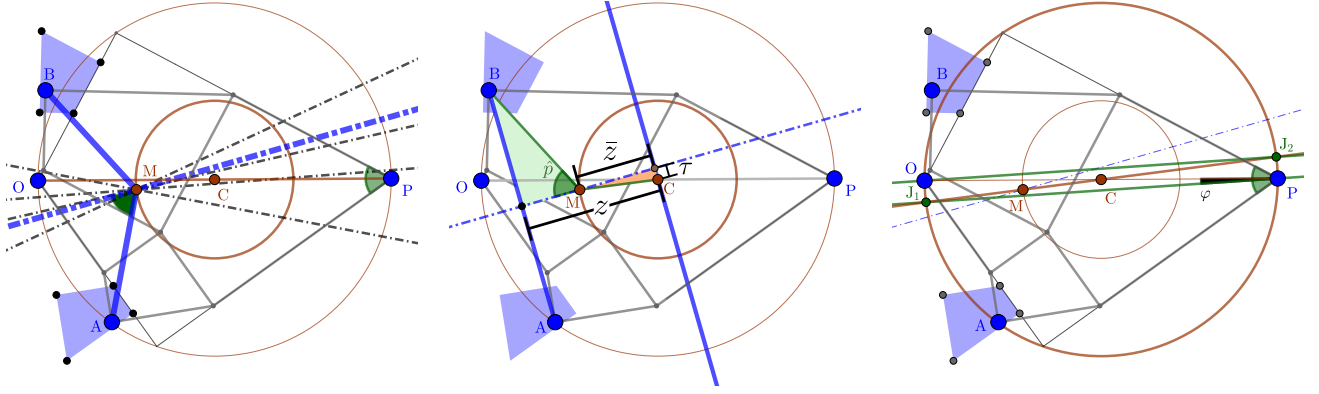


**Figure 7.11:** The range of possible layouts of the approximated four node region for a given value of  $\hat{p} = 63.5^\circ$  and inclination of the line  $R_{AP} - P$ . The shaded regions are  $\mathbb{A}$  and  $\mathbb{B}$ , cyclic quadrilateral with angles  $\hat{p}$ ,  $\frac{\pi}{2}$ ,  $\hat{\phi}$  and  $\frac{\pi}{2}$ , which contain all possible locations of the points  $A$  and  $B$  for the given parameters.

(a)-(d) The layouts corresponding to the corner points of the shaded regions.

(e)-(g) Limits which define edges of the shaded regions.



(a) Perpendicular bisectors of pairs of A, B locations for extreme layouts and pictured layout, intersecting at the centre of rotation M.

(b) Locations of dimensions used for calculation of  $\hat{p}$ . The two solid blue lines are parallel.

(c) Perpendicular bisectors of  $\hat{p}$  at point O, and  $\hat{p}$  at P, are parallel and intersect the line MC at  $J_1$  and  $J_2$ , on the circle with diameter OP.

**Figure 7.12:** Further relationships and quantities for a given value of  $\hat{p}$  and inclination of line  $R_{AP}P$ . The inner circle is centred on point C, the centre point of line OP.

The point M lies on a circle centred on the point C, the midpoint of the line OP. The circle has radius

$$|MC| = 0.5|OP| \cos \hat{p} = |OC| \cos \hat{p} \quad (7.59)$$

As the chosen inclination of  $R_{AP} - P$  is changed, the point M moves around the circle.

It now remains to formulate these relationships as an equation which may be solved to find  $\hat{p}$  from the locations of the points. A number of quantities are defined in Figure 7.12b, which may be easily obtained through simple geometrical operations on the points O, A, B and P. The minimum distance from the perpendicular bisector of AB to point C is denoted by  $\tau$ ,  $z$  is the distance from the line AB to a parallel line through C.  $\bar{z}$  is the distance from the same line through C to the point M. Also used are the distances  $|MC|$ ,  $\frac{|AB|}{2}$  and  $|OC|$ .

Consider the orange right angled triangle in Figure 7.12b, it has leg lengths  $\tau$  and  $\bar{z}$ . The hypotenuse of this triangle has length  $|MC|$ . Thus,

$$\bar{z} = \sqrt{|OC|^2 \cos^2 \hat{p} - \tau^2} \quad (7.60)$$

Next consider the green right-angled triangle with hypotenuse BM and leg lengths  $\frac{|AB|}{2}$  and  $z - \bar{z}$ . The angle marked in Figure 7.12b is equal to  $\hat{p}$ . Therefore this triangle and equation (7.60) imply

$$z - \bar{z} = z - \sqrt{|OC|^2 \cos^2 \hat{p} - \tau^2} = \frac{0.5|AB|}{\tan \hat{p}} = \frac{0.5|AB| \cos \hat{p}}{\sin \hat{p}} \quad (7.61)$$

Square both sides and introduce the notation  $\sin^2 \hat{p} = e$  (therefore  $(1 - e) = \cos^2 \hat{p}$ ) to simplify the equation.

$$z^2 - 2z\sqrt{|OC|^2(1 - e) - \tau^2} + |OC|^2(1 - e) - \tau^2 = \frac{(0.5|AB|)^2(1 - e)}{e} \quad (7.62)$$

$$\left( z^2 e + |OC|^2 e - |OC|^2 e^2 - \frac{|AB|^2}{2} + \frac{|AB|^2}{2} e \right)^2 = \left( 2ze\sqrt{|OC|^2 - |OC|^2 e - \tau^2} \right)^2 \quad (7.63)$$

Expanding this gives a quartic equation in  $e$ .

$$o_4 e^4 + o_3 e^3 + o_2 e^2 + o_1 e + o_0 = 0 \quad (7.64a)$$

where

$$o_4 = |OC|^4 \quad (7.64b)$$

$$o_3 = 2z^2|OC|^2 - 2\frac{|AB|^2}{2}|OC|^2 + 2|OC|^2\tau^2 - 2|OC|^4 \quad (7.64c)$$

$$o_2 = \frac{|AB|^4}{2} + z^4 + |OC|^4 + \tau^4 + 2\frac{|AB|^2}{2}z^2 + 4\frac{|AB|^2}{2}|OC|^2 - 2\frac{|AB|^2}{2}\tau^2 - 2z^2|OC|^2 + 2z^2\tau^2 - 2|OC|^2\tau^2 \quad (7.64d)$$

$$o_1 = 2\left(\frac{|AB|}{2}\right)^2\tau^2 - 2\frac{|AB|^2}{2}z^2 - 2\frac{|AB|^2}{2}|OC|^2 - 2\frac{|AB|^4}{2} \quad (7.64e)$$

$$o_0 = \frac{|AB|^4}{2} \quad (7.64f)$$

The value of  $e$  found from equation (7.64) furnishes a value of  $\hat{p}$ ; some care may be required to ensure that the correct root is chosen such that  $\hat{p}$  is real. Note that there will not always be real roots to this equation; some combinations of locations do not produce a valid region of this type.

The value of  $\hat{p}$  is one of the initially fixed values, the other being the inclination of the line  $R_{AP} - P$ . To represent the inclination as a variable the value  $\varphi$  is used, which is defined as the angle between the line  $OP$  and the angle bisector of  $\hat{p}$  at  $P$ , as shown in Figure 7.12c.

To calculate  $\varphi$ , note that the  $\angle OCM = \angle OCJ_1 = 2\varphi$ . The location of the point  $M$  may be calculated by noting that it lies a distance of  $\frac{|AB|}{2 \tan \hat{p}}$  away from the midpoint of a line  $AB$ , along its perpendicular bisector. The angle formed by these three points may then be found by any suitable method. Alternative methods of calculating  $2\varphi$  are possible, but note that the value of  $\tau$  is frequently very small, so methods which use this can lead to significant errors when limited precision is available.

The values of  $\hat{p}$  and  $\varphi$  found above may imply a layout in which one or more bars have a negative length. To ensure that these are eliminated from consideration, the limiting values (where the bars have zero length) must be considered. These occur when  $A$  and  $B$  lie on the edges of polygons  $\mathbb{A}$  and  $\mathbb{B}$ .

One such limit may be derived from the layout shown in Figure 7.11a, the angle  $\angle AOB$  for any possible region must be less than the  $\angle AOB$  in this case, which is composed of the angles labelled in Figure 7.11e. The lower limit on  $\angle AOB$  is derived from the angle highlighted in Figure 7.11f. Combining these gives

$$\pi - \hat{p} \leq \angle AOB \leq 2\pi - 3\hat{p} \quad (7.65)$$

A further limit is identified in Figure 7.11g. Two of the edges of  $\mathbb{A}$  and  $\mathbb{B}$  are parallel to  $R_{AP} - P$  and  $R_{BP} - P$  respectively, and therefore that lines extended from these edges must meet at an angle  $\hat{p}$ . The point at which these lines meet will be denoted as  $Z$  and lies on the line  $OP$  such that  $|PZ| = |OC|(1 + \cos(2\hat{p}))$ . Therefore the angle  $\angle AZB$  must be less than or equal to  $\hat{p}$  for any feasible region.

The remaining edges (those closest to point  $O$ ) of  $\mathbb{A}$  and  $\mathbb{B}$  do not form an angle with a static point, making direct calculation of their equation complicated. However, note that as  $\mathbb{A}$  and  $\mathbb{B}$  are rotated images, these two edges do not correspond to one another. Therefore we can eliminate these layouts by tightening the bounds on the opposite edge using  $\varphi$ . The required limit is the lower bound in equation (7.65). Thus,

$$\angle AOP \geq \pi - \hat{p} - \varphi \quad (7.66a)$$

$$\angle BOP \geq \pi - \hat{p} + \varphi \quad (7.66b)$$

Once the values of  $\hat{p}$  and  $\varphi$  have been established, the internal lines and points can be easily calculated.

### Summary of calculation method for geometry of discrete region

The overall procedure to calculate the geometry of a potential four node element from the positions of the ground structure nodes therefore proceeds as follows:

- Calculate  $\hat{p}$  value
  - Calculate distances  $|OC|$  and  $0.5|AB|$  (as defined in Figure 7.12b).
  - Calculate the positions of point  $C$  and midpoint of  $AB$
  - Find the lines: through  $C$  and parallel to  $AB$   
through the midpoint of  $AB$  and perpendicular to  $AB$ .
  - Intersect these lines and calculate the values of  $z$  and  $\tau$  (as defined in Figure 7.12b)
  - Find the coefficients of equation (7.64) and solve the quartic equation to find values for  $e = \sin^2 \hat{p}$ . If no real roots exist then discard the potential element.
  - Find corresponding values of  $\hat{p}$ . If no real values exist (e.g.  $e < 0$ ) then discard the potential element.
- Check the value of  $\hat{p}$  is in the range given by equation (7.65) and Figure 7.11e-f.
- Find point  $Z$  and check that the resulting angle  $\angle AZB \leq \hat{p}$  (Figure 7.11g).
- Find  $\varphi$ .
  - Find the position of the point  $M$
  - Calculate the angle  $\angle OCM$ .
  - Use expression  $\varphi = \frac{\angle OCM}{2}$  from Figure 7.12c.
- Check strengthened versions of limits from equation (7.66).
- Calculate lines from nodes  $O$ ,  $A$ ,  $B$  and  $P$  to adjoining  $R$  points.
- Intersect relevant lines to find the location of  $R_{OA}$ ,  $R_{OB}$ ,  $R_{AP}$  and  $R_{BP}$ .
- Find lines connecting to these points going towards  $R_M$ .
- Intersect to find the location of  $R_M$ .



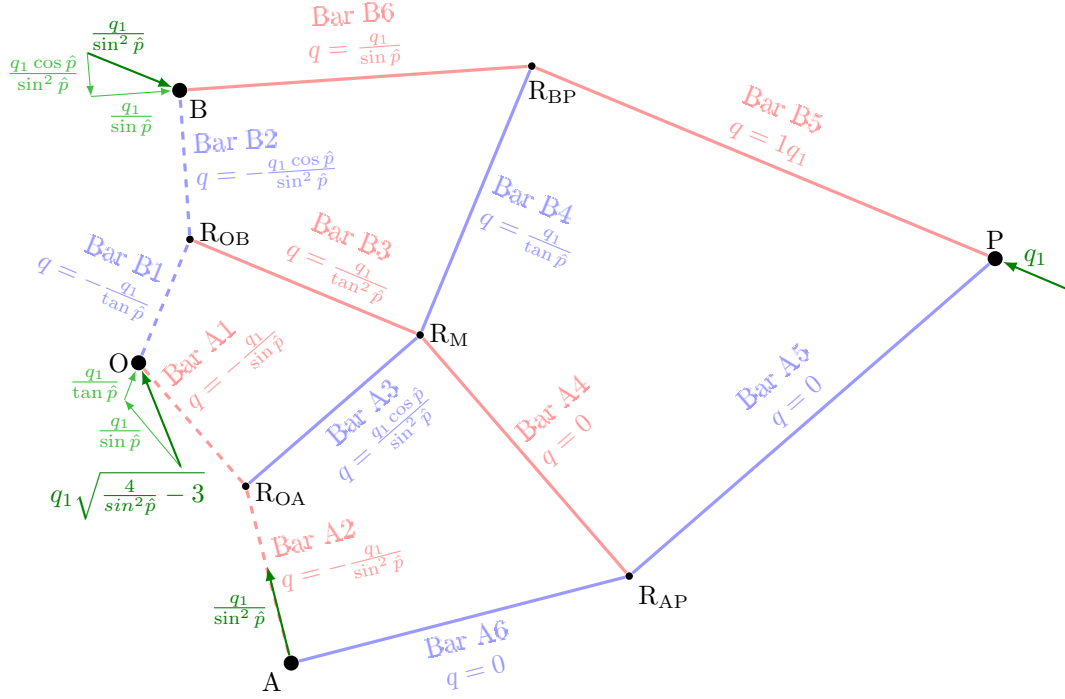


**Figure 7.13:** Primal (static) derivation of a discrete approximated quad element.

### 7.5.2 Static derivation of constraints

The geometry obtained above is subjected to a force of magnitude  $q_1$  applied at the point P and aligned with the bar  $PR_{BP}$ . For convenience, the bars have been assigned names as shown in Figure 7.10a. The internal forces in each bar have been calculated and are shown in Figure 7.13, where positive values denote a force of the ‘expected’ sense for that bar. The resulting forces at the nodes have also been calculated, and when converted to global coordinates give

$$\begin{bmatrix} -\cos \Theta_P^B - \frac{2}{\tan \hat{p}} \sin \Theta_P^B \\ -\sin \Theta_P^B + \frac{2}{\tan \hat{p}} \cos \Theta_P^B \\ (1 - \frac{1}{\tan^2 \hat{p}}) \cos \Theta_P^B + \frac{2}{\tan \hat{p}} \sin \Theta_P^B \\ (1 - \frac{1}{\tan^2 \hat{p}}) \sin \Theta_P^B - \frac{2}{\tan \hat{p}} \cos \Theta_P^B \\ \frac{1}{\sin^2 \hat{p}} \cos \Theta_P^B \\ \frac{1}{\sin^2 \hat{p}} \sin \Theta_P^B \\ -\cos \Theta_P^A \\ -\sin \Theta_P^A \end{bmatrix} q_1 = \begin{bmatrix} f_O^x \\ f_O^y \\ f_A^x \\ f_A^y \\ f_B^x \\ f_B^y \\ f_P^x \\ f_P^y \end{bmatrix} \quad (7.67)$$

where  $\Theta_P^B$  is the angle of the bar  $PR_{BP}$ , (i.e. bar B5) to the global  $x$ -axis.

The volume can be calculated by simply summing the lengths and areas of each bar.

$$V = \frac{q_1}{\sigma} \left( l_{B5} + \frac{l_{B4}}{\tan \hat{p}} + \frac{l_{B6}}{\sin \hat{p}} + \frac{l_{B3}}{\tan^2 \hat{p}} + \frac{l_{A3}}{\tan \hat{p} \sin \hat{p}} - \frac{l_{A1}}{\sin \hat{p}} - \frac{l_{A2}}{\sin^2 \hat{p}} - \frac{l_{B1}}{\tan \hat{p}} - \frac{l_{B2}}{\tan \hat{p} \sin \hat{p}} \right) \quad (7.68)$$

A second independent force variable, which will be denoted  $q_2$ , can be established by the use of similar principles with the force  $q_2$  applied to the bar A5.

### 7.5.3 Example: Michell cantilever

Consider the simple Michell cantilever problem shown in Figure 7.14, the supports are a distance  $2d$  apart, and the force is applied at a distance of  $5d$  from the line of the supports. The force has magnitude  $2Q$  and the material has a limiting stress of  $\sigma$  in both tension and compression. The ground structure consists of 6 nodes, and the initial ground structure contains all possible straight bar elements connecting these points. This problem was previously considered using mixed integer linear programming methods in Section 6.4.3, and the theoretical minimum volume is calculated using expressions from Chan (1960) to be  $V_T = 39.43 \frac{Qd}{\sigma}$ .

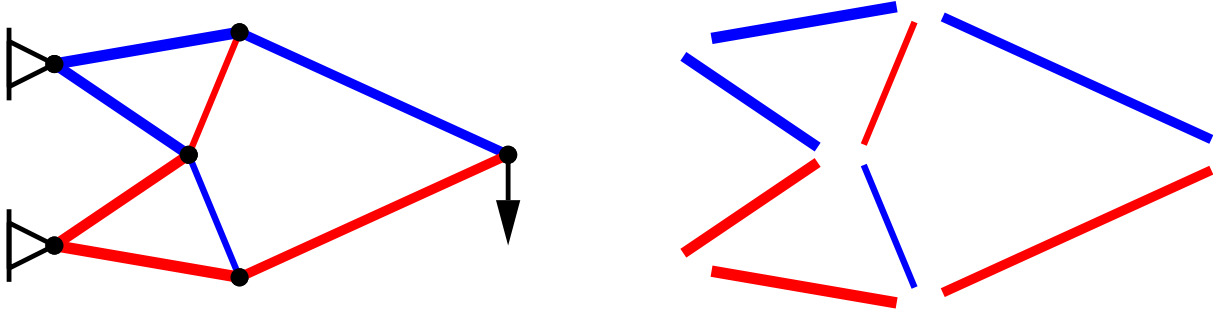


**Figure 7.14:** Michell cantilever: Iteration 1.  $V = 1.056V_T$ . (a) output structure, (b) exploded view.

The output of the first iteration (using the fully connected ground structure of bars) is shown in Figure 7.14. The structure consists of 8 straight bar elements, and has a volume of  $41.62 \frac{Qd}{\sigma}$ .

The dual solution of this problem gives a virtual displacement field; this is checked first to see if any potential straight bar elements have a violated constraint. As all possible bars were included in the ground structure, all such constraints were already considered by the solver and thus no new bar members are added.

As no violated bar members are found, potential fan region elements are now checked. Each triplet of nodes is considered with respect to the constraint of equation (7.53). Two potential regions are found to violate this constraint, both having a relative violation of 5.3%. These elements are therefore added to the ground structure, and the solver is called on the new problem. The result of this second iteration is shown in Figure 7.15, and consists of two discretely approximated fan regions and 6 straight bars.

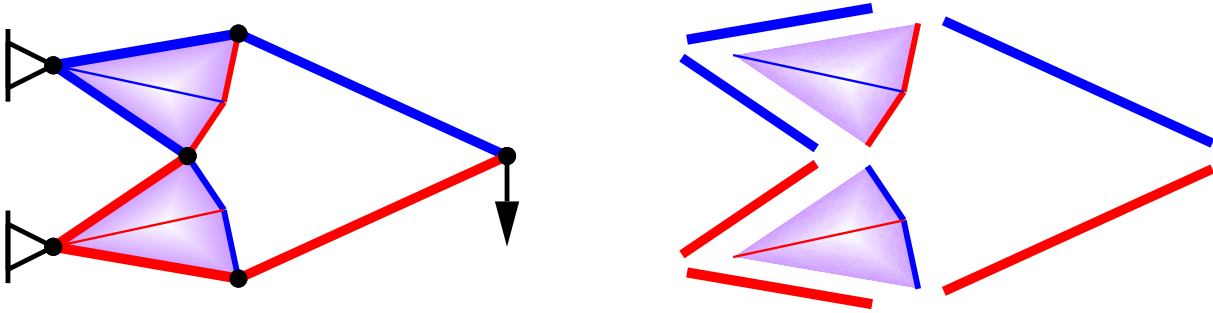


**Figure 7.15:** Michell cantilever: Iteration 2.  $V = 1.046V_T$ . (a) output structure, (b) exploded view.

The virtual displacement field from iteration 2 is now checked, first for violating potential straight bar elements, of which there are none; then for potential violating fan elements, of which there are also none. Therefore checks for four node regions are undertaken, using the dual of equations (7.67) and (7.68). One violating region is found with a relative violation of 14.8% for both the  $q_1$  and  $q_2$  constraints.

This region is added to the ground structure, and the problem is again solved. The result of this third iteration is shown in Figure 7.16. The solution consists of one quad region, two fan regions and four straight bars. The volume of this structure is  $40.05 \frac{Qd}{\sigma}$ , in increase of 1.6% over the theoretical minimum volume. Observe that this matches the result for a structure with 11 joints identified in Figure 6.20.

Finally, the virtual deflection field of the solution in Figure 7.16 is checked, but no bars, fans or four node elements are found to violate a constraint. Therefore this solution is the overall optimum to the problem.

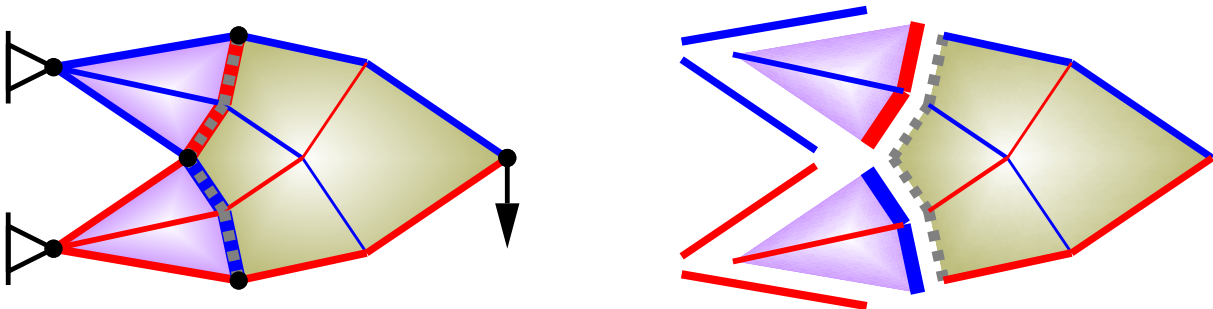


**Figure 7.16:** Michell cantilever: Final (3<sup>rd</sup>) iteration.  $V = 1.016V_T$ . (a) output structure, (b) exploded view.

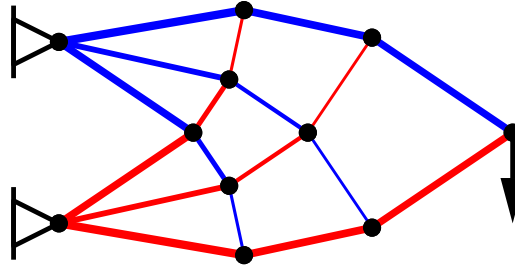


**Figure 7.17:** Michell cantilever: Result with bars and increased no. of ground structure nodes.  $V = 1.016V_T$

including all bars, fans or four node elements connecting these 6 nodes.

It is somewhat challenging to interpret the meaning of bars A1, A2, B1 and B2 (see Figure 7.13) of the four node region in this solution. These bars have been marked with grey dashed lines in Figure 7.16, with the line's thickness corresponding to the magnitude of the force as calculated using the relationships from Figure 7.13. To provide a comparison, the five internal points of this element, as calculated using the geometrical relationships in Section 7.5.1, are added to the problem. This is then solved using a fully connected ground structure of bars, and no region based elements, and the resulting structure is shown in Figure 7.17.

The structures of Figure 7.16 and Figure 7.17 are identical in volume. Furthermore, the areas of all bars, with the exception of A1, A2, B1 and B2, are identical in the two structures. In this case, the bars A1, A2, B1 and B2 are co-incident with the bars of the adjacent fan region, but this will not be the case for arbitrary nodal positions. The area of the bars in Figure 7.17 which are in the location of bars A1, A2, B1 and B2 have an area which may be calculated as follows: take the area of the (dotted) member from the four node region, and subtract it from the area of the co-incident bar from the adjacent fan region.

Whilst this allows us to construct the correct solution from the result of Figure 7.16, it is less clear how this may be applied if there is not an exactly corresponding member (i.e. if the intermediate nodes based calculated from the fans differ from those calculated from the four node element), furthermore, this does not provide a satisfactory physical interpretation. To address this, derivations based on the kinematic form are presented in Appendix C.3.5.

## 7.6 Discussion

This chapter has presented a novel method for numerically identifying Michell structures consisting of a number of regions. This has allowed solutions with volumes within a fraction of a percent of known analytical values to be obtained numerically. However, these results have thus far been limited to solutions with fan type regions.

A more general region, connecting four ground structure nodes, would allow the vast majority of problems to be tackled. A discrete approximation of this region has been presented here, and tested on a simple Michell cantilever problem.

Extensions of the method may also extend the usefulness of the results. When a sufficiently large design domain is used, together with appropriate handling of numerical errors, the output could be altered to show fully strained regions which have zero force. This would be helpful in suggesting potential strain fields which could then be used in analytical solutions to prove their optimality.

Conceptually, this method is very simple to extend to problems with multiple load cases. This could be achieved in a similar manner to the problem with straight bars; each element is assigned a force variable for each load case, and an overall variable representing the maximum absolute force value (analogous to area variables in the standard formulation). There is significant potential for benefits in multiple load case problems due to the complex and overlapping nature of the forms. However, most known problems are too complex to be solved using the elements developed to date.

Initial studies concerning the implementation of the remaining classes of regions may be found in Appendix C. For regions of type  $T_1$  which have two boundary curves OA and OB given by circular arcs (as is very common for regions of type  $T_1$  in the literature), it is found that normalisation in the manner of Figure 7.11 leads to a similar rotational relationship to the one described in Figure 7.12. For implementation in this framework, the  $T_1$  region is the most important as it will be capable of closely approximating other regions, such as those of type  $T_2$ .



## Part IV

# Discussion and closure



# Chapter 8

## Discussion

In the previous chapters, several techniques have been proposed to address issues which could affect the uptake of structural optimization methods in practice. This chapter will discuss how the proposed methods can be used in combination, their applicability to real world problems, and potential further developments and refinements.

How the methods may be used in combination is first discussed in Section 8.1. Generally the approaches described in the previous chapters may be used simultaneously, although there are some aspects in which care must be taken. Section 8.2 discusses numerical issues encountered with the proposed formulations.

Many of the numerical issues associated with the MILP formulations could be sidestepped by use of a more direct method. Section 8.3 directly studies the solution spaces of layout optimization problems in order to develop such an approach. The importance of basic solutions is demonstrated, and vertex enumeration methods are used in order to identify them. This approach has the potential to produce Pareto fronts showing the trade off between efficiency and complexity in a single run. It is also shown that an algorithm designed to tackle cardinality constrained optimization can be successfully adapted to handle a range of complexity measures.

Section 8.4 applies methods from the previous chapters to two case studies drawn from real world problems. This shows how the methods can be used to answer the questions a designer may pose concerning the possible efficiency of a number of typical forms, as well as intermediate solutions combining such designs. A fully three dimensional example is also presented to show how these methods may be applied in such cases.

---

8.1	Combined application of the proposed methods . . . . .	134
8.1.1	Simplification of structures under self-weight loading . . . . .	134
	Symmetry, complexity and self-weight . . . . .	134
8.1.2	Regions in structures under self-weight loading . . . . .	134
8.1.3	Discretisation of solutions from RAGS method . . . . .	135
8.2	Scaling and numerical issues . . . . .	136
8.2.1	Member adding heuristics in distributed self-weight and RAGS methods . . . . .	136
	RAGS method . . . . .	136
	Distributed self-weight method . . . . .	137
8.2.2	Joint costs and $\ell_1$ norms . . . . .	138
8.2.3	Large numbers in integer programming . . . . .	138
8.3	The solution spaces of layout optimization problems . . . . .	140
8.3.1	Degeneracy and determinacy . . . . .	140
8.3.2	Mapping complexity throughout the solution space . . . . .	141
8.3.3	Vertex enumeration methods and layout optimization . . . . .	143
	Example mapped solution spaces . . . . .	143
	Partial vertex enumeration . . . . .	146
8.3.4	Complexity constrained enumeration of structures . . . . .	146
8.4	Simplification and interpretation in practice . . . . .	149
8.4.1	Two span footbridge, Problem specification . . . . .	149
	Minimum weight results . . . . .	149
8.4.2	The spectrum between traditional designs . . . . .	151
	Arches and trusses . . . . .	151
	Cable stays and arches . . . . .	151
8.4.3	Three-dimensional example . . . . .	153
8.4.4	Observations . . . . .	155

---

## 8.1 Combined application of the proposed methods

### 8.1.1 Simplification of structures under self-weight loading

The use of integer programming to identify simpler versions of structures can be easily combined with the distributed self-weight method for problems with a single load case. The curved and non-prismatic bars used in the distributed self-weight method would increase the comparative complexity of the results identified, although for everyday spans the difference in the geometry is negligible, and for slightly larger spans could potentially be considered as part of the pre-camber.

The foundations and counterweights described in Chapter 5 would also be compatible with the addition of constraints on complexity. When complexity is reduced, this generally has the effect of increasing the volume of the structural members more than the magnitude of the reaction forces; as such it is likely that the addition of complexity constraints will lead to a greater use of counterweights and anchorages when other parameters are constant. A similar effect has been observed when the complexity was restricted by the use of a coarse ground structure, see Appendix B. Furthermore, modified versions of the integer programming limits could be applied to allow only a certain number of foundation points or counterweight locations.

#### Symmetry, complexity and self-weight

Issues that arise when simultaneously considering symmetry and complexity limits were discussed in Section 6.4, and a modified constraint was proposed which could ignore joints on the symmetry plane which connected only two parallel members, such as the case shown in Figure 8.1a.

However, if the distributed self-weight method is also to be used, then these members would no longer be perpendicular to the symmetry plane, and an additional member(s) would be required to ensure equilibrium, as shown in Figure 8.1b. This problem is not specific to the distributed self-weight method, as Figure 8.1c shows, the lumped self-weight force also requires the addition of another member. Note that this problem is generally only encountered when both symmetry *and* a limit on the number of members/joints is required; otherwise the additional member added in the layout optimization phase is will often simply be removed during geometry optimization as the joint moves to the appropriate location.

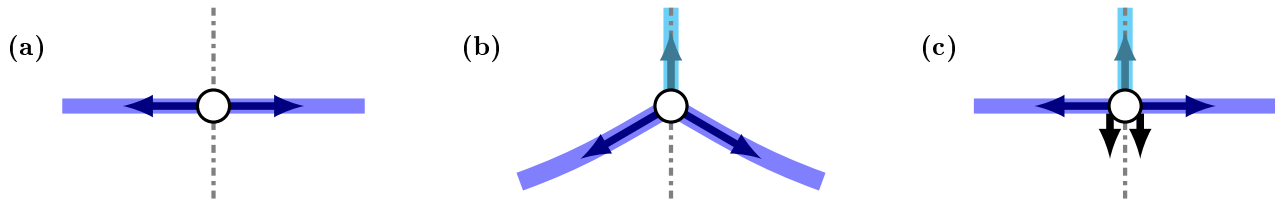


**Figure 8.1:** Visualisation of issues caused by the interaction of self-weight modelling and symmetry conditions. (a) Non-self-weight case. (b) Distributed self-weight method. (c) Lumped self-weight method.

For the distributed self-weight method, it is reasonably easy to calculate the location on the symmetry plane that eliminates the need for an additional member. This is achieved by using the equations describing the equally stressed catenary. The catenary connecting each node to its mirror image can be found, and a node added *a priori* at the point that this curve intersects the symmetry plane. If these new nodes are connected only to the node used to calculate their position, rather than being fully connected to the whole ground structure, this would imply only a moderate increase in the size of the problem ( $O(n)$ ), and could allow simultaneous consideration of self-weight, symmetry and complexity constraints.

### 8.1.2 Regions in structures under self-weight loading

To combine the distributed self-weight method of Chapter 4 with the region based method of Chapter 7, equations describing regions in known solutions subjected to self-weight would be required. Due to the lack of known solutions in the present literature, it is unclear how much of a difficulty this presents. The numerical results of Chapters 4 and 5 appear to show that structures identified using the distributed self-weight method still consist of distinct regions. For example, see the central fan type region of the bridge forms of Figure 4.4 or the doubly curved  $T_1$ -like regions of the Michell cantilevers in Figure 5.4; indeed the results for the extended design domain begin to resemble the strain fields described by Hemp (1973, fig 4.19) or Lewiński & Rozvany (2008b) in the layouts of regions, although the geometry of these is substantially altered.

Figure 8.2 shows layout optimization results of a simple problem using the distributed self-weight method. A single point load, of various inclinations, is to be transmitted to a vertical line of support. The non-self-weight



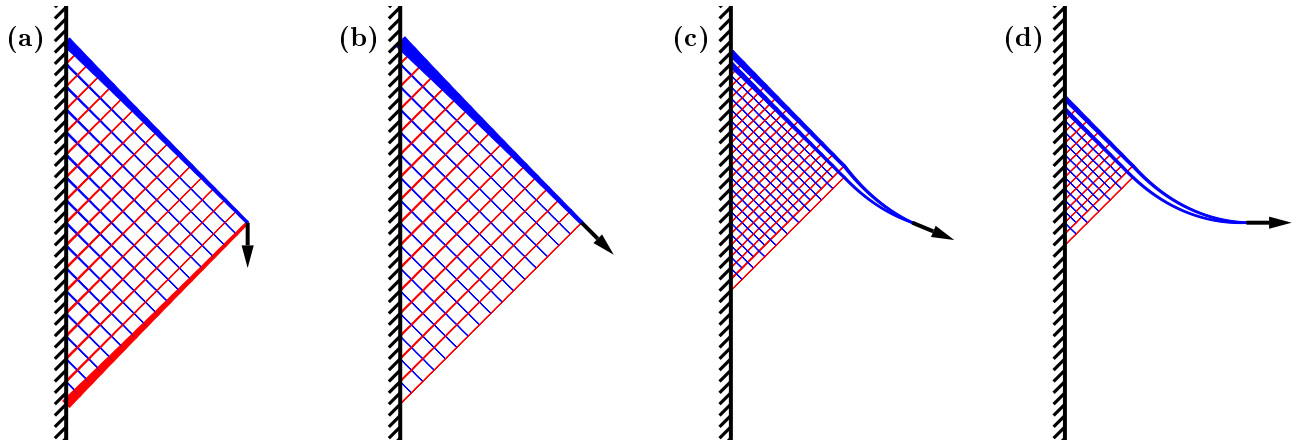


**Figure 8.2:** Solutions for a simple cantilever problem under substantial self-weight loading and a single external point load. (a) Point load vertical. (b) Point load at  $45^\circ$  to horizontal. (c) Point load at  $22.5^\circ$  to horizontal. (d) Point load horizontal.

solution consists of either two orthogonal bars, in cases where the force is less than  $45^\circ$  from vertical, or a single bar in line with the force in other cases. In Figure 8.2 it appears that a similar solution is obtained when the force is close to vertical (8.2a and b) although in order to support straight members, a dense fibrous region of variable thickness members is required. When the force is closer to horizontal, as in Figure 8.2c and d, it is initially supported by a longer catenary member, until the point where that curve of that member reaches approximately  $45$  degrees, at which point it again becomes a straight member supported by a fibrous region, as in Figure 8.2a and b.

This suggests that optimal structures under self-weight may also consist of orthogonal families of members; although the curvature of the finite length bars, and the influence of the underlying ground structure, may obscure some subtle difference. Nonetheless, in the seemingly likely scenario that orthogonal curvilinear coordinates are required, many relationships from Section 7.2.1 and Appendix C will still hold, and an extension to self-weight seems plausible.

### 8.1.3 Discretisation of solutions from RAGS method

The RAGS method described in Chapter 7 has the potential to greatly simplify the manual rationalization process, as the overall structure of the solution is much clearer. Considering how this may be automated is somewhat more complex. A simple solution involving the addition of a fixed number of nodes along e.g. the outer edge of a fan, may work well for some examples, such as the simply supported point load in Figure 7.8.

However such a strategy would be less effective when compatibility between several regions is required. For example, in the multiple span problem of Figure 7.9, it would be logical to align the radial compressive members of all the fans centred at a particular support, thereby producing solutions similar to the split pylon designs from Chapter 4. However, for equilibrium with the connected straight bars, each fan would also require a compressive member connecting to the corner point (A or P) of the fan. This would substantially limit how simple the resulting solution could be.

The problem is further complicated if multiple load case problems are considered. Whilst the RAGS method will be potentially even more valuable for interpreting results in these cases, it may be less suited to automatically producing discretised versions of the solutions. As can be seen from the results of Chapter 6, and particularly Figure 6.24, optimal structures in multiple load case problems no longer display a structure of overlapping layers when complexity limits are imposed. Therefore methods based on discretising the component regions may not be as effective.

Possibly the simplest approach for producing discretised solutions from the region based output of the RAGS method is to use the result to automatically create a customised ground structure, which could then be used with the integer programming methods of Chapter 6. In this way, fewer potential nodes and members would be required, and better solutions may be possible. In single load case scenarios it may be possible to further refine the nodal positions using rules similar to those describing the discretely approximated regions in Sections 7.3.3 and 7.5.

## 8.2 Scaling and numerical issues

### 8.2.1 Member adding heuristics in distributed self-weight and RAGS methods

The order in which potential dual constraints are added in the member adding process can have significant effects on the overall speed. In this thesis, the heuristics used for this have been based mainly on those of Gilbert & Tyas (2003); however more effective options may be available when new features such as distributed self-weight or region based elements are present.

#### RAGS method

For the RAGS method, it has generally been found preferable to consider different element types sequentially. As a demonstration, the problem in Figure 8.3 has been solved using two different heuristics to choose the elements to add. Firstly the single phase, potentially more intuitive, method is used in Figure 8.3a. All potential bar and fan elements are checked every iteration, and up to 4 members (5% of number of members in initial ground structure) and 5 fans with the highest violation are added. Using this method, 0.42s was required to find the solution. When the nodal spacing was halved, the solution could be found in 21.2s and 15 iterations.

A seemingly more efficient alternative is illustrated in Figure 8.3b. In this, the member adding procedure adds only bars until no further violation is found, i.e. the solution of the normal ground structure layout optimization problem is obtained. Only then are the potential fan elements checked and added to the problem. With this method, only 0.34s of CPU time was required for the problem in 8.3, and the problem with halved nodal spacing was solved in 7.6s and 20 iterations.

It can be seen that the first method requires less iterations to obtain the solution; the presence of the fan elements means that a more accurate virtual displacement field is obtained very quickly. Indeed, the problem in Figure 8.3a required less iterations than the same problem using only bar members (equivalent to the first seven iterations of Figure 8.3b). However, the overall CPU time required was lower when the strategy of Figure 8.3b was used, by almost two thirds for the finer nodal resolution. This is due to the reduced number of times that all potential fans must be considered, as the number of potential fans is proportional to  $n^3$ ; this difference could be expected to increase with problem size.

Future work may attempt to improve the speed of these checks. For example, parallel computing could be used to check multiple potential elements simultaneously. Alternatively, heuristics to reduce the number of potential elements checked at the early iterations may prove effective; logical candidates could include beginning with fans centred at external loads or supports, or beginning with the largest or smallest elements. Providing that in the final iteration all potential elements are checked, the use of such heuristics would not affect the rigour of the solution.

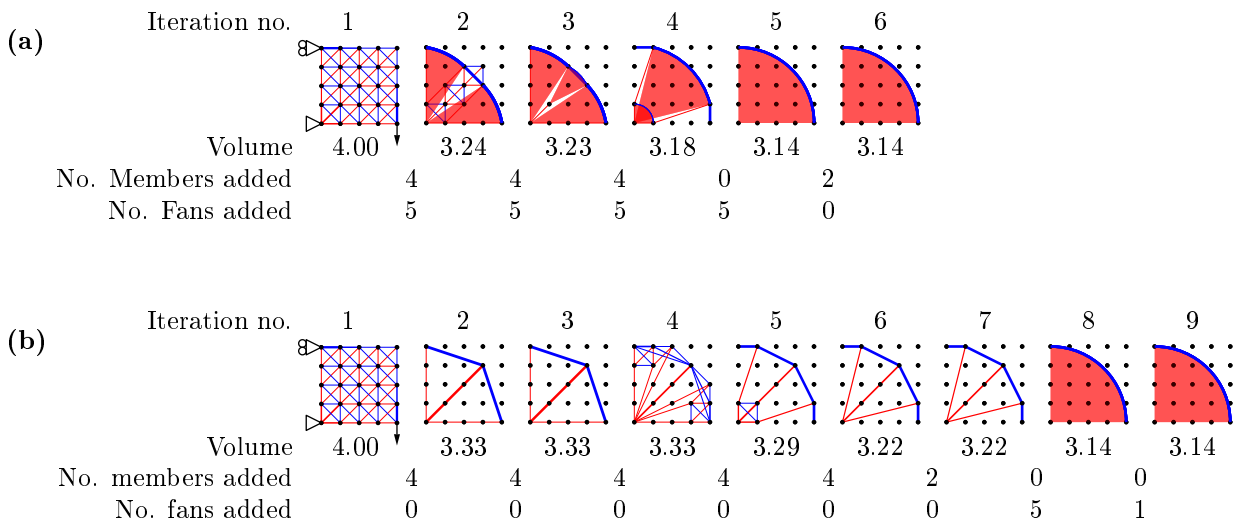


**Figure 8.3:** Comparison of heuristics for member adding sequence. Solutions are shown after each member adding iteration. **(a)** Fan constraints checked violation after every iteration. **(b)** Fan violation checked only if there are no bar members to be added.

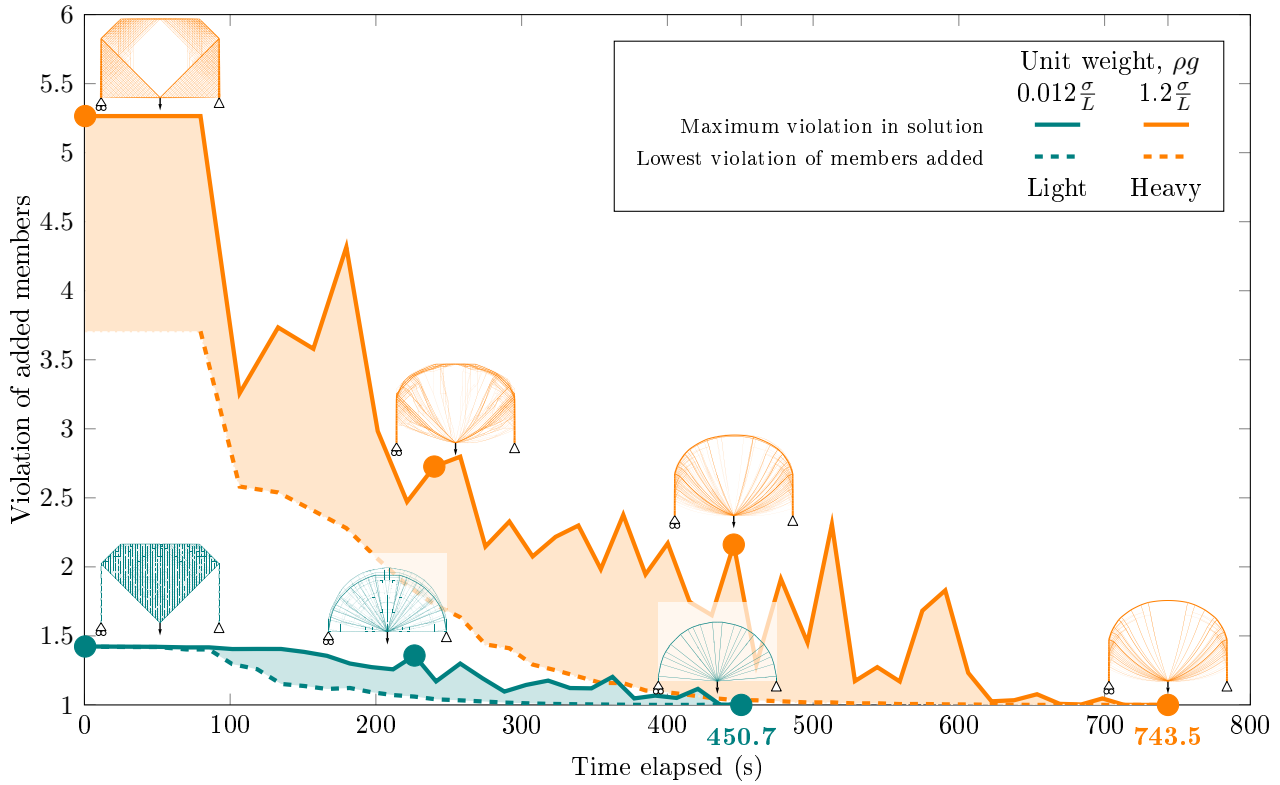


**Figure 8.4:** A comparison of the effectiveness of the member adding method with light (teal) and heavy (orange) materials. Plots show the range of values for the normalised violation of the dual constraints concerning the members added in each iteration, plotted against the time at which that iteration occurs. The corresponding structures for the points marked with dots are also shown.

### Distributed self-weight method

When self-weight is significant, heuristics used in the member adding method are often less effective. Figure 8.4 shows the results for two problems, identical other than the unit weight of the material. The problem consists of a point load, applied midway between a pair of simple supports a distance of  $L$  apart. The material has a strength of  $\sigma$  in tension and compression, and a unit weight of  $0.012 \frac{\sigma}{L}$  in the lightweight case and  $1.2 \frac{\sigma}{L}$  in the heavy case.

Figure 8.4 shows the range of values for normalised violation of the dual constraints corresponding to the members added in each iteration. The violations are normalised as in Gilbert & Tyas (2003), i.e. the normalised violation is defined as the left hand side of the constraint divided by the constant on the right hand side; this means that values above 1 imply the constraint is violated.

When the self-weight is insignificant (see the teal results in Figure 8.4) the final solution is obtained in 450.7 seconds, and requires 29 iterations. It can be seen that the final solution is very similar to the half bicycle wheel, known to be the optimal solution when there is no self-weight. However, when the self-weight is substantial (see orange results of Figure 8.4) the final structure is significantly altered; vertical towers above supports prevent the radial tension members from dipping below the base of the design domain, and fibrous domains with two families of members can be seen on the sides of the structure. This solution requires a computational time of 743.5s (65% longer than the lightweight case) and is obtained in 46 iterations.

In the lightweight case, the solution to the first iteration has a volume 27% above the final optimum, in the heavyweight case this difference is 50%. This may explain why the violations of members in the heavyweight case are so much larger than in the lightweight case.

In the lightweight case, and particularly in the early iterations, the range of violation values for the members added is very small (i.e. there are many members with a similar level of violation). However, in the heavyweight case, only a few members with the highest violations were found, and the ranges are much larger. This may be due to the fact that in the lightweight case, there are many members which are (almost) co-linear, and therefore likely to have similar violation values; in the heavyweight case these each have substantially different curvatures, and therefore the relevant coefficients are more varied, leading to a wider range of violation values.

### 8.2.2 Joint costs and $\ell_1$ norms

The use of the  $\ell_1$  norm is a common mathematical technique to seek sparse solutions (Donoho, 2006; Bach et al., 2011). Applied to the layout optimization problem, this would become

$$\text{minimise } \mathbf{l}^T \mathbf{A} + \tau \|\mathbf{A}\|_1 \quad (8.1a)$$

$$\text{subject to } (\mathbf{B}\mathbf{q}_k = \mathbf{f}_k)_{\forall k} \quad (8.1b)$$

$$\left( \mathbf{A} - \left( \frac{q_k^+}{\sigma_T} + \frac{q_k^-}{\sigma_C} \right) \right)_{\forall k} \geq \mathbf{0} \quad (8.1c)$$

$$\mathbf{q}, \mathbf{A} \geq \mathbf{0} \quad (8.1d)$$

where  $\mathbf{A}$  is the member areas,  $\mathbf{q}_k$  are the member forces for load case  $k$ ,  $\mathbf{B}$  is the geometry matrix and  $\mathbf{f}_k$  is the external loads for load case  $k$ . As  $\mathbf{A}$  is entirely non-negative real numbers,  $\|\mathbf{A}\|_1 = \sum \mathbf{A}$ , so the objective can be written as

$$\text{minimise } \sum_{\forall i} (l_i + \tau) A_i \quad (8.2)$$

However, on inspection of results obtained using this method it seems that they are similar to those found through the existing technique of joint costs developed by Parkes (1975), and used in Chapter 3. This is normally thought of as an addition to the length due to the cost of manufacture of the node, meaning that the  $\mathbf{l}$  matrix is no longer  $[l_i]$ , but instead is  $[l_i + j_{ia} + j_{ib}]$  where  $j_{ia}$  and  $j_{ib}$  are the joint lengths of the nodes at the start and end of member  $i$ . Usually, the joint lengths for all the nodes are set to be equal to a single value  $j$ , so the objective function can be written as

$$\text{minimise } \sum_i (l_i + 2j) A_i \quad (8.3)$$

Comparing this to equation (8.2) clearly shows that these formulations function in the same manner. Nonetheless it is useful to be aware of both interpretations. The engineering description can assist in interpretation and explanation of results, whilst the mathematical background provides confidence in the accuracy and efficacy of the method. Similarly the member adding method (Gilbert & Tyas, 2003), has been shown to correspond to the mathematical technique of column generation (Weldeyesus & Gondzio, 2018), and both interpretations have proved useful in adapting and extending the method.

### 8.2.3 Large numbers in integer programming

For the integer programming formulations shown in Chapter 6, the big- $M$  method was used to add flag variables for members and nodes using the equation,

$$Mw_i - a_i \geq 0 \quad (\text{see 6.2})$$

for the flag variable  $w_i$  which relates to member  $i$ . The equation

$$\hat{M}v_j - \sum_{i \in J_j} a_i \leq 0 \quad (\text{see 6.3})$$

was used for the flag,  $v_j$ , relating to node  $j$ . See Section 6.1.2 for more details.  $M$  and  $\hat{M}$  in these equations represent large numbers. In this context, large means greater than the maximum cross section of any member in the solution for  $M$ , or larger than the sum of cross section areas at any joint for  $\hat{M}$ . If the values chosen are too small, then the preceding equations become limits on the values of the cross section areas,  $a$ . In Chapter 6,  $M$  and  $\hat{M}$  were chosen, based on the imposed forces and material properties, using the relationships

$$M = 20 \frac{|\mathbf{f}|_\infty}{\min(|\sigma_T|, |\sigma_C|)} \quad \hat{M} = 4M \quad (8.4)$$

These are very conservative values, chosen such as to ensure they would not cause inaccuracies in the solution for practical scenarios.

Considering the simple structure shown in Figure 8.5, the force in member 1 is given using the equation

$$q_1 = Q \sqrt{1 + 4 \left( \frac{L}{d} \right)^2} \quad (8.5)$$

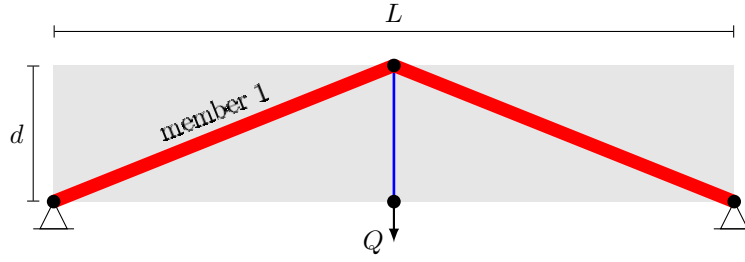


**Figure 8.5:** A simple example to demonstrate the limits of  $M$  and  $\hat{M}$ .

For the value of  $M$  given in equation (8.4) to be limiting in this example,  $\frac{L}{d}$  would need to be equal to 19.9; guidance for initial design (Ioannides & Ruddy, 2000) suggests  $\frac{L}{d}$  of 12 for steel trusses and 12 to 20 for space frames. The example in Section 6.3 has a span to depth ratio of 13.1, whilst the example in Chapter 3 has a span to depth ratio of 5. From this it is seen that the value used in equation (8.4) is conservative, but potentially not far beyond the range which may be encountered in practice.

The choice of  $\hat{M}$  as being 4 times the value of  $M$  is based on the assumption that most joints will lie on the intersection of two families of curves, as in a Michell structure. Naturally this will not always be the case, but equally, it is very unlikely that all members connecting at a joint would be of the largest size possible.

For problems where the value of  $M$  could be altered, this could have a significant effect on the speed with which the solution is found. To test this, a simple two load case problem was solved subject to a limit on the number of joints. The results are shown in Figure 8.6 for limits of 6, 10 and 12 nodes. For simplicity, crossovers were not considered here.

Clearly it is possible for the value of  $\hat{M}$  to significantly affect the solution time, with the quickest results generally being observed when  $\hat{M}$  is near to the limiting value. However, substantial increases in speed are also seen if the value of  $\hat{M}$  is chosen too low, and in this case the solution is also sub-optimal. It is difficult to know if the value of  $\hat{M}$  has influenced the solution based on only a single result. For this reason, the conservative value from equation (8.4) seems reasonable for practical usage, even if better, more problem specific, heuristics may be possible. In the future, more advanced methods to set  $M$  and  $\hat{M}$  may make use of the continuous layout optimization result to adapt the value of  $M$  to the problem.

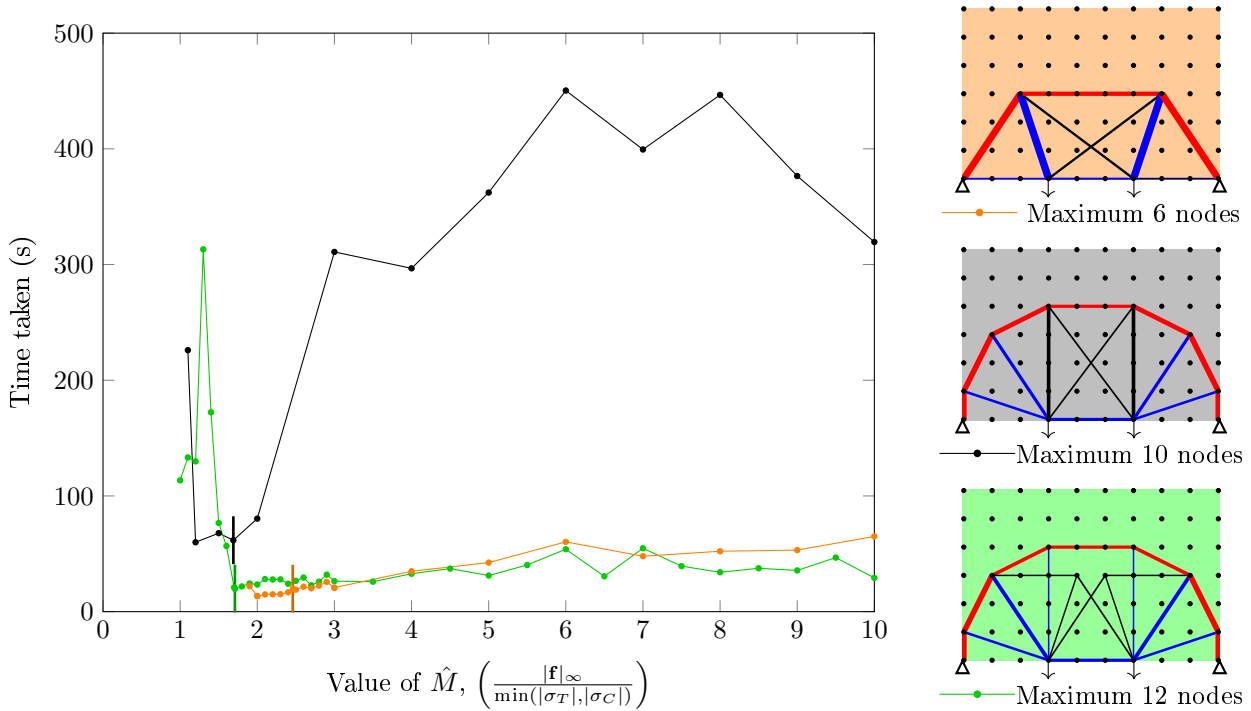


**Figure 8.6:** Variation in time required to solve two load case problem with 70 nodes using various values of  $\hat{M}$ . The number of joints in the solution was limited to 6, 10 or 12 respectively, without considering crossover points. The vertical lines indicate the point where  $\hat{M}$  becomes active as an upper limit on the sum of bar areas at a node; results with values of  $\hat{M}$  below this are inaccurate.

Physically, the values of  $M$  and  $\hat{M}$  have no obvious meaning, as is the case for the (non-integer) values of the flag variables in the initial continuous relaxation of the problem. Overall, the initial relaxation is not particularly intuitive and is also far from the final integer solution, particularly when the complexity constraints are more restrictive. MILP problems usually perform badly when the continuous relaxation is far from the final solution; for example see the rapidly increasing computational times in Figure 6.11 as more onerous minimum area constraints are imposed. To avoid this issue, methods of identifying lightweight and simple structures can be directly sought from the solution space of the original problem (i.e. without integer flag variables). In this way the need for arbitrary parameters such as  $M$  could be circumvented, and a more intuitive approach found. The next section comprises an initial investigation into this possibility.

### 8.3 The solution spaces of layout optimization problems

Studies undertaken in this thesis, e.g. see Figures 3.7 and 6.24 and Table 6.1 have suggested the solution space often contains many possible structures with volumes close to the optimal value. Many of these are likely to provide attractive options for designers, and as such methods which can identify a range of different solutions could be advantageous.

In Chapters 3 and 6 results have been presented as a Pareto front, illustrating the trade off between efficiency and simplicity. This can allow informed decision making and better understanding. However, constructing these diagrams is time consuming and cumbersome as each point has to be individually calculated. This necessitated many, very similar, optimization problems being solved. This section will consider methods by which all of the solution space may be investigated simultaneously, or as part of the same process. It is hoped that this will reduce unnecessarily duplicated computations.

One such method, based on the genetic algorithm, is the multi-objective genetic algorithm (Balling, 2006). This aims to identify a final generation of results widely spread along a Pareto front. However, as it is based on genetic algorithms, it may not identify the true optima. In this section, more rigorous methods of mapping the solution spaces are considered.

#### 8.3.1 Degeneracy and determinacy

Consider the following formulation of the single load case layout optimization problem for  $m$  members and  $n$  nodes in the ground structure, and with  $s$  supported degrees of freedom.

$$\min V = \frac{1}{\sigma^+} \mathbf{q}^+ + \frac{1}{\sigma^-} \mathbf{q}^- \quad (8.6a)$$

$$\text{s.t. } \mathbf{B}\mathbf{q}^+ - \mathbf{B}\mathbf{q}^- = \mathbf{f} \quad (8.6b)$$

$$\mathbf{q}^+, \mathbf{q}^- \geq \mathbf{0} \quad (8.6c)$$

where  $\mathbf{q}^+$  and  $\mathbf{q}^-$  are vectors of compressive and tensile member forces; other symbols are as previously defined.

The problem has  $2m$  variables and  $2n - s$  equality constraints (for the 2D case). For a non-degenerate basic solution, it is therefore expected that there will be  $2n - s$  basic (potentially non-zero) variables. If the ground structure is fully connected then  $m = \frac{n(n-1)}{2}$ .

Any member,  $i$ , of the ground structure which vanishes in the optimal solution will have  $q_i^+ = q_i^- = 0$ . Furthermore, in an optimal solution, all members which remain present can be expected to be fully stressed, i.e. to have either  $q_i^+ = 0$  or  $q_i^- = 0$ . So, if we denote the number of members in the final structure as  $\bar{m}$ , we can say that we expect the optimal solution to have  $\bar{m}$  non-zeros. Therefore we know that

$$\bar{m} \leq 2n - s \quad (8.7)$$

and that this relationship will be satisfied as an equality at non-degenerate basic solutions, and as a strict inequality at degenerate solutions. If the resulting structure is statically determinate (as is usual for single load case problems), then we can say

$$\bar{m} + s = 2\bar{n} \quad (8.8)$$

where  $\bar{n}$  is the number of joints in the final structure.

If we assume that the resulting structure uses all nodes of the ground structure, i.e.  $\bar{n} = n$ , then equation (8.8) is the equality form of equation (8.7), and the solution is non-degenerate. However, from experience, it is very rarely the case that all nodes of the ground structure are present in an optimal solution, and when additional simplification is undertaken this generally has the effect of reducing the number of nodes used even further. As such it should be assumed that all layout optimization problems are likely to be degenerate, and that seeking the most degenerate solutions is potentially a valid strategy for reducing complexity.

### 8.3.2 Mapping complexity throughout the solution space

Consider a simple problem, as shown in Figure 8.7a. For simplicity assume that the applied force is of unit magnitude, the material may be subjected to a unit stress, and the design domain is a unit square. The ground structure consists of 6 nodes, and is fully connected but with overlapping members removed. Self-weight is assumed to be negligible.

The solution space of this problem is unbounded; an unstressed member of arbitrarily large volume could be present at any of the potential locations of the ground structure. However, more interesting are the basic feasible solutions of the problem, three of which are shown in Figure 8.7b-d; these correspond to three vertices of the solution space for this problem. These three points can be used to define a plane, a 2D face of the solution space, which will now be used to allow illustration of some interesting features.

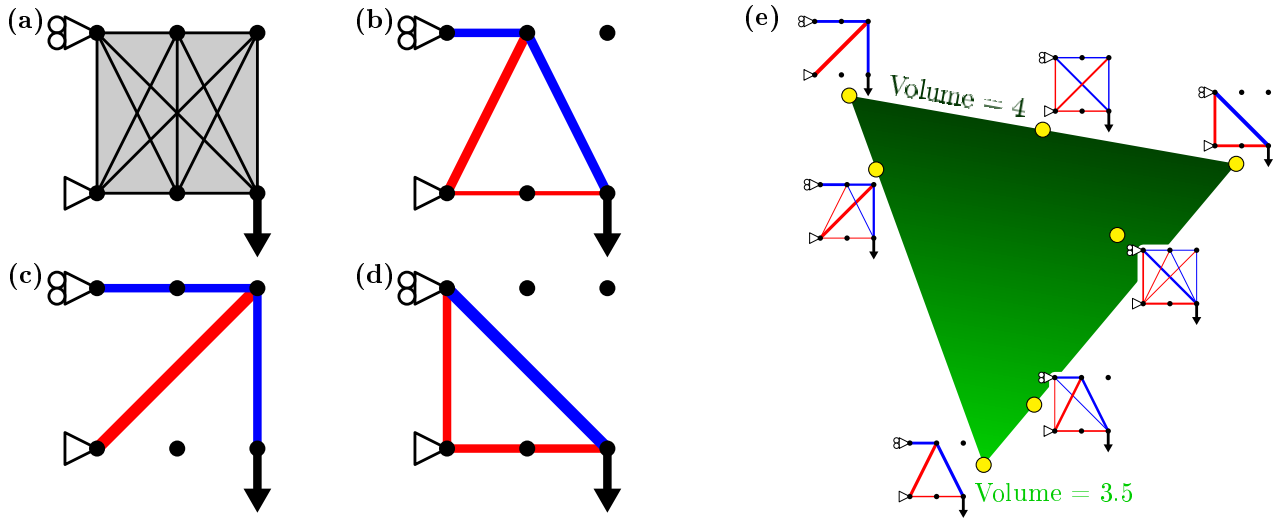


**Figure 8.7:** Square cantilever - 6 node: (a) Problem specification and ground structure. (b) Minimum volume solution, volume = 3.5. (c)-(d) Other basic feasible solutions, volume = 4. (e) A face of the solution space, coloured according to volume, with examples of basic and non-basic solutions.

The points on this plane are non-basic feasible solutions of the problem, formed by a linear combination of the three basic solutions. The volume of any non-basic solution is found by linearly interpolating between the vertices, as shown in Figure 8.7e. However, measuring the complexity of the different solutions is less straightforward.

Figure 8.8 shows the face coloured according to several possible measures of complexity, where paler colours are less complex. Figure 8.8a and 8.8c are based on simple measures of the complexity using only the number of members with non-zero area variables, and the number of nodes to which those members connect. Figure 8.8b and 8.8d use more sophisticated measures, in which crossover nodes and nodes which join only two co-linear members are correctly handled, i.e. two intersecting ground structure bars imply a total of four members in Figure 8.8b, and an additional crossover joint in Figure 8.8d; a joint which connects only two co-linear members is not counted in Figure 8.8d, and the two connected members are counted as one in Figure 8.8b. Figure 8.8e is similar to the angle measure used in Section 6.4; although in this case considering angles formed between crossing members did not lead to any results worse than those at the nodes.

Figure 8.8f shows the complexity based on the minimum cross-section area of any member in the solution. This differs from the other measures as it is not constant over each line segment or region. The minimum area becomes infinitesimal as any line is approached from within the central 2D region, or as a point is approached along an edge line. Furthermore, there are additional local minima at some non-basic solutions. Therefore this measure of complexity has the potential to cause significant additional difficulties to any simplification method based on traversing the interior of the solution space.

For the different measures shown in Figure 8.8, the location of the simplest structure is not consistent, this corroborates previous findings e.g. Figure 6.12. However, it can be observed that the simplest (palest) structure always lies on a node. This suggests that a productive approach may be to consider methods of directly identifying basic solutions, i.e. vertices of the solution space.

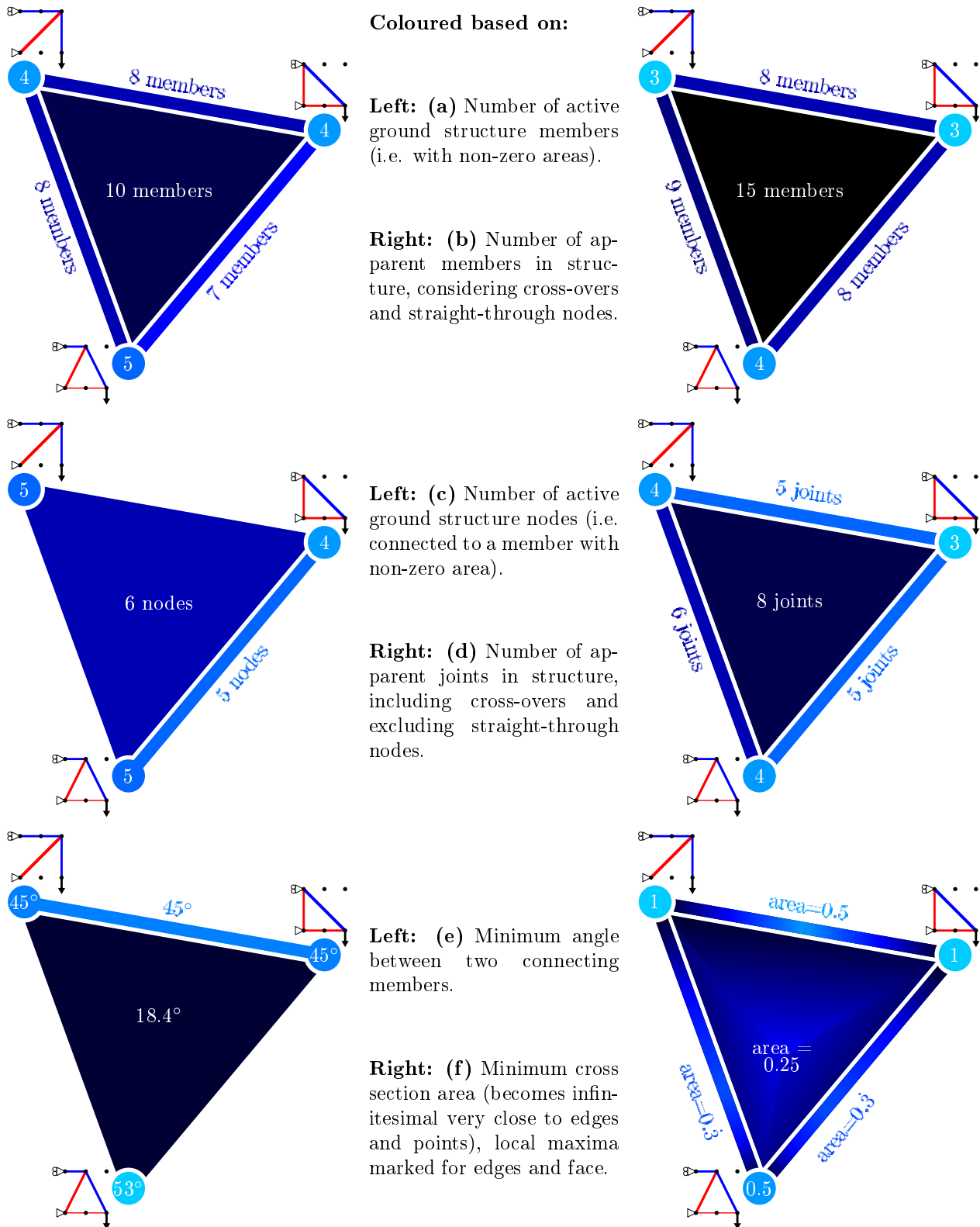


**Figure 8.8:** Square cantilever - 6 nodes: A plane of the solution space as shown in Figure 8.7, coloured based on six different measures of complexity. Paler colours represent less complex structures, and darker colours represent more complex structures. Edge lines and circles represent the 1D and 0D edges and vertices respectively and have been enlarged for visibility. Units for results on the vertices are the same as for the edges and face on the relevant sub-figure. The basic feasible solutions for each vertex are also shown.



### 8.3.3 Vertex enumeration methods and layout optimization

The vertex enumeration problem and its dual, the facet enumeration problem, are well studied problems in mathematics. They concern the conversion between two different representations of a polytope.

$$\mathcal{L} = \{\mathbf{x} \in \mathbb{R}^d : \mathbf{Ax} \geq \mathbf{b}\} \quad (8.9a)$$

$$\mathcal{L} = \{\mathbf{x} \in \mathbb{R}^d : \mathbf{x} = \mathbf{Vz} \text{ for some } \mathbf{z} \text{ where } \mathbf{z} \geq \mathbf{0}, \sum_{\forall s} z_s = 1\} \quad (8.9b)$$

where  $\mathcal{L}$  is the polytope concerned,  $\mathbf{A}$  and  $\mathbf{b}$  contain coefficients for a number of halfspaces of  $\mathbb{R}^d$ , and  $\mathbf{V}$  contains the coordinates of each vertex of  $\mathcal{L}$ .

The description in equation (8.9a) is essentially that given as the constraints in a linear programming problem. The description in (8.9b) represents  $\mathcal{L}$  as a convex combination of its vertices. The vertices, i.e. the basic feasible solutions of the linear program, are represented by the rows of  $\mathbf{V}$ , and  $\mathbf{z}$  gives a convex combination thereof. The vertex enumeration problem is to compute  $\mathbf{V}$  given  $\mathbf{A}$  and  $\mathbf{b}$ , whilst facet enumeration is the reverse, although they can be shown to be mathematically equivalent.

There are two broad categories of algorithm. The first category is graph traversal algorithms (e.g. Avis & Fukuda, 1992), which move from one vertex to an adjacent one in a similar way to a simplex pivot; the facet enumeration equivalent is the gift wrapping algorithm (Chand & Kapur, 1970). The second category is incremental algorithms, which start by constructing a simplex which contains the required polytope, and sequentially considering each half-space and using it to cut off vertices (Motzkin et al., 1953; Fukuda & Prodon, 1995).

For some algorithms, a closed polytope is required. A logical way in which this can be ensured for a layout optimization problem is to add a constraint on the maximum total volume. As the volume is a positive linear combination of all variables (for a formulation in the form of equation (8.6c)), and the variables are constrained to be non-negative, this will always give a closed space.

#### Example mapped solution spaces

To construct the solution spaces for some small scale problems, the double description method (Motzkin et al., 1953; Fukuda & Prodon, 1995) has been used. This method was chosen due to its success at dealing with degenerate problems (Avis et al., 1997) such as those from layout optimization. For the full formulation used see Appendix D.

A version of the problem in Figure 8.7, but containing a ground structure of only 4 nodes, will first be considered. The volume of the optimal layout optimization solution of this problem will be denoted by  $V_0$ . A volume limit of 10% over  $V_0$  has been imposed. The vertices of the solution space have been identified using the double description method, and are illustrated in Figure 8.9, along with the connectivity of the solution space polytope. The vertical position of each point is based on the volume of the associated structure; here all vertices have a volume of either  $V_0$  or  $1.1V_0$  (the upper volume limit). The horizontal positions of the points have been chosen for visual clarity.

Illustrations have been added to certain points to show the corresponding solutions. The two equally optimal structures are illustrated at the bottom. Each of these have seven adjacent points which lie on the upper volume limit (if the volume limit was not imposed these would be unbounded rays). Six of these correspond to increasing the size of a single bar of the ground structure without increasing the force in it. The seventh adjacent point is formed by uniformly scaling up the relevant optimal structure, including its internal forces, and adding an appropriately and inversely scaled version of the other optimal structure to ensure equilibrium at the bottom right node.

The problem of Figure 8.7 with all 6 nodes will now be considered. The minimum volume found for layout optimization in this case will be denoted by  $V_1$ . A volume limit 20% above  $V_1$  has been enforced. The vertices of the solution space are shown in Figure 8.10. Points (a) and (b) are similar to the solutions of the problem with four nodes, although due to the lack of overlapping members in the ground structure they contain 4 members rather than three. Point (c) is the solution to the layout optimization problem. Note that the triangle connecting these three points is the face considered in Figure 8.8.

The remaining points in Figure 8.10 lie on the plane of the upper volume limit. They have been horizontally arranged based firstly on which of the points (a)-(c) they are connected to (note that each is connected to only one of these points). This gives three densely connected groups of nodes. There are far fewer connections occurring between groups; each point has at most one connection to each group of which it is not a member.

The vertices are arranged such that points with the same numbers of members in their corresponding structures form a ring. Each group has 14 points in total in the inner two rings; these correspond to the relevant labelled point (a)-(c), plus one result for each of the 13 members in the ground structure, where that member has been increased in volume with no change in force.

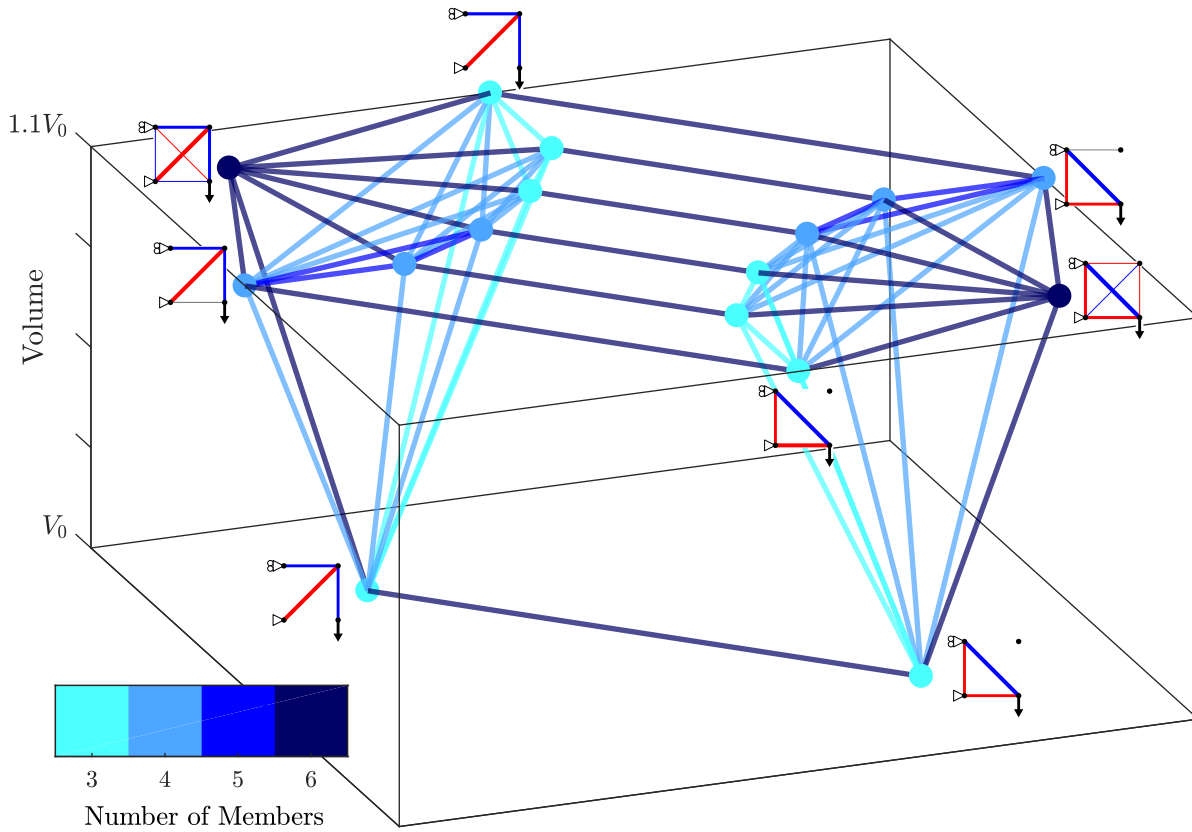


**Figure 8.9:** Square cantilever - 4 nodes: All vertices of simple 4 node problem with the volume constrained to a 10% increase over the minimum volume from layout optimization. Selected vertices are illustrated with their corresponding structures, in these grey elements carry no load. Vertices and edges are coloured based on the number of non-zero area variables of the corresponding solution.

Point (d) is based on structure (c), combined with a version of (a) with the force direction reversed. This is somewhat similar to what was observed in Figure 8.9. However the substantial difference is that the size of the bottom members is smaller in point (d) than point (c); this indicates that if there was not a volume limit this would not be an unbounded ray - it would instead form another basic solution when the bottom members had zero area.

There are few basic solutions in Figure 8.10 with 6 or 7 members. The solution created by combining one of points (a)-(c) with an additional unstressed single bar, generally cause structures with fewer members than this. Other modifying rays/edges must therefore change the internal forces, although they clearly cannot alter the external equilibrium. As such, they generally correspond to the addition of a structural segment which is in a state of self-stress; these involve a certain level of complexity. Points (e) and (f) show two such examples, where point (a) is modified by a rectangular self-stressed component. Note that either sense of the forces is possible; here, (f) would be an unbounded ray if there was no volume limit, but (e) would eventually form a new basic solution when the bottom member had zero area.

Equation (8.7) may appear to suggest that the number of members in a basic solution could be at most  $2n - s = 2 \times 6 - 3 = 9$ . This is not the case, as the addition of the volume limit increases the number of constraints, and therefore basic variables, by one, allowing for basic solutions corresponding to structures with 10 members. However, clearly the number of nodes in the ground structure has not changed; thus the solutions of the outer ring, such as point (g), are statically indeterminate.

Each edge in Figure 8.10 has an equal or larger number of members in the structure than the vertices at each end; there are no vertices, only edges, corresponding to structures with 11 members. This further demonstrates the principle seen in Figure 8.8, that complexity is smallest at the basic solutions.

Overall, there are 147 vertices shown on Figure 8.10, of which only three (i.e. 2%) are likely to be of practical interest. Much computational effort is expended to identify points lying on the upper volume limit, despite their lack of usefulness.

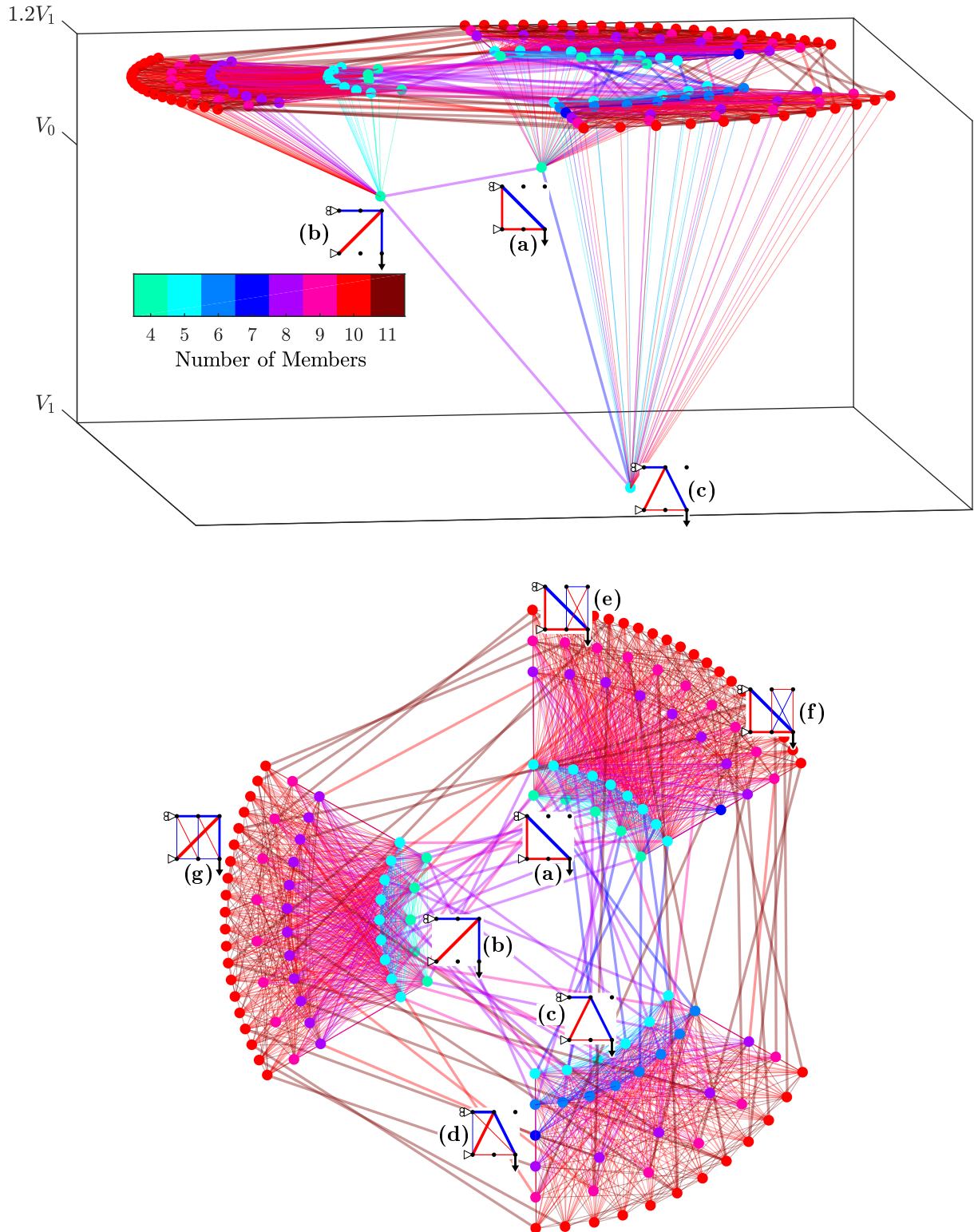


**Figure 8.10:** Square cantilever - 6 nodes: All vertices of the solution space of the problem of Figure 8.7, with a volume limit of  $1.2V_1$ . Two views of a 3d representation; where the vertical axis represents the volume of the solution and the horizontal positions are chosen for clarity. The triangle visible in the perspective view is the facet considered in Figure 8.9. Selected vertices are labelled with their corresponding structures, (a)-(g). Vertices and edges are coloured based on the number of non-zero area variables of the corresponding solution.

### Partial vertex enumeration

Using a pivoting style vertex enumeration algorithm, feasible solutions are found continuously throughout the running of the algorithm. Therefore, it is possible to terminate the process early and still obtain a gallery of feasible solutions. Through this it may be possible to observe characteristics of the solution space of a problem, even if the computational demands would be too great to allow all vertices to be found.

**Complexity measures for non-overlapping ground structures** Recall that the optimal solutions from Figure 8.9 were presented as being more complex (having more members) in Figure 8.10; this is not ideal for accurately representing the complexity of structures. Two different complexity measures will be used here to ameliorate the effect of removing the overlapping members from the ground structure. Instead of number of members, the total length of members will be used. This is calculated using the expression

$$\text{Length of members} = \mathbf{l}^T \mathbf{g} \quad (8.10)$$

where  $\mathbf{l}$  is a vector of the lengths of each member in the ground structure, and  $\mathbf{g} = [g_1, g_2, \dots, g_m]$  is a vector representing the topology of the solution, where  $g_i = \begin{cases} 0 & \text{if } a_i = 0 \\ 1 & \text{if } a_i > 0 \end{cases}$ .

Instead of joints and/or angles between members, we will use a measure of the joint complexity, defined by

$$K = \mathbf{g} \mathbf{K} \mathbf{g}^T \quad \text{where} \quad k_{i,j} = \begin{cases} 0 & \text{if members } i \text{ and } j \text{ do not meet} \\ \frac{\pi}{\theta} - 1 & \text{if members } i \text{ and } j \text{ meet at a node} \end{cases} \quad (8.11)$$

where  $K$  is the joint complexity score,  $\mathbf{g}$  is as defined previously,  $\theta$  is the angle formed by the two members  $i$  and  $j$ , in radians, in the range 0 to  $\pi$ . Note that this means that  $k_{i,j} = 0$  if members  $i$  and  $j$  are in line with one another, and therefore nodes which are only connecting two members in a straight chain make no contribution to the score.

**Example** Again consider an example similar to that in Figure 8.7. The ground structure here consists of 25 nodes and is fully connected, but with overlapping members removed (resulting in 200 members in the ground structure). A pivoting type approach is used (see Appendix D.2 for further details) starting from the solution to the layout optimization problem. Solutions with a volume greater than 4.2 ( $= 1.2V_1$ ) have been discarded, and the process is terminated once a total of 200 basic solutions were produced. The basic solutions were then evaluated using the complexity measures described in equations (8.10) and (8.11), and a constraint on minimum cross-section area. Non-basic solutions formed by the combination of two basic solutions along an edge which had been traversed have also been evaluated by these measures.

Figure 8.11 shows a plot of volume against complexity for each measure with the Pareto optimal points marked; Figure 8.12 shows the structures corresponding to these points. Most of the structures identified are significantly more complex than even the minimum volume solution. The graphs in Figure 8.11 show the pivot steps taken between the structures; generally there are several pockets of simple structures, divided by structures with higher complexity. Some examples of the more complex solutions are available in Figure D.5.

Due to these high ‘walls’ between the regions of simple solutions, there is not an obvious heuristic for choosing the next direction to search. The algorithm managed to find some solutions on the Pareto fronts quickly (4th and 6th pivot), but many of the others were only identified much later (169th and 176th pivot). Several structures which are easily manually identified to be on the Pareto front were not identified within the 200 solutions at all, such as the three member solution similar to that of Figure 8.7c. Overall, this type of method wastes significant computational resources in identifying overly complex structures.

### 8.3.4 Complexity constrained enumeration of structures

Rubin (1975) proposes a modification to the double description method to handle cardinality constrained linear programs, i.e. linear problems with an additional constraint on the number of variables which may be non-zero. The method is based on the observation that the cardinality of a non-basic solution created by combining two basic solutions, must be equal to or greater than the cardinality of each of the two basic solutions. Therefore any vertex which violates the cardinality constraint, cannot be combined with any other vertex to produce a solution which will satisfy the cardinality constraint. Thus any solution violating the cardinality constraint which is found by the double description method can be immediately discarded.

From Figure 8.8, it has been shown that many measures of complexity obey a similar relationship; indeed the number of active ground structure members is simply a cardinality constraint, applied to only the variables representing member areas. It is therefore possible to implement methods similar to Rubin’s to directly limit

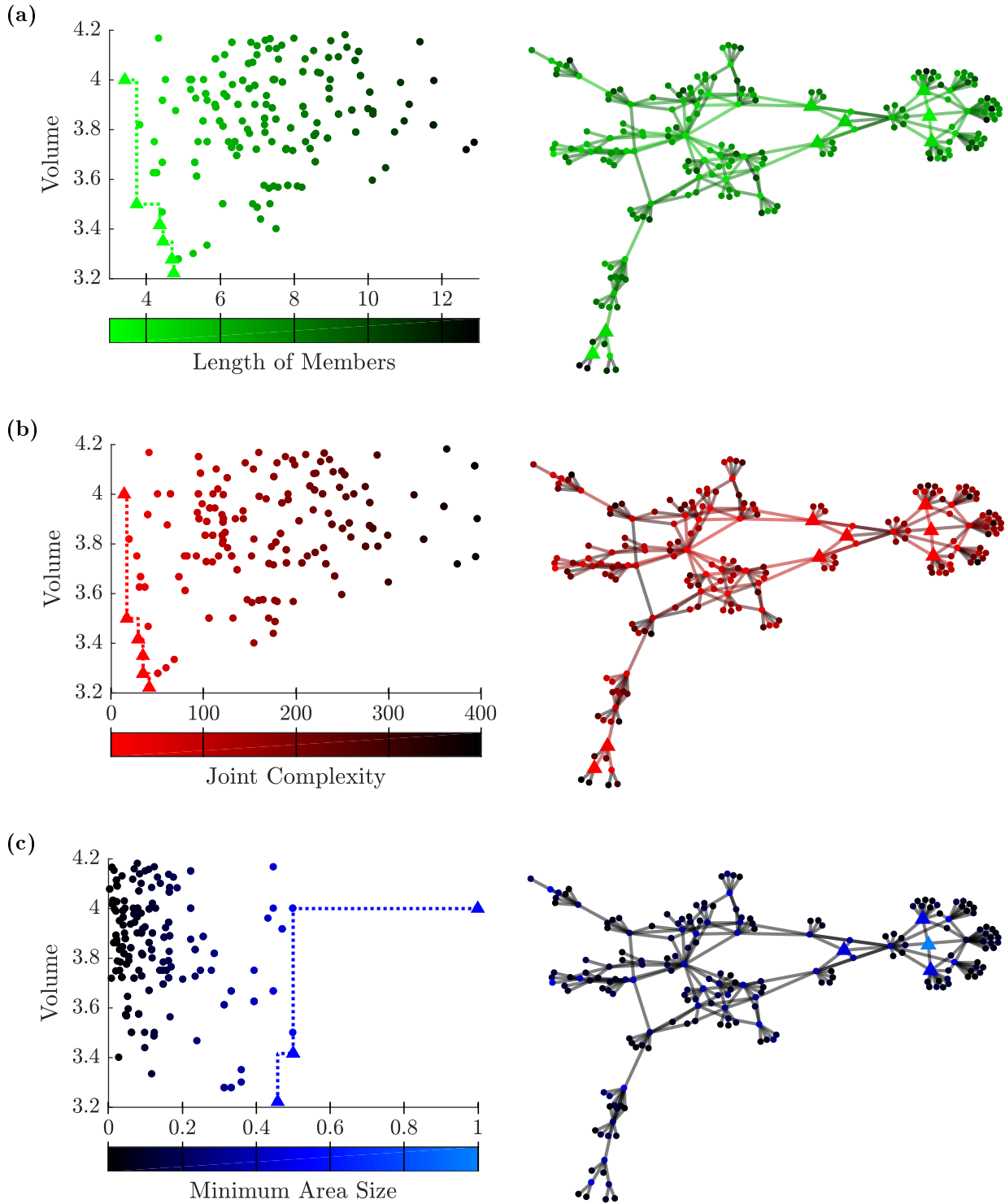


**Figure 8.11:** Square cantilever - 25 nodes: Complexity of 200 basic solutions found by pivoting type method. Left, scatter plots of volume against complexity; some points are co-incident in these plots. Right shows the graph of the points and the traversed edges, coloured using the same scale. The complexity measures used are: (a) Total member length. (b) Joint complexity,  $K$ , defined in equation (8.11). (c) Minimum cross-section area (for graph edges, the colour is based on the point at which the maximum value is obtained).

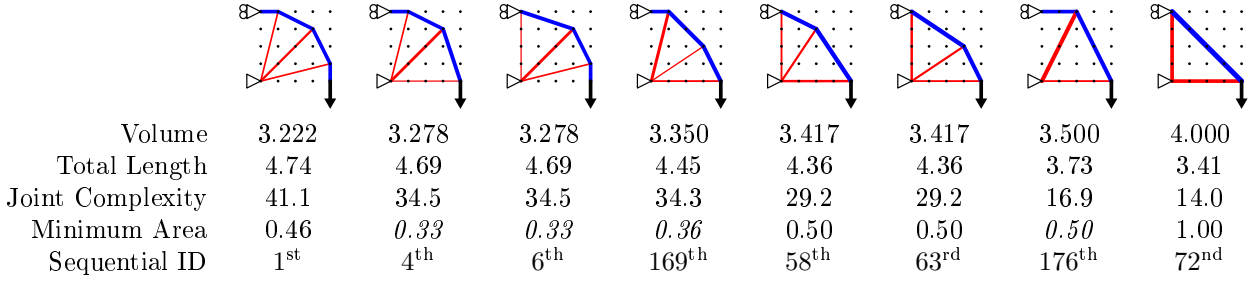


**Figure 8.12:** Square cantilever - 25 nodes: Structural forms for points on the Pareto fronts in Figure 8.11. Values for complexity measures which are given in italics indicate that point does not lie on the Pareto front for that measure.

the complexity (see Appendix D.3). Multiple limits on different measures can be set simultaneously, and adding more limits or tightening existing limits will reduce the computational cost as more intermediate points will be discarded.

An obvious level at which to initially set the complexity constraints is at the level of complexity of the minimum volume layout optimization solution. From Figure 8.11 it can be seen that this will remove a large quantity of potential solutions. This was applied to the problem considered above with a ground structure of nine nodes; the complexity limit was set based on limiting the total member length to less than 3.943 (the total length of members in the layout optimization solution). The results are shown in Figure 8.13a. A limit on the number of members was also tested; this was more complicated to compute and thus took longer to run. The results are shown in Figure 8.13b.

The method is effective at removing the structures with high complexity. However, a number of solutions with high volume were identified. These could be removed by the addition of a maximum volume constraint, but this is likely to add many new unwanted solutions. These solutions are somewhat more interesting than the spurious solutions identified by the pivoting algorithm in Figure 8.11; as the complexity is limited the structures are at least reasonably comprehensible. For example, in Figure 8.13b, structures with a volume of 9 are identified which resemble tensegrity structures (if the influence of cross-over is ignored). Whilst this structure is far from the optimal volume, it may be of interest for reasons such as deploy-ability or aesthetic preferences. Such additional value seems far less likely to occur in structures of moderate volume but un-necessarily high complexity.

This section presents only a very preliminary investigation into the potential for applying vertex enumeration methods to layout optimization. It is known that the double description method can be very sensitive to the order in which constraints are added. A wide range of layout optimization specific heuristics for choosing this may be possible; for example, beginning with members with high virtual strains or which directly connect to external loads. These could have the potential to substantially increase the computational speed.

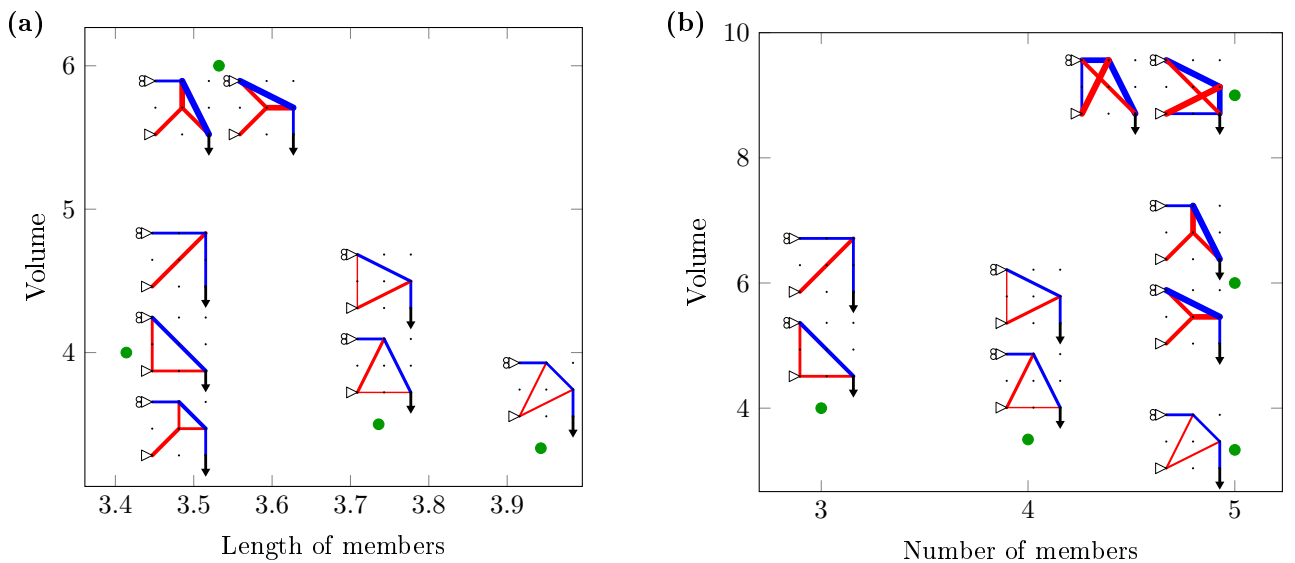


**Figure 8.13:** Square cantilever - 9 nodes: Results of modified double description method implementing complexity limits on (a) total member length or (b) apparent number of members (not considering crossovers).

## 8.4 Simplification and interpretation in practice

To test the developed methods, two real world case studies have been considered. The first focuses on the interpretation of results to assist the design team in decision making. The second is a fully three dimensional example to demonstrate the additional opportunities and challenges that brings.

### 8.4.1 Two span footbridge, Problem specification

The first case study considers the design of a two span footbridge of total length 90m. The project was in the very early stages of design, and the design team were considering three classes of solutions:

- CABLE STAYED BRIDGE, with a single central tower rising up to 18m above the high point of the deck.
- TIED (NETWORK) ARCH BRIDGE, with a height of approximately 12m above the deck, a network arch was also under consideration to better resist the effects of pattern loading.
- TRUSS BRIDGE, with a height above the deck of 2-4m, most likely to be Warren truss style

Two design domains were derived from the specified project geometries and are shown in Figure 8.14. Figure 8.14a relates to the designs of the cable stayed or arch forms, whilst Figure 8.14b is based on the geometries of the truss bridge designs. Symmetry along the centreline is desired for aesthetic reasons. For simplicity, the problem is to be optimized in 2D, although some modifications to create a full 3D design would later be needed.

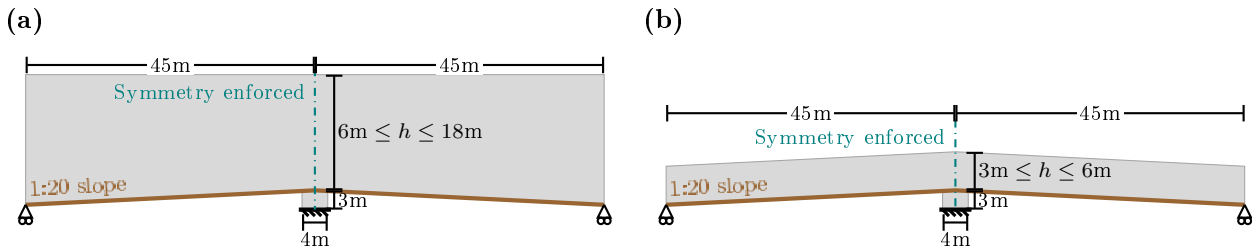


**Figure 8.14:** Two span footbridge: Design domains. (a) For cable stayed and arch type designs. (b) For truss designs.

The bridge is to be designed to carry a dead load of  $5\text{kN/m}^2$  over a 4m wide strip ( $20\text{kN/m}$ ), and a live load of  $5\text{kN/m}^2$  over a 3m wide strip ( $15\text{kN/m}$ ); with loads factored favourably or unfavourably according to the Eurocode factors, leading to a total load of  $49.5\text{kN/m}$  in unfavourable regions, and  $20\text{kN/m}$  in favourable regions. Four loading cases (some of which have an associated mirror image case which is handled implicitly) have been identified for the initial design phase:

- Case 1 - All loading factored unfavourably.
- Case 2 - One span loaded favourably and one un-favourably.
- Case 3 - Outer halves of each span factored un-favourably, and inner halves factored favourably.
- Case 4 - Inner half of one span loaded un-favourably, other loads factored favourably.

The bridge was to be supported on a central piled foundation, capable of resisting vertical, horizontal and moment loading. At the ends, it was to be supported only vertically to allow for the presence of a movement joint. It is to be constructed from S355 steel, and the allowable compressive strength was taken to be half the allowable tensile strength. No further consideration was made for buckling in the optimization as it was assumed that two 2D structures would be connected at high level to improve out of plane buckling resistance.

### Minimum weight results

It is common in very early stages of structural design to consider only the dominant load case explicitly. For example, cable stayed, suspension and arch structures are all primarily designed for a uniform loading. The minimum volume structure for the uniform loading case is shown in Figure 8.15a and b. This includes loading from self-weight; both the distributed and lumped methods were tested, producing volume increases of 0.886% and 0.882% respectively over the case where self-weight was taken as negligible. The layouts for the two different methods of modelling self-weight are minor here; longer spans would increase the disparity.

The single load case optimum resembles a combination of arch type regions with a fan/cable stayed type region providing continuity over the central support. Notice that this is substantially different to the results for infinitely many spans considered in Chapter 4, and much more closely resembles forms found for bridges of



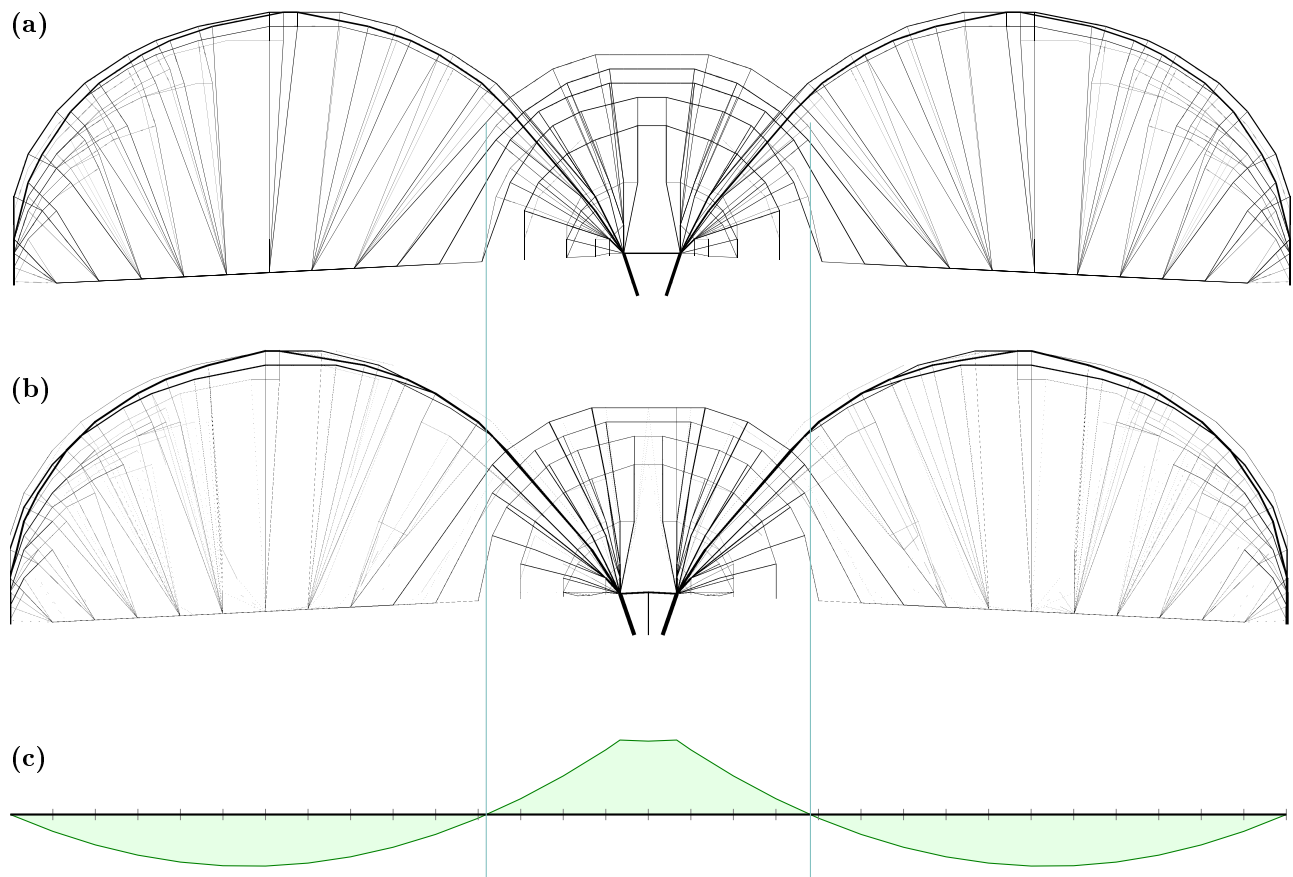


**Figure 8.15:** Two span footbridge: Single load case results. **(a)** Minimum volume structure with distributed self-weight. **(b)** Minimum volume structure with lumped self-weight. **(c)** Bending moment diagram of a beam under the same loading and support conditions (projected to a horizontal line).

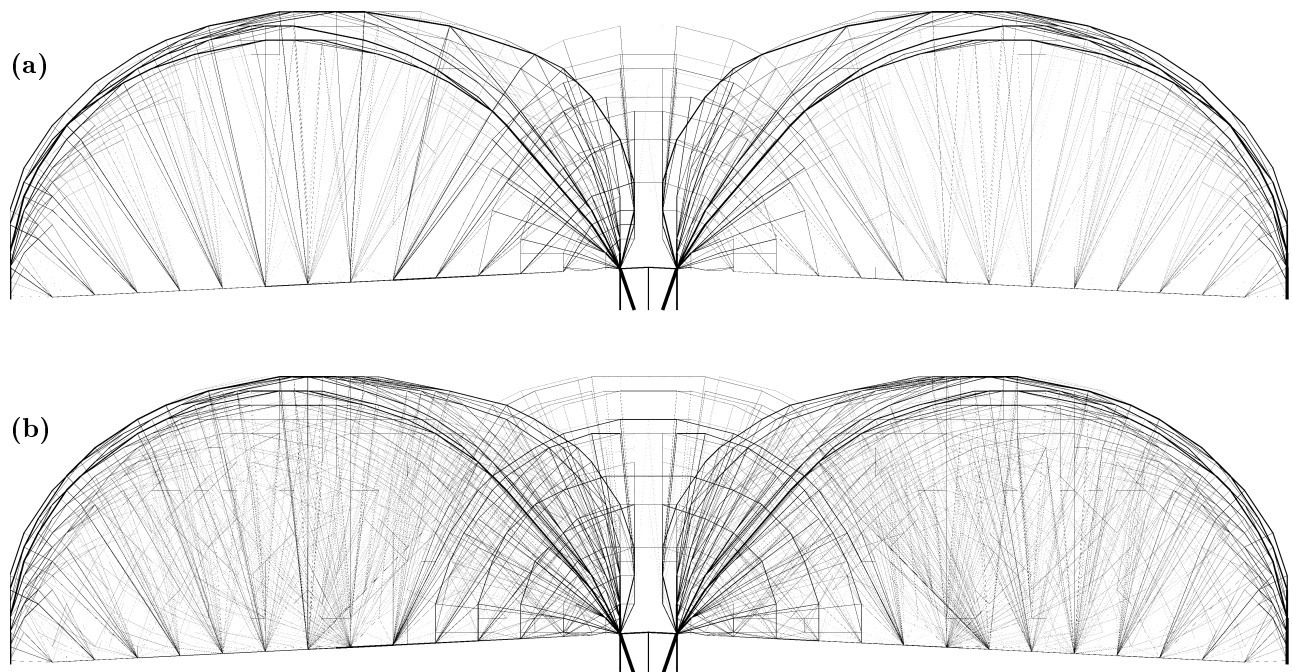


**Figure 8.16:** Two span footbridge: Multiple load case results. **(a)** Minimum volume structure for load cases 1 and 2. **(b)** Minimum volume structure for all load cases (1 to 4).



finite length in Chapter 5. The bending moment diagram for a horizontal beam subject to the same loading and support conditions as the deck of the bridge is shown in Figure 8.15c. The point of zero moment approximately corresponds to the point at which the arches overlap with the topmost of the cable stays; this could provide a useful and intuitive rule of thumb to adapt this hybrid design to other scenarios.

In the single load case problem of Figure 8.15, each point under the arch region is supported by a fan of cables. These fans are narrow, and generally do not interact with adjacent fans until they reach the outer compressive members. Figure 8.16 shows the minimum volume structure for multiple load case scenarios. When more load cases are added, the fans of cables become wider and begin to overlap; the structure now begins to resemble a network arch. The arch also deepens, particularly in the central half, generating pseudo-bending resistance.

The addition of the pattern load cases requires a volume increase of only 3.89% and 4.98% respectively for the solutions in Figure 8.16a and b when compared to the solution of 8.15b.

### 8.4.2 The spectrum between traditional designs

To evaluate the efficiency of the different categories of structures under consideration by the design team, additional constraints are added to push the result towards the desired solution.

The initial minimum weight structure appears most similar to the arch type, although the height used is closer to that of the cable stayed design. Additionally, the optimized design has additional continuity over the central support; if this continuity is removed, the volume increases by 16%, and the resulting design is shown in Figure 8.17 (note that this solution makes use of members on the symmetry line, but that these do not allow force to pass between the two halves).

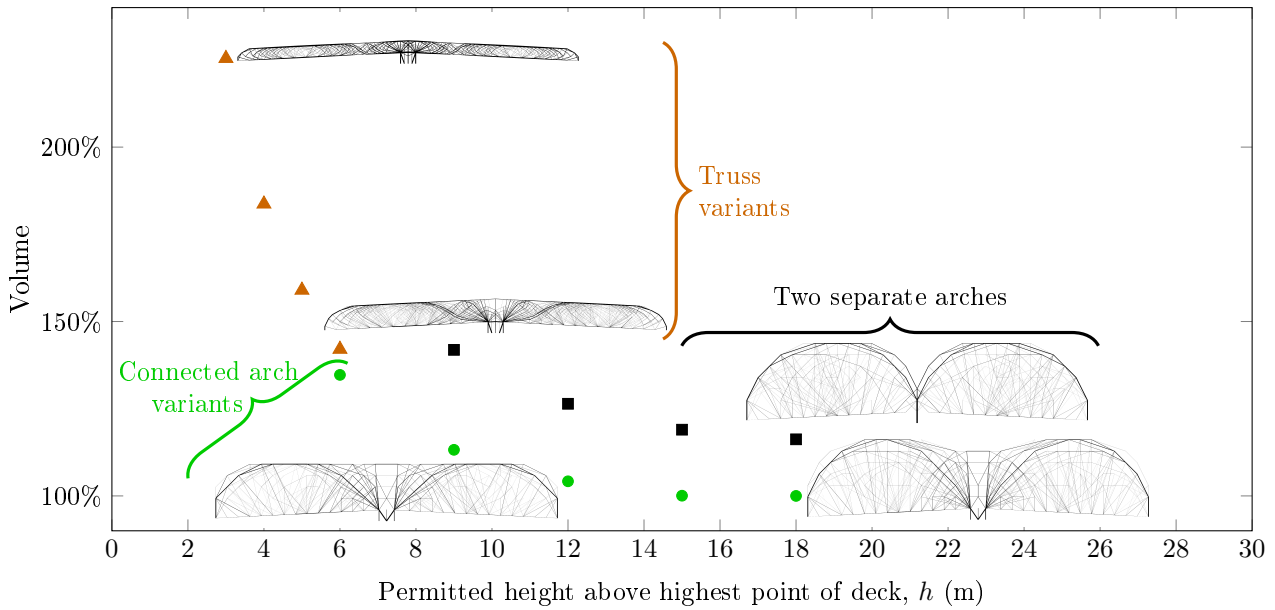


Figure 8.17: Two span footbridge: Intermediate structures between truss and arch designs.

#### Arches and trusses

To test how efficiency changes between the optimized, arch and truss designs, a parametric study of the height of the available design domain was performed. All four load cases were included, and the two geometries of Figure 8.14a and b were used for arch and truss results respectively. Results for two separate arches, without allowing continuity over the central support, were also calculated.

The results can be seen in Figure 8.17. It is evident that the shortest truss solutions are over twice the weight of the optimal structure. However, the tallest truss has a volume comparable to those of the separated arch solutions. Indeed, a continuous truss of 6m height has almost the same volume as two arches of 9m height.

#### Cable stays and arches

To find a progression between cable stayed type structures and the optimized arch type form, integer programming was used to impose a limit on the number of joints. A fan type cable stayed bridge has only a single joint which is not located on a joint or external force (i.e. essential node locations).

This limit was initially imposed on the problem using all four load cases, resulting in the structure shown in Figure 8.18b. Whilst this initially appears to be a cable stayed bridge, closer inspection reveals that the outer ‘cables’ are actually long struts. This is driven by the forces in load case 2 (where only a single span is loaded), and the internal forces relating to one such force in this load case are illustrated on Figure 8.18b. The force is carried up the cable to the top of the tower; the vertical load is then transmitted directly to the central foundation, but the horizontal component remains. It may seem logical for this to be dealt with using a tensile tie to make use of the increased strength in tension; this is shown using dotted arrows in Figure 8.18b. However, the horizontal force cannot be supported at the outer ends, and would result in a compressive force being transmitted the whole way through the deck. The optimal result actually balances the horizontal force using a compressive strut, on the same side as the applied load, this puts a tensile force into the deck, although over a much shorter distance.

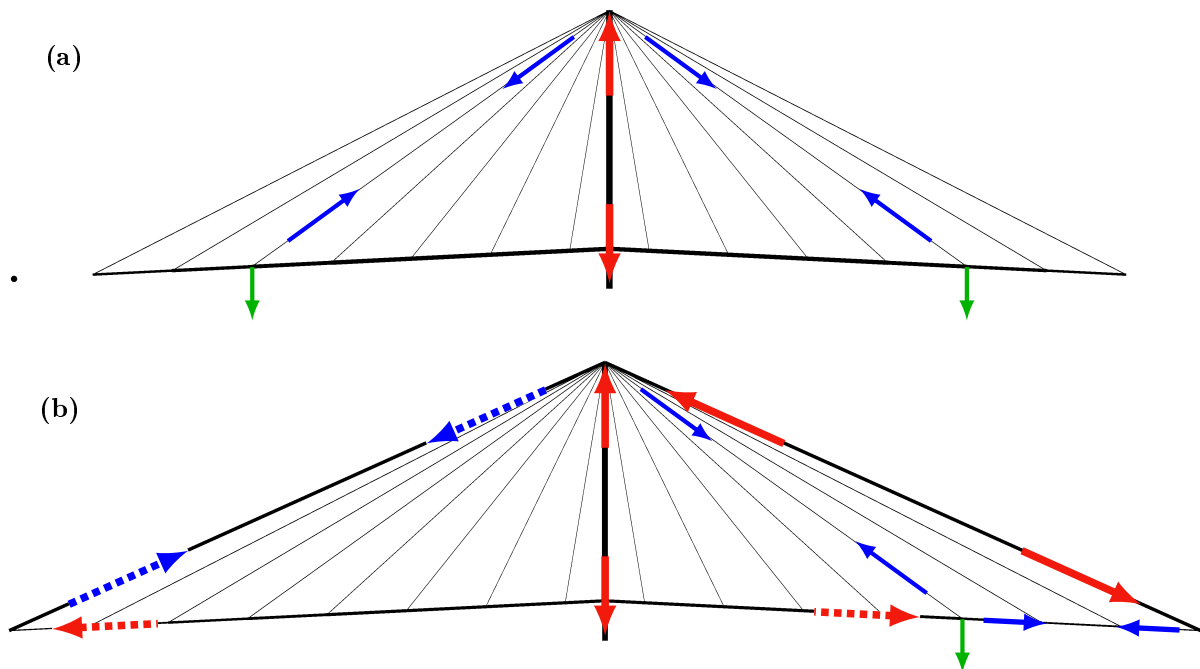


**Figure 8.18:** Two span footbridge: Structures with one non-essential node. (a) Single load case result, note that no cable connects to the outer support. Overlaid with the load path of one pair of imposed loads. (b) Resulting structure from optimization with 4 load cases, overlaid with load path of one of the loads applied in load case 2 (only one span loaded). The dotted arrows show an alternative, non-optimal load path.

In the single load case scenario, the simplest possible structure is indeed a self-anchored cable stayed type structure, shown in Figure 8.18a. When only the symmetrical loading case is considered, the loads balance at the top of the tower, and the deck forces are purely compressive. In this case, the outer supports are not connected to the structure at all, meaning that the structure is inherently unstable as a pin jointed truss and would rely on the bending resistance of the central tower. However, this does allow for a gallery of designs showing the transition from a cable stayed type design to an arch type design. This is shown in Figure 8.19.

Both the standard fan cable stayed form and a split pylon fan variant are identified for low numbers of joints. At higher numbers of joints, connected arches are again found, with many cables connecting to the arch at a single point. These results contain less noise and fewer overlapping members than the results of Figure 8.16; this improves the intuitiveness of the structures. However, solutions where many cables need to be connected at a single point may come with their own practical issues.

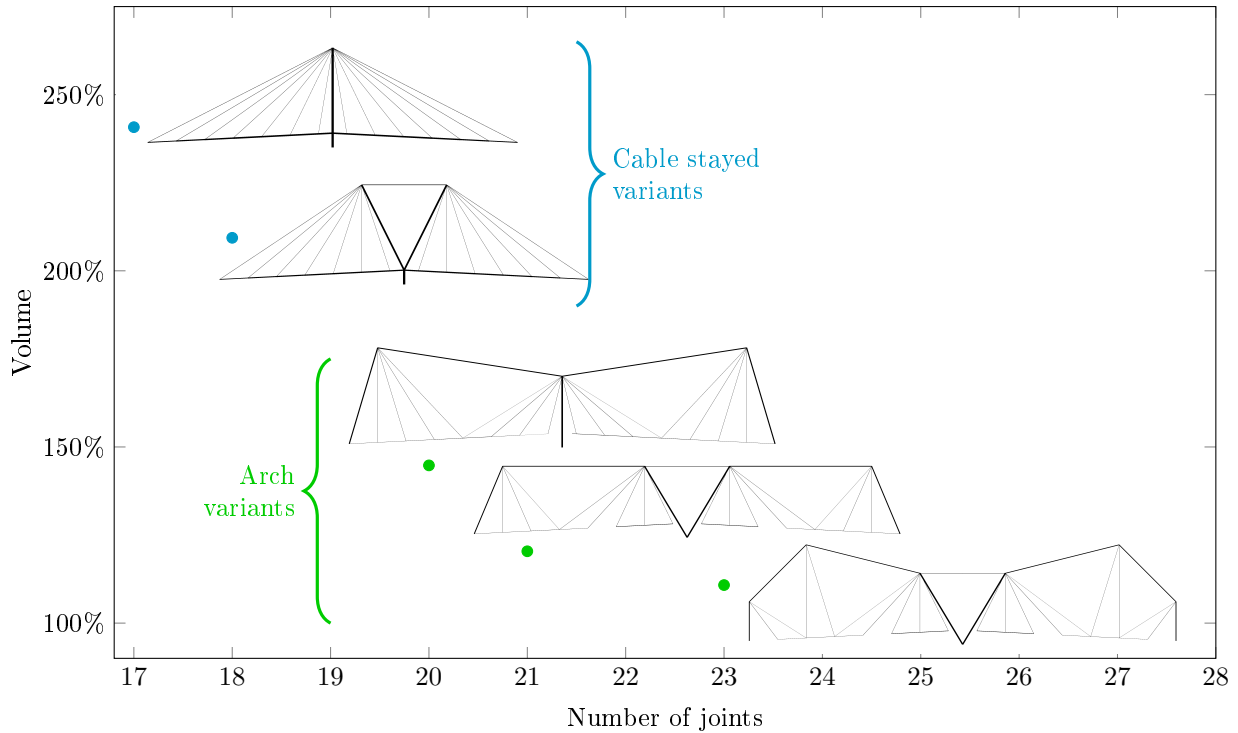


**Figure 8.19:** Two span footbridge: Intermediate structures between cable stayed and arch designs.

### 8.4.3 Three-dimensional example

Most the methods presented in Chapters 4, 5 and 6 are, at least conceptually, trivial to extend to 3D cases. In truly three dimensional problems (i.e. those which are not simply an assemblage of planar structures) interpretation of the results can be very challenging. To demonstrate this, an example problem has been developed from a real world project.

The project concerns the design of a canopy roof. The majority of the roof consists of a series of parallel planar trusses. In one section these are essentially tied arches of span 64m. In the adjacent section, the columns are moved closer, giving a 42.7m central span, and cantilevers of 10.6m off each side. The section shown in Figure 8.20 shows the area where the form changes between these two regions; this is the region which will be considered here. The design is loaded by the cladding purlins at the points indicated. The loading applied to each region is as given in Table 8.1.

The structure is to be symmetrical about the plane marked in Figure 8.20; this implicitly considers the reflected versions of the load cases described in Table 8.1. The layout optimization result using a ground structure with 64 nodes in one half of the domain is shown in Figure 8.21a, this solution is very complex and presents difficulties for both interpretation and construction. Limits on the number of joints will be imposed using the MILP method in Chapter 6 to achieve simpler and possibly more interpretable designs. To avoid the issues illustrated in Figure 8.1, self-weight of the truss was not considered.

Figure 8.21b shows the resulting structure when only 18 joints are permitted (i.e. only the loaded or support locations) and crossover members were prevented using the lazy constraints method from Section 6.4. It broadly consists of two arches (red), balanced by an external tension ring (pale blue). The two long slender members crossing the base of the design domain (dark red) are in compression, allowing the outermost forces to cantilever out.

Figure 8.21c shows the optimal structure containing 19 joints; as this is only a single extra joint, it clearly must lie on the symmetry plane. When 22 joints are permitted, the optimal structure is as shown in Figure 8.21d. Both Figure 8.21c and d can be broadly interpreted as mainly comprising two inclined tied arches (red and pale blue), with the outer loads cantilevering from this (dark red and blue), and transverse struts (pink) to ensure equilibrium of the inclined arches.

The volumes of each of the structures is shown in Figure 8.21e, compared to the volume of the layout solution of the same problem, which contains 69 joints. It can be seen that the simplest solution has a substantial volume penalty, whilst by adding only four additional joints, a solution within 7% of the layout optimization solution is obtained. This solution is also far simpler to interpret than the that found using layout optimization.

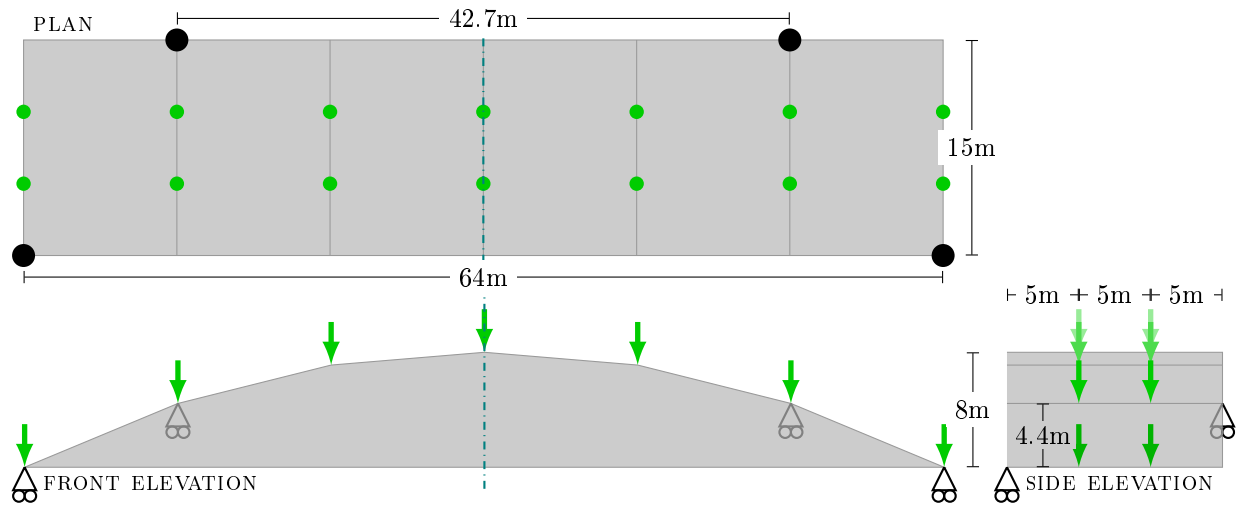


**Figure 8.20:** 3D transfer truss example: Design domain

	Left third	Central third	Right third	
LC1	7.04kPa	5.69kPa	6.29kPa	All loading unfavourable
LC2	7.04kPa	0.65kPa	1.40kPa	Left unfavourable, central and right favourable

**Table 8.1:** 3D transfer truss example: Load case definitions.

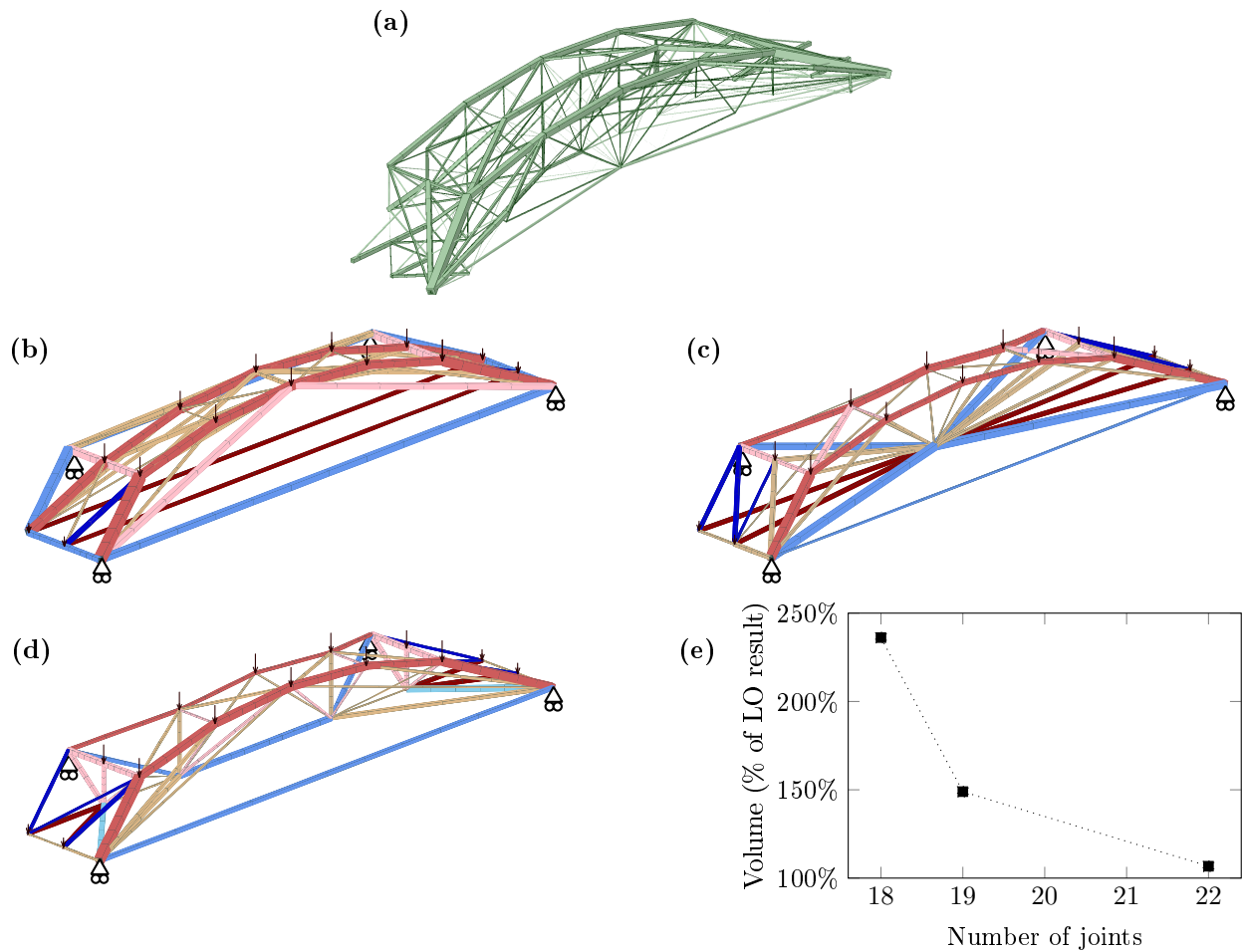


**Figure 8.21:** 3D transfer truss example: Solutions with limited numbers of nodes, manual colouring based on a possible conceptual interpretation of the structure. Limited to (a) 18 joints, (b) 19 joints, (c) 22 joints.

#### 8.4.4 Observations

In this section, the methods proposed in this thesis have been applied to real-world problems. This has led to a number of observations which may provide guidance for future users.

The example shown in Section 8.4.1, has spans of 45m, this would be a fairly long span in the context of building design, although within the context of bridge design it would likely be considered to be a short or medium span length. In this case, the inclusion of self-weight made only a small difference to the overall volume of the resulting structure ( $<1\%$ ). The difference between the distributed and lumped self-weight approaches was even smaller (0.004%). This suggests that explicit consideration of self-weight may be necessary only for long span bridge design. However, as increasing levels of rationalization will increase the magnitude of the self-weight loads, explicit self-weight modelling may become necessary at later design stages for a wider range of problems.

A fan type cable stayed bridge was identified as the optimal result when a severe restriction on the number of joints was imposed. Difficulties were encountered when applying this to the multiple load case problem; this is due to the fact that traditional forms are often designed for a single primary load case, and would resist secondary load cases by the use of bending resistance. Pseudo-bending resistance was observed in standard layout results in Figure 8.16, but the associated increase in complexity means this is not possible when limited numbers of members are permitted. Clearly, adding moment resisting members and joints would increase the difficulty of construction; although how this increase compares to the complexity caused by including additional members is difficult to quantify. Therefore, for practical application, it may be useful to compare a number of models with different assumptions to obtain a more complete understanding of the potential solution and to improve confidence in the proposals.

Interpretation of 3D problems still requires some manual interpretation. This is additionally complicated by the lack of truly 3D examples of traditional structural forms. Nonetheless, as shown in Figure 8.21, structures simplified through the use of integer programming constraints are far easier to interpret than those of simple linear layout optimization.

Although many problems in structural design are three-dimensional, they are often divided into essentially two-dimensional sub-problems. This can be seen in all the real world projects considered in this thesis, the problem of Chapter 3 was split along planes defined by internal walls, the problem in Section 8.4.1 was predominantly one way spanning and therefore to be formed from two planar structures. Although the problem considered in Section 8.4.3 was volumetric, the solution was primarily found to consist of two inclined arches; additionally, the remainder of the project was mainly formed of repeated planar trusses. Therefore, with appropriate decomposition of the design problem, the challenges of application to 3D cases may be mitigated due to the small scale of regions which will be considered in a truly three dimensional manner.



# Chapter 9

## Conclusions

This study has focused on delivering powerful layout optimization-based design tools that enable practitioners in structural engineering design to make informed decisions and obtain candidate design solutions that are both efficient and feasible.

1. For scenarios based on real world problems, it has been found that designs similar to those used in practice may require up to 2.3 times as much material as the theoretical minimum volume design. Even when simplified designs, developed from the benchmark, are considered, the more traditional design for the considered problem still requires 65% more material.
2. A novel method of accurately modelling the self-weight of a structure has been developed. This eliminates the non-conservative errors that are caused by the standard lumped self-weight method. The new method uses ground structure members in the form of equally stressed catenaries, with arching compressive members and sagging tension members. In this way, the self-weight is modelled as a distributed loading throughout the structure, allowing accurate benchmark results to be obtained for any span length.
3. The distributed self-weight method has been applied to the conceptual design of a very long span bridge. The benchmark designs obtained are significantly different to the standard cable stayed and suspension forms generally used in practice. It was found that, for a span of 5km, a cable stayed form required at least 38% more material than the benchmark, whilst suspension forms required at least 70% more material (potentially significantly more for the geometries typically used in practice).
4. Due to the complexity of the benchmark designs, they have been used as inspiration for simplified designs. These novel layouts make use of split pylons instead of the standard vertical pylons used in suspension and cable stayed designs. The proposed layouts typically require only around 5%-10% more material than the benchmark result.
5. The layout optimization method has also been extended to allow modelling of unstressed point masses. This approach can be combined with the distributed self-weight formulation to accurately model long span structures incorporating counterweights, anchorages or abutments.
6. To usefully model designs where anchorages or abutments are used, a support type based on frictional planes has been proposed. This allows for comparisons to be made between ground anchored and self anchored solutions. Application to the design of a simplified bridge problem demonstrated that for very long spans it is likely to be advantageous to make use of ground anchorages, rather than to adopt a self anchored design.
7. A number of different combinations of vertical and frictional supports were tested, and rationalized designs were again manually produced. These novel forms included an asymmetric split pylon layout, and a hybrid tied arch and split pylon layout. These forms provided a compromise between the very high volumes required for self anchored designs, and the large horizontal reaction forces required for fully ground anchored designs.
8. Manually producing simplified structures is time consuming. Therefore integer programming has been used to impose constraints designed to increase buildability. When limits were imposed on the minimum member cross-section area or on the number of joints in a structure, low correlation was found between these two measures of complexity. However, good correlation was observed between the number of joints and number of members in a structure; this is particularly useful as limiting the number of members was

amongst the most computationally challenging approaches, whilst limiting the number of joints was one of the most computationally inexpensive.

9. When limiting the number of joints, or limiting the angles between connected members, it is necessary to consider the joints formed by intersecting members in order to produce meaningful results. The use of so-called lazy constraints was found to be efficient in tackling such problems within an MILP framework, and reduced the required CPU time by a factor of 20.
10. For very simple structures with few nodes, it is possible to exhaustively consider all possible solutions. It was shown that for such structures multiple solutions may be equally optimal, and the optimal solutions can form a non-connected set. However, in most of the simple cases considered, the non-convexity of the problem was low in the vicinity of the optimal solution (i.e. among solutions with similar nodal locations).
11. The MILP approach was combined with a geometry optimization post processing step. In many cases this allowed results to be obtained that agreed with analytically derived results from the literature.
12. It was found that presentation of results as a Pareto front of complexity against material usage provided an effective means of assisting designers in making informed decisions. This allows easy visual comparison between options and can also be used to estimate which structures are likely to be optimal in terms of cost. However, each point along the Pareto front requires a separate optimization run.
13. It has been demonstrated, for a number of common measures of complexity, that the simplest structures occur on vertices of the solution space. As such, many potential structural options can be considered simultaneously by using vertex enumeration methods, which give the ability to rapidly generate complexity vs. efficiency Pareto fronts in a single run. Furthermore, it is possible to directly impose complexity constraints within a modified double description algorithm, and within this framework the computational difficulty is reduced when adding more complexity constraints.
14. A novel method for producing more easily interpretable results has also been proposed. The Region based Adaptive Ground Structure (RAGS) method produces structures that are described in terms of regions, similar to the outputs of analytical methods. When this method is employed the solutions are likely to be easier to interpret, this will also simplify communication between members of the design team. It also suggests how the optimal family of discretised structures should be formed, greatly simplifying the manual rationalization process.
15. The RAGS method has allowed numerical results to be obtained that are within a fraction of a percent of known optimal volumes. This will be beneficial in validating analytical results, as will the suggestion of the forms of regions that should be considered. As such this method can be useful for both academics and practitioners.



# Chapter 10

## Suggestions for future work

A number of potential avenues that would merit further investigation have arisen during this study.

**Self-weight with multiple load cases** The distributed self-weight method introduced here is limited to the consideration of single load case problems. Extending the method to treat multiple load cases is however not straightforward as, unlike when self-weight is negligible, members that are unused in a particular load case are still required to carry a load: the bending from their own weight. Indeed, the load case where no external loading is applied anywhere can be an important concern when self-weight is significant.

A further extension could be to allow multiple scenarios where the self-weight loading acts in different directions. This would be most obviously relevant to aerospace applications, but could also have uses in designing buildings to resist horizontal accelerations from earthquake loading.

**More accurate geotechnical modelling of supports** The frictional supports proposed here have demonstrated that the use of typical pin and roller supports can produce unrealistic results. However the frictional supports are still rather simplified, and greater benefits may result from more accurate modelling of the ground conditions. The DLO method (Smith & Gilbert, 2007) could provide such a modelling capability within a linear programming framework, preserving the computational efficiency of the layout optimization method. This could also allow for modelling of more complex foundation types such as piles.

**Further complexity measures** A range of constraints have been considered to reduce the complexity of the structures identified. However, there is still scope to consider alternative complexity measures. For example, some manufacturing or assembly methods will lead to specific constraints, which may often be possible to consider using the methods described in Chapter 6 or Appendix D; close collaboration with manufacturers is likely to prove valuable.

The use of lazy constraints was shown to be particularly effective when first limiting the number of active ground structure nodes and then using lazy constraints to limit crossover joints. In this case, the initial limit on the number of active ground structure nodes significantly reduced the number of lazy constraints which were required, leading to a reduction in computational time. This logic could be extended to apply several types of constraints simultaneously, using only the computationally simplest constraints initially, and adding more complex constraints only as required. This would ameliorate the increase in computational requirements caused by adding more, method specific, constraints.

**Crossover joints in 3D** The use of lazy constraints to correctly consider crossover joints has here been applied only to 2D problems. The method could be immediately applied to 3D problems if a crossover point is deemed to occur whenever two members' centrelines lie within a predetermined tolerance. However a more realistic model would be to consider a crossover to occur when the outer faces of members intersect.

This would introduce a dependency on the chosen shape of the cross section and, depending on the chosen cross section, the relaxed problem may no longer be linear. Implementation of this is likely to also necessitate an additional integer variable at each crossover joint, indicating whether the members fill the space between their centrelines; an intersection would only be implied if this additional variable, and both flags indicating member existence, were equal to 1. This would lead to a requirement for a huge number of additional integer variables, unless these were also implemented using a pool type approach, as was used here for the implementation of variables to count crossover nodes.

**Obtaining simple structures by vertex enumeration** Minimising volume subject to limits on common measures of complexity implies identifying a particular basic solution of the layout optimization problem, i.e. a particular vertex of the solution space. A preliminary investigation into the application of vertex enumeration algorithms to problems of layout optimization has been performed; it has been shown that they have the potential to simultaneously identify and evaluate many options for a given problem. Further studies are required to establish the most appropriate algorithms, the best performing heuristics and other strategies for improving performance.

**Elements representing additional region types** A number of region types have been implemented and tested within the RAGS framework. However, a number of other regions commonly found in Michell structures known in the literature remain to be implemented. Some initial results for these may be found in Appendix C. Perhaps the most critical region type on which further studies should focus is a general region of type  $T$  with two families of curved coordinate lines (i.e.  $T_1$ ).

Further studies into possible heuristics for the order in which regions are checked and added in the member adding phase may also be effective in reducing the computational requirements of this method. For example, fan regions are usually observed connecting to externally loaded or supported points. Provided that all possible regions are checked at the final iteration, such heuristics will not affect solution quality.

# References

- Achtziger, W. (2007). On simultaneous optimization of truss geometry and topology. *Structural and Multidisciplinary Optimization*, 33(4-5), 285–304.
- Achtziger, W., Bendsøe, M., Ben-Tal, A., & Zowe, J. (1992). Equivalent displacement based formulations for maximum strength truss topology design. *IMPACT of Computing in Science and Engineering*, 4(4), 315–345.
- Achtziger, W., & Stolpe, M. (2007). Truss topology optimization with discrete design variables - Guaranteed global optimality and benchmark examples. *Structural and Multidisciplinary Optimization*, 34(1), 1–20.
- Addis, B. (2013). Toys that save millions - A history of using physical models in structural design. *The Structural Engineer*, 91(4), 12–27.
- Ahrari, A., Atai, A. A., & Deb, K. (2015). Simultaneous topology, shape and size optimization of truss structures by fully stressed design based on evolution strategy. *Engineering Optimization*, 47(8), 1063–1084.
- Akbarzadeh, M., Van Mele, T., & Block, P. (2015). On the equilibrium of funicular polyhedral frames and convex polyhedral force diagrams. *Computer-Aided Design*, 63, 118–128.
- Arafa, M., & Alqedra, M. (2011). Early stage cost estimation of buildings construction projects using artificial neural networks. *Journal of Artificial Intelligence*, 4(1), 63–75.
- Arora, R., Jacobson, A., Langlois, T. R., Huang, Y., Mueller, C., Matusik, W., Shamir, A., Singh, K., & Levin, D. I. W. (2019). Volumetric Michell trusses for parametric design & fabrication. In *Proceedings of the ACM Symposium on Computational Fabrication*, (pp. 6:1–6:13). ACM.
- Asadpoure, A., Guest, J. K., & Valdevit, L. (2015). Incorporating fabrication cost into topology optimization of discrete structures and lattices. *Structural and Multidisciplinary Optimization*, 51(2), 385–396.
- ASCE (2003). *ASCE 7: Minimum design loads for buildings and other structures*. American Society of Civil Engineers.
- Autodesk, Inc (2016). Dynamo BIM - Open source graphical programming for design. Accessed 10/07/2019. URL <https://dynamobim.org/>
- Avis, D., Bremner, D., & Seidel, R. (1997). How good are convex hull algorithms? *Computational Geometry*, 7(5-6), 265–301.
- Avis, D., & Fukuda, K. (1992). A pivoting algorithm for convex hulls and vertex enumeration of arrangements and polyhedra. *Discrete & Computational Geometry*, 8(3), 295–313.
- Azagra, D., & Hay, T. (2012). A case for physical models. *The Structural Engineer*, 90(9), 14–20.
- Baandrup, M., Sigmund, O., & Aage, N. (2019). *Large scale topology optimization of girders in cable supported bridges*. Presented at 13th World Congress of Structural and Multidisciplinary Optimization, Beijing.
- Bach, F., Jenatton, R., Mairal, J., & Obozinski, G. (2011). Convex optimization with sparsity-inducing norms. In S. Sra, S. Nowozin, & S. J. Wright (Eds.) *Optimization for Machine Learning*, (pp. 19–53). Cambridge, MA: MIT press.
- Baker, W. F., Beghini, L. L., Mazurek, A., Carrion, J., & Beghini, A. (2013). Maxwell’s reciprocal diagrams and discrete Michell frames. *Structural and Multidisciplinary Optimization*, 48(2), 267–277.
- Balling, R. (2006). Giving designers a choice of optimal designs. In *Structures Congress 2006: 17th Analysis and Computation Specialty Conference*, (pp. 1–13).

- Barnes, M. R. (1999). Form finding and analysis of tension structures by dynamic relaxation. *International Journal of Space Structures*, 14(2), 89–104.
- Beghini, A., & Baker, W. F. (2015). On the layout of a least weight multiple span structure with uniform load. *Structural and Multidisciplinary Optimization*, 52(3), 447–457.
- Beghini, A., Beghini, L. L., Schultz, J. A., Carrion, J., & Baker, W. F. (2013). Rankine's theorem for the design of cable structures. *Structural and Multidisciplinary Optimization*, 48(5), 877–892.
- Beghini, L. L., Carrion, J., Beghini, A., Mazurek, A., & Baker, W. F. (2014). Structural optimization using graphic statics. *Structural and Multidisciplinary optimization*, 49(3), 351–366.
- Bendsøe, M. P. (1989). Optimal shape design as a material distribution problem. *Structural Optimization*, 1(4), 193–202.
- Bendsøe, M. P., Ben-Tal, A., & Zowe, J. (1994). Optimization methods for truss geometry and topology design. *Structural Optimization*, 7(3), 141–159.
- Bendsøe, M. P., & Haber, R. B. (1993). The Michell layout problem as a low volume fraction limit of the perforated plate topology optimization problem: An asymptotic study. *Structural Optimization*, 6(4), 263–267.
- Bendsøe, M. P., & Sigmund, O. (1999). Material interpolation schemes in topology optimization. *Archive of Applied Mechanics*, 69(9-10), 635–654.
- Bendsoe, M. P., & Sigmund, O. (2004). *Topology optimization: Theory, methods and applications*. Springer.
- Benham, P. P., Crawford, R. J., & Armstrong, C. G. (1996). *Mechanics of engineering materials*. Longman Harlow.
- Bixby, R. E., & Saltzman, M. J. (1994). Recovering an optimal LP basis from an interior point solution. *Operations Research Letters*, 15(4), 169–178.
- Bland, R. G. (1977). New finite pivoting rules for the simplex method. *Mathematics of Operations Research*, 2(2), 103–107.
- Bletzinger, K.-U., & Ramm, E. (2001). Structural optimization and form finding of light weight structures. *Computers & Structures*, 79(22-25), 2053–2062.
- Block, I. (2018). Robots complete span of 3D-printed bridge for Amsterdam canal. Accessed 11/07/2019.  
URL <https://www.dezeen.com/2018/04/17/mx3d-3d-printed-bridge-joris-laarman-arup-amsterdam-netherlands/>
- Block, P. (2009). *Thrust network analysis: Exploring three-dimensional equilibrium*. Ph.D. thesis, Massachusetts Institute of Technology.
- Block, P., DeJong, M., & Ochsendorf, J. (2006). As hangs the flexible line: Equilibrium of masonry arches. *Nexus Network Journal*, 8(2), 13–24.
- Boyd, S., & Vandenberghe, L. (2004). *Convex optimization*. Cambridge University press.
- Brancaleoni, F., Diana, G., Fiammenghi, G., Jamiolkowski, M., Marconi, M., & Vullo, E. (2011). Messina bridge, design, concept, from early days to present. In *Taller, Longer, Lighter, IABSE-IASS symposium London, Special session on the Messina bridge*, (pp. 15–23).
- Brown, E. (2011). London Waterloo station - Billboard - Welcome to Yorkshire. Used under the Creative Commons Attribution 2.0 Generic license. Accessed 19/09/2019.  
URL <https://www.flickr.com/photos/ell-r-brown/6427778705>
- Brown, N. C., & Mueller, C. T. (2016). Design for structural and energy performance of long span buildings using geometric multi-objective optimization. *Energy and Buildings*, 127, 748–761.
- Buchanan, A. H., & Honey, B. G. (1994). Energy and carbon dioxide implications of building construction. *Energy and Buildings*, 20(3), 205–217.
- Bukauskas, A., Shepherd, P., Walker, P., Sharma, B., & Bregulla, J. (2018). Inventory-constrained structural design: New objectives and optimization techniques. In *Proceedings of IASS Annual Symposia*, vol. 11, (pp. 1–8). International Association for Shell and Spatial Structures (IASS).

- Calladine, C. (2015). An amateur's contribution to the design of Telford's Menai suspension bridge: A commentary on Gilbert (1826) 'On the mathematical theory of suspension bridges'. *Philosophical Transactions of the Royal Society of London A: Mathematical, Physical and Engineering Sciences*, 373(2039), 20140346.
- Cammelli, S. (2018). Tianjin CTF finance centre: Wind, form and structure. *The Structural Engineer*, 96(9), 14–21.
- Carnot, N.-L.-S. (1897). Reflections on the motive power of heat and on machines fitted to develop that power. In R. H. Thurston (Ed.) *Reflections on the motive power of heat accompanied by an account of Carnot's theory*. J. Wiley.
- Carter, M., Kite, S., Hussain, N., & Minto, B. (2010). Design of the Forth replacement crossing, Scotland. *Proceedings of the Institution of Civil Engineers-Bridge Engineering*, 163(2), 91–99.
- CEN (2002). *EN 1990: Eurocode 0 - Basis of structural design*. European Committee for Standardisation.
- Chan, A. S. L. (1960). The design of Michell optimum structures. Tech. rep., College of Aeronautics Cranfield.
- Chan, H. S. Y. (1963). Optimum Michell frameworks for three parallel forces. Tech. rep., College of Aeronautics Cranfield.
- Chan, H. S. Y. (1964). Optimum structural design and linear programming. Tech. rep., College of Aeronautics Cranfield.
- Chan, H. S. Y. (1967). Half-plane slip-line fields and Michell structures. *The Quarterly Journal of Mechanics and Applied Mathematics*, 20(4), 453–469.
- Chan, H. S. Y. (1975). Symmetric plane frameworks of least weight. In *Optimization in structural design*, (pp. 313–326). Springer.
- Chand, D. R., & Kapur, S. S. (1970). An algorithm for convex polytopes. *Journal of the ACM (JACM)*, 17(1), 78–86.
- Chern, J. M., & Prager, W. (1972). Optimal design of trusses for alternative loads. *Ingenieur-Archiv*, 41(4), 225–231.
- Chilton, J. (2009). Heinz Isler's infinite spectrum of new shapes for shells. In *Symposium of the International Association for Shell and Spatial Structures 2009, Valencia*.
- Collins, I. F. (1968). The algebraic-geometry of slip line fields with applications to boundary value problems. *Proceedings of the Royal Society of London. Series A. Mathematical and Physical Sciences*, 303(1474), 317–338.
- Cox, H. L. (1965). *The design of structures of least weight*. Pergamon.
- Creese, R. C., & Li, L. (1995). Cost estimation of timber bridges using neural networks. *Cost Engineering*, 37(5), 17–22.
- Croll, J. G. (2019). Assessing structural efficiency: A study of gravity balanced cable-stay bridges. *Proceedings of the Institution of Civil Engineers - Bridge Engineering*, 172(1), 2–12.
- Croll, J. G. A. (1997a). Thoughts on the structural efficiency of cable-stayed and suspension bridges. *The Structural Engineer*, 75(10), 173–175.
- Croll, J. G. A. (1997b). Correspondence - Thoughts on the structural efficiency of cable-stayed and catenary suspension bridges - Author's reply. *The Structural Engineer*, 75(19), 346–347.
- Culmann, C. (1875). *Die graphische statik*, vol. 1. Meyer & Zeller.
- Dalton, H. C. (1997). Correspondence - Thoughts on the structural efficiency of cable-stayed and suspension bridges. *The Structural Engineer*, 75(19), 345.
- Damolini, S. (2009). *Carbon nanotubes and their application to very long span bridges*. Ph.D. thesis, Massachusetts Institute of Technology.
- Dantzig, G., Fulkerson, R., & Johnson, S. (1954). Solution of a large-scale traveling-salesman problem. *Journal of the Operations Research Society of America*, 2(4), 393–410.

- Dantzig, G. B. (1949). Programming in a linear structure. In *Econometrica* 17, (pp. 73–74). The Econometric Society.
- Dantzig, G. B., Ford Jr, L. R., & Fulkerson, D. R. (1956). A primal–dual algorithm. Tech. rep., RAND Corp Santa Monica CA.
- Dantzig, G. B., & Wolfe, P. (1960). Decomposition principle for linear programs. *Operations Research*, 8(1), 101–111.
- Darwich, W., Gilbert, M., & Tyas, A. (2010). Optimum structure to carry a uniform load between pinned supports. *Structural and Multidisciplinary Optimization*, 42(1), 33–42.
- Davidson, S. (2019). Grasshopper - Algorithmic modelling for Rhino. Accessed 10/07/2019.  
URL <https://www.grasshopper3d.com/>
- de Gol, D. (2014). Soap films. Used under the Creative Commons Attribution 4.0 International license.  
URL [https://commons.wikimedia.org/wiki/File:Minimal\\_surface.jpg](https://commons.wikimedia.org/wiki/File:Minimal_surface.jpg)
- de Ville de Goyet, V., Propson, A., Peigneux, C., & Duchene, Y. (2018). The third Bosphorus bridge - Erection sequences of the main span. In *40th IABSE Symposium - Tomorrow's Megastructures*, (pp. S19–17–S19–24).
- Debney, P. (2016). An introduction to engineering optimisation methods. *The Structural Engineer*, 90(3), 34–41.
- Dewhurst, P. (2001). Analytical solutions and numerical procedures for minimum-weight Michell structures. *Journal of the Mechanics and Physics of Solids*, 49(3), 445–467.
- Dewhurst, P., & Collins, I. F. (1973). A matrix technique for constructing slip-line field solutions to a class of plane strain plasticity problems. *International Journal for Numerical Methods in Engineering*, 7(3), 357–378.
- Donoho, D. L. (2006). For most large underdetermined systems of linear equations the minimal  $\ell_1$ -norm solution is also the sparsest solution. *Communications on Pure and Applied Mathematics: A Journal Issued by the Courant Institute of Mathematical Sciences*, 59(6), 797–829.
- Dorn, W. S., Gomory, R. E., & Greenberg, H. J. (1964). Automatic design of optimal structures. *Journal de Mecanique*.
- Drewry, C. S. (1832). *A memoir on suspension bridges, comprising the history of their origin and progress, and of their application to civil and military purposes*. Cambridge University press.
- Duysinx, P., & Bendsøe, M. P. (1998). Topology optimization of continuum structures with local stress constraints. *International Journal for Numerical Methods in Engineering*, 43(8), 1453–1478.
- Eley, D., & Annereau, N. (2018). The structural engineering of the Leadenhall building. *The Structural Engineer*, 96(4), 10–20.
- Espí, M. V. (2013). On the allowance for support costs in Prager-Rozvany's optimal layout theory. *Structural and Multidisciplinary Optimization*, 48(4), 849–852.
- Ewing, D. J. F. (1967). A series-method for constructing plastic slipline fields. *Journal of the Mechanics and Physics of Solids*, 15(2), 105–114.
- Fair Isacc Corp. (2018). Xpress - optimizer reference manual.  
URL <https://www.artelys.com/en/optimization-tools/fico-xpress>
- Fairclough, H. (2015). *Geometry optimization with self weight*. Master's thesis, University of Sheffield.
- Fairclough, H. E., Gilbert, M., Pichugin, A. V., Tyas, A., & Firth, I. (2018). Theoretically optimal forms for very long-span bridges under gravity loading. *Proc Roy Soc A*, 474, 20170726.
- Firth, I. (2017). Going for gold in a changing world. *The Structural Engineer*, 95(2), 16–24.
- Fischer, M., & Tatum, C. B. (1997). Characteristics of design-relevant constructability knowledge. *Journal of Construction Engineering and Management*, 123(3), 253–260.
- Forrest, J. J., & Goldfarb, D. (1992). Steepest-edge simplex algorithms for linear programming. *Mathematical Programming*, 57(1-3), 341–374.

- French, M. J. (1997). Correspondence - Thoughts on the structural efficiency of cable-stayed and suspension bridges. *The Structural Engineer*, 75(19), 345.
- Fruchterman, T., & Reingold, E. (1991). Graph drawing by force-directed placement. *Software - Practice & Experience*, 21(11), 1129–1164.
- Fukuda, K., & Prodon, A. (1995). Double description method revisited. In *Franco-Japanese and Franco-Chinese Conference on Combinatorics and Computer Science*, (pp. 91–111). Springer.
- Galileo, G. (1954). *Dialogues concerning two new sciences. Translation by Henry Crew and Alfonso de Salvio*. Dover publications Inc., New York.
- Ge, Y.-J. (2016). Aerodynamic challenge and limitation in long-span cable-supported bridges. In *Proceedings ACEM16 / Structures16 Conference*. Korea.
- Gerbo, E. J., & Saliklis, E. P. (2014). Optimizing a trussed frame subjected to wind using Rhino, Grasshopper, Karamba and Galapagos. In *Proceedings of IASS Annual Symposia*, vol. 13, (pp. 1–7). International Association for Shell and Spatial Structures (IASS).
- Ghista, D. N., & Resnikoff, M. M. (1968). Development of Michell minimum weight structures. Tech. rep., NASA.
- Gil, L., & Andreu, A. (2001). Shape and cross-section optimisation of a truss structure. *Computers & Structures*, 79(7), 681–689.
- Gilbert, D. (1826). On the mathematical theory of suspension bridges, with tables for facilitating their construction. *Philosophical Transactions of the Royal Society of London*, 116, 202–218.
- Gilbert, M., & Tyas, A. (2003). Layout optimization of large-scale pin-jointed frames. *Engineering Computations*, 20(8), 1044–1064.
- Gill, P. E., Murray, W., Saunders, M. A., Tomlin, J. A., & Wright, M. H. (1986). On projected Newton barrier methods for linear programming and an equivalence to Karmarkar's projective method. *Mathematical Programming*, 36(2), 183–209.
- Gimsing, N. J. (1994). Suspended bridges with very long spans. In *Proceedings of the International Conference of IABSE-FIP*, (pp. 489–504). Deauville.
- Gimsing, N. J., & Georgakis, C. T. (2011). *Cable supported bridges: concept and design*. John Wiley & Sons.
- Gokyu, I. (1970). Parallel cables. US Patent 3,500,625.
- Goldfarb, D., & Reid, J. K. (1977). A practicable steepest-edge simplex algorithm. *Mathematical Programming*, 12(1), 361–371.
- Goldsmith, N. (2016). The physical modeling legacy of Frei Otto. *International Journal of Space Structures*, 31(1), 25–30.
- Gomory, R. (1960). An algorithm for the mixed integer problem. Tech. rep., RAND Corp Santa Monica CA.
- Gonçalves, M. S., Lopez, R. H., & Miguel, L. F. F. (2015). Search group algorithm: A new metaheuristic method for the optimization of truss structures. *Computers & Structures*, 153, 165–184.
- González, J., & Fiorito, F. (2015). Daylight design of office buildings: Optimisation of external solar shadings by using combined simulation methods. *Buildings*, 5(2), 560–580.
- Gorgolewski, M. (2008). Designing with reused building components: Some challenges. *Building Research & Information*, 36(2), 175–188.
- Graczykowski, C., & Lewiński, T. (2006a). Michell cantilevers constructed within trapezoidal domains — Part I: Geometry of Hencky nets. *Structural and Multidisciplinary Optimization*, 32(5), 347–368.
- Graczykowski, C., & Lewiński, T. (2006b). Michell cantilevers constructed within trapezoidal domains — Part II: Virtual displacement fields. *Structural and Multidisciplinary Optimization*, 32(6), 463–471.
- Graczykowski, C., & Lewiński, T. (2007). Michell cantilevers constructed within trapezoidal domains — Part III: Force fields. *Structural and Multidisciplinary Optimization*, 33(1), 27–45.

- Gregorski, T. (1998). Akashi Kaikyo Bridge. *Roads & Bridges*, 36(8), 34–37.
- Groenwold, A. A., & Stander, N. (1997). Optimal discrete sizing of truss structures subject to buckling constraints. *Structural Optimization*, 14(2-3), 71–80.
- Guest, J. K., Draper, P., & Billington, D. P. (2013). Santiago Calatrava’s Alamillo bridge and the idea of the structural engineer as artist. *Journal of Bridge Engineering*, 18(10), 936–945.
- Guest, J. K., & Igusa, T. (2008). Structural optimization under uncertain loads and nodal locations. *Computer Methods in Applied Mechanics and Engineering*, 198(1), 116–124.
- Guo, X., Zhang, W., & Zhong, W. (2014). Doing topology optimization explicitly and geometrically — A new moving morphable components based framework. *Journal of Applied Mechanics*, 81(8), 081009.
- Gurobi Optimization, LLC (2018). Gurobi optimizer reference manual.  
URL <http://www.gurobi.com>
- Hansen, S. R., & Vanderplaats, G. N. (1990). Approximation method for configuration optimization of trusses. *AIAA journal*, 28(1), 161–168.
- Hansford, M. (2012). Cable stay revolution hangs in the balance. *New Civil Engineer*, 05/07/2012, 4–5.
- Harding, J., & Shepherd, P. (2011). Structural form finding using zero-length springs with dynamic mass. In *Proceedings of the IASS Annual Symposium: IABSE-IASS 2011: Taller, Longer, Lighter*.
- Haunert, J.-H., & Wolff, A. (2010). Optimal and topologically safe simplification of building footprints. In *Proceedings of the 18th SIGSPATIAL international conference on advances in geographic information systems*, (pp. 192–201). ACM.
- Havelia, P. (2016). *A ground structure method to optimize topology and sizing of steel frame structures to minimize material, fabrication and erection cost*. Ph.D. thesis, Stanford University.
- He, L., & Gilbert, M. (2015). Rationalization of trusses generated via layout optimization. *Structural and Multidisciplinary Optimization*, 52(4), 677–694.
- He, L., Gilbert, M., Johnson, T., & Smith, C. (2017). Human-in-the-loop layout and geometry optimization of structures and components. In *12th World Congress of Structural and Multidisciplinary Optimization, WCSMO12*, (pp. 227–228). ISSMO.
- He, L., Gilbert, M., & Song, X. (2019). A Python script for adaptive layout optimization of trusses. *Structural and Multidisciplinary Optimization*, 60(2), 835–847.
- Hegemier, G. A., & Prager, W. (1969). On Michell trusses. *International Journal of Mechanical Sciences*, 11(2), 209–215.
- Hemp, W. S. (1958). Theory of structural design. Tech. rep., College of Aeronautics Cranfield.
- Hemp, W. S. (1966). Studies in the theory of Michell structures. In *Applied Mechanics*, (pp. 621–628). Springer.
- Hemp, W. S. (1973). *Optimum structures*. Clarendon Press.
- Hemp, W. S. (1974). Michell framework for uniform load between fixed supports. *Engineering Optimization*, 1(1), 61–69.
- Hemp, W. S. (1976). Michell framework for a force in any definite direction at the mid-point between two supports. *Engineering Optimization*, 2(3), 183–187.
- Heyman, J. (1998). Hooke’s cubico–parabolical conoid. *Notes and Records of the Royal Society of London*, 52(1), 39–50.
- Hill, R. (1950). *The mathematical theory of plasticity*. Oxford University press.
- Hill, R. (1967). On the vectorial superposition of Hencky-Prandtl nets. *Journal of the Mechanics and Physics of Solids*, 15(4), 255–262.
- Hill, R. D., & Rozvany, G. I. N. (1985). Prager’s layout theory: A nonnumeric computer method for generating optimal structural configurations and weight-influence surfaces. *Computer Methods in Applied Mechanics and Engineering*, 49(2), 131–148.



- Hoang, V.-N., & Jang, G.-W. (2017). Topology optimization using moving morphable bars for versatile thickness control. *Computer Methods in Applied Mechanics and Engineering*, 317, 153–173.
- Holland, J. H. (1992). *Adaptation in natural and artificial systems: An introductory analysis with applications to biology, control, and artificial intelligence*. MIT press.
- Hooke, R. (1676). *A description of helioscopes and some other instruments*. Royal Society, London.
- Horn, A. (2015). *Integrating constructability into conceptual structural design and optimization*. Ph.D. thesis, Massachusetts Institute of Technology.
- Horst, R., & Tuy, H. (1995). *Global optimization: Deterministic approaches*. Springer Science & Business Media.
- Huang, X. H., & Xie, Y. (2007). Bidirectional evolutionary topology optimization for structures with geometrical and material nonlinearities. *AIAA journal*, 45(1), 308–313.
- Huerta, S. (2006). Structural design in the work of Gaudi. *Architectural Science Review*, 49(4), 324–339.
- IBM Corp. (2015). CPLEX User’s Manual.  
URL <https://www.ibm.com/analytics/cplex-optimizer>
- Ioannides, S. A., & Ruddy, J. L. (2000). Rules of thumb for steel design. *Modern Steel Construction*, 40(2).
- Ito, M. (1996). Super long span cable-suspended bridges in Japan. In *Proceedings of the 15th Congress of IABSE*, (pp. 1009–1018). Copenhagen, Denmark.
- Jacot, B. P., & Mueller, C. T. (2017). A strain tensor method for three-dimensional Michell structures. *Structural and Multidisciplinary Optimization*, 55(5), 1819–1829.
- Jansen, B., De Jong, J. J., Roos, C., & Terlaky, T. (1997). Sensitivity analysis in linear programming: Just be careful! *European Journal of Operational Research*, 101(1), 15–28.
- Jensen, L., & Bloomstine, M. L. (2009). Application of high strength steel in super long span modern suspension bridge design. In *Nordic Steel Construction Conference*, (pp. 494–501). The Swedish Institute of Steel Construction.
- Johnson, W. (1961). An analogy between upper-bound solutions for plane-strain metal working and minimum-weight two-dimensional frames. *International Journal of Mechanical Sciences*, 3(4), 239–246.
- Kanno, Y. (2013). Topology optimization of tensegrity structures under compliance constraint: A mixed integer linear programming approach. *Optimization and Engineering*, 14(1), 61–96.
- Kanno, Y., & Fujita, S. (2018). Alternating direction method of multipliers for truss topology optimization with limited number of nodes: A cardinality-constrained second-order cone programming approach. *Optimization and Engineering*, 19(2), 327–358.
- Kanno, Y., & Guo, X. (2010). A mixed integer programming for robust truss topology optimization with stress constraints. *International Journal for Numerical Methods in Engineering*, 83(13), 1675–1699.
- Karmarkar, N. (1984). A new polynomial-time algorithm for linear programming. In *Proceedings of the sixteenth annual ACM symposium on Theory of computing*, (pp. 302–311). ACM.
- Kelley, J. E., Jr (1960). The cutting-plane method for solving convex programs. *Journal of the Society for Industrial and Applied Mathematics*, 8(4), 703–712.
- Kennedy, J., & Eberhart, R. (1995). Particle swarm optimization. In *Proceedings of the IEEE international conference on neural networks*, vol. 4, (pp. 1942–1948).
- Kilian, A., & Ochsendorf, J. (2005). Particle-spring systems for structural form finding. *Journal of the International Association for Shell and Spatial Structures*, 46(2), 77–84.
- Kim, G.-H., An, S.-H., & Kang, K.-I. (2004). Comparison of construction cost estimating models based on regression analysis, neural networks, and case-based reasoning. *Building and Environment*, 39(10), 1235–1242.
- Kirkpatrick, S., Gelatt, C. D., Jr, & Vecchi, M. P. (1983). Optimization by simulated annealing. *Science*, 220(4598), 671–680.

- Kirsch, U. (1990). On singular topologies in optimum structural design. *Structural Optimization*, 2(3), 133–142.
- Koumoussis, V. K., & Georgiou, P. G. (1994). Genetic algorithms in discrete optimization of steel truss roofs. *Journal of Computing in Civil Engineering*, 8(3), 309–325.
- Kwok, T.-H., Li, Y., & Chen, Y. (2016). A structural topology design method based on principal stress line. *Computer-Aided Design*, 80, 19–31.
- Lagarias, J. C., Reeds, J. A., Wright, M. H., & Wright, P. E. (1998). Convergence properties of the Nelder-Mead simplex method in low dimensions. *SIAM Journal on Optimization*, 9(1), 112–147.
- Lagaros, N. D. (2018). The environmental and economic impact of structural optimization. *Structural and Multidisciplinary Optimization*, 58(4), 1751–1768.
- Lam, P. T. I., Wong, F. W. H., & Chan, A. P. C. (2006). Contributions of designers to improving buildability and constructability. *Design Studies*, 27(4), 457–479.
- Lamé, G. (1859). *Leçons sur les coordonnées curvilignes et leurs diverses applications*. Mallet-Bachelier.
- Land, A. H., & Doig, A. G. (1960). An automatic method of solving discrete programming problems. *Econometrica*, 28(3), 497–520.
- Leach, J., Nicolin, R., & Burton, M. (2016). Structural workflows and the art of parametric design. *The Structural Engineer*, 94(3), 24–31.
- Lee, G., Kim, W., Oh, H., Youn, B. D., & Kim, N. H. (2019). Review of statistical model calibration and validation — from the perspective of uncertainty structures. *Structural and Multidisciplinary Optimization*, (pp. 1–26).
- Leng, G., & Duan, B. (2012). Topology optimization of planar truss structures with continuous element intersection and node stability constraints. *Proceedings of the Institution of Mechanical Engineers, Part C: Journal of Mechanical Engineering Science*, 226(7), 1821–1831.
- Lewiński, T. (2004). Michell structures formed on surfaces of revolution. *Structural and Multidisciplinary Optimization*, 28(1), 20–30.
- Lewiński, T., & Rozvany, G. I. N. (2007). Exact analytical solutions for some popular benchmark problems in topology optimization II: Three-sided polygonal supports. *Structural and Multidisciplinary Optimization*, 33(4–5), 337–349.
- Lewiński, T., & Rozvany, G. I. N. (2008a). Exact analytical solutions for some popular benchmark problems in topology optimization III: L-shaped domains. *Structural and Multidisciplinary Optimization*, 35(2), 165–174.
- Lewiński, T., & Rozvany, G. I. N. (2008b). Analytical benchmarks for topological optimization IV: Square-shaped line support. *Structural and Multidisciplinary Optimization*, 36(2), 143–158.
- Lewiński, T., Rozvany, G. I. N., Sokół, T., & Bołbotowski, K. (2013). Exact analytical solutions for some popular benchmark problems in topology optimization III: L-shaped domains revisited. *Structural and Multidisciplinary Optimization*, 47(6), 937–942.
- Lewiński, T., Sokół, T., & Graczykowski, C. (2019). *Michell Structures*. Springer.
- Lewiński, T., Zhou, M., & Rozvany, G. I. N. (1994a). Extended exact solutions for least-weight truss layouts — Part I: Cantilever with a horizontal axis of symmetry. *International Journal of Mechanical Sciences*, 36(5), 375–398.
- Lewiński, T., Zhou, M., & Rozvany, G. I. N. (1994b). Extended exact least-weight truss layouts — Part II: Unsymmetric cantilevers. *International Journal of Mechanical Sciences*, 36(5), 399–419.
- Lewis, W. (2012). A mathematical model for assessment of material requirements for cable supported bridges: Implications for conceptual design. *Engineering Structures*, 42, 266–277.
- Lewis, W. (2016). Mathematical model of a moment-less arch. *Proceedings of the Royal Society A: Mathematical, Physical and Engineering Sciences*, 472(2190), 20160019.
- Limitstate Ltd. (2019). Limitstate:3d.  
URL <https://limitstate3d.com/>

- Lin, T., & Chow, P. (1991). Gibraltar Strait crossing - A challenge to bridge and structural engineers. *Structural Engineering International*, 1(2), 53–58.
- Lin, V. C., Gossard, D. C., & Light, R. A. (1981). Variational geometry in computer-aided design. *ACM SIGGRAPH Computer Graphics*, 15(3), 171–177.
- Love, A. E. H. (1920). *A treatise on the mathematical theory of elasticity*. Cambridge University press.
- Lu, H., Gilbert, M., & Tyas, A. (2018). Theoretically optimal bracing for pre-existing building frames. *Structural and Multidisciplinary Optimization*, 58(2), 677–686.
- Lu, K. (2010). The future of metals. *Science*, 328(5976), 319–320.
- Marmulla, R. (2008). Statics model of the Sagrada Familia in Barcelona. Used under the Creative Commons Attribution-Share Alike 3.0 Unported license.  
URL <https://commons.wikimedia.org/wiki/File:SagradaFamiliaStatikmodell.jpg>
- Martinez, P., Marti, P., & Querin, O. M. (2007). Growth method for size, topology, and geometry optimization of truss structures. *Structural and Multidisciplinary Optimization*, 33(1), 13–26.
- Mathur, R., & Molina, A. (2005). The new Tacoma Narrows bridge: Suspension system and anchorage. In *Structures Congress 2005: Metropolis and Beyond*, (pp. 1–12).
- Maute, K., Schwarz, S., & Ramm, E. (1998). Adaptive topology optimization of elastoplastic structures. *Structural Optimization*, 15(2), 81–91.
- Maxwell, J. C. (1864). On reciprocal figures and diagrams of forces. *The London, Edinburgh, and Dublin Philosophical Magazine and Journal of Science*, 27(182), 250–261.
- Maxwell, J. C. (1870). I. On reciprocal figures, frames, and diagrams of forces. *Transactions of the Royal Society of Edinburgh*, 26(01), 1–40.
- Mazurek, A., Baker, W. F., & Tort, C. (2011). Geometrical aspects of optimum truss like structures. *Structural and Multidisciplinary Optimization*, 43(2), 231–242.
- McKeown, J. (1998). Growing optimal pin-jointed frames. *Structural Optimization*, 15(2), 92–100.
- Meier, U. (1987). Proposal for a carbon fibre reinforced composite bridge across the Strait of Gibraltar at its narrowest site. *Proceedings of the Institution of Mechanical Engineers, Part B: Journal of Engineering Manufacture*, 201(2), 73–78.
- Mela, K. (2014). Resolving issues with member buckling in truss topology optimization using a mixed variable approach. *Structural and Multidisciplinary Optimization*, 50(6), 1037–1049.
- Melchers, R. E. (2005). On extending the range of Michell-like optimal topology structures. *Structural and Multidisciplinary Optimization*, 29(2), 85–92.
- Mele, E., Simeone, A., & Tomei, V. (2018). Efficiency vs. irregularity in non-conventional structural patterns: The case of tall buildings. In *Symposium of the International Association for Shell and Spatial Structures, Boston, Creativity in Structural Design*.
- Menn, C., & Billington, D. P. (1995). Breaking barriers of scale: A concept for extremely long span bridges. *Structural Engineering International*, 5(1), 48–50.
- Michell, A. G. M. (1904). The limits of economy of material in frame-structures. *The London, Edinburgh, and Dublin Philosophical Magazine and Journal of Science*, 8(47), 589–597.
- Mortazavi, A., & Toğan, V. (2016). Simultaneous size, shape, and topology optimization of truss structures using integrated particle swarm optimizer. *Structural and Multidisciplinary Optimization*, 54(4), 715–736.
- Mosek ApS (2019). *Modeling cookbook*. MOSEK, 3.1 ed.
- Motzkin, T. S., Raiffa, H., Thompson, G. L., & Thrall, R. M. (1953). The double description method. *Contributions to the Theory of Games*, 2(28), 51–73.
- Mueller, C. T., & Ochsendorf, J. A. (2015). Combining structural performance and designer preferences in evolutionary design space exploration. *Automation in Construction*, 52, 70–82.

- Nagtegaal, J. (1973a). A new approach to optimal design of elastic structures. *Computer Methods in Applied Mechanics and Engineering*, 2(3), 255–264.
- Nagtegaal, J. (1973b). A superposition principle in optimal plastic design for alternative loads. *International Journal of Solids and Structures*, 9(12), 1465–1471.
- Nagtegaal, J., & Prager, W. (1973). Optimal layout of a truss for alternative loads. *International Journal of Mechanical Sciences*, 15(7), 583–592.
- Niehe, P. (2017). Sand printing makes complex casted structural parts affordable. Accessed 11/07/2019.  
URL <https://www.arup.com/news-and-events/sand-printing-makes-complex-casted-structural-parts-affordable>
- Nolan, J. (2016). Cost versus value - The role of the consulting structural engineer. *The Structural Engineer*, 90(2), 13–22.
- Ochsendorf, J. A., & Billington, D. P. (1999). Self-anchored suspension bridges. *Journal of Bridge Engineering*, 4(3), 151–156.
- Ohsaki, M. (1998). Simultaneous optimization of topology and geometry of a regular plane truss. *Computers & Structures*, 66(1), 69–77.
- Ohsaki, M. (2011). *Optimization of finite dimensional structures*. CRC Press.
- Ohsaki, M., & Katoh, N. (2005). Topology optimization of trusses with stress and local constraints on nodal stability and member intersection. *Structural and Multidisciplinary Optimization*, 29(3), 190–197.
- Orr, J. (2008). Survey of structural engineering practice. Tech. rep., MEICON.
- Ostenfeld, K. H. (1996). Comparison between different structural solutions. The Great Belt project. In *Proceedings of the 15th Congress of IABSE*, (pp. 1063–1078). Copenhagen, Denmark.
- Palmer, A. C., & Sheppard, D. J. (1970). Optimizing the shape of pin-jointed structures. *Proceedings of the Institution of Civil Engineers*, 47(3), 363–376.
- Park, P. (2013). *Application of design synthesis technology in architectural practice*. Ph.D. thesis, University of Sheffield.
- Parkes, E. W. (1965). *Braced frameworks: An introduction to the theory of structures*. Pergamon.
- Parkes, E. W. (1975). Joints in optimum frameworks. *International Journal of Solids and Structures*, 11(9), 1017–1022.
- Paulson, B. C., Jr (1976). Designing to reduce construction costs. *ASCE Journal of the construction division*, 102(C04).
- Pedersen, N. L., & Nielsen, A. K. (2003). Optimization of practical trusses with constraints on eigenfrequencies, displacements, stresses, and buckling. *Structural and Multidisciplinary Optimization*, 25(5-6), 436–445.
- Perera, S., & Watson, I. (1998). Collaborative case-based estimating and design. *Advances in Engineering Software*, 29(10), 801–808.
- Perold, A. F. (1980). A degeneracy exploiting LU factorization for the simplex method. *Mathematical Programming*, 19(1), 239–254.
- Pichugin, A. V., Tyas, A., & Gilbert, M. (2012). On the optimality of Hemp’s arch with vertical hangers. *Structural and Multidisciplinary Optimization*, 46(1), 17–25.
- Pichugin, A. V., Tyas, A., Gilbert, M., & He, L. (2015). Optimum structure for a uniform load over multiple spans. *Structural and Multidisciplinary Optimization*, 52(6), 1041–1050.
- Plateau, J. (1869). *Recherches expérimentales et théoriques sur les figures d’équilibre d’une masse liquide sans pesanteur*. Mémoires de l’Académie Royale des Sciences, des Lettres et des Beaux-Arts de Belgique.
- Potts, K. (2008). *Construction cost management: Learning from case studies*. Routledge.
- Prager, W. (1977). Optimal layout of cantilever trusses. *Journal of Optimization Theory and Applications*, 23(1), 111–117.

- Prager, W. (1978a). Nearly optimal design of trusses. *Computers & Structures*, 8(3-4), 451–454.
- Prager, W. (1978b). Optimal layout of trusses with finite numbers of joints. *Journal of the Mechanics and Physics of Solids*, 26(4), 241–250.
- Prager, W., & Hodge, P. G. (1951). *Theory of perfectly plastic solids*. Wiley.
- Prager, W., & Rozvany, G. I. N. (1977). Optimization of structural geometry. In *Dynamical Systems: Proceedings of a University of Florida International Symposium*, (pp. 265–293). Elsevier.
- Prager, W., & Shield, R. (1968). Optimal design of multi-purpose structures. *International Journal of Solids and Structures*, 4(4), 469–475.
- Prager, W., & Shield, R. T. (1967). A general theory of optimal plastic design. *Journal of Applied Mechanics*, 34(1), 184–186.
- Prasannan, S. (2012). Cannon street station new building. Used under the Creative Commons Attribution-Share Alike 3.0 Unported license.  
URL [https://commons.wikimedia.org/wiki/File:Cannon\\_Street\\_station\\_new\\_building.JPG](https://commons.wikimedia.org/wiki/File:Cannon_Street_station_new_building.JPG)
- Prehn, W., & Mertens, M. (2002). Die Rheinquerung der a 44-Darstellung der Gesamtmaßnahme. *Stahlbau*, 71(6), 386–392.
- Pritchard, T. J., Gilbert, M., & Tyas, A. (2005). Plastic layout optimization of large-scale frameworks subject to multiple load cases, member self-weight and with joint length penalties. In *6th World Congress of Structural and Multidisciplinary Optimization*. ISSMO.
- Rafiq, Y., & Beck, M. (2008). A decision support tool for multi-disciplinary conceptual design. *The Structural Engineer*, 86(1), 37–42.
- Ranalli, F., Flager, F., & Fischer, M. (2018). A ground structure method to minimize the total installed cost of steel frame structures. *World Academy of Science, Engineering and Technology International Journal of Civil and Environmental Engineering*, 12(2), 115–123.
- Reddy, G., & Cagan, J. (1995). An improved shape annealing algorithm for truss topology generation. *Journal of Mechanical Design*, 117(2A), 315–321.
- RIBA (2007). Outline plan of work 2007. Tech. rep., Royal Institute of British Architects.
- Rippmann, M., Lachauer, L., & Block, P. (2012). Interactive vault design. *International Journal of Space Structures*, 27(4), 219–230.
- Routh, E. J. (1896). *A treatise on analytical statics: With numerous examples*, vol. 1. Cambridge University Press.
- Rozvany, G. I. N. (1977). Optimal plastic design: Allowance for self-weight. *Journal of the Engineering Mechanics Division*, 103(6), 1165–1170.
- Rozvany, G. I. N. (1989). *Structural design via optimality criteria: The Prager approach to structural optimization*. Kluwer Academic Publishers.
- Rozvany, G. I. N. (1992). Optimal layout theory: Analytical solutions for elastic structures with several deflection constraints and load conditions. *Structural Optimization*, 4(3-4), 247–249.
- Rozvany, G. I. N. (1996). Some shortcomings in Michell’s truss theory. *Structural Optimization*, 12(4), 244–250.
- Rozvany, G. I. N. (1998). Exact analytical solutions for some popular benchmark problems in topology optimization. *Structural Optimization*, 15(1), 42–48.
- Rozvany, G. I. N., Bendsoe, M. P., & Kirsch, U. (1995). Layout optimization of structures. *Applied Mechanics Reviews*, 48(2), 41–119.
- Rozvany, G. I. N., & Birker, T. (1994). On singular topologies in exact layout optimization. *Structural Optimization*, 8(4), 228–235.
- Rozvany, G. I. N., & Hill, R. D. (1978). Optimal plastic design: Superposition principles and bounds on the minimum cost. *Computer Methods in Applied Mechanics and Engineering*, 13(2), 151–173.

- Rozvany, G. I. N., Lewiński, T., Sigmund, O., Gerdes, D., & Birker, T. (1993a). Optimal topology of trusses or perforated deep beams with rotational restraints at both ends. *Structural Optimization*, 5(4), 268–270.
- Rozvany, G. I. N., & Prager, W. (1979). A new class of structural optimization problems: Optimal archgrids. *Computer Methods in Applied Mechanics and Engineering*, 19(1), 127–150.
- Rozvany, G. I. N., & Sokół, T. (2012). Exact truss topology optimization: Allowance for support costs and different permissible stresses in tension and compression - Extensions of a classical solution by Michell. *Structural and Multidisciplinary Optimization*, 45(3), 367–376.
- Rozvany, G. I. N., Sokół, T., & Pomezanski, V. (2014). Fundamentals of exact multi-load topology optimization - Stress-based least-volume trusses (generalized Michell structures) - Part I: Plastic design. *Structural and Multidisciplinary Optimization*, 50(6), 1051–1078.
- Rozvany, G. I. N., & Wang, C. M. (1983). On plane Prager-structures - I. *International Journal of Mechanical Sciences*, 25(7), 519–527.
- Rozvany, G. I. N., & Wang, C. M. (1984). Optimal layout theory: Allowance for selfweight. *Journal of Engineering Mechanics*, 110(1), 66–83.
- Rozvany, G. I. N., Wang, C. M., & Dow, M. (1982). Prager-structures: Archgrids and cable networks of optimal layout. *Computer Methods in Applied Mechanics and Engineering*, 31(1), 91–113.
- Rozvany, G. I. N., & Zhou, M. (1991). The COC algorithm, part I: Cross-section optimization or sizing. *Computer Methods in Applied Mechanics and Engineering*, 89(1-3), 281–308.
- Rozvany, G. I. N., Zhou, M., & Birker, T. (1993b). Why multi-load topology designs based on orthogonal microstructures are in general non-optimal. *Structural Optimization*, 6(3), 200–204.
- Rubin, D. S. (1975). Vertex generation and cardinality constrained linear programs. *Operations Research*, 23(3), 555–565.
- Saka, M. (1990). Optimum design of pin-jointed steel structures with practical applications. *Journal of Structural Engineering*, 116(10), 2599–2620.
- Sakrajda, P. (2010). St Pancras international. Used under the Creative Commons Attribution-Share Alike 3.0 Unported license.  
URL <https://commons.wikimedia.org/wiki/File:StPancrasInternational-PS02.JPG>
- Schek, H.-J. (1974). The force density method for form finding and computation of general networks. *Computer Methods in Applied Mechanics and Engineering*, 3(1), 115–134.
- Schumann, W. (1958). On limit analysis of plates. *Quarterly of Applied Mathematics*, 16(1), 61–71.
- Senatore, G. (2016). *Adaptive building structures*. Ph.D. thesis, University College London.
- Shao, X., Hu, J., Deng, L., & Cao, J. (2013). Conceptual design of superspan partial ground-anchored cable-stayed bridge with crossing stay cables. *Journal of Bridge Engineering*, 19(3), 06013001.
- Sigmund, O. (2001). A 99 line topology optimization code written in Matlab. *Structural and Multidisciplinary Optimization*, 21(2), 120–127.
- Sigmund, O., Aage, N., & Andreassen, E. (2016). On the (non-)optimality of Michell structures. *Structural and Multidisciplinary Optimization*, 54(2), 361–373.
- Sinclair, D. (2013). RIBA plan of work 2013 overview. Tech. rep., Royal Institute of British Architects.
- Smith, C., & Gilbert, M. (2007). Application of discontinuity layout optimization to plane plasticity problems. *Proceedings of the Royal Society A: Mathematical, Physical and Engineering Sciences*, 463(2086), 2461–2484.
- Smith, C., & Gilbert, M. (2013). Identification of rotational failure mechanisms in cohesive media using discontinuity layout optimization. *Geotechnique: International Journal of Soil Mechanics*, 63(14), 1194–1208.
- Sokół, T. (2011a). A 99 line code for discretized Michell truss optimization written in Mathematica. *Structural and Multidisciplinary Optimization*, 43(2), 181–190.
- Sokół, T. (2011b). Topology optimization of large-scale trusses using ground structure approach with selective subsets of active bars. In *19th International Conference on Computer Methods in Mechanics*. Warsaw, Poland.

- Sokół, T., & Lewiński, T. (2010). On the solution of the three forces problem and its application in optimal designing of a class of symmetric plane frameworks of least weight. *Structural and Multidisciplinary Optimization*, 42(6), 835–853.
- Sokół, T., & Rozvany, G. I. N. (2013a). Exact truss topology optimization for external loads and friction forces. *Structural and Multidisciplinary Optimization*, 48(4), 853–857.
- Sokół, T., & Rozvany, G. I. N. (2013b). On the adaptive ground structure approach for multi-load truss topology optimization. In *Tenth World Congress on Structural and Multidisciplinary Optimization*, (pp. 20–24).
- Sokół, T., & Rozvany, G. I. N. (2015). A new adaptive ground structure method for multi-load spatial Michell structures. In *3rd Polish Congress of Mechanics and 21st Computer Methods in Mechanics, Gdańsk*.
- Spillers, W., & Lev, O. (1971). Design for two loading conditions. *International Journal of Solids and Structures*, 7(9), 1261–1267.
- Starossek, U. (1996). Cable-stayed bridge concept for longer spans. *Journal of Bridge Engineering*, 1(3), 99–103.
- Stolpe, M. (2010). On some fundamental properties of structural topology optimization problems. *Structural and Multidisciplinary Optimization*, 41(5), 661–670.
- Stolpe, M. (2016). Truss optimization with discrete design variables: A critical review. *Structural and Multidisciplinary Optimization*, 53(2), 349–374.
- Sved, G., & Ginos, Z. (1968). Structural optimization under multiple loading. *International Journal of Mechanical Sciences*, 10(10), 803–805.
- Taha, H. A. (1975). *Integer programming: Theory, applications, and computations*. Academic Press.
- Taha, H. A. (2007). *Operations research: An introduction*. Pearson.
- Tauriainen, M., Puttonen, J., Saari, A., Laakso, P., & Forsblom, K. (2014). The assessment of constructability: BIM cases. In A. Mahdavi, B. Martens, & R. Scherer (Eds.) *eWork and eBusiness in Architecture, Engineering and Construction*, (pp. 55–61). CRC Press.
- Tedeschi, A. (2014). *AAD – Algorithms-aided design: Parametric strategies using Grasshopper*. Le penseur publisher.
- Александрович, Б. А. (2013). Completed bridge at night. Used under the Creative Commons Attribution-Share Alike 3.0 Unported license.  
URL [https://en.wikipedia.org/wiki/Russky\\_Bridge#/media/File:%22Russian\\_bridge%22\\_in\\_Vladivostok.jpg](https://en.wikipedia.org/wiki/Russky_Bridge#/media/File:%22Russian_bridge%22_in_Vladivostok.jpg)
- Topping, B. H. V. (1983). Shape optimization of skeletal structures: A review. *Journal of Structural Engineering*, 109(8), 1933–1951.
- Torii, A. J., Lopez, R. H., & Miguel, L. F. (2016). Design complexity control in truss optimization. *Structural and Multidisciplinary Optimization*, 54(2), 289–299.
- Trancao, R.-V. (2018). What will structural engineering practice look like in 10–15 years’ time and how can our professional community help us prepare for this? *The Structural Engineer*, 96(9), 10–12.
- Troitsky, M. S. (1988). *Cable-stayed bridges: Theory and design*. BSP Professional.
- Tyas, A. (2002). A mixed integer-linear programming approach to the modelling of strut behaviour in truss topology optimisation. Tech. rep., University of Sheffield.
- Tyas, A., Pichugin, A. V., & Gilbert, M. (2011). Optimum structure to carry a uniform load between pinned supports: Exact analytical solution. *Proceedings of the Royal Society A: Mathematical, Physical and Engineering Sciences*, 467(2128), 1101–1120.
- Van Mellaert, R., Lombaert, G., & Schevenels, M. (2016). Global size optimization of statically determinate trusses considering displacement, member, and joint constraints. *Journal of Structural Engineering*, 142(2), 04015120.
- Van Mellaert, R., Mela, K., Tiainen, T., Heinisuo, M., Lombaert, G., & Schevenels, M. (2018). Mixed-integer linear programming approach for global discrete sizing optimization of frame structures. *Structural and Multidisciplinary Optimization*, 57(2), 579–593.

- Vanderbei, R. J. (2001). *Linear programming: Foundations and extensions*. Springer.
- Villar, J. R., Vidal, P., Fernández, M. S., & Guaita, M. (2016). Genetic algorithm optimisation of heavy timber trusses with dowel joints according to Eurocode 5. *Biosystems Engineering*, 144, 115–132.
- Virlogeux, M. (2018). Long span bridges. In *40th IABSE Symposium - Tomorrow's Megastructures*, (pp. K-65–K-73).
- Wächter, A., & Biegler, L. T. (2006). On the implementation of a primal-dual interior point filter line search algorithm for large-scale nonlinear programming. *Mathematical Programming*, 106(1), 25–57.
- Wainwright, F. (2018). President's inaugural address: Working together for a creative and collaborative future. *The Structural Engineer*, 96(2), 12–19.
- Walladao, J. (2018). Golden Gate bridge splash. Used under the Creative Commons Attribution-Share Alike 4.0 International license.  
URL [https://commons.wikimedia.org/wiki/File:Gg\\_bridge\\_splash\\_11x14.jpg](https://commons.wikimedia.org/wiki/File:Gg_bridge_splash_11x14.jpg)
- Wang, C.-M., & Rozvany, G. I. N. (1983). On plane Prager-structures II: Non-parallel external loads and allowances for selfweight. *International Journal of Mechanical Sciences*, 25(7), 529–541.
- Weldeyesus, A. G., & Gondzio, J. (2018). A specialized primal-dual interior point method for the plastic truss layout optimization. *Computational Optimization and Applications*, 71(3), 613–640.
- Wolpert, D. H., & Macready, W. G. (1997). No free lunch theorems for optimization. *IEEE Transactions on Evolutionary Computation*, 1(1), 67–82.
- Xie, Y. M., & Steven, G. P. (1993). A simple evolutionary procedure for structural optimization. *Computers & Structures*, 49(5), 885–896.
- Xiong, W., Cai, C. S., Zhang, Y., & Xiao, R. (2011). Study of super long span cable-stayed bridges with CFRP components. *Engineering Structures*, 33(2), 330–343.
- Xu, Y.-L. (2013). *Wind effects on cable-supported bridges*. John Wiley & Sons.
- Yang, X.-S. (2010). *Engineering optimization: An introduction with metaheuristic applications*. John Wiley & Sons.
- Zegard, T., & Paulino, G. H. (2014). GRAND — Ground structure based topology optimization for arbitrary 2D domains using MATLAB. *Structural and Multidisciplinary Optimization*, 50(5), 861–882.
- Zegard, T., & Paulino, G. H. (2015). GRAND3 — Ground structure based topology optimization for arbitrary 3D domains using MATLAB. *Structural and Multidisciplinary Optimization*, 52(6), 1161–1184.
- Zhang, W., Zhou, J., Zhu, Y., & Guo, X. (2017). Structural complexity control in topology optimization via moving morphable component (MMC) approach. *Structural and Multidisciplinary Optimization*, 56(3), 535–552.
- Zhou, K., & Li, J. (2004). The exact weight of discretized Michell trusses for a central point load. *Structural and Multidisciplinary Optimization*, 28(1), 69–72.
- Zhou, M., & Rozvany, G. I. N. (1991). The COC algorithm, part II: Topological, geometrical and generalized shape optimization. *Computer Methods in Applied Mechanics and Engineering*, 89(1-3), 309–336.



# Appendices



# Appendix A

## Numerical analysis of regions in known optimal solutions

This appendix collects regions which appear in Michell structures known from the literature. In order that they may be more readily compared, the series expansions of the functions defining the Lamé coefficients are given. The values of the series expansion coefficients are plotted for comparison. It is observed that the relative magnitudes of the series expansion coefficients are frequently similar across different region types.

A brief description of the form of the region or the solution from which it is drawn accompany each result, although detailed problem descriptions are beyond the scope of this section and the interested reader is referred to the relevant original works. Several of the results in this chapter are discussed in more detail in Appendix C.

---

A.1	Definitions of functions and constants	178
A.1.1	Type $T_2$ regions	178
A.1.2	Type $T_1$ regions	178
A.2	Tabulated results	179
A.2.1	Type $T_2$ regions	179
A.2.2	Type $T_1$ regions	180

---

## A.1 Definitions of functions and constants

To simplify the expression of Lamé coefficients in several regions Lewiński et al. (1994a) define the following function,

$$G_n(\alpha, \beta) = \left(\frac{\alpha}{\beta}\right)^{\frac{n}{2}} I_n(2\sqrt{\alpha\beta}) \quad (\text{A.1})$$

where  $I$  is the modified Bessel function of the first kind. Lewiński & Rozvany (2008b) further defines the function  $T_n$ , given below. Here this function will be denoted as  $H_n$  to avoid possible confusion with regions of type  $T_1$  etc.

$$T_n(\alpha, \beta) = H_n(\alpha, \beta) = G_n(\alpha, \beta) + G_{n+1}(\alpha, \beta) \quad (\text{A.2})$$

It is also useful to note from these definitions that  $G_n(\beta, \alpha) = G_{-n}(\alpha, \beta)$  and  $H_n(\beta, \alpha) = H_{-n-1}(\alpha, \beta)$ .

### A.1.1 Type $T_2$ regions

A region of type  $T_2$  consists of one set of straight lines and one set of curves. The coordinates are then the distance along the straight lines for  $\alpha$ , and  $\beta$  is the angle turned through by the curves, i.e.  $\phi = \beta$ . The region is then defined by the functions  $A(\alpha, \beta) = 1$  and  $B(\alpha, \beta) = \alpha + F(\beta)$ . The coefficients of the series expansion of  $F$  will be termed  $D_n$  and will be defined for integers  $1 \leq n \leq \infty$  such that

$$B(\alpha, \beta) = \alpha + F(\beta) = \alpha + \sum_{n=0}^{\infty} \frac{D_{n+1}}{n!} \beta^n \quad (\text{A.3})$$

Table A.1 shows the expressions for  $B(\alpha, \beta)$  and the values of  $D_n$  for a number of regions of type  $T_2$  in solutions in the literature. The values of  $D_n$  for some of these are plotted in Figure A.1. It is shown that the values of  $D_n$  rapidly become small as  $n$  increases for all the regions considered.

### A.1.2 Type $T_1$ regions

Regions of type  $T_1$  are those with two sets of curved coordinate lines containing no inflexions. The coordinates  $\alpha$  and  $\beta$  are then defined as the angles turned through by the coordinate axes, the angle of the  $\alpha$  line to the local  $x$  axis is  $\phi = -\alpha + \beta$ .

The functions which define a region of type  $T_1$  can be expressed as a series expansion with coefficients  $C_n$ , for all integer values of  $n$  from  $-\infty$  to  $\infty$ . This is discussed in detail in Appendix C.3.1. Here we simply note that these constants give the functions  $A$  and  $B$  with either the relationship,

$$A = \sum_{a=0}^{\infty} \sum_{b=0}^{\infty} \frac{1}{a!b!} C_{b-a} \alpha^a \beta^b, \quad B = \sum_{a=0}^{\infty} \sum_{b=0}^{\infty} \frac{1}{a!b!} C_{b-a+1} \alpha^a \beta^b \quad (\text{A.4})$$

or, equivalently,

$$A = \sum_{n=-\infty}^{\infty} C_n \left(\frac{\beta}{\alpha}\right)^{\frac{n}{2}} I_n(2\sqrt{\alpha\beta}) \quad B = \sum_{n=-\infty}^{\infty} C_{n+1} \left(\frac{\beta}{\alpha}\right)^{\frac{n}{2}} I_n(2\sqrt{\alpha\beta}) \quad (\text{A.5})$$

where  $I$  is the modified Bessel function of the first kind.

Table A.2 gives details of the functions  $A(\alpha, \beta)$  and  $B(\alpha, \beta)$  for a number of regions of type  $T_1$  known in the literature, the associated values of the coefficients  $C_n$  are also given. The values of  $C_n$  are also plotted in Figures A.2 and A.3. Figure A.2 shows the results for the regions of type  $T_1$  in the exterior of a square problem, and for the region of equiangular spirals; these are both problems with the whole plane as design domain. Figure A.3 presents results for regions drawn from problems constrained to a long, narrow design domain, note that in this case the values of  $C_n$  may be negative.

Region	Type	Analytical Function for $B$ ( $A = 1$ )	Power series
Michell (1904) Figure 2	Circular fan	$B(\alpha, \beta) = \alpha$	$D_n = 0$
Chan (1963) Fig 4, DCEF	Simply supported cantilever	$B(\alpha, \beta) = \alpha + r \left( I_0(\sqrt{2\pi\beta}) + \sqrt{\frac{\pi}{2\beta}} I_1(\sqrt{2\pi\beta}) \right)$ $= \alpha + r R_0(\frac{\pi}{2}, \beta)$	$D_n = r \left( \frac{(0.5\pi)^{n-1}}{(n-1)!} + \frac{(0.5\pi)^n}{n!} \right)$ $= r \left( (\frac{\pi}{2})^{n-1} \Xi(n) + (\frac{\pi}{2})^n \Xi(n+1) \right)$
Lewiński & Rozvany (2007) Fig 6, CDB <sub>1</sub> 'G <sub>1</sub>	Exterior of a trapezoid	$B(\alpha, \beta) = \alpha + r_0 (H_0(\theta, \beta))$	$D_n = r_0 (\theta^{n-1} \Xi(n) + \theta^n \Xi(n+1))$
Lewiński & Rozvany (2008b) Fig 4, D <sub>1</sub> HH <sub>1</sub> O	Exterior of a square	$B(\alpha, \beta) = \alpha + r (H_0(\frac{\pi}{2}, \beta) + H_0(\frac{\pi}{4}, \beta + \frac{\pi}{4}))$	$D_n = r (I_n(\frac{\pi}{2}) + I_{n-1}(\frac{\pi}{2})$ $+ (\frac{\pi}{2})^{n-1} \Xi(n) + (\frac{\pi}{2})^n \Xi(n+1))$
Lewiński & Rozvany (2008b) Fig 4, H <sub>1</sub> ''SJ <sub>1</sub> ''S <sub>1</sub> ''	Exterior of a square	$B(\alpha, \beta) = \alpha + r (H_0(\frac{\pi}{2}, \beta + \frac{\pi}{4}) + H_0(\frac{\pi}{4}, \beta + \frac{\pi}{2}) + H_0(\frac{3\pi}{4}, \beta))$	$D_n = 2^{\frac{n-1}{2}} I_{n-1}(\frac{\sqrt{2}\pi}{2}) + 2^{\frac{n}{2}} I_n(\frac{\sqrt{2}\pi}{2})$ $+ 0.5^{\frac{n-1}{2}} I_{n-1}(\frac{\sqrt{2}\pi}{2}) + 0.5^{\frac{n}{2}} I_n(\frac{\sqrt{2}\pi}{2})$ $+ (\frac{3\pi}{4})^{n-1} \Xi(n) + (\frac{3\pi}{4})^n \Xi(n+1)$

**Table A.1:** Details of selected known regions of type  $T_2$ . Values of  $r$ ,  $r_0$ ,  $\theta$  and  $h$  refer to geometrical parameters of the original problem classes.  $\Xi$  is the reciprocal gamma function (see Section C.3.4).

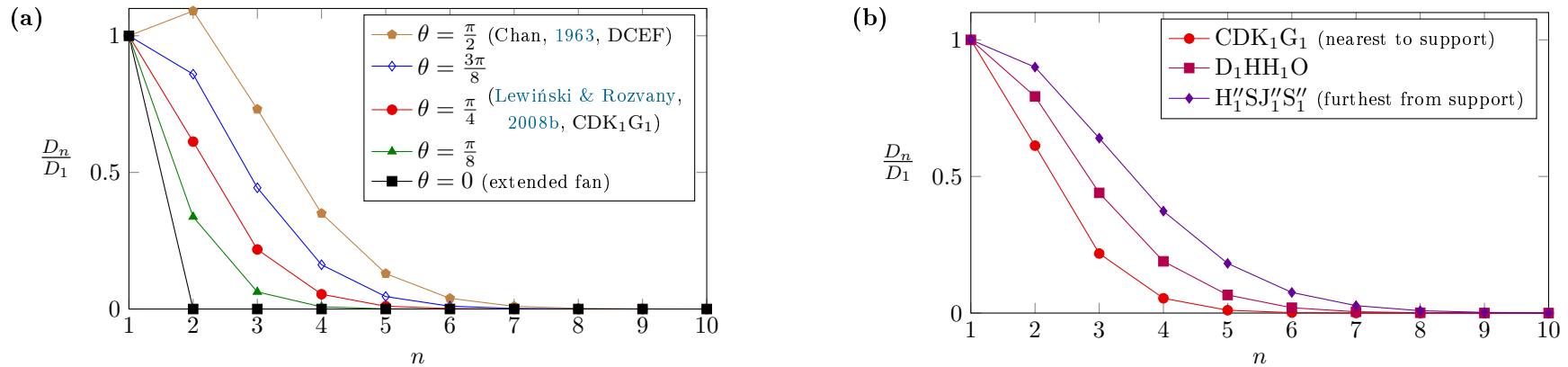


**Figure A.1:** Normalised values of the coefficients  $D_n$  for selected regions of type  $T_2$ . (a) Regions adjacent to type  $T_1$  regions based on circular arcs subtending angle  $\theta$  (i.e. Lewiński & Rozvany, 2007, Fig 6 CDB<sub>1</sub>'G<sub>1</sub>). (b) Regions in the exterior of a square problem (Lewiński & Rozvany, 2008b, Figure 4).

Region	Type	Analytical Function	Double power series
Michell (1904) Figure 1	Equiangular spirals	$A(\alpha, \beta) = B(\alpha, \beta) = r \exp(\alpha + \beta)$	$C_n = r$
Chan (1960) Fig 13, OADB	Arc-Based	$A(\alpha, \beta) = r \left( I_0(2\sqrt{\alpha\beta}) + \sqrt{\frac{\beta}{\alpha}} I_1(2\sqrt{\alpha\beta}) \right)$ $B(\alpha, \beta) = r \left( I_0(2\sqrt{\alpha\beta}) + \sqrt{\frac{\alpha}{\beta}} I_1(2\sqrt{\alpha\beta}) \right)$	$C_n = \begin{cases} r, & \text{if } n = 0, 1 \\ 0, & \text{otherwise} \end{cases}$
Sokoł & Lewiński (2010) Eqn. (2.4) Fig 2, ACDB	Arc-Based (unequal radii)	$A(\alpha, \beta) = r_1 I_0(2\sqrt{\alpha\beta}) + r_2 \sqrt{\frac{\beta}{\alpha}} I_1(2\sqrt{\alpha\beta})$ $B(\alpha, \beta) = r_2 I_0(2\sqrt{\alpha\beta}) + r_1 \sqrt{\frac{\alpha}{\beta}} I_1(2\sqrt{\alpha\beta})$	$C_n = \begin{cases} r_1, & \text{if } n = 0 \\ r_2, & \text{if } n = 1 \\ 0, & \text{otherwise} \end{cases}$
Hemp (1973) Figure 4.15	Cycloid	$\phi = \alpha + \beta \quad \begin{aligned} A(\alpha, \beta) &= 2h \cos(\alpha + \beta) \\ B(\alpha, \beta) &= 2h \sin(\alpha + \beta) \end{aligned}$ $\phi = -\alpha + \beta \quad \begin{aligned} A &= 2h \cos(\alpha - \beta + \frac{\pi}{4}) \\ B &= 2h \sin(\alpha - \beta + \frac{\pi}{4}) \end{aligned}$	$C_n = \begin{cases} h\sqrt{2}, & \text{if } n \bmod 4 = 0, 1 \\ -h\sqrt{2}, & \text{if } n \bmod 4 = 2, 3 \end{cases}$
Lewiński et al. (1994a), Fig 4a DHJG	Symmetrical cantilever	$\frac{A(\alpha, \beta)}{r} = H_{-1}(\alpha, \beta) - H_0(\alpha - \theta, \beta + \theta) - H_{-2}(\alpha + \theta, \beta - \theta)$ $\frac{B(\alpha, \beta)}{r} = H_0(\alpha, \beta) - H_1(\alpha - \theta, \beta + \theta) - H_{-1}(\alpha + \theta, \beta - \theta)$	see Dewhurst (2001)
Lewiński & Rozvany (2008b) Fig 4, B <sub>1</sub> D <sub>1</sub> HD' <sub>1</sub>	Exterior of a square	$A(\alpha, \beta) = r \left( H_{-1} \left( \alpha + \frac{\pi}{4}, \beta \right) + H_{-1} \left( \alpha, \beta + \frac{\pi}{4} \right) \right)$ $B(\alpha, \beta) = r \left( H_0 \left( \alpha + \frac{\pi}{4}, \beta \right) + H_0 \left( \alpha, \beta + \frac{\pi}{4} \right) \right)$	$\frac{C_n}{r} = \left( \frac{\pi}{4} \right)^n \Xi(n+1) + \left( \frac{\pi}{4} \right)^{n-1} \Xi(n)$ $+ \left( \frac{\pi}{4} \right)^{1-n} \Xi(2-n) + \left( \frac{\pi}{4} \right)^{-n} \Xi(1-n)$
Lewiński & Rozvany (2008b) Fig 4, OH <sub>1</sub> SH'' <sub>1</sub>	Exterior of a square	$A(\alpha, \beta) = r \left( H_0 \left( \beta + \frac{\pi}{4}, \alpha + \frac{\pi}{4} \right) + H_0 \left( \beta, \alpha + \frac{\pi}{2} \right) + H_0 \left( \beta + \frac{\pi}{2}, \alpha \right) \right)$ $B(\alpha, \beta) = r \left( H_0 \left( \alpha + \frac{\pi}{4}, \beta + \frac{\pi}{4} \right) + H_0 \left( \alpha + \frac{\pi}{2}, \beta \right) + H_0 \left( \alpha, \beta + \frac{\pi}{2} \right) \right)$	$\frac{C_n}{r} = I_n \left( \frac{\pi}{2} \right) + I_{n-1} \left( \frac{\pi}{2} \right)$ $+ \left( \frac{\pi}{2} \right)^n \Xi(n+1) + \left( \frac{\pi}{2} \right)^{n-1} \Xi(n)$ $+ \left( \frac{\pi}{2} \right)^{1-n} \Xi(2-n) + \left( \frac{\pi}{2} \right)^{-n} \Xi(1-n)$

**Table A.2:** Details of selected known regions of type  $T_1$ . Where alternative choices of origin points were used in the original form, these are shown in grey and an appropriate transformation is used to find comparable expressions. Values of  $r$ ,  $r_1$ ,  $r_2$ ,  $\theta$  and  $h$  refer to geometrical parameters of the original problem classes.  $\Xi$  is the reciprocal gamma function (see Section C.3.4).

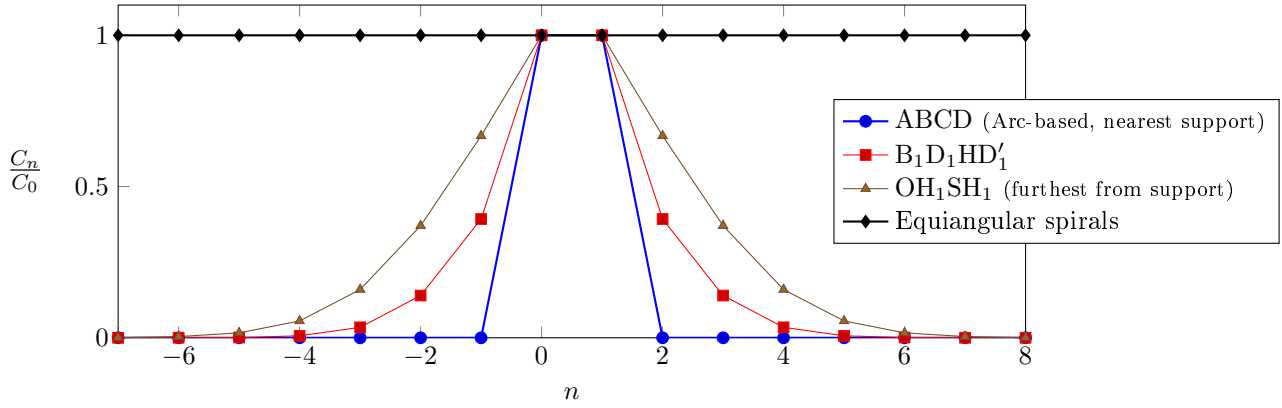


**Figure A.2:** Normalised values of the coefficients  $C_n$  for regions of type  $T_1$  within the solution of Lewiński & Rozvany (2008b) for the exterior of a square problem.

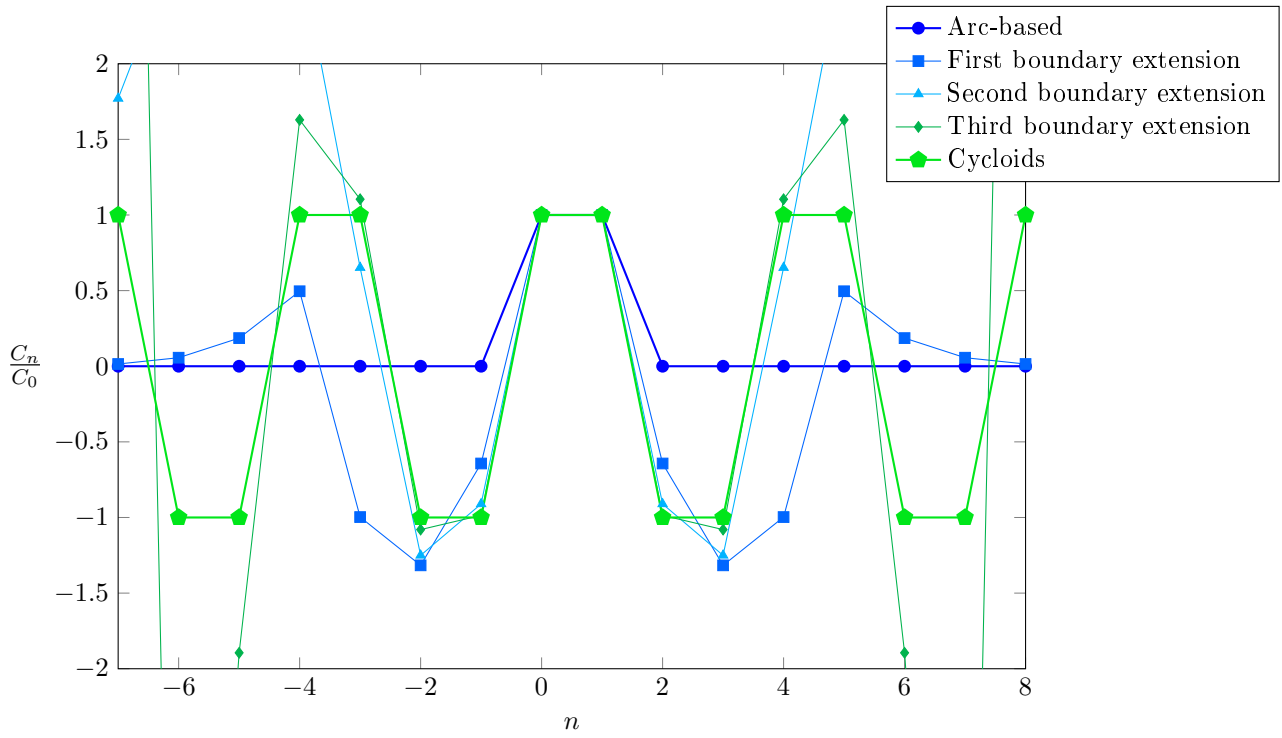


**Figure A.3:** Normalised values of the coefficients  $C_n$  for a region of type  $T_1$  consisting of a series of cycloids Hemp (1973, figure 4.15), and for the first four  $T_1$  type regions in a long cantilever constrained to lie within a parallel sided strip (Dewhurst, 2001, table 2), i.e. where the ‘first boundary extension’ result is equivalent to the result of Lewiński et al. (1994a, fig 4a, DHJG).





## Appendix B

# Further applications of counterweights

This appendix presents some further examples using the counterweight modelling approach discussed in Section 5.3.1. The focus is on scenarios where counterweights are used in practice, the first example is based on a simplified crane design, and the second concerns gravity balanced cable stay bridges.

A number of additional characteristics are observed; firstly that two load case problems using this method do not appear to be entirely approachable using the superposition method. Secondly that counterweight loading may be treated as analogous to transmissible loads with regards to the angles of supporting bars.

The formulation for frictional supports from Section 5.3.2 is also extended to cases where the frictional plane is not horizontal. This provides a more realistic physical interpretation of the larger values for the coefficient of friction which were used in Chapter 5.

---

B.1	Crane structure example . . . . .	184
B.1.1	Influence of structural complexity on counterweight use . . . . .	184
B.1.2	Variations in counterweight cost and material strength . . . . .	186
B.1.3	Inclusion of tower structure . . . . .	186
B.1.4	Multiple load cases . . . . .	188
B.2	Counterbalance bridge example . . . . .	190
B.3	Foundations on inclined frictional planes . . . . .	191
B.3.1	Formulation with inclined frictional supports . . . . .	191
B.3.2	Equivalent values of $\mu$ and $\psi$ . . . . .	191

---

## B.1 Crane structure example

A real world application which frequently makes use of counterweights is the design of cranes. Tower cranes in use today use a wide variety of structural forms, as shown in Figure B.1. However, most designs make use of some form of counterweight, frequently in the form of pre-cast concrete sections.



**Figure B.1:** A variety of designs of tower crane in use.

The simplified design problem considered here is illustrated in Figure B.2. For this scenario, a span of 60m is required, and a back-span of up to 30m from the front of the tower may be utilised. A point load of 22kN must be supported at the far end of the span.

The crane is to be supported on a 4m wide tower. It will be initially assumed that the tower's load carrying capacity is not governed by the loading from this case, but instead by other load cases such as wind loading during survival conditions. Therefore the initial problem will be independent of the total height of the crane.

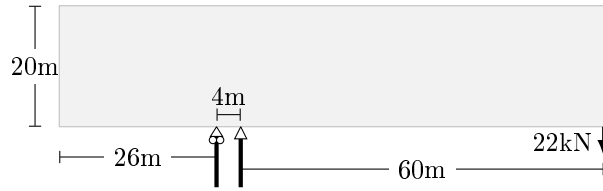


**Figure B.2:** Crane example: Problem specification. The shaded area is the considered design domain.

The structure is initially assumed to be constructed from a material with a unit weight  $\rho g = 80 \frac{\text{kN}}{\text{m}^3}$ , a tensile strength,  $\sigma_T$ , of 300MPa and a compressive strength,  $\sigma_C$ , of 150MPa. The cost of this material is  $3645 \frac{\text{£}}{\text{m}^3}$ . Also available is a cheaper material, which has no strength, but has a unit weight of  $23 \frac{\text{kN}}{\text{m}^3}$  and a unit cost,  $p_U$ , which varies between 0 and  $60 \frac{\text{£}}{\text{m}^3}$ .

Combining these two materials allows the force to be equilibrated in a number of ways, including using a balancing counterweight placed within the back-span, or a moment developed between the two supports. Layout optimization has been performed using a dense nodal grid (0.5m spacing, allowing for almost 26 million potential truss members) for a range of values of  $p_U$  and the results are shown in Figure B.3.

Both the total cost of the structure (i.e. the optimal objective value) and the cost of the structural elements are plotted. When the counterweight material is relatively expensive, the total cost and the cost of the bars are identical. In this region, no counterweights are used and the force is supported entirely by means of the moment generated at the two supports.

Similarly to the cantilever problem in Figure 5.5, the change from a counterweight based solution to a moment supported solution happens abruptly. However, the solutions where counterweights are present are not purely balanced structures except in the case where  $p_U = 0$ , this is evidenced by the presence of a fan of tension members from the back support. Instead, these structures are a hybrid, consisting of an outer area of structure which forms a balance about a point within the main span. This balance point is then supported by the inner structure, which is reminiscent of the classical michell cantilever.

### B.1.1 Influence of structural complexity on counterweight use

The results shown in Figure B.3 make use of a complex structure, as is common in michell type problems. However, for practical usage, simpler structures are generally required. Simplification of these structures will increase the material usage of the truss bars. However it will make little difference to the required counterweight volume, if the location is kept constant.

To investigate the impact that this structural rationalization has on the results, the same problem has been investigated using coarser nodal grids. Figure B.5 shows the results of layout optimization using a nodal grid with 2m spacing. Figure B.4 shows the results of layout optimization using a 4m nodal grid, followed by

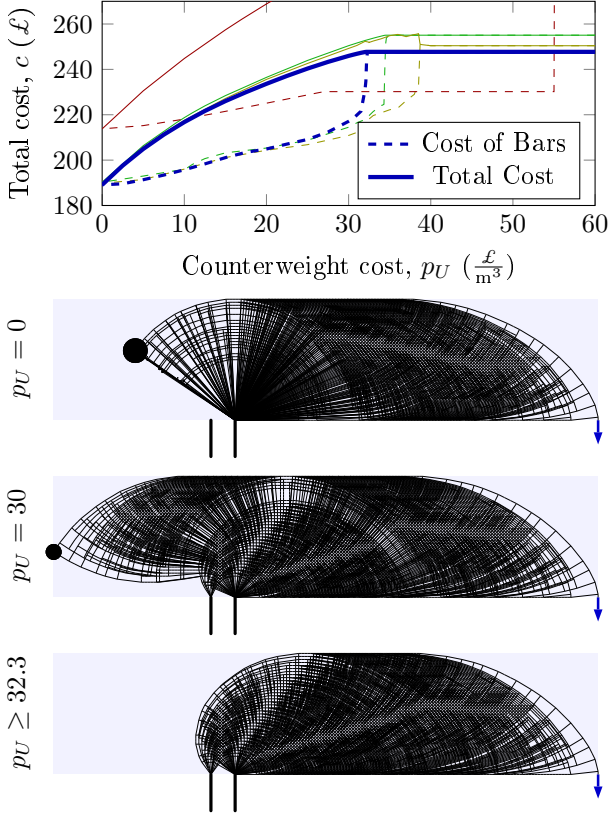


**Figure B.3:** Crane example: Results of layout optimization with 0.5m nodal grid.

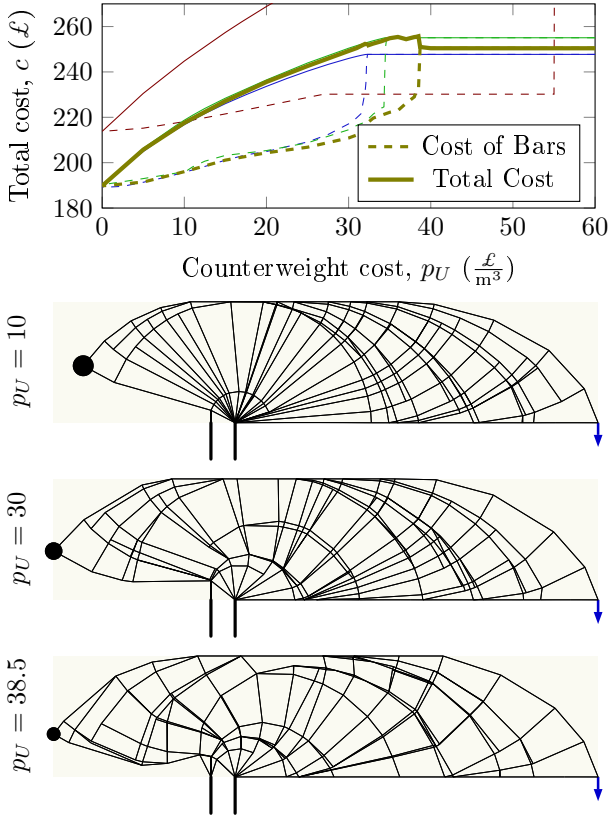


**Figure B.4:** Crane example: Results of layout optimization using 4m nodal grid followed by geometry optimization.

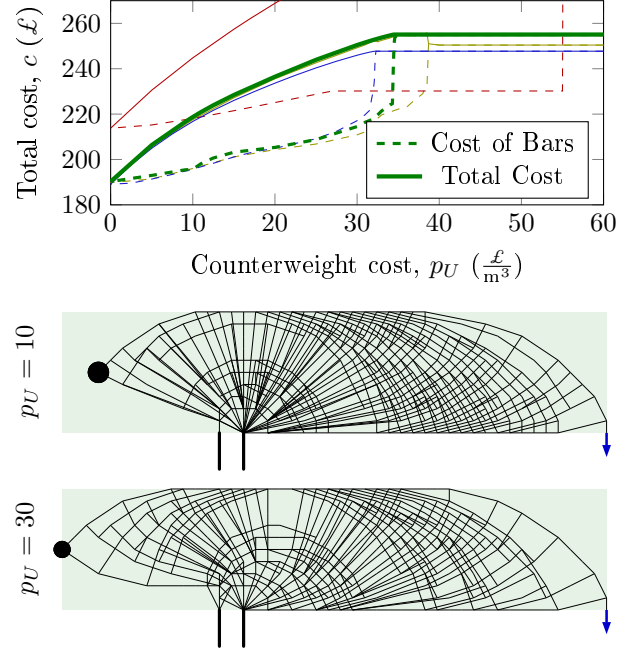


**Figure B.5:** Crane example: Results of layout optimization using 2m nodal grid.

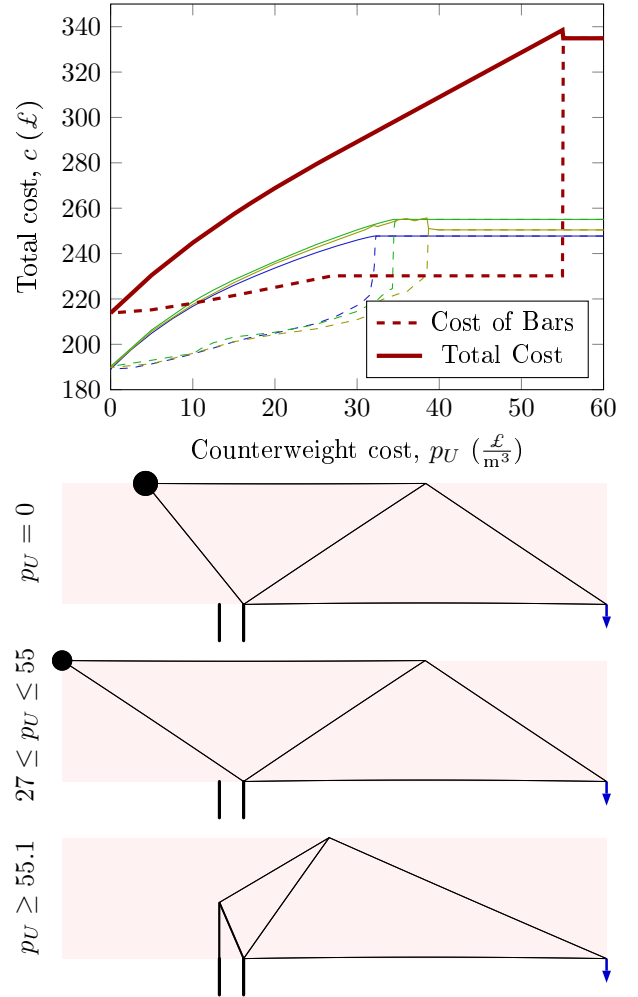


**Figure B.6:** Crane example: Results of layout optimization with minimal nodes followed by geometry optimization.

rationalization using geometry optimization. Figure B.6 shows the results of layout and geometry optimization using a ground structure with nodes at the loads, supports and the points (0m,20m), (25m,10m) and (50m,20m).

The results in Figures B.3-B.5 display similar values for the total costs throughout the cost range investigated, this is particularly pronounced at lower values of  $p_U$ . It can be seen that all cases show a sudden jump where the use of the counterweight becomes advantageous. However, the value of  $p_U$  at which this jump occurs is quite variable, even when the total costs on each side of the jump are very similar.

The optimal cost when counterweights are not used provides an upper bound for the global optimum for any value of  $p_U$ . In Figures B.4 and B.6, i.e. the results which use geometry optimization, it can be seen that local optima have been identified in the region where the change to counterweight use occurs. Therefore, for practical usage with low resolutions and geometry optimization, it may be useful to solve a problem both with and without permitting counterweights to ensure the correct solution is identified.

However, the impact of structural complexity is significant. This can be seen clearly in Figure B.6. The critical value at which the optimal solution changes from a counterweight based form to a moment support form is requires the counterweight material price to be approximately 40% greater than the critical value for a high complexity structure, such as in Figure B.3.

### B.1.2 Variations in counterweight cost and material strength

A series of scenarios were considered using layout optimization with a nodal grid of 0.5m spacing. As previously, the scenarios varied in the values of the unit cost for unstressed material,  $p_U$ . The values of material strength,  $\sigma_T$  and  $\sigma_C$ , were also varied, although the ratio  $\frac{\sigma_T}{\sigma_C}$  was kept constant and equal to 2. The volume of material used in the counterweight is shown in Figure B.7a. When unstressed material is expensive and the available material is strong, counterweights are not used, and a form similar to that shown in Figure B.7b is identified.

As seen in Figures B.3-B.6, the change in form to make use of counterweights is abrupt. The change appears to occur approximately on a line with the form  $p_U \sigma_T = \text{constant}$ . Beyond that line, there is a gradual increase in the volume of the optimal counterweight as either  $p_U$  or  $\sigma_T$  are reduced. As this happens, the location of the counterweight moves horizontally towards the support, as can be seen in the forms shown in Figure B.7c-f.

The positions of the counterweights for results with  $\sigma_T = 100\text{MPa}$ ,  $200\text{MPa}$ ,  $300\text{MPa}$ ,  $400\text{MPa}$  and  $500\text{MPa}$  have been interpolated and the resulting bezier curves are plotted in Figure B.7g, along with the positions of the counterweights for the layouts in Figure B.7c-f. It can be seen that all results follow very similar lines, this demonstrates that points in Figure B.7a with the same colour have very similar layouts.

### B.1.3 Inclusion of tower structure

However, the layouts in Figure B.7 require a variety of different support conditions. If the design of the tower is governed by the currently considered load case, it would be preferable to include this in the formulation. Therefore Figure B.8 shows results where a tower of height 60m is also included. Note that, in this case, the unit cost of the counterweight material must be significantly (by approximately a factor of 10) increased before it ceases to be advantageous to make use of a counterweight. Structures which do not make use of counterweights are as seen in Figure B.7b.

When a counterweight is used, the form is generally as shown in Figure B.8b. This layout, using only one support and also using the full permitted back-span, is not seen in Figure B.7. When the cost of the tower members is included, it is preferable to make use of the largest permitted back-span in order to reduce the mass of the counterweight and therefore the force which must be transmitted by the tower. The same layout is observed throughout the paler blue area of Figure B.8a, with the only minor change being that the volume of the counterweight should balance the increased structural mass when lower material strengths are used. This results in an increase of only 7% between the results with  $\sigma_T = 500$  and  $\sigma_T = 100$ .

Within the transition region in Figure B.8 there is evidence of structures similar to that of B.7c (e.g. Figure B.9a), however the range of cases for which these intermediate structures are optimal is relatively small.

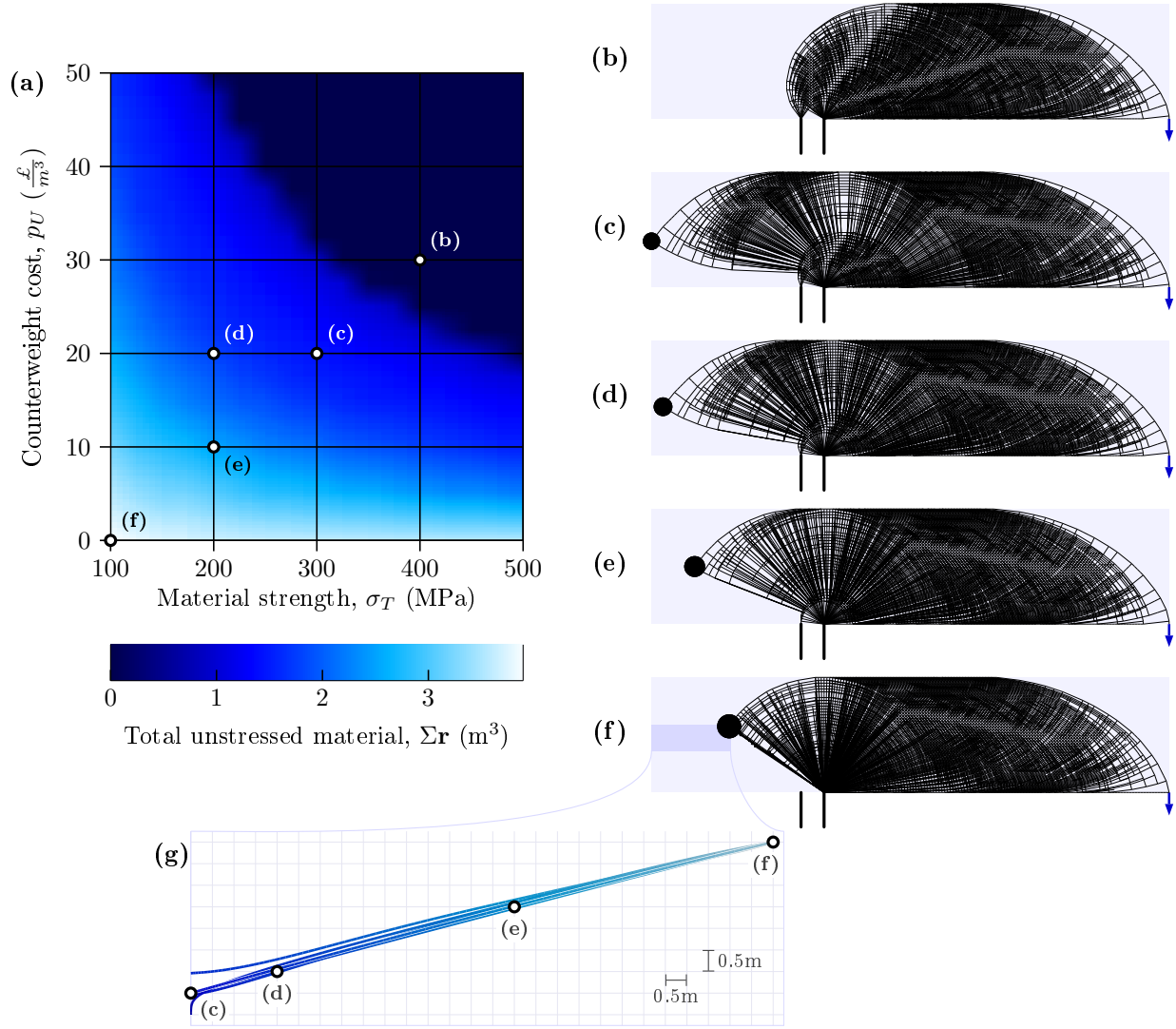


**Figure B.7:** Crane example: Effect of variations in material strengths and costs on the use of counterweights in the optimal structure. Layout optimization results with 0.5m nodal spacing.

**(a)** Total volume of unstressed material in optimal structure for a range of material strengths and unit costs of counterweights.

**(b)-(f)** Optimal layouts for  $p_U$  and  $\sigma_T$  as marked in (a).

**(g)** Magnified view of portion of design domain shown darker in (f), the grid shows the spacing of the ground structure nodes. Counterweight positions for layouts (b)-(f) are shown. Also, bezier curves for  $\sigma_T = 100, 200, 300, 400$  and  $500$  MPa have been interpolated from the positions of the counterweight in all relevant results from (a), these have been coloured using the same colour scale as in (a).

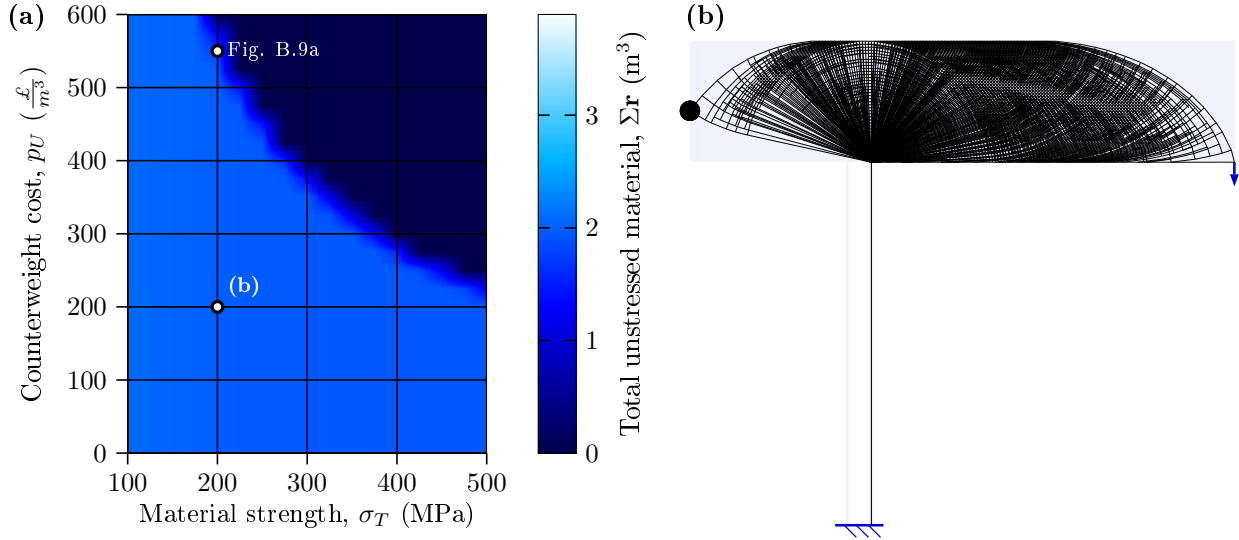


**Figure B.8:** Crane example: Effect of variations in material strengths and costs on the use of counterweights in the optimal structure, when the cost of the material in the tower is included.

(a) Total volume of unstressed material.

(b) Optimal layouts for  $p_U = 200 \frac{\text{£}}{\text{m}^3}$  and  $\sigma_T = 200 \text{ MPa}$ , as marked in (a).

#### B.1.4 Multiple load cases

The structures in Figures B.7f and B.8c make use of only one of the support points. Clearly this would be unstable if the external load was removed. Figures B.7c-e use both supports, but would still be unlikely to withstand the loading of the counterweight if the point load was not present.

To test this, a two load case problem will be studied, consisting of the original case plus an additional case containing no external loading, but still considering the weight of the counterweight. This result is shown in Figure B.9d. Due to the limitations of the distributed self-weight modelling, this result neglects the self-weight of the structural members, and for comparison the single load case result under these assumptions is given in Figure B.9c.

The result of the two load case problem shows a layered structure, as is usual for standard multiple load case problems (i.e. without counterweights or self weight). In such problems, the superposition approach is often used to obtain the solution to the multiple load case problem, from the solutions to two related single load case problems, the sum and difference problems respectively. It may therefore be interesting to consider the results of similar logic to this problem.

If the force imposed by the counterweight is considered as an external force (present in both load cases) then the component load cases used in the superposition principle can be found. The sum load case would consist of the load of the counterweight (at full magnitude) and the external load at half magnitude. The difference load case would consist of only the half magnitude external force, whilst the load from the counterweight would cancel to nothing. Thus, it may be expected that the solution would consist of the result from B.9c combined with a form similar to that of Figure B.9b.

Qualitatively, this seems to be roughly accurate, but closer inspection reveals some differences. For example, in the back span of B.9d, there does not seem to be evidence of the central region of straight lines as seen in B.9. Furthermore, the counterweight in B.9d is only 40% of the volume of the counterweight in Figure B.9c. This suggests that there may be more factors influencing the two load case situation.

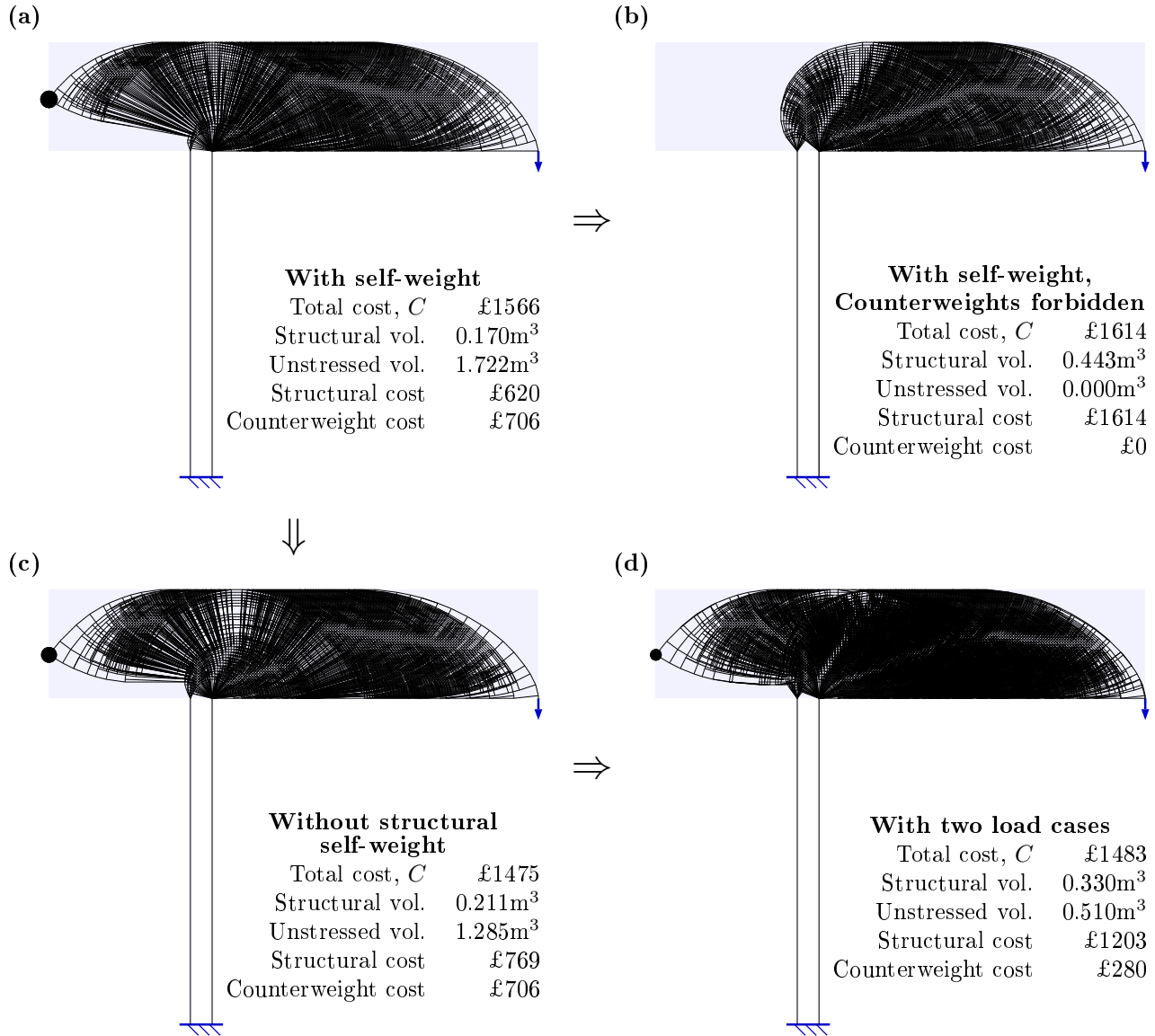


**Figure B.9:** Crane example: Cases with  $\sigma_T = 200\text{MPa}$ ,  $p_U = 550\frac{\text{£}}{\text{m}^3}$  and tower height of 60m.

(a) Single load case - as in Figure B.8. Counterweight is 9.5m above the top of the tower.

(b) As in (a) but with counterbalances not permitted.

(c) As in (a) but with self-weight of structural members neglected. Counterweight is 8m above the top of the tower.

(d) As for (c) but with the addition of a second load case containing no external loads. Counterweight is 8m above the top of the tower.



## B.2 Counterbalance bridge example

Another famous example of a structural layout based on the use of counterweights is the Alamillo bridge, a gravity balanced cable stayed bridge design by Santiago Calatrava. This unusual design has received substantial attention, however it is generally considered to be a very inefficient design, e.g. Croll (2019) state a value of 3.5 to 5.8 times the material required for a comparable harp type cable stayed bridge, whilst Guest et al. (2013) find that the pylon weight is over 10 times that of a cable stayed form, and also compare overall cost with a bridge of a more standard cable stayed design and substantially longer span, finding that the Alamillo bridge has almost twice the cost per  $\text{m}^2$ .

Despite this, it may still be possible that there are certain scenarios for which this design is preferred. One such example is shown in Figure B.10a-c, where a span is pin supported at one end, and has only a horizontal support force at the other. The material has equal strength in tension and compression of  $\sigma$ , and the loaded span has a length of  $0.16 \frac{\sigma}{\rho g}$  (approximately 1km with realistic material values such as in Chapter 4).

The results in Figure B.10a-c show cases where the counterweight material ranges from close to the same price as the structural material, to having no cost. These structures show a number of designs ranging from counterweights located very close to the supports, to structures making use of the whole of the permitted backspan. A very simplified form of these could be imagined where all radial members except the deck and a single outer pylon were eliminated, this would then be very similar to the Alamillo bridge.

In all three cases, the counterweights are supported by pairs of members at  $\pm 45^\circ$ . Similarly in Section B.1, all counterweights are supported by members at approximately the same inclinations, although as that case does not have equal tensile and compressive strengths they are not at  $\pm 45^\circ$ . This property is related to the observation of Lu et al. (2018) that equal strength tension and compression members which meet a pre-existing member (or equivalently a transmissible load) should do so at angles of 45 degrees. The counterweight force is in many ways similar to a transmissible load; in that its location is controlled by the optimization algorithm, although clearly it differs in that its magnitude can also vary.

The structure in Figure B.10c has a total material cost of almost double that of Figure B.10a. However, in the far more likely case that a vertical support could be used at the right end, an arch type form becomes far more efficient (Figure B.10d), with a total material cost of just over a quarter of that in B.10a, i.e. around an eighth of the cost of Figure B.10c.

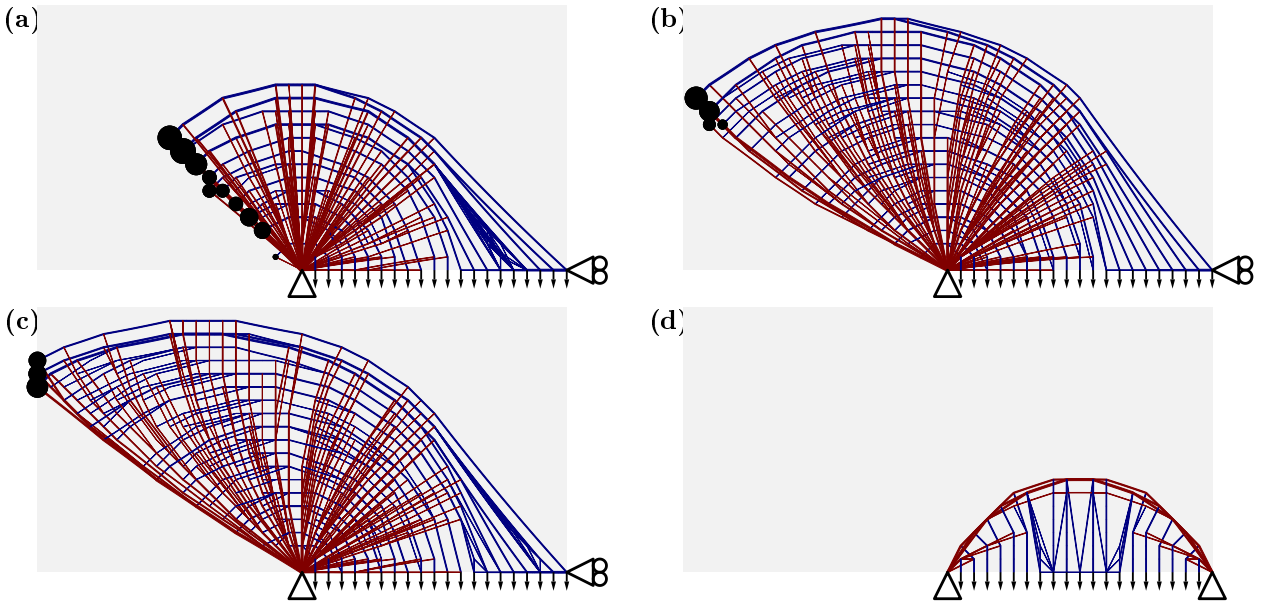


**Figure B.10:** Cantilever bridge example: Resulting structures.

- (a) Counterweight cost,  $p_U = 0$ . Total cost =  $c'$
- (b) Counterweight cost,  $p_U = 10\%$  of structural material costs. Total cost =  $1.15c'$
- (c) Counterweight cost,  $p_U = 99\%$  of structural material cost. Total cost =  $1.96c'$
- (d) With pin supports on both sides. Total cost =  $0.26c'$ .



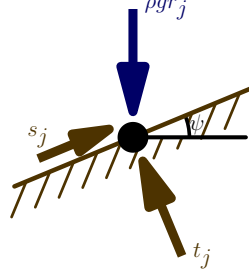


**Figure B.11:** Reaction and counterweight forces acting on a frictional foundation node.

## B.3 Foundations on inclined frictional planes

### B.3.1 Formulation with inclined frictional supports

This section describes an extension to the proposed formulation for frictional foundations to handle cases where a structure is supported on a non-horizontal frictional plane. The angle between the surface and horizontal will be notated as  $\psi$ , as shown in Figure B.11.

The equilibrium constraint (5.9b) will be modified by changing the coefficients of  $\mathbf{C}$  and  $\mathbf{D}$  such that, for a single supported node  $j$ , equation (5.9b) becomes

$$\mathbf{B}_j \mathbf{q} + \rho g \begin{bmatrix} 0 \\ 1 \end{bmatrix} r_j + \begin{bmatrix} \cos \psi_j \\ \sin \psi_j \end{bmatrix} s_j + \begin{bmatrix} -\sin \psi_j \\ \cos \psi_j \end{bmatrix} t_j = \begin{bmatrix} f_j^x \\ f_j^y \end{bmatrix} \quad (\text{B.1})$$

where  $\mathbf{B}_j$  represents the rows of  $\mathbf{B}$  relating to node  $j$ , and  $\psi_j$  is the inclination of the frictional plane at joint  $j$ .

### B.3.2 Equivalent values of $\mu$ and $\psi$

Consider a scenario where the frictional force  $t_j$  is known to act in one (positive) direction, and where the volume of the counterweight,  $r_j$ , is selected so as to ensure that the foundation just resists slipping. Then equation (5.9c) will be satisfied by equality, and the resultants of  $t_j$  and  $s_j$  in the  $x$  and  $y$  directions can be written as

$$t_j(\mu \cos \psi + \sin \psi) = f_x \quad (\text{B.2a})$$

$$t_j(\mu \sin \psi + \cos \psi) = f_y \quad (\text{B.2b})$$

A set of modified values  $\mu^*$  and  $\psi^*$  will produce identical behaviour if they result in the same values of  $f_x$  and  $f_y$  for some value  $t_j^*$ . By equating original and modified versions of equation (B.2), and eliminating  $\frac{t_j}{t_j^*}$ , a relationship between the original and modified values is found. After some rearrangement, this may be conveniently stated as

$$\psi^* + \arctan \mu^* = \psi + \arctan \mu \quad (\text{B.3})$$

For example, a foundation plane where  $\psi = 20^\circ$  and  $\mu = 0.4$  where the structure applies a force which pulls the node uphill, could be equivalently represented by a flat surface,  $\psi^* = 0$  with  $\mu^* \approx 0.9$ .

Note however, that the conditions which have been used to derive this equivalence are rather onerous, and provide little scope for consideration of alternate loading cases or construction stages. The example of the previous paragraph would be equivalent to a flat surface with  $\mu^* \approx 0.03$  if the horizontal force was such that the frictional force changed direction. Additionally, the stability of the sloped plane itself must be taken into consideration.

For these reasons, equation (B.3) is unlikely to be of practical application. This relationship is not incorporated within the optimization formulation, and is instead presented here to provide some element of physical interpretation whilst allowing for investigation of cases where the support conditions approach a pin support, i.e. with large values of  $\mu$ .



## Appendix C

# Derivation of further region types for RAGS method

This appendix discusses potential extensions to the Region based Adaptive Ground Structure (RAGS) method to incorporate the other region types which may be found in Michell structures. These include type  $R$  and  $S$  regions, and further regions of type  $T$ . The latter are again discussed using the special coordinate systems defined by Chan (1960). It is possible to imagine curvilinear coordinate systems that do not fall into any of these three categories, for example regions consisting of two families of curves which contain inflexions. However, such coordinate systems would be more difficult to model than the well defined classes considered here, also it is likely to be reasonable to model such regions as multiple smaller regions. As such the focus here is limited to the cases denoted as  $T_1$ ,  $T_2$  and  $T_3$ .

The majority of this chapter is concerned with regions of truss-like continua, these would allow the identification of the most accurate benchmark structures. Discretised structures, similar to those considered in Section 7.5 are briefly discussed where relevant.

---

C.1	Type $T_3$ regions . . . . .	194
C.2	Type $T_2$ regions . . . . .	195
	C.2.1 Examples from literature . . . . .	195
	C.2.2 Discretised geometry . . . . .	196
C.3	Type $T_1$ regions . . . . .	197
	C.3.1 Numerical approximation methods . . . . .	198
	C.3.2 Examples from literature . . . . .	198
	C.3.3 Circular based regions . . . . .	199
	Possible regions for fixed points O, A and B . . . . .	199
	Possible regions for fixed O and P . . . . .	201
	C.3.4 Fields extended from circular arcs . . . . .	202
	Uniqueness of regions derived from circular based fields . . . . .	204
	Limits at infinity . . . . .	204
	C.3.5 Discretised geometry - kinematic constraints . . . . .	207
C.4	Type $R$ regions . . . . .	210
C.5	Type $S$ regions . . . . .	210

---

### C.1 Type $T_3$ regions

Regions of type  $T_3$  consist of two sets of orthogonal straight lines, the coordinates  $\alpha$  and  $\beta$  are the distances along each set of lines from the origin  $O$ . In these regions,  $\frac{d\phi}{d\alpha} = \frac{d\phi}{d\beta} = 0$ , i.e.  $\phi$  is constant. The corner points of this region, and their associated local displacements illustrated in C.1a and given by

$$A(l_{OA}, 0) : \quad \dot{u}_A^\alpha = \varepsilon l_{OA} \quad \dot{u}_A^\beta = \omega_0 l_{OA} \quad (C.1a)$$

$$B(0, l_{OB}) : \quad \dot{u}_B^\alpha = -\omega_0 l_{OB} \quad \dot{u}_B^\beta = -\varepsilon l_{OB} \quad (C.1b)$$

$$P(l_{OA}, l_{OB}) : \quad \dot{u}_P^\alpha = \varepsilon l_{OA} - \omega_0 l_{OB} \quad \dot{u}_P^\beta = -\varepsilon l_{OB} + \omega_0 l_{OA} \quad (C.1c)$$

These regions are mostly considered trivial cases; and indeed it seems unlikely that there would be a need to consider them explicitly within the framework of the RAGS method as they may be modelled well using the existing straight bar elements. However, as a demonstration of the importance of appropriate selection of constraints, they will be briefly discussed here. Two different means of cancelling  $\omega_0$  from equations (C.1) will be compared.

Using  $\dot{u}_B^\alpha$  from equation (C.1b) to find  $\omega_0$ , and substituting into the equation (C.1c) for  $\dot{u}_P^\alpha$ , gives

$$\begin{aligned} \dot{u}_P^\alpha &\leq \varepsilon l_{OA} + \dot{u}_B^\alpha \\ (u_P^\alpha - u_O^\alpha) - (u_B^\alpha - u_O^\alpha) &\leq \varepsilon l_{OA} \\ u_P^\alpha - u_B^\alpha &\leq \varepsilon l_{OA} \end{aligned} \quad (C.2)$$

Then duality principles are used to give the static form as

$$\begin{bmatrix} -1 \\ 1 \end{bmatrix} q = \begin{bmatrix} f_B^\alpha \\ f_P^\alpha \end{bmatrix}, \quad V = \frac{l_{OA}}{\sigma} \quad (C.3)$$

This can be easily seen to be equivalent of a straight bar element from  $B$  to  $P$ , as shown in Figure C.1b.

Conversely, if the expression for  $\omega_0$  is found from equation (C.1a),

$$\begin{aligned} \omega_0 &= \frac{\dot{u}_A^\beta}{l_{OA}} \\ \dot{u}_P^\alpha &\leq \varepsilon l_{OA} - \frac{l_{OB}}{l_{OA}} \dot{u}_A^\beta \\ (u_P^\alpha - u_O^\alpha) + \frac{l_{OB}}{l_{OA}} (u_A^\beta - u_O^\beta) &\leq \varepsilon l_{OA} \end{aligned} \quad (C.4)$$

Converting this into the primal (static) form gives

$$\begin{bmatrix} -1 \\ -\frac{l_{OB}}{l_{OA}} \\ \frac{l_{OB}}{l_{OA}} \\ 1 \end{bmatrix} q = \begin{bmatrix} f_O^\alpha \\ f_O^\beta \\ f_A^\beta \\ f_P^\alpha \end{bmatrix}, \quad V = \frac{l_{OA}}{\sigma} \quad (C.5)$$

This set of forces is illustrated in Figure C.1c, note that this cannot be easily resolved into a feasible set of internal forces. This illustrates the care that must be taken when formulating constraints from these regions.

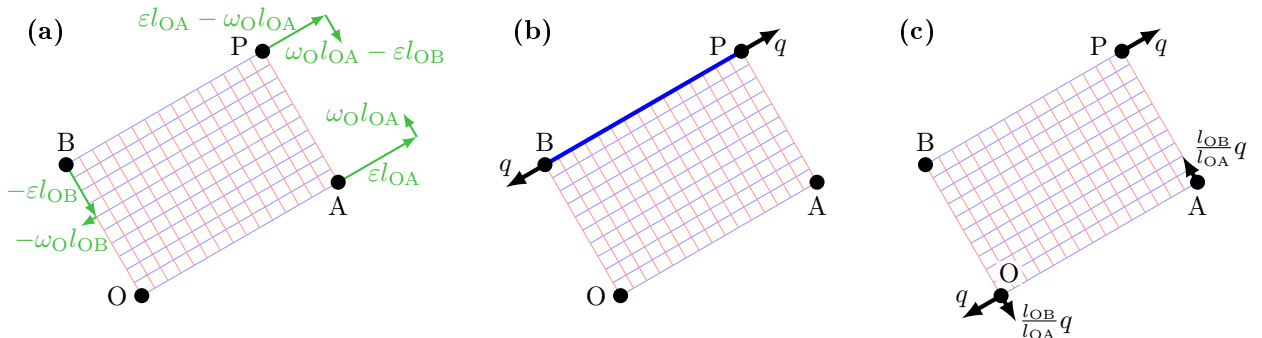


**Figure C.1:** Type  $T_3$  region. (a) Virtual deflections. (b)-(c) Possible static forms from duality principles.

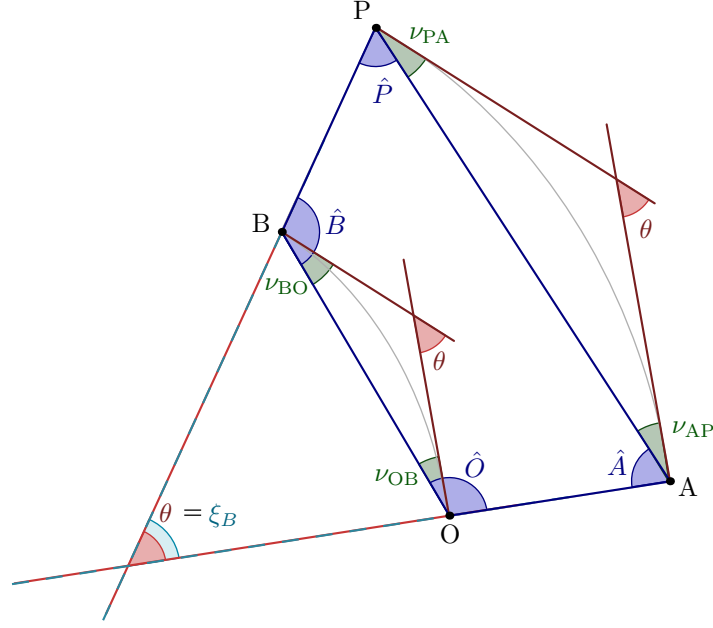


**Figure C.2:** Type  $T_2$  region: Definitions of points and angles.

## C.2 Type $T_2$ regions

Special coordinate system from Chan (1960), contains one set of straight coordinate lines and one set of curved lines. The  $\alpha$  coordinate is defined as the distance along the straight lines from the curve through point O and the  $\beta$  coordinate is the angle turned by the curved coordinate lines from the line OA. This region exists only when  $|OA| = |BP|$ ; all  $\alpha$ -lines then have a length equal to this. Thus, exact regions of this type are unlikely to be of significant use in layout optimization, where precisely placed nodes are not common.

The red lines in Figure C.2 are the tangents to the coordinate curves at the nodes, thus they are perpendicular to the lines OA or BP. Therefore it is easy to see that the angle turned through by the coordinate curves in this region will be equal to the angle between the lines OA and PB.

The limits on the coordinates within the region are given by

$$0 \leq \alpha \leq |OA| = |BP| \qquad 0 \leq \beta \leq \theta = \xi_B \qquad (C.6)$$

where  $\xi_B$  is defined as the angle between the lines OA and BP. These values are easily found from the positions of the four nodes.

The geometry functions for a general region of type  $T_2$  are

$$\phi = \beta \qquad A(\alpha, \beta) = 1 \qquad B(\alpha, \beta) = \alpha + F(\beta) \qquad (C.7)$$

where  $F(\beta)$  is a non-negative, monotonically increasing function.

### C.2.1 Examples from literature

The most common types of  $T_2$  region in the literature are the fan elements already discussed in Section 7.3. For these,  $F(\beta) = 0$  and therefore  $B(\alpha, \beta) = \alpha$ . It may be of interest to be able to construct a similar region of radial bars without them reaching the central points. For such a ‘doughnut’ type region with circular arcs,  $F(\beta) = r_B$  where  $r_B$  is the radius of the innermost arc between O and B. In these cases  $\nu_{OB} = \nu_{BO}$  and  $\nu_{AP} = \nu_{PA}$ .

A number of examples of type  $T_2$  regions drawn from the literature are examined in Table A.1. Generally, these bridge small gaps between adjacent regions of type  $T_1$ . In these cases, the curved  $\beta$  lines generally have zero thickness, this may lead to challenges in implementing these as part of the RAGS method, as it may be difficult to distinguish these regions from those of type  $R$  when a limited level of precision is available.

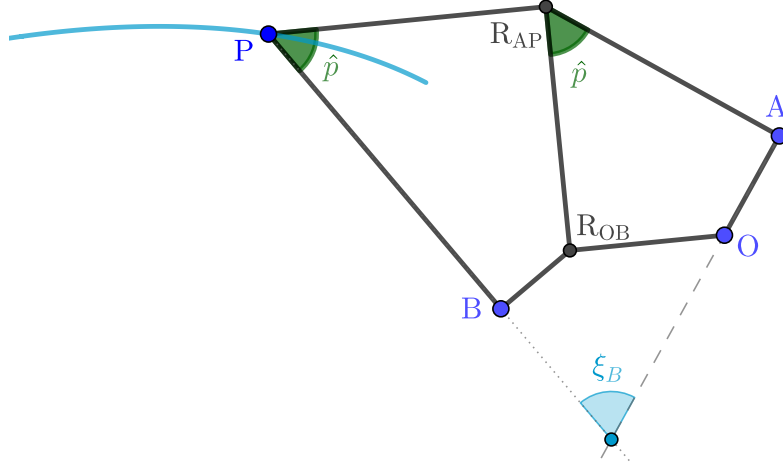


**Figure C.3:** A discrete approximation of a region using a  $1 \times 2$  cell mesh. The blue curve through P shows the locus of possible points for the given locations of A, B, and O.

### C.2.2 Discretised geometry

Discretised geometries following the same rules as Section 7.5 can be defined for  $1 \times n$  grids of mesh cells. In some ways these resemble regions of type  $T_2$ ; two opposing pairs of corner points are connected by straight lines, whilst the other pair are connected by an approximation to a curve. However these regions cannot be defined for points in general position. When three points are fixed, the fourth may only lie on a 1D locus. Figure C.3 shows an example where points O, A and B are fixed, point P may then only fall on the indicated curve. The curve is generated by altering the value of  $\xi_B$ , i.e. by moving the intersection point along the dashed line.

Furthermore, these regions cannot be usefully defined for regions where  $|OA| = |BP|$ , i.e. for any set of points for which a true  $T_2$  region could be defined. This can be seen by examining Figure C.3, note that lines  $OR_{OB}$  and  $R_{AP}P$  are parallel (as both are perpendicular to  $R_{OB}R_{AP}$ ). Line  $OR_{OB}$  must lie inside the line OB (i.e. be concave) whilst line  $R_{AP}P$  must lie outside of AP (i.e. be convex). The only case in which all of the above and  $|OA| = |BP|$  can hold is if all the angles in the quadrilateral OABP are  $90^\circ$ , i.e. the region becomes effectively type  $T_1$ . This is true for  $1 \times n$  grids of mesh cells regardless of the value of  $n$ .

Overall, it seems unlikely that specific implementation of type  $T_2$  regions will be effective in the RAGS method. Recall that this was similarly the case for the exact fan region in Section 7.3.1; a more effective implementation was to derive offset fan elements 7.3.2, which became equal to the exact region in the case  $\iota = 0$ . In the examples shown, the geometry optimization phase proved effective at converging to solutions where  $\iota$  was indeed equal to 0. A similar approach is likely to be fruitful here; either the more generalised form could be explicitly derived, as for the fan element, or a type  $T_1$  region where one set of curves turns through only a very small angle may be sufficiently accurate to approximate these regions.

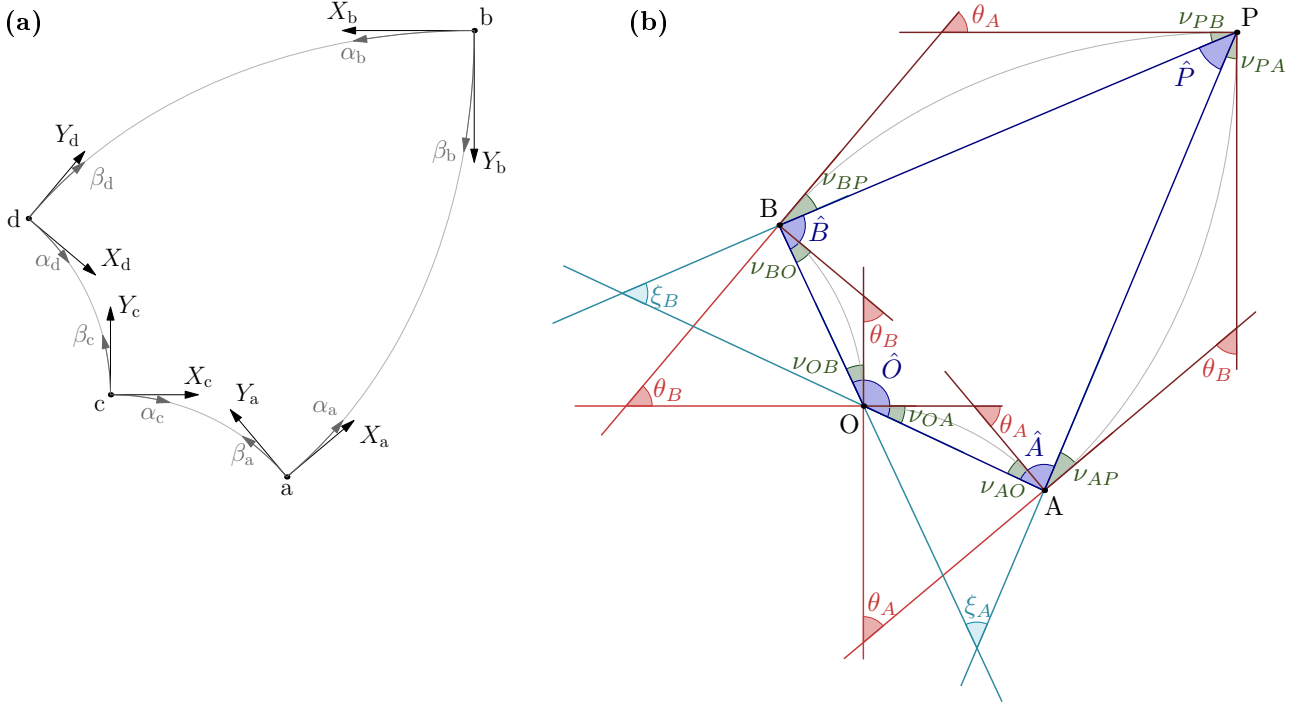


**Figure C.4:** Type  $T_1$  region: Definitions of points and angles. **(a)** Local Cartesian  $X$  and  $Y$  axes, and the curvilinear  $\alpha$  and  $\beta$  axes, if each of the four corner points was to be chosen as the origin  $O$ . **(b)** The bounding coordinate curves of a region of type  $T_1$  (grey), and the corresponding quadrilateral  $OAPB$  (dark blue). The lines of the quadrilateral have been extended (light blue) to their points of intersection. The red lines are the tangents to the coordinate curves at each point. Angles of interest are marked.

### C.3 Type $T_1$ regions

Chan (1960) defines special case 1 of a  $T$  type region to be a where both sets of coordinate lines are curves, and do not contain any points of inflexion. The region is then parametrised using the angles turned through by each set of coordinate curves. This gives four possible expressions for  $\phi$ , differing in the signs of  $\alpha$  and  $\beta$ . These four cases correspond to choosing each of the four corners of a region (as defined here, i.e. bounded by coordinate curves) as the origin of the local coordinate system. This is illustrated in Figure C.4a, where the points a-d correspond to the cases of Chan (1960, fig. 2). Here, we use point  $c$  as the origin, this gives results which are easily comparable to many known solutions. Therefore the expression for  $\phi$  is given as

$$\phi = -\alpha + \beta \quad (\text{C.8})$$

Assigning the labels  $O$ ,  $A$ ,  $B$  and  $P$  as described in equation (7.5), gives the positions shown in Figure C.4b. This also defines a number of useful angles. The interior angles of the quadrilateral  $OAPB$  are defined as  $\hat{O}$ ,  $\hat{A}$ ,  $\hat{B}$  and  $\hat{P}$ , and the angles between opposing sides are  $\xi_A$  and  $\xi_B$ . Angles between the sides of the quadrilateral and the tangents to the coordinate lines at that point are denoted by  $\nu$ , with subscripts denoting the point at which the angle occurs, and the point it faces towards. The total angles turned through by the coordinate lines in this region are defined by  $\theta_A$  and  $\theta_B$ , meaning that the limits for the coordinates  $\alpha$  and  $\beta$  are

$$0 \leq \alpha \leq \theta_A, \quad 0 \leq \beta \leq \theta_B \quad (\text{C.9})$$

Following the methodology of Chan (1960), the derivatives of equation (C.8) can now be used with the equation (7.2), to give

$$\frac{dA}{d\beta} = B, \quad \frac{dB}{d\alpha} = A \quad (\text{C.10})$$

and hence

$$\frac{d^2 A}{d\alpha d\beta} = A, \quad \frac{d^2 B}{d\alpha d\beta} = B \quad (\text{C.11})$$

### C.3.1 Numerical approximation methods

A general solution to the system (C.10) can be written as a double series expansion to reveal a useful pattern in the results.

$$\begin{array}{cccccccc}
 A = & & & C_0 & + & & & \\
 & & & + & & C_1\beta & + & \\
 & & C_{-1}\alpha & + & & + & & \\
 & & + & C_0\alpha\beta & + & \frac{1}{2}C_2\beta^2 & + & \\
 \frac{1}{24}C_{-4}\alpha^4 & + & \frac{1}{6}C_{-3}\alpha^3 & + & \frac{1}{2}C_{-2}\alpha^2 & + & \frac{1}{6}C_{-1}\alpha^2\beta & + & \frac{1}{4}C_0\alpha^2\beta^2 & + & \frac{1}{2}C_1\alpha\beta^2 & + & \frac{1}{6}C_2\alpha\beta^3 & + & \frac{1}{24}C_4\beta^4 \\
 \vdots & & \vdots & & \vdots & & \vdots & & \vdots & & \vdots & & \vdots & & \vdots \\
 & & & & & & & & & & & & & & 
 \end{array} \quad (C.12a)$$

$$\begin{array}{cccccccc}
 B = & & & C_1 & + & & & \\
 & & & + & & C_2\beta & + & \\
 & & C_0\alpha & + & & + & & \\
 & & + & C_1\alpha\beta & + & \frac{1}{2}C_3\beta^2 & + & \\
 \frac{1}{24}C_{-3}\alpha^4 & + & \frac{1}{6}C_{-2}\alpha^3 & + & \frac{1}{2}C_{-1}\alpha^2 & + & \frac{1}{6}C_{-1}\alpha^3\beta & + & \frac{1}{4}C_0\alpha^2\beta^2 & + & \frac{1}{2}C_1\alpha\beta^2 & + & \frac{1}{6}C_2\alpha\beta^3 & + & \frac{1}{24}C_5\beta^4 \\
 \vdots & & \vdots & & \vdots & & \vdots & & \vdots & & \vdots & & \vdots & & \vdots \\
 & & & & & & & & & & & & & & 
 \end{array} \quad (C.12b)$$

where  $C_n$  are any set of coefficients. Visually verifying that this satisfies equation (C.10) is simple, noting that in this layout, differentiation with respect to  $\alpha$  will result in each coefficient moving up and right, whilst a differentiation with respect to  $\beta$  results in each coefficient moving up and left (plus multiplication by the appropriate exponents). More concisely, this relationship can be expressed as

$$A = \sum_{a=0}^{\infty} \sum_{b=0}^{\infty} \frac{1}{a!b!} C_{b-a} \alpha^a \beta^b, \quad B = \sum_{a=0}^{\infty} \sum_{b=0}^{\infty} \frac{1}{a!b!} C_{b-a+1} \alpha^a \beta^b \quad (C.13)$$

Furthermore, by collecting the terms in each column of equations (C.12), it can be expressed as

$$A = \sum_{n=-\infty}^{\infty} C_n \left( \frac{\beta}{\alpha} \right)^{\frac{n}{2}} I_n(2\sqrt{\alpha\beta}) \quad B = \sum_{n=-\infty}^{\infty} C_{n+1} \left( \frac{\beta}{\alpha} \right)^{\frac{n}{2}} I_n(2\sqrt{\alpha\beta}) \quad (C.14)$$

where  $I$  is the modified Bessel function of the first kind (note that for integer  $n$ , as occurs here,  $I_{-n}(z) = I_n(z)$ ).

The values of  $C$  are closely linked to the values used in other numerical methods for approximating Hencky-Prantl nets. For instance, the values  $a_n$  and  $b_n$  of Ewing (1967); Dewhurst & Collins (1973); Dewhurst (2001) are equivalent to  $C_{-n}$  and  $C_{n-1}$  respectively. However, the combination of these into a single set of coefficients, not only highlights the coupled nature of  $A$  and  $B$  but also allows for continuous patterns to be observed in several known regions (see Appendix A).

### C.3.2 Examples from literature

One of the earliest known solutions for a region containing two sets of curved lines is a region of equiangular spirals, given by Michell (1904) as the solution for a cantilever supported on a circular boundary. This consists of two families of equiangular spirals in opposing directions. For such a region, functions  $A$  and  $B$  are generally given (e.g. Hemp, 1973) as

$$A(\alpha, \beta) = B(\alpha, \beta) = \sqrt{2}r_0 e^{\alpha} e^{\beta} \quad (C.15)$$

where  $r_0$  gives the radius of the point  $(\alpha, \beta) = (0, 0)$  from the center of the spirals. With this form, both families of spirals form an angle of  $\frac{\pi}{4}$  with radial lines from the central point. Regions with other values for these angles are rarely mentioned in the literature. Hemp (1958) briefly discusses their applicability in supporting circles which simultaneously provide a torque and a normal pressure, although the examples shown still all have zero normal pressure. These regions are defined by

$$A(\alpha, \beta) = qpe^{p\alpha} e^{\frac{\beta}{p}} \quad (C.16)$$

$$B(\alpha, \beta) = qe^{p\alpha} e^{\frac{\beta}{p}} \quad (C.17)$$



where  $q(= \sqrt{2}r_0)$  is now the global scaling factor, whilst  $p$  controls the angle of the spirals relative to their centres. From this, the coefficients  $C_n$  can be written as

$$C_n = qp^{1-n} \quad (\text{C.18})$$

The commonly found region supporting pure torque occurs when  $p = 1$ , in this case all values of  $C_n$  will be equal to  $q$ .

A number of other regions found in the literature are listed in Table A.2, along with the associated values of  $C_n$ . The next section discusses what is perhaps the most common region of type  $T_1$  in known solutions.

### C.3.3 Circular based regions

A case very commonly found in the literature occurs when the curves OA and OB are circular arcs, whose radii will be denoted by  $r_A$  and  $r_B$  respectively. In this case, the boundary conditions that  $A(\alpha, 0) = r_A$  and  $B(0, \beta) = r_B$  may be combined with the system of equations (C.10), to find the expressions for  $A$  and  $B$  are:

$$A(\alpha, \beta) = r_A I_0(2\sqrt{\alpha\beta}) + r_B \sqrt{\frac{\beta}{\alpha}} I_1(2\sqrt{\alpha\beta}) \quad (\text{C.19a})$$

$$B(\alpha, \beta) = r_B I_0(2\sqrt{\alpha\beta}) + r_A \sqrt{\frac{\alpha}{\beta}} I_1(2\sqrt{\alpha\beta}) \quad (\text{C.19b})$$

where  $I$  is the modified Bessel function of the first kind. Alternatively this can be defined by the series expansion coefficients to give

$$C_n = \begin{cases} r_A, & \text{if } n = 0 \\ r_B, & \text{if } n = 1 \\ 0, & \text{otherwise} \end{cases} \quad (\text{C.20})$$

From this it can be seen that a circular based  $T_1$  region is fully defined by the values of  $r_A$ ,  $r_B$ ,  $\theta_A$  and  $\theta_B$  (plus some global translation/rotation). As 5 parameters are required to define the relative positions of 4 nodes, it appears that this problem may be overdetermined and such regions may not be possible for four points in general position. It be shown that this is indeed the case.

In the circular based case, the triangles formed by the red lines in Figure C.4b and the lines OA and OB are isosceles triangles. Therefore  $\nu_{OB} = \nu_{BO} = \frac{\theta_B}{2}$  and  $\nu_{OA} = \nu_{AO} = \frac{\theta_A}{2}$ . Then, by considering the angle  $\angle AOB$  it can be found that

$$\theta_A + \theta_B = 2\hat{O} - \pi \quad (\text{C.21})$$

In this case, once the angle  $\hat{O}$  is defined, the sum of  $\theta_A + \theta_B$  is fixed. Furthermore, when one of these is set (implicitly giving the value of the other), the radii of the arcs OA and OB can also be easily calculated by

$$r_A = \frac{|\vec{OA}|}{\sin(0.5\theta_A)} \quad r_B = \frac{|\vec{OB}|}{\sin(0.5\theta_B)} \quad (\text{C.22})$$

where  $|\vec{OA}|$  and  $|\vec{OB}|$  are the lengths of straight lines from point O to points A and B respectively.

Thus the parameters which must be set to find the form of a circular based region can now be stated as  $\hat{O}$ ,  $|\vec{OA}|$ ,  $|\vec{OB}|$  and  $\theta_A$  (or  $\theta_B$ ).

#### Possible regions for fixed points O, A and B

Setting the values of  $\hat{O}$ ,  $|\vec{OA}|$  and  $|\vec{OB}|$  is equivalent to defining the relative positions of the three points O, A and B. Once this has occurred, only the value of  $\theta_A$  must be given to fully define the functions  $A(\alpha, \beta)$  and  $B(\alpha, \beta)$  in (C.19) and thus the geometry of the region. This single degree of freedom implies a 1D locus along which the point P must lie. As an example, Figure C.5 shows the outlines of regions under these assumptions for fixed O, A and B across the valid range of  $\theta_A$ .

Each value for  $\theta_A$  has been given a different colour, ranging from red for small values, to green for the largest possible values ( $\theta_A = 2\hat{O} - \pi$ ). In Figure C.5a the coordinate curves  $\alpha = 0$ ,  $\alpha = \theta_A$ ,  $\beta = 0$  and  $\beta = \theta_B$  (i.e. the outline of the region) have been plotted. The locus of the points P can be seen to form an approximately (but not quite) circular arc. The interior angles of the quadrilateral OAPB are shown in Figure C.5b. Clearly  $\hat{O}$  is constant by definition, however it is interesting to note that  $\hat{P}$  changes by only 0.07 radians ( $\approx 4^\circ$ ) over the whole of the possible range.

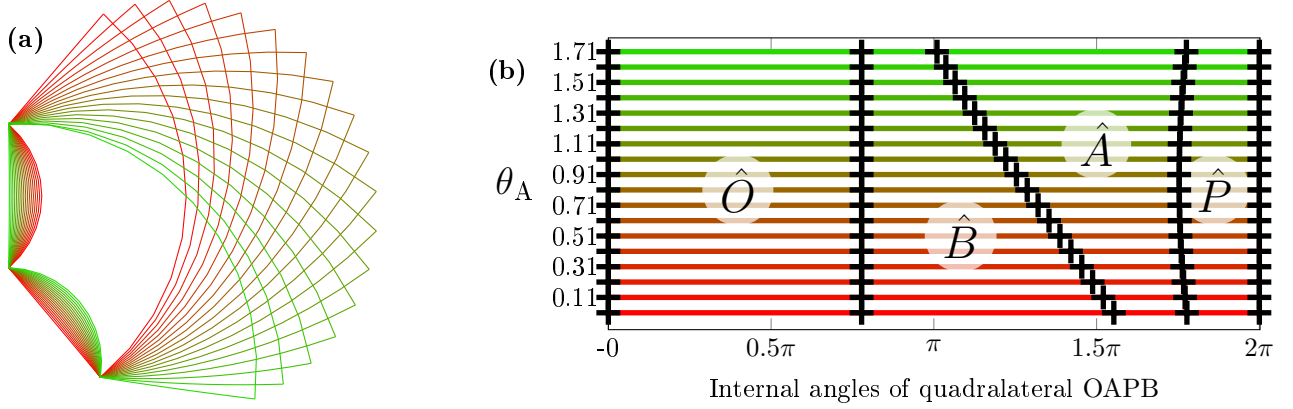


**Figure C.5:** The range of possible regions for a region of type  $T_1$  where the coordinate lines  $\alpha = 0$  and  $\beta = 0$  are both circular arcs, and the positions of O, A, and B are fixed. **(a)** outlines of the potential regions, showing the locus of possible locations for P, each possible region is drawn in a different color. **(b)** internal angles of the quadrilateral OAPB.

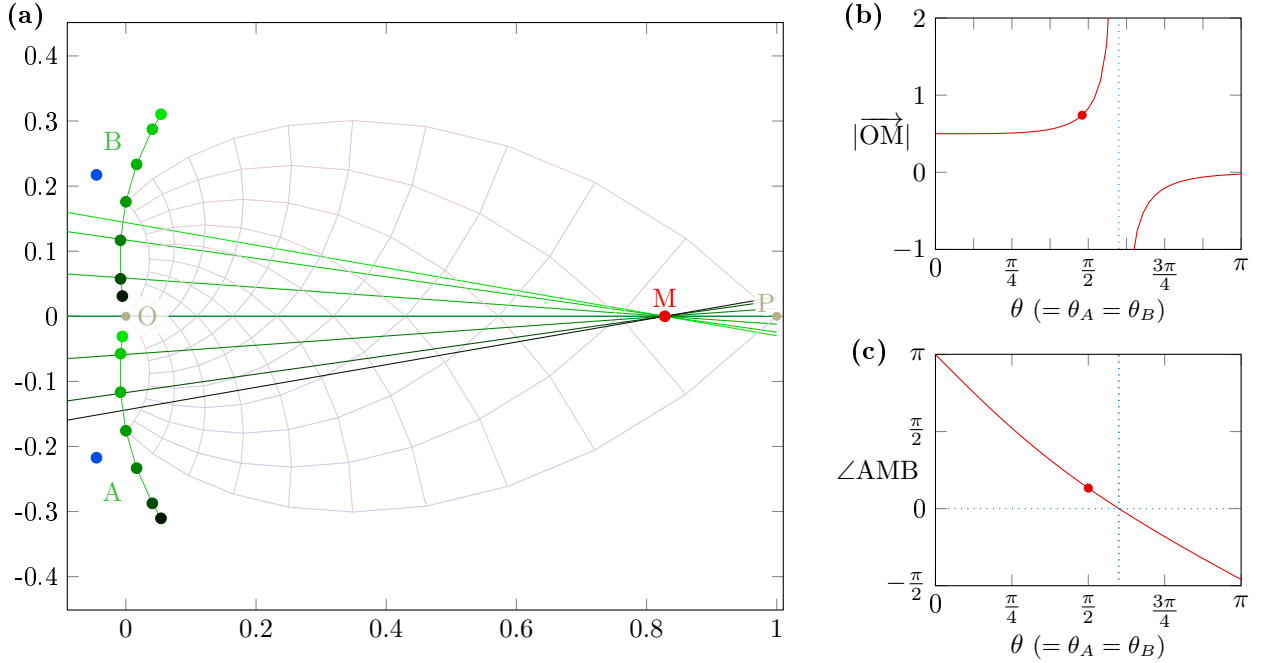


**Figure C.6:** Relationship between different regions constructed from two arcs, where  $\theta_A = \theta_B = \theta$ , for varying  $\frac{r_A}{r_B}$ . Regions are normalised such that  $O = (0, 0)$  and  $P = (1, 0)$ .

**(a)** results for case  $\theta = \frac{\pi}{2}$ . The locations of points A and B for  $\frac{r_A}{r_B} = 0.1$  (brightest green), 0.2, 0.5, 1, 2, 5, 10 (darkest green). The perpendicular bisector of AB for each result is also shown in the corresponding colour. Points A and B for a region of equiangular spirals are shown in blue. Point M is the intersection of all the perpendicular bisectors. Coordinate curves for  $\frac{r_A}{r_B} = 1$  are shown for context.

**(b)** Position of point M for a range of values of  $\theta$ , given as distance from point O (along the line OP).

**(c)** Position of point M for a range of values of  $\theta$ , given as the internal angle at M of the isosceles triangle between M and any pair A and B from the circular based results. Negative values occur when the point M is located behind point O.

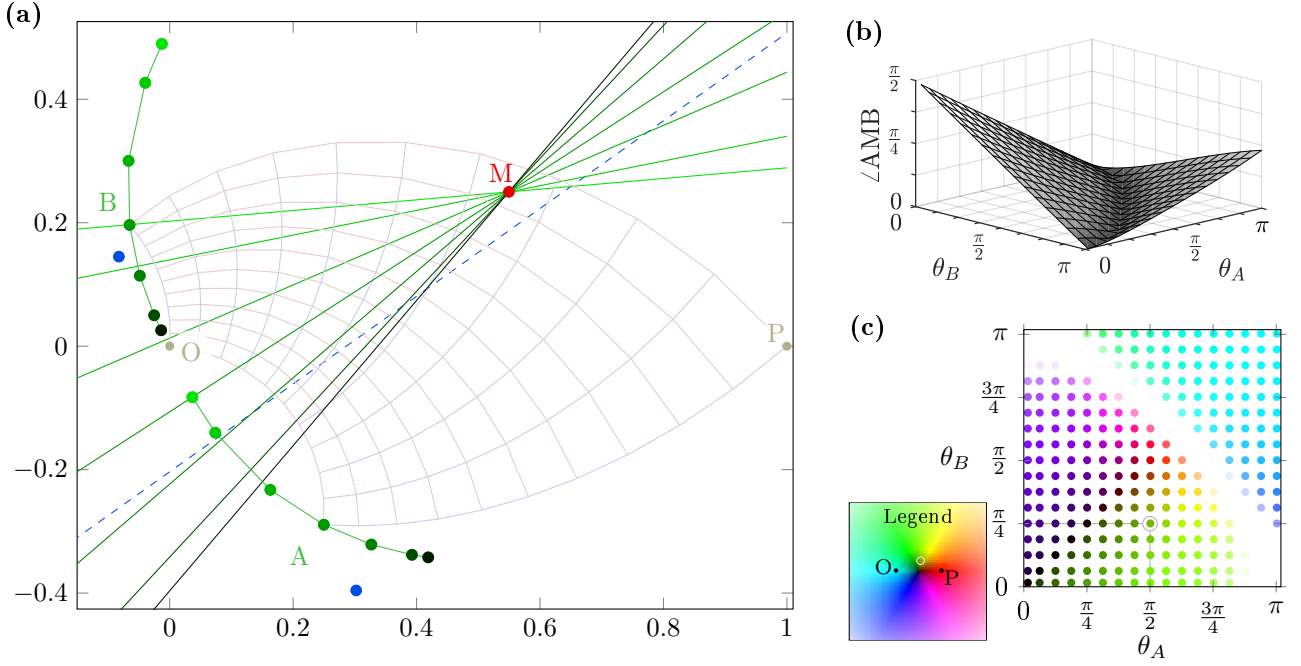


**Figure C.7:** Relationship between different regions constructed from two arcs OA and OB with varying values of  $\theta_A$ ,  $\theta_B$  and  $\frac{r_A}{r_B}$ . Regions are normalised such that O = (0,0) and P = (1,0)

(a) Results for case  $\theta_A = \frac{\pi}{2}$  and  $\theta_B = \frac{\pi}{4}$ . The locations of points A and B for  $\frac{r_A}{r_B} = 0.1$  (darkest green), 0.2, 0.5, 1, 2, 5 and 10 (brightest green) are shown. The perpendicular bisector of AB is also shown in the corresponding colour. Point M is the intersection point of all these perpendicular bisectors. The points A and B are also shown for the region of equiangular spirals (blue) however the bisector of AB (dashed) in this case does not pass through M.

(b) Position of point M relative to points A and B, indicated by angle of the isosceles triangle between M and a pair of points A and B. Results calculated for values of  $\theta_A$  and  $\theta_B$  from 0 to  $\pi$ .

(c) Position of point M for values of  $\theta_A$  and  $\theta_B$  from 0 to  $\pi$ . The colour of the point corresponds to a position relative to points O and P as indicated in the legend. Colours with full brightness are located on the circle through O and P, black is in the centre of the line OP and distant colours are increasingly pale.

### Possible regions for fixed O and P

A quad region can be normalised such that point O lies at the point (0,0) and point P = (1,0) by global translation, rotation and scaling. It is therefore possible to consider such points with no loss of generality (the scale factor can be factored into the Lamé coefficient functions to restore the global scaling as a post-processing step). This is similar to the process used to calculate the geometry of the discretised approximation to this region in Section 7.5 and Figure 7.11.

First, regions where  $\theta_A = \theta_B = \theta$  will be considered. The normalised positions of A and B for  $\theta = \frac{\pi}{2}$  and a number of ratios  $\frac{r_A}{r_B}$  are shown in Figure C.6a. The perpendicular bisector of AB for each of these points passes through the point labelled M. A similar exercise has been undertaken for a range of values of  $\theta$  from almost 0 to  $\pi$ , and it was again found that all bisectors passed through the common point M, which always lay on the line OP. Figures C.6b and c show how the location of M changes as  $\theta$  varies. Two different methods of expressing the position are used, Figure C.6b shows simply the normalised  $x$  coordinate of M, while C.6c shows the angle formed by a corresponding pair of points A and B and the point M. Recall from Figure 7.12a, that the corresponding angle in the discretised case was given by  $2\hat{p}$ .

There is a discontinuity in Figure C.6b which occurs when all the bisectors of AB are parallel. This would correspond to the point at which the angle in Figure C.6c passes through zero, by linear interpolation this is found to occur when  $\theta \approx 0.6005\pi$ , and certainly within the range  $0.6\pi \leq \theta \leq 0.62\pi$ .

This approach can be extended to cases where  $\theta_A \neq \theta_B$ . For example, Figure C.7a shows the case where  $\theta_A = \frac{\pi}{2}$  and  $\theta_B = \frac{\pi}{4}$ . The perpendicular bisectors of AB for regions with circular arcs still meet at a common intersection point M. This point is now located away from the line OP. The perpendicular bisector of AB for the region of equiangular spirals no longer passes through M however.

Calculating the location of M over a range of values for  $\theta_A$  and  $\theta_B$  furnishes Figures C.7b and c. Figure C.7b shows the angle through which point A should be rotated about M to give the corresponding point B (i.e. similar to Figure C.6c). Figure C.7c shows the position of M identified for each pair of values for  $\theta_A$  and  $\theta_B$

tested. For example, the result corresponding to the case in Figure C.7a is circled on the plot. The location of point M for this case has been circled in the legend, relative to the indicated positions of points O and P. The colour at the centre of the circle in the legend gives the colour of the point in the main plot.

From this it can be seen that there is a distinct line of discontinuity where the point M tends to an infinite distance away, this is shown by the white points in Figure C.7c, and the points at which the angle in Figure C.7b are close to zero (i.e. the perpendicular bisectors of AB are parallel for any values of  $\frac{r_A}{r_B}$ ).

This section has shown that it there may be relationships which could lead to a method for identifying a set of parameters  $r_A$ ,  $r_B$ ,  $\theta_A$  and  $\theta_B$  defining a circular based region from a given set of corner points. However, as shown in the previous section, it could not be possible to find such a set for points in general position, this would be a significant obstacle to implementing such regions within a layout optimization based method. It is therefore of interest to consider how this could be expanded to a wider range of possible regions.

### C.3.4 Fields extended from circular arcs

It seems that we cannot expect to be able to construct a region from circular arcs for a general set of four points. However, due to their ubiquity in known results, it will be useful to ensure that the chosen means of identifying regions is capable of selecting these circular based regions when they are required.

This suggests a possible extension which could provide a wider and more useful range of regions. These regions could be cut from an infinitely extended field built from circular arcs.

Consider a field defined by equations (C.24) ranging all the way from  $\alpha, \beta = 0$  to  $\alpha, \beta = \infty$ . Sections of such fields are shown in Figure C.8. Note that portions of these fields do overlap (see the bottom left corners of Figure C.8 particularly), however it is still feasible to consider a range for  $\alpha$  or  $\beta$  in a single layer of the overlapping region. Fields where the ratio of  $r_A$  to  $r_B$  is the same will be uniformly scaled up or down in size, however cases where this ratio vary will produce different fields, as shown in Figure C.8.

To aid in the evaluation some additional notation will be introduced. In the case where  $r_A = r_B = r$ , then equation (A.2) can be used to simplify equation (C.19) to give  $B(\alpha, \beta) = rH_0(\alpha, \beta)$ . To extend this to the more general case, we now define

$$H_n^\gamma(\alpha, \beta) = G_n(\alpha, \beta) + \gamma G_{n+1}(\alpha, \beta) \quad (\text{C.23})$$

where  $G$  is as defined by Lewiński et al. (1994a), and in equation (A.1) of the present work. Thus  $H_n(\alpha, \beta) = H_n^1(\alpha, \beta)$ . Using this notation, equation (C.19) becomes

$$A(\alpha, \beta) = r_A I_0 \left( 2\sqrt{\alpha\beta} \right) + r_B \sqrt{\frac{\beta}{\alpha}} I_1 \left( 2\sqrt{\alpha\beta} \right) = r_B H_{-1}^{\frac{r_A}{r_B}}(\alpha, \beta) \quad (\text{C.24a})$$

$$B(\alpha, \beta) = r_B I_0 \left( 2\sqrt{\alpha\beta} \right) + r_A \sqrt{\frac{\alpha}{\beta}} I_1 \left( 2\sqrt{\alpha\beta} \right) = r_A H_0^{\frac{r_B}{r_A}}(\alpha, \beta) \quad (\text{C.24b})$$

Integration of equation (C.24) can be used to find the geometry of any region cut from this field, not just those regions with the base at  $(\alpha, \beta) = (0, 0)$ . These regions will not be bordered by circular arcs. If we say that the ranges for the angles are denoted by the subscripts  $-$  and  $+$ , then we can express the Lamé coefficients of these fields as either

$$A(\alpha, \beta) = r_B H_{-1}^\gamma(\alpha, \beta), \quad \alpha_- \leq \alpha \leq \alpha_+, \quad \beta_- \leq \beta \leq \beta_+ \quad (\text{C.25a})$$

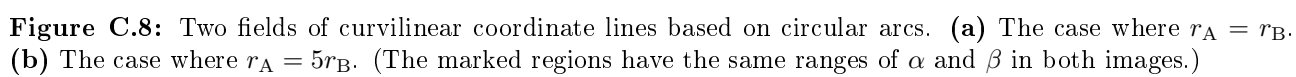
$$B(\alpha, \beta) = r_A H_0^{\bar{\gamma}}(\alpha, \beta), \quad \alpha_- \leq \alpha \leq \alpha_+, \quad \beta_- \leq \beta \leq \beta_+ \quad (\text{C.25b})$$

or as

$$A(\alpha, \beta) = r_B H_{-1}^\gamma(\alpha + \alpha_-, \beta + \beta_-), \quad 0 \leq \alpha \leq (\alpha_+ - \alpha_-), \quad 0 \leq \beta \leq (\beta_+ - \beta_-) \quad (\text{C.26a})$$

$$B(\alpha, \beta) = r_A H_0^{\bar{\gamma}}(\alpha + \alpha_-, \beta + \beta_-), \quad 0 \leq \alpha \leq (\alpha_+ - \alpha_-), \quad 0 \leq \beta \leq (\beta_+ - \beta_-) \quad (\text{C.26b})$$

where  $\gamma = \frac{r_A}{r_B}$  and  $\bar{\gamma} = \frac{r_B}{r_A}$ . The form of equation (C.25) will be used when comparing different possible fields with the same corner points, whilst (C.26) will be useful for comparing the series expansions of regions cut from these fields with other known results.



### Uniqueness of regions derived from circular based fields

A region which has been cut from a portion of an infinite field constructed from two arcs may be determined using 6 parameters: the upper and lower bounds on the coordinates  $\alpha_-$ ,  $\alpha_+$ ,  $\beta_-$  and  $\beta_+$ ; and the two radii of the base arcs  $r_A$  and  $r_B$ . Comparing this with the 5 parameters to describe the relative position of the four nodes suggests that it may be possible that multiple regions could be selected for the same four points.

To test this, an example problem has been investigated. Four nodes, O, A, B and P have been defined as the corner points of the region where  $0 \leq \alpha \leq 1$ ,  $0 \leq \beta \leq 0.5$ ,  $r_A = 1$  and  $r_B = 2$ , this region is shown in Figure C.9ai. The aim was to perturb the parameters, and then use an optimizer to minimise the error in the positions of the points O, A, B and P. This would then have the potential to identify alternative sets of parameters resulting in the same extreme points.

A non-gradient based search algorithm of Lagarias et al. (1998), implemented in MATLAB's `fminsearch` function, was used due to convergence issues with the gradient based alternative. Perturbing of the problem was achieved by rotating the target nodes through different angles (keeping the local Cartesian coordinate system of the field constant). The objective function of the optimization was to minimise the RMS (root mean squared) error in the absolute distance between the (rotated) target nodes, and the corresponding corner point of the current solution.

The optimized values output by the solver are shown in Table C.1, along with the final objective value, the associated layouts of coordinate curves are shown in Figure C.9. The top row of Table C.1 is a verification run, where the un-perturbed target nodes were used, as expected this achieves a very low error in the node positions, and identifies the parameter values which were originally used to select the target nodes. This result is shown in black in Figure C.9.

The trials with increasingly perturbed targets do show a wide range of parameter values. The major changes are increases in the values of  $\alpha_-$  and  $\alpha_+$  and a correlated decrease in the radius  $r_B$ . All the solutions still have a value  $\beta_- = 0$ , i.e. the coordinate curve through O and A is still a circular arc of radius  $r_A$ ; the values of  $r_A$  also have only minor changes. Perhaps most interestingly, the range of  $\alpha$  is almost constant throughout all the results. This seems to suggest that, even if multiple regions are possible for the same points, the angles turned through in each region may be defined by the positions of the points.

It is difficult to definitively conclude from Table C.1 whether the different parameter sets truly correspond to identical nodal positions. The RMS errors are all low, however there is a definite increasing trend as the target points are increasingly perturbed from the exact values. Furthermore, the zoomed in views around each extreme point in Figure C.9 show that the errors are not randomly spread; the regions with larger errors (in red) consistently have points A and B located further outwards, and point P located further inwards. It may therefore be that these different parameter sets are not merely insufficiently converged, but do describe marginally different points.

### Limits at infinity

The series expansion approach described in Section C.3.1 can be applied to examine the behaviour of regions cut from these fields, by expanding the equations (C.24) about a suitable point. This point will become the location of O, the curvilinear coordinates of this point (in the curvilinear coordinate system of the field) will be defined as  $(\chi, \lambda)$ .

Initially, attention will be focused on the field where  $r_A = r_B$  for simplicity. The geometry when both base curves are circular arcs (i.e.  $(\chi, \lambda) = (0, 0)$ ) is given by

$$\begin{aligned} A(\alpha, \beta) &= rH_{-1}(\alpha, \beta) \\ B(\alpha, \beta) &= rH_0(\alpha, \beta) \end{aligned} \quad \rightarrow \quad C_n = \begin{cases} r, & \text{if } n = 0, 1 \\ 0, & \text{otherwise} \end{cases} \quad (\text{C.27})$$

**Expansions about an arbitrary point O** When the point O lies on either the  $\alpha$ -axis or the  $\beta$ -axis, one coordinate curve will be an arc and the other will not. Thus the region may be defined using

$$\begin{aligned} A(\alpha, \beta) &= rH_{-1}(\alpha + \chi, \beta) \\ B(\alpha, \beta) &= rH_0(\alpha + \chi, \beta) \end{aligned} \quad \rightarrow \quad C_n = \begin{cases} 0, & \text{if } n < 0 \\ r \frac{\chi^n}{n!}, & \text{if } n = 0 \\ r \left( \frac{\chi^n}{n!} + \frac{\chi^{n-1}}{(n-1)!} \right), & \text{if } n \geq 1 \end{cases} \quad (\text{C.28})$$

$$\begin{aligned} A(\alpha, \beta) &= rH_{-1}(\alpha, \beta + \lambda) \\ B(\alpha, \beta) &= rH_0(\alpha, \beta + \lambda) \end{aligned} \quad \rightarrow \quad C_n = \begin{cases} r \left( \frac{\lambda^{1-n}}{(1-n)!} + \frac{\lambda^{-n}}{(-n)!} \right), & \text{if } n \leq 0 \\ r \frac{\lambda^{1-n}}{(1-n)!}, & \text{if } n = 1 \\ 0, & \text{if } n \geq 2 \end{cases} \quad (\text{C.29})$$

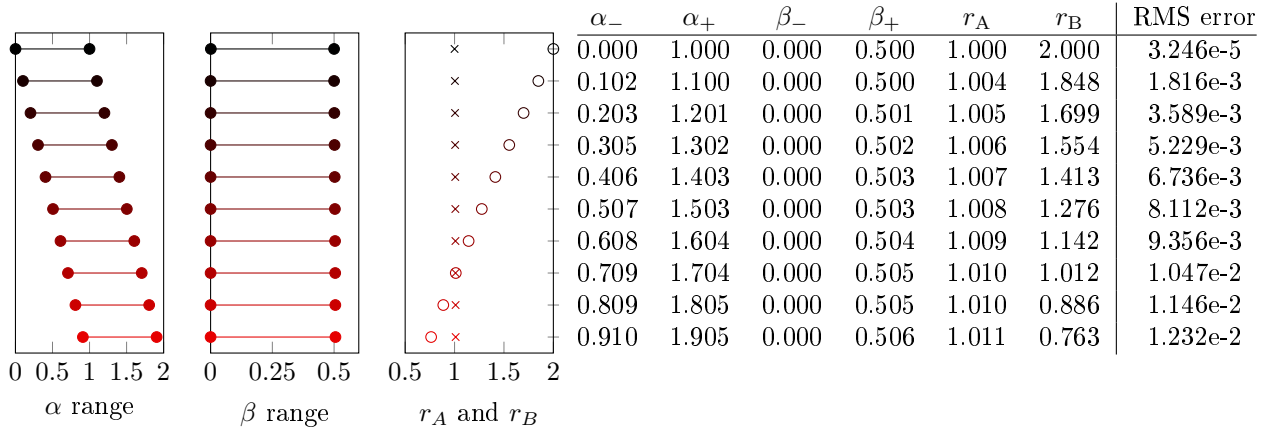


**Table C.1:** Test of uniqueness of areas cut from circular based fields: Resulting optimized parameter values and corresponding (objective) value of RMS error of positions of points O, A,B and P.

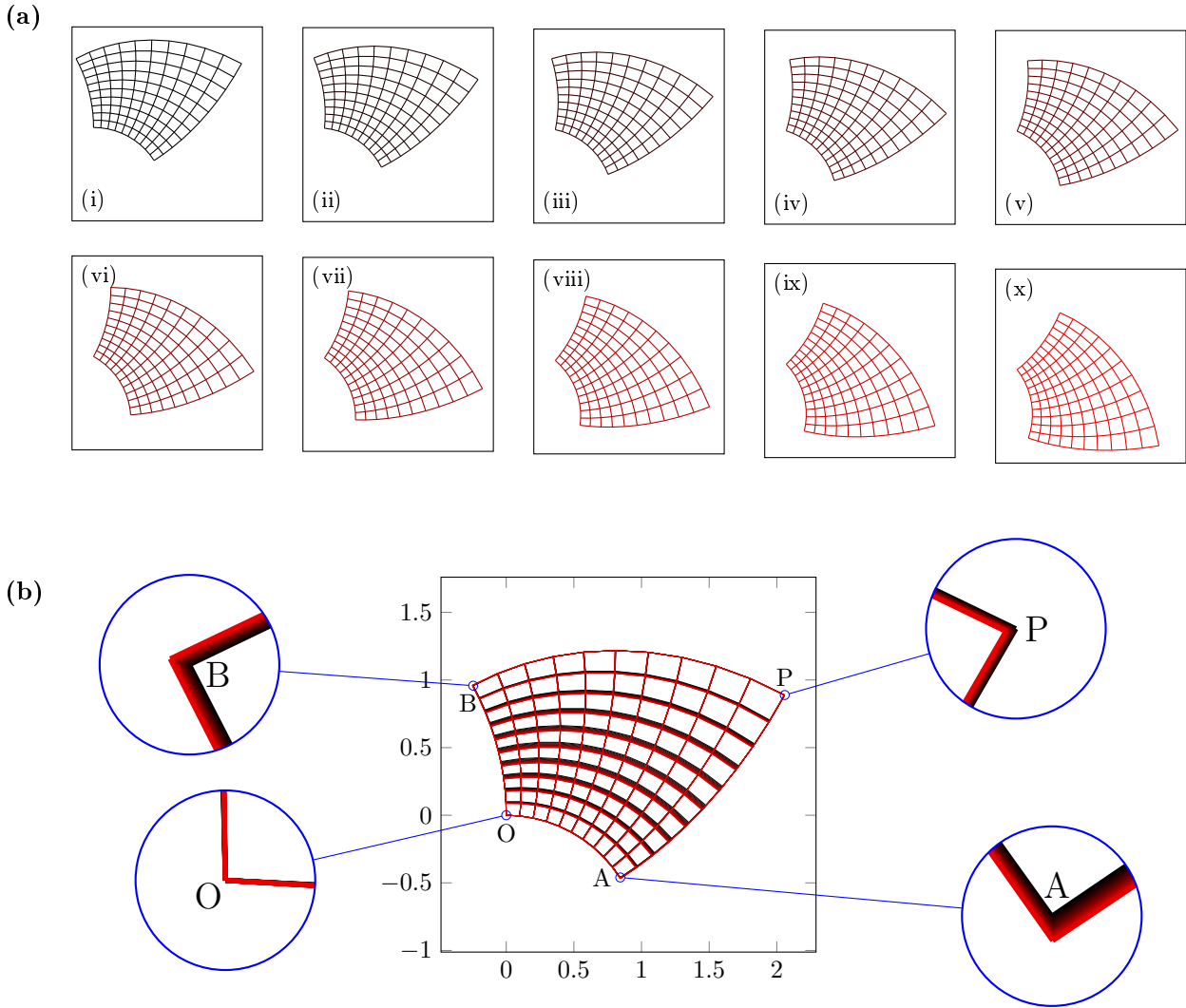


**Figure C.9:** Test of uniqueness of areas cut from circular based fields: Resulting layouts of coordinate curves. (a) For each individual test, where (i) is the originally given parameters. (b) For all tests overlain (after post processing to rotate target points to be co-incident); details at each corner point are also shown.



Note that  $\frac{\chi^n}{n!}$  is equal to 1 when  $n$  is equal to 0, similarly  $\frac{\lambda^{1-n}}{(1-n)!}$  is equal to 1 when  $n$  is equal to 1. Thus the appropriate coordinate axis is still a circular arc with radius  $r$ .

We denote the reciprocal gamma function using  $\Xi$ , i.e.  $\Xi(n) = \frac{1}{\Gamma(n)}$ . The gamma function is equal to  $\Gamma(n) = (n-1)!$  for positive integers, and tends to a value of  $\pm\infty$  when approaching zero and negative integers. Thus,  $\Xi(n) = \frac{1}{(n-1)!}$  if  $n$  is a positive integer and  $\Xi(n) = 0$  if  $n$  is a negative integer or zero. This can be used to simplify the expressions above.

$$\begin{aligned} A(\alpha, \beta) &= rH_{-1}(\alpha + \chi, \beta) \\ B(\alpha, \beta) &= rH_0(\alpha + \chi, \beta) \end{aligned} \quad \rightarrow \quad C_n = r(\chi^n \Xi(n+1) + \chi^{n-1} \Xi(n)) \quad (\text{C.30})$$

$$\begin{aligned} A(\alpha, \beta) &= rH_{-1}(\alpha, \beta + \lambda) \\ B(\alpha, \beta) &= rH_0(\alpha, \beta + \lambda) \end{aligned} \quad \rightarrow \quad C_n = r(\lambda^{1-n} \Xi(2-n) + \lambda^{-n} \Xi(1-n)) \quad (\text{C.31})$$

For a region cut from the field with the point O at an arbitrary point with  $(\alpha, \beta) = (\chi, \lambda)$ , neither base curve will be an arc. The series expansion in this case is

$$\begin{aligned} A(\alpha, \beta) &= rH_{-1}(\alpha + \chi, \beta + \lambda) \\ B(\alpha, \beta) &= rH_0(\alpha + \chi, \beta + \lambda) \end{aligned} \quad \rightarrow \quad C_n = r \left( \left( \frac{\chi}{\lambda} \right)^{\frac{n}{2}} I_n(2\sqrt{\lambda\chi}) + \left( \frac{\chi}{\lambda} \right)^{\frac{n-1}{2}} I_{n-1}(2\sqrt{\lambda\chi}) \right) \quad (\text{C.32})$$

**Comparison to regions in the literature: Equiangular spiral** The equations describing the equiangular spiral region given in (C.17) can also be expanded about an arbitrary point  $(\alpha, \beta) = (\chi, \lambda)$ . This gives

$$\begin{aligned} A(\alpha, \beta) &= qpe^{p(\alpha+\chi)} e^{\frac{\beta+\lambda}{p}} \\ B(\alpha, \beta) &= qe^{p(\alpha+\chi)} e^{\frac{\beta+\lambda}{p}} \end{aligned} \quad \rightarrow \quad C_n = qp^{1-n} e^{p\chi} e^{\frac{\lambda}{p}} \quad (\text{C.33})$$

Note that  $e^{p\chi}$  and  $e^{\frac{\lambda}{p}}$  are constants over all values of  $C_n$ , this implies that the equiangular spiral region changes by only a global scaling factor when the origin is moved. Thus we could rewrite this equation by redefining the value of  $q$  instead. Alternatively, we could normalise the values of  $C_n$  relative to the value of  $C_0$  to remove the global scaling factors completely. For this case, this gives

$$\frac{C_n}{C_0} = \frac{qp^{1-n} e^{p\chi} e^{\frac{\lambda}{p}}}{qp^1 e^{p\chi} e^{\frac{\lambda}{p}}} = p^{-n} \quad (\text{C.34})$$

Normalising the values from equation (C.33) in the same manner, gives

$$\begin{aligned} A(\alpha, \beta) &= rH_{-1}(\alpha + \chi, \beta + \lambda) \\ B(\alpha, \beta) &= rH_0(\alpha + \chi, \beta + \lambda) \end{aligned} \quad \rightarrow \quad \frac{C_n}{C_0} = \left( \frac{\chi}{\lambda} \right)^n \frac{I_n(2\sqrt{\lambda\chi}) + \left( \frac{\chi}{\lambda} \right)^{-\frac{1}{2}} I_{n-1}(2\sqrt{\lambda\chi})}{I_0(2\sqrt{\lambda\chi}) + \left( \frac{\chi}{\lambda} \right)^{-\frac{1}{2}} I_1(2\sqrt{\lambda\chi})} \quad (\text{C.35})$$

To examine the behaviour of regions cut from this circular field at points far from the base circles, set  $\lambda = v\chi$  and let  $\chi$  tend to infinity:

$$\frac{C_n}{C_0} = \left( \frac{1}{v} \right)^n \frac{I_n(2\chi\sqrt{v}) + \sqrt{v} I_{n-1}(2\chi\sqrt{v})}{I_0(2\chi\sqrt{v}) + \sqrt{v} I_1(2\chi\sqrt{v})} \quad (\text{C.36})$$

$$\lim_{\chi \rightarrow \infty} \frac{C_n}{C_0} = v^{-\frac{n}{2}} \quad (\text{C.37})$$

which can be compared with equation (C.34).

Therefore, we can approximate any region of equiangular spirals arbitrarily well by the method of cutting a region from a field extended from two arcs. The region should be chosen such that the origin point, O (with coordinates  $(\alpha, \beta) = (\chi, \lambda)$ ), lies far from the origin curves of the field. As the coordinate values of the origin point increase, the region becomes close to the equiangular spiral region with  $p = \sqrt{\frac{\lambda}{\chi}}$ . To approximate the most common type of equiangular spiral region, where an angle of  $\frac{\pi}{4}$  is formed to the radius by both families, the point O should lie on the line  $\alpha = \beta$ .

This poses a question however, we have now found that all equiangular spiral regions can be approximated from just the field where  $r_A = r_B$ , i.e. where the two base arcs have equal radii. Therefore the distant regions of fields where  $r_A \neq r_B$  must either duplicate this result, or produce some new form.

The values of  $C_n$  for a region where  $r_A \neq r_B$  are

$$\begin{aligned} A(\alpha, \beta) &= r_B H_{-1}^\gamma(\alpha + \chi, \beta + \lambda) \\ B(\alpha, \beta) &= r_A H_0^\gamma(\alpha + \chi, \beta + \lambda) \end{aligned} \quad \rightarrow \quad C_n = r_A \left( \left( \frac{\chi}{\lambda} \right)^{\frac{n}{2}} I_n(2\sqrt{\chi\lambda}) \right) + r_B \left( \left( \frac{\chi}{\lambda} \right)^{\frac{n-1}{2}} I_{n-1}(2\sqrt{\chi\lambda}) \right) \quad (\text{C.38})$$



where  $\gamma = \frac{r_A}{r_B}$  and  $\bar{\gamma} = \frac{r_B}{r_A}$ .

If these values for  $C_n$  are normalised as previously, and the relationship  $\lambda = v\chi$  is again used, then a region cut from a distant portion of this field is also described by the coefficients,

$$\lim_{\chi \rightarrow \infty} \frac{C_n}{C_0} = v^{-\frac{n}{2}} \quad (\text{C.39})$$

This is independent of the ratio of  $r_A$  to  $r_B$ . In other words, it has now been shown that at points distant from the base curves, the form of the region is less affected by the base curves' relative sizes.

**Comparison to regions in the literature: Square line support** Another set of regions of type  $T_1$  which are known from the literature are those present in the solution of Lewiński & Rozvany (2008b). This solution contains 3 different regions of type  $T_1$ , with only the first being a circular based one. This section will discuss whether these may be well modelled by the use of regions cut from circular based fields.

These regions are symmetrical, and thus will be best modelled by regions cut from the field where  $r_A = r_B$ , and where the point O lies on the line  $\alpha = \beta$ . The values of  $C_n$  for such regions are shown as grey and white lines in Figure C.10 for cases where the point O =  $(\alpha_-, \beta_-)$  lies at  $(\frac{\pi}{8}, \frac{\pi}{8}), (\frac{\pi}{4}, \frac{\pi}{4}), \dots, (\pi, \pi)$ . The values of  $C_n$  for the regions in the exterior of a square have been overlain.

This shows that the coefficients from the regions in the exterior of a square do not precisely follow those from a region cut from a circular based region. For example, the region  $B_1D_1HD'_1$  has values of  $C_2$  and  $C_{-1}$  close to those of the region with O =  $(\frac{\pi}{8}, \frac{\pi}{8})$ ; yet the values of  $C_4$  and  $C_{-3}$  are closer to those corresponding to the region where O =  $(\frac{\pi}{4}, \frac{\pi}{4})$ .

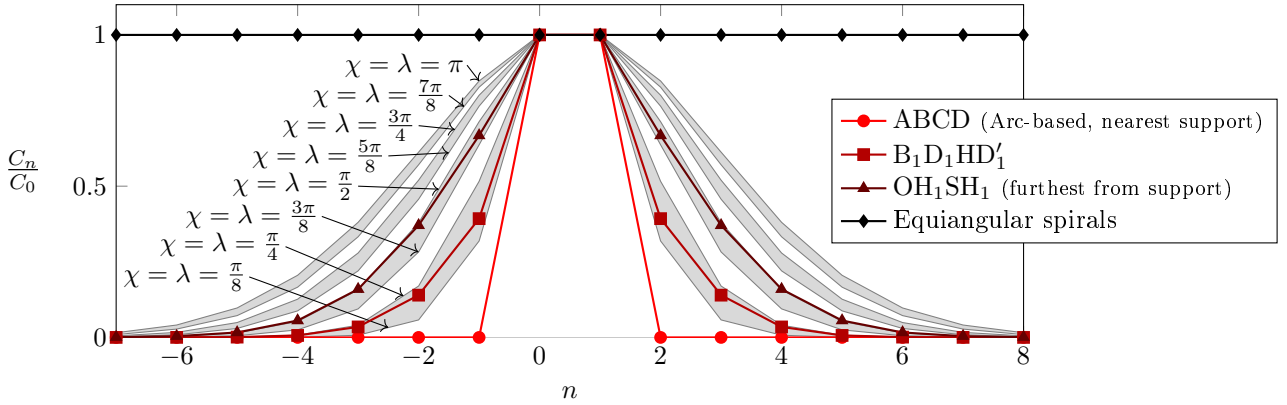


**Figure C.10:** Normalised coefficients of the functions defining regions from the exterior of a square (Lewiński & Rozvany, 2008b, region labels refer to figure 4), and regions cut from the field based on circular arcs with equal radius, where the point O lies on the line  $\alpha = \beta$  (i.e. equation (C.32) with  $\chi = \lambda$ ).

### C.3.5 Discretised geometry - kinematic constraints

The example of Section 7.5.3 showed the results of a Michell cantilever problem solved using a discrete approximation to a type  $T_1$  region. The solution obtained by this method (Figure 7.16) is reproduced in Figure C.11a. To obtain the bar thicknesses on the border between the fan region and the  $T_1$  region, the thickness of the dotted lines of the  $T_1$  region must be subtracted from the thicknesses of the coincident bars of the fan regions.

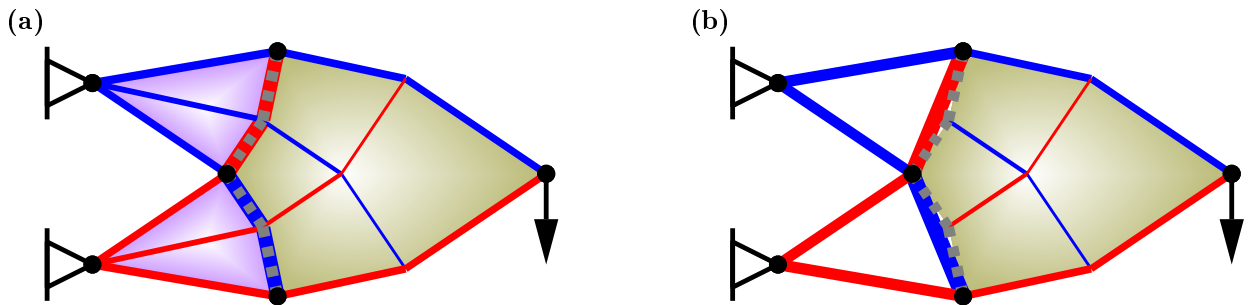


**Figure C.11:** Michell cantilever: Results. (a) With bars, (approximated) fan elements and approximated four node elements,  $V = 1.016V_T$ . (b) With bars and four node elements only,  $V = 1.039V_T$ .

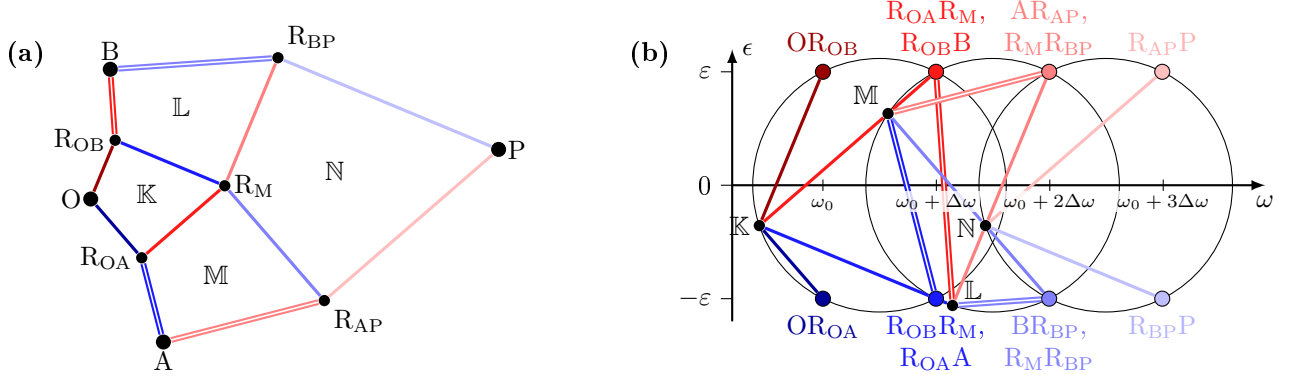


**Figure C.12:** A four cell approximated element. (a) In the physical plane, with labels for each mesh cell. (b) The associated circles of relative displacements; the poles of the circles relating to each mesh cell are labelled.

Figure C.11b shows the result of this problem where fan elements are not considered. The straight bar between these nodes has increased in size to accommodate the forces imposed by these lines, as shown by the increased volume of Figure C.11b compared to Figure C.11a. However, there is now no member directly underlying the grey dotted lines and it is therefore unclear how this should be interpreted into a feasible structure. To seek a clearer derivation, the kinematic setting will now be considered.

To derive the kinematic constraint for the discrete approximation of a  $T_1$  region, the circles of relative displacement (see Figure 7.4) are again used. Figure C.12 shows the form and associated circles of relative displacement for an approximated quad element. The four mesh cells are labelled using double struck letters, and the pole of the relevant circle is indicated in the same way. The circles relating to the mesh cells L and M are co-incident, although the poles are at different locations.

As the strains should be mesh-wise constant, the points representing each bar must lie on the lines  $\epsilon = \pm\epsilon$ . Additionally, bars which are orthogonal in the physical plane will form the diameter of the circle of relative displacements. Therefore the centres of the circles will lie on the line  $\epsilon = 0$ .

It is then simple to calculate, using an isosceles triangle formed by two adjacent points and the centre of the circle, that

$$\Delta\omega = \frac{2\epsilon}{\tan \hat{p}} \quad (C.40)$$

where  $\Delta\omega$  is the change in rotation, as defined in Figure C.12b.

The virtual strains and rotations of each bar are now known. Therefore the virtual displacements of each point may be found by stepping through the layout, calculating the displacement added by each bar. These displacements are shown in these are shown in Figure C.13.

Calculating the displacements is simplest through the sequence of bars B1, B3, B4 and B5 as shown in Figure C.13, as these bars are orthogonal and therefore extension and rotation coefficients may be easily summed. The total displacements at point P are shown in black, and the limits which they imply on the relative deflected position of P are shown in thin black lines. Calculating the appropriate limits from the sequence of bars A1, A3, A4, A5 is also possible, the limit lines calculated in this way are shown in orange. The solid limit lines represent those parallel to the bars B5 and A5 respectively, whilst the dashed lines are those calculated perpendicular to the relevant bar. It can be seen that the solid lines are the tightest limits, suggesting that these would be the most useful to implement, and that the limits shown in dashed lines may be redundant.

Additionally, Figure C.13 also shows the limits on virtual displacements from straight bars OA, OB and OP. It can be seen that the limiting virtual displacements from this region are tighter than the relative constraints from bars OB and OA.

This is likely to link to the aforementioned issue concerning the interpretation of the dotted lines in Figure C.11b, as they both concern the connections between points O and A, and O and B. Further work is required to establish the physical meaning of these results. Numerically, it seems likely that an additional primal variable will be required for each pair of nodes OA and OB (corresponding to the dual constraint between O and either A or B as shown in Figure C.13). A possible static interpretation could be a 2D area of solid structure connecting the space from the edge of the  $T_1$  region and the line of the straight bar/the edge of the fan region. All these connected elements would contribute to the force distribution in the region, although the contribution from the  $T_1$  region would likely be negative (as is the contribution from the dotted bars in equation (7.67)). It would then be simple to add a constraint that the overall volume of this solid area could not be negative. However, further studies are required to establish if this hypothesis is correct.

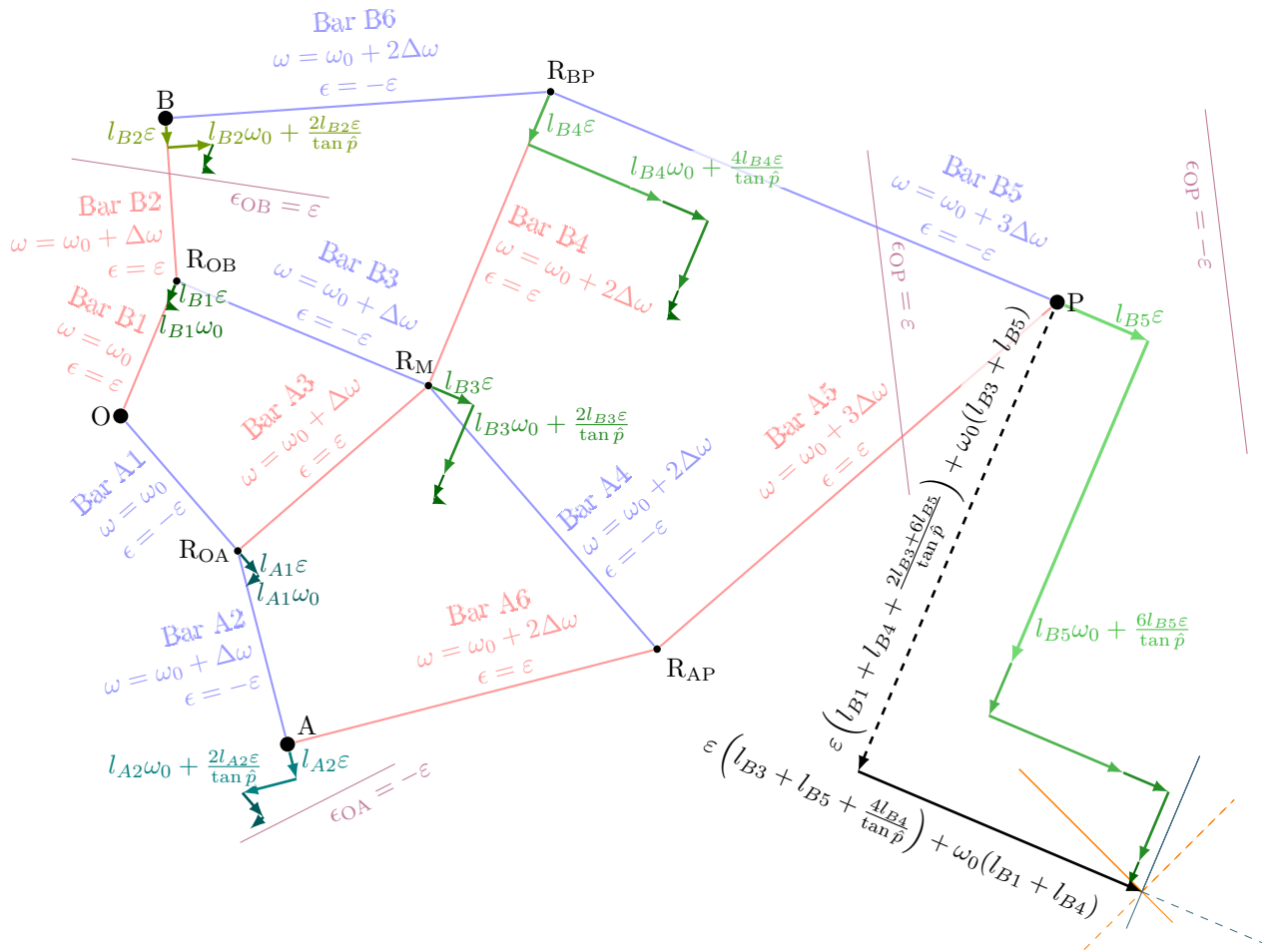


**Figure C.13:** Four cell approximated element: Local displacements of points. The lines of limiting virtual deflections for the straight bars OA and OB are also shown. Note that the deflection parallel to OA or OB which is implied by the quad element is a tighter bound than that enforced by the straight element.

## C.4 Type $R$ regions

Regions of type  $R$  are distinguished by the presence of a principal strain that is strictly less than the limiting values. Strict less than constraints are challenging to incorporate in continuous mathematical optimization problems, and are generally not implemented by commercial software packages or well known algorithms. If the interior point method is used, then the solution will generally not satisfy any constraints with equality, the amount of variability being set by various problem parameters.

For these reasons, type  $R$  regions (and similarly, type  $O$  regions) are unlikely to be effectively implemented as explicit regions in the RAGS framework. However, in the absence of body forces such as self-weight, the fact that a type  $R$  region has members only in one direction means that these members will always be straight. As such regions of type  $T_2$  (or approximations thereof) may be able to accurately model regions of type  $R$  simply by having some of the relevant kinematic constraints satisfied strictly.

## C.5 Type $S$ regions

Type  $S$  regions are those where the limiting strain is reached in all directions. In these regions there are not defined trajectories along which structural members should lie, instead there are infinitely many equally optimal layouts. This can be advantageous, the volume of these regions can often be found quite accurately using the layout optimization method. However, it can also lead to unclear solutions where many bars are superimposed. In layout optimization this can also occur when a triangle of bars of the same sense are present, this is usually observed within regions which are theoretically of type  $R$ , but where the resolution of the numerical method does not allow this to be sufficiently accurately modelled, e.g. Figure C.14. In these cases, a specific region of type  $S$  could make the solution clearer.

Explicit addition of a type  $S$  region would be most practical as a triangular region connecting three nodes, as this results in fewer potential members to check. Unlike the fan region, each of these nodes would be equal, further reducing the number of checks by a third. However, such a region would be functionally identical, in terms of both equilibrium and volume, to simply using the three corresponding existing bars. Furthermore, any valid combination of the three nodes concerned and other nodes within their convex hull is also equivalent. Thus, these  $S$  regions would likely be of use only when joint costs or similar are implemented.

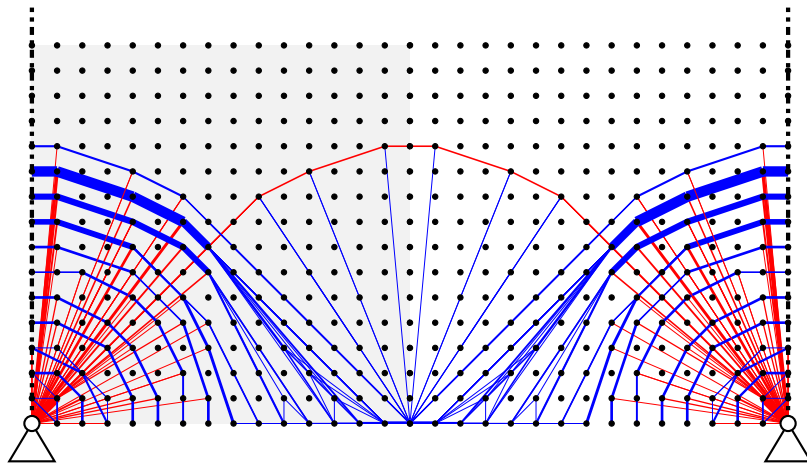


**Figure C.14:** When nodal resolution is limited, apparent regions of type  $S$  can appear, where the theoretical result would give a region of type  $R$ .

## Appendix D

# The solution spaces of layout optimization problems

One of the advantages of linear programming is the wide range of results which may be employed to gather further information on the characteristics of the problem. Here, two methods of exploring the solution spaces of layout optimization problems will be investigated.

Sensitivity analysis (Section [D.1](#)) explores the consequences of changes to the original problem, and how this may affect the optimal solution. This has the potential to suggest how resilient the resulting structure is, with minimal computational cost.

Vertex enumeration (Sections [D.2](#) and [D.3](#)) is a method for converting between representations of a polytope (such as the solution space of a linear programming problem). Applied to truss optimization, this allows all possible solutions to be generated as combinations of the basic solutions. From this, Pareto fronts of efficiency vs. complexity could be obtained in a single step.

---

D.1	Sensitivity analysis of layout optimization problems . . . . .	212
D.1.1	Sensitivity analysis for changing forces . . . . .	212
	Scaling in structural design codes . . . . .	212
	Modelling approaches for sensitivity analysis of applied forces . . . . .	212
D.1.2	Sensitivity analysis for member costs . . . . .	214
	Single load case . . . . .	214
	Multiple load cases . . . . .	214
D.2	Vertex enumeration by pivoting methods . . . . .	217
D.3	Vertex enumeration by incremental algorithms . . . . .	219
D.3.1	Formulation . . . . .	219
D.3.2	Method heuristics . . . . .	219

---

## D.1 Sensitivity analysis of layout optimization problems

Sensitivity analysis, or post-optimal analysis, refers to methods by which additional information can be obtained from the output of the linear programming solver. This is often used to answer ‘what if’ questions about the original problem scenario. Three main categories of information are generally considered; the rate of change of the objective when the right hand sides of the constraints are altered, the range over which this rate is constant, and the range over which changes in objective coefficients lead to a constant rate of change in the objective.

These results can be obtained from standard commercial linear programming solvers, however these results can be unreliable, particularly in cases with degenerate optimal solutions, such as most layout optimization problems. Here the optimal value method (Jansen et al., 1997) is used to obtain accurate values.

The optimal value, as a function of a particular right hand side value or objective coefficient of the original problem, is piecewise linear, consisting of a number of linearity intervals and breakpoints. Sensitivity analysis generally provides a description of the linearity interval(s) in which the optimal solution lies, and their associated breakpoints.

### D.1.1 Sensitivity analysis for changing forces

Perhaps the most obvious ‘what if’ type question with regards to structural optimization problems is: What if the external forces are different to expected? Future change of use, accidental loading or modelling assumptions regarding choice of loading patterns could cause problems. Whilst the field of robust optimization aims to tackle this rigorously (Guest & Igusa, 2008; Lee et al., 2019), the added computational and conceptual difficulty may discourage everyday use. Sensitivity analysis may be of use to provide simple checks and information when the level of variability is reasonably low.

Sensitivity analysis of constraints produces a ‘worth per unit’ (Taha, 2007) and a range over which this is valid. The worth per unit is the rate of change of the objective function relative to the change in the right hand sides. By the strong duality theorem,

$$\text{optimal value of primal} = \mathbf{c}^T \mathbf{x} = \mathbf{b}^T \mathbf{y} = \text{optimal value of dual} \quad (\text{D.1})$$

where  $\mathbf{c}$  are the primal objective coefficients (i.e. the dual right hand sides),  $\mathbf{x}$  are the primal variables,  $\mathbf{b}$  are the primal right hand sides (i.e. the dual objective coefficients) and  $\mathbf{y}$  are the dual variables.

Applied to the layout optimization problem, this implies that the value of the optimal structure for a perturbed problem will be the volume of the original structure plus the change in value of the force times the original virtual displacement at that point. If the direction of the force perturbation opposes the virtual displacement, the volume will decrease. However if the added force is in the direction of the virtual displacement, the optimal volume will increase, implying that the original structure would be non-conservative. This is a particular concern if the force perturbation acts to reduce the magnitude of an applied force.

### Scaling in structural design codes

Structural design codes generally classify loads into different categories, such as live loads (those expected to change frequently, e.g. weight of people and furnishings) and dead loads (those expected to remain mainly constant such as self-weight of the supported structure) (CEN, 2002; ASCE, 2003). These loads have factors applied to give a design value; the factors differ depending on whether a load is favourable or unfavourable.

Identifying which loads are favourable and unfavourable is reasonably easy when the design is fixed, particularly for common layouts. However, for layout optimization, the loads must be factored before the design is found, this can cause issues if the incorrect combinations are chosen. Sensitivity analysis could provide a simple means of highlighting potential issues with the chosen patterns of loading. Any load which acts in the opposite direction to its virtual deflection is likely to be having a favourable effect on the structure, and should be factored as such. This has the advantage of being a simple and relatively intuitive check, Simultaneous sensitivity analysis of different combinations should ideally also be considered, although the number of different possible cases would increase rapidly with the number of applied loads.

### Modelling approaches for sensitivity analysis of applied forces

There are a number of modelling approaches which may be chosen, each of which may result in somewhat different conclusions being drawn from the sensitivity analysis. The simple problem shown in Figure 8.9 has been used to test three different approaches, and the results are shown in Figure D.1 for sensitivity analysis of all 5 free degrees of freedom.

The most straightforward approach is to simply solve the problem as initially posed, e.g. in the case of Figure D.1 to solve a single load case problem, and then to obtain the sensitivity information from this. The results of this are shown in Figure D.1a.

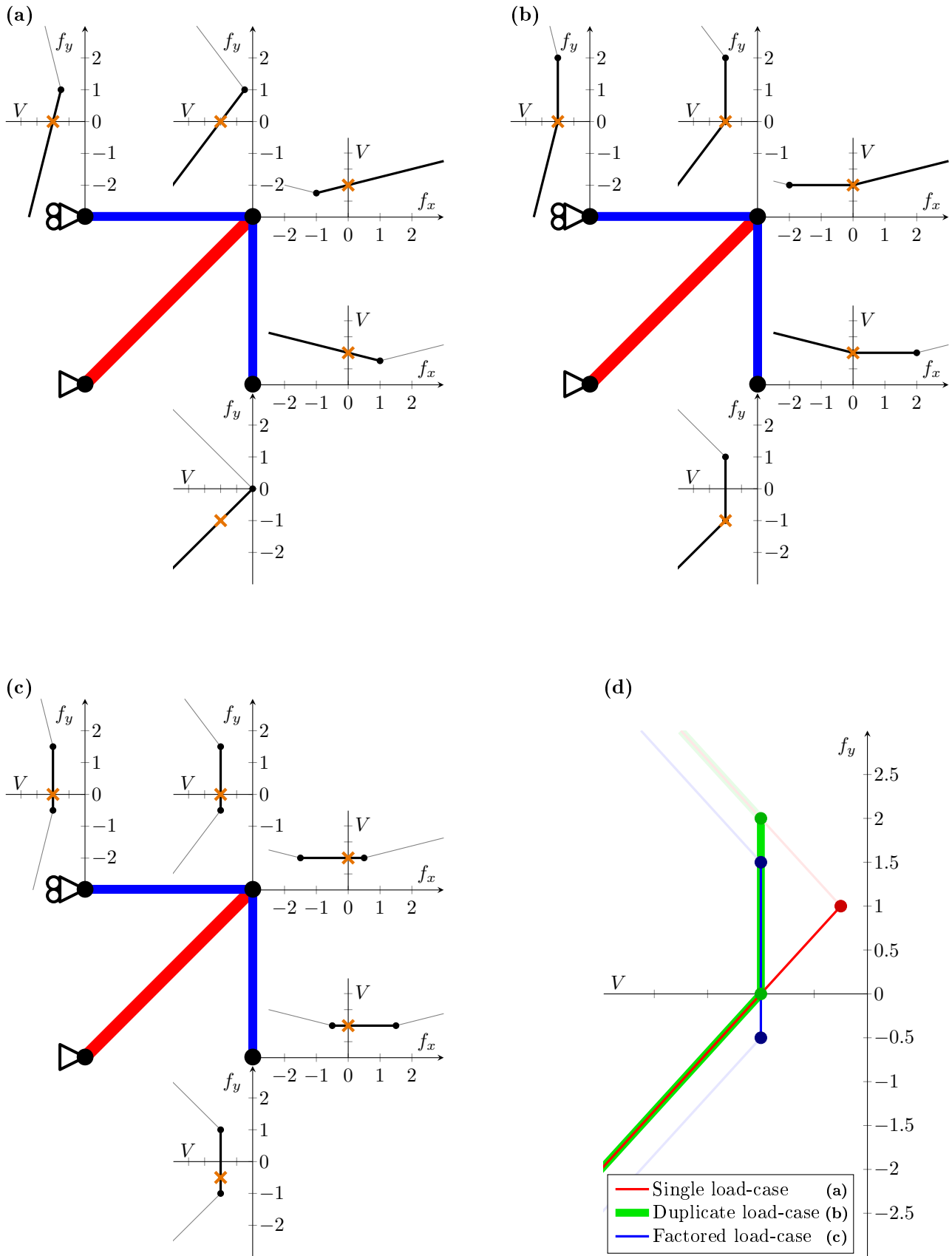


**Figure D.1:** Square cantilever - 4 node: sensitivity analysis for external forces. Orange cross shows initially analysed case. Black results show those available by sensitivity analysis, gray results have been separately calculated for context. (a) perturbation applied to original load case, (b) perturbation applied to duplicate alternate load case, (c) perturbation applied to factored alternate load case. (d) comparison of results for vertical load at top right.

Note that this problem has two equally optimal solutions, and the illustrated relationships between volume and force perturbation are independent of which solution is illustrated. For example, see the plot relating to horizontal force at the lower right node, an additional force to the left would result in a reduction in volume. However, the shown structure clearly could not support such a load, instead the equally optimal triangular structure (see Figure 8.9) should be used, and the bottom member could then be appropriately reduced in size. It may be possible to obtain more practically useful, if less mathematically rigorous, results through the use of optimal basis methods.

The results using this method may be very impractical; for example a vertical unit load applied upwards at top right causes a drastic decrease in the volume, this breakpoint corresponds to a structure consisting of a single bar connecting the two applied forces, and not connecting to the support at all. Thus it may be more appropriate to consider the perturbed loads as acting in a second load case, the results of this are shown in Figure D.1b.

Now, the structure will never decrease in volume, as the original load case must also be carried. Some linearity intervals which are returned are now horizontal, these intervals are of particular practical interest, as they represent alternative load combinations which could be carried by an optimal solution. However, most points lie on a breakpoint, this is likely to cause substantial errors and inaccuracies in the data returned from commercial packages.

A similar approach is shown in Figure D.1c, in this case, the first load case is unchanged, but the second load case halves the magnitude of the original forces. The optimal values now do not lie on breakpoints, which can simplify application. This now gives reasonably useful ranges of possible alternate loads, for example the original structure designed for a downwards load of 1 at the lower right, is also capable of supporting a downwards load of 0.5 at the bottom right concurrently with a rightwards load of 0.5 at the top right.

Figure D.1d compares the results of these three approaches. It can be seen that when the perturbed loads are applied to a duplicated load case (D.1b), this simply removes areas where the single load case result (D.1a) would drop below the original value. Using a factored load case (D.1c) translates the results of Figure D.1b towards the direction of increasing volume from Figure D.1a.

### D.1.2 Sensitivity analysis for member costs

The other major use of sensitivity analysis is the investigation of changes in the coefficients of the objective function. This may not seem immediately applicable to layout optimization as variability in the costs of material and thus members is most likely to affect all members equally. However some interesting results can be obtained.

The linearity ranges for the objective coefficients give the range of costs for a particular member over which a current optimal form remains optimal. From the breakpoints at the ends of the linearity interval, the new objective value obtained when the form changes is obtained. This can be used as a measure of the 'importance' of a certain member of the solution.

**Single load case** For example, Figure D.2a shows the layout optimization result for the single load case problem shown. Sensitivity analysis is used to investigate the influence of increasing the cost of the horizontal member at the top left. The upper end of the linearity interval is calculated to occur when the objective value is increased by 1.7%. Solving the perturbed problem then gives the result shown in Figure D.2b.

Similar investigations have been undertaken for each member present in the initial structure, resulting in the forms in Figure D.2b-f as indicated. Note that the results are not exactly symmetrical about the diagonal axis of symmetry; result D.2c is obtained for only one member, whilst result D.2e is obtained for two. This is because structures D.2b and c and D.2e and f have identical volumes, and are therefore equally optimal if no relevant coefficients have been changed.

The volume increase given by the indicated structure is the minimum volume increase possible by reducing that member. This could make a simple means of guiding a designer during a manual rationalization process such as the one described in Chapter 3, as members could be coloured by the result of the sensitivity analysis.

**Multiple load cases** The method works equally well for multiple load cases, as shown in Figure D.3, where the two loads are applied in separate load cases. However, these results, particularly D.3 show a potential issue whereby a member may be replaced by a set of almost identical members. This also demonstrates why it is important to remove colinear members for sensitivity analysis and vertex enumeration methods, otherwise the members could simply be replaced by a different set of colinear members.

Although the idea of 'removing' the member may appear to imply that this method could lead to simpler structures, this is not the case, for example solutions in D.3e-f are substantially more complex than Figure D.3a. These results do show the importance of the vertical bar on the right in this problem.



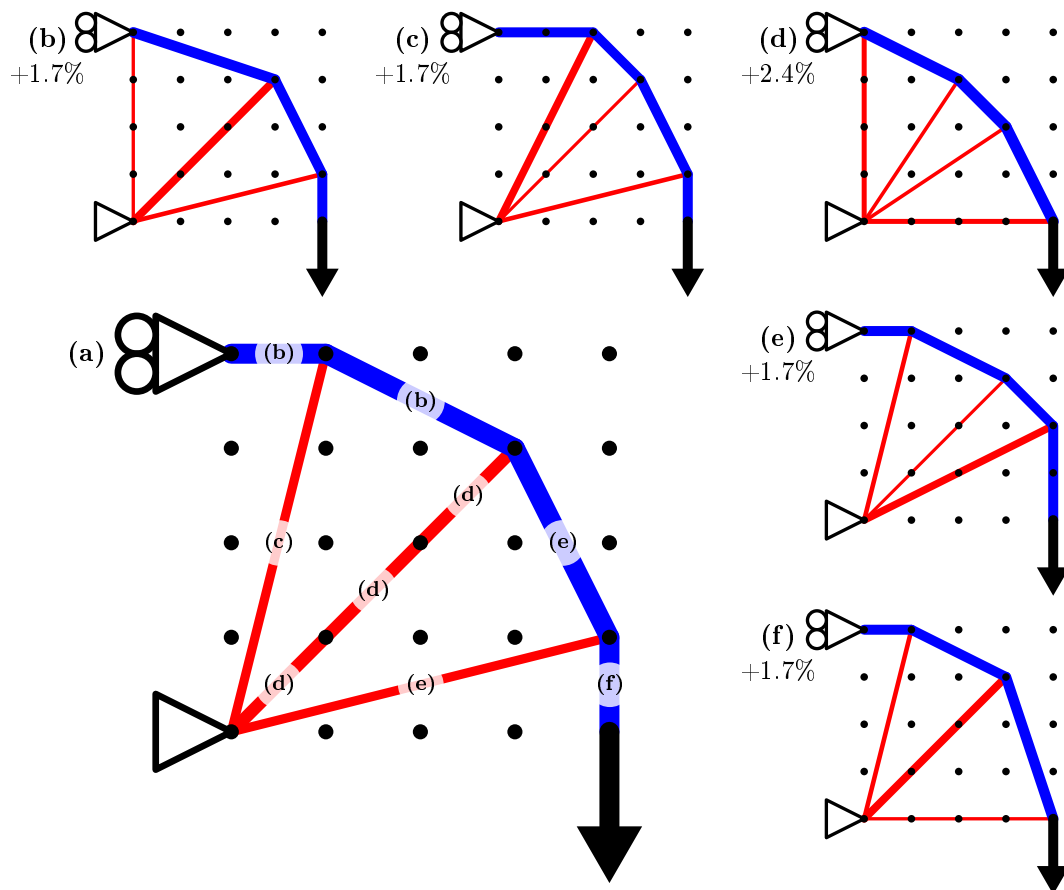


**Figure D.2:** Square cantilever - 25 nodes: Sensitivity analysis of cost coefficients of active members. (a) layout optimization result, each member present is labelled with the new solution found when its objective coefficient is increased just outside of the associated linearity interval. (b)-(f) Minimum volume structures with individual members removed, and associated volume increase.

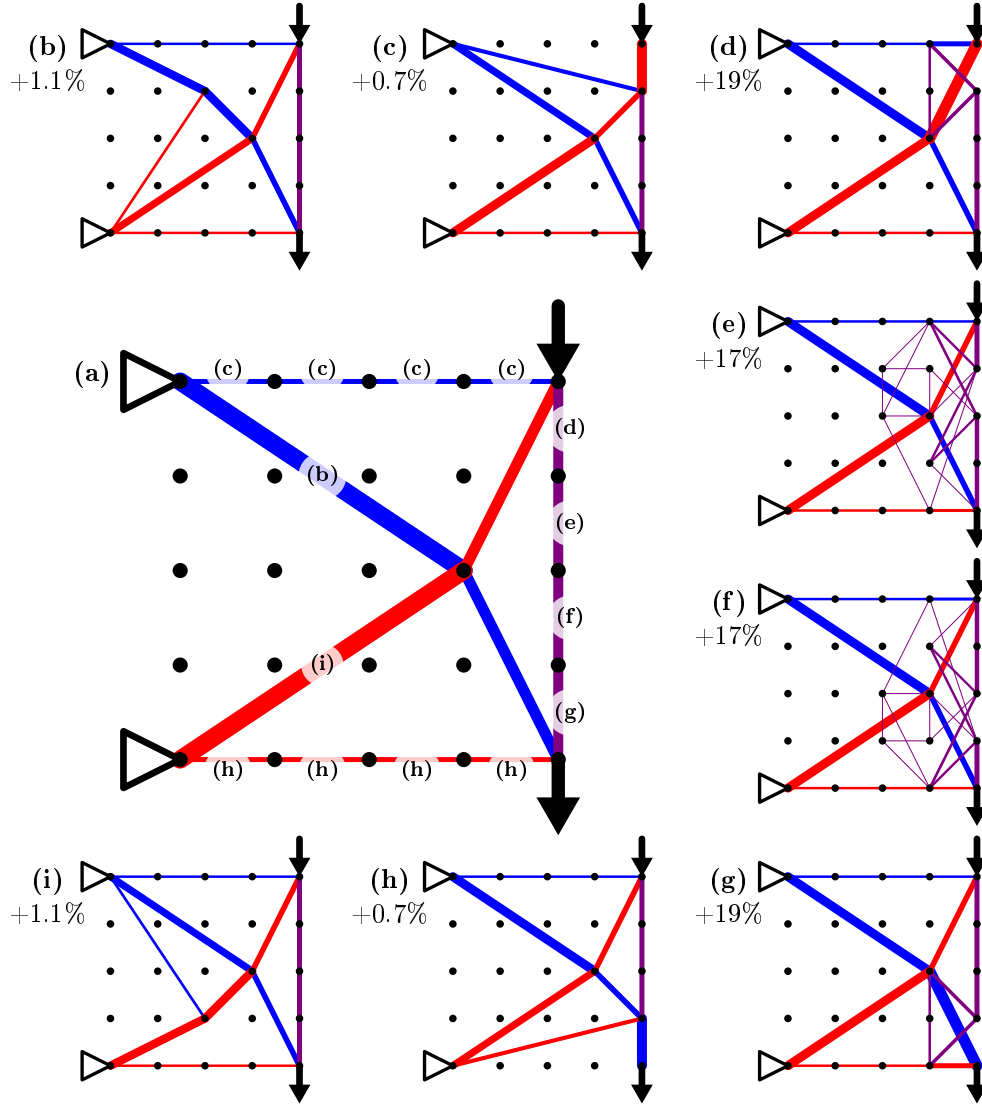


**Figure D.3:** Square cantilever - 25 nodes, 2 load case: Sensitivity analysis of cost coefficients of active members. (a) layout optimization result, each member present is labelled with the new solution found when its objective coefficient is increased just outside of the associated linearity interval. (b)-(i) Minimum volume structures with individual members removed, and associated volume increase. It can be seen that elements forming the bar on the right of the structure imply a much higher volume increase when they are removed.

## D.2 Vertex enumeration by pivoting methods

The sensitivity analysis process described in Section D.1.2 generates new basic solutions to the layout optimization problem. These new solutions are adjacent to the optimal solution. Furthermore, the solutions are guaranteed to be distinct from the optimal solution, i.e. not just an alternative basis representation of the same point.

Repeated application of the method to the results produced will generate further new structures. This effectively becomes a pivoting type vertex enumeration algorithm (similar to those of Chand & Kapur, 1970; Avis & Fukuda, 1992). The obtained solutions, and the graph of the edges traversed to reach them can be stored, and usefully output at any time during the solver operation. The method handles degeneracies well, and is logical and intuitive in its progression.

A number of extra issues must be considered. Firstly, at each iteration after the first, multiple possible solutions will exist and a decision must be made concerning which is to be checked next. Here, the very simple heuristic of choosing the unchecked solution with the lowest complexity (defined as total length of members) was used. The second issue is that loops may occur, this is dealt with by checking the uniqueness of the set of non-zero variables. Any solutions found which duplicate already known bases are discarded, and the new connection is added to the graph. Additionally, any solutions which produced a structure with a volume greater than  $4.2 (=1.2V_1)$  were discarded.

This method is applied to the square cantilever problem of Figure D.2 using a ground structure of 25 nodes. The process was terminated when 200 solutions had been obtained. The graph of the basic feasible points and the edges traversed is shown in Figure D.4, and a number of solutions of interest are shown in Figure D.5. The solutions adjacent to point 1 are the same solutions as those identified in Figure D.2.

The layout of the graph was calculated using the force based method of Fruchterman & Reingold (1991), implemented within MATLAB. A moderate level of symmetry in the graph is observed. This is due to the diagonal axis of symmetry in the problem, for example compare results 4 and 6 or 58 and 63. Symmetrical structures, such as solutions 1, 2 and 72, lie along the central line of the graph.

The vertices of the graph in Figure D.4 are coloured according to the volume of the corresponding structure. At least two pockets of low volume structures can be seen, one in the vicinity of point 1 and the other in the vicinity of point 169. The route that was taken between these two pockets went via results 135, 157 and 168 (shown in Figure D.5). These intermediate results have much higher volume, and higher values for most complexity measures. As the graph in Figure D.4 shows only the edges traversed, there may be an alternate route. However, as lowest complexity was used as the selection heuristic, any alternative route will also cross solutions of high complexity.

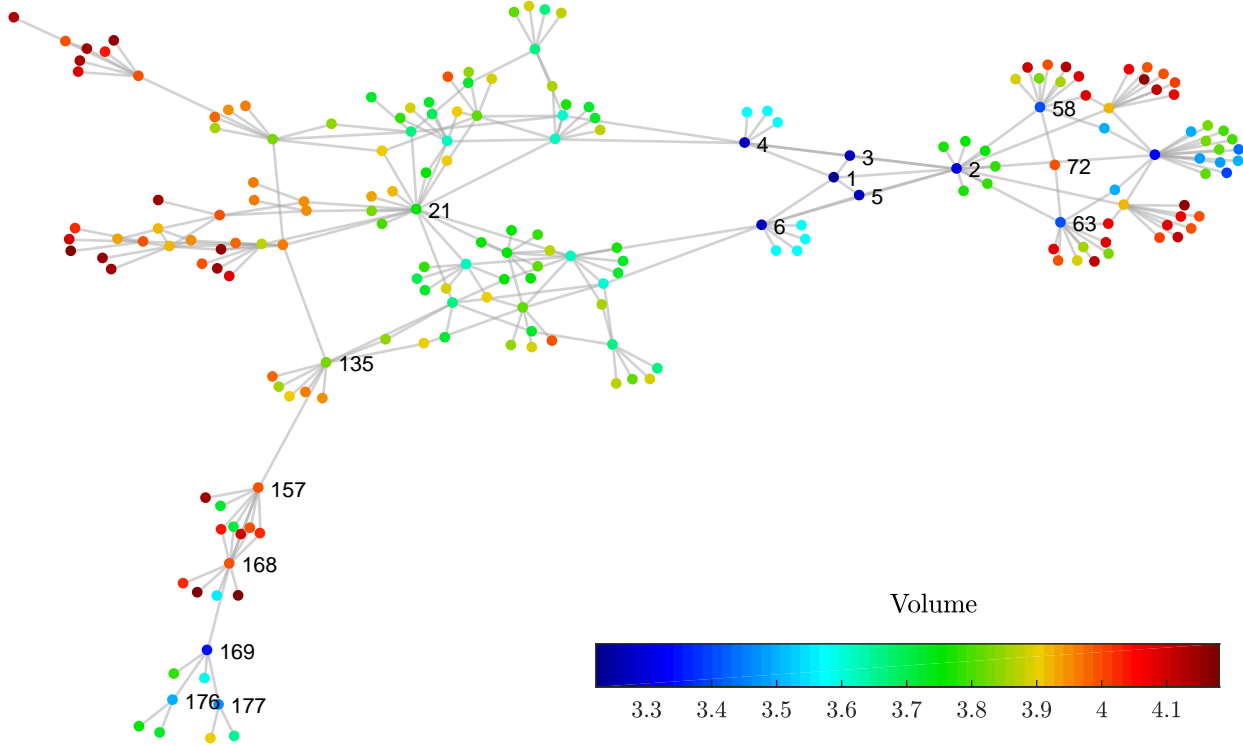


**Figure D.4:** Square cantilever - 25 nodes: Volumes of 200 basic solutions found by pivoting type method. The sequential ID numbers of the solutions illustrated in Figures 8.12 and D.5 are indicated.

Volume	3.222	3.278	3.278	3.350	3.417	3.417	3.500	4.000
Total Length	4.74	4.69	4.69	4.45	4.36	4.36	3.73	3.41
Joint Complexity	41.1	34.5	34.5	34.3	29.2	29.2	16.9	14.0
Minimum Area	0.46	0.33	0.33	0.36	0.50	0.50	0.50	1.00
Sequential ID	1 <sup>st</sup>	4 <sup>th</sup>	6 <sup>th</sup>	169 <sup>th</sup>	58 <sup>th</sup>	63 <sup>rd</sup>	176 <sup>th</sup>	72 <sup>nd</sup>
Volume	3.300	3.278	3.278	3.750	3.833	4.000	4.000	3.467
Total Length	5.27	4.87	4.87	4.22	5.54	5.18	5.23	4.43
Joint Complexity	59.7	50.8	50.8	28.1	110	64.5	94.8	40.3
Minimum Area	0.36	0.31	0.31	0.40	0.24	0.50	0.22	0.24
Sequential ID	2 <sup>nd</sup>	3 <sup>rd</sup>	5 <sup>th</sup>	21 <sup>st</sup>	135 <sup>th</sup>	157 <sup>th</sup>	168 <sup>th</sup>	177 <sup>th</sup>

**Figure D.5:** Square cantilever - 25 nodes: Structural forms for points labelled in Figure D.4.

## D.3 Vertex enumeration by incremental algorithms

### D.3.1 Formulation

For the double description method described in Section 8.3.3, it is required to have the problem formulated using non-negative variables. However, variables for the area are also needed; thus the standard single load case formulation is not ideal. Instead, the following formulation was used.

$$\text{minimise } \mathbf{l}^T \mathbf{a} \quad (\text{D.2a})$$

$$\text{subject to } \mathbf{B}(\mathbf{a}\sigma_T - \mathbf{p}) = \mathbf{f} \quad (\text{D.2b})$$

$$\mathbf{a}(\sigma_T + \sigma_C) - \mathbf{p} \geq \mathbf{0} \quad (\text{D.2c})$$

$$\mathbf{a} \geq \mathbf{0} \quad (\text{D.2d})$$

$$\mathbf{p} \geq \mathbf{0} \quad (\text{D.2e})$$

where  $\mathbf{p}$  is a variable representing the force state of the member, members fully stressed in tension have  $p = 0$  and members fully stressed in compression have equation (D.2c) satisfied with equality.

For the double description method, the constraints should all be inequalities. This is achieved by using Gaussian elimination to reduce the dimension of the problem before applying the algorithm. It may also be achieved by converting each equality constraint into a pair of opposing inequality constraints, although this is likely to be less efficient.

### D.3.2 Method heuristics

The speed of the double description method is known to be very sensitive to the order in which the constraints are considered (Fukuda & Prodon, 1995). Here, the dynamic ordering of Rubin (1975) was used to decide the next constraint to be added; the next row to be added is the row with the minimal value of  $U$ , where  $U$  for each row is found using:

$$U = P + Z + PN \quad (\text{D.3})$$

where  $P$  is the number of points on the positive side of the constraint,  $N$  is the number of points on the negative side of the constraint, and  $Z$  is the number of points lying directly on the plane of the constraint. The value of  $U$  is an upper bound on the number of points/rays which may be present at the end of this iteration, if all pairs of points checked produce a new point. The value  $P + Z$  is a lower bound, assuming no new points are produced.

Figure D.6 shows the number of points and rays at each iteration during the solution of the problem of Figure 8.13. The black lines at each point represent the upper bound (i.e.  $U$ ) and lower bound (i.e.  $P + Z$ ) on the possible number of points and rays in the next iteration. It can be seen that neither bound is particularly well correlated with the resulting number of points/ray. This may suggest that better adding orders are possible.

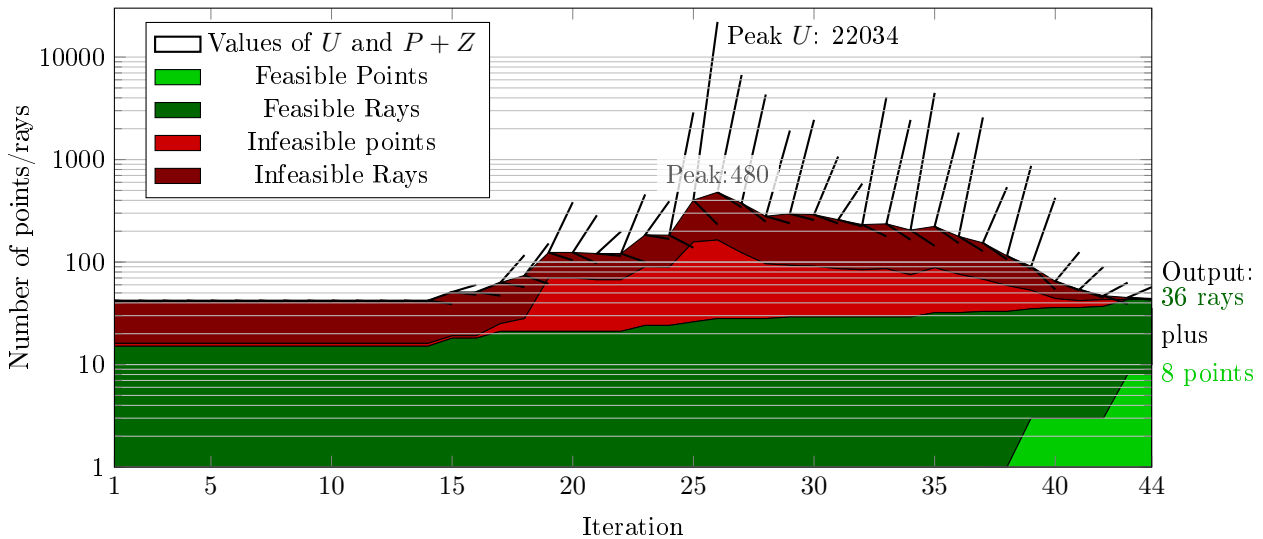


**Figure D.6:** Number of points and rays at each step of complexity constrained double description method. Also shown are the upper and lower limits of the number of points and rays at the next step, for the chosen constraint.



# Appendix E

## Additional contributions to the literature

This appendix provides copies of additional material which has been published as part of this study. Note that in addition to the contributions below, Chapters 4 and 5 are each drawn from a paper, see the prefaces of the relevant chapters for more information.

Sections E.1 and E.2 are based on the real world case study of Chapter 3. These sections use the case study to present the opportunities of layout optimization to a wider audience of researchers and practitioners respectively.

Section E.3 describes an initial study which eventually led to the frictional foundations described in Chapter 5. This initial study uses a simpler model where the horizontal reaction forces are limited without reference to the vertical reaction force at the point.

Sections E.4, E.5 and E.6 relate to the integer programming methods described in Chapter 6. Sections E.4 and E.5 compare different possible complexity measures, with E.5 extending this to 3D cases. Section E.6 covers the use of lazy constraints to improve the computational efficiency of the MILP problem, and the derivation of benchmarks for validation.

---

E.1	Application of layout optimisation for building structures . . . . .	222
E.1.1	Abstract . . . . .	223
E.1.2	Poster . . . . .	225
E.2	Optimisation-driven conceptual design: Case study of a large transfer truss . . . . .	226
E.3	Optimization-driven conceptual design of long span bridges . . . . .	234
E.4	Automatic identification of structurally efficient layouts with limited complexity . . . . .	243
E.4.1	Abstract . . . . .	244
E.4.2	Poster . . . . .	246
E.5	Balancing complexity and structural efficiency in the design of optimal trusses . . . . .	247
E.6	Layout optimization of simplified trusses using MILP with runtime generation of constraints . . . . .	256

---

## E.1 Application of layout optimisation for building structures

The material in this section was prepared for the Young Researchers' Conference 2017, hosted by the Institute of Structural Engineers. This conference brings together PhD researchers from all areas of structural engineering research. This section contains the submitted abstract, and the poster which was presented at the conference. The was awarded first prize in the poster category at the conference.

This primarily concerns the case study considered in Chapter 3, although the constraints of the poster format mean that only the major results are discussed.

---

<sup>†</sup> Fairclough, H., (2017) Application of layout optimisation for building structures. In *Proceedings of the 19th Young Researchers' Conference*. The Institute of Structural Engineers, (pp. 44-45).



## Application of Layout Optimization for Building Structures

**Helen Fairclough**  
University of Sheffield

### Introduction

Reducing the volume of material used in building structures is becoming increasingly important. There are many reasons why this may be a priority: reduced carbon emissions from material production, easier transportation and erection of lighter components, or to limit the loads imposed on existing structures or earthworks. However, the forms of almost all structures are still designed by engineering judgement and past experience, often using forms identified many centuries ago. This makes it difficult to establish whether the proposed solutions are efficient, or whether significant savings may be made by considering alternatives.

The problem of finding a minimum weight structure to transmit loads to supports has been the subject of significant academic study. Pioneering work by Michell (1904) allowed manually derived exact solutions to be obtained for simple problems. Later, computational methods, such as those derived by Dorn (1964) and Bendsøe (1989), allowed approximate solutions for more complex scenarios to be obtained. However, many issues remain which prevent widespread application of these methods in daily design practice in the field of structural engineering.

### Project objectives and goals

The aim of this project is to identify the most critical issues preventing widespread application of structural optimisation methods in the field of structural engineering. Various methods of tackling these issues will be developed, including modifying the basic methods and post-processing the solutions obtained to increase their practicality.

This study uses a number of optimisation methods, combined with manual interpretation, to produce a series of structures ranging from theoretical benchmarks to typically used forms. This results in a family of potential forms, and their associated volume costs, and allows for informed decisions to be made on the impact of the design choices involved. The case study chosen for this is drawn from a real industry project, and through close collaboration with engineers at Expedition Engineering, it is ensured that a wide ranging and realistic set of construction and architectural constraints are considered. From this, limitations in both the process and the results can be identified and addressed.

### Description of method and results

For this study, a ground structure based layout optimisation method, similar to that described by Pritchard et al. (2005) is used. This identifies structural design solutions in the form of line-element models which are well suited to construction using a series of individual elements. This method also has superior performance when compared to continuum optimisation methods for problems where the structure occupies only a small fraction of the available design domain.

The basic problem is to minimise the total volume, with constraints on the maximum permitted stresses and equilibrium enforced under all load cases. This is implemented as a linear program, which allows the use of efficient gradient based methods, and eliminates the risk of finding local optima.

Analysis of initial case studies has established three key areas in which improvements to the classical layout optimisation methods are necessary:

- Accurate and efficient modelling of buckling.
- Appropriate rationalisation of complex forms.
- Assessment of robustness of the solutions found.

A number of possible solutions have been identified for each issue. Choosing the most appropriate method to tackle each of these will require evaluation of the method's effectiveness, computational efficiency and ease of application.

### Potential for application of results

Layout optimisation has the potential to be applied to a wide variety of structural types; case study problems looked at so far include transfer structures in tall buildings, roofs and bridges. In each of these it has been found that improvements in structural efficiency are possible, with the most savings found when there is significant freedom of form.

**References**

Bendsøe, M. P. (1989). Optimal shape design as a material distribution problem, *Structural optimization* 1:4, 193-202.

Dorn, W. S. (1964). Automatic design of optimal structures, *Journal de Mecanique*, 3, 25-52.

Michell, A. G. M. (1904). The limits of economy of material in frame-structures, *The London, Edinburgh, and Dublin Philosophical Magazine and Journal of Science*, 8:47, 589-597.

Pritchard, T. J., Gilbert, M., & Tyas, A. (2005). Plastic layout optimization of large-scale frameworks subject to multiple load cases, member self-weight and with joint length penalties, In *6th World Congress of Structural and Multidisciplinary Optimization*.

**Funding body**

Engineering and Physical Science Research Council (EPSRC) and Expedition Engineering.

**Further information**

Helen Fairclough (E: [hefairclough1@sheffield.ac.uk](mailto:hefairclough1@sheffield.ac.uk)) or  
Professor Matthew Gilbert (E: [m.gilbert@sheffield.ac.uk](mailto:m.gilbert@sheffield.ac.uk))  
<http://www.build-opt.org/>

**Collaborators**

This research forms part of a larger EPSRC funded project involving the Universities of Bath, Edinburgh & Sheffield and Expedition Engineering, Aecom, Arup, Buro Happold, IStructE, Ramboll and the SCI.

## Introduction

In structural design, the overall shape and layout of a structure is most commonly chosen based on the precedents of existing structures and the engineer's past experience. Additionally, often, little is done to assess how material-efficient a structure could theoretically be or to assess the impact each decision made by the design team has on structural weight.

The main aims of this project are to:

- Establish **benchmarks** to inform how efficient a structure is,
- Provide tools to help designers understand the implications of each **design choice** on structural weight,
- Offer methods to **rationalise** the designs produced by optimisation methods to comply with fabrication constraints.

Here initial findings made on a real-world case study are presented.

## A practical case study

The case study considers the design of a **steel transfer structure** with a 50m span, which needs to fit within a 10m deep design domain. The structure is to be constructed from hollow square sections, fabricated from S355 steel.

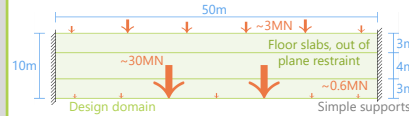


Figure 1: Problem description, loading values un-factored.

The structure must resist the loads shown in Figure 1, and comply with an increasingly restrictive set of constraints designed to increase its buildability.

The structure is modelled as a pin jointed truss. As it is a planar truss, resistance to out-of-plane buckling must be provided. This is available at the floor slabs.

## Details of optimisation methodology

The method of optimisation used is called Layout Optimisation. In this, the design domain (Figure 2a) is filled with nodes (2b), which are then connected in all possible pairings to give a 'ground structure' of potential truss members (2c). Linear programming algorithms are then used to find the globally optimal set of these members (2d) to support the loads.

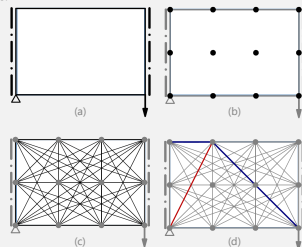


Figure 2: The stages of the layout optimisation process.

The output of this technique applied to the current case study with nodes at 0.25m spacing (32 million possible members) is shown in figure 4 row (a). The complexity of this structure is common in the outcomes of optimisation processes, this is a major factor in the low uptake of optimisation techniques in structural design practice

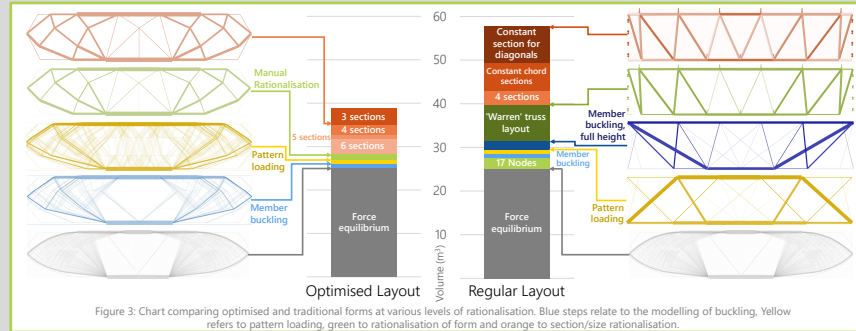


Figure 3: Chart comparing optimised and traditional forms at various levels of rationalisation. Blue steps relate to the modelling of buckling. Yellow refers to pattern loading, green to rationalisation of form and orange to section/size rationalisation.

Description		Form and total volume	
Optimised Layout	(a) Reference solution, minimum volume possible for force equilibrium at ultimate limit state.	High complexity	25.10m³
	(b) + Nodes restrained out of plane by being located on slab lines		25.48m³
	(c) + Compressive strength reduced according to effective length of members, to account for member buckling.		26.02m³
	(d) + Pattern Loading, using load case where one of the larger (~30MN) loads is factored as being favourable		27.03m³
	(e) + Penalty applied to optional (i.e. non load or support) nodes, representing weight of the joint.		27.40m³
	(f) + Manual removal of members and optimisation of node positions		30.52m³
	(g) + Optimisation using all possible connections between existing nodes.		27.44m³
	(h) + Manual removal of members and optimisation of node positions	Complexity	28.32m³
	(i) + Only 4 different cross sections permitted		34.98m³
	(j) Nodes only at top and bottom of domain, on loaded points or supports (includes pattern loading and member buckling)		29.44m³
Regular Layout	(k) + No out of plane buckling restraint provided to members where they cross interim slab lines		31.49m³
	(l) + Only 4 different cross sections permitted		37.66m³
	(m) + Topology restricted to Warren truss type		39.83m³
	(n) + Only 4 different cross sections permitted		42.86m³
	(o) + Continuous cross section along top and bottom chord	Low complexity	49.39m³
	(p) + Uniform cross section for all diagonals		57.85m³
			0m³ 10m³ 20m³ 30m³ 40m³ 50m³ Volume

Figure 4: Resulting structures for example problem from most complex theoretical structures to increasingly constrained forms.

## Details of rationalisation methods

The complex structures in figure 4, row (d) and earlier are simplified using an iterative procedure combining optimisation techniques with manual intervention using the Limstate-Form software developed at Sheffield University. This procedure is described in figure 5.

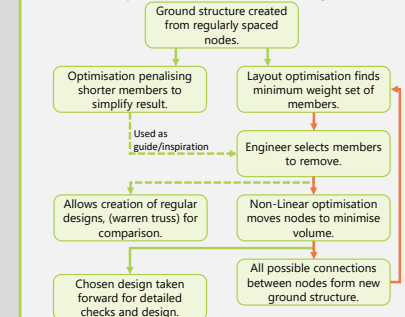


Figure 5: Rationalisation method incorporating manual intervention. The loop in orange is carried out as many times as required to produce a solution which satisfies all desired fabrication constraints.

After this process, forms using a limited number of different cross sections are found. This is currently done as a post processing step and the node locations and topology are not changed.

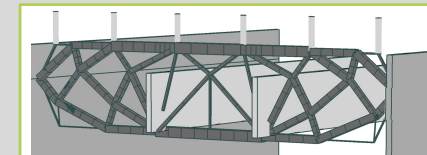


Figure 6: Rationalised truss using optimised topology (dark grey), showing supporting walls (mid grey) and main loading sources (light grey)

## Results

Figures 3 and 4 show the resulting potential structures found for the current problem. In figure 3 they are separated into optimised and regular layout. This allows a visual representation of the significance of the different **design choices**.

Figure 4 shows the changes in form and volume as additional constraints are added. Note that with the chosen cross section and modelling type (i.e. pin jointed) lines 4(a) to 4(c) are not resistant to buckling. Further work will be required if a **benchmark** which does not depend on design decisions is desired.

Rows 4(f) and 4(g) of show some of the structures produced during the iterative **rationalisation** process described in figure 5. Row 4(h) shows the chosen design which was used for the studies to reduce the numbers of cross sections, and is shown in figure 6. The proposed method allows flexible interpretation of fabrication constraints, and this is just one of many potential designs available to the designer.

This case study has shown that these methods can produce a wide range of structural options for a design team, with the potential for significant material savings, even once fabrication constraints are considered. This will allow informed decisions to be made when considering design choices, and may provide additional options which make use of highly efficient structural forms which are not yet commonly considered.

## E.2 Optimisation-driven conceptual design: Case study of a large transfer truss

This section contains an article<sup>†</sup> which has been accepted for publication in *The Structural Engineer*, the magazine of the Institute of Structural Engineers. The aim of this article was to demonstrate, to practitioners, what can be achieved through the use of currently available optimization methods.

The article considers the case study considered in Chapter 3, although the focus here is on the strengths and opportunities the methods present, rather than on identifying issues to be addressed.

---

<sup>†</sup> Fairclough, H., Gilbert, M., Thirion, C., Tyas, A., & Winslow, P. (in press) Optimization-driven conceptual design: Case study of a large transfer truss. *The Structural Engineer*.

# Optimisation-driven conceptual design: case study of a large transfer truss

HELEN FAIRCLOUGH

MEng

Research Engineer, Expedition Engineering, London; and University of Sheffield, UK

MATTHEW GILBERT

BEng, PhD, CEng, MICE, MASCE

Professor, University of Sheffield, UK

CLEMENT THIRION

MEng, MSc, CEng, MICE

Senior Associate, Passage Projects, London, UK (formerly Expedition Engineering, London)

ANDY TYAS

BEng, PhD

Professor, University of Sheffield, UK

PETE WINSLOW

MEng, MA, PhD, CEng, MStructE

Associate, Expedition Engineering, London, UK

## SYNOPSIS

This article describes the use of structural optimisation at the conceptual design stage to identify materially efficient solutions which incorporate buildability considerations. In the proposed approach, a minimum-weight solution is first identified, providing a benchmark against which other designs can be judged.

However, as this solution will often be complex in form (and effectively impossible to construct in practice), additional constraints are then gradually introduced to rationalise it, and to explore the regions of the solution space which separate it from simpler, more familiar solutions. This enables the designer to balance material efficiency and complexity in a more informed manner.

The efficacy of the approach is demonstrated via application to a case study of a transfer truss design.

## Introduction

Recent advances in affordable computing power mean that optimisation techniques, once primarily the preserve of aerospace and high-end automotive designers, are becoming accessible to the wider structural design community. The most general forms of structural optimisation are *topology optimisation* or, for frame structures, *layout optimisation*. Both of these involve starting with a blank space, the *design domain*, and generating a geometry for the structure based on mathematical rules. These techniques have the potential to achieve the most materially efficient designs possible, but are not currently commonly used in structural engineering practice, partly due to the complexity of the forms they generate.

For example, consider the 50m span basement transfer truss required for a hotel development project (Figure 1). A range of designs for the problem are presented in Figure 2. Figure 2a shows the basic truss structure derived manually, which resembles a Warren truss. In contrast, the solution shown in Figure 2c, obtained using numerical layout optimisation, would in theory consume much less material. However, this comprises many thin members, each of different length and cross-section. This is a close approximation to the true theoretical solution for this problem, which can be obtained based on the principles set out by Michell in 1904<sup>1</sup>, and which includes an infinite number of infinitely thin members.

Application of new manufacturing methods has the potential to remove some barriers to fabrication. For example, additive manufacturing, or '3D printing', techniques are being developed

for a range of materials, including concrete<sup>2</sup> and steel joints<sup>3</sup>. Alternatively, steel joints cast using 3D printed moulds can provide a means of avoiding issues with scale and certification. The use of 3D printing in the production of joints for a truss may reduce the costs associated with unusual joint configurations and may ultimately allow more tailored designs to be considered.

It is also possible to rationalise optimum forms to make them easier to fabricate. Previous studies have shown that simplified structures that are similar in form to the optimal layout have the potential to retain a significant level of material efficiency with much lower complexity<sup>4</sup>. This is explored here. One such simplified structure is shown in Figure 2b; this has a weight which is little higher than the identified optimum form, and less than half that of the manually derived truss (Figure 2a).

Based on this observation, the method described here involves first finding a minimum-weight structure without imposing limits on complexity, and then gradually rationalising the design by accounting for practical considerations. Here, the term 'structural complexity' is used to refer to a range of features; considering minimum-weight structures, the number of members and the number of different cross-sections are both commonly identified as major issues. Therefore, the method progressively removes members and/or standardises cross-sections, to lead to a gallery of candidate designs.

However, it is unlikely to be possible to find forms that are both very simple and very lightweight. Instead, a choice will need to be made concerning the trade-off between material efficiency and

complexity (Figure 3). A demonstration of this will be provided, using the hotel basement transfer structure problem already referred to, from a project by Expedition Engineering.

To achieve this, a number of numerical layout-optimisation methods developed at the University of Sheffield are employed. These methods are implemented in the commercially available LimitState:FORM<sup>6</sup> design-optimisation software. A feature of the software is that the user can manually remove or modify individual structural members during the optimisation process. The study demonstrates the potential to achieve greater material efficiency through exploration of the solution space, the set of all possible feasible solutions to a problem.

It is found that a wide range of possibilities lie between the mathematically optimal, but impractical, forms at one extreme, and the forms typically used in practice today at the other extreme. This allows the design team to make informed decisions on the implications of using a less conventional layout and to indicate where an investment in more complex detailing may be justified. Conversely, it will also indicate when benefits are marginal, and therefore when a more standardised design is likely to provide the most economical choice.

#### Available optimisation techniques

Heuristic optimisation methods, such as genetic algorithms, have proved popular in recent years, largely due to the ease with which a non-specialist user can include real-world constraints; a description of several such approaches and their application has been given by Debney<sup>6</sup>.

However, these methods have severe drawbacks. For example, the starting points for these methods are usually randomly generated, or based on intuition, but will often influence the final output, likely leading to a suboptimal design being obtained (i.e. corresponding to a 'local hollow', which may be much higher than the 'valley bottom' shown in Figure 4).

Additionally, with these methods, there is no way of knowing how much further benefit is possible once a solution has been found. This may lead either to unnecessarily inefficient designs being accepted, or alternatively to substantial effort being wasted attempting to improve on a design which is already optimal or near-optimal.

Here, an alternative two-step optimisation approach is proposed. In the first step, the problem is simplified so that only the essential physics is modelled; in this case, meaning that only equilibrium and stress limit considerations remain. This allows a reference solution to be obtained, providing a lower bound on the structural volume (or weight). The second step is to apply various methods to move through the solution space to locate promising solutions, if possible in close proximity to the reference solution (Fig. 4b).

For the identification of minimum-weight structures, continuum-based topology-optimisation methods are commonly used. These routines are now included in many

FIGURE 1: Basement transfer truss: configuration and applied load magnitudes

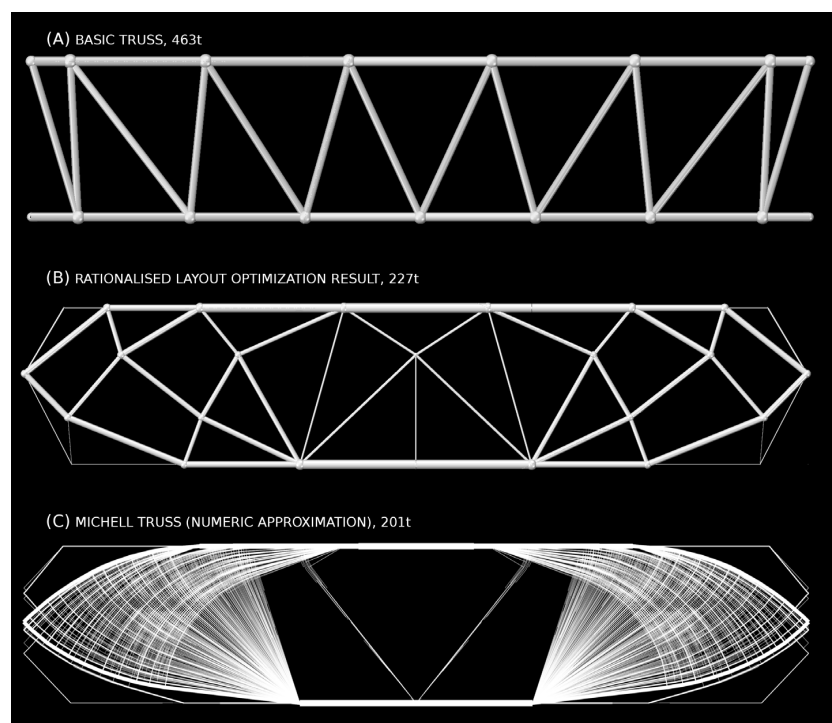
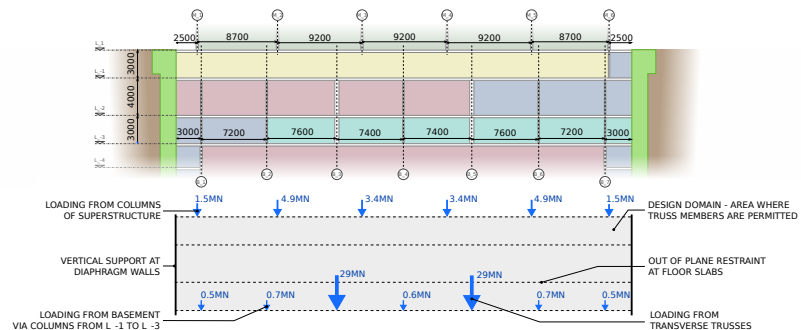


FIGURE 2: Basement transfer truss: sample discrete designs for problem shown in Fig. 1

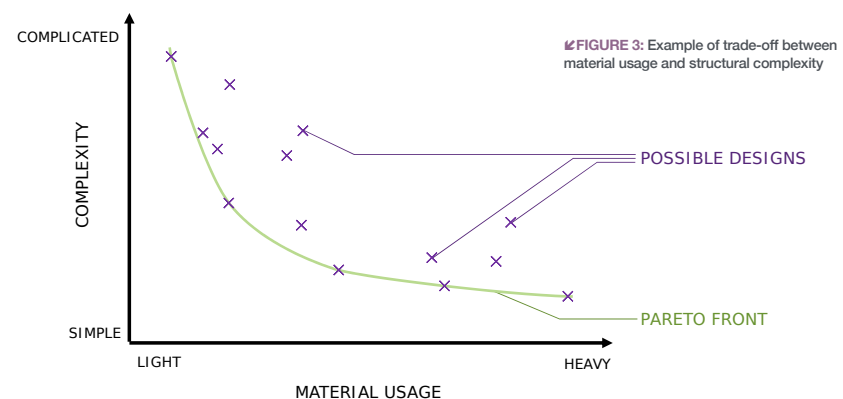
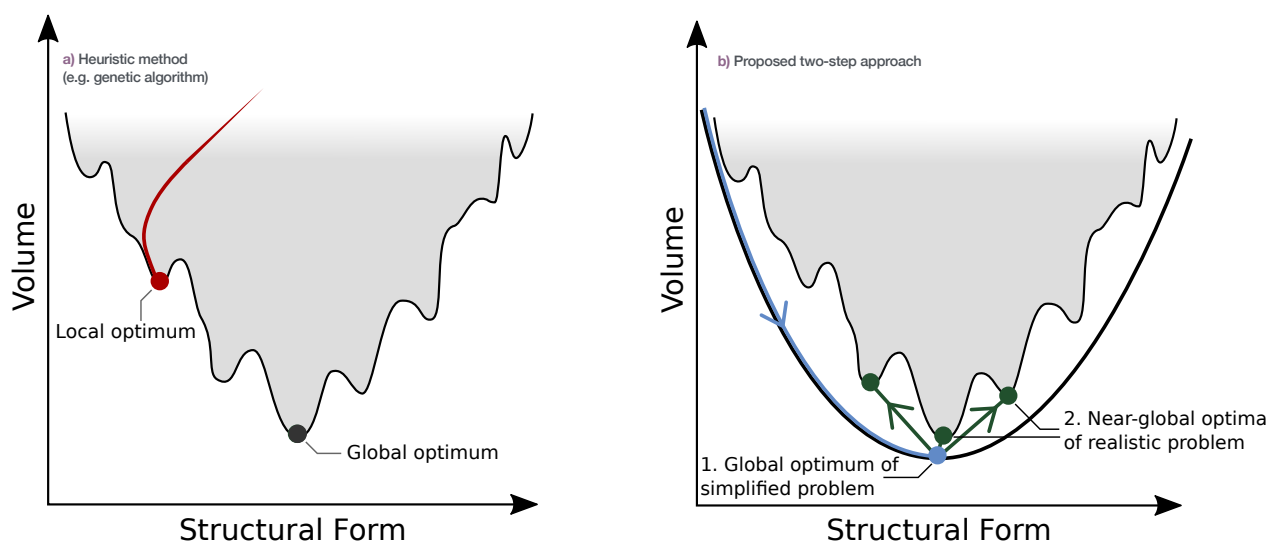


FIGURE 3: Example of trade-off between material usage and structural complexity

### Technical Optimisation-driven conceptual design



**FIGURE 4:** Methods of treating real-world, non-convex design problems

general-purpose finite-element software packages, and are widely used in the aerospace and automotive industries.

However, they are less obviously useful in the design of building structures. This is because a typical building structure comprises a sparse assembly of discrete elements, with a very low associated volume fraction (the proportion of original design domain which is occupied by structure after the optimisation), beyond the normal working range of continuum topology-optimisation routines. **Figure 5** shows an example continuum optimisation result for the present case study, produced using the freely available MATLAB script developed by Sigmund<sup>7</sup>.

For building frames, it is more appropriate to instead work with discrete structural elements, as is proposed here. In this case, numerical layout optimisation employing a

ground structure<sup>8</sup> can be used, in which the design domain is populated with nodes, then interconnected by potential members (**Figure 6**). Mathematical routines can then be used to identify the subset of members which form, for example, the structure which consumes the minimum amount of material.

In the low-resolution example shown in **Fig. 6**, this resembles a deep Warren truss; at higher resolutions, the minimum-weight solution closely resembles a bicycle half-wheel, with a semi-circular compression member and many radial ties. This demonstrates key characteristics of minimum-weight structures: members are axially stressed and bending is eliminated; furthermore, compression and tension members are approximately orthogonal and lie along lines of principal virtual strain.

Here, the optimisation problem considered throughout is to minimise the volume of material consumed, subject to equilibrium and strength constraints, using a plastic multiple-load-case formulation<sup>9</sup>. The mathematical optimisation problem is linear, which ensures that the global optimum for the given problem can be found, and the availability of efficient solvers allows problems with millions of potential members to be solved in seconds on an ordinary desktop computer. A Python script implementing the ground structure-based layout-optimisation method is freely available<sup>10</sup>.

### Case study: basement transfer truss

The case study concerns the conceptual design of a steel transfer truss providing a 50m clear span between the retaining walls on opposite sides of a deep basement (**Fig. 1**). This carries the loads from a five-storey building and a garden at ground level. It also supports a pair of 50m span transverse trusses which apply a substantial load at the bottom of the design domain. The permitted structural depth is 10m, covering three levels below ground-floor level. The intermediate floors can be used to provide out-of-plane bracing against buckling of the truss elements.

This provides an ideal application for optimisation methods. The combination of loading from the transverse trusses and the building above provides a specific and unusual configuration, meaning that the minimum-volume solution may not be familiar or immediately intuitive. Also, because the basement levels through which the truss passes are primarily plant and 'back of house' spaces, there are far fewer constraints on the locations of structural members than in more visible areas of the project – although the approach described is equally applicable to arbitrary design domains. Finally, the structure is to be constructed using fabricated hollow square sections, constructed from S355 steel plate.

The LimitState:FORM software was used to undertake the optimisation study described; this implements the ground structure-based layout-optimisation procedure described in the previous section. The software also allows deflection limits to be specified and irregularly shaped design domains to be defined, as well as permitting some further basic structural analysis internally and allowing export to external software (e.g. Oasys GSA<sup>11</sup>) to enable more detailed analysis and design to be undertaken.

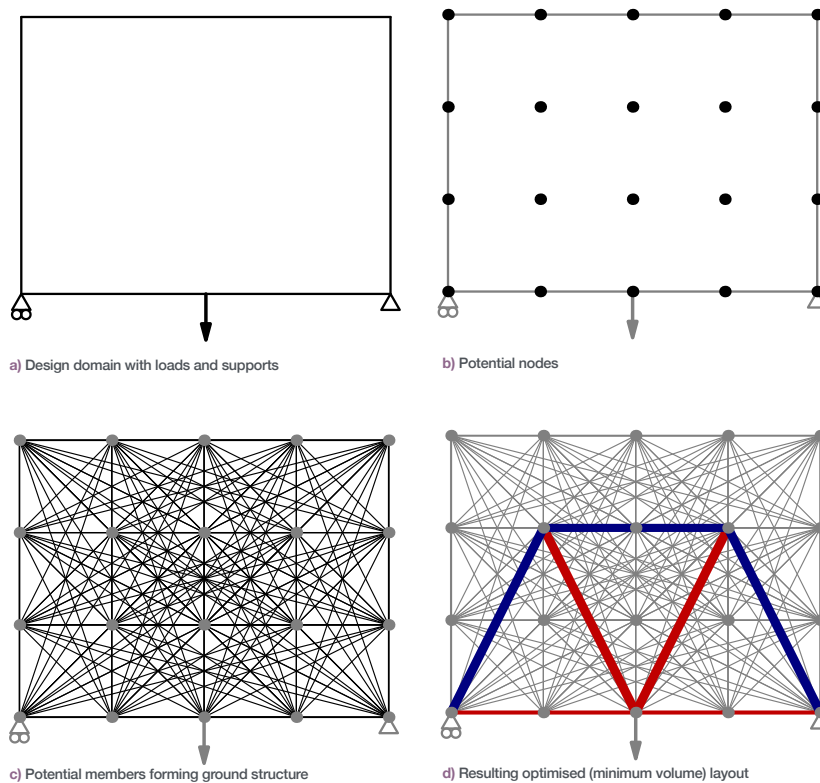
“  
**THE AVAILABILITY OF EFFICIENT SOLVERS ALLOWS PROBLEMS WITH MILLIONS OF POTENTIAL MEMBERS TO BE SOLVED IN SECONDS**



**FIGURE 5:** Basement transfer truss: continuum topology optimisation solution



↓FIGURE 6: Stages in numerical layout-optimisation method

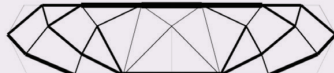
**Step 1: Identification of global optimum for simplified problem**

Numerical ground structure-based layout-optimisation method used to find minimum volume, considering stress and equilibrium constraints

**Output from step 1:****Step 2: Move to identify practical solution, applicable to real-world problem**

Manual rationalisation used to take account of complexity constraints, including:

- reducing number of members/nodes
- removing complex joints (number of, or angles of, connected members)
- standardising cross-sections
- moving towards more common or understandable layouts

**Output from step 2:**

↑FIGURE 7: Proposed two-step process (where step 2 may involve several iterations)

For the purposes of this exploratory study, the permissible strength in compression was reduced to approximate the effect of member buckling; the value of limiting compressive strength varied from 95% of the yield strength in the shortest members, to zero in members unrestrained for over 19m. Both uniform and pattern loading (with the transverse truss on one side only factored favourably) cases were considered, resulting in three load cases in the optimisation problem.

Using layout optimisation, the structure is usually modelled as a pin-jointed truss; therefore, any node which is not supported out-of-plane by a floor plate or support will be unrestrained against buckling. It would be possible to resist this form of buckling by using nodes/joints with moment capacity. However, in order to ensure all designs were comparable, in this study, joints were permitted to lie only on floor levels and up the sides of the design domain.

Although deflections are often critical in the design of long-span structures, for the sake of simplicity, in the present study, only the ultimate limit state was considered initially (i.e. stress constraints). However, the software used can also account for deflections, and deflection-governed problems actually offer greater potential savings with the use of optimisation methods; this is discussed later in the article.

**Interactive rationalisation of structure**

The LimitState:FORM software allows the engineer to interactively edit an optimised solution, e.g. to make it easier to build. This forms the second step of the two-step process outlined in Fig. 4, i.e. moving from the solution of the simplified problem to a design that is a feasible solution for the real-world problem (Figure 7).

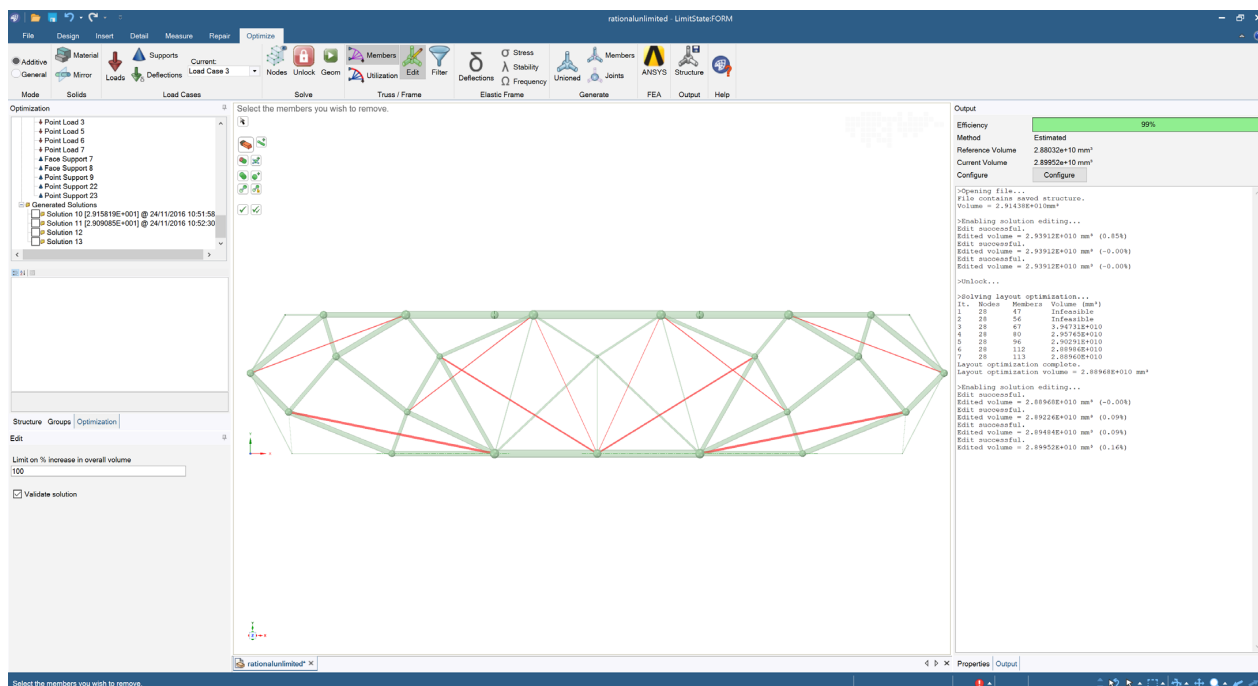
Following a manual edit, a secondary optimisation problem is solved to ensure the edited structure is both stable and as lightweight as possible. This uses the same volume-minimising objective function and equilibrium/stress constraints as the initial problem; however, the reduced ground structure used in the manual editing stage allows simpler structures to be produced. This process can be repeated a number of times if desired.

Each secondary optimisation problem includes linear size optimisation and non-linear geometry optimisation steps, where the latter allows joint positions to be adjusted. Each of these optimisation problems can be solved very quickly, in just a few seconds for the problems shown here, permitting rapid exploration of the solution space.

In the interactive step, the designer can individually choose members to add or remove from the structure (Figure 8), with the influence



## Technical Optimisation-driven conceptual design



of such edits on the required volume of material to form the structure clear at all times. The designer can choose their modifications based on any potential criteria, such as minimum angles between members, total numbers of joints, etc., but is free to break rules if they wish. This allows for a flexible definition of complexity, which may be specific to the problem at hand or vary as the designer reacts to solutions identified by the optimiser.

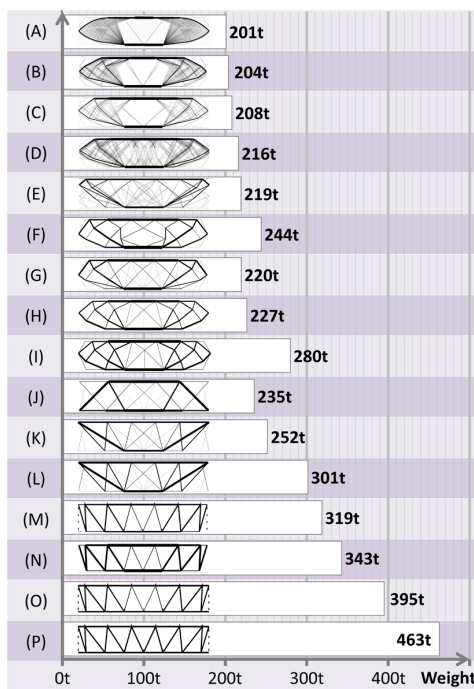
### Results

The results of the proposed approach are presented in **Figure 9** with an increasing number of constraints applied to the structure.

The output of the layout optimisation technique is shown in **Fig. 9a**. These results use a grid of nodes at 0.25m spacing, which results in 32 million possible members. This provides a numerical approximation to the Michell truss for this problem. While this structure would clearly be challenging to construct, it provides a close approximation of the lower-bound reference solution, which uses the minimum possible amount of material to carry the applied load.

In **Fig. 9b**, the nodes are restricted to lie only on the slab lines where lateral restraint is provided; in **Fig. 9c**, the permitted compressive strength is reduced to account for member buckling. At this point, the structure can be said to be physically possible – although unlikely to be buildable using currently available technology. **Fig. 9d** shows the result when the pattern loading cases are considered.

**Fig. 9e** shows the results of automatic rationalisation using the joint-length method<sup>12</sup>. A series of designs following manual rationalisation steps are shown in **Figs. 9f–h**. After this,



↑ **FIGURE 9:** Basement transfer truss: derived concept designs

forms using a limited number of different cross-sections are found; the result with four cross-sections is shown in **Fig. 9i**. This is currently performed as a post-processing step with the node locations and layout remaining unchanged.

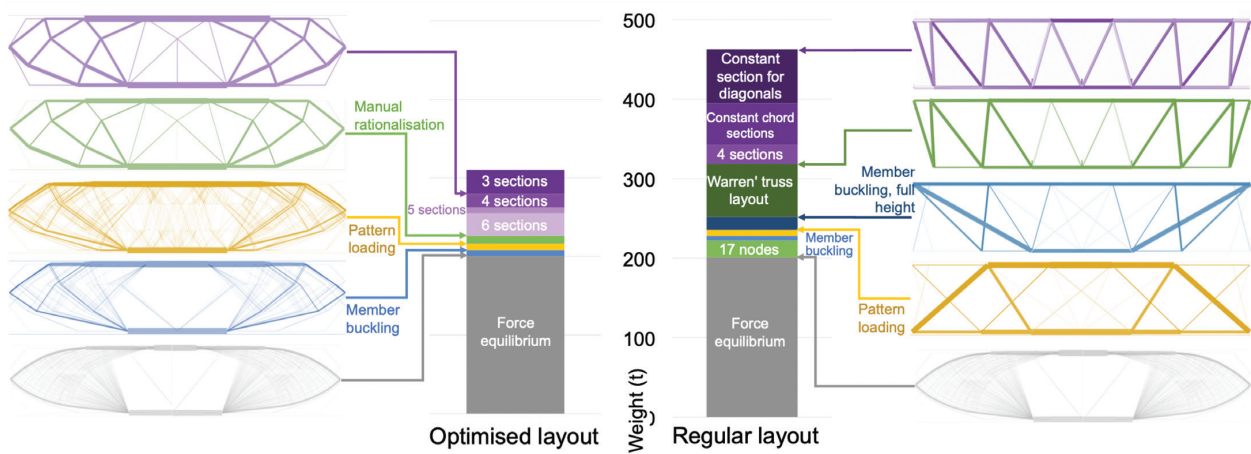
FIGURE 8: User interface – red members manually marked for deletion

**Fig 9j** shows the results of layout optimisation where nodes are only permitted to lie at loading points and at the top and bottom of the supports; **Fig. 9k** shows the case where these members are not restrained from buckling in the out-of-plane direction by the floor plates that they pass through. In **Fig. 9l**, the number of different cross-sections used in this case is limited to four. The manual rationalisation method can be used to force the structure to take on easily recognisable forms, such as the Warren truss like form shown in **Fig. 9m**.

For cases where the number of different cross-sections is further limited, the outcomes are shown in **Figs. 9n–p**, with the design in **Fig. 9n** allowing four cross-sections in any configuration, the design in **Fig. 9o** having equal cross-sections along the top and bottom chords, and the design in **Fig. 9p** also having a single cross-section for all diagonals.

The options presented in **Fig. 9** provide the designer with the information needed to quickly appraise the trade-off between complexity of form and weight of steel required for this particular design problem.

Another way of thinking about the journey through the solution space is to consider the outcome at each step following a given design



↑ **FIGURE 10:** Basement transfer truss: volume increases due to imposed design constraints

decision; this is illustrated in **Figure 10** for the basement transfer truss case study. This means that the engineer can take an informed view on the consequence of each design decision. For example, moving to a familiar Warren-like truss layout leads to a significant increase in the required steel tonnage, even when compared with other solutions with the same number of joints (e.g. the structure shown directly below has the same number of joints).

### Commentary

The proposed method provides a quick way of finding a number of possible design concepts. This allows the impact of different design decisions on the overall structure to be evaluated, informing the decision-making process.

As with all optimisation methods, it is important that the problem passed to the optimiser accurately represents the real demands on the design. For example, a structure optimised only for a uniformly distributed loading may not be able to resist pattern loading cases, if these are not also included in the problem specification at the outset. While post-optimisation checks can identify such issues, better solutions will generally be obtained if these are included in the initial model.

As a relatively long-span structure, deflections are also likely to be important. Therefore, an understanding of how the stiffness of the optimised designs compares to more traditional layouts is of interest. It has been previously demonstrated that for single-load-case problems, the optimal truss layout will be the same irrespective of whether the design is governed by stress limits or deflection limits<sup>13</sup>.

This is based on a minimum-weight truss structure for a single load case being statically determinate and fully stressed. This means that the constituent truss members will be uniformly strained and, therefore, that the internal strain energy will be proportional to the volume of material used. Since the external work done by an applied load is proportional to the deflection

of that load, and as external and internal work must be equal, the layout of the lowest-volume design with stress limits will correspond to the layout with the lowest deflection (when all members are subjected to a given stress).

To move between the stress-based solution and the deflection-based one, all cross-section areas in the solution can be scaled by an appropriate factor. As the minimum volume layout has both the least material and the highest stiffness, it produces the minimum volume result for a given deflection when scaled

tonnage than the optimal value. The volume penalty on the rationalised form also increases slightly; however, it still offers an increased saving compared with the Warren-like truss. This shows that the potential advantages of layout optimisation are further magnified when the design is governed by deflections.

Seeking the minimum volume of material is a clear quantifiable goal for use in the optimisation process. This value can potentially be used as a surrogate for other quantities, such as embodied carbon or material cost, although in reality both of these will also be influenced by other factors, including the complexity of the structure.

In addition to complexity, the manual rationalisation method also allows concerns such as construction sequence and aesthetic considerations to be addressed intuitively. Therefore, it may be necessary to maintain some element of manual control even when more automated methods are used. This also provides the designer with more freedom to explore the design landscape than when using traditional optimisation methods, which output only a single design solution.

The truss-based nature of the layout-optimisation method means that interaction with solutions should be fairly intuitive to anyone familiar with more conventional frame analysis programs. Developing a feel for the best members to add or remove comes with practice. This intuition may be obtained through experience, although it will be informed by knowledge of the fundamental features of minimum-weight structures (such as preferring the use of purely axially loaded members, and noting that tension and compression members should ideally intersect at close to 90° in problems dominated by a single load case).

In our increasingly resource-conscious society, the training of future structural engineers should foster a culture of inquisitiveness around optimisation and a desire to improve the efficiency of our structures, making use of effective software tools to facilitate this.



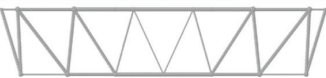




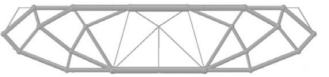




“  
**IT IS IMPORTANT THAT THE PROBLEM PASSED TO THE OPTIMISER ACCURATELY REPRESENTS THE REAL DEMANDS ON THE DESIGN**”

(this can be interpreted as the stiffest structure for a given volume). As rationalisation moves a design further from the optimum, its volume increases and also its stiffness reduces. For deflection-governed designs, these effects compound and cause even greater differences in volume.

However, this is not generally the case in multiple-load-case problems. While this study does have multiple load cases, the fully loaded case dominates the design. The top row of **Figure 11** shows stress-based designs; the Warren-like truss (right) has both a 40% higher volume than the optimised structure (left) and also a 32% higher deflection.

If a range of mid-span deflections is imposed in the fully loaded case (**Fig. 11**), for each of the deflection-governed cases, the Warren-like truss now requires around 64% higher steel

## Technical ■ Optimisation-driven conceptual design

	Optimised (benchmark)	Rationalised	Warren-like truss
No deflection limit (stress based)			
<b>Weight</b>	228t = +0%	<b>Weight</b> 233t = +2.2%	<b>Weight</b> 319t = +40%
<b>Deflection</b>	148mm = +0%	<b>Deflection</b> 164mm = +11%	<b>Deflection</b> 196mm = +32%
Span/500 (100mm)			
<b>Weight</b>	342t = +0%	<b>Weight</b> 359t = +4.9%	<b>Weight</b> 562t = +64.3%
Span/1000 (50mm)			
<b>Weight</b>	679t = +0%	<b>Weight</b> 711t = +4.7%	<b>Weight</b> 1116t = +64.4%
Span/2000 (25mm)			
<b>Weight</b>	1358t = +0%	<b>Weight</b> 1418t = +4.4%	<b>Weight</b> 2227t = +64.0%

### Conclusions

Structural optimisation techniques have the potential to help structural engineering designers to realise significant savings in material usage, embodied carbon and/or cost. While it is important that care is taken in formulating a design problem, and in performing detailed checks on design solutions generated, the case study described here, of a 50m span hotel basement transfer truss, clearly demonstrates the usefulness of optimisation, and that available tools are now becoming sufficiently mature for use in engineering practice at the conceptual design stage.

The two-step optimisation approach presented addresses some of the major concerns that have previously limited uptake of optimisation in practice. Using this approach, a wide range of structural options can be generated, helping the design team to make informed decisions on the balance to be struck between complexity and material efficiency. The results show the potential for significant material savings, even once fabrication constraints are accounted for. This provides an opportunity for designers to explore options derived from highly efficient structural forms, which may not initially be obvious.

### Acknowledgements

This paper is based on a poster prepared by Helen Fairclough that was awarded 1st Prize at the 2017 IStructE Young Researchers' Conference.

The authors acknowledge the financial support of Expedition Engineering and the EPSRC under grant reference EP/N023471/1.

LimitState, a Sheffield University spinout

company cofounded by Matthew Gilbert, Andy Tyas and two other academics, provided access to its LimitState:FORM design optimisation software for the purposes of this study.

FIGURE 11: Basement transfer truss: effect of limiting mid-span deflection

### REFERENCES

- 1) Michell A.G.M. (1904) 'The limits of economy of material in frame-structures', *Philosophical Magazine*, 8 (47), pp. 589–597
- 2) Richardson V. (2017) '3D printing becomes concrete: exploring the structural potential of concrete 3D printing', *The Structural Engineer*, 95 (10), pp. 10–17
- 3) Galjaard S. (2019) *Additive Manufacturing, Design method for critical structural steel elements* [Online] Available at: [www.arup.com/projects/additive-manufacturing](http://www.arup.com/projects/additive-manufacturing) (Accessed: June 2019)
- 4) Prager W. (1978) 'Optimal layout of trusses with finite numbers of joints', *J. Mech. Phys. Solids*, 26 (4), pp. 241–250
- 5) LimitState Ltd (2017) *LimitState:FORM* [Online] Available at: <https://limitstate3d.com/> (Accessed: August 2018)
- 6) Debney P. (2016) 'An introduction to engineering optimisation methods', *The Structural Engineer*, 94 (3), pp. 34–41
- 7) Sigmund O. (2001) 'A 99 line topology optimization code written in Matlab', *Struct. Multidisc. Optim.*, 21 (2), pp. 120–127
- 8) Dorn W.S., Gomory R.E. and Greenberg H.J. (1964) 'Automatic design of optimal structures', *Journal de Mecanique*, 3, pp. 25–52
- 9) Pritchard T.J., Gilbert M. and Tyas A. (2005) 'Plastic layout optimization of large-scale frameworks subject to multiple load cases, member self-weight and with joint length penalties', *Proc. 6th World Congress of Structural and Multidisciplinary Optimization*, Rio de Janeiro, Brazil
- 10) He L., Gilbert M. and Song X. (2019) 'A Python script for adaptive layout optimization of trusses', *Struct. Multidisc. Optim.*, 60 (2), pp. 835–847
- 11) Oasys (2019) *GSA – Structural Design & Analysis Software* [Online] Available at: [www.oasys-software.com/products/structural/gsa/](http://www.oasys-software.com/products/structural/gsa/) (Accessed: September 2019)
- 12) Parkes E.W. (1975) 'Joints in optimum frameworks', *Int. J. Solid Struct.*, 11 (9), pp. 1017–1022
- 13) Nagtegaal J.C. and Prager W. (1973) 'Optimal layout of a truss for alternative loads', *Int. J. Mech. Sci.*, 15 (7), pp. 583–592

HAVE  
YOUR  
SAY



tse@istructe.org



@IStructE

#TheStructuralEngineer

### E.3 Optimization-driven conceptual design of long span bridges

This section contains a paper prepared for the symposium of the International Association of Bridge and Structural Engineers. This paper was presented to an audience which consisting of both practitioners and academics within the fields of bridge design.

This paper describes an initial study into the feasibility of including novel support types within the layout optimization formulation. However, unlike the study of Chapter 5, here the supports may carry a fixed horizontal load, which is not affected by the value of the vertical reaction. This is a simpler, albeit less realistic approach. The approach is also combined with the distributed self-weight method described in chapter 4.

---

<sup>†</sup> Fairclough, H., Gilbert, M., Tyas, A., Pichugin, A., (2018) Optimization-driven conceptual design of long span bridges. In *IABSE symposium, Nantes 2018 Tomorrow's Megastructures, report*, (pp. S13-67 - S13-74).



40th IABSE Symposium, 19-21 September 2018, Nantes, France.  
Tomorrow's Megastructures

## Optimization-driven Conceptual Design of Long Span Bridges

Helen Fairclough, Matthew Gilbert, Andrew Tyas

*University of Sheffield, United Kingdom*

Aleksey Pichugin

*Brunel University London, United Kingdom*

**Contact:** [m.gilbert@sheffield.ac.uk](mailto:m.gilbert@sheffield.ac.uk)

### Abstract

This paper explores the potential for structural optimization to be used at the conceptual design stage for long span bridge structures. A discrete numerical layout optimization procedure is used to automatically identify the most structurally efficient forms for prescribed design problems. The study builds on previous work which identified designs ranging from cable stayed to tied arch bridge forms, depending on the specified limiting tensile/compressive stress ratio. Here this work is extended to encompass a wider range of support types and the impact of self-weight is now considered to allow very long spans to be treated, beyond what is realisable today. To permit comparison with traditional bridge forms an idealized 3-span bridge design problem is considered. It is found that optimized forms that consume considerably less material than traditional bridge forms are identified using the optimization procedure described. This theoretically extends the distance that can be spanned when using a given material, notwithstanding that these forms are likely to be challenging to construct using current practices.

**Keywords:** conceptual design; optimization; long span bridges; layout optimization; topology optimization; cable stayed; suspension; tied arch; self-weight.

### 1 Introduction

The choice of form has far reaching impacts on all subsequent aspects of the design of a bridge. When large spans are required, cable-supported forms have been found to be more efficient than arches and cantilever truss forms, in large part due to the high tensile resistance of cables in comparison with compressive elements. In turn cable supported structures come in a wide range of forms, with to date the traditional suspension bridge form finding favour for the longest spans.

As spans increase, the advantages gained from choosing a more materially efficient form are magnified, as are the penalties for choosing an inefficient form, due to the need for the structure to carry its own weight. For example, in the main 1,991m span of the Akashi Kaikyo bridge, the cable superstructure has a weight half that of the deck;

for the proposed 3,300m span for the Strait of Messina crossing bridge, the proposed design has a cable weight of 1.5 times the weight of the deck [1].

At extreme spans, the ratio of superstructure weight to imposed load rises steeply and a given form eventually becomes impossible to realise in practice. The less materially efficient the form, the shorter the span which can be achieved. In the case of the suspension bridge in steel, the max. span has been suggested to be 5-7km [2].

This poses a question: what are the most materially efficient forms when very long spans are required? To help answer this question various mathematical techniques can potentially be applied, in particular the so-called layout optimization technique [3,4].



40th IABSE Symposium, 19-21 September 2018, Nantes, France.  
Tomorrow's Megastructures

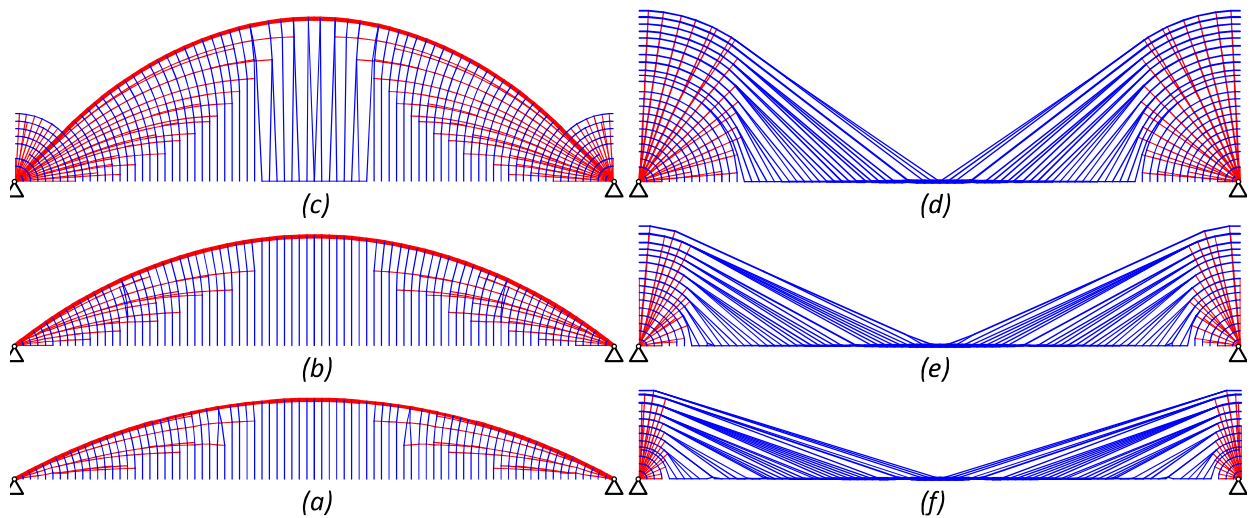


Figure 1 Optimized forms for idealized short multi-span bridge structures for different limiting compressive and tensile stresses,  $\sigma_C$  and  $\sigma_T$ : (a)  $\sigma_C = 10\sigma_T$ , (b)  $\sigma_C = 5\sigma_T$ , (c)  $\sigma_C = 2\sigma_T$ , (d)  $2\sigma_C = \sigma_T$ , (e)  $5\sigma_C = \sigma_T$ , (f)  $10\sigma_C = \sigma_T$ . After [6].

Layout optimization involves finding the arrangement of structural elements requiring the minimum volume of material for a given set of loads and supports. Since its fundamental building blocks are structural members, which likely occupy only a tiny proportion of the design domain in the optimal solution, it is more immediately useful for the conceptual design of bridges than the more widely known ‘topology optimization’ technique [5].

Considering idealized multi-span bridge forms, Pichugin et al [6] used layout optimization to show that a family of bridge forms, from arch to cable-stayed, could be generated by changing the ratio of limiting tensile to compressive stress (Figure 1). Interestingly, for cases where the limiting tensile stress is much higher than the limiting compressive stress, cable stayed forms with multiple split pylons radiating out from the supports were generated; in the interests of practicality these could very efficiently be replaced by two or three pylons, in contrast to the single vertical pylons usually employed in practice. Also, suspension bridge forms were not found to be optimal for the assumptions made.

However, the bridge models considered in [6] were highly idealized. For example, although the forms considered were notionally multi-span, only a single load case was considered - which is only justifiable in practice if traffic loads are very small

in comparison with self-weight loads (i.e. assuming that unbalanced traffic loads in adjacent spans do not significantly influence the generated design). Also self-weight effects were neglected.

In this contribution the optimized cable-supported bridge forms considered in [6] are revisited, though now considering more realistic boundary conditions and taking account of self-weight effects, with a view to assessing the viability of layout optimization being used as a conceptual design tool for bridge designers. Note that although many of the optimized forms are complex, these can potentially be simplified to render them more practical, though this post-processing step is beyond the scope of the present contribution.

The paper is organized as follows: first the layout optimization method is introduced. Then methods of modelling self-weight are considered and the means by which alternative boundary conditions can be treated are discussed. The influence of alternative boundary conditions on the optimized forms are initially explored for short span bridges, comparing these with traditional cable stayed and suspension layouts. Finally, long spans are considered, including self-weight and alternative boundary conditions, and conclusions are drawn.

40th IABSE Symposium, 19-21 September 2018, Nantes, France.  
Tomorrow's Megastructures

## 2 Layout optimization

Numerical layout optimization involves identifying the most efficient structure to carry prescribed loads. This entails populating a prescribed design domain with nodes, which are interconnected by members to form a 'ground structure' comprising every possible member which could feasibly form part of the solution. When a fine nodal discretization is used a close approximation of the theoretical optimum solution can be obtained. (Note that the vast majority of members in the 'ground structure' will have an area of zero.)

In the formulation force equilibrium constraints are enforced at each node in each load case, with additional constraints set up to ensure that the area of each member is large enough to support the forces in that member (for a specified limiting stress, which can be different in tension and compression). The objective of the optimization is to minimize the total volume of all members, calculated by summing the cross sectional area of each member multiplied by its length. Steps in the optimization procedure are shown in Figure 2.

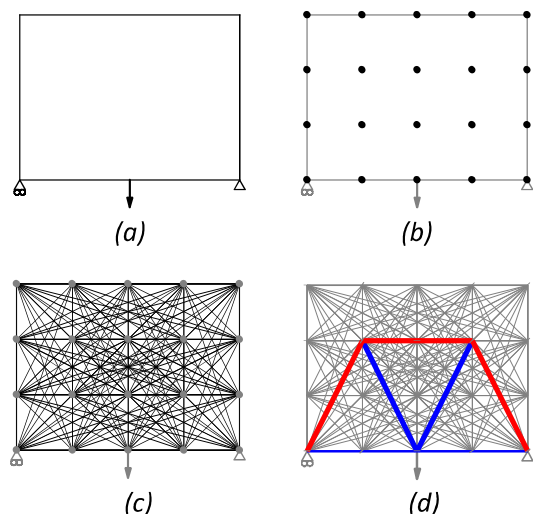


Figure 2. Steps in the layout optimization procedure: (a) details of example problem, (b) nodes distributed across the design domain, (c) interconnecting members forming the 'ground structure', (d) members forming the optimal structure, identified via linear optimization.

Finding the cross-sectional area values is a linear optimization problem, which is therefore very quick to solve, especially if the adaptive 'member adding' method of Gilbert and Tyas [4] is employed, and is guaranteed to find the global optimum for the given nodal discretization.

## 3 Modelling self-weight & foundations

Standard layout optimization does not account for the influence of structural self-weight. This quickly becomes non-conservative at even moderate spans. This can be addressed as follows.

### 3.1 Lumped mass self-weight method

In much of the existing literature, self-weight is accounted for by adding an additional term based on the area of each member [7]. Half of the weight ( $\rho g A l$ ) of each member of density  $\rho$ , length  $l$  and cross-sectional area  $A$  is added to the node at each of its ends, as shown in Figure 3b, where  $g$  is the acceleration due to gravity.

However, this is non-conservative because the area of the member is not increased to enable it to carry the bending moment imposed by its own self weight. For dense materials or long spans this leads the optimizer to favour solutions which include very long members, further compounding the error.

However, for short to medium spans, this method can provide an acceptable approximation, and it can be applied to multiple load case problems.

### 3.2 Distributed self-weight method

Recently the present authors have developed a new method for incorporating self-weight continuously throughout the structure. This method involves replacing each straight member in the ground structure with an equally stressed catenary, i.e. an arch or sagging cable depending on whether the member is in compression or tension. This has a higher volume than the equivalent straight member, and also imposes an additional downward force on the end nodes, see Figure 3c; for more details see [8]. This method is accurate for all spans, although can only be used for single load case problems.

40th IABSE Symposium, 19-21 September 2018, Nantes, France.  
Tomorrow's Megastructures

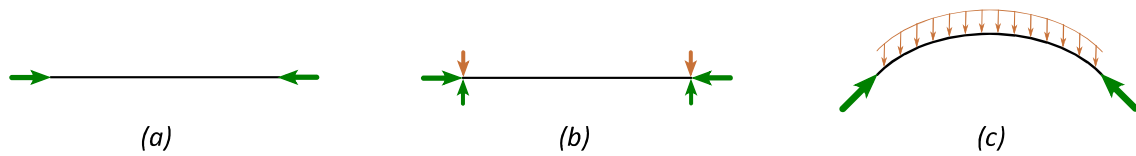


Figure 3. Methods of incorporating self-weight; (a) self-weight ignored (potentially very non-conservative), (b) lumped mass self-weight (non-conservative), (c) distributed self-weight method (accurate).

### 3.3 Foundations

In structural layout optimization, boundary conditions are applied to nodes in the 'ground structure'. Foundations are usually modelled as fixed pin or pin/roller type supports; herein the term pin/roller will be taken to mean vertical support with no restraint horizontally.

In reality, the ground conditions and chosen construction type employed for the foundation will impose limits on the forces which can be sustained. Horizontal forces in particular can have a significant influence on the cost and complexity of a foundation design.

To address this, the classical layout optimization formulation can be modified to explicitly include reaction forces as variables. This allows limits to be placed on their values. This potentially allows a wider range of optimum structures to be found than those generated with standard support types.

## 4 Idealized optimized bridge designs

### 4.1 Short span bridges

The optimum form of an idealized bridge type structure is first considered, initially with self-weight effects ignored. Thus the forms obtained are relevant for short span bridges. The bridge consists of a main span of length  $L$ , and two side spans each with length  $L/2$ . The maximum height of the structure is also  $L/2$ . Suppose the structure is constructed from material with limiting stress of 1500MPa in tension and 150MPa in compression. The structure is modelled with a uniform imposed load (over the whole design domain) of  $\omega$  per unit length (i.e. for sake of simplicity uneven traffic loadings are not considered).

Initially, the boundary conditions are modelled as fixed pin supports at both the potential anchorage

points and the pylon bases; the resulting structure for this scenario is shown in Figure 4a.

It can be seen that this form resembles a cable stayed structure, although the pylons are split, like the forms identified in [6]. i.e. the pylons are not vertical as are commonly found in practice. Volumes of the structures herein will be normalized relative to the volume of this structure, taken as  $V_0$ .

Note that the horizontal forces in the deck are carried exclusively in tension and require a very large horizontal support force of  $1.02 \omega L$  in each anchorage. The horizontal forces in the pylon base supports are zero, and this form is therefore unchanged if the supports here are assumed to be pin/roller supports.

To eliminate the large reaction force at the anchorages, the optimization can be re-run with

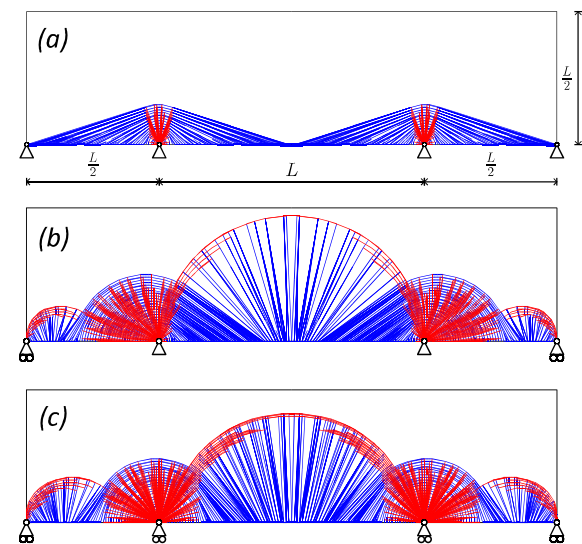


Figure 4. Idealized optimized short span bridge forms generated using standard support types.

the edge supports modelled as roller supports. The resulting structure is shown in Figure 4b, comprising an arch structure in the central span,



40th IABSE Symposium, 19-21 September 2018, Nantes, France.  
Tomorrow's Megastructures

with edge spans incorporating arched elements and fan type nets to give continuity between the spans. This structure imposes a horizontal force of  $0.36\omega L$  on each of the pylon support points.

Whilst this horizontal load is much less than the previous design, it may still be undesirable to transmit. Therefore, Figure 4c shows the resulting structure when all supports are idealized as roller pins.

However, the reduced support requirements of the structures shown in Figure 4b,c come at a significant cost; as well issues of practicality the normalized volume of material required to form the structures increases to  $1.50V_0$  and  $1.59V_0$  in the last two cases respectively. It is thus of interest to seek structures where the horizontal reaction forces are limited to a range of intermediate values. These solutions should permit structural and foundation costs to be balanced.

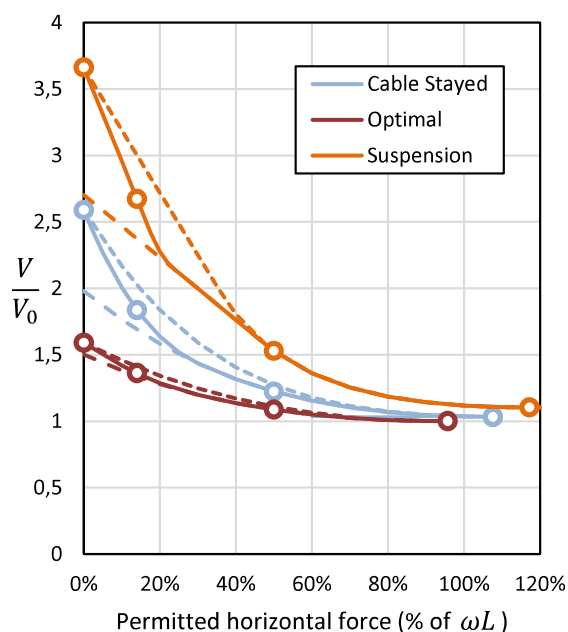


Figure 5. Short span bridge forms: volumes for optimized, cable stayed and suspension forms. Dotted line = pin/roller pylon base; dash-dot line = pinned pylon base; solid line = pylon base capable of resisting same load as anchorage. Marked points correspond to structures shown in Figure 6.

#### 4.2 Intermediate foundation conditions

The amount of horizontal force that can be carried by the anchorage foundation will now be varied. For the foundation at the base of the pylon, three

cases are considered: pinned, pin/roller and one where this may carry a horizontal force with the same limit as the anchorage support.

The normalized volumes for the various horizontal reactions are shown in Figure 5. The volume reduces quickly at lower horizontal forces, suggesting that any associated additional foundation cost to carry a part of the horizontal force may be worthwhile, whilst it may be less so to design supports to carry the whole of the horizontal force.

Forms for a range of representative bridge structures are shown in Figure 6a, with the associated required horizontal support forces indicated. These show a family of designs which range from arch forms associated with roller supports to cable stayed forms associated with pinned supports.

#### 4.3 Comparison to existing forms

The optimized forms are now compared to a range of traditional layouts. To ensure that the latter are directly comparable, solutions were obtained by artificially constraining the optimization problem.

To generate the cable stayed bridge designs, nodes were restricted to lie only directly above the pylon supports, or on the deck. For the pin/roller support case this generates a harp style structure, with a span:dip ratio of 2. For the pinned support case the stays are no longer evenly spaced and the span to dip ratio increases to 6.6. These and forms with intermediate support conditions are shown in Figure 6b.

To generate the suspension bridge designs, compression was only permitted in the pylon and, for the self-anchored cases, in the deck spanning between supports. The resulting forms are shown in Figure 6c. When high horizontal support forces are available, ground anchored suspension bridge forms are preferred, with span to dip ratio up to 9.4. When less horizontal restraint is available, self-anchored suspension bridges are produced, with span:dip ratios as low as 2.8.

40th IABSE Symposium, 19-21 September 2018, Nantes, France.  
Tomorrow's Megastructures

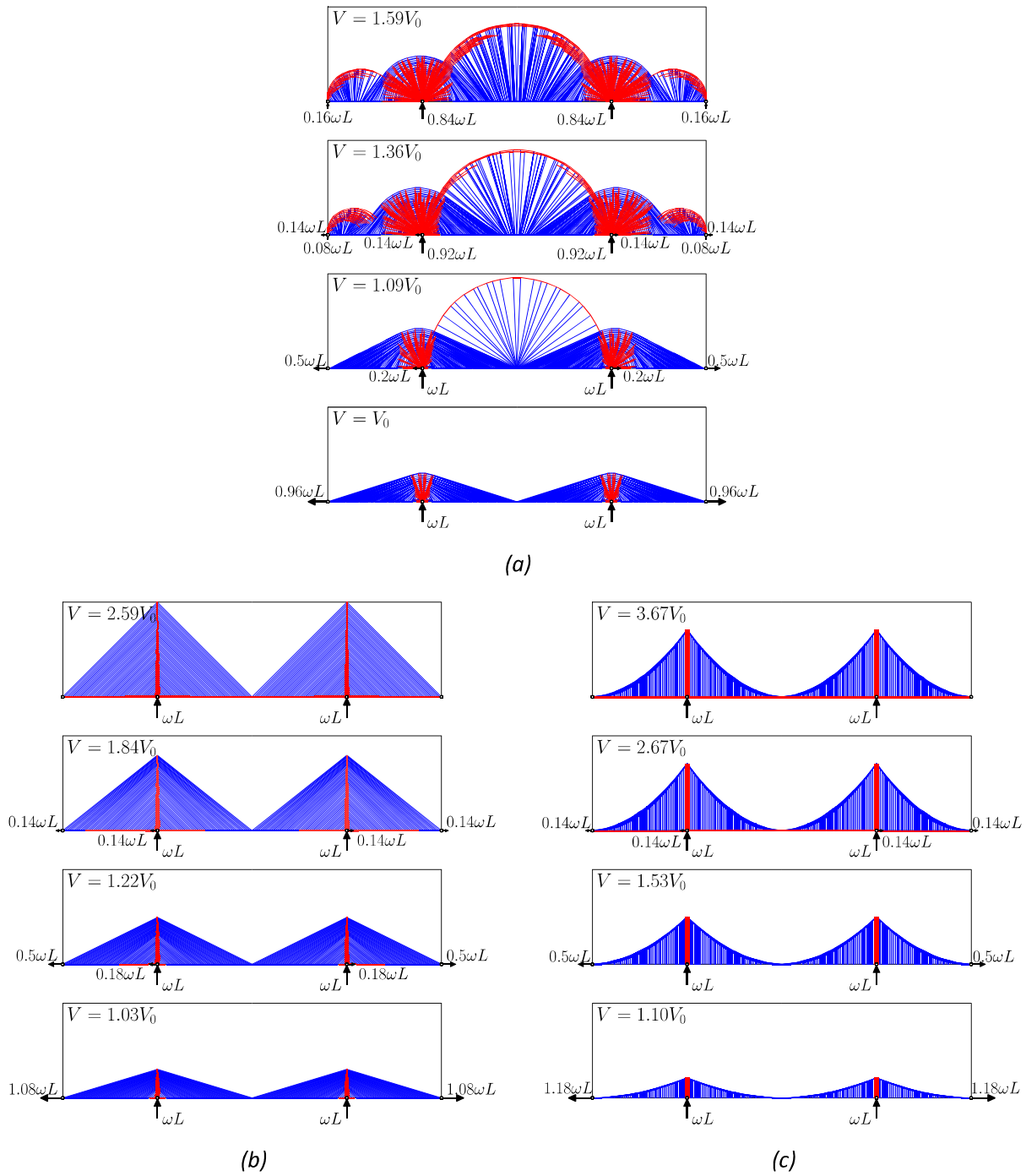


Figure 6. Short span bridge forms: (a) idealized optimized, (b) cable stayed, (c) suspension. Maximum permitted horizontal reaction forces at each support: 0,  $0.14\omega L$ ,  $0.5\omega L$  and unlimited.

40th IABSE Symposium, 19-21 September 2018, Nantes, France.  
Tomorrow's Megastructures

#### 4.4 Long span bridges

For long span bridges it is necessary to explicitly consider the impact of self-weight on the optimal form. Here self-weight is modelled using the distributed method described in Section 3.2, assuming steel is used (unit weight taken as  $80\text{kN/m}^3$ ). In the interests of brevity only the maximum horizontal force =  $0.5\omega L$  case is described here. The resulting volumes, normalized by span, for the previously considered forms are shown in Figure 7.

It is evident that the forms identified as being less optimal at short spans incur an increasing penalty as spans increase. For example, for the maximum horizontal force =  $0.5\omega L$  case the suspension form consumes 40% more material than the optimal form for short spans, but with 5km and 10km spans this increases to 76% and 172% respectively.

The forms of each structure type are shown for spans of 5km and 10km in Figure 8. The optimized form now has an asymmetrical form above the intermediate supports, allowing some of the self-weight to act as a counterbalance to the main span. Also, the large central arch is no longer present.

The cable stayed form is largely unchanged, except that the stays now exhibit cable sag which

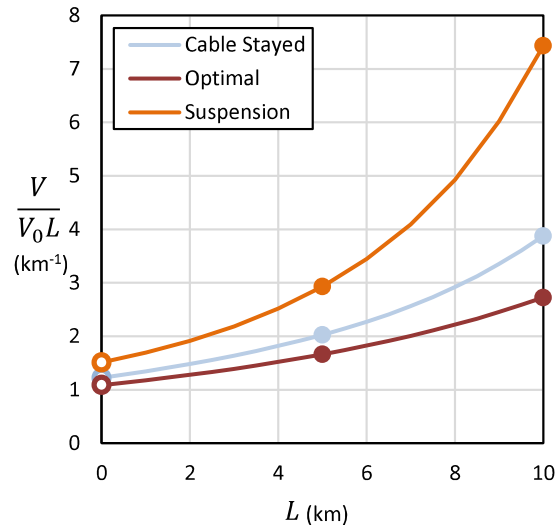


Figure 7. Structural volume vs span for bridges with foundations capable of resisting a maximum horizontal force of  $0.5\omega L$ . The associated forms for the solid data points are shown in Figure 8.

causes the optimal pylon height to increase.

The suspension form is also largely similar to before, the pylon cross section now varying with height as each section must now carry the weight of the pylon above. The pylon also has an increased height. Additionally, the shape of the main cable begins to transition from a parabolic curve to a catenary one.

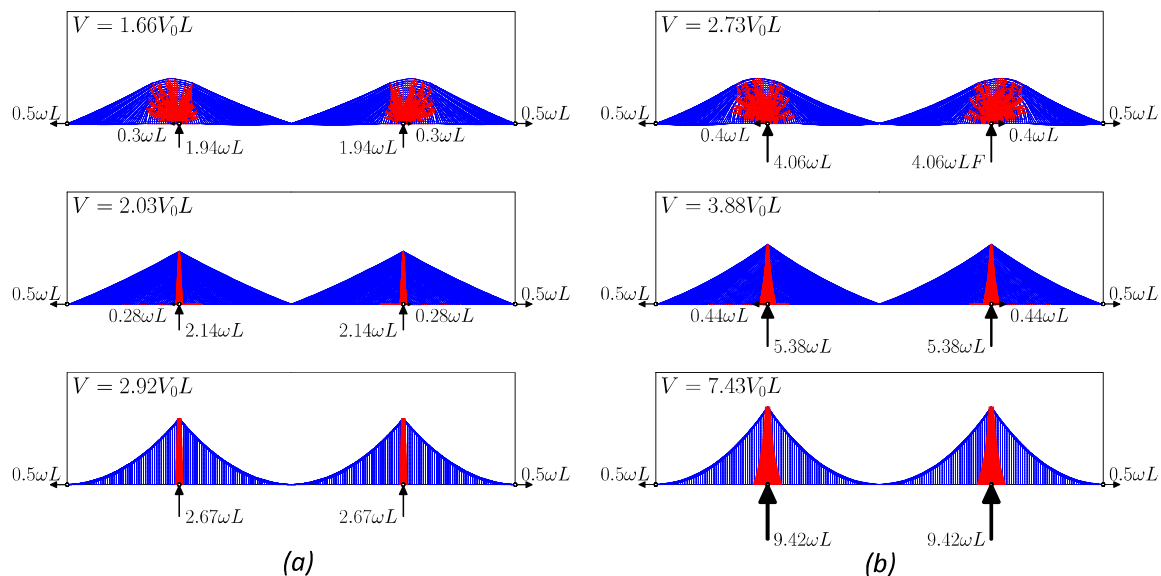


Figure 8. Long span idealized optimized, cable stayed and suspension forms for spans of: (a) 5km, (b) 10km. Maximum horizontal reaction force taken as  $0.5\omega L$  at each support.

40th IABSE Symposium, 19-21 September 2018, Nantes, France.  
Tomorrow's Megastructures

## 5 Concluding remarks

This paper has briefly explored the potential for structural layout optimization to be used at the conceptual design stage for short and long span bridge structures.

Although it can justifiably be argued that the idealizations made for the purposes of the present study render the specific outcomes of primarily academic rather than practical interest (e.g. thermal effects, multiple load cases, dynamic effects and aerodynamic considerations have not been considered), the study has provided a clear indication of the potential usefulness of layout optimization in the field of bridge engineering.

For example, the present study has clearly illustrated the strong influence of boundary conditions on the optimal form and associated volume of material required to form a bridge. More specifically the study has shown that standard support types may not produce the most effective design solutions if the costs of both the superstructure and foundations are taken into account.

A family of new forms which lie between cable stayed and tied arch type structures has been generated for intermediate support restraint scenarios, potentially allowing designers to identify 'best compromise' solutions. Even more realistic models of foundation behaviour could potentially be used, bringing further benefits.

It has also been shown that the optimized bridge forms identified in the study consume significantly less material than corresponding traditional forms (e.g. cable stayed and suspension bridge forms). This is particularly true when long spans are considered. Indeed, if very long spans are desired, such optimized forms may be the only choice for a given material.

Finally, in the interests of practicality the complex spoke-pylon arrangements present above the supports in the optimized bridge forms identified in the study could easily be replaced by two or three split pylons, with little loss of structural efficiency. However, long span bridges employing split pylons would nevertheless likely be challenging to construct using current practices.

## 6 Acknowledgements

The financial support of EPSRC under grant reference EP/N023471/1 and Expedition Engineering is gratefully acknowledged. Also thanks to Ian Firth of COWI for his comments on a draft of the paper and Linwei He for providing a coloured version of Figure 1.

## References

- [1] Brancaleoni, F., Diana, G., Fiammenghi, G., Jamiolkowski, M., Marconi, M., and Vullo, E. Messina bridge - Design, concept, from early days to present. *Taller, Longer, Lighter - Special session on the Messina Bridge* (pp. 15 - 22). London: IABSE – IASS; 2011.
- [2] Meier, U. Proposal for a carbon fibre reinforced composite bridge across the Strait of Gibraltar at its narrowest site. *Proceedings of the Institution of Mechanical Engineers*. 1987; **201**(B2): 73 - 78.
- [3] Dorn, W. S., Gomory, R. E., and Greenberg, H. J. Automatic design of optimal structures. *J. de Mechnique*. 1964; **3**(1): 25-52.
- [4] Gilbert, M., and Tyas, A. Layout Optimization of large scale pin jointed frames. *Engineering Computations*. 2003; **20**(8): 1044-1064.
- [5] Bendsoe, M. P., and Sigmund, O. *Topology Optimization: theory, methods and applications*. Springer Science and Business Media; 2003.
- [6] Pichugin, A. V., Tyas, A., Gilbert, M., and He, L. Optimum structure for a uniform load over multiple spans. *Structural and Multidiciplinary Optimization*. 2015; **52**(6): 1041-1050.
- [7] Pritchard, T. J., Gilbert, M., and Tyas, A. Plastic layout optimization of large-scale frameworks subject to multiple load cases, member self weight and with joint length penalties. *6th World Congress of Structural and Multidisciplinary Optimization*; 2005.
- [8] Fairclough, H., Gilbert, M., Tyas, A., and Pichugin, A., *Self Weight in Layout Optimization, CMD group report CMD/17-1, University of Sheffield, UK*; 2017.

## E.4 Automatic identification of structurally efficient layouts with limited complexity

The material in this section was prepared for the Young Researchers' Conference 2018, hosted by the Institute of Structural Engineers. This conference brings together PhD researchers from all areas of structural engineering research. This section contains the submitted abstract, and the poster which was presented at the conference.

This section primarily concerns the case study considered in Section 6.3, and focuses on the comparison between different measures of complexity.

---

<sup>†</sup> Fairclough, H., (2018) Automatic Identification of structurally efficient layouts for building structures. In *Proceedings of the 20th Young Researchers Conference*. The Institute of Structural Engineers, (pp. 46-47).

## Automatic identification of structurally efficient layouts for building structures

**Helen Fairclough**  
University of Sheffield

The problem of finding a suitable arrangement of elements to form a building is fundamental to structural design. Increasing resource scarcity drives us to search for structures which can provide the required levels of strength and comfort whilst consuming as little material as possible. This is known as the problem of topology or layout optimisation. However, the resulting optimal structural forms can be complex and here the focus is on identifying practical, near-optimal, forms.

### Background

Various well established methods allow us to find the absolute minimum weight structure capable of transmitting a given set (or sets) of loads to supports. Analytical methods, such as those developed by Michell (1904), allow exact solutions to be found for simple problems, such as the cantilever analysed by Chan (1960). Later, numerical and computational methods such as those derived by Dorn (1964), and Bendsøe (1989), allowed solutions for more complex scenarios to be approximated using discrete (truss based) or continuous models respectively.

However, whichever method is used to find a minimum weight structure, we find that they display similar, and generally undesirable, characteristics. In all but the most trivial cases, the theoretical solution will consist of a 'truss-like continuum': this is a structure which is made up of an infinite number of infinitesimally thin and short bars. Clearly this is impractical for real world construction.

There is still value in identifying these minimum volume structures however. Prager (1974) has shown that trusses with a fairly low number of bars/joints can, when arranged correctly, require an increase of only a few percent over the minimum possible volume. However, manual methods such as his cannot easily be applied to more complex problems such as those found in real world design situations.

### Project objectives and goals

This project seeks to use numerical and computational methods to produce structures which can feasibly be constructed using current (or near-future) methods, whilst still retaining significant material savings.

### Description of method and results

In this study a ground structure layout optimisation will be employed, similar to that described by Pritchard et al. (2005). This method allows for easy conceptual interpretation of the solutions into a series of truss members connected at joints. It is also a convex optimisation problem, which eliminates the risk of falling into a local optimum.

In order to reduce the complexity of the structures, the integer programming optimisation method will be used. This allows limits or penalties to be set for a range of key real-world constraints, such as:

- Number of members,
- Number of joints,
- Complexity of joints (i.e. number of members which meet at a given joint),
- Minimum cross-sectional area.

In this study, we will apply these constraints to a case study derived from a real world project, chosen in collaboration with engineers from Expedition Engineering. Our case study is a 21m roof truss, subjected to two load cases, a uniform and a pattern load case, the loading is applied via secondary beams at 6m spacing. The original optimised design for the problem is shown in Fig 1; this is also the design corresponding to the uppermost (lowest volume/most joints) point in Fig 2.

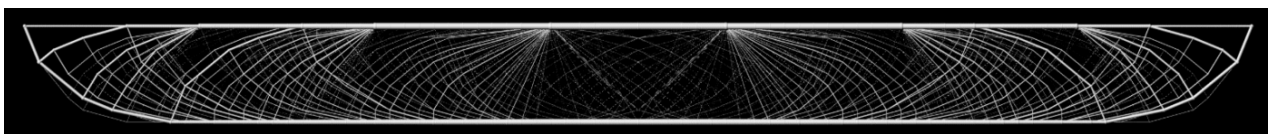


**Fig 2** Results from layout optimisation of the case study problem with high complexity permitted.

Each type of constraint will produce a family of possible structures, providing different trade-offs between the complexity of the structure and the volume of material required. This is valuable to a designer as it allows them to make an informed decision on the implication of various design decisions. The options can be shown in the form of a Pareto front, a common presentation method in the field of multi-objective optimisation. This involves plotting the best solutions found against two objectives (here: volume and complexity), showing the desired edge of the feasible region. An example of a Pareto front based on the number of nodes is shown in Fig 2.

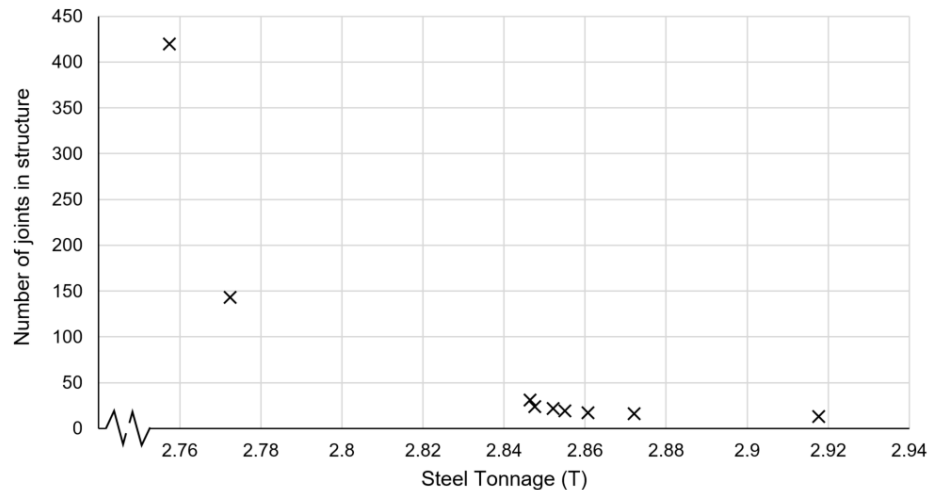


**Fig 2** A range of possible designs for the case study of varying complexity.

### Potential for application of results

The method is capable of handling both 2D and 3D problem and multiple load cases. It has potential for application to a wide variety of structure types. Initial studies show that the greatest savings are in spanning structures, as opposed to tower type structures. Case studies so far have included transfer structures, roofs and bridges.

### References

- Bendsøe, M. P. (1989). Optimal shape design as a material distribution problem, *Structural Optimization* 1:4, 193-202.
- Chan, A. S. L. (1960). *The design of Michell optimum structures*, College of Aeronautics Cranfield.
- Dorn, W. S. (1964). Automatic design of optimal structures, *Journal de Mecanique*, 3, 25-52.
- Michell, A. G. M. (1904). LVIII. The limits of economy of material in frame-structures, *Philosophical Magazine*, 8:47, 589-597.
- Prager, W. (1974). A note on discretized Michell structures. *Computer Methods in Applied Mechanics and Engineering*, 3:3, 349-355.
- Pritchard, T. J., Gilbert, M., & Tyas, A. (2005). Plastic layout optimization of large-scale frameworks subject to multiple load cases, member self-weight and with joint length penalties, In *6th World Congress of Structural and Multidisciplinary Optimization*, Rio de Janeiro.

### Funding body

Engineering and Physical Science Research Council (EPSRC) and Expedition Engineering.

### Further information

Helen Fairclough (E: [hefairclough1@sheffield.ac.uk](mailto:hefairclough1@sheffield.ac.uk)) or  
 Professor Matthew Gilbert (E: [m.gilbert@sheffield.ac.uk](mailto:m.gilbert@sheffield.ac.uk))  
<http://www.build-opt.org/>

### Collaborators

This research forms part of a larger EPSRC funded project involving the Universities of Bath, Edinburgh & Sheffield and Expedition Engineering, Aecom, Arup, Buro Happold, IStructE, Ramboll and the SCI.





## Automatic identification of structurally efficient layouts with limited complexity

Helen Fairclough, Department of Civil and Structural Engineering, Sheffield



### Introduction

Various well established methods allow us to find the absolute minimum weight structure capable of transmitting a given set (or sets) of loads to supports. However, these structures are too complex to be suitable for practical usage.

Here, we seek to identify structural forms which are as **lightweight** as possible, whilst additionally requiring that they are **simple enough** that they could be constructed with current or emerging technologies.

Previous work in this area has generally been quite ad hoc or required significant manual intervention. Our method uses Integer Programming, which guarantees global optimality and does not require any **user input** once the problem is set up.

### What is Complexity?

The complexity of a given structural scheme is difficult to precisely define, and may vary by project. Generally, the key considerations are anything which impacts on the cost or speed of the construction. A range of **quantifiable characteristics** can be used to **approximate** the complexity, for example:

- Number of joints
- Number of members
- Number of members meeting at a joint
- Angles between members meeting
- Minimum cross-section area
- Number of different cross-section areas
- Number of different member lengths

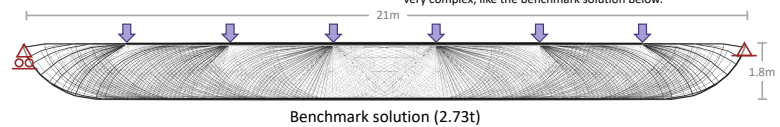
It is possible to conceive structures which are simple by some measures, but complex by others. However, we hope that limiting any of these characteristics will produce a reduction in complexity. Here we compare two measures, number of joints and minimum cross-section area to see if limiting one also affects the other.

### Example Problem

Our example problem consists of a transfer truss, with;

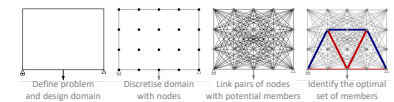
- Span 21m
- Maximum 1.8m depth.
- Loading from 6 evenly spaced beams above
- Simply supported at the ends of the top chord
- S355 steel, (with 75% reduction in compressive strength assumed to account for buckling)

For this loading, the theoretical minimum weight solution would be a tied arch. However, the design domain here is rather restricted and therefore the optimal form (below) is more compact, although the ends of the domain do still show a curved reduction in depth.



### Layout Optimisation

Layout optimisation is a **numerical method** which seeks to identify the minimum weight structure for a given problem. The steps required are illustrated here:

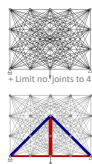


As this is a linear programming problem, high resolutions can be **computed relatively quickly**. These produce good at approximations for volumes and forms of minimum weight structures. These forms are very complex, like the benchmark solution below.

### Integer Programming

Integer programming can extend the layout optimisation method to allow us to **impose limits or penalties** on our quantifiable measures of complexity. It is **very computationally expensive** and can only be used on low resolution problems (<50 nodes).

The different measures have different levels of difficulty, with limiting the number of nodes being the least computationally difficult.

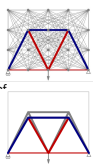


### Geometry Optimisation

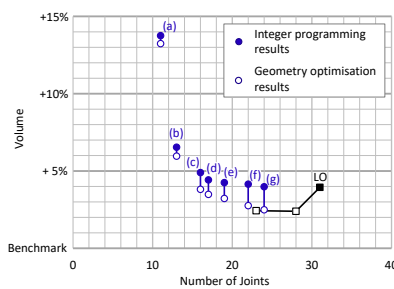
At low to medium resolutions the results of layout optimisation (with or without integer programming) can be improved by geometry optimisation.

This involves **moving the joint positions** and altering cross section areas to further **reduce the volume** of the structure. This may also include merging nodes which become close together.

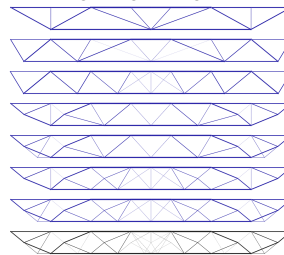
This is a non-convex problem, so may not find the globally optimal solution.



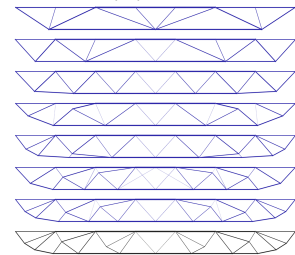
### Results: Limiting number of joints



#### Integer Programming Forms



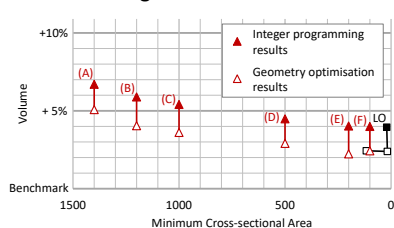
#### Geometry Optimisation Forms



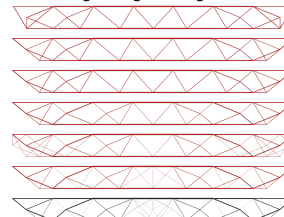
#### CPU time

(a)	00:03:15
(b)	00:00:58
(c)	00:00:27
(d)	00:01:49
(e)	00:01:39
(f)	00:00:39
(g)	00:00:42
LO	00:00:02

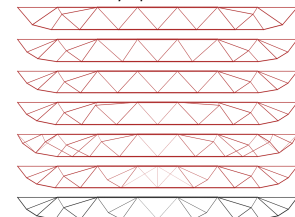
### Results: Limiting minimum cross-section area



#### Integer Programming Forms



#### Geometry Optimisation Forms



#### CPU time

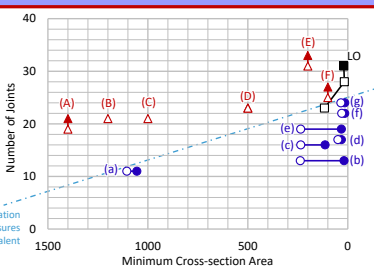
(A)	11:11:15
(B)	00:20:08
(C)	00:06:11
(D)	00:00:59
(E)	00:00:20
(F)	00:00:53
LO	00:00:02

### Comparison of complexity measures

For each of the forms shown above we can now easily calculate the values of any of our complexity measures. The number of joints and the minimum cross-section area for each of the forms are plotted against each other to determine the level of correlation between the two measures.

This shows that when one complexity measure is limited, there is **minimal effect** on the other complexity measure. Generally, the forms are fairly complex in the measure they were not restricted in. Indeed, sometimes tightening the restriction on one measure causes an increase in complexity of the other, as for form (E).

To obtain the most appropriate and simplest structures imposing constraints on **multiple complexity measures** may be required. This is likely to further increase the computing time required.



### Conclusions

Integer programming has been shown to provide a possible extension to the layout optimisation method to allow **buildability constraints** to be imposed.

Various quantitative values have been used to approximate the complexity level of a structure, and these affect the computational difficulty of the integer programming problem. Limiting the number of joints has been shown to be much easier than that of limiting the minimum cross-section area. However, the different complexity measures are generally quite independent, so simultaneous application of limits to multiple complexity measures may be required.

Overall, the computational difficulty of integer programming means that it is only possible to use it for **relatively simple problems**. Therefore it may be of more use for benchmarking alternative methods than as a practical design tool.



## E.5 Balancing complexity and structural efficiency in the design of optimal trusses

This section contains a paper<sup>†</sup> which was presented at the symposium of the International Association for Shell and Spatial Structures. This paper was presented to an audience of researchers, practising engineers and practising architects, mainly specialising in the design of shell structures or frameworks of complex geometry.

This paper includes the case study considered in Section 6.3, and also includes as three dimensional example problem to demonstrate the efficacy of the method in 3D.

---

<sup>†</sup> Fairclough, H., Gilbert, M., Thirion, C., & Tyas, A. (2018). Balancing complexity and structural efficiency in the design of optimal trusses. In *Proceedings of IASS Annual Symposia 2018: Creativity in Structural Design*. International Association for Shell and Spatial Structures (IASS)



*Proceedings of the IASS Symposium 2018*  
Creativity in Structural Design  
July 16-20, 2018, MIT, Boston, USA  
Caitlin Mueller, Sigrid Adriaenssens (eds.)

## Balancing complexity and structural efficiency in the design of optimal trusses

Helen FAIRCLOUGH<sup>\*a</sup>, Matthew GILBERT<sup>a</sup>, Clement THIRION<sup>b</sup>, Andy TYAS<sup>a</sup>

<sup>\*a</sup>Department of Civil and Structural Engineering, University of Sheffield  
Mappin Building, Mappin St, Sheffield S1 3JD

<sup>\*</sup>hefairclough1@sheffield.ac.uk

<sup>b</sup>Expedition Engineering, London

### Abstract

Attempts to apply topology or layout optimization methods at the conceptual design stage can be hampered by the complex and impractical nature of the forms which are often generated. Here, the standard truss layout optimization formulation is extended to allow introduction of constraints designed to increase buildability and reduce fabrication costs. Specifically, means of controlling the numbers of joints and eliminating overly thin members in the resulting structures are investigated, although the basic method presented can be extended to incorporate a range of other constraints. Through application to both 2D and 3D examples it is shown that it is possible to find forms that are almost as lightweight as the corresponding theoretical optimums, but are far simpler to construct. These forms are presented graphically, allowing the designer to make informed decisions on the appropriate level of compromise between material consumption and buildability.

**Keywords:** Layout optimization, MILP, conceptual design, transfer truss, buildability, Pareto front, topology optimization

### 1. Introduction

In a world increasingly driven by resource scarcity, optimization based design methods have the potential to offer significant benefits in fields such as structural engineering. However, uptake of such methods in practice can be derailed by the complexity of the structures identified, which would often be economically prohibitive to construct using current methods.

Minimum weight structures generally take the form of truss-like continua, comprising an infinite number of infinitesimally thin members [1]. Although such forms can be rationalized (e.g. as in [2]), they may often still be challenging to construct. Prager [3] demonstrated that significant material savings can be maintained in simplified variants of optimum solutions, though he only considered small problems.

Here, solutions to a range of larger problems are found by using mixed integer linear programming (MILP) constraints added to the standard truss layout optimization formulation. The simplicity of the proposed formulation permits far more complex problems to be treated than has hitherto been possible (e.g. [4]), permitting layout optimization, rather than just size optimization, problems to be considered.

### 2. Example problem: transfer truss

In this paper, the methods will first be tested using a case study drawn from a real world project. The case study concerns the identification of a structural layout for a transfer truss of 21m span, as shown in figure 1. The truss is to carry 6 equally spaced column loads of equal magnitude in the Ultimate Limit State (ULS) load case, and a pattern load case is also included. The structure is to be constructed from S355 steel, giving a maximum stress of 355MPa in tension, reduced to 266MPa in compression to approximate the effects of buckling. The symmetry of the problem is exploited to require only half the design domain to be modelled.

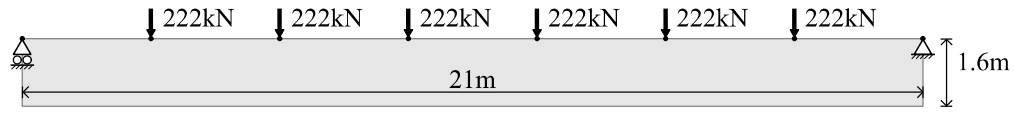


Figure 1. Transfer truss - problem description (ULS load case shown)

### 3. Minimum volume trusses with high complexity

Many methods are available for the identification or approximation of minimum volume structures without restrictions on complexity. Here, ‘ground structure’ based layout optimization is used, after Dorn [5]. This method been extended to allow inclusion of additional considerations (e.g. see [6]) and to improve the computational efficiency (e.g. see [7]). The method is outlined in figure 2. This method is ideal for structural engineering applications as the results are discrete truss forms which can be produced at large physical scales much more easily than the solid forms produced by continuum topology optimization methods such as [8]. The method is also ideal as it allows intuitive post processing methods (e.g. [9]), or further analysis using familiar truss or frame based methods.

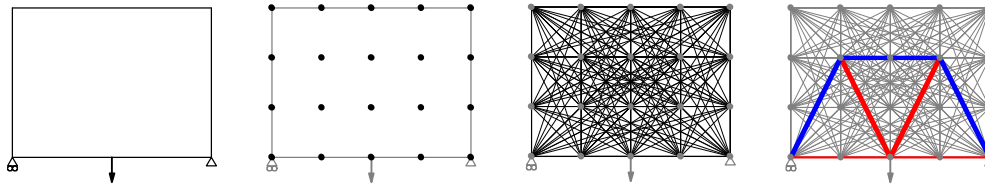


Figure 2. Layout optimization: (a) specification of design domain, loading and supports; (b) design domain discretized using nodes; (c) each pair of nodes connected by potential truss member; (d) optimal set of truss members with non-zero areas identified by solving the linear problem in equation 1.

The layout optimization method uses linear programming to identify the optimal member areas and internal forces for each load case. For a multiple load case problem with a ground structure containing  $m$  potential members and  $n$  potential nodes, to be constructed from a material with allowable tensile and compressive stresses of  $\sigma^+$  and  $\sigma^-$  respectively, the linear programming problem is stated as:

$$\begin{aligned}
 \min \quad & V = \mathbf{l}^T \mathbf{A} & (1a) & \quad \text{Objective function: minimize total volume.} \\
 \text{subject to} \quad & (\mathbf{B}\mathbf{q}_k = \mathbf{f}_k)_{\forall k} & (1b) & \quad \text{Equilibrium constraint at all nodes, for each load case.} \\
 & (\sigma_c \mathbf{A} + \mathbf{q}_k \geq 0)_{\forall k} & (1c) & \quad \text{Compressive stresses in each load case are allowable.} \\
 & (\sigma_t \mathbf{A} - \mathbf{q}_k \geq 0)_{\forall k} & (1d) & \quad \text{Tensile stresses in each load case are allowable.} \\
 & \mathbf{A} \geq 0 & (1e) & \quad \text{Member areas must be non-negative.}
 \end{aligned}$$

where  $V$  is the total structural volume,  $\mathbf{A}$  is a vector containing variables representing member cross sectional areas  $[A_1, A_2, \dots, A_m]^T$ ,  $\mathbf{l}$  is a vector of member lengths,  $\mathbf{q}_k$  contains the variables representing the internal member forces in load case  $k$  (with tensile forces positive),  $\mathbf{f}_k$  is a vector containing external forces in load case  $k$ , and  $\mathbf{B}$  is a suitable  $2n \times m$  equilibrium matrix.

As the resolution of the ground structure nodes is increased, this method produces good approximations to both the form and weight of the theoretical minimum volume structure. The efficiency of linear programming solvers means high resolution problems can be solved on standard desktop computers. For example, the structure shown in figure 3 is calculated from a ground structure of over a million potential members (in the modelled half of the domain), and was solved using the Limitstate:FORM software [10] running on an i7-6700HQ CPU in under 4 minutes. This structure requires 2.73t of steel; this will be used as the benchmark value against which the weights of simplified structures can be compared.



Figure 3. Transfer truss - numerical approximation of minimum volume truss - steel weight 2.73t

#### 4. Minimum weight trusses with low complexity

For trusses where very low complexity is desired, there are only limited options for possible forms. For a structure to be a true truss (i.e. with no bending stresses) it is necessary to ensure that a node is present at each applied load and support. Simply connecting these essential nodes will often provide a ground structure which is suitable for use to identify the minimum volume truss with fewest possible nodes.

##### 4.1 Trusses comprising 9 nodes

For our case study, all the loads and supports are co-linear. Therefore, at least one additional node is required to form a feasible truss structure. To ensure symmetry, this node should be located on the central symmetry plane of the problem. Also, to create the lightest structure, this node should be placed to maximize the depth of the truss, as shown in figure 4.



Figure 4. Transfer truss - minimum weight design when 9 nodes are permitted - steel weight 6.19t

The form shown in figure 4 has a weight over double that of the benchmark truss shown in figure 3. For practical design purposes, structures which provide a compromise between these extremes are desired.

##### 4.2 Trusses comprising 11 nodes

To provide a lower weight, a pair of additional nodes will be added to the design. As this adds only two degrees of freedom (the horizontal and vertical location of the new nodes), it is possible to enumerate the minimum structural volume for each possible position, see figure 5. A 25mm spacing between adjacent locations was used, resulting in 27,365 structures analyzed in a total time of 7 minutes. The optimal location is shown in the lightest blue, and illustrated in figure 5d.

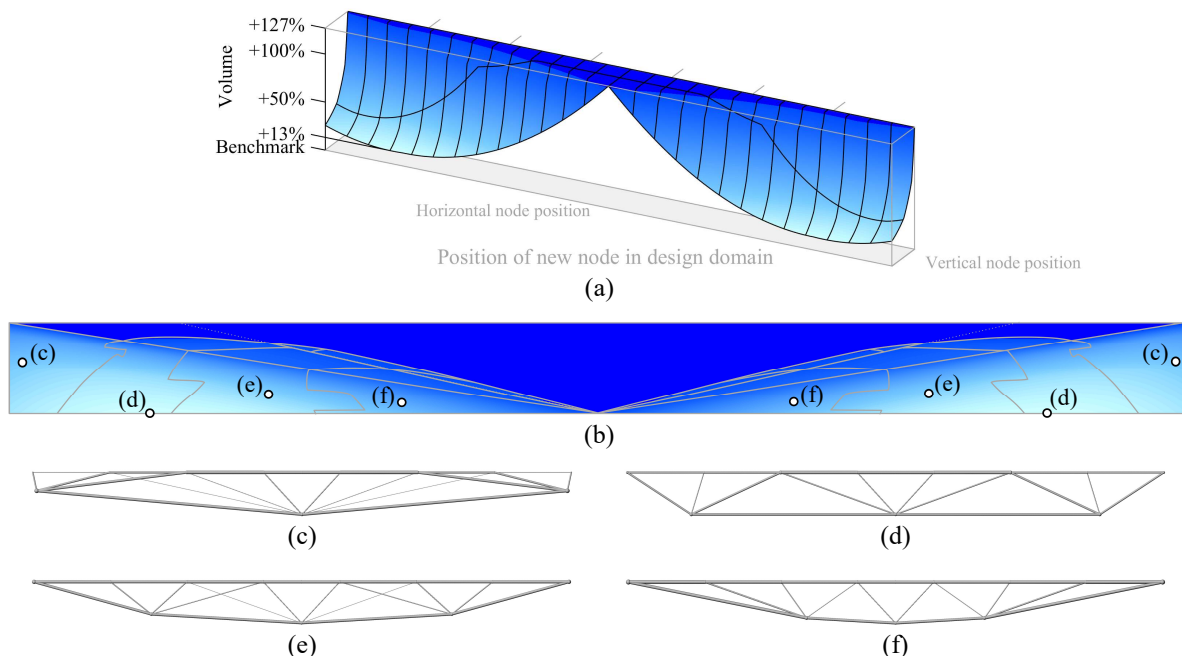


Figure 5. Transfer truss - possible structures with 11 nodes: (a) total structural volume for each position of the newly added pair of nodes within the design domain; (b) positions of the newly added nodes within the design domain, showing regions where the minimum volume topology is uniform, and locations of added nodes for the sample layouts shown. The central (darkest) region represents where the additional nodes were ignored and the structure in figure 4 was identified as optimal, the remaining unmarked regions represent where extra members from the top nodes to the central node are added to the main topologies; (c) – (f) show sample layouts for the main 4 topologies identified, total volumes 42%, 13%, 34% and 62% greater than the benchmark value respectively.

#### 4. Minimum weight trusses with intermediate complexity

As more nodes are added to the structure, the dimensionality of the problem quickly makes testing every location impractical. For example, adding one more pair of nodes to the previous problem will square the number of points which must be checked, leading to an expected computational time of 19 weeks. The non-convexity of the solution spaces of these problems (as shown in figure 5a), means that more refined methods based on further sequential development of the problem (such as [11]) become problematic, leaving them susceptible to identifying local optima (e.g. see [2]).

Instead a mixed integer-linear programming (MILP) formulation based on the layout optimization problem is used here; this allows additional constraints to be imposed, such as restrictions on the total number of nodes in the final structure. The formulation involves using binary variables to represent the presence of each node in the ground structure, and is formed by adding the following constraints to the problem in equation 1:

$$(Mv_j - \sum_{i \in j} A_i \geq 0)_{\forall j} \quad (2a) \quad \text{The active node indicator } v_j \text{ for node } j \text{ is 1 if sum of attached member cross section areas is } > 0, \text{ or 0 otherwise.}$$

$$\sum_{\forall i} v_i \leq \eta \quad (2b) \quad \text{The sum of all } v_j \text{ values must be within the specified limit.}$$

$$v \in [0,1] \quad (2c) \quad \text{Active node indicator variables may only take binary values.}$$

where  $v$  is the vector of active node indicator variables  $[v_1, v_2, \dots, v_n]$  and  $M$  is a large positive value, chosen such that it is larger than the maximum sum of member areas at any node, but sufficiently small to prevent scaling issues. It should be noted that adding a contribution from the  $v$  variables to the objective function will allow this to be converted from being used to limit the number of nodes to being an added cost according to the number of nodes.

MILP solvers are guaranteed to find the global optimum of the given problem; i.e. the solution of a high resolution problem formulated as equation 2 will give the globally minimum volume truss with the required number of nodes. However, MILP problems have greatly increased computational demands compared to standard linear problems. This necessitates the use of lower resolutions, which restricts the possible solutions. Here, a ground structure comprising 36 nodes and 666 potential members is used. Figure 6a shows the result of standard layout optimization at this resolution; this structure is 4% heavier than the benchmark, and the form is quite restricted by the underlying Cartesian grid of nodes.

To counter this, the resulting solutions of the layout optimization and MILP problems are subject to a second optimization stage. This involves using the geometry optimization procedure developed by He and Gilbert [2], where the layout is fixed and the nodal positions and member areas are varied. This method is also applied to the low resolution layout optimization result, both with and without the merging of nearby nodes. This produces simpler solutions, with lower weights (shown in figures 6b and 6c), although there is little control over the level of simplification required, and some regions of the forms may still be challenging to construct.

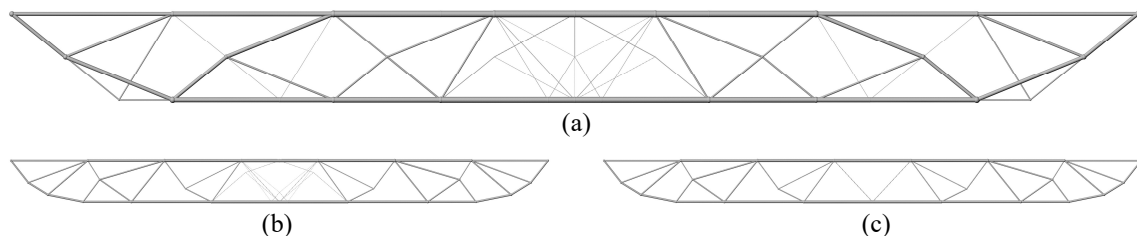


Figure 6. Transfer truss - optimized structural forms obtained using a coarse nodal grid: (a) layout optimization solution - 3.0% heavier than benchmark; (b) layout optimization and geometry optimization - 2.4% heavier; (c) layout optimization and geometry optimization with node merging - 2.5% heavier.

The MILP problems have been solved using the Gurobi solver whilst the non-linear geometry optimization step was solved using the IPOPT solver, via the Limitstate:FORM software [9]. The problems were solved as previously, with the MILP solutions shown in figure 7 requiring CPU times of between 27 and 195 seconds.

*Proceedings of the IASS Symposium 2018*  
*Creativity in Structural Design*

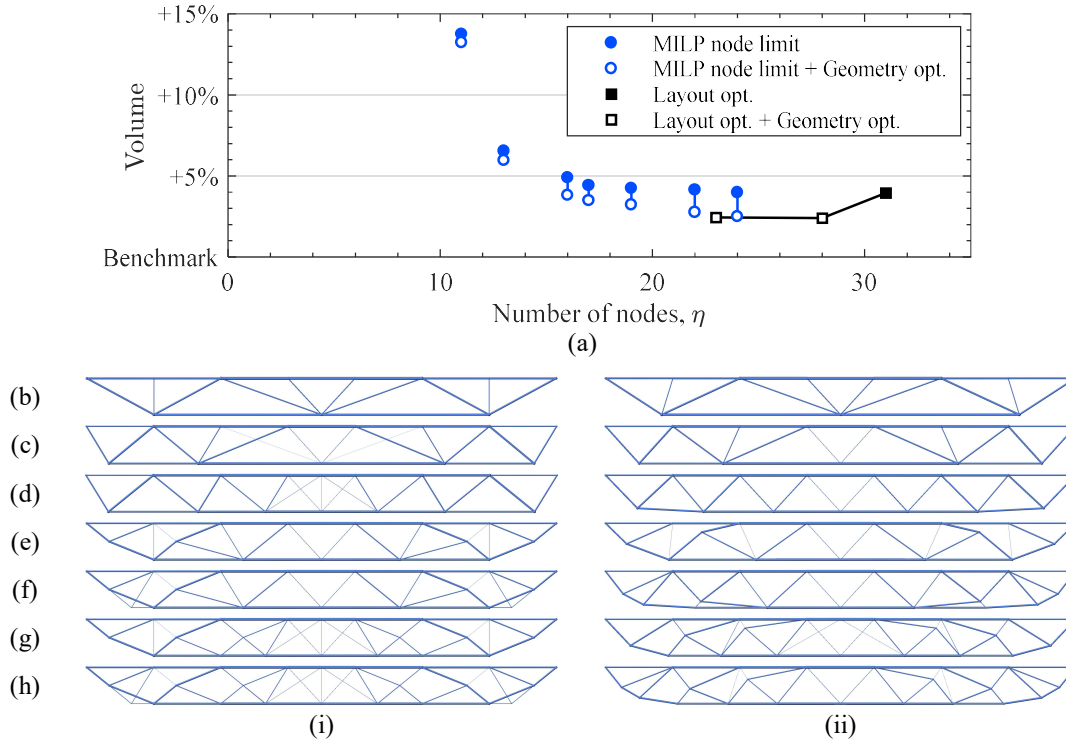


Figure 7. Transfer truss - results for limiting the number of nodes permitted: (a) volumes for forms in figures 6 and 7; (b)-(h) forms identified by (i) MILP and (ii) MILP plus geometry optimization for each limit value.

From figure 7 it can be seen that the solution identified for 11 nodes after geometry optimization is identical to that illustrated in figure 5d. It has also been successfully verified that imposing a limit of 9 nodes produces the form shown in figure 4.

The Pareto front shown in figure 7a provides a powerful tool for designers, allowing them to choose the appropriate level of compromise between complexity and lightness required for a given project. It also places the options in context, both against each other and against the theoretical benchmark solution. The resulting structures from standard layout optimization with geometry optimization and node merging are seen to have similar volumes compared with the MILP results at similar complexities.

### 5. Alternative member-based complexity measure

Limiting the number of joints in a structure is a simple means of increasing likely buildability, but the MILP method can be used to impose a wide range of other potential limits, including:

- Total number of members.
- Number of members meeting at a joint.
- Minimum cross section area.
- Elimination of members which cross/pass close without a joint.
- Minimum angle between members meeting at a joint.
- Number of different member lengths within the structure.
- Number of different cross sections within the structure.
- Member cross sections restricted to known (e.g. catalogue) sections.

Note that the final two constraint types are formulated in a slightly different manner, which would require additional integer variables, similar to the approach in [12]. For most of the remaining types, they are formulated in a similar manner to equation 2; however, instead of requiring the  $1 \times n$  vector  $\mathbf{v}$ , a  $1 \times m$  vector containing an active member indicator for each potential member is required, denoted by  $\mathbf{w}$ . As the MILP problem must be posed with all possible members present,  $m$  will be roughly proportional to  $n^2$ . This will dramatically increase the computational expense of the problem. As an example, a limit will be imposed on the minimum cross section area of members in the solution.



To impose a limit on the minimum cross section area of a member, the following constraints should be added to the problem in equation 1:

$$(Mw_i - A_i \geq 0)_{\forall i} \quad (3a) \quad \text{The active member indicator } w_i \text{ for member } i \text{ is 1 if the member cross section area is } > 0, \text{ or 0 otherwise.}$$

$$M(1 - w) + A \geq \alpha \quad (3b) \quad \text{If the active member indicator} = 1, \text{ the member area must be greater than the limit } \alpha.$$

$$\mathbf{w} \in [0,1] \quad (3c) \quad \text{Active member indicator variables may only take binary values.}$$

where  $\mathbf{w}$  is the vector of active member indicator variables  $[w_1, w_2, \dots, w_m]$ , and  $M$  is still a large positive value, although now it is only necessary to ensure that it is larger than the value of any single area value. Initial tests have shown this to be among the quickest to solve of the constraint types listed previously, likely due to the decoupled nature of these constraints. Nonetheless, when solved under the same conditions as previously, the forms shown in figure 8 required up to 11 hours to solve on a desktop PC.

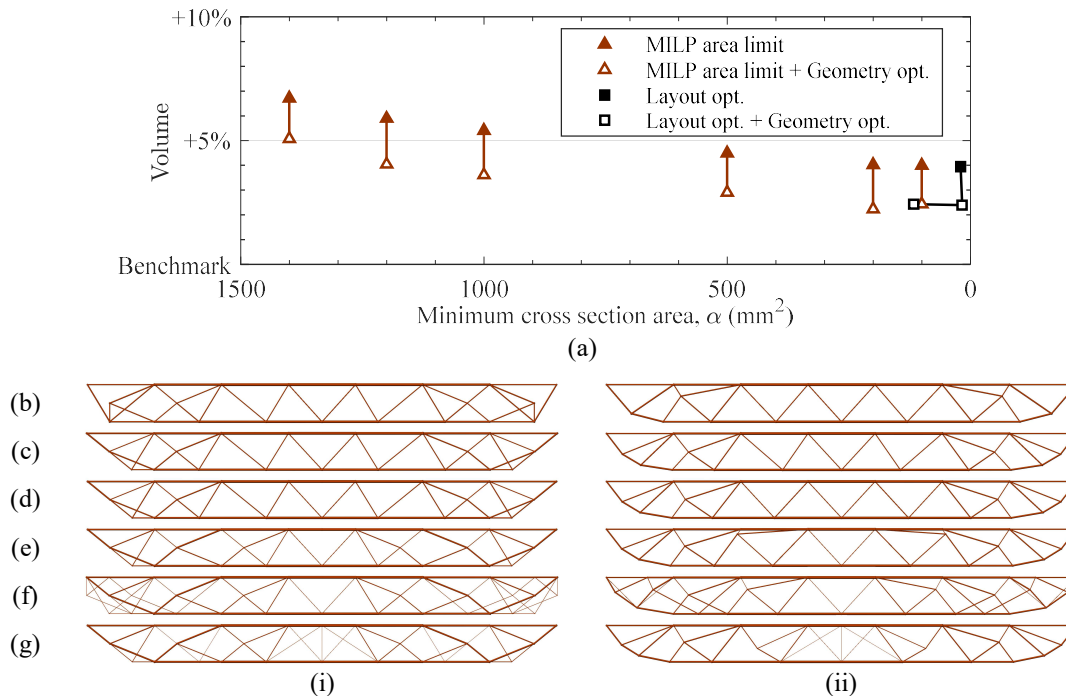


Figure 8. Transfer truss - results for limiting the minimum cross section area: (a) volumes of forms in figures 6 and 8; (b)-(g) forms identified by (i) MILP and (ii) MILP plus geometry optimization for each limit value.

As the computational demands of producing the structures in figure 8 are so much higher than that of figure 7, it would be desirable if the limit on number of nodes could be used as a surrogate for other measures of complexity. However, figure 9 shows the values of both investigated complexity measures for each of the structures identified, and it can be seen that the correlation, particularly for the MILP based results, is low.

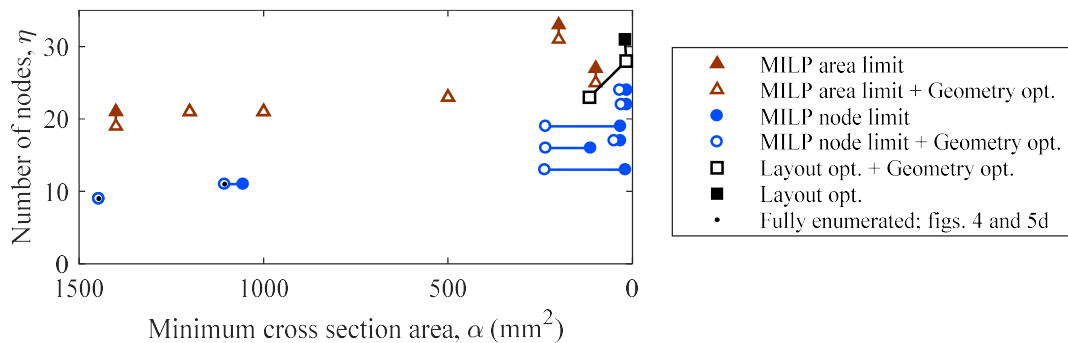


Figure 9. Transfer truss - comparison between the measures of complexity for forms in figures 4, 5b, 6, 7 & 8.

### 6. 3D canopy example problem

The method is also applicable to 3D problems, although the size of problems that can be solved is limited. Nonetheless, a simple problem has been modelled; this concerns a design for a canopy supported at its bottom corners, and loaded in 4 symmetrical locations as shown in figure 9a. The symmetry of the problem has been exploited so that only one eighth of the domain needs to be modelled.

A reasonably high resolution layout optimization (with 336 potential nodes, 56280 potential members) was performed to establish a benchmark volume. To enable MILP to be used a coarser ground structure (45 potential nodes, 990 potential members) was used; see figure 9a. For this, the minimum volume structure is shown in figure 9c, and has a volume 6.7% above the benchmark. It is likely to be possible to reduce this increase by the use of geometry optimization, although this has not been investigated here.

The MILP method has been used to restrict the number of joints in the considered segment. Most of the results are shown in figure 9b. Additionally, the optimal structure with 4 joints per segment was shown to have a volume 57% above the benchmark and it was found that no structure with  $\leq 3$  joints per segment was possible. The structures shown in 9d and 9e are respectively 1.1% and 2.7% heavier than the structure shown in figure 9c, whilst the reduction in complexity is significant.

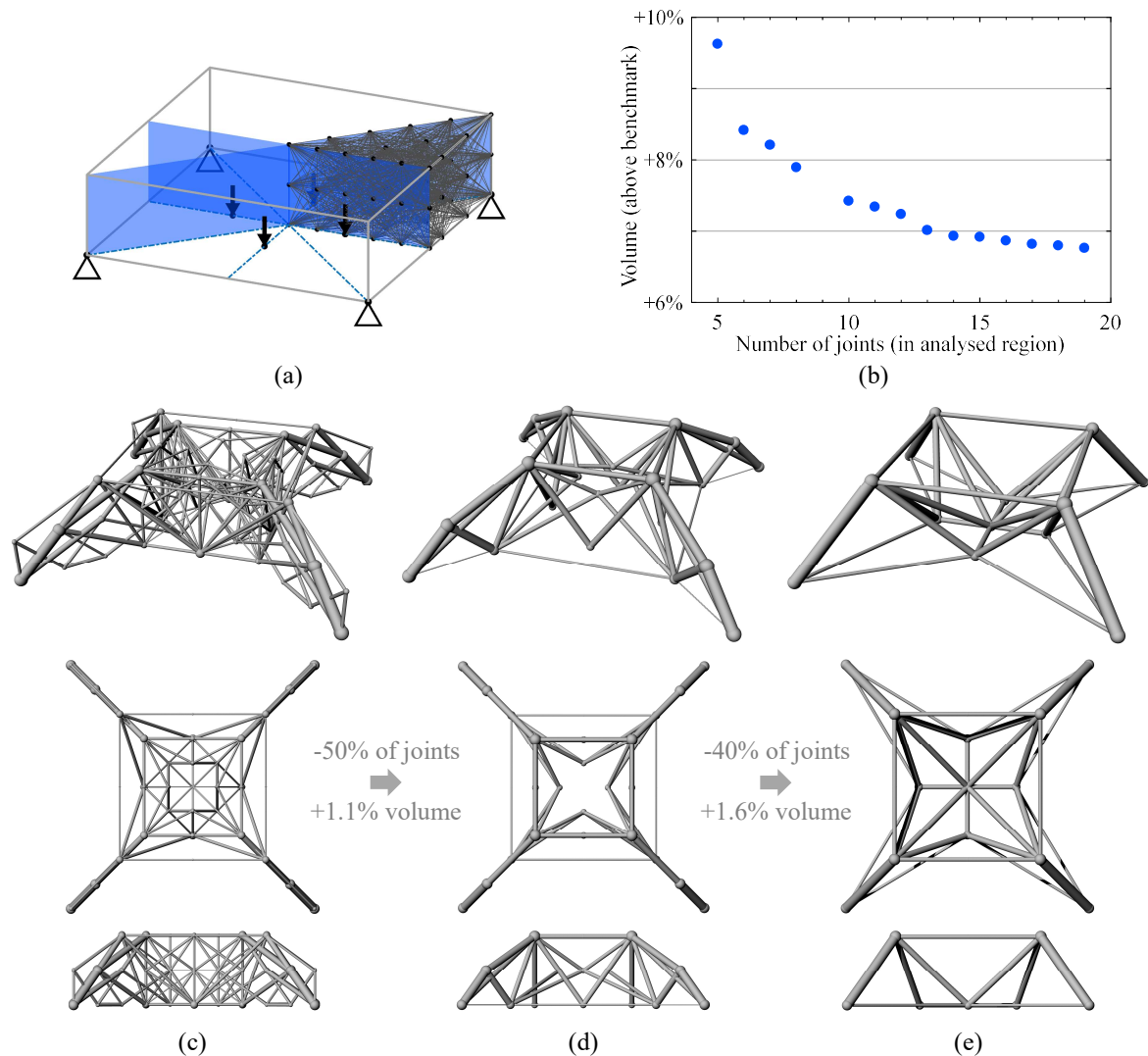


Figure 9. 3D canopy example – complexity study: (a) design domain showing the four symmetry planes and low resolution ground structure; (b) volumes of optimal structures with various numbers of joints; (c) optimal form with no complexity constraint; (d) optimal form with 8 joints in the analyzed region; (e) optimal form with 5 joints in the analyzed region.



## 7. Discussion and conclusions

The addition of MILP constraints to the standard layout optimization problem formulation has been shown to provide an effective means of including buildability constraints for low to medium resolution truss topology optimization problems in 2D or 3D. The method is flexible, allowing a wide range of possible measures of complexity to be controlled, either in the form of limits or additional costs.

The most severe drawback associated with the use of MILP constraints is computational cost, which limits the nodal resolutions that can be used. This restriction can be mitigated somewhat via the use of geometry optimization as a second phase. For the simple structures investigated herein this was found to allow identification of the globally optimal design.

The method allows exploration of areas of the design space between simpler structures, of the sort that may be postulated by designers, and the considerably more complex structures which result from application of classical optimization methods. It thus enables designers to make more informed decisions on the compromises that can be struck between material usage and structural complexity.

## Acknowledgements

The authors wish to thank colleagues at Expedition Engineering for their help in identifying the first case study problem described herein, and for their continued support. The financial support of EPSRC under grant number EP/N023471/1 and Expedition Engineering is also gratefully acknowledged.

## References

- [1] A. G. M. Michell, "The limits of economy of material in frame-structures," *Philosophical Magazine*, vol. 8, no. 47, pp 589-597, 1904.
- [2] L. He and M. Gilbert, "Rationalisation of trusses generated via layout optimization," *Structural and Multidisciplinary Optimization*, vol. 52, no. 4, pp 677-694, 2015.
- [3] W. Prager, "Optimal layout of trusses with finite numbers of joints," *Journal of the Mechanics and Physics of Solids*, vol. 26, no. 4, pp 241-250, 1978.
- [4] R. Van Mellaert, K. Mela, T. Tiainen, M. Heinisuo, G. Lombaert and M. Schevenels, "Mixed-integer linear programming approach for global discrete sizing optimization of frame structures," *Structural and Multidisciplinary Optimization*, vol. 57, no. 2, pp 579-593, 2018.
- [5] W.S. Dorn, R. E. Gomory and H. J. Greenberg, "Automatic design of optimal structures," *Journal de Mecanique*, vol. 3, pp. 25-52, 1964.
- [6] T. J. Pritchard, M. Gilbert, and A. Tyas, "Plastic layout optimization of large-scale frameworks subject to multiple load cases, member self weight and with joint length penalties," in *6th World Congress of Structural and Multidisciplinary Optimization, Rio de Janeiro, Brazil*, 2005.
- [7] M. Gilbert and A. Tyas, "Layout optimization of large-scale pin-jointed frames," *Engineering Computations*, vol. 20, no. 8, pp 1044-1064, 2005.
- [8] M. P. Bendsoe, O. Sigmund, *Topology optimization: theory, methods, applications*. Springer, 2013.
- [9] L. He, M. Gilbert, P. Shepherd, J. Ye, A. Koronaki, H.E. Fairclough, B. Davison, A. Tyas, J. Gondzio, and A.G. Weldeyesus, "A new conceptual design optimization tool for frame structures", in *Proceedings of the IASS symposium 2018: Creativity in Structural Design, Boston, USA*, 2018
- [10] Limitstate Ltd., "Limitstate:FORM version 3.2", 2017 [online]. Available: <http://limitstate3d.com>. [Accessed: April 17th 2018]
- [11] P. Martinez, P. Marti, O.M. Quierin, "Growth method for size, topology, and geometry optimization of truss structures," *Structural and Multidisciplinary Optimization*, vol. 33, no. 1, pp 13-26, 2007.
- [12] M. Rasmussen and M. Stolpe, "Global optimization of discrete truss topology design problems usein a parallel cut-and-branch method," *Computers & Structures*, vol. 86, pp 1527-1538, 2008.

## E.6 Layout optimization of simplified trusses using mixed integer linear programming with runtime generation of constraints

This section contains a paper which has been accepted for publication<sup>†</sup> in the journal *Structural and Multidisciplinary Optimization*.

This paper concerns the application of lazy constraints within the layout optimization problem. Much of the material herein has also appeared in [Chapter 6](#).

---

<sup>†</sup> Fairclough, H. & Gilbert, M. (in press) Layout optimization of simplified trusses using mixed integer linear programming with runtime generation of constraints. *Structural and Multidisciplinary Optimization*

# Layout optimization of simplified trusses using mixed integer linear programming with runtime generation of constraints

H. Fairclough<sup>1</sup> · M. Gilbert<sup>1</sup>

Received: date / Accepted: date

**Abstract** Traditional truss layout optimization employing the ground structure method will often generate layouts that are too complex to fabricate in practice. To address this, mixed integer linear programming can be used to enforce buildability constraints, leading to simplified truss forms. Limits on the number of joints in the structure and/or the minimum angle between connected members can be imposed, with the joints arising from crossover of pairs of members accounted for. However, in layout optimization the number of constraints arising from ‘crossover joints’ increases rapidly with problem size, along with computational expense. To address this here crossover constraints are dynamically generated and added at runtime only as required (so-called ‘lazy constraints’); speedups of more than 20 times are observed whilst ensuring that there is no loss of solution quality. Also, results from the layout optimization step are shown to provide a suitable starting point for a non-linear geometry optimization step, enabling results to be obtained that are in agreement with literature solutions. It is also shown that symmetric problems may not have symmetric optimal solutions, and that multiple distinct and equally optimal solutions may be found.

**Keywords** Layout Optimization · Topology Optimization · Discrete Optimization · Truss Optimization · Multiple Load Cases · Mixed-Integer Linear Programming

---

H. Fairclough · M. Gilbert

E-mail: m.gilbert@sheffield.ac.uk

<sup>1</sup> Department of Civil and Structural Engineering,  
The University of Sheffield, Sir Frederick Mappin Building,  
Mappin Street, Sheffield, S1 3JD, UK

## 1 Introduction

Reducing the volume of material consumed in construction projects is a challenge of increasing importance. The theory of minimum volume structures is well established (Michell, 1904) and can provide benchmark values to help evaluate the structural efficiency of proposed designs. However, for practical usage, the truss-like continua generated by classical methods are often challenging or impossible to construct in practice. Whilst novel construction methods may allow more complex designs to be realized in the future, more immediate benefits may arise through the use of optimization methods capable of generating less complex solutions.

Numerical topology and layout optimization methods allow structurally efficient forms to be identified. These methods can be divided into continuum based approaches and discrete truss / frame based methods. Perhaps the best known of the continuum based approaches is the SIMP method (Bendsøe and Sigmund, 1999). This uses penalization to drive the solution to a distinct structural form. A number of extensions to the SIMP method have been suggested to control the complexity of the forms identified. For example, minimum length scale (Zhou et al, 2015) and maximum perimeter length (Park et al, 2018) constraints have been proposed. However, the quantities involved are not intuitive when considered in the context of a typical structural engineering design problem. More generally, interpreting solutions from a continuum topology optimization in a structural engineering context will often be challenging, and is likely to necessitate considerable manual post-processing effort. Furthermore, the fraction of the available design space occupied by structural members in a typical building or bridge structure will generally be very small, such that very high numerical

resolutions are required to achieve accurate results (see e.g. Aage et al, 2017).

Here, attention is therefore focussed on methods that directly represent the structure as a frame or truss composed of a series of discrete members. The most well known numerical method of this type is the ground structure layout optimization method (Dorn et al, 1964), in which an optimal set of members are chosen from a dense initial ground structure. The commonly used plastic design formulation gives rise to a problem that can be solved using linear programming, allowing problems involving large numbers of potential members to be solved rapidly.

One potential method for limiting the complexity of a truss structure was suggested by Parkes (1975). This involves adding a volume penalty to represent the material required in the connections joining each member in the structure, known as a joint cost. The penalty is linearly related to the member volume, allowing this method to readily be integrated with numerical ground structure based layout optimization methods, whilst retaining computational efficiency. However, as this method penalizes short members, rather than the number of members, its efficacy is problem dependent.

Another, similar concept was presented by Prager (1977); however, here the cost of a joint was assumed to be constant. With Prager's approach minimum volume trusses with fixed numbers of joints are first found, with the ranges of costs for which they are optimal later established. The minimum volume trusses are based on use of a mesh-wise constant strain field, furnishing a set of geometrical rules for the joints. Mazurek et al (2011) identify the same rules by direct optimization of joint positions for simple structures, building on the principles of graphical statics. These rules imply that the angles between members at every unsupported joint should be identical. Prager (1978) extends these rules to the case where  $\sigma_T \neq \sigma_C$ , where  $\sigma_T$  and  $\sigma_C$  are respectively the limiting stress in tension and compression. Each of the aforementioned authors applies their approach to three-force problems, such as the classical Michell cantilever problem (where two of the three forces are support reactions).

Of these approaches, only the linear joint cost method is applicable to multiple load-case problems. When multiple load-cases are present, the optimal solutions for elastic and plastic design problems diverge. The plastic problem gives rise to the simplest numerical formulation and is accepted by many structural design codes so will be considered here.

Optimality criteria for multiple load case plastic design problems were first given by Prager and Shield (1967). For scenarios with two load-cases, it is possible

to use the superposition principle derived by Nagtegaal and Prager (1973) to split the problem into two single load-case problems that can then be superimposed. The superposition principle was later extended to problems with more than two load-cases by Rozvany and Hill (1978), although this has a restricted range of applicability. However, numerical results for various problems demonstrate the 'overlapping' nature of many of the optimal layouts identified. In such cases, manually identifying the layout of a discretized structure becomes challenging.

Various means of characterizing the complexity of a given structure are possible. However, whatever the chosen complexity measure, it generally results in a non-smooth problem that can be challenging to solve numerically. Conceptually, the simplest measures of complexity are the numbers of joints or members in a given structure. Additionally, significant attention has been devoted to limiting the numbers of different cross sections present in a given solution.

Kanno and Fujita (2018) limit the number of joints in solutions whilst minimizing the compliance of the structure, considering both a heuristic method and a mathematical programming formulation including integer variables. However, although the resulting mixed integer second order cone programming (MISOCP) problem could solve problems with up to 1500 potential members reasonably quickly (in a time of 112 seconds), conditions were not imposed to prevent intersecting or overlapping members. Therefore, many of their results contain members that cross, which would likely be interpreted as additional joints by practitioners, therefore limiting the usefulness of the results obtained.

A similar approach based on plastic design principles with volume minimization was used by Park (2013), resulting in a mixed integer linear programming (MILP) problem. Here, complexity was reduced by imposing limits on the numbers of members in the solution; he also used a similar approach to identify tensegrity forms.

Tensegrity forms were also identified by Kanno (2013), using another MILP formulation considering both compliance and stress constraints, as well as a number of practical considerations. This formulation prevents the inclusion of intersecting members, by including constraints for every intersecting pair of potential members in the ground structure. As the problems considered are limited in size (with ground structures containing up to 18 nodes and 99 potential members), the number of potential intersection points is small ( $\leq 32$ ). Nonetheless, the problems took up to 67,000 seconds to solve, and the number of intersection points

and the time required would rapidly increase at higher resolutions.

The great majority of work on truss based optimization methods with discrete constraints has focused on restricting the cross sections of each member to be chosen from a given list of catalogue sections. A comprehensive review of methods for approaching this problem can be found in Stolpe (2016), covering both deterministic (e.g. integer programming) and meta-heuristic methods. In this it is observed that complex formulations generally restrict the size of problems, such that these fall within the realm of ‘size optimization’ rather than true layout or topology optimization. Identification of global optima (deterministic methods) generally has a high computational cost; for example when Achtziger and Stolpe (2007) identify the global optimum for a problem with 131 potential members and 6 possible cross sections, the associated computational time is 488,592 seconds.

Heuristic methods are simple to implement and are therefore popular with many researchers (e.g. Ahrari et al, 2015; Mortazavi and Toğan, 2016; Gonçalves et al, 2015). However, the number of independent design variables is limited ( $\ll 100$ ). Therefore these methods generally employ very low resolution and/or restricted ground structures, often tailored to individual problems.

The Moving Morphable Components (MMC) method, developed by Guo et al (2014), combines a continuum level-set model and explicit description of geometry. Although this does not obviate the need to employ high resolutions, this does allow complexity to be controlled in intuitive ways. For example Hoang and Jang (2017) limit the thickness of members, and Zhang et al (2017) limit the number of ‘effective components’ ( $\approx$  number of members). However, the problem is highly non-linear and prone to identification of local optima; there are also issues treating problems with low volume fractions.

Identification of local optima is also an issue for ground structure based methods involving continuous non-linear approximations, such as those of Asadpoure et al (2015) and Torii et al (2016), which are usually non-convex. Leng and Duan (2012) use a continuum approximation based on the Heaviside function to prevent intersecting bars; however, only problems with up to 68 potential members are considered, and there is no indication of the associated computational cost.

Ohsaki and Katoh (2005) also include a constraint on member intersection, as well as nodal stability and stress constraints. They use non-linear programming (NLP) and MILP in combination to provide both upper and lower bounds on solutions; problems solved have a

maximum of 72 bars, and the ground structure is such that very few members can intersect. Times of up to 3000 seconds are reported.

Ohsaki (2016) also considers the truss topology optimization problem with discrete cross-sections, and additionally considers the problem of combined topology and geometry optimization of trusses, i.e. where the nodal locations are also included as design variables. In this, it is noted that these problems may be both non-convex and non-smooth, and therefore solving them is very difficult. A number of other means of addressing this are also possible, such as the implicit programming approach of Achtziger (2007), and the post-processing method used by He and Gilbert (2015).

MILP formulations have also been used to incorporate a range of other constraints, including buckling (Groenwold and Stander, 1997; Mela, 2014), stress constraints (Kanno and Guo, 2010), and the requirements of real world design codes (Van Mellaert et al, 2018). Complex real world and design code constraints have also been studied using meta-heuristic methods (e.g. Koumoussis and Georgiou, 1994; Villar et al, 2016; Huang and Xie, 2007). However, for both MILP and metaheuristic methods the additional complexity that these cause limit their applicability to size optimization or very low resolution layout optimization (up to around 200 potential member) problems.

Most numerical approaches in the literature that consider buildability constraints can therefore be seen to fall into one of the following categories: (i) those that present topology optimization problem formulations of such complexity that only trivial scenarios can be solved; (ii) those that present solution algorithms that produce structures with no guarantee or measure of optimality. The methodology presented in this paper seeks to extend the scale of truss layout optimization problems with basic buildability constraints that are solvable, so as to provide a potentially useful conceptual design tool for practitioners. To this end, an MILP formulation is used to find a globally optimal solution for a ground structure of finite resolution. The main contribution of this paper is to substantially increase the speed by which problems can be solved, and hence also the scale of problems solvable. This is achieved through the runtime generation of some constraints (so-called ‘lazy constraints’), as part of a two stage design process. The MILP problem forms the first stage, followed by an optional second non-linear refinement stage. Application of the developed procedure to a range of problems allows observations to be drawn on the nature of the structures identified as optimal under the imposed buildability constraint, with results compared with an-

alytical solutions in the case of one of the problems considered.

The paper is organized as follows: Section 2 describes the layout optimization formulations that will be employed in the present study; Section 3 describes the non-linear geometry optimization stage; Section 4 describes application of the methods described to a range of numerical example problems; conclusions from the study are then drawn in Section 5.

## 2 Truss layout optimization formulations

### 2.1 Linear programming formulation

The well known plastic layout optimization formulation for volume minimization of trusses subject to stress constraints (Dorn et al, 1964) is used herein; the process involves setting up a ground structure (figure 1) and solving the following linear programming problem:

$$\text{minimize } V = \mathbf{l}^T \mathbf{a} \quad (1a)$$

$$\text{subject to } (\mathbf{B}\mathbf{q}_k = \mathbf{f}_k)_{\forall k} \quad (1b)$$

$$(\sigma_T \mathbf{a} - \mathbf{q}_k \geq 0)_{\forall k} \quad (1c)$$

$$(\sigma_C \mathbf{a} + \mathbf{q}_k \geq 0)_{\forall k} \quad (1d)$$

$$\mathbf{a} \geq 0 \quad (1e)$$

where  $V$  is the total volume of all members,  $\mathbf{l}$  is a vector of all potential member lengths,  $\mathbf{a}$  is a vector of all potential member areas.  $\mathbf{B}$  is a suitable  $2m \times 2n$  equilibrium matrix (for planar problems), where  $n$  is the number of nodes and  $m$  the number of potential truss members in the ground structure.  $\mathbf{q}_k$  is the vector of member internal forces, and  $\mathbf{f}_k$  is the externally applied loading, in load-case  $k$ .  $\sigma_T$  and  $\sigma_C$  are the limiting stresses in tension and compression. Note that in this formulation, buckling of members may be considered only in a highly simplified manner, by reducing  $\sigma_C$ .

Note that when limitations on structural complexity are imposed (see section 2.2) it is useful to include overlapping members in the ground structure. For example, considering the problem shown in figure 1, if it is required that the solution contains no more than four joints (or members), it is evident that the structure shown in figure 1d is not feasible, whereas the structure shown in figure 1f is feasible, where these structures were generated respectively without and with overlapping members in the ground structure. In the former case this would result in an alternative, suboptimal, solution being generated. Thus overlapping members are included in the ground structures of all problems considered herein.

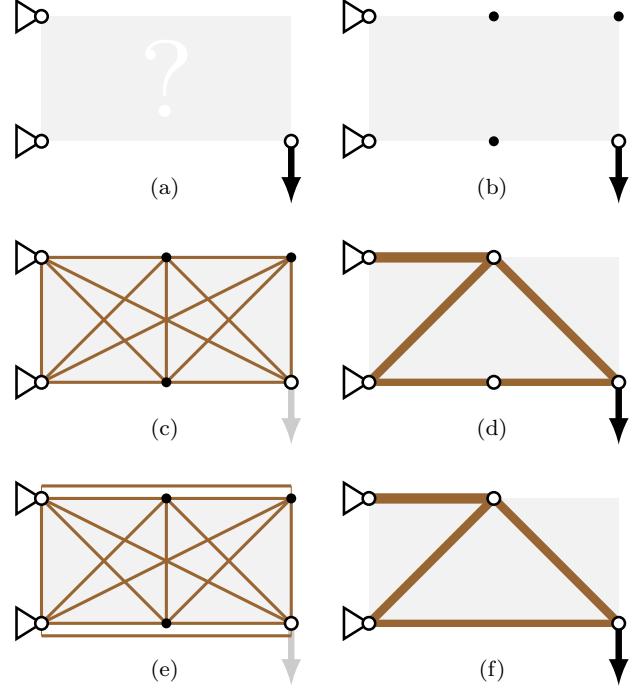


**Fig. 1:** Truss layout optimization: (a) problem specification (applied load(s), supports and design domain); (b) discretization with nodes; (c) ground structure without overlapping members; (d) unique optimal solution associated with (c); (e) ground structure including overlapping members (as used herein); (f) alternative optimal solution obtainable only when using (e).

### 2.2 MILP formulations

#### 2.2.1 Addition of discrete flag variables

The previous formulation can be extended using mixed integer linear programming (MILP) to provide a flexible method capable of imposing a wide range of constraints, including constraints designed to increase the practicality and buildability of a truss structure. In this formulation a new set of binary variables are added that represent e.g. the existence of a given potential member or node. The member flag variables are set based on the cross section areas:

$$M\mathbf{w} - \mathbf{a} \geq 0 \quad (2a)$$

$$w_i \in \{0, 1\} \quad i = 1, 2, \dots, m \quad (2b)$$

where  $\mathbf{w} = [w_1, w_2, \dots, w_m]^T$  is the vector of flag variables for each potential member in the ground structure.  $M$  is a large number, which becomes effectively an upper bound on the cross section areas and must therefore be larger than any required cross section in the final solution. However, if  $M$  is too large, numerical issues can arise; here  $M$  was pragmatically chosen to

be 20 times the maximum magnitude of any point load divided by the minimum limiting stress.

To provide flag variables to represent the existence of a joint, the sum of all members linked to the relevant node is used:

$$\hat{M}v_j - \sum_{i \in J_j} a_i \geq 0 \quad j = 1, 2, \dots, n \quad (3a)$$

$$v_j \in \{0, 1\} \quad j = 1, 2, \dots, n \quad (3b)$$

where  $J_j$  is the set of member indices for all members connected to node  $j$ .  $\mathbf{v} = [v_1, v_2, \dots, v_n]^T$  is the vector of flag variables, such that  $v_j$  is relevant to the presence of node  $j$ .  $\hat{M}$  is another sufficiently large number. In this case  $\hat{M}$  should be bigger than the total area of members connected to any node; here  $\hat{M}$  was pragmatically taken to be 4 times  $M$ .

The modelling of equation (3a) is similar to that found in the literature (e.g. Kanno and Fujita, 2018) when only the number of nodes are limited. However in light of the presence of integer flags for member existence in the present formulation, an equivalent formulation whereby  $\mathbf{v}$  and  $\mathbf{w}$  are linked is possible. This was found to produce inferior performance compared to equation (3a); for more details see appendix A.

These flag variables can then be used to form constraints to increase the practicality of the forms produced.

### 2.2.2 Limits on the number of joints, including ‘crossover joints’

Due to the much lower number of nodes compared to potential members ( $\propto n$  instead of  $\propto n^2$ ), imposing a limit on the number of nodes is comparatively computationally efficient. The simplest method to limit the number of joints to some given value  $\eta$  is to add the following constraint

$$\sum_{j=1}^n v_j \leq \eta \quad (4)$$

and constraints (3) to the problem given in (1).

However, this formulation may produce a structure which contains members which intersect each other partway between their ends. These ‘crossover joints’ will appear to be additional joints from the point of view of the designer, but will by default not be counted as such in the formulation.

To prevent this, constraints can be added for each pair of intersecting members, preventing both of them

from being present in the solution at the same time:

$$\sum_{j=1}^n v_j \leq \eta \quad (5a)$$

$$(w_h + w_i \leq 1)_{\forall \{h,i\} \in X} \quad (5b)$$

where  $X$  is a set containing unordered pairs of indices,  $\{h, i\}$ , for each pair of intersecting elements.

However, the size of  $X$  increases at a very high rate ( $\propto n^4$ ), meaning that the full form of this problem will be extremely computationally expensive to formulate and solve. Fortunately, since only a small subset of these constraints are likely to be used, these can instead be generated on-the-fly, during the running of the solver. Most commercial solvers, including CPLEX (IBM Corp., 2015) and Gurobi (Gurobi Optimization LLC, 2018), are capable of implementing these so-called ‘lazy constraints’ by allowing user defined code (often referred to as a callback function) to be called at intervals *during* a single run of the solver. As any intermediate solution which violates one or more potential constraints will be eliminated, this methodology does not alter the final solution, which remains identical to the solution of the full MILP problem containing all constraints from the beginning.

Lazy constraints have previously been used when solving the travelling salesman and related problems (Dantzig et al, 1954), where they have been shown to provide significant advantages in terms of computational efficiency. More recently Haunert and Wolff (2010) have applied them to the simplification of building outlines for maps. Here it is shown that, when applied to truss structures, the use of lazy constraints enables true topology optimization problems to be solved, i.e., layout optimization problems utilizing fully connected, non-problem specific, ground structures to identify optimal topologies under various different constraints.

The problem is initially provided to the solver without the constraints of (5b) (see appendix B for the full problem statement). In the initial problem, all member flags in  $\mathbf{w}$  can be assumed to be equal to 1 without violating any of the initial constraints. This can be used as a partial warm start, although the speed advantage in explicitly doing so was found to be modest. When a feasible solution is found, the set of members with non-zero areas are identified and each pair from this set (of which there are several orders of magnitude fewer than all pairs of potential members) is checked to see if a crossover joint is produced. If a crossover is found, then an appropriate constraint of the form of equation (5b) is added to the problem, and remains present in the active problem until the final solution is found.

Note also that for multiple load-case problems, optimal solutions are often made up of multiple, almost independent, forms overlain on top of each other. Therefore it is preferable to allow crossovers in the solutions, and to take account of them when computing the total number of joints. i.e. equation (5) becomes:

$$\sum_{j=1}^n v_j + \sum_{g=1}^b \bar{v}_g \leq \eta \quad (6a)$$

$$(w_h + w_i - \bar{v} \leq 1)_{\forall h, i \in X} \quad (6b)$$

where  $\bar{\mathbf{v}} = [\bar{v}_1, \bar{v}_2, \dots, \bar{v}_b]^T$  is a vector of flag variables representing the existence of each possible crossover between members of the ground structure. The length of  $\bar{\mathbf{v}}$ , denoted by  $b$ , will be approximately proportional to  $n^4$ , although it will also depend on the exact positions of the ground structure nodes.

The constraints of equation (6) describe the case where two lines overlap. A similar constraint could be derived for a point where three or more lines intersect. However, identifying these points becomes reliant on the tolerances used in the calculations, and such cases are unlikely to occur in practical situations. As such, this extension will not be considered further in this paper. Note that the general case of three members intersecting at three points (i.e. forming a triangle) is handled correctly by the constraints of equation (6).

When the constraints of equation (6) are implemented using lazy constraints, the size of  $\bar{\mathbf{v}}$  can be greatly reduced.  $\bar{\mathbf{v}}$  becomes a pool of variables, which are assigned to crossovers as required. The pool size should be chosen to be larger than the number of lazy constraints expected to be added, but small enough to not require excessive memory. For the problems shown here, a pool size of 100 was found to be sufficient. In this case, the variables in  $\bar{\mathbf{v}}$  can be set to zero without affecting the optimality of the problem as initially provided; this affects the problem in a similar manner to the variables in  $\mathbf{w}$ .

Initial tests suggested that it was more advantageous to check and impose these lazy constraints each time a feasible integer solution was identified, rather than each time a continuous relaxation was solved. This also reduced the number of times the check was performed, and meant a smaller pool of constraints could be used. This approach has therefore been adopted here. As the solution is not changed by the proposed method, these heuristics impact only the speed with which the solution is obtained, and not the solution itself.

The procedure used to dynamically generate these constraints is shown in figure 2 and algorithm 1. The process to instead forbid crossovers is similar, except

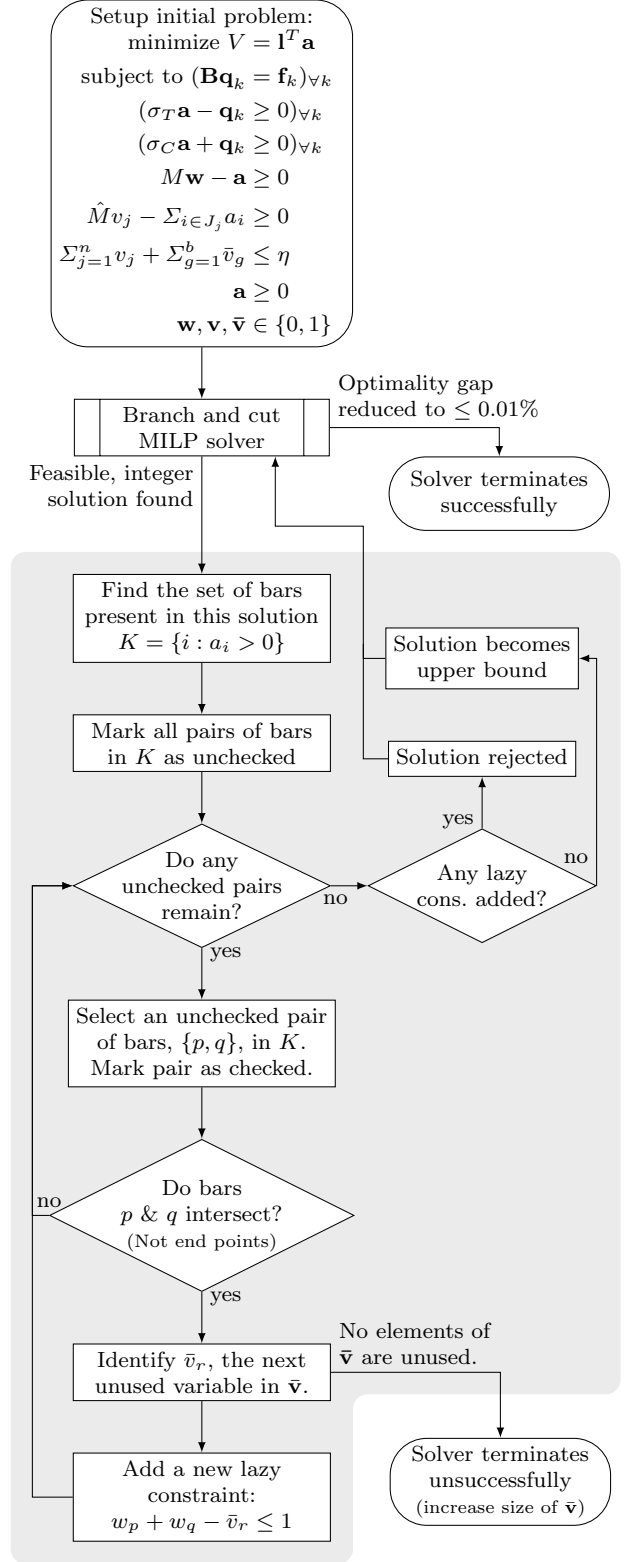


**Fig. 2:** Procedure for runtime constraint generation. Problem shown involves imposing a limit on the number of joints, including ‘crossover joints’. The steps in the shaded region are performed within the callback function which is called by the MILP solver (e.g. Gurobi).



**Algorithm 1** Callback function to limit number of joints, including ‘crossover joints’ (pseudocode).

---

```

# Values from solver for newly found solution:
list of bar member areas, areas
# Data stored from problem setup:
nodes attached to each member, connectivity
coordinates for each node, nodeLocations
list of pointers to  $\bar{\mathbf{v}}$  variables, variablePool
list of pointers to  $\mathbf{w}$  variables, flagVars
# Persistent data throughout an optimization run:
index of most recently used value of  $\bar{\mathbf{v}}$ ,  $r = 0$ 
pairs of members for each lazy constraint, poolPairs = []
# Function called periodically during solver execution:
function CALLBACK( )
    if new integer solution identified then
        realBars  $\leftarrow \{i | \text{areas}(i) > 0\}$ 
        for each pair  $\{p, q\}$  from realBars do
            # Calculate if bars  $p$  and  $q$  intersect using
            data from connectivity and nodeLocations:
            if  $p$  and  $q$  intersect &  $\{p, q\} \notin \text{poolPairs}$  then
                 $r = r + 1$ 
                # Add the constraint:
                flagVars[ $p$ ]+flagVars[ $q$ ]+variablePool[ $r$ ]  $\leq 1$ 
                append  $\{p, q\}$  to poolPairs
            end if
        end for
    end if
    # If no lazy constraints added, the solution is
    accepted as incumbent
end function

```

---

that all references to  $\bar{\mathbf{v}}$  are removed, and the newly added lazy constraint is instead  $w_p + w_q \leq 1$ .

In the procedure, once a constraint has been added to the current reduced problem, it will not be removed. This ensures that the solution obtained by successively adding dynamically generated constraints will converge to the globally optimal solution for the original full problem (i.e., the problem that includes all constraints from the outset). This will occur when the solution for the current reduced problem, comprising only a subset of all possible constraints, is also found to be feasible for the original full problem. For continuous linear optimization problems a similar principle underpins the cutting plane method (Kelley, 1960) and analogous column generation method (Dantzig and Wolfe, 1960), which has been successfully used by Gilbert and Tyas (2003) to develop a computationally efficient ‘member adding’ procedure for large-scale truss layout optimization problems.

Finally, note that the optional geometry optimization post-processing step (see section 3) is not shown in figure 2 and algorithm 1, and is performed following a successful termination of the solver.

### 2.2.3 Imposing symmetry

For a given problem with symmetrical design domain, loads and supports, it is known (Stolpe, 2010) that truss optimization with discrete cross sections may have an optimal solution that is not symmetrical; it will be shown that this is also the case when the MILP problem formulation proposed here is used to impose limits on the number of joints in the structure.

However, it is useful to consider how a requirement for a symmetrical solution can be imposed as an additional constraint, since symmetry will often be preferred for reasons of standardization or aesthetics. It also allows problem size to be significantly reduced, as only half of the design domain needs to be explicitly modelled. To impose a symmetry condition, each symmetrical pair of members is assigned only a single area variable. Additionally, only one integer flag is added to each symmetrical pair of members or nodes. Members that cross the defined line of symmetry, or ‘mirror plane’, are not included, as they can be approximately modelled using nodes that lie on the mirror plane, as shown in figure 3. Thus the number of potential members (and therefore variables) will be reduced to approximately a quarter of the initial number.

To achieve this some modifications to the constraints are needed. A node which lies on the mirror plane, and which is connected only to members which are perpendicular to the mirror plane will not appear to be a joint in the final design. Therefore for nodes lying on the mirror plane, equation (3a) is replaced by

$$\hat{M}v_j - \sum_{i \in J'_j} a_i \geq 0 \quad j = 1, 2, \dots, n \quad (7)$$

where  $J'_j$  is the set of member indices for members connected to node  $j$ , but not including those members which are perpendicular to the mirror plane.

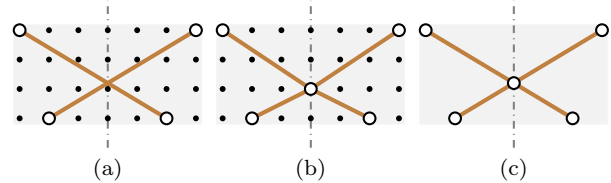


**Fig. 3:** Approximation of members crossing a mirror plane in part of a layout optimization solution: (a) members crossing the mirror plane (shown as a dash-dotted line) permitted, noting that the crossover joint will be counted due to equation (6); (b) members crossing the mirror plane not permitted, with a node on the mirror plane used to approximate (a); (c) geometry optimization used improve (b), with the node on the mirror plane in this case moving to the same location as in (a).

The constraint on the total number of joints must also be modified such that joints that are formed by crossovers or nodes lying remote from the mirror plane are counted twice in the computations.

#### 2.2.4 Limits on the angle between members

A feature that can make Michell structures difficult to manufacture is the presence of small angles between adjacent members, especially in fan-type regions. To prevent this, integer constraints can be added in the layout optimization stage as follows:

$$(w_h + w_i \leq 1)_{\forall \{h,i\} \in D} \quad (8)$$

where  $D = \{\{h_1, i_1\}, \{h_2, i_2\}, \dots\}$  is the set containing unordered pairs of indices for all pairs of members that form an angle that is smaller than  $\mu$ , the minimum permitted joint angle. Note that this angle may be formed either at a node which is common to both members or at a point where the members intersect, partway along one or both of their lengths.

Again, the full formulation is very time consuming to compute as the number of these constraints is approximately proportional to  $n^4$ . These constraints are therefore also implemented as lazy constraints. The procedure is similar to that outlined in figure 2; however references to  $\bar{\mathbf{v}}$  are removed, and the check on each pair of members,  $p$  &  $q$ , is to identify if they form an angle (either at a crossover point or at an end node) which is outside the permitted range.

### 3 Geometry optimization post-processing step

Once the integer programming stage has been completed, the resulting structure can be further refined by the use of the geometry optimization (GO) post-processing rationalization method developed by He and Gilbert (2015). This adds the nodal positions of the structure as design variables, resulting in a non-linear and non-convex problem. This stage is optional as the structure generated by solving the MILP problem will satisfy all the specified design constraints. However it is attractive as it further reduces the volume and may allow results which match analytically derived solutions from the literature to be obtained.

As the geometry optimization problem is non-convex, it is not generally possible to solve this to a guaranteed globally optimal solution, thus this method relies on the starting point provided by the topology optimization being sufficiently close to the optimal point. A finding of this paper is that the solution of the MILP problem may successfully be used as the starting point for geometry optimization.

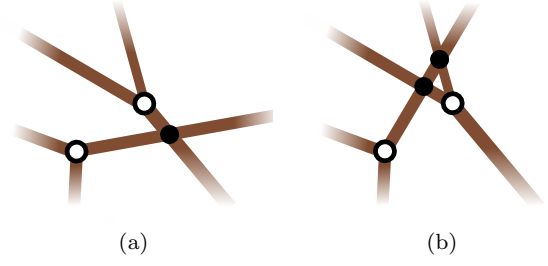


**Fig. 4:** Detail of a layout, showing the importance of converting ‘crossover joints’ to standard joints between the MILP and geometry optimization post-processing stages when imposing a limit on the total number of joints: (a) before geometry optimization, containing 3 joints in this region; (b) after geometry optimization, containing 4 joints in this region.

During the geometry optimization stage, it will be important to ensure that the solutions continue to be feasible with respect to the practical constraints imposed in the previous sections. The remainder of this section will outline the required modifications to the algorithm proposed by He and Gilbert (2015). Note that the original buildability constraints, involving integer variables, need not be included at this stage, as the overall topology is generally not significantly changed. Instead the buildability constraints are reformulated as constraints on the nodal positions, leading to a non-linear but continuous problem.

When a limited number of joints are permitted, no additional constraints will be required in the geometry optimization stage. This is because the number of joints in the problem generally remain constant, or will reduce due to joint merging, or due to all connected members at a joint vanishing.

The only possible means by which new joints can appear is if the topology is changed by a member passing over another joint, as shown in figure 4. However, this situation can easily be avoided by converting the topology between the MILP and GO stages such that all ‘crossover joints’ become standard joints.

When a limit on the angle between members has been imposed, this must be converted to a continuous constraint on the joint coordinates. This will be in the form:

$$\frac{\vec{CA} \cdot \vec{CB}}{|\vec{CA}| |\vec{CB}|} \leq \cos(\mu) \quad (9)$$

where C is the joint common to two members, A and B are the other joints of each member, and  $\mu$  is the imposed minimum angle. Note that this requires point C to be a standard joint; therefore ‘crossover joints’ must again be converted to standard joints before the geometry optimization stage.

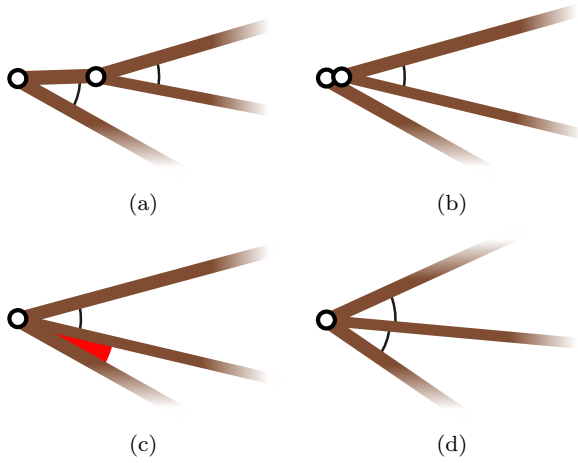


**Fig. 5:** Detail of area containing branched members during the geometry optimization post-processing step: (a) initial branched member topology; (b) joints moving closer together, though as the bottom and middle member do not meet, the angle between them is not checked; (c) joints are merged, but the bottom and middle members now have an angle constraint, which is violated; (d) the feasibility restoration phase finds a point at which all constraints are satisfied, but the geometry is now quite different to the MILP starting point.

In some cases where a minimum angle is imposed, additional parameters may be required for the geometry optimized results to be meaningful. For example, when a branch type form (as shown in figure 5a) is identified as the optimal solution of the integer programming problem, the branch joint tends to move towards the ‘root’ joint, as in figure 5b. The joint merging phase will then combine the two joints, and there then may be pairs of members which violate the angle constraint, figure 5c. If the permitted movement radius of the joints is sufficiently large, the feasibility restoration phase of the non-linear solver is likely to be able to find a new feasible solution using the new topology, figure 5d.

This new form may now be notably different from the initial starting point, and therefore potentially inefficient. However, simply eliminating the joint merging step would result in a final design where two joints were infinitesimally close together. A minimum member length constraint can be added to prevent this, i.e.

$$|\overrightarrow{AB}| \geq l_{min} \quad (10)$$

where A and B are the end points of the member, and  $l_{min}$  is the minimum permitted length. This constraint is only explicitly required in the geometry optimization stage, since during layout optimization short members can simply be omitted from the ground structure. Here, length limits have generally been added only in the geometry optimization stage, with  $l_{min}$  being set at or

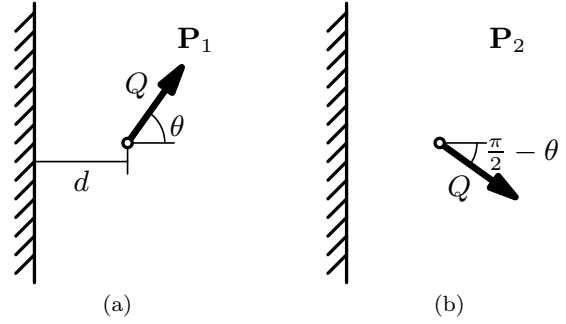


**Fig. 6:** Simple cantilever: details of applied load cases, (a)  $P_1$ , and (b)  $P_2$ .

below the nodal spacing of the original ground structure.

Within the examples of this paper, it has been observed that the geometry optimization procedure did not need to make use of several considerations of He and Gilbert (2015), due to the simplified nature of the starting structures. For example, new cross-over joints were added only at the initialization geometry optimization. Also, the joint merging procedure was triggered only in the cases with branching type structures. From this, it can be seen that the structures produced by geometry optimization are generally topologically very similar to the solutions obtained at the end of the initial MILP stage.

## 4 Numerical examples

All numerical example problems were run on an Intel Core i7-6700HQ CPU @ 2.60GHz, with 16GB of RAM. Gurobi 7.0.1 (Gurobi Optimization LLC 2018) was used to solve the MILP problems, with 4 physical cores available for use. All problems mentioned were solved to a 0.01% optimality gap (the default value when using Gurobi). For practical usage, this level of accuracy may not be required, and a higher value can be used to reduce computation time. All other Gurobi parameters were set to their default value. The computational times reported are wall clock times, and include the time taken to set up the problem.

### 4.1 Simple cantilever

The first example involves the setup shown in figure 6. This consists of two load-cases denoted as  $P_1$  and  $P_2$ . These each contain a single point load, which are both applied at a given angle  $\theta$  to the horizontal at point  $(d, 0)$ , and have magnitude,  $Q$ .

Derivations of the minimum volume structures, both unconstrained and with a maximum of 3 joints, can be found in appendix C. The optimal member sizes and support locations are shown in figure 8.

It can be seen that even for this very simple problem, the behaviour is quite complex and unintuitive. The rationalized structures are not closely linked to the equivalent un-rationalized form, which may make such structures difficult to obtain by intuitive or mathematical post processing. The volume penalty caused by imposing the three joint limit is at most 20.3%.

Table 1 shows the difference between the theoretical and numerical results for this example. The MILP results were found with nodes permitted only along the support, at  $0.02d$  spacing over  $-1.5d \leq y \leq 1.5d$  (i.e. 152 nodes, including the loaded node). As none of the members in the ground structure crossed, crossover constraints were not required. Geometry optimization (GO) was also performed to further refine the results.

The numerical and analytical volumes can be observed to be in close agreement. At  $\theta = \theta_2$  a discontinuity occurs, where two distinct results are equally optimal (see appendix C.2.3). Here, the MILP solver identifies one of these solutions. Then, use of the interior point method for the GO stage perturbs this solution, resulting in identification of the alternative solution.

When a limit on the angle between members is imposed, solutions may be more complex in form, involving members that do not simply directly connect the loaded point and a point on the support. Therefore numerical solutions for joint angle limits have been calculated using a  $5 \times 13$  grid of nodes, and a fully connected ground structure ( $m = 2080$ ).

Figure 7 shows results for the problem with angle  $\theta = \frac{3\pi}{8}$ , i.e. as shown in figure 8e and 8i. The scenario is subjected to limits on the minimum angles between members of  $35^\circ$  and  $45^\circ$ . The unusual topologies identified demonstrate the difficulty in trying to identify optimal solutions for this problem analytically or manually.

The problem was solved firstly by imposing all angle constraints from the outset ('basic formulation'), and then by implementing the angle limit (i.e. equation (8)) using lazy constraints. Both implementations produced identical final results; however it can be seen that the use of lazy constraints reduced the time required by approximately a factor of 20.

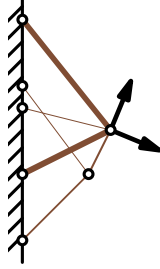
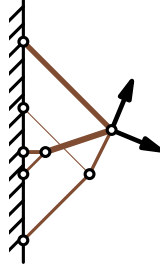
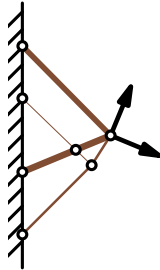
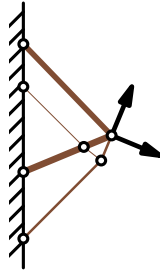
Figure 7 also shows the result of applying geometry optimization post-processing. Despite the different topologies identified in the MILP stage, similar topologies are found after geometry optimization. Additionally, it can be observed that the volumes after geometry optimization are both lower than the three joint form

shown in figure 8i, demonstrating that the more complex topology is beneficial, albeit only by 3.6% and 2.8% respectively. This suggests that, although the geometry optimization process is non-convex and therefore cannot be proven to identify a global optimum, the starting points provided by the MILP formulation appear to be sufficient to provide good results.

## 4.2 Michell cantilever

### 4.2.1 Problem specification

The proposed methods are now applied to a classical Michell cantilever problem, as shown in figure 9. The theoretical minimum volume can be found using equations derived by Chan (1960) to be  $V_T = 39.43Qd$ . Discretized versions of this problem have been studied by Prager (1977) and Achtziger and Stolpe (2007). In both cases, the topology of the optimal structures was man-

	Minimum angle	$35^\circ$	$45^\circ$
Results after MILP			
	Volume	2.160	2.198
	Time (basic formulation)	167 seconds	180 seconds
	Time (lazy constraints)	7 seconds	11 seconds
	Speedup	$23.8\times$	$16.3\times$
Results after MILP + GO			
	Volume	2.082	2.099

**Fig. 7:** Simple cantilever: numerical results for problem with specified minimum angles between members (load inclination  $\theta = \frac{3\pi}{8}$ ).

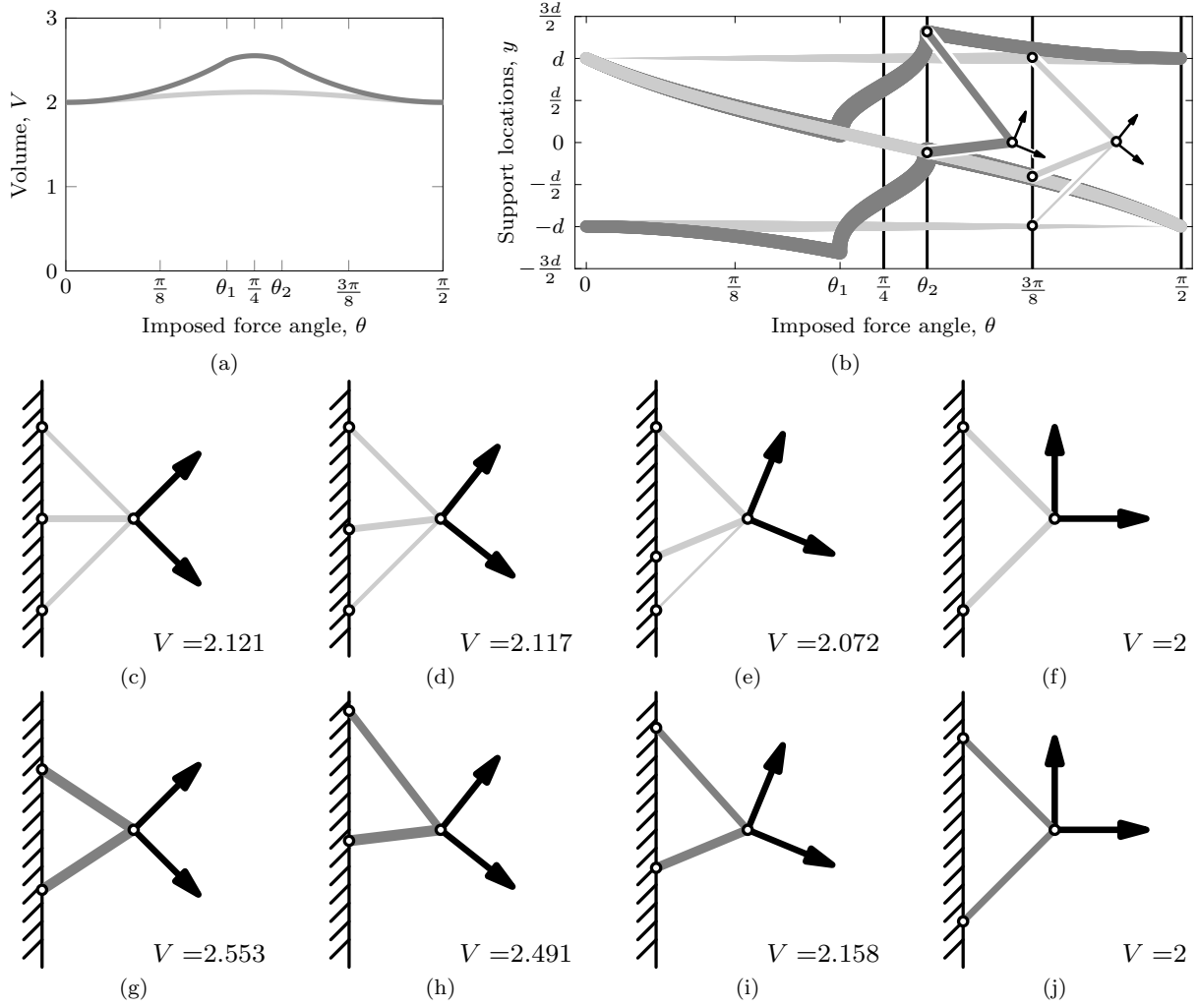


**Fig. 8:** Simple cantilever: theoretical results, (a) volumes of optimal structures with unlimited complexity (light grey) and maximum 3 joints (dark grey) for values of  $\theta$  between 0 and  $\frac{\pi}{2}$ ; (b) locations of support points for optimal structures with unrestricted complexity (light grey) and maximum 3 joints (dark grey), with line width proportional to the area of the member which connects there (forms (e) and (h) shown for context); (c)-(f) forms of optimal structures with unlimited complexity for  $\theta = \frac{\pi}{4}, \theta_2, \frac{3\pi}{8}, \frac{\pi}{2}$ ; (g)-(j) forms of optimal structures with only 3 joints for  $\theta = \frac{\pi}{4}, \theta_2, \frac{3\pi}{8}, \frac{\pi}{2}$ .

**Table 1:** Simple cantilever: comparison of theoretical and numerical methods for problem with 3 joints. (Where  $y_A$  and  $y_b$  refer to the vertical distance between the height at which the point loads are applied, and the upper and lower support locations respectively.  $\theta_2$  is as marked in figure 8b. For more information see appendix C.)

$\theta$	Theoretical			MILP results				MILP + GO results		
	$y_A(d)$	$y_B(d)$	$V\left(\frac{dQ}{\sigma}\right)$	$y_A(d)$	$y_B(d)$	$V\left(\frac{dQ}{\sigma}\right)$	Time (s)	$y_A(d)$	$y_B(d)$	$V\left(\frac{dQ}{\sigma}\right)$
$\frac{\pi}{4}$	0.657	0.657	2.553	0.660	0.660	2.553	10	0.659	0.659	2.553
$\theta_2$	1.308	0.116	2.491	1.300	0.120	2.491	7	1.222	0.174	2.491
	1.222	0.174								
$\frac{3\pi}{8}$	1.117	0.414	2.158	1.120	0.420	2.162	3	1.117	0.414	2.158
$\frac{\pi}{2}$	1.000	1.000	2.000	1.000	1.000	2.000	2	1.000	1.000	2.000

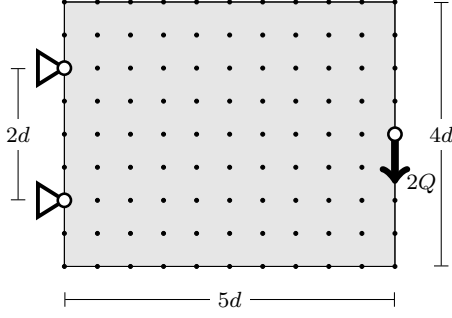


**Fig. 9:** Michell cantilever: problem specification. (Fully connected ground structure used.)

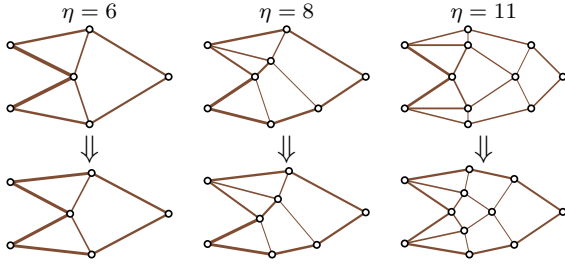


**Fig. 10:** Michell cantilever: Results after MILP (top) and GO (bottom) stages. The volume difference between MILP and GO solutions is 1%, 1.4% and 1.6% respectively.

ually inferred from the continuum form; however their observations are useful for comparative purposes.

A fully connected ground structure of 99 nodes is used here; this contains 4851 potential members. The solution to the standard layout optimization problem at this resolution has a volume of  $40.45Qd$ , an increase of 2.6% over  $V_T$ , although this reduces to +0.8% after GO is applied, and the resulting solution has 20 joints.

#### 4.2.2 Limiting the number of joints

To set up the problem with all crossover constraints from the beginning requires checking 11,763,675 pairs of members, of which 2,795,779 produce a constraint. (Simply performing these checks was found to take nearly 20 minutes with the C++ code used here.)

Alternatively, using lazy constraints, the problem can be set up almost instantly, producing an initial problem with 14,553 variables and 14,844 constraints. The problem was first solved using lazy constraints to prevent crossovers but without limiting the number of joints. This produced a structure with 12 joints, and required 240 lazy constraints, around 0.01% of the full number. This is shown as the 12 joint result in table 2 and figure 11.

The problem was then solved with limits imposed on the maximum numbers of joints,  $\eta$ , from 3 to 11. The results can be seen in table 2 and figures 11 and 10, with further details available in Online Resource 1. Note that the longest time taken to solve any of these problems was under 5 minutes, around a quarter of the time needed just to formulate the full problem.

It may be observed that the forms for 3, 6, or 11 joints agree with those found by Prager (1977)<sup>1</sup>. Additionally the solution with 8 joints corresponds to similar ones mentioned by Mazurek et al (2011, fig 22).

#### 4.2.3 Other related problems

Prager extended his results to postulate a solution to the related problem of minimizing total cost, comprising a material cost and a fixed cost per joint. It is possible to reformulate the integer programming problem to consider this directly, by changing the objective function to be of the form

$$\text{minimize } \mathbf{l}^T \mathbf{a} + c_j \mathbf{v} \quad (11)$$

where  $c_j$  is the normalized cost of a joint.

However, (11) may alternatively be expressed in the form of an equation, plotted as a straight line on figure 11. The example objective function shown on figure 11, is a line of constant cost when the joint cost,  $c_j$ , is equal to the cost of a volume increase of 0.7% of the minimum volume,  $V_T$ . In this case, the solutions with 6 and 8 joints are equally optimal. However, the 7 joint solution has a higher cost; it is therefore not optimal for any objective function in the form of equation (11).

Prager's solution to this problem over a range of values for  $c_j$  consisted of only the 3, 6 and 11 joint solutions. From figure 11 this can now be extended to add solutions with 4, 5, and 8 joints. The ranges of joint cost  $c_j$  for which each solution is optimal is shown in the final column of table 2.

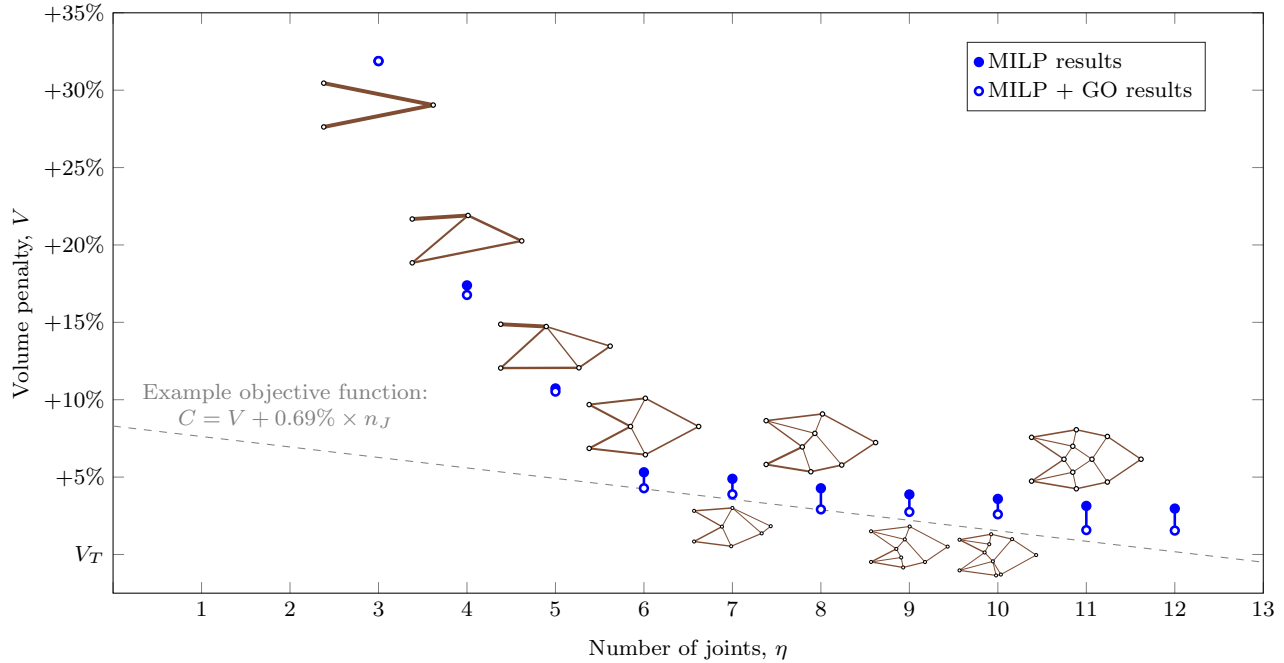
Limiting the number of members in a solution is another concern for ensuring practicality. As this is a single load-case problem, and due to the Simplex solver used to solve the LP sub-problems of the MILP problem, the optimal structures identified are all likely to be statically determinate, meaning that the number of joints is directly linked to the number of members (number of members =  $2\eta - 4$ ). Therefore this method can also be used as a proxy for limiting the number of members.

<sup>1</sup> Note that Prager (1977) gives a volume of  $36.41Qd$  for the 11 joint solution; this can clearly be seen to be incorrect, as it is lower than the minimum value from the equations of Chan (1960). However, the form given by Prager is correct.



**Table 2:** Michell cantilever: results with limits imposed on the total number of joints.

Permitted no. of joints	Number of Lazy constraints added	Time <sup>a</sup> (s)	Volume after		Optimal for joint costs		
			MILP	MILP+GO			
3	0	10	+31.9%	+31.9%	15.11%	$\leq c_j \leq$	$\infty$
4	0	16	+17.4%	+16.8%	6.25%	$\leq c_j \leq$	15.11%
5	3	74	+10.7%	+10.5%	6.24%	$\leq c_j \leq$	6.25%
6	4	72	+ 5.3%	+ 4.3%	0.69%	$\leq c_j \leq$	6.24%
7	4	117	+ 4.9%	+ 3.9%	N/A		
8	0	257	+ 4.3%	+ 2.9%	0.45%	$\leq c_j \leq$	0.69%
9	3	291	+ 3.9%	+ 2.8%	N/A		
10	9	196	+ 3.6%	+ 2.6%	N/A		
11	17	133	+ 3.1%	+ 1.6%	0.09%	$\leq c_j \leq$	0.45%
12 <sup>c</sup>	240	44	+ 3.0%	+ 1.5%			
20 <sup>d</sup>	—	4	+ 2.6%	+ 0.8%			

<sup>a</sup> Elapsed time for MILP stage.<sup>b</sup> Assumes next optimal design is the continuous layout optimization solution; designs with 13-19 joints may increase this value.<sup>c</sup> Result of preventing crossovers without limiting the total number of joints.<sup>d</sup> Continuous layout optimization result, after crossover generation.**Fig. 11:** Michell cantilever: results with limits imposed on the total number of joints. (Volume shown as percentage above theoretical minimum volume,  $V_T = 39.43Qd$ . Forms shown after MILP and GO. An example cost function is also shown where each joint has a constant cost, equal to an increase in volume 0.7% of  $V_T$ .)

#### 4.2.4 Limiting the angles between members

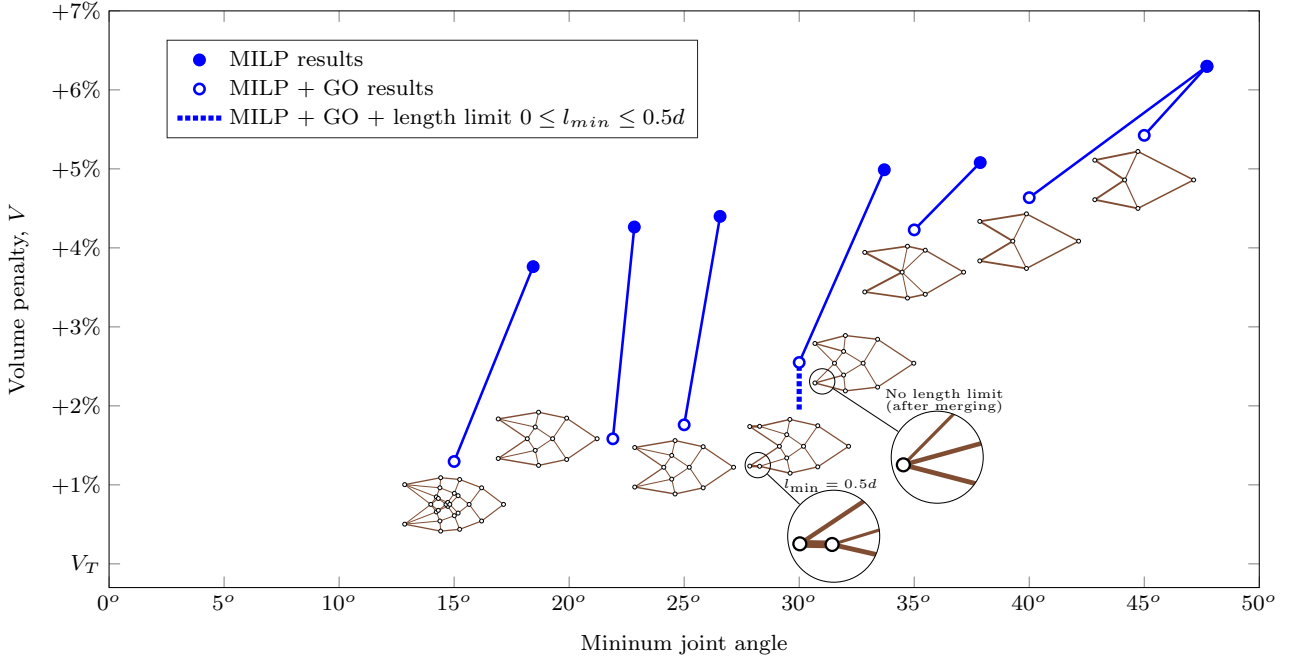
Solutions for the same Michell truss problem, but with imposed minimum angle limits, from  $15^\circ$  to  $45^\circ$  are shown in table 3 and figure 12, with further details provided in Online Resource 2. It can be seen that the topologies shown in figure 12 are symmetrical, and several are distinct from those shown in figure 11.

In the layout optimization stage only a limited number of member angles are available; therefore the structures identified do not have a minimum angle that exactly corresponds to the limit. Generally, once the geometry optimization post-processing step has been applied, the angle limits become active, although this is not always the case (e.g. in the case of the  $20^\circ$  limit). In some cases, such as the  $40^\circ$  and  $45^\circ$  solutions, the same initial result is identified for multiple angle limits, and

**Table 3:** Michell cantilever example: results with limited joint angle. (Volume shown as percentage above theoretical minimum volume.)

Permitted angle between members	Number of lazy constraints added	Time (s)	After MILP Min. angle	Volume	After MILP+GO Min. angle	Volume
45°	3462	2341	47.7°	+6.3%	45°	+5.4%
40°	1415	2009	47.7°	+6.3%	40°	+4.6%
35°	805	234	37.9°	+5.1%	35°	+4.2%
30°	1377	537	33.7°	+5.0%	30°	+2.5% <sup>a</sup>
25°	665	344	26.6°	+4.4%	25°	+1.8%
20°	349	91	22.8°	+4.3%	21.9°	+1.6%
15°	73	21	18.4°	+3.8%	15°	+1.3%

<sup>a</sup> GO with a length limit of  $0.5d$  (i.e. equal to shortest length in ground structure) gives volume of +2.51%, GO without a length limit and after joint merging and subsequent feasibility restoration gives a volume of +2.55%.

**Fig. 12:** Michell cantilever: results with limited joint angle. (Volume given as percentage above theoretical minimum volume. Forms shown after MILP and GO. For branched forms, results both with and without a length limit are shown.)

the solutions only diverge in the geometry optimization stage.

Most results in figure 12 are shown after geometry optimization with no length limit imposed. However, for the limit of 30°, a branching form similar to that shown in figure 5 was identified. During the geometry optimization stage for this result, the merging of the ‘root’ and ‘branch’ joint occurred, leading to a significant change in topology. The solution reduces in volume as the distance between the branching joints approaches zero, but then increases again in order to restore feasibility of the new angle constraint.

A length limit was therefore imposed to produce more meaningful results. For practical purposes, this

is likely to be defined by the same manufacturing process that dictates the minimum angle between members; here  $l_{min}$  will be set at or below the length of the shortest member in the ground structure ( $0.5d$ ). When  $l_{min} = 0.5d$ , the new volume was only slightly smaller (+2.51% vs. +2.55%). However, for small values of  $l_{min}$  the volume reduced to +1.9%; this is shown as a dotted line in figure 12. Both the result with no length limit, and with  $l_{min} = 0.5d$ , are illustrated in figure 12.

By comparing the results in table 2 and 3, it can be seen that the angle limits require a greater number of lazy constraints to be added, leading to correspondingly longer execution times. This is likely to be due to the fact that, when a limit on the number of joint is



imposed, the initial constraints significantly reduce the number of feasible integer topologies before any lazy constraints are required. However, the maximum number of lazy constraints added in table 3 was at most 0.3% of the total number possible (for the  $45^\circ$  limit), showing that the advantage of using lazy constraints is still very significant.

#### 4.3 Spanning example

A more complex, two load-case problem is now considered. This consists of two point loads which are applied separately, and transmitted to a pair of pinned supports; the problem specification is shown in figure 13.

This is a symmetrical problem, and therefore the minimum volume structure is also symmetrical when no discrete buildability constraints are imposed. The minimum volume solution,  $V_T$ , is given by Sokół and Rozvany (2013) as  $3.44363 \frac{Qd}{\sigma}$ . The design domain is discretized using a grid of 90 nodes. The layout and geometry optimization solution for this resolution had a volume 1.2% greater than the theoretical optimal value.

The problem was first solved without imposing a requirement for a symmetrical solution. Solutions with maximum numbers of joints,  $\eta$ , ranging from 5 to 9 were found. Solutions with odd numbers of joints were found to be symmetrical, and were equal to the corresponding results shown in figure 15 and table 4. However, the solutions with 6 and 8 joints were asymmetric, as shown in figure 14. Note that the 8 joint example approximately consists of one half from each of the topologies with 7 and 9 joints.

Due to these findings, and the general preference in practice for symmetrical designs, the model was modified to explicitly impose a symmetry condition about the centre line, using equation (7) and the method outlined in section 2.2.3. Solutions were again sought for 6 and 8 joints; however, the optimal solutions were found to be identical to the solutions for 5 and 7 joints respectively. This demonstrates the lack of a symmetrical optimal solution, a characteristic previously noted in the solutions of truss optimization problems with discrete cross sections, is also a characteristic of the problem with continuous cross sections when limits are imposed on the numbers of joints.

Results for various numbers of joints are given in table 4 and figure 15, with further details provided in Online Resource 3. The use of the constraints from equation (5) (to prevent ‘crossover joints’) and equation (6) (to include ‘crossover joints’ in the total number of joints, to be limited), have both been tested. When ‘crossover joints’ are not permitted, only structures with up to 17 joints can be identified; results in

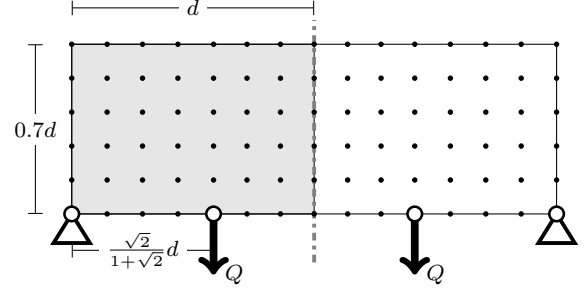


**Fig. 13:** Spanning example: problem specification, after Sokół and Rozvany (2013). (The two point loads are applied separately. Grey shading shows the area modelled when the symmetry condition is imposed.)

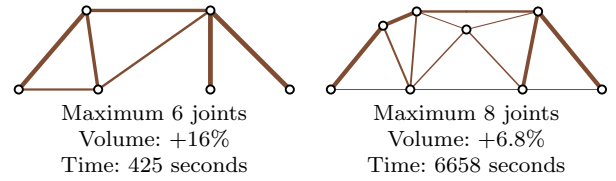


**Fig. 14:** Spanning example: results after MILP and GO showing asymmetric optimal solutions.

the range  $17 < \eta < 45$  can only be identified by allowing ‘crossover joints’ and explicitly including them in the total limit.

The problem of including the ‘crossover joints’ is a more relaxed version of the problem where ‘crossover joints’ are prevented. Therefore solutions from the MILP problems that take account of crossovers must be at least as good as solutions found when these are prevented. However, the geometry optimization stage is non-linear, and therefore local optima may result, depending on the initial point provided. It can be seen that for the 15 and 17 joint solutions, local optima have been identified; both methods appear to be susceptible to this. However, the volume difference is less than 0.2%, demonstrating that at this point multiple options are available of similar volume and complexity, any one of which would likely be suitable for practical application. Many commercial solvers (e.g. IBM Corp. 2015; Gurobi Optimization LLC 2018) provide the ability to record a pool of nearly optimal solutions, which may be of use in addressing this issue.

As a multiple load case problem, the solutions identified are generally not statically determinate and therefore there is not a direct relationship between number of members and number of joints. However, figure 16 shows that there is still a very strong correlation between the number of members and the number of joints. Therefore, for practical purposes, this method is still

likely to produce useful results when structures with few members are desired.

#### 4.4 Commentary

The numerical examples described here have demonstrated the applicability of the method to single

and multiple load case problems in 2D. The method described could also be immediately applied to 3D problems, if crossovers are considered to occur at points where the centrelines of two members intersect exactly, or to within some predefined tolerance. Some modification of the approach described would be necessary in order to prevent the outer faces of members intersecting, taking into account the chosen member cross-section

**Table 4:** Spanning example: results with symmetry condition imposed and limits on numbers of joints. (Bold values highlight when the two methods produce different results.)

Permitted number of joints	Counting ‘crossover joints’				Preventing ‘crossover joints’			
	No. of lazy cons. added	Time <sup>a</sup> (s)	Volume after		No. of lazy cons. added	Time <sup>a</sup> (s)	Volume after	
			MILP	MILP+GO			MILP	MILP+GO
5	0	7	+59.5%	+58.1%	0	6	+59.5%	+58.1%
7	0	56	+8.8%	+8.4%	0	31	+8.8%	+8.4%
9	7	52	+5.9%	+5.1%	14	77	+5.9%	+5.1%
11	26	345	+5.2%	+4.1%	33	154	+5.2%	+4.1%
13	24	528	<b>+4.5%</b>	+3.3%	154	446	<b>+4.5%</b>	+3.3%
15	28	436	<b>+3.5%</b>	<b>+2.7%</b>	48	184	<b>+3.7%</b>	<b>+2.5%</b>
17	40	504	<b>+3.4%</b>	<b>+2.3%</b>	444 <sup>b</sup>	455 <sup>b</sup>	<b>+3.5%</b>	<b>+2.4%</b>
19	76	8150	+3.1%	+2.4%				
21	68	6833	+3.0%	+2.0%				
31	90	138265	+2.7%	+1.8%				
45 <sup>c</sup>	–	6	+2.3%	+1.2%				

<sup>a</sup> Elapsed time for MILP stage.

<sup>b</sup> Refers to forbidding crossovers with no limit on number of joints, which produces a structure with 17 joints.

<sup>c</sup> Layout optimization result, which produces structure with 45 joints.

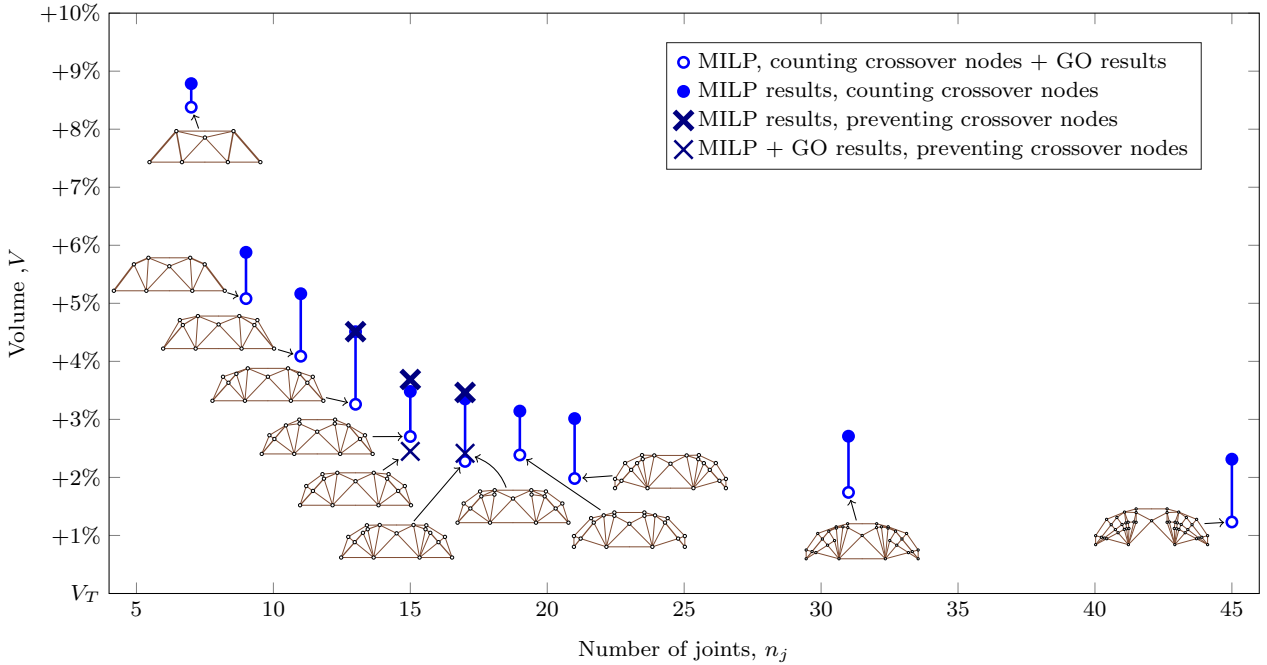


**Fig. 15:** Spanning example: results with limited numbers of joints. (Volume shown as percentage above theoretical minimum volume. Forms shown are after MILP and GO, with symmetrical solutions required. Results preventing crossover joints are shown only where they differ from the result of counting the crossover joints.)

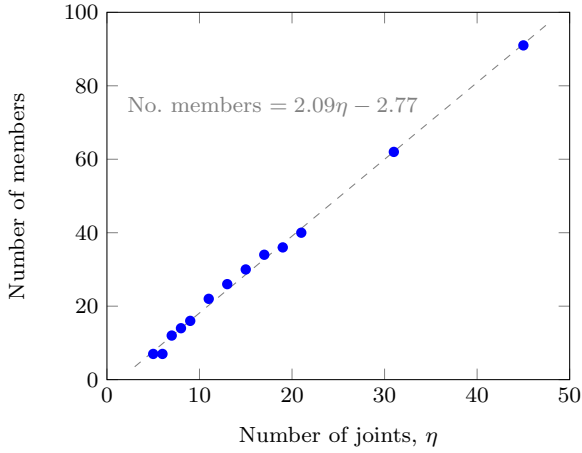


**Fig. 16:** Spanning example: number of joints and members in solutions where the number of joints has been limited, also showing best fit line. ( $R^2 = 0.997$ ).

form. As is generally the case with layout optimization methods, a greater number of nodes would be required to fill a 3D domain to a similar density compared to a 2D domain, increasing the computational requirements.

The method has proved effective at identifying simple truss structures. However, from a practical point of view, the simplest structure may not be a truss. For example, in the case of the spanning example considered in section 4.3, a single beam along the base of the domain would generally be considered to provide a simpler, albeit less efficient, solution. When bending is involved the chosen cross-section form needs to be taken into account, and the associated numerical formulation is somewhat more complex. However, many of the principles described herein are still applicable in this case.

## 5 Conclusions

It was found that the use of dynamically generated lazy constraints can significantly reduce the computational time required to solve layout optimization problems with discrete buildability constraints. Specifically, the use of lazy constraints permitted ‘crossover joints’ to be dealt with in a computationally efficient manner. Improvements in speed of over a factor of 20 were observed for relatively small problems; this difference is likely to increase further as problem size increases. This allows the proposed method to be used for problem sizes that would be intractable using the standard formulation.

Rationalized structures with limited numbers of joints or limited angles between adjacent members have been identified for a range of problems, including those

with multiple load cases, using a two stage process incorporating a layout optimization stage and a geometry optimization stage. Using this process, results were found to agree with analytically derived results from the literature, suggesting that the proposed separation of topology and geometry/shape optimization is effective, and that MILP solutions are suitable starting points for a non-linear optimization stage.

The rationalized structures were often found to have a volume within a few percent of the corresponding minimum volume Michell structure, whilst being far more feasible to construct. A number of interesting features of these solutions have been observed:

- Symmetrical problems do not always have symmetrical optimal solutions when limits on the numbers of joints are imposed. Therefore, the decision to use symmetry to reduce the computational expense of a problem should be made with care.
- Multiple optimal or near optimal solutions are possible. Many numerical methods, such as geometry optimization, will identify only one of these, although there may be many which would be acceptable for practical use.
- When the angle between adjacent members is limited, ‘branching’ type structures may occur. This may then require the addition of a minimum length constraint to produce practical results.
- When the number of joints is limited, it was found that the number of members in the solution was strongly linked to the number of joints. This may provide a computationally efficient proxy problem.

**Acknowledgements** The authors would like to thank LimitState Ltd and Linwei He for access to code implementing the geometry optimization procedure. The financial support of Expedition Engineering and EPSRC (under grant number EP/N023471/1) is gratefully acknowledged.

*Conflict of Interest:* The authors declare that they have no conflict of interest.

## A Comparison of problem formulations

Several equivalent formulations are possible to ensure that the variables  $\mathbf{v}$  accurately represent the existence of each node. The method that is used within this paper links the value of  $v_j$  to the sum of the members connected to node  $j$  using equation (3a), reproduced here:

$$\hat{M}v_j - \sum_{i \in J_j} a_i \geq 0 \quad j = 1, 2, \dots, n \quad (12)$$

This formulation will be referred to as formulation A.

An alternative formulation, which may be considered to be more standard in the general integer programming community, is to link the value of  $v_j$  to the flag variables of the members connected to node  $j$ :

$$Nv_j - \sum_{i \in J_j} w_i \geq 0 \quad j = 1, 2, \dots, n \quad (13)$$

In this formulation, the arbitrary large number,  $\hat{M}$ , is replaced by  $N$ , the maximum number of members which will be permitted to connect to any node. This formulation will be referred to as formulation  $\mathcal{W}$ .

For both  $\mathcal{A}$  and  $\mathcal{W}$ , the remainder of the formulation is as described in section 2.2. The two formulations produce identical solutions; however the computational requirements may differ.

To investigate this, both formulations have been used to test the Michell cantilever problem with a limit imposed on the number of joints. Full results using form  $\mathcal{A}$  were given in table 2. A comparison of the speed of the two formulations is given in table 5.

It can be seen that formulation  $\mathcal{A}$  takes roughly half the time to solve the problems compared to formulation  $\mathcal{W}$ . This is as expected if the characteristics of the two formulations prior to the addition of any lazy constraints is considered. Formulation  $\mathcal{A}$  initially begins with all the member flags,  $\mathbf{w}$ , unconstrained; i.e. they may all be set equal to 1 without making any potential solution infeasible. It only becomes necessary to begin to branch on any variable  $w_i$  once the member  $i$  is part of an added crossover constraint.

In contrast, formulation  $\mathcal{W}$  couples all integer variables from the outset, leading to a much more challenging initial problem. This outweighs the potential benefits of eliminating  $\hat{M}$ .

Formulation  $\mathcal{A}$  has therefore been used to generate all results contained in the main body of the present paper.

Note that the findings in this section apply only to problems where the number of joints is limited, as limiting the angle between members does not require the presence of member flags,  $v_j$ .

## B Full problem statements

For clarity, full problem statements for the problems solved in this paper are given here. Symbols are as defined in the main body of the paper, and are also summarized in table 6. Firstly, the problem to restrict the number of joints in a

**Table 5:** Speed comparison between formulations for defining the node flag variables,  $\mathbf{v}$ . Problem is the Michell cantilever with limited number of joints, as shown in table 2 and figure 11.

Permitted number of joints	Formulation $\mathcal{A}$		Formulation $\mathcal{W}$	
	No. of lazy cons. added	Time (s)	No. of lazy cons. added	Time (s)
3	0	10	0	14
4	0	16	0	58
5	3	74	8	137
6	4	72	0	95
7	4	117	7	222
8	0	257	0	686
9	3	291	1	571
10	9	196	10	376
11	17	133	17	224

solution, whilst preventing crossover nodes is given by:

$$\text{minimize } V = \mathbf{l}^T \mathbf{a} \quad (14a)$$

$$\text{subject to } (\mathbf{B}\mathbf{q}_k = \mathbf{f}_k)_{\forall k} \quad (14b)$$

$$(\sigma_T \mathbf{a} - \mathbf{q}_k \geq 0)_{\forall k} \quad (14c)$$

$$(\sigma_C \mathbf{a} + \mathbf{q}_k \geq 0)_{\forall k} \quad (14d)$$

$$\mathbf{M}\mathbf{w} - \mathbf{a} \geq 0 \quad (14e)$$

$$\hat{M}v_j - \sum_{i \in J_j} a_i \geq 0 \quad j = 1, 2, \dots, n \quad (14f)$$

$$\sum_{j=1}^n v_j \leq \eta \quad (14g)$$

$$(w_h + w_i \leq 1)_{\forall \{h,i\} \in X} \quad (14h)$$

$$\mathbf{a} \geq 0 \quad (14i)$$

$$w_i \in \{0, 1\} \quad i = 1, 2, \dots, m \quad (14j)$$

$$v_j \in \{0, 1\} \quad j = 1, 2, \dots, n \quad (14k)$$

The problem initially supplied to the solver is as above but excluding the constraints of (14h), which are generated as required during the running of the solver.

The problem to count ‘crossover joints’ as contributing to the limiting number of joints is fully stated as:

$$\text{minimize } V = \mathbf{l}^T \mathbf{a} \quad (15a)$$

$$\text{subject to } (\mathbf{B}\mathbf{q}_k = \mathbf{f}_k)_{\forall k} \quad (15b)$$

$$(\sigma_T \mathbf{a} - \mathbf{q}_k \geq 0)_{\forall k} \quad (15c)$$

$$(\sigma_C \mathbf{a} + \mathbf{q}_k \geq 0)_{\forall k} \quad (15d)$$

$$\mathbf{M}\mathbf{w} - \mathbf{a} \geq 0 \quad (15e)$$

$$\hat{M}v_j - \sum_{i \in J_j} a_i \geq 0 \quad j = 1, 2, \dots, n \quad (15f)$$

$$\sum_{j=1}^n v_j + \sum_{g=1}^b \bar{v}_g \leq \eta \quad (15g)$$

$$(w_h + w_i - \bar{v} \leq 1)_{\forall h,i \in X} \quad (15h)$$

$$\mathbf{a} \geq 0 \quad (15i)$$

$$w_i \in \{0, 1\} \quad i = 1, 2, \dots, m \quad (15j)$$

$$v_j \in \{0, 1\} \quad j = 1, 2, \dots, n \quad (15k)$$

$$\bar{v}_g \in \{0, 1\} \quad j = 1, 2, \dots, b \quad (15l)$$

When implemented using lazy constraints, the constraints of (15h) are omitted from the initially provided problem, and generated as required during the running of the solver. In addition,  $b$  may be reduced to a value less than the total number of potential crossover points.

The problem of eliminating small angles between members can be stated as:

$$\text{minimize } V = \mathbf{l}^T \mathbf{a} \quad (16a)$$

$$\text{subject to } (\mathbf{B}\mathbf{q}_k = \mathbf{f}_k)_{\forall k} \quad (16b)$$

$$(\sigma_T \mathbf{a} - \mathbf{q}_k \geq 0)_{\forall k} \quad (16c)$$

$$(\sigma_C \mathbf{a} + \mathbf{q}_k \geq 0)_{\forall k} \quad (16d)$$

$$\mathbf{M}\mathbf{w} - \mathbf{a} \geq 0 \quad (16e)$$

$$(w_h + w_i \leq 1)_{\forall \{h,i\} \in D} \quad (16f)$$

$$\mathbf{a} \geq 0 \quad (16g)$$

$$w_i \in \{0, 1\} \quad i = 1, 2, \dots, m \quad (16h)$$

Symbol	Description
$\mathbf{a} = [a_1, a_2, \dots, a_m]$	Vector of member cross sectional areas
$\mathbf{B}$	Matrix of member direction cosines
$b$	Total number of intersections between potential members
$D$	Set containing all pairs of potential members which form an angle of less than $\mu$
$f_k$	Vector of external forces at nodes in loadcase $k$
$g$	Index of a potential 'crossover joint'
$h, i$	Indices of potential members
$j$	Index of ground structure node
$k$	Index of load-case
$\mathbf{l} = [l_1, l_2, \dots, l_m]$	Vector of member lengths
$M, \hat{M}$	Large numbers
$m$	Number of potential members in the ground structure
$n$	Number of nodes in the ground structure
$\mathbf{q}_k$	Vector of member internal forces in loadcase $k$
$\mathbf{v} = [v_1, v_2, \dots, v_n]$	Vector of flags indicating existence of ground structure nodes
$\bar{\mathbf{v}} = [v_1, v_2, \dots, v_b]$	Vector of flags indicating existence of joints at crossovers
$\mathbf{w} = [w_1, w_2, \dots, w_n]$	Vector of flags indicating existence of members
$X$	Set containing all pairs of potential members which intersect
$\sigma_T, \sigma_C$	Allowable stress in tension and compression respectively
$\eta$	Number of joints permitted
$\mu$	Minimum permitted joint angle

Table 6: Symbols used in problem statements.

When implemented using lazy constraints, the problem is initially provided to the solver omitting constraints (16f), which are generated as required during the running of the solver.

## C Derivation of global solutions for simple cantilever problem

### C.1 Minimum volume solution

To provide a global solution for validation, a simple problem is considered. This consists of 2 load-cases denoted as  $\mathbf{P}_1$  and  $\mathbf{P}_2$ . These each contain a single point load, which are both applied at the point with coordinates  $(d, 0)$ , and with the same magnitude,  $Q$ . The two loads are applied orthogonally, and the load in  $\mathbf{P}_1$  is at an angle of  $\theta$  to the horizontal (figure 17a-b), cases where  $0 \leq \theta \leq \frac{\pi}{2}$  will be considered. Two special cases of this, with  $\theta = 0$  and  $\theta = \frac{\pi}{4}$ , were studied by Rozvany et al (2014).

First the component load-cases are calculated, the sum component load-case<sup>2</sup>  $\mathbf{P}_1^* = (\mathbf{P}_2 + \mathbf{P}_1)/\sqrt{2}$  contains a point load of magnitude  $Q$  and inclined at an angle of  $\theta - \frac{\pi}{4}$  (figure 17c). The difference component  $\mathbf{P}_2^* = (\mathbf{P}_2 - \mathbf{P}_1)/\sqrt{2}$  is also of magnitude  $Q$  and inclined at an angle of  $\theta - \frac{3\pi}{4}$  (figure 17d).

The solution for  $\mathbf{P}_1^*$  consists of a single member inclined at the same angle as the force (figure 17e), i.e. connecting to the support at  $y = -d \tan(\theta - \frac{\pi}{4})$ . The member has an internal force of  $-Q$ . The length of the member is  $\frac{d}{\cos(\theta - \frac{\pi}{4})}$ . Therefore the component volume is

$$V_1^* = \frac{Qd}{\sigma \cos(\theta - \frac{\pi}{4})} \quad (17)$$

<sup>2</sup> Note that here we use the component load form of Rozvany and Hill (1978) which allows for generalizations to more than two load cases.

For  $\mathbf{P}_2^*$  the external load is again of magnitude  $Q$  and its direction varies by  $\frac{\pi}{4}$  either side of vertical, the solution to this was given by Rozvany et al (1995). This consists of 2 symmetrical, orthogonal members, which connect to the support at heights  $y = \pm d$  (figure 17f). The length of each member is  $d\sqrt{2}$ . The internal force in the top member is  $Q \sin \theta$  and in the bottom member is  $Q \cos \theta$ . Therefore the volume in this component is

$$V_2^* = \frac{Qd}{\sigma} \sqrt{2} \cos \theta + \sqrt{2} \sin \theta \quad (18)$$

By the superposition principle, these two component solutions are combined to give the optimal design (figure 17g-h). The total volume is given by:

$$V = \frac{V_1^* + V_2^*}{\sqrt{2}} = \frac{Qd}{\sigma} \left( \frac{1}{\sqrt{2} \cos(\theta - \frac{\pi}{4})} + \cos \theta + \sin \theta \right) \quad (19)$$

As there are no co-incident members, the final member areas are given by dividing the component areas by  $\sqrt{2}$ .

### C.2 Limited complexity solution

#### C.2.1 Internal member forces

It is now required to find the minimum volume solution to the same problem, but with the additional constraint that only 3 joints are permitted. This permits only a single topology; two members reaching from the point of application of the forces to the support line. Therefore all potential solutions to this problem can be enumerated using 2 degrees of freedom, the vertical locations of the two support points, which will be denoted  $y_A$  and  $y_B$  (figure 17i-j).

The two component load-cases are identical to the previous section. The lengths of the members are given by  $l_A = \sqrt{y_A^2 + d}$  and  $l_B = \sqrt{y_B^2 + d}$  respectively.

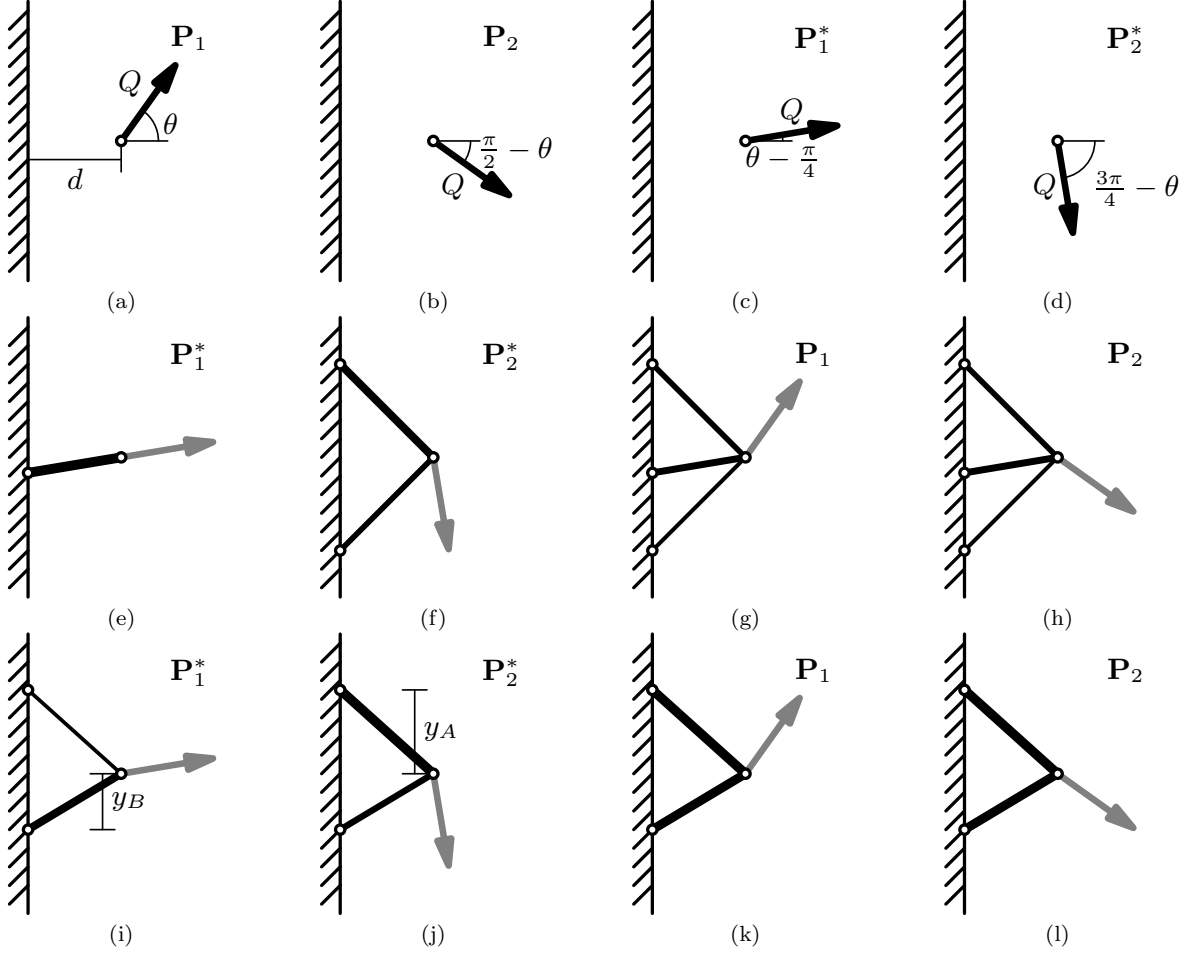


**Fig. 17:** Simple cantilever: problem specification and component load-cases, (a)-(b), imposed load-cases; (c)-(d), component load-cases; (e)-(f) component solutions with unlimited complexity; (g)-(h) final optimal solution with unlimited complexity; (i)-(j) component solutions with only 2 members. (k)-(l) final solution with only 2 members.

The member forces are found from equilibrium equations at the loaded point. In  $\mathbf{P}_1^*$  the member forces in members  $A$  and  $B$  are

$$q_1^A = Q \frac{(\sin(\frac{\pi}{4} + \theta)y_B - \cos(\frac{\pi}{4} + \theta)d)\sqrt{y_A^2 + 1}}{d(y_A - y_B)} \quad (20)$$

$$q_1^B = Q \frac{(-\sin(\frac{\pi}{4} + \theta)y_A + \cos(\frac{\pi}{4} + \theta)d)\sqrt{y_B^2 + 1}}{d(y_A - y_B)} \quad (21)$$

In  $\mathbf{P}_2^*$  the member forces are

$$q_2^A = -Q \frac{(-\cos(\frac{\pi}{4} + \theta)y_B - \sin(\frac{\pi}{4} + \theta)d)\sqrt{y_A^2 + 1}}{d(y_A - y_B)} \quad (22)$$

$$q_2^B = -Q \frac{(\cos(\frac{\pi}{4} + \theta)y_A + \sin(\frac{\pi}{4} + \theta)d)\sqrt{y_B^2 + 1}}{d(y_A - y_B)} \quad (23)$$

The superposition principle is again used to find the overall design (figure 17k-l), and define the total volume as:

$$V = \frac{V_1^* + V_2^*}{\sqrt{2}} = \frac{(|q_1^A l_A| + |q_1^B l_B|) + (|q_2^A l_A| + |q_2^B l_B|)}{\sigma\sqrt{2}} \quad (24)$$

By inspection of the graph for all values of  $0 \leq \theta \leq \frac{\pi}{2}$  (see examples in figure 18), it can be seen that the minimum volume solution falls within or on the border of the region where the member forces in  $\mathbf{P}_1^*$  are in the same direction, and the member forces in  $\mathbf{P}_2^*$  are in opposing directions. Based on this, the expression for  $V$  is re-written without using the absolute value operator, using the sign convention that tensile stresses are negative.

$$V = \frac{-q_1^A l_A - q_1^B l_B - q_2^A l_A + q_2^B l_B}{\sqrt{2}} \quad (25)$$

Additionally the cusps of the plots in figure 18 must be considered, these define the limits of the region within which equation (25) is valid. They are given by:

$$q_1^A \leq 0 \quad q_2^A \leq 0 \quad (26)$$

$$q_1^B \leq 0 \quad q_2^B \geq 0 \quad (27)$$

For a given value of  $\theta$ , these equations each define a vertical plane. Equations (26) are planes with constant  $y_B$ , and equations (27) are planes with constant  $y_A$ .

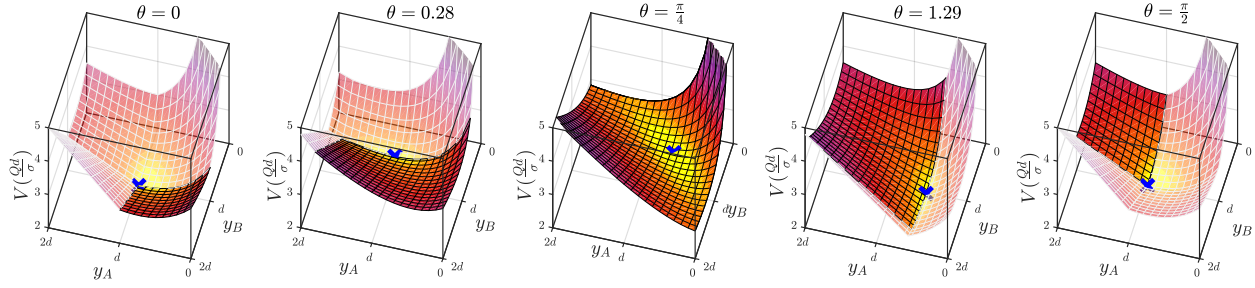


**Fig. 18:** Simple cantilever: volume of two member truss with for  $0 \leq y_A \leq 2d$  and  $0 \leq y_B \leq 2d$  for various force inclinations,  $\theta$ . (The solid region shows where  $q_1^A < 0$ ,  $q_1^B < 0$ ,  $q_2^A < 0$  and  $q_2^B > 0$ , the blue cross shows the globally minimum volume/design to resist each set of forces.)

### C.2.2 Optimal values in each region

The equations which describe the optimal solution vary depending upon the value of  $\theta$ . Three regions are possible, and each of these are considered separately.

When  $\theta > \theta_2$  (where  $\theta_2$  is a critical value, approximately equal to 0.9), the minimal value is found on the cusp of the volume function defined by  $q_1^A = 0$ . The optimal point lies on the minima of the cusp line, i.e. where the partial derivative  $V_{y_A} = 0$ . In this region, the optimal values of  $y_A$  and  $y_B$ , and the optimal volume  $V$  are given by:

$$y_A = \frac{1}{\tan(\frac{\pi}{4} + \theta)} + \frac{\sqrt{2}}{\sin(\frac{\pi}{4} + \theta)} \quad (28a)$$

$$y_B = \frac{-1}{\tan(\frac{\pi}{4} + \theta)} \quad (28b)$$

$$V = \frac{\sqrt{2} \left( \sin(\theta + \frac{\pi}{4}) + 2\sqrt{2} + 3 \cos(\theta + \frac{\pi}{4}) \right)}{2 \sin^2(\theta + \frac{\pi}{4})} \quad (28c)$$

Similarly, for values of  $\theta \leq \theta_1$  (where  $\theta_1 \approx 0.65$ ), the minimal value is found on the intersection of  $V_{y_B} = 0$  and  $q_1^B = 0$ . This gives

$$y_A = \frac{1}{\tan(\frac{\pi}{4} + \theta)} \quad (29a)$$

$$y_B = \frac{-1}{\tan(\frac{\pi}{4} + \theta)} + \frac{\sqrt{2}}{\sin(\frac{\pi}{4} + \theta)} \quad (29b)$$

$$V = \frac{\sqrt{2} \left( \sin(\theta + \frac{\pi}{4}) + 2\sqrt{2} - 3 \cos(\theta + \frac{\pi}{4}) \right)}{2 \sin^2(\theta + \frac{\pi}{4})} \quad (29c)$$

In the inner region, where  $\theta_1 \leq \theta \leq \theta_2$ , the minimum volume structure is found at the local minima of equation (25), i.e. where  $V_{y_A} = 0$  and  $V_{y_B} = 0$ . In this region, values for pairs of  $y_A$  and  $y_B$  are given by the equation:

$$\begin{aligned} 0 = & y_B^4 \\ & - 2y_A^2 y_B^3 + 2y_A y_B^3 \\ & - 2y_A^3 y_B^2 + 4y_A y_B^2 \\ & + 2y_A^3 y_B + 4y_A^2 y_B + 4y_A y_B - 2y_B \\ & + y_A^4 - 2y_A - 2 \end{aligned} \quad (30)$$

To calculate the corresponding value of  $\theta$  for such a pair, the values of  $y_A$  and  $y_B$  are simply substituted into either

$V_{y_A} = 0$  or  $V_{y_B} = 0$ . For this region, it is quite difficult to begin with a value of  $\theta$  and calculate the optimal values of  $y_A$  and  $y_B$ .

### C.2.3 Boundaries between regions

The final task is to establish the boundary values,  $\theta_1$  and  $\theta_2$  between the outer and inner regions. To do this some points of interest must first be defined. The point C is defined as the minimum volume point lying on the cusp  $q_1^A = 0$ , this is the point given by the equations (28), and is the optimal value when  $\theta \geq \theta_2$ .

Next, the stationary points of equation (25) are considered, these lie on the line defined by equation (30). There are at most 2 stationary points in the region in which this function is valid. To characterize these, the discriminant of this function,  $\Delta = V_{y_A y_A} V_{y_B y_B} - (V_{y_A y_B})^2$  is calculated. The stationary point at which  $\Delta > 0$  is defined as point M, this is a local minima, and additionally represents the optimal value in the central region ( $\theta_1 \leq \theta \leq \theta_2$ ). The stationary point where  $\Delta < 0$  is defined as S, this is a saddle point of the function. The critical value  $\theta_2$  is the point at which the optimal value switches from point C to point M.

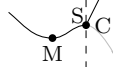
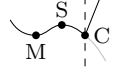
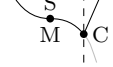
Table 7 gives values of  $y_A$ ,  $y_B$  and  $V$  for these three points at notable values of  $\theta$ . Additionally it provides illustrations of the topography of the volume function in the vicinity of C, M and P; these illustrations show the approximate profile the volume function at the bottom of a 'valley' which runs roughly parallel to the plane  $y_A + y_B = 1$ . This valley may also be observed in the plots in figure 18, particularly when  $\theta = \frac{\pi}{4}$ .

When  $\theta < 0.900110$ , the point S is outside of the valid region for equation (25). Point S enters the valid region when the relations from equations (28a-b) are substituted into equation (30), giving  $\theta = 0.900110$ . Here, points S and C are co-incident and have a volume which is 0.005% greater than the optimal value at M.

At the point where  $V_{y_A} = 0$ ,  $V_{y_B} = 0$  and  $\Delta = 0$  a single degenerate stationary point is formed as points S and M become co-incident. This occurs when  $\theta = 0.900874$ , and the volume at points S and M is 0.0008% higher than the volume at C. Therefore the value  $\theta_2$ , at which points M and C are equally optimal must lie in the region  $0.900110 \leq \theta_2 \leq 0.900874$ .

The value of  $\theta_2$  is found at the point where  $V_{y_A} = 0$ ,  $V_{y_B} = 0$  and the right hand side of equation (28c) is equal to the right hand side of equation (25) (where the values of

**Table 7:** Simple cantilever: behaviour of volume function in vicinity of optimal values for force inclinations in the vicinity of  $\theta_2$ . (Point M is a local minimum, point S is a saddle point, and point C is the minimum value along the cusp at line  $q_1^A = 0$ . Values in boldface are the optimal points for that problem, note that when  $\theta = 0.90068$  two equally optimal solutions exist.)

$\theta$	Point	$y_A$	$y_B$	$V$	
0.90011	C	1.30835	0.11521	2.49230	
	S				
	M	1.19519	0.19318	<b>2.49217</b>	
0.90068	C	1.30786	0.11580	<b>2.49136</b>	
	S	1.27886	0.13492	2.49138	
	M	1.22241	0.17384	<b>2.49136</b>	
0.90087	C	1.037709	0.11599	<b>2.49106</b>	
	S				
	M	1.25026	0.15444	2.49108	

$y_A$  and  $y_B$  refer to the point M). From this it is found that  $\theta_2 = 0.9006836427$ . By a similar logic,  $\theta_1 = 0.6701126839$ .

It has been shown that within the region  $0.900110 \leq \theta \leq 0.900874$ , the range of volumes is small ( $< 0.005\%$ ) over a wide range of possible values for  $y_A$  and  $y_B$  (of up to  $0.1d$ ). This may cause problems for numerical methods if accuracy levels are not set high enough. Additionally, when  $\theta = \theta_1$  or  $\theta_2$ , two distinct solutions are equally optimal.

## Replication of Results

A detailed derivation of the analytical results mentioned in the paper can be found in appendix C.

Details of the results found by the proposed numerical method and shown in figures 11, 12, 14 and 15 are available in the Online Resources.

Implementation of the proposed numerical method was undertaken using the C++ interface of Gurobi

## References

- Aage N, Andreassen E, Lazarov BS, Sigmund O (2017) Gigavoxel computational morphogenesis for structural design. *Nature* 550(7674):84
- Achtziger W (2007) On simultaneous optimization of truss geometry and topology. *Structural and Multidisciplinary Optimization* 33(4-5):285–304
- Achtziger W, Stolpe M (2007) Truss topology optimization with discrete design variables - guaranteed global optimality and benchmark examples. *Structural and Multidisciplinary Optimization* 34(1):1–20
- Ahrari A, Atai AA, Deb K (2015) Simultaneous topology, shape and size optimization of truss structures by fully stressed design based on evolution strategy. *Engineering Optimization* 47(8):1063–1084
- Asadpoure A, Guest JK, Valdevit L (2015) Incorporating fabrication cost into topology optimization of discrete structures and lattices. *Structural and Multidisciplinary Optimization* 51(2):385–396
- Bendsøe MP, Sigmund O (1999) Material interpolation schemes in topology optimization. *Archive of Applied Mechanics* 69(9-10):635–654

- Chan ASL (1960) The design of Michell optimum structures. Tech. rep., College of Aeronautics Cranfield
- Dantzig G, Fulkerson R, Johnson S (1954) Solution of a large-scale traveling-salesman problem. *Journal of the operations research society of America* 2(4):393–410
- Dantzig GB, Wolfe P (1960) Decomposition principle for linear programs. *Operations Research* 8(1):101–111
- Dorn W, Gomory RE, Greenberg HJ (1964) Automatic design of optimal structures. *J de Mecanique* 3:25–52
- Gilbert M, Tyas A (2003) Layout optimization of large-scale pin-jointed frames. *Engineering Computations* 20(8):1044–1064
- Gonçalves MS, Lopez RH, Miguel LFF (2015) Search group algorithm: a new metaheuristic method for the optimization of truss structures. *Computers & Structures* 153:165–184
- Greenwold A, Stander N (1997) Optimal discrete sizing of truss structures subject to buckling constraints. *Structural optimization* 14(2-3):71–80
- Guo X, Zhang W, Zhong W (2014) Doing topology optimization explicitly and geometrically—a new moving morphable components based framework. *Journal of Applied Mechanics* 81(8):081009
- Gurobi Optimization LLC (2018) Gurobi optimizer reference manual. URL <http://www.gurobi.com>
- Haunert JH, Wolff A (2010) Optimal and topologically safe simplification of building footprints. In: *Proceedings of the 18th sigspatial international conference on advances in geographic information systems*, ACM, pp 192–201
- He L, Gilbert M (2015) Rationalization of trusses generated via layout optimization. *Structural and Multidisciplinary Optimization* 52(4):677–694
- Hoang VN, Jang GW (2017) Topology optimization using moving morphable bars for versatile thickness control. *Computer Methods in Applied Mechanics and Engineering* 317:153–173
- Huang XH, Xie Y (2007) Bidirectional evolutionary topology optimization for structures with geometrical and material nonlinearities. *AIAA journal* 45(1):308–313
- IBM Corp (2015) CPLEX User's Manual. URL <https://www.ibm.com/analytics/cplex-optimizer>
- Kanno Y (2013) Topology optimization of tensegrity structures under compliance constraint: a mixed integer linear programming approach. *Optimization and Engineering* 14(1):61–96
- Kanno Y, Fujita S (2018) Alternating direction method of multipliers for truss topology optimization with limited number of nodes: A cardinality-constrained second-order cone programming approach. *Optimization and Engineering* 19(2):327–358
- Kanno Y, Guo X (2010) A mixed integer programming for robust truss topology optimization with stress constraints. *International Journal for Numerical Methods in Engineering* 83(13):1675–1699
- Kelley JE Jr (1960) The cutting-plane method for solving convex programs. *Journal of the Society for Industrial and Applied Mathematics* 8(4):703–712
- Koumoutsis VK, Georgiou PG (1994) Genetic algorithms in discrete optimization of steel truss roofs. *Journal of Computing in Civil Engineering* 8(3):309–325
- Leng G, Duan B (2012) Topology optimization of planar truss structures with continuous element intersection and node stability constraints. *Proceedings of the Institution of Mechanical Engineers, Part C: Journal of Mechanical Engineering Science* 226(7):1821–1831



- Mazurek A, Baker WF, Tort C (2011) Geometrical aspects of optimum truss like structures. *Structural and Multidisciplinary Optimization* 43(2):231–242
- Mela K (2014) Resolving issues with member buckling in truss topology optimization using a mixed variable approach. *Structural and Multidisciplinary Optimization* 50(6):1037–1049
- Michell AGM (1904) The limits of economy of material in frame-structures. *Philosophical Mag* 8(47):589–597
- Mortazavi A, Toğan V (2016) Simultaneous size, shape, and topology optimization of truss structures using integrated particle swarm optimizer. *Structural and Multidisciplinary Optimization* 54(4):715–736
- Nagtegaal J, Prager W (1973) Optimal layout of a truss for alternative loads. *International Journal of Mechanical Sciences* 15(7):583–592
- Ohsaki M (2016) *Optimization of finite dimensional structures*. CRC Press
- Ohsaki M, Katoh N (2005) Topology optimization of trusses with stress and local constraints on nodal stability and member intersection. *Structural and Multidisciplinary Optimization* 29(3):190–197
- Park J, Sutradhar A, Shah JJ, Paulino GH (2018) Design of complex bone internal structure using topology optimization with perimeter control. *Computers in Biology and Medicine* 94:74–84
- Park P (2013) Application of design synthesis technology in architectural practice. PhD thesis, University of Sheffield
- Parkes E (1975) Joints in optimum frameworks. *International Journal of Solids and Structures* 11(9):1017–1022
- Prager W (1977) Optimal layout of cantilever trusses. *Journal of Optimization Theory and Applications* 23(1):111–117
- Prager W (1978) Optimal layout of trusses with finite numbers of joints. *Journal of the Mechanics and Physics of Solids* 26(4):241–250
- Prager W, Shield R (1967) A general theory of optimal plastic design. *Journal of Applied Mechanics* 34(1):184–186
- Rozvany G, Hill R (1978) Optimal plastic design: superposition principles and bounds on the minimum cost. *Computer Methods in Applied Mechanics and Engineering* 13(2):151–173
- Rozvany GI, Sokół T, Pomezanski V (2014) Fundamentals of exact multi-load topology optimization—stress-based least-volume trusses (generalized Michell structures)—Part I: Plastic design. *Structural and Multidisciplinary Optimization* 50(6):1051–1078
- Rozvany GIN, Bendsoe MP, Kirsch U (1995) Layout optimization of structures. *Applied Mechanics Reviews* 48(2):41–119
- Sokół T, Rozvany G (2013) On the adaptive ground structure approach for multi-load truss topology optimization. In: 10th World Congress on Structural and Multidisciplinary Optimization, pp 19–24
- Stolpe M (2010) On some fundamental properties of structural topology optimization problems. *Structural and Multidisciplinary Optimization* 41(5):661–670
- Stolpe M (2016) Truss optimization with discrete design variables: a critical review. *Structural and Multidisciplinary Optimization* 53(2):349–374
- Torii AJ, Lopez RH, Miguel LF (2016) Design complexity control in truss optimization. *Structural and Multidisciplinary Optimization* 54(2):289–299
- Van Mellaert R, Mela K, Tiainen T, Heinisuo M, Lombaert G, Schevenels M (2018) Mixed-integer linear programming approach for global discrete sizing optimization of frame structures. *Structural and Multidisciplinary Optimization* 57(2):579–593
- Villar JR, Vidal P, Fernández MS, Guaita M (2016) Genetic algorithm optimisation of heavy timber trusses with dowel joints according to eurocode 5. *Biosystems Engineering* 144:115–132
- Zhang W, Zhou J, Zhu Y, Guo X (2017) Structural complexity control in topology optimization via moving morphable component (mmc) approach. *Structural and Multidisciplinary Optimization* 56(3):535–552
- Zhou M, Lazarov BS, Wang F, Sigmund O (2015) Minimum length scale in topology optimization by geometric constraints. *Computer Methods in Applied Mechanics and Engineering* 293:266–282